GOETHE UNIVERSITÄT
FRANKFURT AM MAIN

First Principles Studies of Frustrated Spin Systems: From Low-Energy Models to Experiments.

Dissertation
zur Erlangung des Doktorgrades
der Naturwissenschaften

vorgelegt beim Fachbereich Physik
der Johann Wolfgang Goethe-Universität
in Frankfurt am Main

von

Kira Marina Riedl

geboren in Friedberg

Frankfurt am Main, Juli 2019
(D 30)

Vom Fachbereich Physik
der Johann Wolfgang Goethe-Universität
als Dissertation angenommen.

Dekan:
Prof. Dr. Michael Lang

Gutachter:
Prof. Dr. Roser Valentí
Prof. Dr. Peter Kopietz

Datum der Disputation:
23. Januar 2020

Zusammenfassung

Das Feld der kondensierten Materie zeichnet sich durch die Untersuchung von Phänomenen aus, die aufgrund des Zusammenspiels einer makroskopischen Anzahl an Teilchen entstehen. Die wissenschaftliche "Kunst" besteht dabei in der Identifizierung derjenigen Freiheitsgrade, welche eine essentielle Rolle bei der Charakterisierung physikalischer Phänomene im Bereich der experimentell relevanten Energieskalen spielen. Dies ermöglicht die angemessene Beschreibung konkreter Materialien mithilfe von effektiven Modellen, die auf einen relevanten Unterraum des Hilbertraums beschränkt sind.

In dieser Arbeit konzentrierten wir uns auf die Untersuchung von Kristallen, die in erster Linie durch ihre magnetischen Eigenschaften ausgezeichnet sind. In magnetischen Isolatoren sind die Ladungsfreiheitsgrade gefroren, sodass die niederenergetischen Eigenschaften solcher Kristalle mithilfe von effektiven Spinmodellen beschrieben werden können. Solche Modelle können exotische, magnetische Zustände beinhalten, wie beispielsweise den berühmten Quantenspinflüssigkeitszustand, welcher 1973 von Anderson vorgeschlagen wurde. Als Faustregel hat es sich etabliert, Modelle und Materialien mit frustrierten Wechselwirkungen und starken Quantenfluktuationen als vielversprechend einzuordnen. In der Physik zeichnen sich frustrierte Systeme dadurch aus, dass sie konkurrierende Wecheselwirkungen beherbergen, die nicht gleichzeitig befriedigt werden können. Ein Beispiel dafür ist das zweidimensionale anisotrope Dreiecksgitter. Für antiferromagnetische Wechselwirkungen, d.h. die magnetischen Momente optimieren die Gesamtenergie durch eine antiparallele Konfiguration, ist es auf dem Dreiecksgitter nicht möglich, die Energie jeder Bindung durch eine identische globale Spinkonfiguration zu minimieren. Solch eine Situation stellt einen guten Startpunkt in der Suche nach einer Quantenspinflüssigkeit dar, in welcher ausgeprägte, lokale magnetische Momente existieren, aber keine langreichweitige magnetische Ordnung realisiert wird. Es hat sich allerdings herausgestellt, dass eine präzisere Definition dieses Zustands mithilfe seiner Anregungen möglich ist, sodass heutzutage eine Spinflüssigkeit in der Regel anhand von fraktionellen Anregungen identifiziert wird.

Um eine Brücke zwischen experimentellen Beobachtungen und theoretischen Modellen zu schlagen, haben wir in dieser Arbeit zwei komplementäre Strategien verfolgt. Eine Stragie basierte auf *first principles* Methoden, welche die theoretische Vorhersage von elektronischen Eigenschaften echter Materialien allein aufgrund der Kristallstruktur ermöglichen. Basierend auf diesen elektronischen Eigenschaften können magnetische Modelle bestimmt werden, die auf die untersuchten Materialien speziell zugeschnitten sind. Weitere theoretische Modellierung ermöglicht dann den Vergleich mit experimentellen Beobachtungen. Unsere zweite Strategie bestand darin, experimentelle Daten als Ausgangspunkt zu verwenden, gewonnen beispielsweise aus inelastischer Neutronenstreuung (INS), und dann durch Vergleich mit theoretischen Vorhersagen, basierend auf plausiblen magnetischen Parametern, eine geeignetes Modell zu identifizieren. Beide Ansätze erlauben es, theoretische magnetische Modelle mit echten Materialien in Beziehung zu setzen und die Suche nach neuen frustrierten Materialien oder vielversprechenden Theorien anzuleiten.

Diese Arbeit ist folgendermaßen aufgebaut. In Kapitel 1 führen wir die zugrundeliegenden Konzepte ein, welche für die Projekte, die anschließend in Kapitel 2–6 besprochen werden, relevant sind. Als eine der Hauptmotivationen zur Untersuchung frustrierter Spinsysteme, führen wir das Konzept der Quantenspinflüssigkeit ein, insbesondere im Hinblick auf fraktionelle Anregungen als einer ihrer definierenden Eigenschaften. Fraktionelle Anregungen können indirekt in Experimenten beobachtet werden oder als Lösung von bestimmten Spinmodellen erscheinen. Als eine Standardmethode, um solch ein Spinmodell zu erhalten, führen wir das Konzept der Störungstheorie ein, in welcher die kinetische Energie von Elek-

tronen perturbativ behandelt wird. Anschließend besprechen wir das Konzept der Dichtefunktionaltheorie (DFT) als mächtiges Werkzeug um elektronische Eigenschaften von spezifischen Kristallstrukturen zu erhalten. Abschließend stellen wir verschiedene Möglichkeiten vor magnetische Modelle von *first principles* abzuleiten. Unter anderem gehen wir dabei auf die sogenannte Hybridmethode ein, welche in einigen Projekten, die in dieser Arbeit vorgestellt werden, Anwendung fand. In dieser Methode wird DFT auf dem elektronischen Level verwendet und mit exakter Diagonalisierung mit anschließender Projektion auf den niederenergetischen Unterraum kombiniert, um effektive Spinmodelle zu bestimmen.

In Kapitel 2 und Kapitel 3 beschreiben wir dann die magnetischen Eigenschaften von organischen Ladungstransfer-Salzen. In diesen Materialien ist es möglich, die komplizierte Kristallstruktur auf das wohlbekannte anisotrope Dreiecksgitter abzubilden.

Zunächst beschreiben wir in Kapitel 2 die Untersuchung magnetischer Eigenschaften von vier κ-$(ET)_2X$ Salzen. In diesem Fall kann jedes ET-Dimer in der organischen Schicht auf einen magnetischen Gitterplatz abgebildet werden, welcher Spin 1/2 trägt. Die Wahl der anorganischen Schicht, bestimmt durch das Anion X in den κ-$(ET)_2X$ Materialien, ermöglicht es das Verhältnis der magnetischen Austauschparameter zu modifizieren. Dies führt zu der ungewöhnlichen Situation, dass ein ganzes Phasendiagramm für eine bestimmte Geometrie, dem anisotropen Dreiecksgitter, experimentell zugänglich ist. Aufgrund der moderaten Korrelation im Vergleich zur kinetischen Energie, befinden sich die organischen Ladungstransfer-Salze in der Nähe des Mott-Übergangs. Daher ist eine Beschreibung mit rein magnetischen Modellen nur dann sinnvoll, wenn auch Terme höherer Ordnung berücksichtigt werden.

Um ein niederenergetisches, effektives Modell zu erhalten, verwendeten wir die Hybridmethode. In dieser Methode werden Wechselwirkungen von unterschiedlicher Größenordnung gleichberechtigt behandelt. Aus diesem Grund können insbesondere kleinere Austauschparameter, welche von Spin-Bahn-Kopplung stammen, wie die Dzyaloshinksii-Moriya-Wechwelwirkung (DM-Wechselwirkung), oder Spinterme höherer Ordnung, wie der Vierspin-Ringaustausch, vergleichsweise akkurat behandelt werden. Darüber hinaus berücksichtigten wir den Einfluss von externen Magnetfeldern mithilfe der sogenannten Peierlsphase, welche die Hüpfamplituden im Hubbardmodell aufgrund eines Magnetfeldes erhalten. Dies führt dann auf der Ebene der Spinmodelle zu zusätzlichen Termen mit ungerader Anzahl an Spinoperatoren.

Als Repräsentant für den Quadratgitter-Grenzwert des anisotropen Dreiecksgitters diente das magnetisch ordnende κ-$(ET)_2Cu[N(CN)_2]Cl$ (κ-Cl). Konsistent mit den experimentellen Beobachtungen bestimmten wir Verhältnisse der Austauschwechselwirkungen, welche eine magnetische Néel-Ordnung mit einem kleiner Spinneigung aufgrund endlicher DM-Wechselwirkung vorhersagt. Zudem stellten wir zwar einen signifikanten Beitrag des Ringaustauschterms fest, in der Nähe des quadratischen Grenzwerts wird jedoch kein großer Einfluss auf den Grundzustand erwartet. Feldinduzierte, anisotrope Beiträge zum effektiven Spinmodell in Form eines lokalen anisotropen gyromagnetischen Tensors und der skalaren Spinchiralität, welche drei Spinoperatoren beinhaltet, haben wir als endlich berechnet und sollten demnach in zukünftigen Analysen von Experimenten unter Magnetfeldern berücksichtigt werden. Das quasieindimensionale Limit wurde mit κ-$(ET)_2B(CN)_4$ (κ-BCN) abgedeckt, wobei das Verhältnis der dominanten, isotropen Spinaustauschterme mit der experimentell beobachteten reduzierten Dimensionalität übereinstimmte. Für die beiden Spinflüssigkeitskandidaten κ-$(ET)_2Ag_2(CN)_3$ (κ-Ag) and κ-$(ET)_2Cu_2(CN)_3$ (κ-Cu) haben wir Heisenbergwechselwirkungen bestimmt, die näherungsweise isotrop sind. Die berechneten signifikanten Beiträge von Vierspin-Ringaustauschtermen sind ebenfalls konsistent mit der experimentell beobachteten Unterdrückung magnetischer Ordnung. Bekannte Phasendiagramme des anisotropen Dreiecksgitters aus der Literatur haben in diesem Zusammenhang vorhergesagt, dass solche Terme magnetischer Ordnung entgegenwirken, wenn die Heisenbergterme ähnliche Werte aufweisen.

In Kapitel 3 haben wir den Spinflüssigkeitskandidaten κ-Cu darauf aufbauend detaillierter untersucht. Um die Handhabung des Spinmodells zu erleichtern, führten wir eine effektive Beschreibung der anisotropen Wechselwirkungen im Spin-Hamiltonoperator ein. Hierbei orientierten wir uns an wohlbekannten Strategien im Kontext von eindimensionalen Spinketten. In solch einer effektiven Beschreibung werden durch lokale Rotationen der Koordinatensysteme die Effekte der anisotropen Spinwechselwirkungen mithilfe eines effektiven, gitterplatzabhängigen Magnetfeldes beschrieben. Solch eine Behandlung reduziert die anisotropen Effekte auf die Einspin-Terme im magnetischen Modell und

erleichtert somit die Handhabung erheblich.

Anschließend verglichen wir zwei mögliche Szenarios, um das mysteriöse Verhalten der magnetischen Eigenschaften von κ-Cu zu erklären. Das erste Szenario war inspiriert von Experimenten mit externem Magnetfeld in κ-Cu, welche im Rahmen von exotischen, kritischen Exponenten diskutiert wurden. Aus diesem Grund war das erste Szenario, das wir testeten, ein kritisches Szenario mit Magnetfeld als treibenden Parameter, in dem Effekte der anisotropen Terme mithilfe der obigen effektiven Theorie beschrieben werden konnten. Während es durchaus möglich war die Beobachtungen in Myon-Spinrotations-Experimenten (μSR-Experimente) zu erklären, versagte dieses Szenario im Kontext von Messungen des magnetischen Drehmoments von κ-Cu. Wir berücksichtigten dabei eine Vielzahl an möglichen Ordnungsparametern, doch kein kritisches Szenario ermöglichte es, die Kernmerkmale der Experimente zu reproduzieren.

Als Alternative untersuchten wir deshalb ein weiteres Szenario, in welchem κ-Cu als Valenzbindungsglas (VBG) interpretiert wird. In solch einem Zustand führen nichtmagnetische Störstellen zu lokalisierten, magnetischen Momenten, sogenannten Waisenspins, welche die magnetischen Eigenschaften des Systems dominieren. Solch ein VBG-Zustand kann durch Unordnung im Material in Kombination mit einem Einfrieren von fluktuierenden Valenzbindungen einer gewöhnlichen Spinflüssigkeit hervorgerufen werden. Die Unordnung führt dann zur Ausprägung einer Vielzahl von Domänenwänden zwischen verschiedenen Ordnungsmustern der Valenzbindungen, so dass ein glasartiger Zustand eingenommen wird. Solch ein Übergang könnte beispielsweise die Anomalie bei $T_* = 6\,\mathrm{K}$ erklären, welche in κ-Cu in einer Reihe von Experimenten beobachtet wurde und wofür bisher keine befriedigende Erklärung geliefert werden konnte. Das Verhalten des magnetischen Drehmoments konnte jedenfalls in der Tat in diesem Szenario konsistent beschrieben werden.

Darüber hinaus bietet das VBG-Szenario eine mögliche Vereinigung von experimentellen Beobachtungen, die scheinbar widersprüchlich sind. Während in der Messung von thermischer Leitfähigkeit eine Anregungslücke festgestellt wurde, wurden in Messungen von spezifischer Wärme gegenteilige Hinweise beobachtet. Die Anregungslücke ist jedoch ein entscheidender Faktor bei der Klassifizierung von Spinflüssigkeiten. Beide Experimente können im Rahmen des VBG-Szenarios erklärt werden, da lokale Fluktuationen von Domänenwänden niederenergetischen Anregungen entsprechen, die bei der Messung von spezifischer Wärme beobachtbar sind. Da eine Umstrukturierung der Domänenwände infinitesimale Energie benötigt, würde dies in Form einer linearen Temperaturabhängigkeit in der spezifischen Wärme zum Ausdruck kommen, was einem lückenlosen Spektrum entspricht. Auf der anderen Seite können lokale Anregungen nicht zur thermischen Leitfähigkeit beitragen, so dass in diesem Experiment Anzeichen einer Anregungslücke auftreten.

Insgesamt scheint es also möglich zu sein, das magnetische Verhalten von κ-Cu im Rahmen eines Valenzbindungsglas-Szenarios zu interpretieren. Weiterführende Studien, insbesondere in Bezug auf eine Theorie für μSR-Experimente unter Berücksichtigung von Unordnung, sind essentiell, um dieses Szenario weiteren Prüfungen zu unterziehen.

Nach der erfolgreichen Anwendung der Hybridmethode für die organischen Dreiecksgitter-Materialien, verwendeten wir diese zur Bestimmung von bilinearen Spin-1/2-Modellen, inklusive anisotroper Beiträge, für dreidimensionale Pyrochlor-Materialien in Kapitel 4.

In der Hybridmethode wird zunächst das elektronische Hubbardmodell mit Hilfe von *ab-initio* Methoden unter Berücksichtigung der spezifischen Materialeigenschaften bestimmt. Darauf aufbauend wird dann das Energiespektrum für kleine Cluster von Gitterplätzen im elektronischen Modell durch exakte Diagonalisierung berechnet. Die Projektion auf einen angemessenen niederenergetischen Unterraum dieses Spektrums erlaubt dann die Bestimmung eines effektiven magnetischen Modells. Aufgrund der hohen Symmetrie in Pyrochlor-Systemen eignet sich solch eine Geometrie besonders gut, um die Hybridmethode im Zusammenhang mit anisotropen Wechselwirkungen zu testen. Anhand der Regeln von Moriya können Einschränkungen für die mögliche Ausrichtung von anisotropen Wechselwirkungen bereits anhand von Kristallsymmetrien hergeleitet werden. Die Erfüllung dieser Einschränkungen können dann in der numerischen Implementierung der Hybridmethode überprüft werden.

Als Beispielsystem untersuchten wir den Ferromagneten $Lu_2V_2O_7$. In diesem Fall erhielten wir ein magnetisches Modell, welches die anisotrope DM-Wechselwirkung konsistent mit den Regeln von Moriya enthält. Neben der symmetrisch bestimmten Ausrichtung, ermöglichte es die Hybridmethode

aber auch, die materialspezifischen Eigenschaften des Vorzeichens der DM-Wechselwirkung und den Betrag des DM-Vektors, in Abhängigkeit von Modellparametern wie der Hubbard-Abstoßung und der Hund'schen Kopplung, für $Lu_2V_2O_7$ zu bestimmen. Zusätzlich fanden wir einen bedeutenden Beitrag des anisotropen pseudodipolaren Tensors, welcher in vorherigen Studien dieses Materials vernachlässigt wurde. Dennoch sollte diese Studie erweitert werden durch die Berechung von längerreichweitigen, isotropen Wechselwirkungen und der Berücksichtigung von Korrekturen der bilinearen Terme durch Berechnungen auf größeren Clustern. Eine solche Verfeinerung des magnetischen Modells für $Lu_2V_2O_7$ könnte hilfreich sein bei der Erklärung der zugrundeliegenden Mechanismen des Magnon-Hall-Effekts, welcher in $Lu_2V_2O_7$ beobachtet wurde.

Als weiteres Material haben wir das Spin-1/2-Pyrochlor $Lu_2Mo_2O_5N_2$ untersucht, welches als Spinflüssigkeitskandidat vorgeschlagen wurde. Bisher war es nicht möglich für dieses Material Einkristalle zu züchten und die verfügbaren Puderproben leiden vermutlich unter starken Einflüssen von Unordnung. In einer hypothetischen Untersuchung einer Kristallstruktur eines reinen Materials bestimmten wir die bilinearen, anisotropen Wechselwirkungen, welche in einem magnetischen Modell für ein solches System auftreten würden. Damit konnten wir bestätigen, dass eine reine Version von $Lu_2Mo_2O_5N_2$ in einem Bereich des Phasendiagramms einzuordnen wäre, in dem sich laut Rechnungen im Rahmen der Pseudofermion-Funktionalen-Renormierungsgruppe (PFFRG) ebenfalls eine Spinflüssigkeitsphase befindet. Weitere Untersuchungen, und vor allem das Züchten von Einkristallen, sind aus diesem Grund vielversprechend.

Kapitel 5 und Kapitel 6 waren dann der Untersuchung einer anderen Art von Frustration gewidmet, realisiert in dem Kitaev-Material α-$RuCl_3$. Dieses Material kann im Rahmen eines zweidimensionalen Honigwabengitters beschrieben werden, welches nicht geometrisch frustriert ist. Allerdings beinhaltet das Honigwaben-Kitaev-Modell magnetisch frustrierte, bindungsabhängige Kompasswechswelwirkungen, welche unter anderem in α-$RuCl_3$ auftreten.

In Kapitel 5 folgten wir der anfangs erwähnten, zweiten Strategie zur Bestimmung von magnetischen Modellen für konkrete Materialien. Aufgrund des Fehlens eines eindeutigen experimentellen Nachweises, der für alle Spinflüssigkeitstypen gültig ist, ist die Suche nach solch einem exotischen, magnetischen Zustand extrem herausfordernd. Hoffnung wurde geschöpft, als Jackeli und Khalilluin einen Mechanismus vorschlugen, in welchem Übergangsmetalle mit Honigwaben-Gitterstruktur und starker Spin-Bahn-Kopplung als mögliche Kandidaten identifiziert wurden, um eine Kitaev-Wechselwirkung zu realisieren. Diese Beobachtung war insbesondere deswegen aufregend, weil der Grundzustand des exakt lösbaren Honigwaben-Kitaev-Modells einer Majorana-Spinflüssigkeit entspricht. Die Möglichkeit experimentelle Daten unter Berücksichtigung eines exakt gelösten Modells zu interpretieren wirkte zunächst äußerst vielversprechend. Daher war es auch nicht weiter überraschend, dass ein Anregungskontinuum, welches bei Messungen inelastischer Neutronenstreuung (INS) von α-$RuCl_3$ beobachtet wurde, sofort im Sinne von fraktionellen Anregungen in Form von Majorana-Fermionen diskutiert wurde. Es war allerdings bereits aus Experimenten bekannt, dass α-$RuCl_3$ bei tiefen Temperaturen eine langreichweitige, magnetische Ordnung ausprägt und somit kein reines Spinflüssigkeits-Material sein kann. Das Anregungskontinuum wurde dann als Anzeichen von Majorana-Anregungen interpretiert, die aufgrund der Nähe zur reinen Kitaev-Spinflüssigkeit immer noch in α-$RuCl_3$ beobachtbar sind.

Um das Majorana-Fermion-Szenario zu testen haben wir, angeleitet von mikroskopischen Einsichten von vorherigen DFT-Studien, die INS-Intensitäten mithilfe von exakter Diagonalisierung für eine Reihe von magnetischen Modellen berechnet. Dabei fanden wir heraus, dass das ursprünglich vorgeschlagene Nächste-Nachbarn-Heisenberg-Kitaev-Modell unzureichend ist, um die experimentell beobachteten Schlüsselmerkmale ausreichend zu erklären. In qualitativer Übereinstimmung mit den DFT-Vorhersagen für die aktuelle Kristallstruktur, stellten wir fest, dass das vielverprechendste Modell für α-$RuCl_3$ dominante, ferromagnetische Kitaev-Wechselwirkungen beinhaltet, zusätzlich aber auch längerreichweitige, isotrope Heisenberg-Wechselwirkungen und bindungsabhängige, anisotrope, außerdiagonale Wechselwirkungen. Interessanterweise scheinen die beobachteten Merkmale nicht aufgrund der Nähe zur Kitaev-Spinflüssigkeit aufzutreten. Das Anregungskontinuum konnte stattdessen im Rahmen von Magnon-Zerfallsprozessen konsistent erklärt werden. Diese sind in der Gegenwart von bindungsabhängigen, anisotropen Wechselwirkungen erlaubt und verursachen in der Tat ein Anregungskontinuum im INS-Spektrum. Somit kann ein Anregungskontinuum nicht als eindeutiges Merkmal einer Spinflüssigkeit in-

terpretiert werden. Neben der Bestimmung eines vielversprechenden magnetischen Modells für α-$RuCl_3$, konnten wir also auch Anregungskontinua Magnon-Zerfallsprozessen zuordnen, welche in Gegenwart von bindungsabhängigen, anisotropen Wechselwirkungen auftreten können, selbst in der magnetisch geordneten Phase.

In Kapitel 6 stellen wir die Untersuchen eines Regimes vor, in welchem langreichweitige, magnetische Ordnung in α-$RuCl_3$ durch die Effekte eines Magnetfelds unterdrückt werden. Dabei haben wir angenommen, dass das magnetische Modell, welches im vorherigen Kapitel bestimmt wurde, geeignet ist um α-$RuCl_3$ angemessen zu beschreiben. Nachdem wir das Modell um einen anisotropen gyromagnetischen Tensor erweiterten, widmeten wir uns zwei Schlüsselcharakteristika unter Einfluss eines externen Magnetfelds.

Das magnetische Drehmoment τ von α-$RuCl_3$ wies für Feldrotationen aus der Honigwabenebene heraus experimentell eine sägezahnförmige Winkelabhängigkeit auf. Wir identifizierten diese Winkelabhängigkeit als ein charakteristisches Merkmal von Modellen, welche eine magnetische Vorzugsebene besitzen. Diese Eigenschaft besitzt α-$RuCl_3$ aufgrund der Anisotropie im gyromagnetischen Tensor und der bindungsabhängigen, anisotropen, außerdiagonalen Wechselwirkungen. Während diese beiden Terme ähnliche Winkelabhängigkeiten für moderate Magnetfelder aufweisen, sagten wir unterschiedliches Verhalten für hohe Felder voraus. In diesem Fall führt der anisotrope Spinaustauschterm zu einer verschwindenden Dremoment-Magnetisierung τ/H, während sie konstant sein sollte, falls sie allein durch die Gegenwart des gyromagnetischen Tensors hervorgerufen wird.

Im Rahmen der theoretischen Berechnung des magnetischen Drehmoments unter Verwendung des Modells, welches wir im vorherigen Kapitel bestimmten, konnten wir in den ED-Rechnungen nur Hinweise auf einen einzelnen Phasenübergang feststellen. Dies ist insbesondere im Kontext einer exotischen Übergangsphase interessant, welche laut Spekulationen zwischen der magnetisch geordneten und der polarisierten Phase liegen sollte. In diesem Sinne wurden unter anderem auch INS-Daten interpretiert. Die feldinduzierten Verschiebungen von INS-Intensitäten konnten wir allerdings aufgrund der Präsenz der bindungsabhängigen, anisotropen, außerdiagonalen Wechselwirkungen erklären. Diese führen zu der unintuitiven Situation, dass bei niedrigen Feldern die niederenergetischen Anregungen an anderen Stellen im reziproken Raum liegen als die Ordnungswellenvektoren. Für höhere Felder in der Nähe des kritischen Feldes sind sie allerdings identisch, sodass eine Erhöhung des Magnetfelds zwangsweise zu einer Umverteilung der Intensitäten in solchen Systemen führt. INS-Experimente, welche weitere Bereiche in der Brillouin-Zone untersuchen, könnten diese Hypothese bestätigen.

Die theoretische Berechnung von Elektron-Spin-Resonanz-Intensitäten erlaubte dann die Bestimmung von spezifischen Beiträgen zum dynamischen Strukturfaktor am Γ-Punkt und enthüllte Ein- und Multi-Magnon-Charakteristika, welche experimentell beobachteten Moden zugeordnet werden konnten, und damit die Identifizierung einer polarisierten Phase oberhalb des kritischen Feldes bestätigten.

Um zusammenzufassen, die Beobachtungen im Kitaev-Material α-$RuCl_3$ können konsistent im Rahmen von Magnon-Zerfallsprozessen, welche in Gegenwart von anisotropen, bindungsabhängigen, außerdiagonalen Wechselwirkungen erlaubt sind, erklärt werden. Nichtsdestotrotz bleibt es eine offene Frage, ob Majorana-Fermionen oder Magnonen einen größeren Überlapp mit den echten physikalischen Anregungen in α-$RuCl_3$ haben.

Diese Arbeit wird mit einer Zusammenfassung und einem Ausblick in Kapitel 7 abgeschlossen. In der Untersuchung von frustrierten Materialien, welche auf die ein oder andere Art mit dem Zustand der Quantenspinflüssigkeit verwandt sind, müssen allgemein eine Vielzahl an Hürden überwunden werden. Aufgrund des Mangels eines allgemeinen, eindeutigen experimentellen Nachweises für alle Klassen von Spinflüssigkeiten, hat sich die Interpretation der verschiedenen experimentellen Beobachtungen als notorisch schwierig herausgestellt. Die theoretische Handhabung von komplizierten niederenergetischen Modellsystemen steht dem in Sachen Schwierigkeit allerdings nicht nach. Da die Untersuchung einer Spinflüssigkeit naturgemäß mit niedrigen Temperaturen einher geht, sind kleine Wechselwirkungsparameter wie Spin-Bahn-Kopplung nicht *a priori* zu vernachlässigen. Wir haben den signifikanten Einfluss dieser Wechselwirkung in Materialien mit schwacher Spin-Bahn-Kopplung in den organischen Materialien, mit moderater Spin-Bahn-Kopplung in den Pyrochlor-Systemen, und mit starker Spin-Bahn-Kopplung im Kitaev-Material α-$RuCl_3$ untersucht. In allen Fällen hatte Spin-Bahn-Kopplung signifikanten Einfluss und war in den meisten Fällen aufgrund der resultierenden komplizierten Form

der magnetischen Modelle schwierig zu handhaben. Künftige Studien sollten einem besseren intuitiven Umgang mit solch anisotropen Wechselwirkungstermen entgegen streben, sodass typische Merkmale wie Anregungskontinua schnell identifiziert werden können. Darüber hinaus könnte es eine intuitive Handhabung solcher Terme ermöglichen neue Mechanismen zu entdecken, etwa wie die bahnbrechende Arbeit von Kitaev mit seiner exakten Lösung eines Modells, das ohne starke Spin-Bahn-Kopplung gar nicht realisiert werden könnte.

Ein anderer Aspekt, der einen wichtigen Bestandteil dieser Arbeit ausgemacht hat, insbesondere in Hinsicht auf die organischen Materialien, war das Phänomen der Unordnung. In echten Materialien ist es meist schwierig, Unordnung vollständig zu vermeiden. Nichtsdestotrotz arbeitet die Mehrzahl von theoretischen Ansätzen, inklusive der meisten DFT-Studien, unter der Annahme der idealen Situation eines reinen Materials. Ein wichtiges Gegenbeispiel für die allgemeine Berechtigung solcher Annahmen haben wir mit dem Spinflüssigkeitskandidaten κ-Cu betrachtet, in dem die magnetischen Eigenschaften bei niedrigen Temperaturen von Unordnungs-Effekten dominiert zu sein scheinen. Diese Erkenntnis geht mit der etwas entmutigenden Botschaft einher, dass Unordnungs-Effekte wichtiger sein könnten als bisher angenommen. Andererseits beinhaltet es auch die optimistische Botschaft, dass es lohnenswert zu sein scheint, in weitere Entwicklung von Unorndungs-Theorien zu investieren. Solche Theorien können es sicherlich ermöglichen bisher unerklärte physikalische Beobachtungen zu interpretieren und darüberhinaus neue Phänomene im Feld des frustrierten Magnetismus zu entdecken.

Contents

1 Introduction **5**
- 1.1 Quantum Spin Liquids . . . 6
  - 1.1.1 Resonating valence bond state . . . 6
  - 1.1.2 Spinons as fractionalized excitations . . . 7
  - 1.1.3 QSL candidate materials . . . 8
- 1.2 Spin Hamiltonian from perturbation theory . . . 9
  - 1.2.1 Spin-orbit coupling in the electronic Hamiltonian . . . 9
  - 1.2.2 Single-orbital second order perturbation theory . . . 10
- 1.3 Description of real materials: Density functional theory . . . 14
  - 1.3.1 Hohenberg-Kohn theorems . . . 14
  - 1.3.2 Kohn-Sham equations . . . 15
  - 1.3.3 Approximations for the exchange correlation functional . . . 15
- 1.4 Low-energy spin models for real materials . . . 16
  - 1.4.1 Total energy calculations . . . 16
  - 1.4.2 "Hybrid" methods: Hubbard Hamiltonian from first principles . . . 16
- 1.5 Outline of this thesis . . . 18

2 Magnetic interactions in triangular lattice organics **21**
- 2.1 Introduction . . . 21
- 2.2 Extended Hubbard Hamiltonian for the κ-$(ET)_2X$ family . . . 22
- 2.3 Main experimental observations in triangular organics . . . 25
  - 2.3.1 Canted Néel order: κ-Cl . . . 25
  - 2.3.2 Quasi one-dimensionality: κ-BCN . . . 26
  - 2.3.3 QSL candidates: κ-Cu and κ-Ag . . . 26
- 2.4 Review of phases on the anisotropic triangular lattice . . . 27
- 2.5 Effective spin Hamiltonian for triangular lattice organics . . . 30
  - 2.5.1 Higher order perturbation theory . . . 30
  - 2.5.2 Linked cluster expansion . . . 34
  - 2.5.3 Bilinear spin Hamiltonian . . . 35
  - 2.5.4 Higher order spin terms . . . 37
- 2.6 Summary . . . 40

3 Criticality vs. Valence Bond Glass scenario in κ-Cu **41**
- 3.1 Introduction . . . 41
- 3.2 Criticality and observed unconventional exponents . . . 42
  - 3.2.1 The concept of quantum criticality . . . 42
  - 3.2.2 Proposed critical exponents for κ-Cu . . . 43
- 3.3 Coupling to a magnetic field for κ-$(ET)_2X$ materials . . . 44
  - 3.3.1 Anisotropic interactions in a magnetic field . . . 44
  - 3.3.2 Symmetry restrictions on magnetic field coupling in κ-$(ET)_2X$ . . . 48
- 3.4 Critical scenario in κ-Cu? . . . 50
  - 3.4.1 Theoretical magnetization expressions including SOC . . . 50

3.4.2 Fit of μSR linewidth including SOC . . . 52
3.4.3 Theoretical magnetic torque expressions . . . 53
3.4.4 Theoretical magnetic torque in κ-Cu . . . 57
3.5 κ-Cu as a Valence Bond Glass . . . 59
3.5.1 Orphan spins in κ-Cu . . . 59
3.5.2 Theoretical local moment torque expressions . . . 60
3.5.3 Total torque response of κ-Cu . . . 62
3.5.4 Outlook: Interacting orphan spins . . . 62
3.6 Summary . . . 63

4 Anisotropic magnetic interactions in the pyrochlore lattice 65
4.1 Introduction . . . 65
4.2 Magnetic exchange parameters in pyrochlores . . . 66
4.2.1 The pyrochlore lattice . . . 67
4.2.2 Moriya's rules: Symmetry constraints in the pyrochlore lattice . . . 67
4.2.3 Pyrochlore spin Hamiltonian representations in the literature . . . 69
4.3 Extended Hubbard Hamiltonian for d block electrons . . . 71
4.3.1 Hopping parameters from *ab-initio* calculations . . . 71
4.3.2 Two-particle interaction term . . . 72
4.3.3 Spin-orbit coupling term . . . 74
4.4 The pyrochlore ferromagnet $Lu_2V_2O_7$ . . . 75
4.4.1 *Ab-initio* determination of hopping and spin-orbit parameters . . . 77
4.4.2 Importance of Hund's coupling and all five d orbitals . . . 79
4.4.3 Projection onto low-energy subspace . . . 80
4.4.4 Effective Spin Hamiltonian for $Lu_2V_2O_7$ . . . 83
4.4.5 Discussion of $Lu_2V_2O_7$ spin Hamiltonian . . . 87
4.5 The pyrochlore gearwheel QSL candidate $Lu_2Mo_2O_5N_2$ . . . 88
4.5.1 Theoretical modelling of O/N occupation . . . 89
4.5.2 *Ab-initio* determination of hopping and spin-orbit parameters . . . 90
4.5.3 Effective Anisotropic Spin Hamiltonian for $Lu_2Mo_2O_5N_2$ . . . 91
4.5.4 Discussion of $Lu_2Mo_2O_5N_2$ spin Hamiltonian . . . 93
4.6 Discussion . . . 94

5 Magnetic excitations in the honeycomb Kitaev material α-$RuCl_3$ 95
5.1 Introduction . . . 95
5.2 The honeycomb Kitaev model . . . 96
5.2.1 Exact solution of the honeycomb Kitaev model . . . 96
5.2.2 Kitaev interaction in real materials . . . 99
5.3 Extended honeycomb Kitaev model for α-$RuCl_3$ . . . 103
5.3.1 Spin Hamiltonian representations for Kitaev materials . . . 103
5.3.2 *Ab-initio* studies of α-$RuCl_3$ . . . 104
5.3.3 Phase diagram of the minimal model for α-$RuCl_3$ . . . 106
5.4 Key experimental observations for α-$RuCl_3$ . . . 107
5.5 Dynamical correlation functions from exact diagonalization . . . 109
5.5.1 Lanczos method . . . 109
5.5.2 Correlation functions in the Lanczos subspace . . . 112
5.5.3 Correspondence to INS intensity . . . 114
5.6 Magnetic excitations in α-$RuCl_3$ . . . 116
5.6.1 Details of Exact Diagonalization Calculations . . . 117
5.6.2 Nearest neighbour Heisenberg-Kitaev (nnHK) models . . . 119
5.6.3 Extended AFM Kitaev models . . . 120
5.6.4 Extended FM Kitaev models . . . 122
5.6.5 Magnon stability beyond LSWT . . . 126
5.7 Discussion . . . 129

6 Beyond order: α-$RuCl_3$ under magnetic field **131**
6.1 Introduction . . . 131
6.2 Extended model under magnetic field . . . 132
6.3 Magnetic torque in α-$RuCl_3$ . . . 134
6.3.1 Anisotropic field-dependent phase diagram for α-$RuCl_3$ . . . 135
6.3.2 Torque and Magnetotropic Coefficient of α-$RuCl_3$ . . . 137
6.3.3 Magnetic torque in limiting models . . . 139
6.3.4 Summary . . . 141
6.4 Magnetic excitations in α-$RuCl_3$ under magnetic field . . . 141
6.4.1 AFM zigzag domains and influence of in-plane field directions . . . 142
6.4.2 Magnetic excitations in the Brillouin zone . . . 143
6.4.3 Dissection of the Γ-point continuum . . . 145
6.4.4 Summary . . . 146
6.5 Discussion . . . 147

7 Summary and Outlook **149**

A Useful relations **153**
A.1 Useful relations of spinor operators . . . 153
A.2 Isotropy of spin contribution in scalar spin chirality . . . 153
A.3 Permutation operator and ring exchange . . . 154

B Anisotropy in pyrochlores **155**
B.1 DM orientations in the pyrochlore lattice . . . 155
B.2 Pseudo-dipolar tensor in the pyrochlore lattice . . . 156

C Hopping on the honeycomb lattice **159**
C.1 Tight binding model on the honeycomb lattice . . . 159
C.2 Symmetrically allowed hopping terms in Kitaev materials . . . 160

References **163**

Chapter 1

Introduction

In the field of condensed matter physics, phenomena are studied, which are generated by a macroscopic number of particles and, specifically, their interplay. Anderson formulated this picture explicitly in his article *"More is different"* [1]. The scientific "art" is then to identify the degrees of freedom that are crucial to capture the physics at the experimentally relevant energy scales. Materials can then be described theoretically with effective models that live in a low-energy subspace of the full Hilbert space.

In this thesis, we investigate phenomena that are observable in crystals dominated by their magnetic properties. For magnetic insulators with frozen charge degrees of freedom, the low-energy properties of such crystals can be described in terms of effective spin models. These models may host exotic magnetic states, such as the famous quantum spin-liquid (QSL) state, proposed by Anderson in 1973 [2]. As a rule of thumb, frustration and strong quantum fluctuations have been established as promising ingredients to find such a state in models or materials [3].

To create the connection between exotic model theories and real materials, a powerful method is density functional theory (DFT). This method requires solely the crystal structure of the investigated compound as input from experiment. Therefore, the physical properties deduced from DFT are also referred to as models determined from first principles. From this starting point, it is possible to extract electronic models that capture the low-energy properties of the investigated compounds. However, in this thesis the materials of interest are described by spin models, so that additional steps are necessary to build the low-energy models. A well-established method often allowing for analytical expressions is perturbation theory. We will take advantage of this method to gain intuition what to expect from more accurate approximations such as exact diagonalization (ED). With the option to find the connection between models and experiments, it is also possible to go the other way and refine from experimental insights, such as inelastic neutron scattering (INS) measurements, the spin models under consideration.

The materials investigated in this thesis are frustrated magnets, in which the influence of spin-orbit coupling (SOC) plays an important role. Through this interaction, the magnetic and spatial degrees of freedom talk to each other, which manifests through the presence of anisotropic contributions in the effective spin models. The geometries of the systems discussed in this thesis are shown in Fig. 1.1, which represent various realizations of frustration. In physics, frustrated systems are those, in which competing forces cannot be satisfied simultaneously [4, 5]. In Fig. 1.1(a) is the two-dimensional anisotropic triangular lattice illustrated. In general, a triangular motif in the lattice geometry is a promising indicator for magnetic frustration. For antiferromagnetic interactions, i.e. the magnetic moments optimize the total energy for antiparallel arrangements, it is not possible to minimize the energy of each bond within a single global spin configuration. As a result, the relative strength of quantum fluctuations is enhanced. This situation is a good starting point in the search for a quantum spin liquid state, where well-formed local magnetic moments lack long-range magnetic order. Such a state is illustrated in the figure by the disordered orientations of the spins. In Fig. 1.1(b), we show the so-called pyrochlore lattice. It contains, in form of corner-sharing tetrahedra, a three-dimensional version of the triangular motif and is hence geometrically frustrated as well. The higher dimensionality hampers, however, the dominance of the quantum fluctuations in many cases in real materials [5]. A different source for frustration is shown in Fig. 1.1(c), with the two-dimensional honeycomb lattice. This

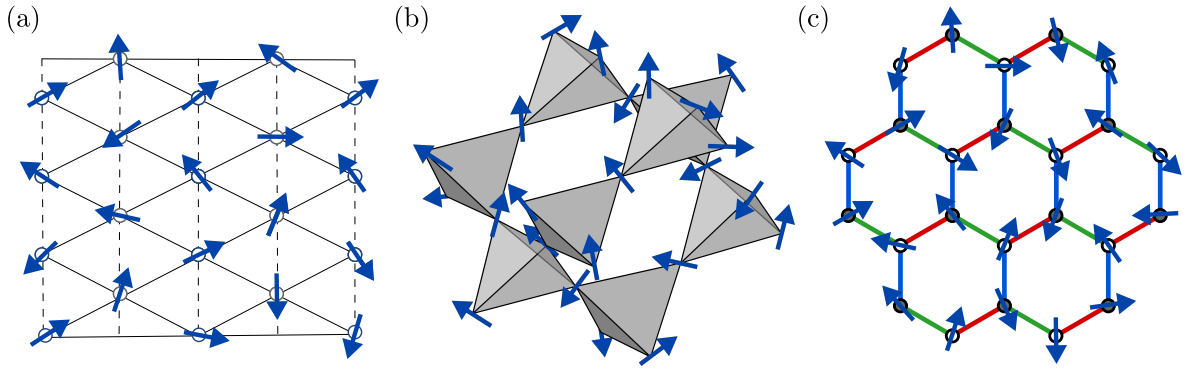

Figure 1.1: Examples for frustrated spin systems, studied in this thesis. (a) Two-dimensional anisotropic triangular lattice, (b) three-dimensional pyrochlore lattice of corner-sharing tetrahedra, (c) two-dimensional honeycomb lattice with frustration due to magnetic compass interactions.

lattice is not geometrically frustrated in the sense that it is indeed possible to realize an antiparallel arrangement of spins on all bonds in a consistent configuration. However, magnetic frustration is achieved for bond-dependent anisotropic interactions, indicated by the differently coloured bonds. For bond-dependent Ising interactions, the famous honeycomb Kitaev model [6] is realized, which is exactly solvable with a quantum spin liquid ground state.

1.1 Quantum Spin Liquids

The topic of quantum spin liquids has been the subject of a number of books, reviews and lecture notes [3, 5, 7–9]. Here, we briefly introduce the concept and main ideas.

Spin liquids are members of the family of Mott insulators, where the electrons of the crystal are localized, but, in contrast to band insulators, maintain their spin degree of freedom. Conventionally, materials with magnetic moments are driven into a magnetically ordered state upon cooling below the Néel temperature T_N. At the lowest temperature $T = 0\,\mathrm{K}$, all typical magnetic materials are expected to have a magnetically ordered ground state, assuming disorder effects are not dominant. In 1973, Anderson [2] proposed a mechanism, in which specific magnetic systems exhibit quantum fluctuations so strong that they persist until $T = 0\,\mathrm{K}$ and prevent the system to magnetically order. Inspired by the analogy to a classical liquid phase, where molecules are highly correlated without static order, Anderson's scenario was referred to as "quantum spin liquid" model. If the spin fluctuations are thermally driven, the system is classified as a classical spin liquid [3]. A famous example is the spin ice, where the spins are frozen at $T = 0$ in the 2-in-2-out rule, in analogy to the conventional water ice [3, 5]. In the following, we will restrict the explanations to the quantum case with spin 1/2.

1.1.1 Resonating valence bond state

The proposed mechanism [2, 10] is based on the idea that it may be energetically favourable for two spins to build, with a partner, a spin singlet state $|\mathrm{VB}\rangle = \frac{1}{\sqrt{2}}(|\uparrow\downarrow\rangle - |\downarrow\uparrow\rangle)$, the so-called "valence bond". By construction, the magnetization of such a valence bond vanishes, $\sum_i \langle \mathbf{S}_i \rangle = 0$, in spite of well-defined moments on each site, fulfilling the criterion for a QSL. If building valence bonds is energetically preferred for all sites in the lattice, there are two possible realizations for the ground state nature, shown in Fig. 1.2. It may be possible that a specific order of valence bonds optimizes the total energy, illustrated in Fig. 1.2(a), so that the system is a valence bond solid (VBS). Such a state has no net magnetization, but it breaks the lattice symmetries since the valence bond configuration is usually not unique. The second class of states hosting valence bonds is illustrated in Fig. 1.2(b). Such a resonating valence bond (RVB) state conserves the symmetry of the system and has no net magnetization down to $T = 0\,\mathrm{K}$. In this case, the valence bonds are not ordered in a specific pattern, but are fluctuating,

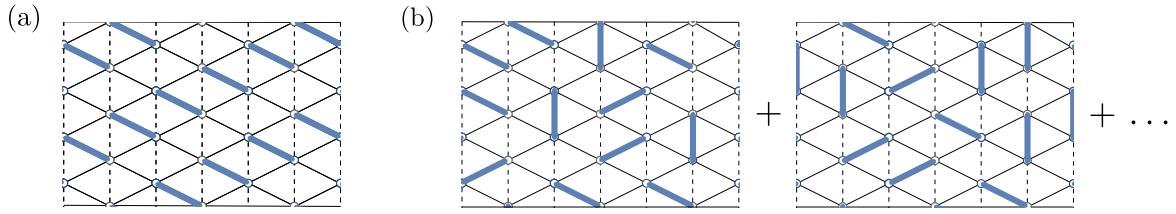

Figure 1.2: Valence bond states on the anisotropic triangular lattice, singlet bonds $\frac{1}{\sqrt{2}}(|\uparrow\downarrow\rangle - |\downarrow\uparrow\rangle)$ are indicated in blue. (a) Valence bond solid (VBS) state, (b) Short-ranged resonating valence bond (RVB) state.

where a snapshot would correspond to a random arrangement throughout the lattice. The RVB state is a coherent quantum superposition of an exponential number of valence bond configurations. Due to the large number of possible arrangements, the state of linear combinations preserves the lattice symmetry and meets the above mentioned analogy as a valence-bond "liquid". Due to the exponential number of possible superpositions, the number of RVB states is vast. Note, that we illustrate in Fig. (b) a short-ranged RVB state. In principle, there is no reason why a valence bond should be built only between nearest neighbour magnetic sites. If the state is a superposition including valence bonds between further neighbours, it is referred to as a long-range RVB state. Such long-range valence bonds are more weakly bound. One important consequence is that, in principle, a gapless energy spectrum of the system is possible, since an infinitesimally small amount of energy is sufficient to break such a valence bond, i.e. excite the RVB state. In contrast, in the case of the depicted short-range RVB, where a valence bond is bound much stronger, the energy spectrum is expected to be gapped.

1.1.2 Spinons as fractionalized excitations

Spin liquids, such as the RVB state, are often expected to display unconventional magnetic excitations. In conventional condensed matter systems, excitations can be either described by electrons, with spin 1/2 and a charge e or, in the case of ordered magnetic systems, the excitations may be magnons. Magnons are excitations of spin systems with $S = 1$ and neutral charge.

As an example case for systems deviating from these conventional systems, we consider a one-dimensional chain of spins that are coupled via the isotropic Heisenberg interaction $\mathcal{H} = J\sum_{\langle ij\rangle} \mathbf{S}_i \cdot \mathbf{S}_j$. According to the Mermin-Wagner theorem, there is no magnetic order possible in this case. This theorem states that for short-range spin models in one- and two-dimensional systems with continuous symmetries, there cannot be spontaneous ordering at finite temperature. However, for discrete symmetries like e.g. the two-dimensional Ising model, symmetries can be spontaneously broken, even for $T = 0$. In one-dimensional systems in general, elementary excitations are so-called spinons. Spinons are quasiparticles that carry $S = 1/2$, like electrons, but are charge neutral. In a one-dimensional spin chain it corresponds to half of a $\Delta S = \pm 1$ excitation in form of a spin flip. Two spinons are generated by such a flip and can then propagate in the chain over large distances. Due to this independent movement, they can be seen as independent, elementary quasiparticles.

In principle, these quasiparticles could also be observable in higher dimensions, $d > 1$. In a RVB state, two spinons would be created by breaking a valence bond. In valence bond solids, the spin singlets are ordered. Therefore, the spinons created by breaking a valence bond cannot travel through the lattice and act as independent elementary excitations. In contrast, in a RVB state, the exponential number of valence-bond configurations results in a spatially uniform state. Rearranging the valence bond pattern would project onto a valence bond configuration already contained in the superposition of the RVB state. In this case, the spinons can travel through the lattice and are deconfined down to $T = 0$. This offers a more precise definition of a quantum spin-liquid state, with respect to the nature of its quasiparticles. In this framework, a quantum spin liquid is defined by the fact that it sustains *fractional* spin 1/2 excitations, also in two and three dimensions.

In order to treat these fractional excitations theoretically, a very successful "trick" is the decompo-

sition of the spin operators in terms of neutral spin 1/2 quasi-particles. The challenge in solving such a problem is then to choose for the decomposition the appropriate quasiparticle basis for each investigated system. On the mean-field level, the introduced quasiparticles are treated as free particles. Beyond this approximation, they interact via gauge fluctuations, so that the nature of a QSL state can be classified through its quasiparticles and the corresponding gauge field [11].

1.1.3 QSL candidate materials

In the case of real materials, the final determination for the presence of a QSL state has proven to be notoriously difficult. The main problem is the absence of a "smoking gun" experiment to identify a quantum spin liquid material directly, independent of its classification. Features according to the definition of the absence of magnetic order, down to the experimentally inaccessible temperature $T = 0$, or the more precise definition in terms of fractionalized excitations that can only be created in pairs in experiment, are only indirectly identifiable. So far, the most successful strategy was to combine the complementary approaches of indirect experimental evidence with appropriate theoretical models with a QSL ground state.

One of the most prominent QSL candidate materials is Herbertsmithite, $ZnCu_3(OH)_6Cl_2$. It is a spin 1/2 material, where the magnetic sites form layers of a nearly perfect Kagome lattice [12, 13]. This lattice consists of corner-sharing triangles, revealing the typical triangular motif for QSL candidate geometries mentioned above. Theoretically, a nearest neighbour Heisenberg spin model on such a lattice has been discussed in terms of a quantum spin liquid [14–19]. In Herbertsmithite, no magnetic order was observed for temperatures down to $T \approx 50\,\mathrm{mK}$ [20] and signatures of fractionalized excitations have been reported in the context of inelastic neutron scattering measurements [21, 22].

Another geometry, with several QSL candidate materials, is the anisotropic triangular lattice. In this geometry, the interaction along one bond direction, J', differs from the other two directions, J, as illustrated by the dashed and solid lines in Fig. 1.1(a). Theoretically, QSL states have been discussed for specific ratios J/J' and additional four-spin ring exchange terms [23–26]. An initially much discussed spin 1/2 QSL candidate was the compound Cs_2CuCl_4, where inelastic neutron scattering experiments showed signatures of fractionalized excitations [27]. However, the observations turned out to belong to a framework of dimensional reduction [28–30], where spinon signatures stem from descendents of the one-dimensional excitations in individual chains. The observed dispersion transverse to the chain can be explained in this framework through so-called triplon excitations that represent a bound state of a pair of spinons that may hop between the chains. Another class of spin-liquid candidates on the anisotropic triangular lattice are the organic charge transfer salts with the most prominent examples $EtMe_3Sb[Pd(dmit)_2]_2$ and κ-$(ET)_2Cu_2(CN)_3$ (κ-Cu) [8, 31, 32]. For the dmit compound, NMR experiments showed no signatures of magnetic ordering down to $T = 20\,\mathrm{mK}$ [33], and evidence for gapless excitations were found consistently in thermal transport [34] and specific heat experiments [35]. NMR studies for κ-Cu showed also no signatures of magnetic order at low temperatures [32, 36]. Specific heat experiments reported signatures of a gapless QSL nature [37], while thermal transport was interpreted in terms of a gapped system [38]. All of these experiments reported the emergence of a mysterious anomaly at $T_* = 6\,\mathrm{K}$. We will revisit this compound in detail within this thesis. Recently, much attention has been drawn to the anisotropic triangular lattice material $YbMgGaO_4$, where inelastic neutron scattering experiments showed signatures of fractionalized excitations as well [39, 40]. However, theoretical studies interpreted the experimental evidence in terms of disorder effects as a QSL mimicry rather successfully [41, 42].

On the two-dimensional honeycomb lattice, illustrated in Fig. 1.1(c), to date all Kitaev materials such as α-$RuCl_3$, Na_2IrO_3, or α-Li_2IrO_3, have revealed magnetic order at low temperatures [43–46]. Nevertheless, for the material α-$RuCl_3$, there was recently much discussion in terms of an induced QSL state under magnetic field due to signatures in inelastic neutron scattering [47] and thermal transport experiments [48]. The question whether a field-induced QSL state is the only possible interpretation of the magnetic response of α-$RuCl_3$ under magnetic field is one of the topics discussed in this thesis.

1.2 Spin Hamiltonian from perturbation theory

With the QSL state, we introduced an exotic magnetic state that may be the ground state of specific spin Hamiltonians. In order to gain intuition about the origin and importance of the parameters involved in general spin Hamiltonians, we present in this section the derivation within second order perturbation theory. Since all the materials investigated in this thesis are subject to spin-orbit coupling, we consider in particular these effects.

There are several methods to construct an effective spin Hamiltonian from electronic models for Mott insulators. We will revisit better approximations for real materials in Section 1.4. For perturbation theory, the starting point is in general the Hubbard Hamiltonian, $\mathcal{H} = \mathcal{H}_{\text{hop}} + \mathcal{H}_{\text{int}}$, with electronic creation and annihilation operators $d^\dagger$ and d, respectively:

$$\mathcal{H} = -\sum_{ij}\sum_{\alpha\beta}\sum_{\sigma} t_{i\alpha,j\beta} d^\dagger_{i\alpha\sigma} d_{j\beta\sigma} + \sum_{ijkl}\sum_{\alpha\beta\alpha'\beta'}\sum_{\sigma\sigma'} U^{ijkl}_{\alpha\beta\alpha'\beta'} d^\dagger_{i\alpha\sigma} d^\dagger_{j\beta\sigma'} d_{l\beta'\sigma'} d_{k\alpha'\sigma}, \tag{1.1}$$

where $\{i,j,k,l\}$ are magnetic site indices, $\{\alpha,\beta,\alpha',\beta'\}$ orbital indices, and $\{\sigma,\sigma'\}$ spin indices. The kinetic energy of the electrons is given by the hopping parameters $t_{i\alpha,j\beta}$ and two-particle interaction, such as e.g. Coulomb repulsion, is represented by the parameters $U^{ijkl}_{\alpha\beta\alpha'\beta'}$. Note, that in Eq. (1.1) spin-orbit coupling effects are not incorporated yet. Since there are several options to include SOC on the electronic level, we will discuss this issue in more detail.

1.2.1 Spin-orbit coupling in the electronic Hamiltonian

In general, spin-orbit coupling can be captured in second quantization by the following expression[1]:

$$\mathcal{H}_{\text{SOC}} = \lambda \sum_{i}\sum_{\alpha\beta}\sum_{\sigma\sigma'} \langle i\alpha\sigma|\mathbf{L}\cdot\mathbf{S}|i\beta\sigma'\rangle d^\dagger_{i\alpha\sigma} d_{i\beta\sigma'} + \text{h.c.}, \tag{1.2}$$

where $\mathbf{L}$ is the angular momentum operator, $\mathbf{S}$ the spin operator, and λ the strength of spin-orbit coupling.

A possible strategy to obtain SOC effects in the effective spin Hamiltonian was presented by Moriya in the 60s [49], where he separated the perturbation theory into two steps. First, Moriya considered the single-ion Hamiltonian $\mathcal{H}_i$ without a hopping term $\mathcal{H}_{\text{hop}}$, and calculated the energy correction and basis wave functions in first order in the SOC strength λ. The full Hamiltonian in terms of those basis wave functions consists then of spin-dependent hopping terms. In the second step, Moriya computed the second order energy correction with the hopping parameters as the small parameter. This strategy can be useful for systems with small spin-orbit coupling, i.e. $U \gg \lambda$, and where analytical expressions of the SOC matrix elements $\langle i\alpha\sigma|\mathbf{L}\cdot\mathbf{S}|i\beta\sigma'\rangle$ are unknown or difficult to determine.

In cases where the SOC matrix elements are known analytically, a higher accuracy can be achieved by treating spin-orbit coupling exact and not as a perturbation. Instead, the full Hamiltonian can be transformed into the eigenbasis of the single-site Hamiltonian. This strategy was proposed by Yildrim *et al.* [50] in the context of d orbitals. The resulting Hamiltonian contains then, like it was the case with Moriya's ansatz, a spin-dependent hopping term. The important difference is that in this case λ is treated up to infinite order.

To obtain a spin-dependent hopping term we follow Ref. [50] and start with the single-site, single-particle Hamiltonian, including spin-orbit coupling:

$$\mathcal{H}_i = \sum_{\alpha\sigma} \varepsilon_\alpha d^\dagger_{\alpha\sigma} d_{\alpha\sigma} + \lambda \sum_{\sigma\sigma'}\sum_{\alpha\beta} \langle \alpha\,\sigma|\mathbf{L}\cdot\mathbf{S}|\beta\,\sigma'\rangle\, d^\dagger_{\alpha\sigma} d_{\beta\sigma'}. \tag{1.3}$$

Here, ε_α is the on-site energy for orbital α. Diagonalization of this Hamiltonian requires a unitary basis transformation $d \to c$ in terms of some matrix $\mathbb{U}$ consisting of the eigenstates of $\mathcal{H}_i$:

$$\mathcal{H}_i = \sum_{as} E_a c^\dagger_{as} c_{as} \qquad \text{with} \qquad E_a = (\mathbb{U}_{\beta\alpha,\sigma'\sigma})^* \big(\varepsilon_\alpha + \lambda\langle\alpha\,\sigma|\mathbf{L}\cdot\mathbf{S}|\beta\,\sigma'\rangle\big)\mathbb{U}_{\alpha\beta,\sigma\sigma'}, \tag{1.4}$$

[1] We will use the convention $\hbar = 1$ throughout this thesis.

where we introduced a as a pseudo-orbital and s as a pseudo-spin in the eigenbasis of $\mathcal{H}_i$. The single-particle Hamiltonian $\mathcal{H}_{1\mathrm{p}}$ includes then, next to $\mathcal{H}_i$, the hopping contribution $\mathcal{H}_{\mathrm{hop}}$ between different sites $i \neq j$:

$$\mathcal{H}_{1\mathrm{p}} = \sum_i \mathcal{H}_i - \sum_{i\neq j} \sum_{\alpha\beta} \sum_{\sigma} \left[t_{i\alpha\sigma,j\beta\sigma}\, d^\dagger_{i\alpha\sigma} d_{j\beta\sigma} + \mathrm{H.c.} \right]. \tag{1.5}$$

In the eigenbasis of $\mathcal{H}_i$ the single-particle Hamiltonian gathers an effective spin-dependent hopping part simply due to the fact that the two-site contribution $\mathcal{H}_{\mathrm{hop}}$ is diagonal with respect to the spin $\{\sigma, \sigma'\}$, but not with respect to the pseudo-spin $\{r, s\}$:

$$\mathcal{H}_{1\mathrm{p}} = \sum_i \sum_{as} E_{ia} c^\dagger_{ias} c_{ias} - \sum_{i\neq j} \sum_{ab} \sum_{rs} \tilde{t}_{iar,jbs} \left[c^\dagger_{ias} c_{jbr} + \mathrm{H.c.} \right]. \tag{1.6}$$

In the spin 1/2 case, it is convenient to work with a (pseudo-)spinor representation of the ladder operators:

$$\underline{c}_{ia} = \begin{pmatrix} c_{ia\uparrow} \\ c_{ia\downarrow} \end{pmatrix} \qquad \text{and} \qquad \tilde{\mathbb{T}}_{ia,jb} = \begin{pmatrix} \tilde{t}_{ia\uparrow,jb\uparrow} & \tilde{t}_{ia\uparrow,jb\downarrow} \\ \tilde{t}_{ia\downarrow,jb\uparrow} & \tilde{t}_{ia\downarrow,jb\downarrow} \end{pmatrix}, \tag{1.7}$$

which leads to the following single-particle Hamiltonian in spinor representation:

$$\mathcal{H}_{1\mathrm{p}} = \sum_i \sum_a E_{ia} \underline{c}^\dagger_{ia} \underline{c}_{ia} - \sum_{i\neq j} \sum_{ab} \left[\underline{c}^\dagger_{ia} \tilde{\mathbb{T}}_{ia,jb}\, \underline{c}_{jb} + \mathrm{H.c.} \right]. \tag{1.8}$$

The hopping matrix in the eigenbasis of $\mathcal{H}_i$ can be calculated with the unitary transformation on the different sites i and j, which differ from each other in case of site-dependent local coordinates:

$$\tilde{\mathbb{T}}_{ia,jb} = \mathbb{U}^\dagger_{i\alpha\beta} \cdot \mathbb{T}_{i\alpha,j\beta} \cdot \mathbb{U}_{j\alpha\beta}. \tag{1.9}$$

With the help of the Pauli matrices σ, this hopping matrix can be separated into a (pseudo)spin-dependent and a (pseudo)spin-independent part:

$$\tilde{\mathbb{T}}_{ia,jb} = \tau_{ia,jb} \mathbb{1}_2 + i \vec{\lambda}_{ia,jb} \cdot \vec{\sigma}, \tag{1.10}$$

where $\vec{\lambda} \cdot \vec{\sigma} = \lambda^x \sigma^x + \lambda^y \sigma^y + \lambda^z \sigma^z$. Note, that his choice is not unique, since there is the identification of the pseudo-spin "up" and "down" is ambiguous. However, the energy spectrum, and with that the observables, are not effected by this choice.

The hopping parameters introduced this way contain information about the crystal field splitting via the parameters ε_α, the spin-orbit coupling strength λ and the matrix elements $\langle \alpha\, \sigma | \mathbf{L} \cdot \mathbf{S} | \beta\, \sigma' \rangle$ in the original basis. They are real and fulfil the following relations:

$$\tau_{ia,jb} = \tau_{jb,ia} \qquad \text{and} \qquad \vec{\lambda}_{ia,jb} = -\vec{\lambda}_{jb,ia}. \tag{1.11}$$

From this derivation follows the important consequence that, spin-orbit coupling generally leads to complex hopping terms.

1.2.2 Single-orbital second order perturbation theory

From now on, we assume the single-orbital case with hopping $t_{i\alpha,j\beta} \to t_{ij}$, and with homogeneous Coulomb repulsion for all sites, $U^{ijkl}_{\alpha\beta\alpha'\beta'} \to U$, in Eq. (1.1). In the limit $U = 0$, the electrons are fully determined by their kinetic energy and can move freely in the lattice, which corresponds to a metallic state[2]. Increasing the ratio U/t_{ij} introduces a penalty for double occupancy of a site, so that the electrons become increasingly more localized. At a critical ratio, the system undergoes a quantum phase transition from a metal to an insulator, the so-called Mott transition. Further increase of U/t_{ij} drives

[2] Here, we assumed that the material is not a band insulator.

the system further deep into the Mott insulating phase, until the electrons for $t_{ij} = 0$ are completely frozen. Here, we consider the case of strong localization in the regime $U \gg t_{ij}$.

Starting point is the single-particle Hamiltonian after the SOC basis transformation, given by Eq. (1.8), in addition to the two-particle interaction term $\mathcal{H}_{\text{int}}$ in the single-orbital case and nearest-neighbour hopping:

$$\mathcal{H} = \sum_i E_i \underline{c}_i^\dagger \underline{c}_i - \sum_{\langle ij \rangle} \left[\underline{c}_i^\dagger \tilde{\mathbb{T}}_{i,j} \, \underline{c}_j + \text{H.c.} \right] + U \sum_i n_{i\uparrow} n_{j\downarrow}, \tag{1.12}$$

with the particle operator $n_{i\sigma} = c_{i\sigma}^\dagger c_{i\sigma}$ in the eigenbasis of the single-particle Hamiltonian. In the limit $U \gg \tau_{ji}, |\vec{\lambda}_{ji}|$ the single-site Hamiltonian represents the unperturbed part,

$$\mathcal{H}_0 = \sum_i E_i \underline{c}_i^\dagger \underline{c}_i + U \sum_i n_{i\uparrow} n_{j\downarrow}, \tag{1.13}$$

whereas the hopping contribution is perturbative:

$$\mathcal{H}_1 = - \sum_{\langle ij \rangle} \left[\underline{c}_i^\dagger \tilde{\mathbb{T}}_{i,j} \, \underline{c}_j + \text{H.c.} \right]. \tag{1.14}$$

To express the energy correction in terms of the ground states $|\psi_{ij}\rangle$ and the excited states $|\phi_{ij}\rangle$, we group the possible spin states in the following way:

$$|\psi_{ij}\rangle = \{|\uparrow_i, \uparrow_j\rangle, |\uparrow_i, \downarrow_j\rangle, |\downarrow_i, \uparrow_j\rangle, |\downarrow_i, \downarrow_j\rangle\}, \tag{1.15}$$

$$|\phi_{ij}\rangle = \{|\uparrow_i \downarrow_i, 0\rangle, |0, \uparrow_j \downarrow_j\rangle\}. \tag{1.16}$$

In perturbation theory, the zeroth order is constant with respect to the spin, where the energy is the matrix element of the unperturbed Hamiltonian with the ground states $E_0 = \langle \psi_{ij} | \mathcal{H}_0 | \psi_{ij} \rangle$. The first order energy correction vanishes, due to the fact that a single hopping process does not transform a ground state into another ground state[3]. The first non-trivial contribution is therefore the second-order term. The general expression for the effective Hamiltonian in second-order Rayleigh-Schrödinger perturbation theory is for a degenerate model space given by the following expression [51]:

$$\mathcal{H}_{\text{eff}} = \mathbb{P}\mathcal{H}_1 \mathbb{R} \mathcal{H}_1 \mathbb{P} \tag{1.17}$$

$$= \sum_{\langle ij \rangle} \sum_{\psi\psi'} \sum_{\phi} \frac{|\psi_{ij}\rangle\langle\psi_{ij}|\mathcal{H}_1|\phi_{ij}\rangle\langle\phi_{ij}|\mathcal{H}_1|\psi'_{ij}\rangle\langle\psi'_{ij}|}{\langle\psi_{ij}|\mathcal{H}_0|\psi_{ij}\rangle - \langle\phi_{ij}|\mathcal{H}_0|\phi_{ij}\rangle}, \tag{1.18}$$

where we introduced the projector operator onto the ground state, $\mathbb{P}$, and the resolvent $\mathbb{R}$, which is a renormalized projector onto the excited states[4]:

$$\mathbb{P} = \sum_{\psi} |\psi_{ij}\rangle\langle\psi_{ij}| \qquad \text{and} \qquad \mathbb{R} = \sum_{\phi} \frac{|\phi_{ij}\rangle\langle\phi_{ij}|}{\langle\psi_{ij}|\mathcal{H}_0|\psi_{ij}\rangle - \langle\phi_{ij}|\mathcal{H}_0|\phi_{ij}\rangle}. \tag{1.19}$$

The denominator of the projector $\mathbb{R}$ onto the excited states is within this approximation the energy difference between the singly occupied ground states and double occupied excited states, which is for the single-orbital case simply the Hubbard repulsion U:

$$\langle\psi_{ij}|\mathcal{H}_0|\psi_{ij}\rangle - \langle\phi_{ij}|\mathcal{H}_0|\phi_{ij}\rangle = (2E_i + U) - 2E_i = U. \tag{1.20}$$

Since the matrix elements of $\mathcal{H}_1$ with the ground states $|\psi_{ij}\rangle$ vanish:

$$\langle\psi_{ij}|\underline{c}_i^\dagger(\tau_{ij}\,\mathbb{1}_2 + i\vec{\lambda}_{ij}\cdot\vec{\sigma})\,\underline{c}_j|\psi_{ij}\rangle = 0, \tag{1.21}$$

[3] This is not surprising, since time-reversal symmetry forbids odd power spin terms in the absence of an external field.

[4] Note, that the projection operators are defined in such a way that they project onto the investigated bond i-j. For calculations including more than two sites, the projection operators can be redefined accordingly.

the sum over the excited states $|\phi_{ij}\rangle$ can be treated effectively as a complete sum:

$$\sum_{\phi}\langle\psi_{ij}|\mathcal{H}_1|\phi_{ij}\rangle\langle\phi_{ij}|\mathcal{H}_1|\psi'_{ij}\rangle = \langle\psi_{ij}|\mathcal{H}_1\mathcal{H}_1|\psi'_{ij}\rangle. \tag{1.22}$$

The effective Hamiltonian is therefore:

$$\mathcal{H}_{\text{eff}} = -\frac{1}{U}\sum_{\langle ij\rangle}\sum_{\psi\psi'}|\psi_{ij}\rangle\langle\psi_{ij}|\big[\underline{c}_i^\dagger(\tau_{ij}\mathbb{1}_2 + i\vec{\lambda}_{ij}\cdot\vec{\sigma})\underline{c}_j + \text{H.c.}\big]^2|\psi'_{ij}\rangle\langle\psi'_{ij}|. \tag{1.23}$$

These matrix elements can be evaluated according to their order in τ and $\vec{\lambda}$. For this we use the Abrikosov pseudo-fermion representation for spin 1/2 operators $\mathbf{S}_i = \frac{1}{2}\underline{c}_i^\dagger\vec{\sigma}\underline{c}_i$:

$$c_{i\uparrow}^\dagger c_{i\downarrow} = S_i^+, \qquad c_{i\downarrow}^\dagger c_{i\uparrow} = S_i^-, \qquad c_{i\uparrow}^\dagger c_{i\uparrow} = \frac{1}{2} + S_i^z \qquad \text{and} \qquad c_{i\downarrow}^\dagger c_{i\downarrow} = \frac{1}{2} - S_i^z. \tag{1.24}$$

The following properties of spinors, detailed in Appendix A, will be useful throughout this section:

$$(\mathbf{a}\cdot\vec{\sigma})(\mathbf{b}\cdot\vec{\sigma}) = (\mathbf{a}\cdot\mathbf{b})\mathbb{1}_2 + i(\mathbf{a}\times\mathbf{b})\cdot\vec{\sigma}, \tag{1.25}$$

$$(\mathbf{a}\cdot\vec{\sigma})(\mathbf{b}\cdot\vec{\sigma})(\mathbf{c}\cdot\vec{\sigma}) = (\mathbf{a}\cdot\mathbf{b})(\mathbf{c}\cdot\vec{\sigma}) + i(\mathbf{a}\times\mathbf{b})\cdot\mathbf{c}\ \mathbb{1}_2 - (\mathbf{a}\cdot\mathbf{c})(\mathbf{b}\cdot\vec{\sigma}) + (\mathbf{c}\cdot\vec{\sigma})(\mathbf{a}\cdot\mathbf{b}), \tag{1.26}$$

$$\underline{c}_i\underline{c}_i^\dagger = \frac{1}{2}\mathbb{1}_2 - \mathbf{S}_i\cdot\vec{\sigma}. \tag{1.27}$$

First, we evaluate the matrix elements that stem from terms including only spin-independent hopping terms:

$$M_{\tau\tau} = (\tau_{ij})^2\langle\psi_{ij}|\big[\underline{c}_i^\dagger\underline{c}_j\underline{c}_i^\dagger\underline{c}_j + \underline{c}_i^\dagger\underline{c}_j\underline{c}_j^\dagger\underline{c}_i + \underline{c}_j^\dagger\underline{c}_i\underline{c}_i^\dagger\underline{c}_j + \underline{c}_j^\dagger\underline{c}_i\underline{c}_j^\dagger\underline{c}_i\big]|\psi'_{ij}\rangle, \tag{1.28}$$

where two annihilation operators on the same site give no contribution since the ground states are singly occupied. With the relation given by Eq. (1.27) spin operators are introduced:

$$\begin{aligned} M_{\tau\tau} =&(\tau_{ij})^2\langle\psi_{ij}|\big[\underline{c}_i^\dagger(\frac{1}{2}\mathbb{1}_2 - \mathbf{S}_j\cdot\vec{\sigma})\,\underline{c}_i + \underline{c}_j^\dagger(\frac{1}{2}\mathbb{1}_2 - \mathbf{S}_i\cdot\vec{\sigma})\,\underline{c}_j\big]|\psi'_{ij}\rangle \\ =&(\tau_{ij})^2\langle\psi_{ij}|\big[\frac{1}{2}(\underline{c}_i^\dagger\underline{c}_i + \underline{c}_j^\dagger\underline{c}_j) - \underline{c}_i^\dagger(\mathbf{S}_j\cdot\vec{\sigma})\,\underline{c}_i - \underline{c}_j^\dagger(\mathbf{S}_i\cdot\vec{\sigma})\,\underline{c}_j\big]|\psi'_{ij}\rangle. \end{aligned} \tag{1.29}$$

The first term is a constant, since $\mathbb{P}\underline{c}_i^\dagger\underline{c}_i = 1$ as a consequence of the Abrikosov spin representation according to Eq. (1.24). Using the fact that spin operators on different sites commute:

$$\begin{aligned} M_{\tau\tau} =&(\tau_{ij})^2\langle\psi_{ij}|\big[1 - \mathbf{S}_j\cdot(\underline{c}_i^\dagger\vec{\sigma}\underline{c}_i) - \mathbf{S}_i\cdot(\underline{c}_j^\dagger\vec{\sigma}\underline{c}_j)\big]|\psi'_{ij}\rangle \\ =&(\tau_{ij})^2\langle\psi_{ij}|\big[1 - 4\,\mathbf{S}_i\cdot\mathbf{S}_j\big]|\psi'_{ij}\rangle. \end{aligned} \tag{1.30}$$

leads to the well-known isotropic Heisenberg expression.

Next, we evaluate the matrix element with one real hopping and one spin-dependent hopping term. Starting point is also an expression where only terms with annihilation operators on different sites $i \neq j$ are considered, the Abrikosov spin representation Eq. (1.24) is employed, as well as the antisymmetry $\vec{\lambda}_{ji} = -\vec{\lambda}_{ij}$:

$$\begin{aligned} M_{\tau\lambda} &= i\tau_{ij}\langle\psi_{ij}|\big[\underline{c}_i^\dagger\underline{c}_j\underline{c}_i^\dagger(\vec{\lambda}_{ij}\cdot\vec{\sigma})\,\underline{c}_j + \underline{c}_i^\dagger\underline{c}_j\underline{c}_j^\dagger(\vec{\lambda}_{ji}\cdot\vec{\sigma})\,\underline{c}_i + \underline{c}_j^\dagger\underline{c}_i\underline{c}_i^\dagger(\vec{\lambda}_{ij}\cdot\vec{\sigma})\,\underline{c}_j + \underline{c}_j^\dagger\underline{c}_i\underline{c}_j^\dagger(\vec{\lambda}_{ji}\cdot\vec{\sigma})\,\underline{c}_i\big]|\psi'_{ij}\rangle + \text{H.c.} \\ &= -i\tau_{ij}\langle\psi_{ij}|\big[\underline{c}_i^\dagger(\frac{1}{2}\mathbb{1}_2 - \mathbf{S}_j\cdot\vec{\sigma})(\vec{\lambda}_{ij}\cdot\vec{\sigma})\,\underline{c}_i - \underline{c}_j^\dagger(\frac{1}{2}\mathbb{1}_2 - \mathbf{S}_i\cdot\vec{\sigma})(\vec{\lambda}_{ij}\cdot\vec{\sigma})\,\underline{c}_j\big]|\psi'_{ij}\rangle + \text{H.c.} \\ &= -i\tau_{ij}\langle\psi_{ij}|\big[\frac{1}{2}\underline{c}_i^\dagger(\vec{\lambda}_{ij}\cdot\vec{\sigma})\,\underline{c}_i - \frac{1}{2}\underline{c}_j^\dagger(\vec{\lambda}_{ij}\cdot\vec{\sigma})\,\underline{c}_j - \underline{c}_i^\dagger(\mathbf{S}_j\cdot\vec{\sigma})(\vec{\lambda}_{ij}\cdot\vec{\sigma})\,\underline{c}_i \\ &\qquad + \underline{c}_j^\dagger(\mathbf{S}_i\cdot\vec{\sigma})(\vec{\lambda}_{ij}\cdot\vec{\sigma})\,\underline{c}_j\big]|\psi'_{ij}\rangle + \text{H.c.} \end{aligned} \tag{1.31}$$

The product of Pauli matrices can be simplified using Eq. (1.25):

$$\begin{aligned} M_{\tau\lambda} = -i\tau_{ij}\langle\psi_{ij}|\big[&\vec{\lambda}_{ij}\cdot\mathbf{S}_i - \vec{\lambda}_{ij}\cdot\mathbf{S}_j - \underline{c}_i^\dagger\big(\mathbf{S}_j\cdot\vec{\lambda}_{ij} + i(\mathbf{S}_j\times\vec{\lambda}_{ij})\cdot\vec{\sigma}\big)\,\underline{c}_i \\ &+ \underline{c}_j^\dagger\big(\mathbf{S}_i\cdot\vec{\lambda}_{ij} + i(\mathbf{S}_i\times\vec{\lambda}_{ij})\cdot\vec{\sigma}\big)\,\underline{c}_j\big]|\psi'_{ij}\rangle + \text{H.c.}, \end{aligned} \tag{1.32}$$

where the single spin contributions are imaginary and cancel with contributions from the hermitian conjugate. Using the Abrikosov spin representation,

$$\begin{aligned} M_{\tau\lambda} &= \tau_{ij}\langle\psi_{ij}|\big[-(\mathbf{S}_j\times\vec{\lambda}_{ij})\cdot(\underline{c}_i^\dagger\vec{\sigma}\underline{c}_i) + (\mathbf{S}_i\times\vec{\lambda}_{ij})\cdot(\underline{c}_j^\dagger\vec{\sigma}\underline{c}_j)\big]|\psi'_{ij}\rangle + \text{H.c.} \\ &= \tau_{ij}\langle\psi_{ij}|\big[-(\mathbf{S}_j\times\vec{\lambda}_{ij})\cdot\mathbf{S}_i + 2\,(\mathbf{S}_i\times\vec{\lambda}_{ij})\cdot\mathbf{S}_j\big]|\psi'_{ij}\rangle + \text{H.c.} \end{aligned} \tag{1.33}$$

and a cyclic permutation in the triple product $\mathbf{a}\cdot(\mathbf{b}\times\mathbf{c}) = \mathbf{c}\cdot(\mathbf{a}\times\mathbf{b})$, we finally obtain the following simplified expression:

$$\begin{aligned} M_{\tau\lambda} &= \tau_{ij}\langle\psi_{ij}|\big[-4\,(\mathbf{S}_i\times\mathbf{S}_j)\cdot\vec{\lambda}_{ij}\big]|\psi'_{ij}\rangle + \text{H.c.} \\ &= -4\tau_{ij}\langle\psi_{ij}|\,\vec{\lambda}_{ij}\cdot(\mathbf{S}_i\times\mathbf{S}_j)\big]|\psi'_{ij}\rangle + \text{H.c.} \end{aligned} \tag{1.34}$$

The hermitian conjugate contribution leads to an identical real part, so that the final result reads:

$$M_{\tau\lambda} = -\,8\tau_{ij}\langle\psi_{ij}|\,\vec{\lambda}_{ij}\cdot(\mathbf{S}_i\times\mathbf{S}_j)\big]|\psi'_{ij}\rangle. \tag{1.35}$$

The cross product of spins is proportional to the so-called Dzyaloshinskii-Moriya interaction [49, 52], which represents the antisymmetric anisotropic contribution in bilinear spin Hamiltonians.

Finally, we evaluate the expression of the matrix element with only spin-dependent hopping parameters:

$$\begin{aligned} M_{\lambda\lambda} &= \langle\psi_{ij}|\big[-\underline{c}_i^\dagger(i\vec{\lambda}_{ij}\cdot\vec{\sigma})\underline{c}_j\underline{c}_j^\dagger(i\vec{\lambda}_{ij}\cdot\vec{\sigma})\,\underline{c}_i - \underline{c}_j^\dagger(i\vec{\lambda}_{ij}\cdot\vec{\sigma})\underline{c}_i\underline{c}_i^\dagger(i\vec{\lambda}_{ij}\cdot\vec{\sigma})\,\underline{c}_j\big]|\psi'_{ij}\rangle \\ &= -\langle\psi_{ij}|\big[\underline{c}_i^\dagger(\vec{\lambda}_{ij}\cdot\vec{\sigma})(\frac{1}{2}\mathbb{1}_2 - \mathbf{S}_j\cdot\vec{\sigma})(\vec{\lambda}_{ij}\cdot\vec{\sigma})\,\underline{c}_i + \underline{c}_j^\dagger(\vec{\lambda}_{ij}\cdot\vec{\sigma})(\frac{1}{2}\mathbb{1}_2 - \mathbf{S}_i\cdot\vec{\sigma})(\vec{\lambda}_{ij}\cdot\vec{\sigma})\,\underline{c}_j\big]|\psi'_{ij}\rangle \\ &= -\langle\psi_{ij}|\big[\frac{1}{2}\underline{c}_i^\dagger(\vec{\lambda}_{ij}\cdot\vec{\sigma})(\vec{\lambda}_{ij}\cdot\vec{\sigma})\,\underline{c}_i + \underline{c}_i^\dagger(\vec{\lambda}_{ij}\cdot\vec{\sigma})(\mathbf{S}_j\cdot\vec{\sigma})(\vec{\lambda}_{ij}\cdot\vec{\sigma})\,\underline{c}_i \\ &\quad + \frac{1}{2}\underline{c}_j^\dagger(\vec{\lambda}_{ij}\cdot\vec{\sigma})(\vec{\lambda}_{ij}\cdot\vec{\sigma})\,\underline{c}_j + \underline{c}_j^\dagger(\vec{\lambda}_{ij}\cdot\vec{\sigma})(\mathbf{S}_i\cdot\vec{\sigma})(\vec{\lambda}_{ij}\cdot\vec{\sigma})\,\underline{c}_j\big]|\psi'_{ij}\rangle. \end{aligned} \tag{1.36}$$

If the indices are relabelled $i \leftrightarrow j$ in the last two terms and under consideration of the antisymmetry $\vec{\lambda}_{ij} = -\vec{\lambda}_{ji}$, they are identical to the first two terms:

$$M_{\lambda\lambda} = -\langle\psi_{ij}|\big[\underline{c}_i^\dagger(\vec{\lambda}_{ij}\cdot\vec{\sigma})(\vec{\lambda}_{ij}\cdot\vec{\sigma})\,\underline{c}_i + 2\underline{c}_i^\dagger(\vec{\lambda}_{ij}\cdot\vec{\sigma})(\mathbf{S}_j\cdot\vec{\sigma})(\vec{\lambda}_{ij}\cdot\vec{\sigma})\,\underline{c}_i\big]|\psi'_{ij}\rangle. \tag{1.37}$$

With the relations for Pauli matrix products given by Eq. (1.25) and Eq. (1.26), this expression can be simplified as follows:

$$\begin{aligned} M_{\lambda\lambda} &= -\langle\psi_{ij}|\big[\underline{c}_i^\dagger[(\vec{\lambda}_{ij}\cdot\vec{\lambda}_{ij})\,\underline{c}_i + i(\vec{\lambda}_{ij}\times\vec{\lambda}_{ij})\cdot\vec{\sigma}] \\ &\qquad + 2\underline{c}_i^\dagger[(\vec{\lambda}_{ij}\cdot\mathbf{S}_j)(\vec{\lambda}_{ij}\cdot\vec{\sigma}) + i(\vec{\lambda}_{ij}\times\mathbf{S}_j)\cdot\vec{\lambda}_{ij} - (\vec{\lambda}_{ij}\cdot\vec{\lambda}_{ij})(\mathbf{S}_j\cdot\vec{\sigma}) + (\vec{\lambda}_{ij}\cdot\vec{\sigma})(\vec{\lambda}_{ij}\cdot\mathbf{S}_j)]\underline{c}_i\big]|\psi'_{ij}\rangle \\ &= -\langle\psi_{ij}|\big[(\vec{\lambda}_{ij}\cdot\vec{\lambda}_{ij}) + 8(\vec{\lambda}_{ij}\cdot\mathbf{S}_j)(\vec{\lambda}_{ij}\cdot\mathbf{S}_i) - 4(\vec{\lambda}_{ij}\cdot\vec{\lambda}_{ij})(\mathbf{S}_j\cdot\mathbf{S}_i)\big]|\psi'_{ij}\rangle \\ &= -\langle\psi_{ij}|\big[(\vec{\lambda}_{ij}\cdot\vec{\lambda}_{ij})(1 - 4\mathbf{S}_j\cdot\mathbf{S}_i) + 8(\vec{\lambda}_{ij}\cdot\mathbf{S}_j)(\vec{\lambda}_{ij}\cdot\mathbf{S}_i)\big]|\psi'_{ij}\rangle. \end{aligned} \tag{1.38}$$

This contribution contains a relativistic correction to the isotropic Heisenberg term, as well as the so-called symmetric pseudo-dipolar contribution.

Considering these results in the expression for the effective Hamiltonian with Eq. (1.23), we obtain the most general expression for a spin 1/2 bilinear Hamiltonian:

$$\mathcal{H}_{\text{spin}} = \sum_{ij}\big[J_{ij}\mathbf{S}_i\cdot\mathbf{S}_j + \mathbf{D}_{ij}\cdot(\mathbf{S}_i\times\mathbf{S}_j) + \mathbf{S}_i\cdot\Gamma_{ij}\cdot\mathbf{S}_j)\big]. \tag{1.39}$$

In the single-orbital limit, the energy coefficients follow from comparison with the prefactors in Eq. (1.30), Eq. (1.35), and Eq. (1.38):

$$J_{ij} = 4\frac{(\tau_{ij})^2 - (\vec{\lambda}_{ij})^2}{U}, \qquad \mathbf{D}_{ij} = 8\frac{\tau_{ij}\vec{\lambda}_{ij}}{U}, \qquad \Gamma_{ij} = 8\frac{\vec{\lambda}_{ij}\otimes\vec{\lambda}_{ji}}{U}. \tag{1.40}$$

1.3 Description of real materials: Density functional theory

Having demonstrated a possibility to obtain an effective spin Hamiltonian from the electronic picture in terms of the Hubbard Hamiltonian, in this case via perturbation theory, the natural question is how to parametrize such a Hubbard Hamiltonian for real materials. A powerful tool to obtain information about the electronic structure of a material from first principles, i.e. without additional experimental input is density functional theory (DFT). For a more detailed introduction, we refer to the many books and reviews devoted to this subject [53–57].

In general, the many-body Hamiltonian of a specific material contains the kinetic and potential energy terms of the nuclei and electrons present in the crystal structure[5]:

$$\mathcal{H} = -\sum_i \frac{1}{2M_i}\nabla^2_{\mathbf{R}_i} - \sum_i \frac{1}{2}\nabla^2_{\mathbf{r}_i} - \sum_{ij} \frac{Z_i}{|\mathbf{R}_i - \mathbf{r}_j|} + \frac{1}{2}\sum_{i\neq j} \frac{1}{|\mathbf{r}_i - \mathbf{r}_j|} + \frac{1}{2}\sum_{i\neq j} \frac{Z_i Z_j}{|\mathbf{R}_i - \mathbf{R}_j|}. \tag{1.41}$$

Here, M_i is the nuclei mass at position $\mathbf{R}_i$, $\mathbf{r}_i$ the position of the i^{th} electron, and Z_i is the atomic number. Since it is impossible to solve this Hamiltonian exactly, i.e. determine the eigenvalues and corresponding wave functions, approximations are unavoidable. Here, we demonstrate the framework of density functional theory in order to tackle this problem.

A common first approximation, not only in the context of DFT, is the so-called Born-Oppenheimer approximation. In this framework, the heavier nuclei are considered to be much slower than the electrons and can be approximated to be frozen. It is then possible to describe the crystal solely in terms of the electrons, which move in a potential that is determined by the position and nature of the nuclei. The kinetic energy of the nuclei, i.e. the first term in Eq. (1.41), vanishes within this approximation, while the last term, the potential associated with the nuclei-nuclei interaction, is treated as a constant background potential. The Hamiltonian in Born-Oppenheimer approximation can be expressed in terms of the kinetic energy of the electrons $\hat{T}$, the potential energy associated with the electrons $\hat{V}$ and the effectively external potential due to the frozen nuclei $\hat{V}_{\text{ext}}$:

$$\mathcal{H} = \hat{T} + \hat{V} + \hat{V}_{\text{ext}}. \tag{1.42}$$

Here, the material specific information is entirely encoded in $\hat{V}_{\text{ext}}$ due to the positions and nature of the nuclei of the investigated crystal.

A powerful tool to tackle this still unsolvable electronic problem is the framework of DFT.

1.3.1 Hohenberg-Kohn theorems

In 1964, Hohenberg and Kohn published two theorems that established the density as a key entity to determine electronic properties of crystals [58].

In the *first Hohenberg-Kohn theorem*, the authors derived that there is a unique mapping between the ground-state density $\rho(\mathbf{r})$ of a many-electron system and the external potential V_{ext}. Consequently, the ground-state expectation value of an observable $\mathcal{O}$ is a unique functional of the ground-state electron density:

$$\langle\psi|\mathcal{O}|\psi\rangle = O[\rho]. \tag{1.43}$$

This unique mapping is more powerful than it might seem on the first glance. Its important consequence is that the ground-state density of a system contains all relevant information and therefore enables the determination of the electronic properties of a given system with a single function $\rho(\mathbf{r})$ without having to calculate the wave function.

According to the *second Hohenberg-Kohn theorem*, the total energy functional of the ground-state density $\langle\psi|\mathcal{H}|\psi\rangle = E[\rho]$ can be expressed as follows:

$$\begin{aligned} E[\rho] &= \langle\psi|\hat{T} + \hat{V}|\psi\rangle + \langle\psi|\hat{V}_{\text{ext}}|\psi\rangle \\ &= F_{\text{HK}}[\rho] + \int \rho(\mathbf{r})\mathrm{d}\mathbf{r}. \end{aligned} \tag{1.44}$$

[5] The expression for the exact many-body Hamiltonian is given in atomic units.

In this expression, the universal Hohenberg-Kohn density functional $F_{\mathrm{HK}}[\rho]$ was introduced, which is minimal for the ground-state density uniquely connected to V_{ext}. The Hohenberg-Kohn functional does not depend on the material-specific details, which are solely encoded in the ground-state density $\rho(\mathbf{r})$. Note, that this theorem is only valid for the ground-state properties of a system. When using results based on first principles, excited states are not included in such a treatment.

1.3.2 Kohn-Sham equations

The practical aspect to the Hohenberg-Kohn theorems was added one year later by Kohn and Sham [59]. A breakthrough gave the insight that the electronic ground-state density ρ of a real system can be calculated by a mapping onto a non-interacting electron gas. This non-interacting electron gas is a formal trick and has no physical meaning. However, through the unique mapping of a density to the total energy functional, the problem is solved completely. This can be seen by rearranging the Hohenberg-Kohn functional $F_{\mathrm{HK}}[\rho] = \langle\psi|\hat{T} + \hat{V}|\psi\rangle$, which can be divided into:

$$F_{\mathrm{HK}}[\rho] = T_0[\rho] + V_H[\rho] + V_{xc}[\rho], \tag{1.45}$$

where $T_0[\rho]$ is the kinetic energy of a non-interacting electron gas, $V_H[\rho]$ is the Hartree contribution:

$$V_H[\rho] = \frac{1}{2}\int \mathrm{d}\mathbf{r} \int \mathrm{d}\mathbf{r}' \frac{\rho(\mathbf{r})\rho(\mathbf{r}')}{|\mathbf{r} - \mathbf{r}'|}, \tag{1.46}$$

and $V_{xc}[\rho]$ is the so-called exchange-correlation potential. V_{xc} consists of the many-body correlations that are not captured by V_H, so that the contributions most difficult to determine are gathered in this term. The energy functional can then be explicitly formulated:

$$E[\rho] = T_0[\rho] + V_H[\rho] + V_{xc}[\rho] + V_{\mathrm{ext}}[\rho]. \tag{1.47}$$

Here, ρ can be interpreted as the density of a non-interacting electron gas that is subject to the external potential of the nuclei and to the exchange correlation potential.

The ground state density of a free electron gas can then be expressed as the product of *single-particle* wave functions:

$$\rho(\mathbf{r}) = \sum_i [\phi_i(\mathbf{r})]^* \phi_i(\mathbf{r}), \tag{1.48}$$

where the Kohn-Sham wave functions $\phi_i(\mathbf{r})$ are determined by the Kohn-Sham equation:

$$\mathcal{H}_{\mathrm{KS}}\, \phi_i = \varepsilon_i \phi_i. \tag{1.49}$$

Solving the Schrödinger equation for a non-interacting system is a problem that can be tackled numerically, e.g. with a self-consistency cycle. Note, that the Kohn-Sham wave functions are constructs corresponding to a fictitious electron gas and do not correspond to real physical wave functions.

1.3.3 Approximations for the exchange correlation functional

So far, every expression given in this section was exact, at least in the limits of the Born-Oppenheimer approximation. However, the exact exchange correlation functional $V_{xc}[\rho]$ is generally unknown and has to be approximated. The most simple, but surprisingly successful, approximation is the so-called local density approximation (LDA):

$$E_{xc}^{\mathrm{LDA}} = \int \rho(\mathbf{r})\varepsilon_{xc}(\rho(\mathbf{r}))\mathrm{d}\mathbf{r}, \tag{1.50}$$

where $\varepsilon_{xc}(\rho(\mathbf{r}))$ is the exchange correlation energy of the homogeneous electron gas, which has been solved numerically. Within this approximation, it is assumed that at each point $\mathbf{r}$, the energy contribution depends only on the local ε_{xc}, independent of the density at other places in the system. A more sophisticated approach is the so-called generalized gradient approximation (GGA), where dependencies on the neighbouring densities are also taken into account, so that the gradient of the density is additionally considered.

1.4 Low-energy spin models for real materials

With the framework of DFT, we introduced a powerful method to determine the electronic structure of a specific material based on its crystal structure. However, to obtain an effective spin model for materials, additional steps are required. In this section, we describe two methods to extract spin Hamiltonians from DFT. The latter was applied for projects incorporated in this thesis and described in the feature article Ref. [60].

1.4.1 Total energy calculations

One way to determine magnetic exchange parameters from DFT are total energy calculations, discussed, for example, in a review by Xiang *et al.* [61]. Especially in the case of isotropic exchange parameters, it has proven to be a very successful approach [62–66]. This method is - for materials with not too large unit cells - comparably inexpensive and allows for the determination of further neighour interactions. It is based directly on the DFT ground-state energy, where the spin degree of freedom is considered by calculation of two different densities, $\rho_\uparrow$ and $\rho_\downarrow$, in addition to the description given in Section 1.3. The energies obtained from DFT can be interpreted as "classical" spin energies, since spin fluctuations cannot be taken into account in the single-particle picture [67–69].

To illustrate the underlying principle, we consider a single bond, where the magnetic sites are coupled by an isotropic Heisenberg interaction J. The ground state energy for two different classical spin configurations follows from the Heisenberg Hamiltonian:

$$E_\mathrm{T} = J\langle\uparrow_1\uparrow_2 |\mathbf{S}_1 \cdot \mathbf{S}_2| \uparrow_1\uparrow_2\rangle = \frac{J}{4} \tag{1.51}$$

$$E_\mathrm{BSS} = J\langle\uparrow_1\downarrow_2 |\mathbf{S}_1 \cdot \mathbf{S}_2| \uparrow_1\downarrow_2\rangle = -\frac{J}{4}. \tag{1.52}$$

Due to the classical treatment of spin, an antiferromagnetic state is considered, $|\uparrow_1\downarrow_2\rangle$, which is not an eigenstate of the Heisenberg Hamiltonian. Therefore, Noodleman referred to it as a "broken symmetry singlet" state [62, 63]. The exchange parameter can be deduced from a system of equations, where the energies can be obtained from DFT calculations for the imposed spin configurations:

$$J = 2(E_\mathrm{T} - E_\mathrm{BSS}). \tag{1.53}$$

In a crystal, the different exchange parameters in the effective spin Hamiltonian can then be determined from least squares fitting of an overdetermined set of equations corresponding to various spin configurations. Note that, since the materials of interest are Mott insulators, "pure" DFT usually fails to capture the properties of the highly correlated electrons sufficiently. Due to the missing localization of the electrons, magnetic exchange parameters may be overestimated by orders of magnitude. One possible solution is the so-called DFT+U approach, where a correlation parameter U is imposed artificially for the most correlated electronic orbitals. In the case of isotropic spin exchange, such a method has been applied successfully in a number of cases [65, 70–73].

While this is a very intriguing method, problems may arise in the determination of anisotropic interactions, such as the Dzyaloshinskii-Moriya interaction or the pseudo-dipolar tensor. In these cases, the number of free parameters in the spin Hamiltonian is vast compared to most isotropic cases. Therefore, a much larger number of spin configurations has to converge on the DFT level to obtain an overdetermined set of equations. However, as mentioned above, DFT is a ground-state theory. If spin configurations are chosen that are very far away from the true ground state, they may describe the real situation poorly.

1.4.2 "Hybrid" methods: Hubbard Hamiltonian from first principles

An alternative are "hybrid" methods that combine first principles with many-body techniques. The contribution from DFT is in these cases the determination of a material-specific Hubbard Hamiltonian, which can then be treated further with other techniques, e.g. perturbation theory as discussed in Section 1.2 or exact diagonalization, as we will discuss in Chapter 4. The explanations below for the extraction of the Hubbard Hamiltonian follow essentially Ref. [74].

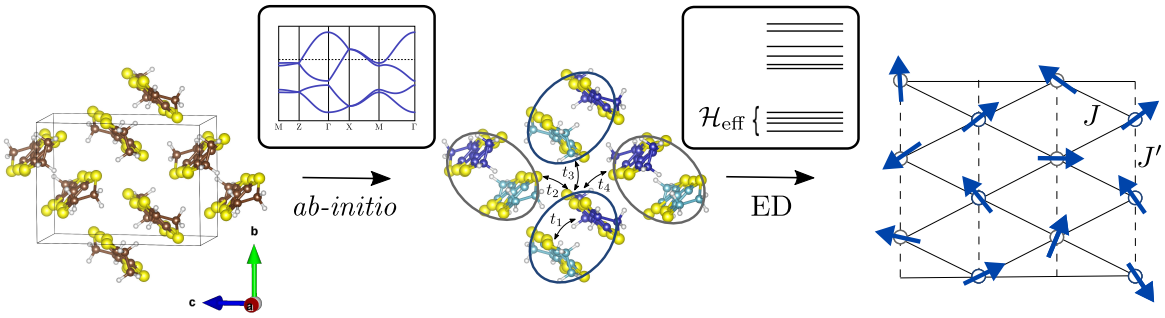

Figure 1.3: Illustration of the involved steps in the "hybrid" method for determination of effective spin Hamiltonians on the example of the anisotropic lattice organic κ-$(ET)_2Cu_2(CN)_3$. In a first step, hopping parameters are determined with *ab-initio* from the crystal structure. Second, the effective Hamiltonian $\mathcal{H}_{\text{eff}}$ can be determined via exact diagonalization (ED) and projection onto the low-energy subspace. $\mathcal{H}_{\text{eff}}$ determines then the magnetic exchange parameters as e.g. J, J'.

The information about the material-specific properties is encoded in the hopping parameters $t_{i\alpha,j\beta}$. It is possible to extract them from the DFT cycle described in Section 1.3 via localized Wannier functions $\psi_{i\alpha\sigma}(\mathbf{r})$. In practice, these Wannier functions can be constructed from first principles by various procedures such as the maximally-localized Wannier functions algorithm or projectors techniques [56, 74–76]. The Hubbard Hamiltonian can then be formulated with the Wannier functions as the one-electron basis:

$$\mathcal{H} = \mathcal{H}_{\text{hop}} + \mathcal{H}_{\text{int}} + \mathcal{H}_{\text{DC}}, \tag{1.54}$$

where $\mathcal{H}_{\text{DC}}$ contains a double counting correction that cancels the part of the electron-electron interaction already accounted for in the LDA part. The hopping Hamiltonian contains the information from DFT:

$$\mathcal{H}_{\text{LDA}} = -\sum_{\sigma}\sum_{ij}\sum_{\alpha\beta} t_{i\alpha,j\beta} d^{\dagger}_{i\alpha\sigma} d_{j\beta\sigma} + \text{H.c.} \tag{1.55}$$

through the hopping parameters, which can be extracted from the Wannier functions as follows:

$$t_{i\alpha,j\beta} = -\int \mathrm{d}\mathbf{r}\, \psi^{*}_{i\alpha\beta}(\mathbf{r})[-\frac{1}{2}\nabla^2]\psi_{i\beta\sigma}, \tag{1.56}$$

The two-particle interaction is defined in this basis generally as

$$\hat{U} = \sum_{ijkl}\sum_{\sigma\sigma'}\sum_{\alpha\beta\alpha'\beta'} U^{ijkl}_{\alpha\beta\alpha'\beta'} d^{\dagger}_{i\alpha\sigma} d^{\dagger}_{j\beta\sigma'} d_{l\beta'\sigma'} d_{k\alpha'\sigma}, \tag{1.57}$$

where the matrix elements are, in principle, also determined by the Wannier functions extracted from DFT:

$$U^{ijkl}_{\alpha\beta\alpha'\beta'} = \frac{1}{2}\int \mathrm{d}\mathbf{r}_1 \int \mathrm{d}\mathbf{r}_2 \frac{\psi^{*}_{i\alpha\sigma}(\mathbf{r}_1)\psi^{*}_{j\beta\sigma'}(\mathbf{r}_2)\psi_{l\beta'\sigma'}(\mathbf{r}_2)\psi_{k\alpha'\sigma}(\mathbf{r}_1)}{|\mathbf{r}_1 - \mathbf{r}_2|}. \tag{1.58}$$

These matrix elements can be estimated by methods such as the constrained random phase approximation (cRPA), but are often also fixed with typical values for the considered correlated atoms. The contribution $\mathcal{H}_{\text{int}} - \mathcal{H}_{\text{DC}}$ is a short-range many-body correction to DFT [56]. It has to be taken into account for correlated or heavy electrons (d or f shells), where "pure" DFT fails qualitatively. The double counting correction is a delicate issue, since the exchange-correlation contribution for the interacting case of the real electrons cannot be extracted from DFT. There are several successful double counting correction schemes, which are especially important for techniques, e.g. DFT+DMFT (dynamical mean-field theory), that take both, correlated and uncorrelated electrons into account. For the hybrid

methods discussed in this thesis, where the effective spin Hamiltonian is constructed based on the correlated electrons, the main effect can be approximated as a constant shift in energy. However, it should be noted that the hopping parameters extracted from first principles also always contain contributions from correlation.

With the electronic Hubbard Hamiltonian determined, the effective spin Hamiltonian can be extracted from many-body techniques. In Fig. 1.3, we illustrate the main idea for the "hybrid" method used in Chapter 2 and Chapter 4, where the many-body technique in the second step is exact diagonalization. The starting point is the crystal structure, here illustrated with the organic layer of the compound κ-Cu. As discussed above, the hopping parameters for the electronic Hubbard model can be determined from first principles. With exact diagonalization (ED), it is then possible to determine an effective Hamiltonian $\mathcal{H}_{\text{eff}}$, from which through projection onto the low-energy subspace, the spin model Hamiltonian can be determined. It contains, in the case of the anisotropic lattice, magnetic exchange parameters such as the Heisenberg parameters J and J'. We will detail these steps in Chapter 4.

1.5 Outline of this thesis

This thesis is organized as follows. In Chapter 2 and Chapter 3, we discuss the magnetic properties of anisotropic lattice organics. In Chapter 2, we determine the effective spin Hamiltonian of four specific compounds. These charge transfer salts belong to the κ-$(ET)_2X$ family, where the organic layers consist of ET molecules and the magnetic properties are varied through the different anorganic anions X. Since these materials are insulators close to the Mott transition, higher order terms in the effective spin models become relevant, which we introduce via perturbation theory. In the context of theoretical predictions for models on the anisotropic triangular lattice and the experimental observations for the materials, we determined then the effective spin Hamiltonian with the "hybrid" method of *ab-initio* and ED. The investigated compounds represent examples of different exchange parameters limits in the anisotropic triangular lattice, from proximity to the square limit, through the almost isotropic triangular lattice, to the quasi-one-dimensional limit. Then, in Chapter 3, we focus on one of the four compounds with the QSL candidate κ-Cu (κ-$(ET)_2Cu_2(CN)_3$) in the context of the experimental observations in muon spin rotation (μSR) and magnetic torque experiments. Since both of these experiments are performed in the presence of an external magnetic field, we discuss first the influence of a field onto the relevant terms in the effective spin Hamiltonian. Then, we consider two scenarios and check their consequences against the experimental facts. First, the response of κ-Cu is interpreted in terms of a critical scenario, which is consistent with the μSR observations, but fails to explain the magnetic torque response. Therefore, we consider then a second scenario, in which κ-Cu is interpreted as a valence bond glass at low temperatures. Together with the consideration of disorder effects, such a scenario offers a consistent explanation of the experimental observations. The results of these two chapters are published in Ref. [77, 78].

In Chapter 4, we demonstrate the details of the hybrid method with ED as the many-body technique on the example of two three-dimensional pyrochlore materials. A special focus is the determination of anisotropic magnetic interactions caused by spin-orbit coupling, such as the Dzyaloshinskii-Moriya interaction and the pseudo-dipolar tensor. Since the pyrochlore lattice is a highly symmetrical geometry, symmetry restrictions according to Moriya's rules for these contributions play an important role, which we present at the beginning of the chapter. Then, we demonstrate the hybrid method on the example of the ferromagnet $Lu_2V_2O_7$ and determine the most general spin 1/2 bilinear spin Hamiltonian for this material. Finally, the same method is used to determine the anisotropic contributions in the effective spin Hamiltonian for the QSL candidate $Lu_2Mo_2O_5N_2$. The results in this chapter are published in Ref. [79, 80].

In Chapter 5 and Chapter 6, we study the honeycomb Kitaev material α-$RuCl_3$. We start Chapter 5 with a brief review of the Kitaev honeycomb model, its solution and possible realization in real materials. Then, we focus on the Kitaev material α-$RuCl_3$. Since in inelastic neutron scattering experiments signatures of fractionalized excitations have been observed, although the material is known to magnetically order below $T_N = 14\,\text{K}$, we focused on the study of magnetic excitations for this material. We tackled this problem via exact diagonalization of dynamical correlation functions based on specific spin Hamiltonians. This approach allows the theoretical prediction of inelastic neutron scattering (INS)

intensities for a series of spin models to narrow down the relevant terms and their ratios in an appropriate effective model for α-$RuCl_3$. It turned out that the most consistent model with the experimental findings is explainable in the context of magnon-decay processes rather than fractionalized quasiparticles. In Chapter 6, we extend the determined model for α-$RuCl_3$ to the presence of a magnetic field. This situation was proposed previously to host a field-induced QSL state. In order to search for the corresponding phase transitions thermodynamic probes, such as magnetic torque experiments, seem the appropriate method of choice. Therefore, we calculated the theoretical torque response for the proposed model under field and compared with the experimental observations. The magnetic excitations in the presence of a magnetic field were calculated with the previously established method of exact diagonalization of dynamical correlation functions and the results were compared to experimental INS and electron spin resonance (ESR) intensities under field. The findings described in these two chapters are published in Ref. [81–83]

Finally, in the last chapter, we conclude the thesis with a summary and outlook.

Chapter 2

Magnetic interactions in triangular lattice organics

2.1 Introduction

In this chapter, we discuss the magnetic interactions in a two-dimensional geometry, which has proven to host a variety of interesting physical phases: The anisotropic triangular lattice. In fact, the antiferromagnetic Heisenberg spin 1/2 model on the isotropic triangular lattice was first proposed to host a resonating valence bond (RVB) state as a realization of a QSL state by Anderson [2] in 1973. Later, it was established that this model orders magnetically in a 120° Néel state by variational, ED, and DMRG methods [84–88]. However, it remains an intensive research field to investigate modified versions of this model. For example, the introduction of anisotropy [26, 89] allows to extrapolate continuously between three widely studied lattice models, the square lattice, the isotropic triangular lattice and the quasi one-dimensional chains. In addition, the stabilization of exotic phases by higher order exchange terms on the triangular lattice attracted a lot of attention [25, 90–92].

To connect this theoretical framework with materials, the family of organic κ-$(ET)_2X$ salts is a promising choice. Despite their complicated crystal structure, it is possible to map the organic layer of ET dimers onto the anisotropic triangular lattice, where every dimer corresponds to a magnetic site with spin 1/2. The choice of the inorganic layer, given by X in κ-$(ET)_2X$ materials, enables to fine-tune the ratio of magnetic interaction parameters within the organic layer throughout a large region of the anisotropic triangular lattice phase diagram. Moreover, while the exchange of X corresponds to a chemical pressure, the soft organic crystals can be also influenced strongly with hydrostatic pressure, where moderate values of a few kbar can already be sufficient to drive the system from the Mott insulating to the metallic state [93]. This creates a unique situation of an experimentally accessible phase diagram for a certain geometry and hence raised strong interest from both, the theoretical and the experimental side.

While the possible ground states of the triangular lattice organics include exotic phases like unconventional superconductivity, charge order and many more [8, 31, 93, 94], we focus here on the insulating phase, which may be described by an effective spin model. A disadvantage of the organics, in comparison to most inorganic materials, is the limited size of grown organic crystals. This is the reason why it is extremely challenging to directly probe the microscopic spin structure with inelastic neutron scattering, the "default" experimental setup for these kind of questions under other circumstances. After some reports of experiments with extremely small crystals [95–97], other routes to determine the magnetic response were pursued instead [38, 93, 98]. Therefore, an analysis based on first principles calculations, considering more indirect experimental probes of magnetic properties, are necessary to tackle the issue of finding the appropriate spin Hamiltonian for a range of κ-ET materials.

Since the magnetism is delocalized over the relatively extended ET molecules, total energy DFT calculations fail in this case to provide a suitable spin description, already at the isotropic level. The proximity to the Mott transition due to $t \sim U$ results in the lack of a single small parameter, which

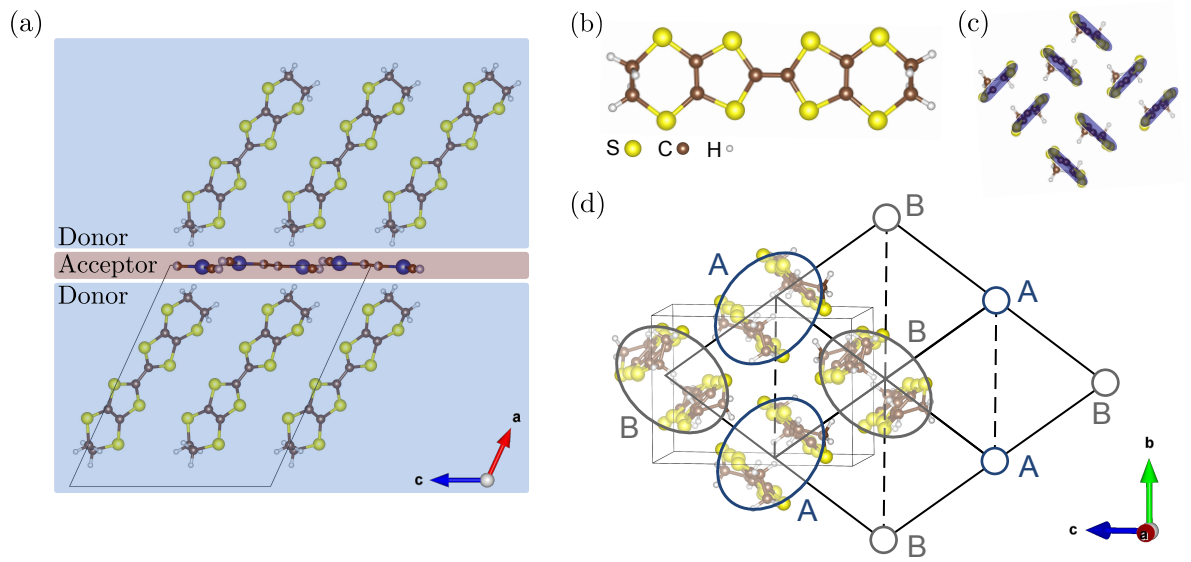

Figure 2.1: (a) Illustration of layered structure with organic electron donor layers and inorganic acceptor layers, for the example κ-Cu. (b) BEDT-TTF or ET molecule. (c) κ packing motif. (d) Mapping onto anisotropic triangular lattice with the sublattice sites labelled A and B, for the example κ-Cu. Figure (d) adapted from Ref. [78].

questions the applicability of perturbation theory. Moreover, due to the light S, C, H atoms in an ET dimer, spin-orbit coupling effects have been thought to be negligible in the early descriptions of the organic charge transfer salts. However, it has been argued that SOC effects can play an important role in the low-temperature physics of these materials [3, 93]. Therefore, a hybrid method of *ab-initio* and many-body methods is a promising choice.

After a short discussion of the electronic properties of the κ-$(ET)_2X$ family in Section 2.2, we review in Section 2.3 the most important experimental observations in the materials investigated in this chapter. In Section 2.4, we give a short overview of the phases hosted by the triangular lattice known from literature. This enables a more sophisticated judgement of the computed spin Hamiltonians in the context of experimentally known facts. In Section 2.5, we present in particular the spin Hamiltonian of four members of the κ-$(ET)_2X$ family governing different limits on the anisotropic triangular lattice. As a representative of the magnetically ordered case we will investigate κ-$(ET)_2Cu[N(CN)_2]Cl$ (abbreviated κ-Cl), with two QSL candidates we will discuss κ-$(ET)_2Cu_2(CN)_3$ (κ-Cu) and its sister compound κ-$(ET)_2Ag_2(CN)_3$ (κ-Ag), and as an example for a quasi one-dimensional material serves κ-$(ET)_2B(CN)_4$ (κ-BCN). For these four members we determined the symmetrically allowed spin Hamiltonian using the hybrid method mentioned above. The calculated exchange parameters are partly published in Ref. [77] and partly in Ref. [78]. In addition, due to proximity to the Mott transition, κ-$(ET)_2X$ materials are suspected to be significantly influenced by higher order spin ring-exchange terms [93]. Since the induced frustration by these higher order terms is known to suppress magnetic order [25, 90–92], their determination might be crucial in understanding the nature of the magnetic states present. These higher order terms are given for all four investigated materials in Section 2.5.

2.2 Extended Hubbard Hamiltonian for the κ-$(ET)_2X$ family

The κ-$(ET)_2X$ organic charge transfer salts are structured in layers of inorganic electron acceptors and organic electron donors, illustrated in Fig. 2.1(a) on the example of κ-Cu. The organic layers consist of BEDT-TTF (bis(ethylenedithio)tetrahiafulvalene), commonly abbreviated with “ET”, molecules, shown in Fig. 2.1(b). They are arranged in the so-called κ packing motif, where dimers of ET molecules are

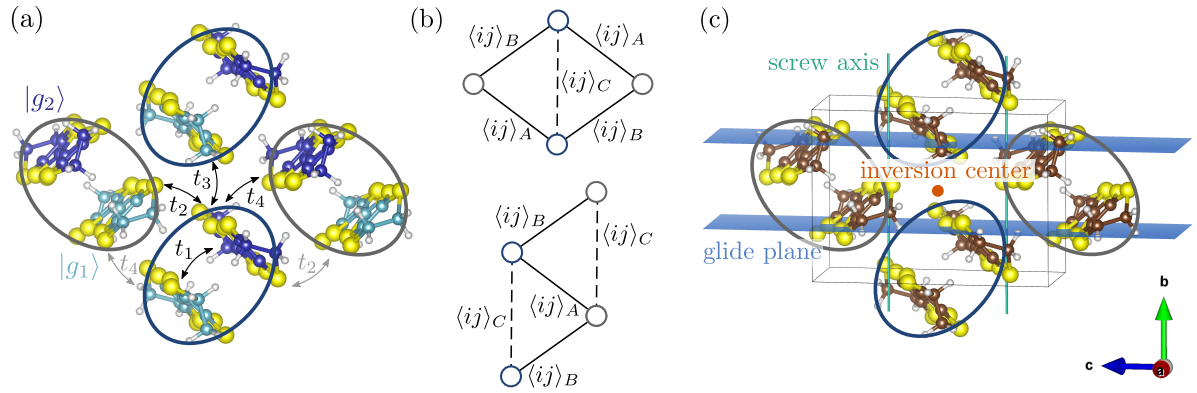

Figure 2.2: (a) Definition of hopping parameters $t_{1...4}$ between molecular orbitals 1 and 2. (b) Corresponding indexing of bonds $\langle ij\rangle_{A...C}$ due to different involved hopping integrals as introduced in Eq. (2.4) for the two different 4-dimer cluster shapes. (c) Symmetry elements present in κ-$(ET)_2X$ materials, here shown for the $P2_1/c$ space group. Figure (c) adapted from Ref. [78].

approximately perpendicular to each other. The κ packing motif from the top view of the organic layer is shown in Fig. 2.1(c).

In this chapter, we will restrict the analysis to cases with monovalent anions, so that on average one electron per ET dimer is transferred to the anion layer (κ-$(ET)_2^+X^-$). Hence, it is possible to describe the magnetism in these compounds in a spin 1/2 hole picture with one hole per ET dimer. In Fig. 2.1(d) we illustrate the mapping of the organic layer onto a simple anisotropic lattice with one magnetic site representing a dimer of ET molecules. The different orientations in the κ-packing motif are translated into two distinct sublattices, here labelled A and B. The most simple approach is a description, where each dimer is treated as one magnetic site. At first, it was common to discuss the κ-$(ET)_2X$ compounds in the framework of this so-called dimer model [93, 99, 100]. It corresponds to a single-orbital Hubbard model considering effective hopping parameters t and t' on the anisotropic triangular lattice. However, it has been pointed out [101–103] that the so-called molecule picture, which includes the inner degrees of freedom of the ET dimers, captures mechanisms not observable in the simple dimer model. The consideration of the molecular structure in the dimers corresponds to a description with a multi-orbital Hubbard model:

$$\mathcal{H}_{\text{tot}} = \mathcal{H}_{\text{hop}^*} + \mathcal{H}_{\text{int}}. \tag{2.1}$$

For large enough Hubbard repulsion, each ET dimer is occupied by a single hole occupying the antibonding orbital:

$$|\text{a}\rangle = \frac{1}{\sqrt{2}}(|g_1\rangle + |g_2\rangle), \tag{2.2}$$

where $|g_i\rangle$ is the HOMO (highest occupied molecular orbital) of an isolated ET molecule i. The corresponding bonding orbital:

$$|\text{b}\rangle = \frac{1}{\sqrt{2}}(|g_1\rangle - |g_2\rangle), \tag{2.3}$$

is then occupied by two electrons and therefore empty and higher in energy in the hole picture.

The orbital energies in the hole picture, $\varepsilon_a = -t_1$ and $\varepsilon_b = t_1$, correspond to the intradimer hopping integral t_1. In the molecule picture, four distinct hopping amplitudes $t_{1...4}$ as defined in Fig. 2.2(a) are considered. The dimer model can be extracted from these hopping parameters with the approximation $t = (t_2 + t_4)/2$ and $t' = t_3/2$. In the basis of molecular orbitals labelled $|g_i\rangle = \{1, 2\}$, the hopping

Hamiltonian, containing real hopping parameters, is expressed as follows:

$$\mathcal{H}_{\text{hop}} = -\sum_{i} t_1 c_{i1}^{\dagger} c_{i2} - \sum_{\langle ij\rangle_A} \left[t_2 c_{i2}^{\dagger} c_{j1} + t_4 c_{i1}^{\dagger} c_{j1}\right] - \sum_{\langle ij\rangle_B} \left[t_2 c_{i1}^{\dagger} c_{j2} + t_4 c_{i2}^{\dagger} c_{j2}\right] - \sum_{\langle ij\rangle_C} t_3 c_{i1}^{\dagger} c_{j2} + \text{h.c.} \tag{2.4}$$

The definition of the hopping integrals $t_{1\ldots4}$ and the bond labelling $\langle ij\rangle_{A\ldots C}$ are illustrated in Fig. 2.2(a,b).

The spin-orbit coupling matrix corresponding to the molecular orbitals of the ET molecules cannot be easily described by analytical expressions. To include SOC effects nevertheless, we consider them through complex hopping terms [50]:

$$\mathcal{H}_{\text{hop}^*} = \sum_{ij}\sum_{\alpha\beta} \mathbf{c}_{i\alpha}^{\dagger} \left(t_{i\alpha,j\beta}\mathbb{1}_{2\times2} + \frac{i}{2}\vec{\lambda}_{i\alpha,j\beta}\cdot\vec{\sigma}\right)\mathbf{c}_{j\beta}. \tag{2.5}$$

In Section 1.2 we demonstrated that complex hopping parameters are a direct consequence of SOC and may be obtained e.g. via first order perturbation theory in terms of the SOC strength λ. The transformation into the hole picture ($c_i^{\dagger} \rightarrow c_i$) causes a sign change of the real hopping parameters ($t_{ij}c_i^{\dagger}c_j \rightarrow -t_{ij}c_j^{\dagger}c_i \rightarrow -t_{ij}c_i^{\dagger}c_j$), with $t_{ij} = t_{ji}$. In contrast, the complex hopping terms are invariant under this transformation ($\vec{\lambda}_{ij}c_i^{\dagger}c_j \rightarrow -\vec{\lambda}_{ij}c_j^{\dagger}c_i \rightarrow \vec{\lambda}_{ij}c_i^{\dagger}c_j$) with $\vec{\lambda}_{ij} = -\vec{\lambda}_{ji}$.

In Fig. 2.2(b), we show the two distinct four-dimer clusters necessary to capture all non-equivalent exchange contributions. In principle, the choice of these clusters breaks the lattice symmetry, we will revisit how to fix this issue in Section 2.5. Here, we show that the electronic Hamiltonian on only two distinct four-dimer clusters, contains the information for a large variety of clusters. In addition, computational effort can be reduced, since the *ab-initio* calculation of the hopping parameters $t_{i\alpha,j\beta}$ and $\vec{\lambda}_{i\alpha,j\beta}$ on one solid and one dashed bond is sufficient to build all four-dimer clusters by taking advantage of the symmetry relations between the bonds.

The four investigated materials in this chapter have the two space groups *Pnma* (for κ-Cl and κ-BCN) and $P2_1/c$ (for κ-Cu and κ-Ag). In both cases, there are two distinct ET dimers per unit cell, indicated by the differently oriented and coloured ellipses in Fig. 2.2 and there are four symmetry operations which build the κ packing motif in the considered materials: The identity operation E, the 2_1 screw axis referred to as a C_2 operation, the inversion operation i at the inversion center, and the glide plane σ_h. On the example of the $P2_1/c$ space group, these symmetry elements are illustrated in Fig. 2.2(c). By convention, the 2_1 screw axis is aligned along the crystallographic b axis, in contrast to the *Pnma* materials, where it is conventionally aligned along the c axis. In general, the symmetries within the organic layers are identical for the materials in the two space groups, they differ only with respect to their interlayer symmetries.

The symmetry relations between the possible four-site clusters on the anisotropic triangular lattice are shown in Fig. 2.3. In Fig. 2.3(a), we show all four-site clusters containing a specific solid bond, indicated in red. The two rows contain the two distinct cluster shapes shown in Fig. 2.2(b). Consideration of the indicated symmetry relations allows to relate hopping parameters on different bonds. For example, from the inversion operation in the top row, it follows directly that $\vec{\lambda}_{01} = \vec{\lambda}_{23}$. Therefore, if the hopping on bond 0-1 is determined from DFT, then the hopping parameters on bond 2-3, 1-2, and 0-3 can be fully determined by the indicated symmetry operations without additional *ab-initio* calculations. In case of the comparatively large number of atoms per unit cell in the organic charge transfer salts, this leads to a significant time saving. Note that, while the shown clusters are symmetrically related, they are not symmetrically equivalent. This is especially important for the the pseudo-vector $\vec{\lambda}_{i\alpha,j\beta}$. In this case, bonds on clusters related by a C_2 or σ_h operation gather an additional minus sign for the component of $\vec{\lambda}_{i\alpha,j\beta}$ that is along the 2_1 axis in the corresponding space group of the material. In Fig. 2.3(b), we show the symmetry operations that are necessary to obtain all clusters containing a specific dashed bond, indicated in blue. Note that due to inversion symmetry at the center of the dashed bonds, there is no finite $\vec{\lambda}$ along this bond.

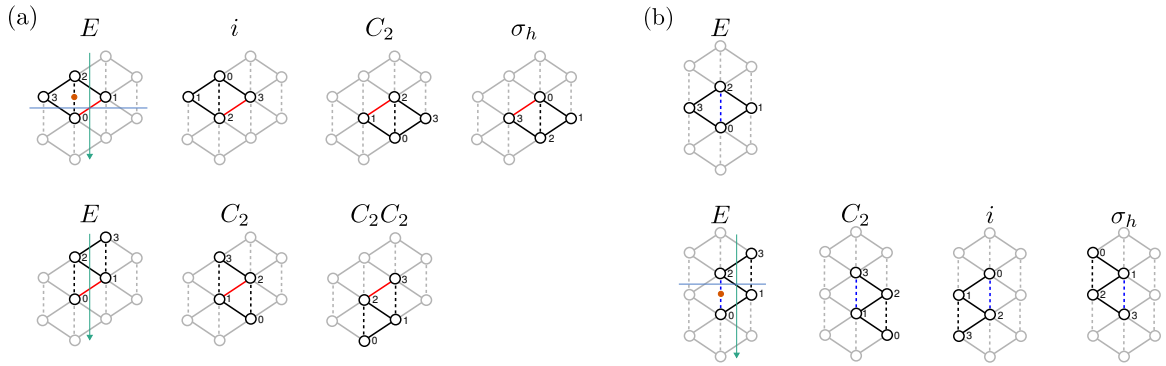

Figure 2.3: Symmetry related clusters on the anisotropic triangular lattice with the symmetries present in the κ-$(ET)_2X$ family: The identity operation E, the inversion operation i, the 2_1 screw axis referred to as C_2, and the glide plane σ_h. Hopping parameters between specific bonds can thus be related solely based on symmetry operations. (a) Symmetry-related solid bonds, indicated in red, for the two different cluster shapes introduced in Fig. 2.2(b). For example, from the inversion operation i follows directly the relation $\vec{\lambda}_{01} = \vec{\lambda}_{23}$ for the cluster indicated by E in the top row. (b) Symmetry-related dashed bonds, indicated in blue, for the two different cluster shapes.

For the two-particle interaction part, we consider Hubbard repulsion and Hund's coupling effects:

$$\mathcal{H}_{\text{int}} = \sum_i \left[U n_{i,a} n_{i,b} + U \sum_\alpha n_{i\alpha\uparrow} n_{i\alpha\downarrow} + J_H \sum_{\sigma\sigma'} (c^\dagger_{ia\sigma} c^\dagger_{ib\sigma'} c_{ia\sigma'} c_{ib\sigma} + c^\dagger_{ia\sigma} c^\dagger_{ia\sigma'} c_{ib\sigma'} c_{ib\sigma}) \right] + V \sum_{ij} \sum_{\alpha\beta} n_{i\alpha} n_{j\beta}. \tag{2.6}$$

where $\{\alpha, \beta\}$ are orbital indices, $\{a, b\}$ label the specific anti-bonding and bonding orbitals, and $n_{ia} = n_{ia\uparrow} + n_{ia\downarrow}$. Since in the case of the organic materials the orbitals are relatively extended, an inter-site Coulomb repulsion, here indicated with V, may have relevant effects.

2.3 Main experimental observations in triangular organics

In this section, we summarize shortly the main experimental observations and corresponding unresolved questions for the four compounds discussed in this chapter.

2.3.1 Canted Néel order: κ-Cl

κ-Cl is a compound for which the magnetic ground state seems to have been settled experimentally since the end of the 90s. In 1995, Miyagawa *et al.* [104] performed ^{1}H NMR and magnetization measurements, revealing an antiferromagnetic transition at $T_N = 27\,\text{K}$, with weak ferromagnetism deduced from a finite magnetization below T_N. Furthermore, the authors suggested that the magnetic ordering is commensurate with the dimer structure in κ-Cl. Eight years later, Smith *et al.* [105] refined these insights further with a ^{13}C NMR study under field with $H = 8.3\,\text{T}$, well above the spin-flop field. The authors proposed a microscopic model to explain the observed spin ordering. The authors assigned the weak ferromagnetism, which implies small spin canting, to the existence of a finite Dzyaloshinskii-Moriya interaction with $|\mathbf{D}| = 3.5\,\text{K}$. For the Heisenberg exchange, they assumed a simple antiferromagnetic, isotropic structure on the triangular lattice with an estimated exchange parameter of $J = 580\,\text{K}$.

Some of the authors refined this analysis one year later [106] to determine the orientation of the DM interaction by field angle sweeps. In this case, a discontinuity in the NMR shift is thought to appear for $\mathbf{H} \parallel \mathbf{D}$, since at this point a spin reorientation is triggered for sufficiently high fields. This analysis suggests an angle $\phi_a \approx 46°$ with the DM vector lying in the a-b plane. Moreover, ESR

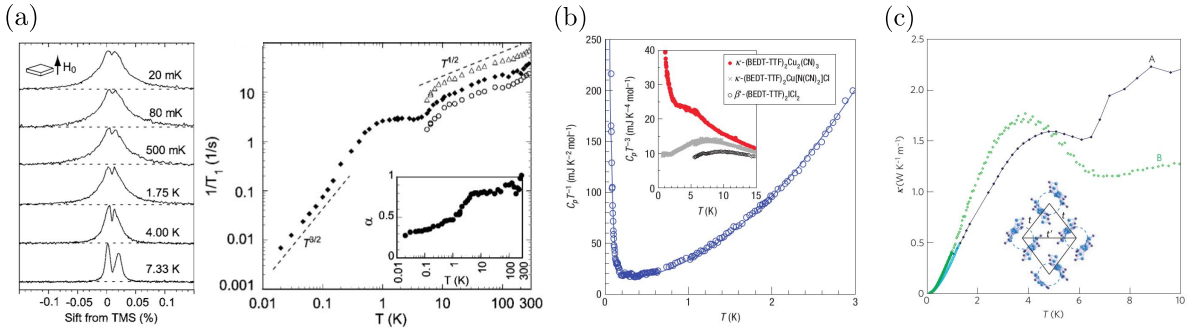

Figure 2.4: Selected experimental reports over the last decade for κ-Cu. (a) ^{13}C NMR spectra and spin-lattice relation rate $1/T_1$, where the inset shows the exponent α from a stretched exponential fit reported by Shimizu *et al.* [36]. (b) Normalized heat capacity C_p/T as a function of temperature T, reported by S. Yamashita *et al.* [37]. (c) Thermal conductivity κ as a function of temperature T, reported by M. Yamashita *et al.* [38]. Fig. (a) reprinted from Ref. [36], Fig. (b) reprinted from Ref. [37], Fig. (c) reprinted from Ref. [38].

measurements [107] revealed a finite DM interaction with $|\mathbf{D}| = 5\,\mathrm{K}$ from classical model calculations of the free energy and fit to frequency versus resonance field. This fit gave also an estimate for the Heisenberg exchange, which was also assumed to be isotropic on the triangular lattice with $J = 600\,\mathrm{K}$. Divergences at fixed frequencies for different angles of certain mode resonances appear when the field is tilted in the direction of the DM interaction. Based on this observation, the ESR measurements show that the DM interaction lies within the a-b plane with an angle $\phi_a \approx 45°$ towards the a axis.

2.3.2 Quasi one-dimensionality: κ-BCN

Recently, the compound κ-BCN attracted attention within the organics community, when in 2015 Yoshida *et al.* [108] presented a detailed study classifying it as a quasi-one-dimensional material on the triangular lattice. ^{1}H NMR experiments showed no signature of magnetic ordering down to $T = 1.5\,\mathrm{K}$ and static magnetic susceptibility studies were consistent with a fit to high-temperature series expansion of the Heisenberg model with $J'/J = 2.0$. Based on DFT calculations, the authors speculated that effect might become more pronounced at low temperatures reaching ratios like $J'/J \approx 3.0$. As a reason for the surprisingly strong anisotropy, the authors propose the significantly higher displacement of ET molecules along the t bonds, reducing the overlap of the corresponding HOMOs and with that the value of the overlap integral t. This is a nice demonstration of the influence of the anion structure, which is thought to be responsible for the increased displacement, onto the hopping parameters and the possibility to tune from different places in the phase diagram of the anisotropic triangular lattice to others by replacing the anion in the κ-$(\mathrm{ET})_2\mathrm{X}$ family. In the low temperature regime, the static susceptibility shows a drop below $T = 5\,\mathrm{K}$ toward zero, which is identified in Ref. [108] as a signature of a second-order phase transition from a paramagnetic state into a gapped non-magnetic state. As possible realizations they proposed a spin-Peierls or a valence bond crystal state, which could be distinguished by low-temperature structural analysis, which was, up to our knowledge, not followed upon to date.

2.3.3 QSL candidates: κ-Cu and κ-Ag

In 2003, Shimizu *et al.* [32] proposed κ-Cu as a spin liquid candidate based on ^{1}H NMR and static susceptibility measurements. A fitting to high-temperature series expansion of the spin 1/2 isotropic triangular lattice gave a first estimate for the order of magnitude of the Heisenberg exchange constant with $J = 250\,\mathrm{K}$. The absence of a splitting of the NMR spectra suggested the absence of long-range order down to 32 mK. This proposal was further refined by a ^{13}C NMR study down to 20 mK of the same authors [36] in 2006. The NMR spectra, shown in Fig. 2.4(a), do not contain splitting down to

20 mK, confirming that the result of the earlier study was not an artefact. The spin-lattice relaxation rate $1/T_1$, as well as the exponent α in the stretched exponential, show clearly the famous $T_* = 6\,\mathrm{K}$ anomaly in κ-Cu. We will see below, that the mysterious anomaly, which is still not unambiguously assigned to a specific phenomenon, can be observed in a number of independent experiments for κ-Cu. In Ref. [36], the small value of α below $T_* = 6\,\mathrm{K}$ was interpreted as a hint towards the emergence of impurities or grain boundaries in this temperature region. In the next chapter we will elaborate on this interpretation, considering the effective spin Hamiltonian determined in this chapter.

S. Yamashita *et al.* [37] reported in 2008 heat capacity measurements on κ-Cu down to 75 mK, shown in Fig. 2.4(b). In contrast to κ-Cl, κ-Cu showed signatures of a contribution linear in temperature to the heat capacity while the compound is insulating. This would be consistent with the presence of a spinon density of states, i.e. gapless excitations of an RVB model. The authors reported also a broad hump in the specific heat, for example visible in the inset in Fig. 2.4(b), around $T_* = 6\,\mathrm{K}$. Due to independence of T_* on magnetic field, they excluded it as a signature for a phase-transition to long-range magnetic order. Note, that they observed an appreciable sample dependence and pointed out the possibility of paramagnetic impurity contributions, although the authors dismissed it as the primary source of the observed behaviour due to convergence of better quality samples to a consistent finite linear contribution.

One year later, M. Yamashita *et al.* [38] contradicted the suggestion of gapless excitations from specific heat with thermal conductivity measurements hinting towards a *gapped* spin liquid behaviour, shown in Fig. 2.4(c). The authors argued that the specific heat results might be ambiguous due to possibly large nuclear Schottky contributions below 1 K. Note, that both measurements agree in the observation of the 6 K anomaly. On the basis of a κ/T vs T^2 plot, the authors argued that κ/T vanishes for $T \to 0$, which immediately indicates the absence of low-lying fermionic excitations. The prediction from Lee *et al.* [91] that $\kappa/T \propto T^{-2/3}$ in the case of a material with a spinon Fermi surface, i.e. gapless excitations, seemed to be not confirmed for κ-Cu in this experiment.

More insight into this issue could be gained by the synthesis of the sibling compound κ-Ag, reported by Shimizu *et al.* [109] in 2016. The declared goal was to push the QSL phase into a larger U/t region by decreasing t due to negative chemical pressure and hence expanded triangular lattice. In the limit of large U/t, higher order correction terms like e.g. ring-exchange are suppressed and a nearest neighbour two-spin model offers a sufficient description. For the nearest neighbour isotropic case ($J \approx J'$), the spiral ordered state is the ground state [26], therefore tuning the ratio U/t with fixed $t \approx t'$ could allow to experimentally probe the quantum phase transition from a QSL to a magnetically ordered phase. To gain a first estimate for the Heisenberg exchange, the authors fitted the static spin susceptibility, which shows similarly to κ-Cu a broad maximum as a function of temperature, to high temperature expansion results and obtained the value $J = 175\,\mathrm{K}$. Similarly to the observation in κ-Cu, the specific heat has a finite contribution linear in temperature. Based on that, the authors argued κ-Ag to be a gapless QSL. Shimizu *et al.* also discussed the reduced sample dependence due to the silver substitution, compared to the copper compound, where the paramagnetic Cu^{2+} impurities remain to be an issue. Moreover, the authors pointed out that the terminal ethylene groups are ordered in the eclipsed type conformation below 300 K, contrasting the disordered staggered conformation in κ-Cu.

2.4 Review of phases on the anisotropic triangular lattice

One of the goals in this chapter is to place the previously introduced materials at the appropriate position in the phase diagram of the anisotropic lattice. Therefore, we review here shortly the theoretically determined ground states for various parameter regimes in the literature.

As mentioned in the introduction, the nearest-neighbour Heisenberg Hamiltonian on an isotropic triangular lattice was the first system proposed to host a QSL state [2]. However, it was shown with variational methods [84–86] and later by exact diagonalization (ED) [87] and density matrix renormalization group (DMRG) calculations [88], that in the isotropic case the ground state is a three-sublattice Néel state, forming the so-called "120° order". While this insight might seem rather disappointing, hope was regained with the question how anisotropy or higher-order spin terms influence this result.

It is well-known that tuning the exchange parameters far into the one-dimensional limit drives the

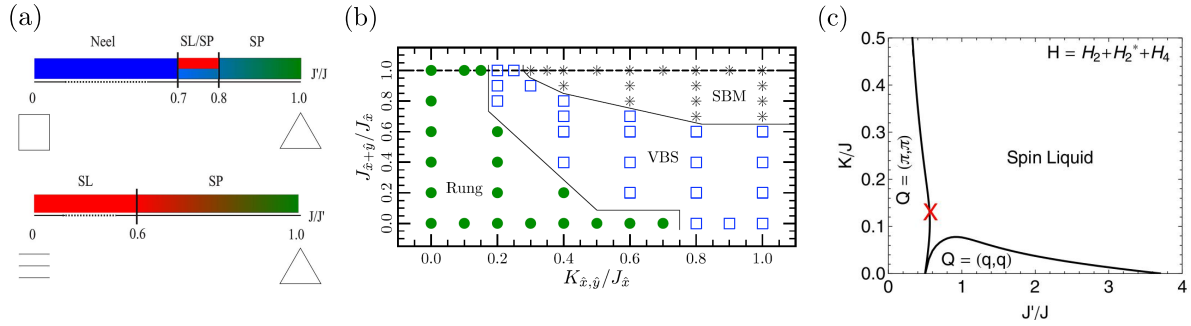

Figure 2.5: Selected theoretical results for the anisotropc triangular lattice. (a) Phases inbetween the limits of the square lattice, the isotropic triangular lattice and the one-dimensional limit, determined with variational Monte Carlo by Ghorbani *et al.* [26]. (b) Influence of finite four spin ring-exchange determined with DMRG by Block *et al.* [92], indicated are the magnetically ordered rung phase, a valence bond solid (VBS) phase, and a spin Bose-metal (SBM) phase that corresponds to a QSL phase. (c) Influence of a finite four spin ring-exchange term determined semiclassically by Holt *et al.* [25], indicated are the Néel ordered phase with ordering wave vector $Q = (\pi, \pi)$, a spiral phase with $Q = (q, q)$ and the spin liquid phase at sufficient ring exchange K. Fig. (a) reprinted from Ref. [26], (b) reprinted from Ref. [92], (c) reprinted from Ref. [25].

system into a spin liquid type state [110–112]. In the opposite limit, the square lattice, the nearest neighbour Heisenberg model orders in a (π, π) Néel state. The physical mechanisms between those well-studied limits are still subject of current research, although there exist a number of studies on that issue [23, 24, 26]. In Fig. 2.5(a) we show, for example, results from variational Monte Carlo calculations by Ghorbani *et al.* [26], tuning the ratio J'/J to connect the limits of the square lattice, the isotropic triangular lattice and one-dimensional chains. Between the square and the isotropic triangular lattice, the authors found the expected ordered Néel state for $J'/J = 0$ and the 120° order for $J'/J = 1$, here referred to as a spiral (SP) state. The colour gradient in the phase diagram indicates a continous change of the spiral pitch angle away from $\theta = 2/3\pi$, corresponding to 120°. On this part of the phase diagram they found also a region, where the energy difference between spin liquid (SL) states and an ordered spiral state is on the order of $10^{-4}J$. It is therefore inconclusive to decide which state is the ground state, but emphasizes the strong competition between the two phases. This result, which was also subject to speculation before [24], is insightful in the sense that a spin liquid phase is in this case favoured in a region that could be classified as "less frustrated" on the classical level. Tuning between the one-dimensional limit and the isotropic triangular case, the authors of Ref. [26] found the expected spin liquid for one-dimensional chains, with a phase transition towards the ordered spiral state for $J/J' = 0.6$.

On the isotropic triangular lattice, it has been suggested by variational Monte-Carlo calculations that weak AFM Heisenberg next nearest neighbour interactions of $\approx 0.1J$ may induce QSL state [113]. Such higher order terms appear naturally in extended clusters with more than two sites. In this case, higher order spin-exchange terms, such as the four-spin ring exchange may also be considered [25, 87, 90, 92, 114].

One of these studies was performed by Motrunich [90] on the isotropic triangular lattice with variational Monte Carlo calculations. In this work, he compared antiferromagnetically ordered ground states with projected Fermi sea states as a representative of the spin liquid ground state. For parameters corresponding to $K/J \geq 0.12$, he found that the QSL states are energetically favoured. Note however, that the ratio $K/J \geq 0.12$ corresponds to the notation used in Ref. [90], where a different normalization convention for four-spin terms is followed than in this thesis. In the context of this picture for a QSL state, he proposed several experimental probes: (i) constant spin susceptiblity χ_{spin} at $T = 0$, (ii) constant nuclear spin relaxation rate $1/(T_1T)$ in NMR measurements, (iii) non-Fermi-liquid behaviour in specific heat with $C \propto T^{2/3}$. At almost the same time, Lee *et al.* [91] tackled the QSL on the Hubbard

model in the triangular lattice with a slave-rotor method. They could essentially confirm the results by Motrunich [90], with the additional prediction that in the case of a spinon Fermi surface the thermal conductivity in the clean limit should behave as $\kappa/T \propto T^{-2/3}$. We will see below that, despite the clear predictions regarding experimental results from theory, the determination of the nature of the QSL can be very challenging in the case of the triangular lattice organics.

The influence of higher order four-spin ring exchange terms onto the *anisotropic* triangular lattice was studied, for example, by Block *et al.* [92] with density matrix renormalization group (DMRG) calculations. In this work, the authors used the concept of a spin Bose-metal (SBM) for the QSL state, emphasizing that this phase possesses metal-like properties for spins while it maintains bosonic character. For the DMRG calculations, they considered a four-leg ladder model, as an extension of a previous two-leg ladder study [114]. The resulting phase diagram is shown in Fig. 2.5(b). In the square lattice limit, the authors identified a "rung" phase, which was assigned as a ladder descendent from the square lattice Néel phase. They also found a VBS phase, in which translational symmetry was broken, while the signatures of magnetic ordering vanished. Motivated by perturbation theory, the relation $K/K' = J/J'$ was fixed for all calculations. Note, that the normalization of the ring exchange parameter shown in Fig. 2.5(b) differs by a factor of 8 from the convention used in this chapter.

Holt *et al.* [25] studied the phase diagram including four-spin ring exchange terms on the anisotropic semiclassically. They identify three phases in their phase diagram shown in Fig. 2.5(c): the Néel phase with ordering wave vector $\mathbf{q} = (\pi, \pi)$, a quantum disordered phase labelled as spin liquid, and an ordered spiral phase with $\mathbf{q} = (q, q)$, with the special case of $\mathbf{q} = (2\pi/3, 2\pi/3)$ for $J = J'$ corresponding to the 120° ordered phase. As the "most striking feature" of their phase diagram the authors identify the fact that even in a semiclassical theory quantum fluctuations destroy long-range magnetic order over large areas in the investigated phase space. This results effectively in a suppression of long-range order in the presence of four-spin ring-exchange with $K/J > 0.1$ and a sufficiently large J'/J ratio. They argue that this can be understood from the preference of the two-spin contributions towards a collinear ground state and the competition with the preferred spiral ground state of the four-spin terms. Note, that the notation in Ref. [25] differs from the notation used in this thesis. In agreement with Holt *et al.*, we rescale the four-spin terms with S^2 in order to keep a reasonable limit for $S \to \infty$. However, we order the parameters according to specific combinations of spins. In contrast, Holt *et al.* divide the terms according to the source in perturbation theory. The two-spin term along the solid bonds follows the relation $J = J_{\mathrm{Holt}} + 2K_{\mathrm{Holt}} + 3K'_{\mathrm{Holt}}$, while along the dashed bonds we have $J' = J'_{\mathrm{Holt}} + K_{\mathrm{Holt}} + 4K'_{\mathrm{Holt}}$. Since we do not calculate on clusters with more than four sites, the four-spin exchange terms are equivalent, $K = K_{\mathrm{Holt}}$ and $K' = K'_{\mathrm{Holt}}$. The two-spin terms stemming from fourth order perturbation theory are denoted with H_2^* in Ref. [25], so that the phase diagram shown in Fig. 2.5(c) for the Hamiltonian $H = H_2 + H_2^* + H_4$ refers to the same Hamiltonian considered in this chapter. In contrast, the axes $J'_{\mathrm{Holt}}/J_{\mathrm{Holt}}$ and $K_{\mathrm{Holt}}/J_{\mathrm{Holt}}$ refer to rescaled parameter ratios. Expansion in $K/J \ll 1$ and using the approximate relation $K/K' = J/J'$ gives:

$$\frac{J'_{\mathrm{Holt}}}{J_{\mathrm{Holt}}} = \frac{J' - K - 4K'}{J - 2K - 3K'} = \frac{J'}{J}\left(\frac{1 - \frac{J}{J'}\frac{K}{J} - 4\frac{K}{J}}{1 - 2\frac{K}{J} - 3\frac{J'}{J}\frac{K}{J}}\right) = \frac{J'}{J}\left(1 + \left(-2 - \frac{J}{J'} + 3\frac{J'}{J}\right)\frac{K}{J} + \mathcal{O}(\tfrac{K^2}{J^2})\right) \tag{2.7}$$

which is for $J \approx J'$ a relatively small correction. The same statement holds for:

$$\frac{K_{\mathrm{Holt}}}{J_{\mathrm{Holt}}} = \frac{K}{J - 2K - 3K'} = \frac{K}{J}\left(\frac{1}{1 - 2\frac{K}{J} - 3\frac{J'}{J}\frac{K}{J}}\right) = \frac{K}{J}\left(1 + \left(2 - 3\frac{J'}{J}\right)\frac{K}{J} + \mathcal{O}(\tfrac{K^2}{J^2})\right) \tag{2.8}$$

Especially in the case of κ-Cu, it was hotly debated where to place it in the phase diagram and whether terms like the four-spin ring exchange are negligible. Therefore, it is crucial to track also small corrections caused by differences in notation and normalization.

2.5 Effective spin Hamiltonian for triangular lattice organics

Stephen M. Winter, **Kira Riedl**, and Roser Valentí,
Importance of spin-orbit coupling in layered organic salts,
Phys. Rev. B **95**, 060404(R) (2017)
[77]

In the previous sections we introduced the questions we tackle now with the determination of an effective magnetic model for four selected charge transfer salts, published in Ref. [77]. With κ-Cl we introduced a well-studied compound which magnetically orders and shows evidence for a finite DM interaction. Previous *ab-initio* calculations determined hopping parameters corresponding to $t'/t \approx 0.45$ [115, 116]. A systematic theoretical investigation of the microscopic exchange parameters can be benchmarked against those literature values, so that the determined smaller anisotropic and four-spin exchange can be justified. With κ-BCN we also consider a more recently discovered compound that does not order and is suspected to be quasi one-dimensional. κ-Cu and κ-Ag do not show signatures of magnetic order as well. Due to experimental hypothesis of an isotropic triangular lattice it is an interesting question why they do not show a 120° order. DFT calculations for κ-Cu determined hopping parameters corresponding to $t'/t \approx 0.8 - 0.9$ [115–117]. In this case, the question for the theoretical analysis here is whether the isotropic character can be confirmed and whether higher order terms appear, which are thought to suppress magnetic order. In κ-Cu there is furthermore the issue of contradicting experimental results regarding the nature of the QSL - gapped or gapless - and the mysterious appearance of the $T_* = 6\,\mathrm{K}$ anomaly. The latter two issues are discussed in the next chapter, based on the spin Hamiltonian determined in this section.

For the determination of the effective spin Hamiltonian we used a hybrid method of *ab-initio* methods and exact diagonalization. In this case, a Hubbard Hamiltonian as introduced in Section 2.2 on finite clusters contains the *ab-initio* hopping parameters and chosen two-particle interaction parameters. The energy spectrum can then be extracted via exact diagonalization and projection onto the low-energy subspace, which provides an approximate description in terms of pseudo-spins, in the same spirit as it is the case for perturbation theory, discussed in Section 1.2 and Section 2.5.1. In Chapter 4 we will discuss the steps of this procedure in more detail on the example of the pyrochlore lattice.

Since in the organic materials the hopping parameters t and the Hubbard repulsion U are on the same order of magnitude (see also the supplemental material of Ref. [77]), it has been argued that higher order terms in the spin Hamiltonian play an important role. This has two consequences: (i) Higher order terms in the perturbation theory sense might modify the nearest-neighbour interactions with significant corrections. In the hybrid-method, this is equivalent to larger cluster sizes, where higher order hopping processes are considered. (ii) Higher order terms in the spin Hamiltonian, like e.g. four-spin ring exchange terms might have a significant contribution. Because of these reasons we determined for the κ-$(\mathrm{ET})_2\mathrm{X}$ compounds the magnetic exchange interactions of clusters of up to eight ET molecules, i.e. four magnetic sites.

2.5.1 Higher order perturbation theory

To provide context for the numerical results, we discuss first terms in the spin Hamiltonian beyond bilinear exchange from the perspective of perturbation theory.

As a reminder, we give first some useful properties of spinors, also given Appendix A:

$$(\mathbf{a}\cdot\vec{\sigma})(\mathbf{b}\cdot\vec{\sigma}) = (\mathbf{a}\cdot\mathbf{b})\mathbb{1}_2 + i(\mathbf{a}\times\mathbf{b})\cdot\vec{\sigma}, \tag{2.9}$$

$$(\mathbf{a}\cdot\vec{\sigma})(\mathbf{b}\cdot\vec{\sigma})(\mathbf{c}\cdot\vec{\sigma}) = (\mathbf{a}\cdot\mathbf{b})(\mathbf{c}\cdot\vec{\sigma}) + i(\mathbf{a}\times\mathbf{b})\cdot\mathbf{c}\;\mathbb{1}_2 - (\mathbf{a}\cdot\mathbf{c})(\mathbf{b}\cdot\vec{\sigma}) + (\mathbf{c}\cdot\vec{\sigma})(\mathbf{a}\cdot\mathbf{b}), \tag{2.10}$$

$$\underline{c}_i\underline{c}_i^\dagger = \frac{1}{2}\mathbb{1}_2 - \mathbf{S}_i\cdot\vec{\sigma} \tag{2.11}$$

$$[\underline{c}_1^\dagger\underline{c}_2, \underline{c}_3^\dagger\underline{c}_4] = \underline{c}_1^\dagger\underline{c}_4\delta_{23} - \underline{c}_3^\dagger\underline{c}_2\delta_{14}. \tag{2.12}$$

Since we are interested in higher order corrections due to proximity to the Mott transition, we divide

the spin Hamiltonian with respect to the number of spin operators per term $\mathcal{H}_{(n)} \sim \mathcal{O}(\mathbf{S}^n)$:

$$\mathcal{H} = \mathcal{H}_{(2)} + \mathcal{H}_{(3)} + \mathcal{H}_{(4)} + \dots, \tag{2.13}$$

where finite odd order terms are permitted in the presence of an external magnetic field.

Four-spin ring exchange

Due to time reversal symmetry, only exchange terms with an even number of spins contribute to effective spin Hamiltonians in the absence of an external magnetic field. Hence, the relevant contributions beyond bilinear exchange are four-spin ring exchange terms:

$$\mathcal{H}_{(4)} = \mathbb{P}\mathcal{H}_1\mathbb{R}\mathcal{H}_1\mathbb{R}\mathcal{H}_1\mathbb{R}\mathcal{H}_1\mathbb{P}, \tag{2.14}$$

where $\mathbb{P}$ projects onto the singly occupied ground state and $\mathbb{R}$ is the renormalized projector onto the excited states, analogously defined to Eq. (1.19). In this case, eight-operator terms are important, which can be rearranged using Eq. (2.11) as follows[1]:

$$\begin{aligned}
\underline{c}_i^\dagger\underline{c}_j\underline{c}_j^\dagger\underline{c}_k\underline{c}_k^\dagger\underline{c}_l\underline{c}_l^\dagger\underline{c}_i &= \underline{c}_i^\dagger(\frac{1}{2}\mathbb{1}_2 - \mathbf{S}_j\cdot\vec{\sigma})(\frac{1}{2}\mathbb{1}_2 - \mathbf{S}_k\cdot\vec{\sigma})(\frac{1}{2}\mathbb{1}_2 - \mathbf{S}_l\cdot\vec{\sigma})\underline{c}_i \\
&= \frac{1}{8}\mathbb{1}_2 - \frac{1}{4}\underline{c}_i^\dagger\big[((\mathbf{S}_j\cdot\vec{\sigma}) + (\mathbf{S}_k\cdot\vec{\sigma}) + (\mathbf{S}_l\cdot\vec{\sigma})\big]\underline{c}_i \\
&\quad + \frac{1}{2}\underline{c}_i^\dagger\big[(\mathbf{S}_j\cdot\vec{\sigma})(\mathbf{S}_k\cdot\vec{\sigma}) + (\mathbf{S}_j\cdot\vec{\sigma})(\mathbf{S}_l\cdot\vec{\sigma}) + (\mathbf{S}_k\cdot\vec{\sigma})(\mathbf{S}_l\cdot\vec{\sigma})\big]\underline{c}_i \\
&\quad + \underline{c}_i^\dagger(\mathbf{S}_j\cdot\vec{\sigma})(\mathbf{S}_k\cdot\vec{\sigma})(\mathbf{S}_l\cdot\vec{\sigma})\underline{c}_i.
\end{aligned} \tag{2.15}$$

Only terms with $i \neq j \neq k \neq l$ contribute, since in terms with more than one annihilation and creation operator on the same site either (i) a double occupied state is the result, which vanishes sandwiched in the projectors $\mathbb{P}$, or (ii) a term where $\mathbb{R}$ acts on the ground state is created, which vanishes as well. Then, there are $4! = 24$ finite terms, resulting from permutations of clockwise hopping processes ($i \to j$, $j \to k$, $k \to l$, $l \to i$). In addition, 4! terms contribute from permutations of anti-clockwise hopping ($i \to l$, $l \to k$, $k \to j$, $j \to i$), which represent the Hermitian conjugate terms to the clockwise hopping.

The four-spin ring exchange stems from terms with the product of three Pauli matrices, as can be seen using the Pauli matrix relation given by Eq. (2.10):

$$\begin{aligned}
\underline{c}_i^\dagger(\mathbf{S}_j\cdot\vec{\sigma})(\mathbf{S}_k\cdot\vec{\sigma})(\mathbf{S}_l\cdot\vec{\sigma})\underline{c}_i &= \underline{c}_i^\dagger\big[(\mathbf{S}_j\cdot\mathbf{S}_k)(\mathbf{S}_l\cdot\vec{\sigma}) + i(\mathbf{S}_j\times\mathbf{S}_k)\cdot\mathbf{S}_l\ \mathbb{1}_2 \\
&\qquad - (\mathbf{S}_j\cdot\mathbf{S}_l)(\mathbf{S}_k\cdot\vec{\sigma}) + (\mathbf{S}_l\cdot\vec{\sigma})(\mathbf{S}_j\cdot\mathbf{S}_k)\big]\underline{c}_i \\
&= 4(\mathbf{S}_j\cdot\mathbf{S}_k)(\mathbf{S}_l\cdot\mathbf{S}_i) - 2(\mathbf{S}_j\cdot\mathbf{S}_l)(\mathbf{S}_k\cdot\mathbf{S}_i) + i(\mathbf{S}_j\times\mathbf{S}_k)\cdot\mathbf{S}_l.
\end{aligned} \tag{2.16}$$

The purely imaginary three-spin term cancels with its Hermitian conjugate.

To gain some intuition, we investigate the sum of the four "connected" clockwise hopping processes and the four "connected" anti-clockwise hopping processes. Here, we refer to terms, where each creation operator $\underline{c}_\alpha^\dagger$ matches the index of the annihilation operator on its left $\underline{c}_\alpha$ as "connected". The odd-order terms vanish due to the some with the Hermitian conjugate terms, and the sum follows from index relabelling in Eq. (2.16):

$$\sum_{\substack{\text{conn.}\\ \text{permut.}}} \underline{c}_i^\dagger(\mathbf{S}_j\cdot\vec{\sigma})(\mathbf{S}_k\cdot\vec{\sigma})(\mathbf{S}_l\cdot\vec{\sigma})\underline{c}_i = 16(\mathbf{S}_i\cdot\mathbf{S}_j)(\mathbf{S}_k\cdot\mathbf{S}_l) + 16(\mathbf{S}_i\cdot\mathbf{S}_l)(\mathbf{S}_j\cdot\mathbf{S}_k) - 16(\mathbf{S}_i\cdot\mathbf{S}_k)(\mathbf{S}_j\cdot\mathbf{S}_l). \tag{2.17}$$

The non-connected hopping processes can be related back to these expressions with the commutation relation Eq. (2.12). As a consequence, we have for example:

$$\begin{aligned}
\underline{c}_i^\dagger\underline{c}_j\underline{c}_j^\dagger\underline{c}_k\underline{c}_l^\dagger\underline{c}_i\underline{c}_k^\dagger\underline{c}_l &= \underline{c}_i^\dagger\underline{c}_j\underline{c}_j^\dagger\underline{c}_k\,[(\underline{c}_k^\dagger\underline{c}_l)(\underline{c}_l^\dagger\underline{c}_i) + \underline{c}_l^\dagger\underline{c}_l\delta_{ik} - \underline{c}_k^\dagger\underline{c}_i\delta_{ll}] \\
&= \underline{c}_i^\dagger\underline{c}_j\underline{c}_j^\dagger\underline{c}_k\underline{c}_k^\dagger\underline{c}_l\underline{c}_l^\dagger\underline{c}_i - \underline{c}_i^\dagger\underline{c}_j\underline{c}_j^\dagger\underline{c}_k\underline{c}_k^\dagger\underline{c}_i,
\end{aligned} \tag{2.18}$$

[1] In this section we use a simplified notation, in which the projectors are not explicitly given, e.g. $\mathbb{P}\underline{c}_i^\dagger\underline{c}_j\mathbb{Q}\underline{c}_j^\dagger\underline{c}_k\mathbb{Q}\underline{c}_k^\dagger\underline{c}_l\mathbb{Q}\underline{c}_l^\dagger\underline{c}_i\mathbb{P} \to \underline{c}_i^\dagger\underline{c}_j\underline{c}_j^\dagger\underline{c}_k\underline{c}_k^\dagger\underline{c}_l\underline{c}_l^\dagger\underline{c}_i$, where $\mathbb{Q} = \mathbb{1} - \mathbb{P}$ projects onto the excited states without renormalization.

where we used that $i \neq j \neq k \neq l$ in the singly occupied ground state. With that a "connected" hopping process is expressed on the right-hand side, with additional six-operator contributions. These contributions lead to corrections on the bilinear level. Considering, that there are six possibilities to connect the four hopping processes, the four-spin contribution to the spin Hamiltonian is in total:

$$\mathcal{H}_{(4)} = \frac{1}{S^2} \sum_{\langle ijkl \rangle} K_{\langle ijkl \rangle} \left[(\mathbf{S}_i \cdot \mathbf{S}_j)(\mathbf{S}_k \cdot \mathbf{S}_l) + (\mathbf{S}_i \cdot \mathbf{S}_l)(\mathbf{S}_j \cdot \mathbf{S}_k) - (\mathbf{S}_i \cdot \mathbf{S}_k)(\mathbf{S}_j \cdot \mathbf{S}_l) \right], \tag{2.19}$$

with the ring-exchange parameter $K_{\langle ijkl \rangle}/S^2 = 96\tau_{ij}\tau_{jk}\tau_{kl}\tau_{li}/U^3$. This expression is consistent with the known form of the four-spin ring exchange [118, 119].

Three-spin exchange in a magnetic field

Since we also considered, for the case of κ-Cu, experiments under magnetic field [98, 120], it is furthermore crucial to investigate the influence of a field onto the effective spin Hamiltonian. In the presence of an external magnetic field, exchange terms with an odd number of spins become finite. To lowest order in perturbation theory, third-order hopping processes give then a non-vanishing contribution. The so-called Peierls phase captures the influence of a magnetic field for moving electrons as a phase factor of the hopping parameters:

$$\tau_{ij} = |\tau_{ij}| \, \mathrm{e}^{i a_{ij}} \qquad \text{with} \qquad a_{ij} = q \int_i^j \mathbf{A} \cdot \mathrm{d}\mathbf{l}, \tag{2.20}$$

where $\mathbf{A}$ is the vector potential with $\mathbf{A} = \frac{1}{2}\mathbf{r} \times \mathbf{H}$ for a homogenous magnetic field. The relation $\tau_{ij} = \tau_{ji}^*$ follows directly from Eq. (2.20). The starting point for perturbation theory is the one band Hubbard model with the additional phase on the hopping parameters:

$$\mathcal{H}_{\mathrm{hop}^*,\mathbf{H}} = \sum_{ij} \underline{c}_i^\dagger \tau_{ij} \underline{c}_j + U \sum_i n_{i\uparrow} n_{i\downarrow} + h.c. \tag{2.21}$$

For simplicity, we neglect spin-orbit coupling effects at this point.

In second order, the Peierls phase has no influence on the final result, since it cancels in all contributing terms. We demonstrate this for the isotropic Heisenberg exchange; compare with the result given in Section 1.2:

$$\begin{aligned} M_{\tau\tau^*} =& |\tau_{ij}|^2 \langle \psi_{ij} | \left[\mathrm{e}^{i(a_{ij}+a_{ij})} \, \underline{c}_i^\dagger \underline{c}_j \underline{c}_i^\dagger \underline{c}_j + \mathrm{e}^{i(a_{ij}-a_{ij})} \, \underline{c}_i^\dagger \underline{c}_j \underline{c}_j^\dagger \underline{c}_i \right. \\ & \left. + \mathrm{e}^{i(-a_{ij}+a_{ij})} \, \underline{c}_j^\dagger \underline{c}_i \underline{c}_i^\dagger \underline{c}_j + \mathrm{e}^{-i(a_{ij}+a_{ij})} \, \underline{c}_j^\dagger \underline{c}_i \underline{c}_j^\dagger \underline{c}_i \right] | \psi'_{ij} \rangle \\ =& |\tau_{ij}|^2 \langle \psi_{ij} | \left[1 - 4 \, \mathbf{S}_i \cdot \mathbf{S}_j \right] | \psi'_{ij} \rangle \end{aligned} \tag{2.22}$$

The Peierls phase cancels for the anisotropic matrix elements in the same way.

In contrast, the Peierls phase has a significant effect in third order. Considering only terms that give a finite contribution for singly occupied ground states, there are 3! possibilities of clockwise hopping (permutation of $i \to k$, $k \to j$, $j \to i$) and 3! possibilities of anticlockwise hopping (permutation of $i \to j$, $j \to k$, $k \to i$). With the commutator given by Eq. (2.12) six-operator products (with $i \neq j \neq k$) can be related to each other in the same fashion used for the eight-operator products above:

$$\begin{aligned} \underline{c}_j^\dagger \underline{c}_k \underline{c}_i^\dagger \underline{c}_j \underline{c}_k^\dagger \underline{c}_i &= \left[\underline{c}_j^\dagger \underline{c}_j \delta_{ik} - \underline{c}_i^\dagger \underline{c}_k \delta_{jj} + (\underline{c}_i^\dagger \underline{c}_j)(\underline{c}_j^\dagger \underline{c}_k) \right] \underline{c}_k^\dagger \underline{c}_i \\ &= -\underline{c}_i^\dagger \underline{c}_k \underline{c}_k^\dagger \underline{c}_i + \underline{c}_i^\dagger \underline{c}_j \underline{c}_j^\dagger \underline{c}_k \underline{c}_k^\dagger \underline{c}_i \\ &= -\frac{1}{2} + 2\mathbf{S}_i \cdot \mathbf{S}_k + \underline{c}_i^\dagger \underline{c}_j \underline{c}_j^\dagger \underline{c}_k \underline{c}_k^\dagger \underline{c}_i. \end{aligned} \tag{2.23}$$

The total contribution to third order consists of distinct six terms corresponding to three clockwise and three anti-clockwise hoppings. All six terms have a prefactor of two, since not connected hopping

processes can be translated into these terms via Eq. (2.23). Due to the corresponding permutation of the fermionic operators, the corresponding two-spin terms have to be subtracted:

$$\begin{aligned} M_{\tau\tau\tau^*} = \tau_{ij}\tau_{jk}\tau_{ki}\big\{2\,\langle\psi_{ij}|\,\big[\,&\mathrm{e}^{i(a_{ij}+a_{jk}+a_{ki})}\left(\underline{c}_i^\dagger\underline{c}_j\underline{c}_j^\dagger\underline{c}_k\underline{c}_k^\dagger\underline{c}_i + \underline{c}_k^\dagger\underline{c}_i\underline{c}_i^\dagger\underline{c}_j\underline{c}_j^\dagger\underline{c}_k + \underline{c}_j^\dagger\underline{c}_k\underline{c}_k^\dagger\underline{c}_i\underline{c}_i^\dagger\underline{c}_j\right) \\ &+ \mathrm{e}^{i(-a_{ij}-a_{jk}-a_{ki})}\left(\underline{c}_j^\dagger\underline{c}_i\underline{c}_i^\dagger\underline{c}_k\underline{c}_k^\dagger\underline{c}_j + \underline{c}_i^\dagger\underline{c}_k\underline{c}_k^\dagger\underline{c}_j\underline{c}_j^\dagger\underline{c}_i + \underline{c}_k^\dagger\underline{c}_j\underline{c}_j^\dagger\underline{c}_i\underline{c}_i^\dagger\underline{c}_k\right)\big]\,|\psi'_{ij}\rangle \\ &+ \mathrm{e}^{i(a_{ij}+a_{jk}+a_{ki})}(-\frac{3}{2} + 2\mathbf{S}_i\cdot\mathbf{S}_k + 2\mathbf{S}_i\cdot\mathbf{S}_j + 2\mathbf{S}_j\cdot\mathbf{S}_k) \\ &+ \mathrm{e}^{-i(a_{ij}+a_{jk}+a_{ki})}(-\frac{3}{2} + 2\mathbf{S}_i\cdot\mathbf{S}_k + 2\mathbf{S}_i\cdot\mathbf{S}_j + 2\mathbf{S}_j\cdot\mathbf{S}_k)\big\}. \end{aligned} \tag{2.24}$$

A six operator term with "connected" indices gives with $\underline{c}_i\underline{c}_i^\dagger = \frac{1}{2}\mathbb{1}_2 - \mathbf{S}_i\cdot\vec{\sigma}$ and $(\mathbf{S}_j\cdot\vec{\sigma})(\mathbf{S}_k\cdot\vec{\sigma}) = (\mathbf{S}_j\cdot\mathbf{S}_k) + i(\mathbf{S}_j\times\mathbf{S}_k)\cdot\vec{\sigma}$ (see Eq. (2.9)):

$$\begin{aligned} \underline{c}_i^\dagger\underline{c}_j\underline{c}_j^\dagger\underline{c}_k\underline{c}_k^\dagger\underline{c}_i &= \underline{c}_i^\dagger(\frac{1}{2}\mathbb{1}_2 - \mathbf{S}_j\cdot\vec{\sigma})(\frac{1}{2}\mathbb{1}_2 - \mathbf{S}_k\cdot\vec{\sigma})\underline{c}_i \\ &= \frac{1}{4}\mathbb{1}_2 - \mathbf{S}_j\cdot\mathbf{S}_i - \mathbf{S}_k\cdot\mathbf{S}_i + \underline{c}_i^\dagger(\mathbf{S}_j\cdot\vec{\sigma})(\mathbf{S}_k\cdot\vec{\sigma})\underline{c}_i \\ &= \frac{1}{4}\mathbb{1}_2 - \mathbf{S}_j\cdot\mathbf{S}_i - \mathbf{S}_k\cdot\mathbf{S}_i + \mathbf{S}_j\cdot\mathbf{S}_k + 2i(\mathbf{S}_j\times\mathbf{S}_k)\cdot\mathbf{S}_i. \end{aligned} \tag{2.25}$$

From cyclic permutations of the indices, the other terms in Eq. (2.24) can be evaluated equivalently. The sum of the clockwise hopping processes leads to:

$$\underline{c}_i^\dagger\underline{c}_j\underline{c}_j^\dagger\underline{c}_k\underline{c}_k^\dagger\underline{c}_i + \underline{c}_k^\dagger\underline{c}_i\underline{c}_i^\dagger\underline{c}_j\underline{c}_j^\dagger\underline{c}_k + \underline{c}_j^\dagger\underline{c}_k\underline{c}_k^\dagger\underline{c}_i\underline{c}_i^\dagger\underline{c}_j = \frac{3}{4}\mathbb{1}_2 - \mathbf{S}_i\cdot\mathbf{S}_j - \mathbf{S}_k\cdot\mathbf{S}_j - \mathbf{S}_i\cdot\mathbf{S}_k + 6i\,(\mathbf{S}_i\times\mathbf{S}_k)\cdot\mathbf{S}_j \tag{2.26}$$

Similarly, the sum of the anti-clockwise permutations results in:

$$\underline{c}_j^\dagger\underline{c}_i\underline{c}_i^\dagger\underline{c}_k\underline{c}_k^\dagger\underline{c}_j + \underline{c}_i^\dagger\underline{c}_k\underline{c}_k^\dagger\underline{c}_j\underline{c}_j^\dagger\underline{c}_i + \underline{c}_k^\dagger\underline{c}_j\underline{c}_j^\dagger\underline{c}_i\underline{c}_i^\dagger\underline{c}_k = \frac{3}{4}\mathbb{1}_2 - \mathbf{S}_j\cdot\mathbf{S}_i - \mathbf{S}_k\cdot\mathbf{S}_i - \mathbf{S}_j\cdot\mathbf{S}_k + 6i\,(\mathbf{S}_j\times\mathbf{S}_k)\cdot\mathbf{S}_i \tag{2.27}$$

With the dimensionless flux like quantity $\Phi = \oint_{\partial\mathcal{S}}\mathbf{A}\cdot\mathrm{d}\mathbf{l} = a_{ij}+a_{jk}+a_{ki}$, the matrix element Eq. (2.24) can be expressed as:

$$\begin{aligned} M_{\tau\tau\tau^*} = 2\tau_{ij}\tau_{jk}\tau_{ki}\big\{\,&\mathrm{e}^{i\Phi}\,\big[\frac{3}{4}\mathbb{1}_2 - \mathbf{S}_i\cdot\mathbf{S}_j - \mathbf{S}_k\cdot\mathbf{S}_j - \mathbf{S}_i\cdot\mathbf{S}_k + 6i\,(\mathbf{S}_i\times\mathbf{S}_k)\cdot\mathbf{S}_j \\ &\qquad -\frac{3}{4}\mathbb{1}_2 + \mathbf{S}_i\cdot\mathbf{S}_k + \mathbf{S}_i\cdot\mathbf{S}_j + \mathbf{S}_j\cdot\mathbf{S}_k\big] \\ &+ \mathrm{e}^{-i\Phi}\,\big[\frac{3}{4}\mathbb{1}_2 - \mathbf{S}_j\cdot\mathbf{S}_i - \mathbf{S}_k\cdot\mathbf{S}_i - \mathbf{S}_j\cdot\mathbf{S}_k + 6i\,(\mathbf{S}_j\times\mathbf{S}_k)\cdot\mathbf{S}_i \\ &\qquad -\frac{3}{4}\mathbb{1}_2 + \mathbf{S}_i\cdot\mathbf{S}_k + \mathbf{S}_i\cdot\mathbf{S}_j + \mathbf{S}_j\cdot\mathbf{S}_k\big] \\ = 24\sin\Phi\,\tau_{ij}\tau_{jk}\tau_{ki}\,&\mathbf{S}_i\cdot(\mathbf{S}_j\times\mathbf{S}_k). \end{aligned} \tag{2.28}$$

With $J_\chi/S = 24\sin\Phi\,\tau_{ij}\tau_{jk}\tau_{ki}/U^2$, we obtain the so-called scalar spin chirality term:

$$\mathcal{H}_{(3)} = \frac{1}{S}\sum_{\langle ijk\rangle} J_\chi^{ijk}\,\mathbf{S}_i\cdot(\mathbf{S}_j\times\mathbf{S}_k). \tag{2.29}$$

To ensure reasonable expressions in the $S\to\infty$ limit, we follow the convention to rescale three-spin terms with $1/S$ and four-spin terms with $1/S^2$. In the limit of a vanishing field, the flux vanishes, $\Phi\to 0$, and with that the three-spin term vanishes as well. This is a also a consequence of time reversal invariance of the spin Hamiltonian. The flux is field dependent:

$$\Phi = \frac{q}{\hbar}\mu_B A_{\text{triangle}}\mathbf{H}^{\mathrm{T}}\cdot\mathbf{n}, \tag{2.30}$$

where A_{triangle} is the area of the triangular plaquette of the sites i,j,k and $\mathbf{n}$ is the normal vector to the plaquette. This implies that the scalar spin chirality depends on the field strength and on the direction of the field relative to the sites enclosing Φ

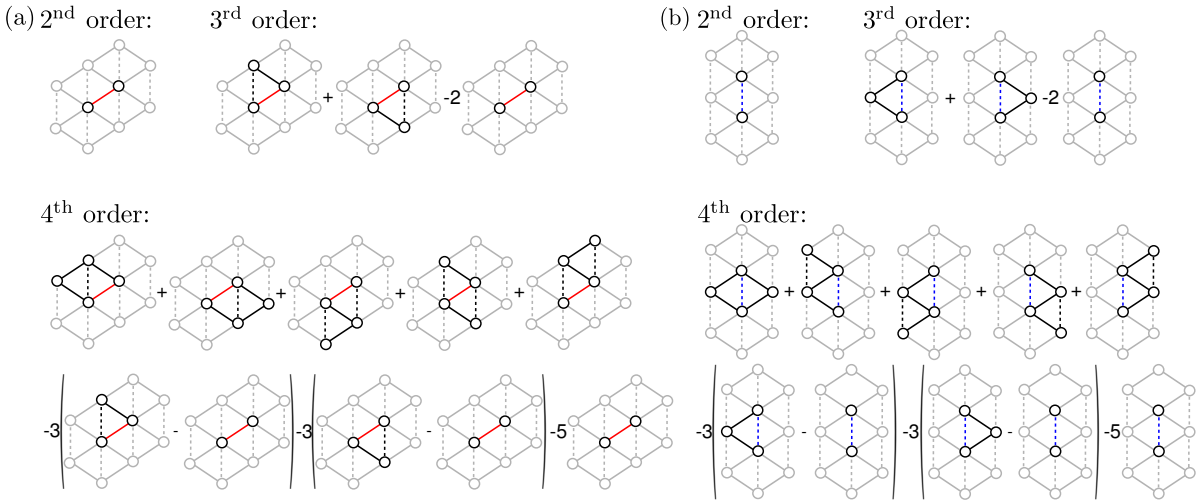

Figure 2.6: Linked cluster expansion up to fourth order for (a) nearest neighbour exchange couplings, marked in red, and (b) next nearest neighbour exchange couplings, marked in blue.

2.5.2 Linked cluster expansion

As mentioned above, in order to incorporate higher order terms, we computed the interactions on up to four dimers. Since these clusters break the symmetry of the crystal, higher order corrections have to be incorporated in a specific scheme. For this, we used the so-called linked cluster expansion [121], where the exchange interactions J are determined by the sum over clusters $\{C\}$:

$$J = \sum_{\{C\}} \tilde{J}_C \qquad \text{with} \qquad \tilde{J}_C = J_C - \sum_{\{C'\}\in C} \tilde{J}_{C'}. \tag{2.31}$$

$\tilde{J}_C$ describes the "pure" contribution of a certain cluster, which is obtained by taking the contriubtion of cluster J_C and substracting the contributions from all subclusters C' within cluster C. This is illustrated in Fig. 2.6 in (a) for the solid bonds and in (b) for the dashed bonds up to fourth order. Here, the order corresponds to the number of considered sites. The 2nd order represents the trivial lowest order for bilinear exchange couplings. In 3rd order, the exchange interaction J, marked in red, is part of two three-site clusters. The "pure" contribution J_C consists of the sum of the exchange on those two clusters, with two times the 2nd order contribution $\tilde{J}_{C'}$ substracted, since the "cluster" from the 2nd order C' appears twice in the 3rd order clusters. At 4th order, the bond marked in red appears in five distinct four-site clusters. In those five clusters each three-site cluster appears three times and the two-site "cluster" five times. The resulting "pure" 4th order contribution J_C is shown in the lower panel of Fig. 2.6(a). The total exchange contribution with corrections up to fourth order is then the sum of those three "pure" contributions. In this case, the two-site contributions cancel and J consists of the sum of the five four-site clusters with two times the three-site cluster substracted. The weight is therefore equivalent to one bond, as expected. With this approach, the crystal symmetry is rehabilitated and hopping processes including paths up to four magnetic sites were taken into account, leading to higher order corrections. Similar methods include the so-called contractor renormalization (CORE) technique [122–124], where the sum of connected clusters with substracted contributions from embedded sub-clusters are used to determine effective Hamiltonians, as well as the more evolved perturbative continuous unitary transformations (pCUT) [125] and continuous unitary transformations (gCUTs) [126].

Note that, in principle, open clusters not considered in Fig. 2.6 could also contribute. For example, a straight three-site line in the third order contribution is in principle also a three-site "cluster" containing the two-site subcluster. However, as mentioned below, these types of open clusters have only a minor influence on the end result.

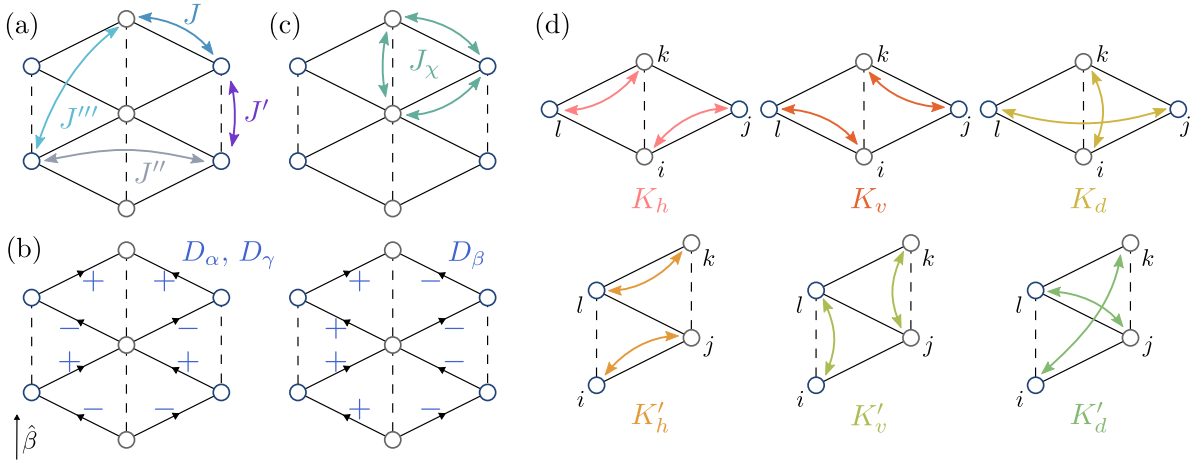

Figure 2.7: Definition of magnetic exchange parameters on anisotropic triangular lattice. (a) Isotropic Heisenberg exchange up to fourth nearest neighbours. (b) Sign of DM interactions with $\hat{\beta} \parallel b$ for $P2_1/c$ materials and $\hat{\beta} \parallel c$ for *Pnma* materials. (c) 3-spin scalar spin chirality exchange J_χ on a triangular plaquette. (d) 4-spin ring-exchange terms on two distinct four site plaquettes. Figure adapted from Ref. [78].

2.5.3 Bilinear spin Hamiltonian

We start the analysis of the concrete Hamiltonian for each investigated material on the level of the bilinear Hamiltonian $\mathcal{H}_{(2)}$. An expression for the most general bilinear spin 1/2 Hamiltonian was introduced in Section 1.2:

$$\mathcal{H}_{(2)} = \sum_{\langle ij \rangle} J_{ij} \left(\mathbf{S}_i \cdot \mathbf{S}_j\right) + \mathbf{D}_{ij} \cdot \left(\mathbf{S}_i \times \mathbf{S}_j\right) + \mathbf{S}_i \cdot \Gamma_{ij} \cdot \mathbf{S}_j. \tag{2.32}$$

In Fig. 2.7(a,b), we show the definitions and symmetry allowed patterns of the Heisenberg and DM interactions. By convention, we label the interaction terms along the solid bonds with J, $\mathbf{D}$, Γ, while the interaction terms along the dashed bonds are indicated with J', $\mathbf{D}'$, Γ'. According to Moriya's rules [49], see also Section 4.2, the presence of an inversion center prevents the DM interaction to be finite. This is the case at the center of the bonds indicated with dashed lines for all four investigated compounds, consequently $|\mathbf{D}'| = 0$. To leading order, the pseudo-dipolar tensor nearly vanishes in this case as well, $||\Gamma'|| \approx 0$, since it is proportional to the DM interaction if Hund's coupling effects are neglected, demonstrated for second order perturbation theory in Section 1.2.

In Table 2.1 we present the bilinear exchange interactions calculated with linked cluster expansion on four-dimer clusters using the hybrid method detailed in Chapter 4. Here, the electronic model obtained from *ab-initio* is the two-orbital Hubbard model including spin-orbit coupling effects, given by the hopping Hamiltonian $\mathcal{H}_{\text{hop}^*}$, defined in Eq. (2.5). The interaction term $\mathcal{H}_{\text{int}}$ is defined in Eq. (2.6) and we used for all four investigated materials the parameter set $U = 0.55\,\text{eV}$, $J_H = 0.2\,\text{eV}$, and $V = 0.15\,\text{eV}$. This is consistent with those computed with cRPA plus MLWO by Nakamura *et al.* [127], but the parameters have been scaled by a factor $\approx 2/3$ after comparison to experiment. The material specific *ab-initio* hopping parameters $t_{1\ldots4}$ and $\vec{\lambda}_{1\ldots4}$ were determined by Stephen M. Winter using the local quantum chemistry package ORCA at the PBE0/def2-VDZ level [128]. The specific values and the procedure how to obtain the spin-dependent hopping parameters are given in the supplemental information of Ref. [77]. Note, that we do not give values for the pseudo-dipolar tensor Γ in Table 2.1, since these are negligibly small on the order of mK.

For the canted Néel compound κ-Cl we found a ratio of $J'/J = 0.34$. This is not surprising, since this ratio corresponds in the phase diagram given in Fig. 2.5(a) to the Néel ordered region, in agreement with experimental observation [104, 105]. Regarding the anisotropic terms, we determined

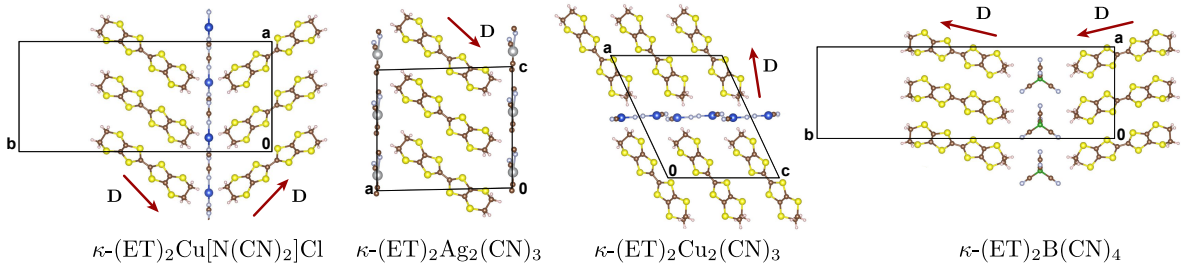

Figure 2.8: Computed orientation of **D** in the plane perpendicular to the 2_1 axis for κ-Cl, κ-Ag, κ-Cu, and κ-BCN. In each case, **D** is nearly along the long axis of the molecule. Figure adapted from Ref. [77].

$|\mathbf{D}| = 5.1\,\mathrm{K}$, which is in very good agreement with the experimental value from ESR measurements [107] with $|\mathbf{D}_{\mathrm{exp}}| = 5.0\,\mathrm{K}$. Also, the orientation is in good agreement with experiment, with the DM vector lying approximately in the a-b plane with an angle toward the a axis $\phi_a = 44.5°$, compared to $\phi_{a,\mathrm{exp}} = 46°$ from the ESR estimate. In Fig. 2.8, we show the orientation of the computed DM interaction for all four investigated compounds. The experimentally confirmed orientation of the DM vector in κ-Cl reveals an almost parallel orientation to the long axis of the ET molecules. Microscopically, this is expected since the hopping vector $\vec{\lambda}$ points approximately along the long axes of the ET molecules and perturbation theory predicts a parallel orientation of the DM interaction, although this is not precisely true in the case of finite Hund's coupling. We therefore confirmed the proposed scenario of a finite DM interaction, inspired by the observation that the magnetic Néel order has a small ferromagnetic contribution resulting in a weak canting of the magnetic moments [104]. The direction of the DM vector shows a staggered (π, π) pattern within the triangular plane and a stripy $(0, \pi)$ pattern along the 2_1 axis, which corresponds to the crystallographic c axis for materials with $Pnma$ space group. This pattern is schematically illustrated in Fig. 2.7(b) for both relevant space groups. With κ-Cl being a relatively uncontroversial material regarding the magnetic properties, we confirmed on that example that the hybrid method works well in the case of the organic κ-$(\mathrm{ET})_2\mathrm{X}$ materials. Next, we apply the procedure to materials with less established experimental facts.

The computed nearest-neighbour Heisenberg parameters for κ-BCN place this material, in agreement with Ref. [108], in the quasi-one dimensional limit with $J'/J = 2.79$. Similarly to κ-Cl, the DM interaction has the smallest contribution along the 2_1 screw axis, placing the vector for the $Pnma$ materials approximately in the a-b plane, with a steeper angle $\phi_a = 76°$ and a similar order of magnitude $|\mathbf{D}| = 4.3\,\mathrm{K}$. Since the quasi one-dimensional character is probably dominant in this regime of the phase diagram, the presence of the DM interaction might have a less significant impact on the magnetic properties of this material. However, we will see in the next chapter, in the context of κ-Cu, that the presence of a staggered DM vector might have influence on other properties like e.g. the response to an external magnetic field. Therefore, the existence of a DM interaction on the order of 5 K might be significant in future studies of low temperature experiments under field or similar circumstances.

The two QSL candidates, κ-Ag and κ-Cu, are indeed computed to be roughly in the isotropic regime

Material	Space Group	C_2	J	J'	J''	J'''	**D**	J'/J
κ-$(\mathrm{ET})_2\mathrm{Cu}[\mathrm{N}(\mathrm{CN})_2]\mathrm{Cl}$	$Pnma$	c	482.0	164.7	38.0	7.9	$(-3.6, -3.6, -0.2)$	0.34
κ-$(\mathrm{ET})_2\mathrm{Ag}_2(\mathrm{CN})_3$	$P2_1/c$	b	250.2	157.8	10.3	3.8	$(-2.9, -0.9, -2.9)$	0.63
κ-$(\mathrm{ET})_2\mathrm{Cu}_2(\mathrm{CN})_3$	$P2_1/c$	b	227.5	268.1	9.5	5.1	$(+3.3, +0.9, +1.0)$	1.18
κ-$(\mathrm{ET})_2\mathrm{B}(\mathrm{CN})_4$	$Pnma$	c	131.1	365.9	1.3	6.1	$(+1.0, +4.2, -0.1)$	2.79

Table 2.1: Space group, crystal axis parallel to C_2 screw axis, bilinear exchange parameters J, J', J'', J''', **D** (defined in Fig. 2.7(a,b)) in K, and ratio of the dominant Heisenberg exchange J'/J.

Material	$J_{(2)}$	$J'_{(2)}$	J	J'	K_h	K_v	K_d	K'_h	K'_v	K'_d
κ-$(ET)_2Cu[N(CN)_2]Cl$	470.9	94.6	482.0	164.7	56.0	51.4	-77.9	20.3	17.2	-24.1
κ-$(ET)_2Ag_2(CN)_3$	235.7	119.6	250.2	157.8	18.9	16.8	-24.1	12.1	11.5	-14.3
κ-$(ET)_2Cu_2(CN)_3$	217.0	219.3	227.5	268.1	16.5	13.6	-21.3	17.0	17.7	-20.5
κ-$(ET)_2B(CN)_4$	110.5	363.1	131.1	365.9	5.15	4.9	-5.5	12.1	14.6	-17.0

Table 2.2: All exchange parameters are given in K. Heisenberg exchange parameters on 2-dimer clusters $J_{(2)}$, $J'_{(2)}$ and for comparison J, J' computed via linked cluster expansion on 4-dimer clusters. 4-dimer ring exchange parameters K and K' as defined in Fig. 2.7(d).

with $J'/J = 0.63$ and $J'/J = 1.18$ respectively[2]. In materials with space group $P2_1/c$, the 2_1 screw axis is parallel to the crystallographic b axis and hence the contribution of the DM interaction is in this direction for both compounds the smallest. The pattern follows the one illustrated in Fig. 2.7(b), with $\hat{\beta} \parallel b$, along the 2_1 screw axis. As can be seen in Fig. 2.8, the DM vector is roughly along the long axes of the ET molecules and lies approximately in the a-c plane. The angle toward the a axis of the projection onto the a-c plane is $\phi_a = 45°$ and $\phi_a = 16.5°$ respectively. The DM interaction is on the same order of magnitude as in the other two salts with $|\mathbf{D}| = 4.2\,\mathrm{K}$ for κ-Ag and $|\mathbf{D}| = 3.5\,\mathrm{K}$ for κ-Cu. We will elaborate in the next chapter on the consequences of a staggered contribution of the DM vector in the case of κ-Cu.

2.5.4 Higher order spin terms

From perturbation theory in (t/U) it becomes obvious that for materials close to the Mott transition, i.e. with $t \sim U$, it might not be sufficient to terminate an effective description at low orders. In the case of the four investigated materials $t_1 \approx 200\,\mathrm{meV}$ (see supplemental material of Ref. [77]), which is the same order of magnitude as the estimated Hubbard repulsion $U = 550\,\mathrm{meV}$. In the picture of effective spin Hamiltonians, $t \sim U$ implies a non-negligible contribution from higher order corrections. For κ-Cu, the results discussed here are published in Ref. [78].

One aspect of these higher order corrections are the importance of hopping processes including more than two dimers for bilinear exchange parameters. As discussed above, we included hopping processes with up to four dimers via the linked cluster expansion. To judge the corrections obtained with this method, we show in Table 2.2 the two dominant Heisenberg exchange couplings computed from two-dimer clusters, $J_{(2)}$ and $J'_{(2)}$, and compare them to the corresponding value obtained from four-dimer clusters. Indeed, in some cases there appear significant corrections, like e.g. in the case of κ-Cl with $(J' - J'_{(2)})/J' = 0.425$. In addition, the significance of the corrections vary from case to case. For example, in the case of κ-BCN there is with $(J' - J'_{(2)})/J' = 0.008$ almost no deviation from the lower order value. We speculate, that this effect stems from cancellation of various correction terms. However, since this cancellation does not seem to appear systematically over the variety of materials, a calculation of higher order corrections seems to be crucial in this class of materials.

In addition to the higher order corrections to bilinear contributions, higher order spin terms like $\mathcal{H}_{(4)}$ in Eq. (2.13), may not be negligibly small in the organic materials. We define the isotropic four spin ring-exchange in terms of the product of Heisenberg exchange like terms on four-dimer plaquettes:

$$\mathcal{H}_{(4)} = \frac{1}{S^2} \sum_{\langle ijkl \rangle} K_{ijkl} (\mathbf{S}_i \cdot \mathbf{S}_j)(\mathbf{S}_k \cdot \mathbf{S}_l). \tag{2.33}$$

The involved plaquette sites in the scalar product determine then the labelling of the exchange parameters according to a horizontal (K_h), vertical (K_v), and a diagonal (K_d) interaction, see also Fig. 2.7(d). For example, on a cluster $\langle ijkl \rangle$ with the shape shown in the upper panel of Fig. 2.7(d), the ring-exchange

[2] Note that a test calculation for κ-Cu including open clusters in the linked cluster expansion gave with $J_{\mathrm{lin}} = 226.1\,\mathrm{K}$ and $J'_{\mathrm{lin}} = 265.6\,\mathrm{K}$ very small corrections to the presented results.

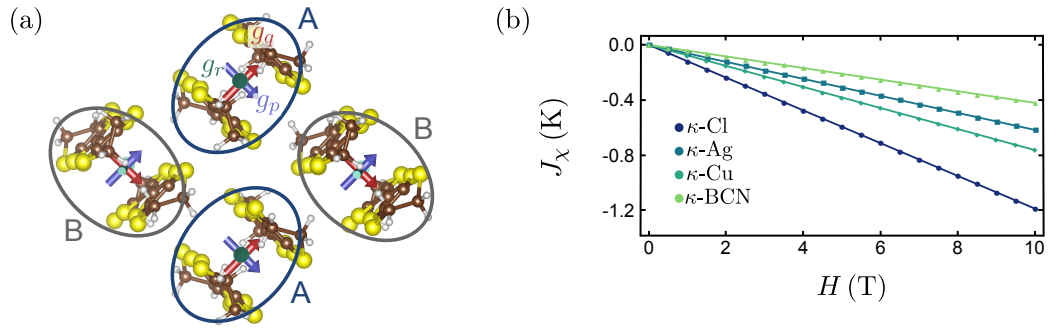

Figure 2.9: (a) Staggered pattern of g tensors in κ-$(ET)_2$ materials, here for κ-Cu. (b) Field dependence of chiral exchange parameter J_χ (K) for a variety of κ-$(ET)_2$ materials, with $\mathbf{H} \parallel \mathbf{n}$ where $\mathbf{n}$ is the out-of-plane unit vector.

term consists of the following contributions:

$$\mathcal{H}_{\langle ijkl\rangle} = \frac{1}{S^2}\left[K_h(\mathbf{S}_i\cdot\mathbf{S}_j)(\mathbf{S}_k\cdot\mathbf{S}_l) + K_v(\mathbf{S}_i\cdot\mathbf{S}_l)(\mathbf{S}_j\cdot\mathbf{S}_k) + K_d(\mathbf{S}_i\cdot\mathbf{S}_k)(\mathbf{S}_j\cdot\mathbf{S}_l)\right]. \tag{2.34}$$

This is why the ring-exchange term is also often defined in terms of permutation operators in the literature. For instance, in Ref. [25] the term $\frac{K}{S^2}\sum_{\langle ijkl\rangle}(\hat{P}_{ijkl}+\hat{P}_{lkji})$ is introduced among others. Here, the operator $\hat{P}_{ijkl} = \hat{P}_{ij}\hat{P}_{jk}\hat{P}_{kl}$ cyclically permutes four spins around a plaquette with $\hat{P}_{ij} = 2\mathbf{S}_i\cdot\mathbf{S}_j + \frac{1}{2}$. The normalization with S^2 is chosen to keep a meaningful classical limit for $S\to\infty$, where the two-spin exchange would otherwise be negligible compared to the four-spin terms. We follow the same convention in this thesis. Writing the four spin ring-exchange term in terms of the permutation operators implies $K_h = K_v = -K_d$ and also the relation $K' = \frac{J'}{J}K$, as it follows from Eq. (A.7), detailed in Appendix A. This relation was assumed in previous works, in which ring-exchange terms have been considered [25, 92]. However, these relations are not enforced by symmetry. Interestingly, as shown in Table 2.2, we found that such relations do not hold when considering the full electronic structure of the dimers.

The ring-exchange results for the four investigated materials are given in Table 2.2. The strongest contribution from ring-exchange is found for κ-Cl. However, considering the phase diagram from semi-classical calculations by Holt *et al.* [25], shown in Fig. 2.5(c), a significant ring-exchange is unlikely to drive the system out of the Néel ordered state, which is in agreement with the experimental observation. In case of the QSL candidate materials, ring-exchange has a better chance to play a significant role. Close to the isotropic point $J = J'$, the semiclassical calculation suggests that a finite ring-exchange drives the system out of a magnetically ordered spiral phase into the spin liquid phase. Using average values for the ring exchange and the relation to the notation used in Ref. [25] given by Eq. (2.7) and Eq. (2.8), κ-Cu should be placed at $J'_{\mathrm{Holt}}/J_{\mathrm{Holt}} = 1.2$ and $K_{\mathrm{Holt}}/J_{\mathrm{Holt}} = 0.07$, while κ-Ag should be placed at $J'_{\mathrm{Holt}}/J_{\mathrm{Holt}} = 0.55$ and $K_{\mathrm{Holt}}/J_{\mathrm{Holt}} = 0.08$. Both materials enter with these values the QSL phase in Fig. 2.5(c), although they appear rather close to magnetically ordered phases. However, it should be kept in mind that structural and numerical uncertainties hamper this method to give a precise answer to such an accuracy. Nevertheless, our calculations confirmed the general importance of four spin ring-exchange effects especially with regard to the experimentally observed suppression of magnetic order in the two QSL candidate materials. Another interesting observation is that the ring-exchange in κ-Ag seems to be only suppressed on the four-site plaquette indicated with K', although the initial motivation to investigate this material was to increase the distance to the Mott transition [109]. This is yet another case where we find that the higher order corrections are difficult to predict solely based on the electronic Hubbard model, implicating the importance of the inner dimer structure.

As mentioned above, the presence of an external magnetic field allows for finite odd spin terms in

Material	(g_p, g_q, g_r)	$\hat{p}$	$\hat{q}$	$\hat{r}$
κ-Cl	$(2.0028, 2.0085, 2.0099)$	$(+0.7, \pm 0.5, -0.6)$	$(-0.4, \mp 0.5, -0.8)$	$(\mp 0.7, +0.7, \mp 0.1)$
κ-Ag	$(2.0026, 2.0078, 2.0101)$	$(\mp 0.4, +0.5, +0.8)$	$(-0.7, \mp 0.7, \pm 0.1)$	$(\pm 0.6, -0.5, +0.6)$
κ-Cu	$(2.0024, 2.0075, 2.0102)$	$(+0.1, -0.1, \pm 1.0)$	$(\pm 0.7, \mp 0.7, -0.1)$	$(+0.7, +0.7, \pm 0.1)$
κ-BCN	$(2.0024, 2.0071, 2.0097)$	$(\mp 0.6, \pm 0.7, \pm 0.4)$	$(\pm 0.1, \mp 0.4, \pm 0.9)$	$(+0.8, +0.6, +0.2)$

Table 2.3: Computed local g-tensors for the four investigated materials in terms of the principal axes $\hat{p}$, $\hat{q}$, $\hat{r}$, illustrated in Fig. 2.9(a). The upper sign corresponds to sublattice sites A, the lower sign to sublattice sites B.

the Hamiltonian. To lowest order, this manifests in the Zeeman term:

$$\mathcal{H}_{(1)} = \mu_B \mathbf{H}^{\mathrm{T}} \cdot \sum_i \mathbb{G}_i \cdot \mathbf{S}_i, \tag{2.35}$$

where $\mathbb{G}_i$ is the local g tensor on dimer i. Spin-orbit coupling effects may cause anisotropy in the g tensor. In the case of the κ-$(\mathrm{ET})_2\mathrm{X}$ materials, the direction of the g tensor is sublattice dependent, as illustrated in Fig. 2.9(a), with the sublattices labelled A and B. Due to symmetry, the local g tensor can be expressed in terms of a uniform $\mathbb{G}_u$ and a staggered $\mathbb{G}_s$ component:

$$\mathbb{G}_i = \mathbb{G}_u + \eta_i \mathbb{G}_s \tag{2.36}$$

$$\eta_i = \begin{cases} +1 & i \in \text{sublattice A} \\ -1 & i \in \text{sublattice B} \end{cases} \tag{2.37}$$

We computed the g tensor for the four materials with the quantum chemistry package ORCA on isolated dimers at the PBE0/IGLO-III level [128, 129]. The results are summarized in Table 2.3. They are almost indistinguishably similar for all four components with the largest value $g_r \approx 2.010$ along the long axis of the ET molecules, the second largest $g_q \approx 2.008$ along the axis connecting two ET molecules within a dimer, and the smallest $g_p \approx 2.002$ along the short axis of an ET molecule. Due to the light C, S, H atoms in an ET molecule, the relativistic effects are relatively weak. However, we will see in the next chapter that a small deviation from the isotropic case can have a significant impact on the response of the material under the right circumstances.

The next lowest odd spin term is the so-called scalar spin chirality [90] with the three-spin term $\mathcal{H}_{(3)}$. In Section 2.5.1 we derived this term from third order perturbation theory, where the presence of a magnetic field is captured through a modification of the electronic Hamiltonian through the Peierls phase, as given by $\mathcal{H}_{\mathrm{hop}^*,\mathbf{H}}$ defined in Eq. (2.21). From cluster exact diagonalization on three-dimer clusters we computed the scalar spin chirality term:

$$\mathcal{H}_{(3)} = \frac{1}{S} \sum_{\langle ijk \rangle} J_\chi^{ijk} \mathbf{S}_i \cdot (\mathbf{S}_j \times \mathbf{S}_k), \tag{2.38}$$

as a function of the external magnetic field. To capture the largest possible contribution, the direction of the field $\mathbf{H}$ was chosen parallel to the out-of-plane unit vector $\mathbf{n}$. Due to $J_\chi \propto \mathbf{H}^{\mathrm{T}} \cdot \mathbf{n}$, this is the maximal contribution possible. The perturbation theory result suggested a linear dependence of the exchange parameter J_χ on the external field. As demonstrated in Fig. 2.9(b), this linear dependence is not broken by higher order corrections included in the cluster diagonalization. To simplify comparison, we introduce here another notation to introduce a field-independent exchange parameter. For this we assume a perfect linear dependence on the field and use for the flux the following approximation:

$$\Phi = \frac{q}{\hbar} \mu_B A_{\langle ijk \rangle} \mathbf{H}^{\mathrm{T}} \cdot \mathbf{n}. \tag{2.39}$$

where $A_{\langle ijk \rangle}$ is the area of the plaquette $\langle ijk \rangle$. The scalar spin chirality can then be expressed as:

$$\mathcal{H}_{(3)} = -\mu_B j_\Phi (\mathbf{H}^{\mathrm{T}} \cdot \mathbf{n}) \sum_{\langle ijk \rangle} \tilde{\mathbf{S}}_i \cdot (\tilde{\mathbf{S}}_j \times \tilde{\mathbf{S}}_k), \tag{2.40}$$

with the dimensionless plaquette operator:

$$j_\Phi = -\frac{1}{S}\frac{q}{\hbar}\frac{A_{\langle ijk\rangle}}{\Phi}J_\chi^{ijk}, \tag{2.41}$$

which is independent of the field for $J_\chi^{ijk} \propto \Phi$. For κ-Cu, we estimate $\mu_B j_\Phi/k_B \sim 0.03\,\mathrm{K/T}$. Due to the small flux Φ in one triangular plaquette, the values for all four κ-phase materials are relatively small. Nevertheless, in a critical region the anisotropy due to the dependence on the field direction may influence the magnetic response of a system.

2.6 Summary

In this chapter, we presented the determination of effective spin Hamiltonians for four anisotropic lattice organics. The method of choice was a "hybrid" approach of *ab-initio* and many-body methods, for the specific details of the method we refer also to Chapter 4. This approach is especially powerful in the treatment of anisotropic interactions caused by spin-orbit coupling, and terms with a higher power in spins like the four-spin ring exchange discussed in this chapter, because it has no intrinsic difficulties with interactions having widely different orders of magnitude. These higher order terms are suspected to have significant influence in the κ-ET salts, due to proximity to the Mott transition and anisotropic influence on low-temperature properties.

Since the extended Hubbard Hamiltonian is an essential ingredient of the hybrid method, we discussed specialities in the case of the κ-$(ET)_2X$ family. Especially consideration of the intradimer structure and opportunities to save computational effort in the *ab-initio* determination of hopping parameters by taking advantage of certain symmetry relations. In Section 2.3, we discussed the known experimental facts for the four investigated materials, including the seemingly contradicting observations in the case of κ-Cu. The influence of the different magnetic exchange terms of the anisotropic triangular lattice with antiferromagnetic exchange was reviewed in Section 2.4, by discussing known phases from the literature. Tuning exchange parameters promises to drive a system from a (π, π) order on a square lattice, through the 120° order on the isotropic triangular lattice, to spin liquid like behaviour in the one-dimensional limit. In addition, significant four-spin ring exchange is suspected to suppress magnetic order.

In Section 2.5, we presented the concrete calculations for the four compounds investigated in this chapter. To obtain insight about the higher order terms, we extended the second order perturbation theory, discussed in Chapter 1, to higher orders and considered in addition the effects of an external magnetic field via the Peierls phase. Since four-dimer clusters break in general the crystal symmetry, we first introduced the linked cluster expansion, which was used to restore the symmetry for the final magnetic model Hamiltonian. As a representative of the square lattice limit, we discussed then κ-Cl (κ-$(ET)_2Cu[N(CN)_2]Cl$), confirming exchange parameters that match the experimental observation of magnetic Néel order and a small spin canting due to a finite DM interaction. The order of magnitude and the angle of the Dzyaloshinskii-Moriya vector agreed very well with the experimentally determined values by ESR. The significant ring-exchange is not expected to influence the magnetic order strongly for these ratios of J'/J. Anisotropic contributions under field from a local g-tensor and scalar spin chirality are present and should be considered in experiments under field. The quasi one-dimensional limit was covered by κ-BCN (κ-$(ET)_2B(CN)_4$), consistent with the original proposal of reduced dimensionality. The influence of the finite DM interaction may be considered in future studies of this compound. The ring-exchange was found to be small compared to the dominant Heisenberg exchange and is therefore considered as less important in this particular compound. For the two QSL candidates κ-Ag (κ-$(ET)_2Ag_2(CN)_3$) and κ-Cu (κ-$(ET)_2Cu_2(CN)_3$), we found approximately isotropic Heisenberg exchange with a significant contribution of four-spin ring exchange. This provides a possible explanation for the experimentally observed suppression of magnetic order. Interestingly, for κ-Ag we found a more significant ring exchange than expected for a compound with smaller hopping amplitudes than its sister compound κ-Cu. The anisotropic terms in κ-Cu, especially the pattern and magnitude of the DM interaction and the local g-tensor, will be the basis of the investigation presented in the next chapter, where we will tackle some of the mysteries of κ-Cu, the $T_* = 6\,\mathrm{K}$ anomaly and the contradicting QSL classifications based on thermal transport - as a gapped QSL - and on specific heat - as a gapless QSL.

Chapter 3

Criticality vs. Valence Bond Glass scenario in κ-Cu

Kira Riedl, Roser Valentí, and Stephen M. Winter
Critical spin liquid versus valence-bond glass in a triangular-lattice organic antiferromagnet,
Nat. Commun. **10**, 2561 (2019)
[78]

3.1 Introduction

With the effective spin Hamiltonian established, we present in this chapter the corresponding consequences for the magnetic response in the case of κ-Cu (κ-$(ET)_2Cu_2(CN)_3$). As one of the most promising QSL candidates it has been the subject of intensive experimental studies for more than a decade, as briefly described in Section 2.3. Despite those efforts, a number of mysteries about this compound remain unsolved. Arguably the most prominent puzzle is the $T_* = 6\,\mathrm{K}$ anomaly [32, 36–38, 130–134], which has proven to be notoriously difficult to solve. Moreover, there are the seemingly contradicting experimental results, where specific heat reveals features of a gapless QSL nature [37], while thermal transport shows signatures of a gap [38]. One attempt to explain the mysterious behaviour of κ-Cu was the proposal of a low-temperature quantum critical scenario, inspired by unconventional scaling of the μSR linewidth as a function of magnetic field [98]. This idea was further pushed in the context of magnetic torque measurements where the corresponding torque susceptibility showed unconventional scaling in terms of field and temperature [120].

In this chapter, we present the theoretical analysis of the magnetic response in the framework of such a critical scenario, on the basis of the previously determined model Hamiltonian for κ-Cu. While in the case of the μSR data this scenario gives compelling agreement, we will show that a number of features in the torque response cannot be reconciled with criticality. Instead, we propose an alternative scenario, in which local "orphan" spins dominate the low-temperature response of κ-Cu. In this scenario, κ-Cu is understood as a "vanilla" QSL with resonating valence bonds above T_*. For $T < T_*$, the valence bonds freeze, leading to a valence bond glass (VBG) state. In such a host system, non-magnetic vacancies and structural inhomogeneity can lead to localized magnetic moments, which may dominate the magnetic response of the compound at low temperature. In the case of κ-Cu, this scenario provides a consistent explanation of the features observed in the torque experiment and offers a possible interpretation of the T_* anomaly, as well as the seemingly contradicting results from specific heat and thermal transport experiments.

This chapter is organized as follows. First, we briefly introduce the concept of criticality and the experimentally observed unconventional exponents of the μSR linewidth $B_e \propto m$ [98] and torque susceptibility χ_τ [120] as a function of magnetic field H, which were interpreted as exotic critical exponents. In Section 3.3, we demonstrate how anisotropic interactions can be "gauged" away if certain symmetry

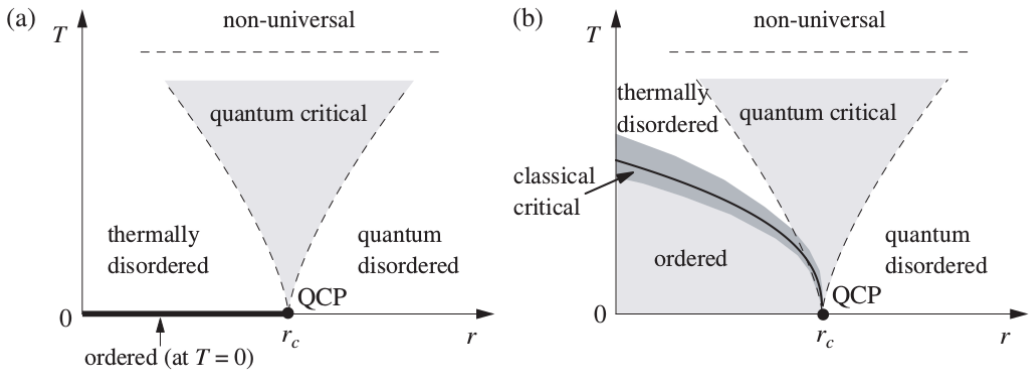

Figure 3.1: Schematic phase diagrams of a critical scenario as a function of the tuning parameter r and temperature T from the review article by Matthias Vojta [135]. While the quantum critical fan is a general feature of the phase diagrams, at low temperatures it is distinguished between models (a) without order and (b) with order at finite temperature. Fig. reprinted from Ref. [135].

restrictions are met. This framework is extremely useful in the analysis of magnetization m and susceptibility χ, circumventing the challenge to solve arbitrarily complicated Hamiltonians. We apply this concept then in Section 3.4, where we discuss the scaling of m and χ in a critical scenario for κ-Cu. While the μSR linewidth can be explained through the presence of anisotropic interactions, a number of the experimentally observed features in the magnetic torque are absent. Finally, in Section 3.5, we propose the valence bond glass scenario and theoretically analyse the corresponding implications.

The analysis in the context of the μSR response is published in Ref. [77], the analysis regarding the magnetic torque response is published in Ref. [78].

3.2 Criticality and observed unconventional exponents

The critical scenario for κ-Cu was proposed based on the experimental observations in μSR [98] and the magnetic torque response [120]. In the center of the analysis was the interpretation of the measured data in terms of exotic critical exponents. Before we discuss these interpretations, we introduce first briefly the concept of criticality and critical exponents.

3.2.1 The concept of quantum criticality

The subject of criticality and quantum phase transitions is detailed in many textbooks and review articles, e.g. Ref. [135–139]. Here, we introduce briefly the basic ideas with focus on the concept of critical exponents and refer for further reading to the mentioned references.

A quantum phase transition occurs at a quantum critical point (QCP), which can be reached by tuning some parameter r. For simplicity, we consider a hypothetical Hamiltonian $\mathcal{H} = \mathcal{H}_0 + r\mathcal{H}_1$ with non-degenerate energy spectrum and where $\mathcal{H}_0$ and $\mathcal{H}_1$ commute. In this case, $\mathcal{H}_0$ and $\mathcal{H}_1$ have a shared set of eigenstates that is independent of r. However, the eigenenergies can be tuned through r, so that one can imagine some critical value r_c with a level-crossing of the two lowest eigenenergies. Therefore, ground state energy as a function of r is non-analytic at r_c. Such a non-analyticity is the observable signature for a quantum phase transition. In the more general case, where $\mathcal{H}_0$ and $\mathcal{H}_1$ do not commute, the quantum phase transition is defined analogously. However, note that in this case the non-analyticity can only be realized for infinite lattice sizes. The gap between the energy of the ground state and the first excited state is then the relevant energy scale for such a critical system.

Since these considerations refer to the ground state, a quantum critical point is only well-defined for $T = 0$. For finite temperatures, the interplay between quantum and thermal fluctuations leads to finite temperature crossovers, enclosing a quantum critical fan, as depicted in Fig. 3.1. In this region,

the physics is controlled by thermal excitations of the quantum critical ground state. In the case of systems that do not order at finite temperature, illustrated in Fig. 3.1(a), the remaining regions are dominated either only by thermal fluctuations, in the thermally disordered region ($T \gg |r - r_c|$), or only by quantum fluctuations, in the quantum disordered region ($r - r_c \gg T$; $r > r_c$). In the case of order at finite temperature, illustrated in Fig. 3.1(b), it is necessary to consider additionally a region where the order is destroyed by thermal fluctuations. Since in this case asymptotically close to the phase transition the thermal fluctuations always dominate the critical behaviour of the system, the phase transition can be described entirely classical.

Within the quantum critical fan, due to the non-analyticity of the ground state energy, several thermodynamic observables exhibit diverging power-law behaviour. Such power laws are characterized by the so-called critical exponents. If $g = |r - r_c|$ measures the distance to the QCP, then the thermodynamic observables behave for $g \to 0$ as follows:

$$f_s \propto g^{2-\alpha}, \tag{3.1}$$

$$m \propto g^{\beta}, \tag{3.2}$$

$$\chi \propto g^{-\gamma}, \tag{3.3}$$

$$m(H, g = 0) \propto H^{1/\delta}, \tag{3.4}$$

with the free energy density f_s, the order parameter of the ordered phase m and the susceptibility χ. Note, that in the case of the order parameter there is a distinction between the critical exponent β, corresponding to the control parameter g, and the critical exponent δ, corresponding to the conjugate field at the critical point ($g = 0$). Therefore, the choice of labelling already implies a statement about the nature of the control parameter. This will be important in the context of the critical scenario for κ-Cu. When the system approaches a quantum critical point, the correlation length ξ diverges and fluctuations occur on all scales, so that the system is scale invariant. The critical behaviour of a material is in this case independent of microscopic details and hence materials can be divided into universality classes according to their critical exponents. Very different physical systems may be a member of the same universality class.

3.2.2 Proposed critical exponents for κ-Cu

In 2011, Pratt *et al.* [98] proposed, based on μSR and NMR experiments, an H-T phase diagram for κ-Cu, shown in Fig. 3.2(a). The authors introduced a critical field H_c, above which the transverse-field μSR linewidth becomes field-dependent. Field-dependent scans of this linewidth at different temperatures gave then a series of $H_c(T)$ points that determine the phase boundary between quantum critical (QC) and weakly antiferromagnetic (WAF) phases. The authors argued that a small magnetic field, with $H > H_0$, induces a quantum phase transition between a gapped spin-liquid (GS) phase and a low-field $\mathrm{WAF_L}$ phase. They proposed a Bose-Einstein condensation of spin excitations with an extremely small spin gap as a possible explanation. With a fit to a two-dimensional BEC model for the phase boundary shape in the H-T diagram, the QCP was located for $T = 0$ at $H_0 = 5.2\,\mathrm{mT}$. At higher field, with $H = H_1$, they suggested a second transition to a high-field $\mathrm{WAF_H}$ phase. In this critical scenario, where the field takes the role of the tuning parameter that drives the system through the QCP, the magnetization can be expressed with respect to the external magnetic field via the critical exponent β, as introduced above. The authors argued that the μSR linewidth is proportional to the local magnetization, $B_e \propto m$, which was interpreted as an order parameter, so that it obeys the following scaling relation:

$$B_e \propto (H - H_c)^{\beta}. \tag{3.5}$$

From a fit of the experimental data at $T = 0.8\,\mathrm{K}$, shown in Fig. 3.2(b), the authors extracted a critical exponent in the low field region with $\beta_L \approx 0.36$. They identified for the second QCP $H_1 \approx 4\,\mathrm{T}$, where the field dependence of B_e changes drastically yielding a high-field critical exponent $\beta_H \approx 0.83$. The fitting shown in Fig. 3.2(b) suggests a crossover from the low-field critical exponent β_L to the high-field critical exponent β_H, which was interpreted as an indication for an exotic quantum critical point.

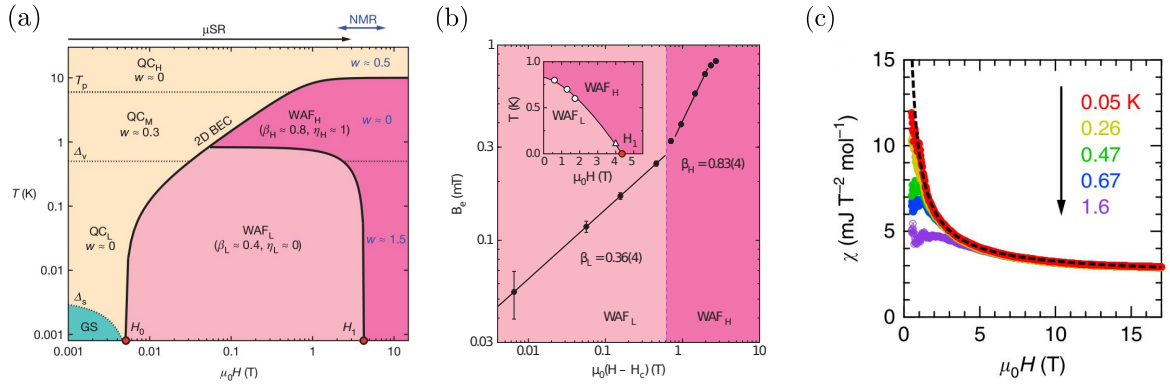

Figure 3.2: (a) H-T phase diagram for κ-Cu, proposed by Pratt *et al.* [98] based on μSR and NMR experiments. The authors identify a weakly antiferromagnetic (WAF) phase, a quantum critical (QC) region and assign gapped spin-liquid (GS) phase. (b) Scaling of μSR linewidth as a function of field [98], where two different regions are identified according to different critical exponents [98]. (c) Experimental field dependence of torque susceptibility [120], diverging at low fields. The dashed line corresponds to the fitted curve $\chi(H) \propto H^{-p}$ with $p = 0.83$. Fig. (a,b) reprinted from Ref. [98], Fig. (c) reprinted from Ref. [120].

In 2016, Isono *et al.* [120] also proposed a critical scenario for κ-Cu under field, inspired by the results of their magnetic torque measurements. For an illustration of a magnetic torque setup, see also Fig. 3.6(a). If the investigated compound contains anisotropic features, a rotated magnetic field $\mathbf{H}$ leads to the observation of an angle-dependent magnetic torque $\tau(\theta)$. The authors of Ref. [120] reported a sinusoidal angle dependence $\tau \propto \sin 2(\theta - \theta_0)$ with an angle shift θ_0 that increases for low temperatures and fields. The extracted torque susceptibility $\chi_\tau = \tau/H^2$ as a function of field is shown in Fig. 3.2(c). Fitting of the susceptibility to a generic formula $\chi(H) \propto H^{-p}$ revealed a scaling exponent $p = 0.83$. These findings were interpreted in terms of a zero-field QCP with a field-induced spin liquid regime. The authors identified a low-field, low-temperature regime below $H = 1\,\mathrm{T}$ and $T = 0.1\,\mathrm{K}$ as a weak AF ordered phase, where the above identified scaling is violated, and proposed a field-induced QSL regime for low enough temperatures up to fields $H = 10\,\mathrm{T}$.

3.3 Coupling to a magnetic field for κ-$(ET)_2X$ materials

The critical scenario proposed in Ref. [98, 120] is based on the assumption that in the case of κ-Cu the tuning parameter r is the magnetic field $\mathbf{H}$. In order to analyze the consequences in a complete fashion, anisotropic interactions, as determined in the previous chapter, have to be considered. To enable an effective treatment of these interactions, we follow in this section a strategy described by Shekhtman *et al.* [140] in 1992. There, the authors proposed that under specific circumstances it is possible to "gauge" the anisotropic interactions away by local rotations of the coordinate system. The price to pay for such an effective picture is an additional term in the magnetic field part. Since the Zeeman term contains only single-spin terms, this simplifies solving the Hamiltonian significantly.

3.3.1 Anisotropic interactions in a magnetic field

Our starting Hamiltonian is the most general nearest neighbour spin 1/2 Hamiltonian, without an external magnetic field:

$$\mathcal{H} = \sum_{ij} J_{ij}\mathbf{S}_i \cdot \mathbf{S}_j + \mathbf{D}_{ij} \cdot (\mathbf{S}_i \times \mathbf{S}_j) + \mathbf{S}_i \cdot \Gamma_{ij} \cdot \mathbf{S}_j. \tag{3.6}$$

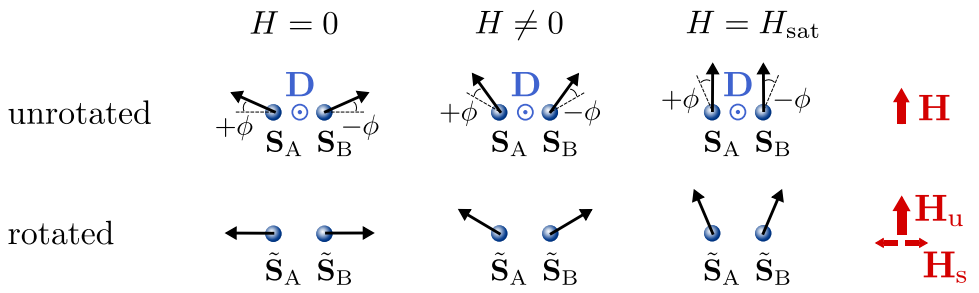

Figure 3.3: Local rotations of each spin about the canting angle ϕ, so that the DM interaction is gauged away. Fig. adapted from Ref. [78].

In order to gauge the anisotropic interactions away, the strategy is to apply local rotations to each spin. This is illustrated in the left panel of Fig. 3.3 for a hypothetical case with an out-of-plane DM vector. Since each site "feels" four Dzyaloshinskii-Moriya interactions, a requirement onto this strategy is, that the local rotation has to be consistent for the four attached bonds, indicated by solid lines in the previous chapter. As it turns out, this is the case for a uniform and for a staggered (π, π) DM pattern[1]. For DM configurations in a $(\pi, 0)$ or $(0, \pi)$ configuration, it is *not* be possible to find local transformations that gauge away all anisotropic interactions consistently.

An important approximation for the following derivation is the negligence of Hund's coupling effects. With $J_H = 0$, the symmetric pseudo-dipolar tensor can be expressed in terms of the DM vector, as can be seen easily from the second order perturbation theory results in Section 1.2, $\Gamma \propto \mathbf{D} \otimes \mathbf{D}$.

To determine which local rotations eliminate explicit anisotropic spin-spin interactions, we consider the sublattice dependent canting angle $(\eta_i \phi)$, where we use the previously introduced sublattice dependent parameter from Section 2.5:

$$\eta_i = \begin{cases} +1 & i \in \text{sublattice A} \\ -1 & i \in \text{sublattice B} \end{cases} \tag{3.7}$$

In order to find an expression for the canting angle, we consider a simple classical picture in which the energy on a bond depends only on the angle between the two spins on the two sublattices A and B:

$$E = J|\mathbf{S}_\mathrm{A}||\mathbf{S}_\mathrm{B}| \cos\varphi + |\mathbf{D}||\mathbf{S}_\mathrm{A}||\mathbf{S}_\mathrm{B}| \sin\varphi. \tag{3.8}$$

The Γ term has no contribution in the plane perpendicular to the DM vector due to $\Gamma = \mathbf{D} \otimes \mathbf{D}$. The expression of the energy Eq. (3.8) is minimized for:

$$\begin{aligned} J \sin\varphi - |\mathbf{D}| \cos\varphi &= 0 \\ \tan\varphi &= \frac{|\mathbf{D}|}{J}. \end{aligned} \tag{3.9}$$

As illustrated in Fig. 3.3 in the unrotated picture, the angle between the spins in terms of the canting angle is $\varphi = \pi - 2\phi$. In second order perturbation theory, see Eq. (1.40), the ratio of DM and Heisenberg interaction in terms of hopping parameters is given by:

$$\frac{|\mathbf{D}|}{J} = \frac{2\tau|\vec{\lambda}|}{\tau^2 - |\vec{\lambda}|^2} = \frac{2\tau/|\vec{\lambda}|^2}{\tau^2/|\vec{\lambda}|^2 - 1} \tag{3.10}$$

Together with the trigonometric relation $\tan\varphi = -\tan(2\phi) = -\frac{2\tan\phi}{1-\tan^2\phi} = \frac{2\tan\phi}{\tan^2\phi - 1}$, we obtain for the canting angle the following expression:

$$\phi = \arctan\left(\frac{\tau}{|\vec{\lambda}|}\right). \tag{3.11}$$

[1]The wave vectors for the DM patterns such as (π, π) in the staggered case are given with respect to the square lattice.

Using Rodrigues' rotation formula we get for the two spins of one bond the transformation rules:

$$\mathbf{S}_i = (1-\cos\phi)[\mathbf{d}\cdot\tilde{\mathbf{S}}_i]\mathbf{d} + \cos\phi\tilde{\mathbf{S}}_i + \eta_i \sin\phi\,\tilde{\mathbf{S}}_i \times \mathbf{d}, \tag{3.12}$$

where $\tilde{\mathbf{S}}$ is in the global coordinate system and $\mathbf{S}$ is locally rotated.

Rotating the Heisenberg term leads to a contribution to the Heisenberg term in the rotated system, as well as to the effective DM interaction and the effective pseudo-dipolar tensor:

$$\begin{aligned}\mathbf{S}_\mathrm{A}\cdot\mathbf{S}_\mathrm{B} = {}& (1-\cos\phi)^2[\mathbf{d}\cdot\tilde{\mathbf{S}}_\mathrm{A}]\mathbf{d}[\mathbf{d}\cdot\tilde{\mathbf{S}}_\mathrm{B}]\mathbf{d} + (1-\cos\phi)\cos\phi[\mathbf{d}\cdot\tilde{\mathbf{S}}_\mathrm{A}]\tilde{\mathbf{S}}_\mathrm{B}\cdot\mathbf{d} \\ & - (1-\cos\phi)\sin\phi[\mathbf{d}\cdot\tilde{\mathbf{S}}_\mathrm{A}]\mathbf{d}\cdot(\tilde{\mathbf{S}}_\mathrm{B}\times\mathbf{d}) + \cos\phi(1-\cos\phi)\tilde{\mathbf{S}}_\mathrm{A}[\mathbf{d}\cdot\tilde{\mathbf{S}}_\mathrm{B}]\cdot\mathbf{d} \\ & + \cos^2\phi\,\tilde{\mathbf{S}}_\mathrm{A}\cdot\tilde{\mathbf{S}}_\mathrm{B} - \cos\phi\sin\phi\,\tilde{\mathbf{S}}_\mathrm{A}\cdot(\tilde{\mathbf{S}}_\mathrm{B}\times\mathbf{d}) + \sin\phi(1-\cos\phi)[\mathbf{d}\cdot\tilde{\mathbf{S}}_\mathrm{B}](\tilde{\mathbf{S}}_\mathrm{A}\times\mathbf{d})\cdot\mathbf{d} \\ & + \sin\phi\cos\phi(\tilde{\mathbf{S}}_\mathrm{A}\times\mathbf{d})\cdot\tilde{\mathbf{S}}_\mathrm{B} - \sin^2\phi\,(\tilde{\mathbf{S}}_\mathrm{A}\times\mathbf{d})(\tilde{\mathbf{S}}_\mathrm{B}\times\mathbf{d}).\end{aligned} \tag{3.13}$$

Using the relation $(\mathbf{a}\times\mathbf{b})\cdot(\mathbf{c}\times\mathbf{d}) = (\mathbf{a}\cdot\mathbf{c})(\mathbf{b}\cdot\mathbf{d}) - (\mathbf{a}\cdot\mathbf{d})(\mathbf{b}\cdot\mathbf{c})$ we can simplify further:

$$\begin{aligned}\mathbf{S}_\mathrm{A}\cdot\mathbf{S}_\mathrm{B} = {}& (1-\cos\phi)^2[\mathbf{d}\cdot\tilde{\mathbf{S}}_\mathrm{A}][\mathbf{d}\cdot\tilde{\mathbf{S}}_\mathrm{B}] + (1-\cos\phi)\cos\phi[\mathbf{d}\cdot\tilde{\mathbf{S}}_\mathrm{A}][\tilde{\mathbf{S}}_\mathrm{B}\cdot\mathbf{d}] + \cos\phi(1-\cos\phi)[\tilde{\mathbf{S}}_\mathrm{A}\cdot\mathbf{d}][\mathbf{d}\cdot\tilde{\mathbf{S}}_\mathrm{B}] \\ & + \cos^2\phi\,\tilde{\mathbf{S}}_\mathrm{A}\cdot\tilde{\mathbf{S}}_\mathrm{B} - \cos\phi\sin\phi\,\tilde{\mathbf{S}}_\mathrm{A}\cdot(\tilde{\mathbf{S}}_\mathrm{B}\times\mathbf{d}) - \sin\phi\cos\phi\,\mathbf{d}\cdot(\tilde{\mathbf{S}}_\mathrm{A}\times\tilde{\mathbf{S}}_\mathrm{B}) \\ & - \sin^2\phi[\tilde{\mathbf{S}}_\mathrm{A}\cdot\tilde{\mathbf{S}}_\mathrm{B} - (\tilde{\mathbf{S}}_\mathrm{A}\cdot\mathbf{d})(\tilde{\mathbf{S}}_\mathrm{B}\cdot\mathbf{d})].\end{aligned} \tag{3.14}$$

Ordering according to the spin exchange terms leads to:

$$\begin{aligned}\mathbf{S}_\mathrm{A}\cdot\mathbf{S}_\mathrm{B} = {}& \tilde{\mathbf{S}}_\mathrm{A}\cdot\tilde{\mathbf{S}}_\mathrm{B}[\cos^2\phi - \sin^2\phi] - \mathbf{d}\cdot(\tilde{\mathbf{S}}_\mathrm{A}\times\tilde{\mathbf{S}}_\mathrm{B})[2\cos\phi\sin\phi] \\ & + (\mathbf{d}\cdot\tilde{\mathbf{S}}_\mathrm{A})(\mathbf{d}\cdot\tilde{\mathbf{S}}_\mathrm{B})[(1-\cos\phi)^2 + 2\,(1-\cos\phi)\cos\phi + \sin^2\phi].\end{aligned} \tag{3.15}$$

With the trigonometric relations $2\sin x\cos x = \sin(2x)$ and $\cos^2 x - \sin^2 x = \cos(2x)$ we finally obtain:

$$\mathbf{S}_\mathrm{A}\cdot\mathbf{S}_\mathrm{B} = \cos(2\phi)\tilde{\mathbf{S}}_\mathrm{A}\cdot\tilde{\mathbf{S}}_\mathrm{B} - \sin(2\phi)\mathbf{d}\cdot(\tilde{\mathbf{S}}_\mathrm{A}\times\tilde{\mathbf{S}}_\mathrm{B}) + 2\sin^2\phi(\mathbf{d}\cdot\tilde{\mathbf{S}}_\mathrm{A})(\mathbf{d}\cdot\tilde{\mathbf{S}}_\mathrm{B}). \tag{3.16}$$

Rotating the spins in the DM term with Eq. (3.12) leads as well to contributions to all of the interaction terms in the rotated coordinate system:

$$\begin{aligned}\mathbf{d}\cdot(\mathbf{S}_\mathrm{A}\times\mathbf{S}_\mathrm{B}) = {}& (1-\cos\phi)^2\mathbf{d}(\mathbf{d}\cdot\tilde{\mathbf{S}}_\mathrm{A})(\mathbf{d}\cdot\tilde{\mathbf{S}}_\mathrm{B})(\mathbf{d}\times\mathbf{d}) + (1-\cos\phi)\cos\phi(\mathbf{d}\cdot\tilde{\mathbf{S}}_\mathrm{A})\mathbf{d}\cdot(\mathbf{d}\times\tilde{\mathbf{S}}_\mathrm{B}) \\ & -(1-\cos\phi)\sin\phi\,(\mathbf{d}\cdot\tilde{\mathbf{S}}_\mathrm{A})\mathbf{d}[\mathbf{d}\times(\tilde{\mathbf{S}}_\mathrm{B}\times\mathbf{d})] + \cos\phi(1-\cos\phi)(\mathbf{d}\cdot\tilde{\mathbf{S}}_\mathrm{B})\mathbf{d}\cdot(\tilde{\mathbf{S}}_\mathrm{A}\times\mathbf{d}) \\ & + \cos^2\phi\,\mathbf{d}\cdot(\tilde{\mathbf{S}}_\mathrm{A}\times\tilde{\mathbf{S}}_\mathrm{B}) - \cos\phi\sin\phi\,\mathbf{d}\cdot[\tilde{\mathbf{S}}_\mathrm{A}\times(\tilde{\mathbf{S}}_\mathrm{B}\times\mathbf{d})] \\ & + \sin\phi(1-\cos\phi)\mathbf{d}\cdot[(\tilde{\mathbf{S}}_\mathrm{A}\times\mathbf{d})\times\mathbf{d}](\mathbf{d}\cdot\tilde{\mathbf{S}}_\mathrm{B}) \\ & + \sin\phi\cos\phi\,\mathbf{d}\cdot[(\tilde{\mathbf{S}}_\mathrm{A}\times\mathbf{d})\times\tilde{\mathbf{S}}_\mathrm{B}] - \sin^2\phi\,\mathbf{d}\cdot[(\tilde{\mathbf{S}}_\mathrm{A}\times\mathbf{d})\times(\tilde{\mathbf{S}}_\mathrm{B}\times\mathbf{d})].\end{aligned} \tag{3.17}$$

With the relation $\mathbf{a}\times(\mathbf{b}\times\mathbf{c}) = \mathbf{b}(\mathbf{a}\cdot\mathbf{c}) - \mathbf{c}(\mathbf{a}\cdot\mathbf{b})$ this expression can be simplified:

$$\begin{aligned}\mathbf{d}\cdot(\mathbf{S}_\mathrm{A}\times\mathbf{S}_\mathrm{B}) = {}& \cos^2\phi\,\mathbf{d}\cdot(\tilde{\mathbf{S}}_\mathrm{A}\times\tilde{\mathbf{S}}_\mathrm{B}) - \cos\phi\sin\phi\,\mathbf{d}\cdot[\tilde{\mathbf{S}}_\mathrm{B}(\tilde{\mathbf{S}}_\mathrm{A}\cdot\mathbf{d}) - \mathbf{d}(\tilde{\mathbf{S}}_\mathrm{A}\cdot\tilde{\mathbf{S}}_\mathrm{B})] \\ & + \sin\phi(1-\cos\phi)\mathbf{d}\cdot[\mathbf{d}(\tilde{\mathbf{S}}_\mathrm{A}\cdot\mathbf{d}) - \mathbf{d}(\tilde{\mathbf{S}}_\mathrm{A}\cdot\mathbf{d})](\mathbf{d}\cdot\tilde{\mathbf{S}}_\mathrm{B}) \\ & - \sin\phi\cos\phi\,\mathbf{d}\cdot[\tilde{\mathbf{S}}_\mathrm{A}(\tilde{\mathbf{S}}_\mathrm{B}\cdot\mathbf{d}) - \mathbf{d}(\tilde{\mathbf{S}}_\mathrm{A}\cdot\tilde{\mathbf{S}}_\mathrm{B})] - \sin^2\phi\,\mathbf{d}\cdot(\tilde{\mathbf{S}}_\mathrm{A}\times\tilde{\mathbf{S}}_\mathrm{B}).\end{aligned} \tag{3.18}$$

Using trigonometric relations we obtain the following expression for the DM interaction in the rotated framework:

$$\mathbf{d}\cdot(\mathbf{S}_\mathrm{A}\times\mathbf{S}_\mathrm{B}) = \sin(2\phi)\,\tilde{\mathbf{S}}_\mathrm{A}\cdot\tilde{\mathbf{S}}_\mathrm{B} + \cos(2\phi)\,\mathbf{d}\cdot(\tilde{\mathbf{S}}_\mathrm{A}\times\tilde{\mathbf{S}}_\mathrm{B}) - \sin(2\phi)(\mathbf{d}\cdot\tilde{\mathbf{S}}_\mathrm{A})(\mathbf{d}\cdot\tilde{\mathbf{S}}_\mathrm{B}). \tag{3.19}$$

Without Hund's coupling the pseudo-dipolar tensor depends only on the DM interaction. Since we perform a rotation about the DM vector and the pseudo-dipolar tensor consists solely of terms that project the spin onto the DM vector, the pseudo-dipolar tensor is invariant under the rotation:

$$(\mathbf{d}\cdot\mathbf{S}_\mathrm{A})(\mathbf{d}\cdot\mathbf{S}_\mathrm{B}) = (\mathbf{d}\cdot\tilde{\mathbf{S}}_\mathrm{A})(\mathbf{d}\cdot\tilde{\mathbf{S}}_\mathrm{B}). \tag{3.20}$$

Now, we add the prefactors of the different spin exchange contributions in Eq. (3.16), Eq. (3.19), and Eq. (3.20). The following trigonometric relations are useful:

$$\cos(2\phi) = \frac{1-\tan^2\phi}{1+\tan^2\phi} = \frac{1-|\vec{\lambda}|^2/\tau^2}{1+|\vec{\lambda}|^2/\tau^2} = \frac{\tau^2-|\vec{\lambda}|^2}{\tau^2+|\vec{\lambda}|^2} \tag{3.21}$$

$$\sin(2\phi) = \frac{2\tan\phi}{1+\tan^2\phi} = \frac{2\vec{\lambda}|/\tau}{1+|\vec{\lambda}|^2/\tau^2} = \frac{2\tau|\vec{\lambda}|}{\tau^2+|\vec{\lambda}|^2} \tag{3.22}$$

$$\sin^2\phi = \frac{\tan^2\phi}{1+\tan^2\phi} = \frac{|\vec{\lambda}|^2/\tau^2}{1+|\vec{\lambda}|^2/\tau^2} = \frac{|\vec{\lambda}|^2}{\tau^2+|\vec{\lambda}|^2} \tag{3.23}$$

The prefactor to the isotropic part $\frac{4}{U}(\tilde{\mathbf{S}}_\mathrm{A}\cdot\tilde{\mathbf{S}}_\mathrm{B})$ is:

$$\begin{aligned}(\tau^2-|\vec{\lambda}|^2)\cos(2\phi)+2\tau|\vec{\lambda}|\sin(2\phi) &= (\tau^2-|\vec{\lambda}|^2)\frac{\tau^2-|\vec{\lambda}|^2}{\tau^2+|\vec{\lambda}|^2}+2t|\vec{\lambda}|\frac{2\tau|\vec{\lambda}|}{\tau^2+|\vec{\lambda}|^2} = \frac{(\tau^2+|\vec{\lambda}|^2)^2}{\tau^2+|\vec{\lambda}|^2}\\ &= \tau^2+|\vec{\lambda}|^2.\end{aligned} \tag{3.24}$$

The prefactor for the DM interaction vanishes:

$$\begin{aligned}(\tau^2-|\vec{\lambda}|^2)(-\sin(2\phi))+2\tau|\vec{\lambda}|\cos(2\phi) &= -(\tau^2-|\vec{\lambda}|^2)\frac{2\tau|\vec{\lambda}|}{\tau^2+|\vec{\lambda}|^2}+2\tau|\vec{\lambda}|\frac{\tau^2-|\vec{\lambda}|^2}{\tau^2+|\vec{\lambda}|^2}\\ &= 0,\end{aligned} \tag{3.25}$$

as well as the prefactor for the pseudo-dipolar contribution:

$$\begin{aligned}(\tau^2-|\vec{\lambda}|^2)2\sin^2\phi+2|\vec{\lambda}|^2-2\tau|\vec{\lambda}|\sin(2\phi) &= 2(\tau^2-|\vec{\lambda}|^2)\frac{|\vec{\lambda}|^2}{\tau^2+|\vec{\lambda}|^2}+2|\vec{\lambda}|^2\frac{\tau^2+|\vec{\lambda}|^2}{\tau^2+|\vec{\lambda}|^2}-2\tau|\vec{\lambda}|\frac{\tau^2-|\vec{\lambda}|^2}{\tau^2+|\vec{\lambda}|^2}\\ &= 0.\end{aligned} \tag{3.26}$$

Therefore, the rotated spin Hamiltonian is isotropic, where the relativistic correction to the Heisenberg exchange has the opposite sign:

$$\tilde{\mathcal{H}} = \sum_{ij}\frac{4(\tau^2+|\vec{\lambda}|^2)}{U}(\mathbf{S}_i\cdot\mathbf{S}_j) = \sum_{ij}\tilde{J}_{ij}(\tilde{\mathbf{S}}_i\cdot\tilde{\mathbf{S}}_j). \tag{3.27}$$

Note, that this is insight can be generalized to higher order perturbation theory, so that spin interactions are effectively isotropic at every order as soon as $\vec{\lambda}$ can be "gauged" away.

Finite magnetic field

For a finite magnetic field, the DM interaction is gauged away by applying the rotation, as shown above, but it induces an effective staggered magnetic field, shown in the middle panel of Fig. 3.3. Note, that we assume an isotropic g-tensor for simplicity at this point. The more realistic analysis considering the anisotropy will be discussed below. The spin exchange with the external magnetic field via the Zeeman term is in the rotated basis expressed as:

$$\begin{aligned}\mathbf{H}\cdot\tilde{\mathbf{S}}_i &= (1-\cos\phi)[\mathbf{d}\cdot\tilde{\mathbf{S}}_i][\mathbf{H}\cdot\mathbf{d}]+\cos\phi\,\mathbf{H}\cdot\tilde{\mathbf{S}}_i+\eta_i\sin\phi\,\mathbf{H}\cdot(\tilde{\mathbf{S}}_i\times\mathbf{d})\\ &= \big[(1-\cos\phi)(\mathbf{H}\cdot\mathbf{d})\mathbf{d}+\cos\phi\mathbf{H}-\eta_i\sin\phi(\mathbf{H}\times\mathbf{d})\big]\cdot\tilde{\mathbf{S}}_i,\end{aligned} \tag{3.28}$$

Here, it is possible to identify a sublattice independent uniform magnetic field, and a sublattice dependent staggered field contribution:

$$\mathbf{H}_u = (1-\cos\phi)(\mathbf{H}\cdot\mathbf{d})\mathbf{d}+\cos\phi\mathbf{H} \qquad \text{and} \qquad \mathbf{H}_s = \sin\phi(\mathbf{H}\times\mathbf{d}). \tag{3.29}$$

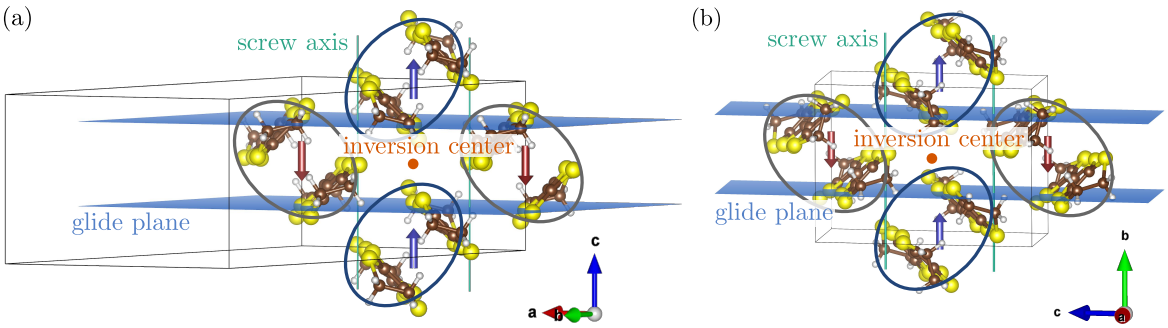

Figure 3.4: (a) Symmetries in *Pnma* materials with antiferromagnetic **l** spin configuration, defined in Eq. (3.31). (b) Symmetries in $P2_1/c$ materials with **l** configuration. In both cases, the spin quantization axis is chosen along the 2_1 screw axis for illustration purposes.

Note, that the staggered contribution of the effective field is perpendicular to the DM vector and to the applied external field.

In the limit of $|\mathbf{D}|/J \ll 1$, the definition of the canting angle given by Eq. (3.9) implies $\sin\phi = \sin(\frac{1}{2}\arctan(|\mathbf{D}|/J) \approx \frac{|\mathbf{D}|}{2J}$ and $\cos\phi \approx 1$. This allows to obtain the following approximate expressions for the effective fields:

$$\mathbf{H}_u \approx \mathbf{H} \qquad \text{and} \qquad \mathbf{H}_s \approx \frac{1}{2J}(\mathbf{H} \times \mathbf{D}). \tag{3.30}$$

In the right panel of Fig. 3.3 it is illustrated that for fields in the saturated limit $H = H_{\text{sat}}$, a finite DM interaction has still a noticeable effect. As a consequence, up to the polarized phase, the DM interaction allows the field always to "talk" to a (π, π) ordered magnetic configuration.

3.3.2 Symmetry restrictions on magnetic field coupling in κ-$(ET)_2X$

We discussed in the previous chapter the symmetrically allowed pattern of the DM interaction in the κ-$(ET)_2X$ materials, see also Fig. 2.7(b). In these compounds, the DM contribution along the 2_1 screw axis of the respective space groups follows a stripy $(0, \pi)$ pattern. This pattern is not compatible with the procedure to gauge anisotropic interactions away, as discussed above. Here, we show that an external magnetic field is "blind" with respect to the DM component parallel to the 2_1 screw axis, so that the influence of an external magnetic field can be discussed in the picture of the above introduced effective picture nevertheless.

Which magnetic configurations are realizable and how they couple to a magnetic field is restricted by the crystal symmetry. A detailed introduction to this topic can be found, for example, in Ref. [141]. To gain intuition for the κ-$(ET)_2X$ materials, we consider first the magnetically ordered member κ-Cl. For this compound, the magnetic order is known to be a canted Néel order [142]. Due to the experimental observation that its magnetic unit cell is equal to the crystallographic unit cell [104, 105], only magnetic configurations are realizable that can be described without a magnetic supercell. Since a unit cell contains two ET dimers, this requirement reduces the possibilities to the following two magnetic configurations:

$$\mathbf{m} = \mathbf{S}_1 + \mathbf{S}_2 \qquad \text{and} \qquad \mathbf{l} = \mathbf{S}_1 - \mathbf{S}_2, \tag{3.31}$$

where the spin is treated within the classical limit for convenience. The antiferromagnetic **l** configuration is shown in Fig. 3.4 for *Pnma* materials in (a) and for $P2_1/c$ materials in (b). The corresponding point group for both space groups is C_{2h}, which contains four symmetry operations: The identity operation E, the two-fold rotation C_2, the inversion operation i and the reflection σ_h. In the space group, the C_2 operation corresponds to the depicted 2_1 screw axis and σ_h to the depicted glide plane in Fig. 3.4. The

(a)

	E	C_2	i	σ_h	
m_a	+	−	+	−	B_g
m_b	+	+	+	+	A_g
m_{c^*}	+	−	+	−	B_g
l_a	+	+	+	+	A_g
l_b	+	−	+	−	B_g
l_{c^*}	+	+	+	+	A_g

(b)

C_{2h}	E	C_2	i	σ_h
A_g	+	+	+	+
B_g	+	−	+	−
A_u	+	+	−	−
B_u	+	−	−	+

(c)

C_{2h}	A_g	B_g	A_u	B_u
A_g	A_g	B_g	A_u	B_u
B_g	B_g	A_g	B_u	A_u
A_u	A_u	B_u	A_g	B_g
B_u	B_u	A_u	B_g	A_g

Table 3.1: (a) Characters and corresponding representations of the two spin configurations $\mathbf{m}$ and $\mathbf{l}$ for the symmetry operations in the C_{2h} point group, (b) C_{2h} character table, (c) C_{2h} product table [143].

transformation of the three spatial contributions[2] of $\mathbf{m}$ and $\mathbf{l}$ under the four symmetry operations are given in Table 3.1(a). Since we are eventually interested in describing the response of κ-Cu, we will here focus on the $P2_1/c$ space group and work in the (a, b, c^*) coordinate system with the screw axis along the crystallographic b axis. If the magnetic configuration is invariant under a symmetry operation, it is indicated by the character "+", if the transformed magnetic configuration changes sign, it is indicated by the character "−"[3].

The character table for the point group C_{2h} is given in Table 3.1(b), so that the appropriate representations can be assigned in the last column in Table 3.1(a) to the components of $\mathbf{m}$ and $\mathbf{l}$. It turns out that only the two representations A_g and B_g are relevant for the considered magnetic configurations. Since both representations appear for $\mathbf{m}$ and $\mathbf{l}$, a simultaneous ferromagnetic and antiferromagnetic order is symmetrically allowed, which results in the so-called weak ferromagnetism.

According to the Ginzburg-Landau theory, the free energy $\mathcal{F}$ of a system can be expressed as a function of the corresponding order parameter. Here, we are interested in a transition between a magnetically ordered phase and a QSL state, so that the order parameter should be magnetic and correspond to a linear combination of the possible magnetic configurations, $\mathbf{m}' = \alpha\,\mathbf{m} + \beta\,\mathbf{l}$, where α and β are in general tensors. Due to time reversal symmetry, the free energy consists in the absence of a magnetic field only of even orders in the magnetic order parameter. Under the assumption that $\mathcal{F}$ is quadratic in the order parameter to leading order, it can be expressed as $\mathcal{F}(\mathbf{m}') = c_1\,(\mathbf{m}')^2$. The free energy of a system has to transform as the representation A_g within the point group of the crystal. According to the product table of the point group C_{2h}, given in Table 3.1(c), the combinations that transform as A_g are the diagonal elements, i.e. $A_g \otimes A_g$ and $B_g \otimes B_g$. That implies that the components of the magnetic configurations within $(\mathbf{m}')^2$ can couple only within certain combinations:

$$A_g \otimes A_g: \quad \{m_b^2,\ l_a^2,\ l_{c^*}^2,\ m_b l_a,\ m_b l_{c^*},\ l_a l_{c^*}\}, \tag{3.32}$$

$$B_g \otimes B_g: \quad \{m_a^2,\ m_{c^*}^2,\ l_b^2,\ m_a m_{c^*},\ m_a l_b,\ l_{c^*} l_b\}. \tag{3.33}$$

Using the definitions of the magnetic configurations $\mathbf{m}$ and $\mathbf{l}$ in Eq. (3.31) and omitting the contributions on a single site[4], as well as the quadratic contributions, which give rise to a Heisenberg term, we find the following terms:

$$A_g \otimes A_g: \quad \{(-S_{1,b}S_{2,a} + S_{2,b}S_{1,a}),\ (-S_{1,b}S_{2,c^*} + S_{2,b}S_{1,c^*}),\ (-S_{1,a}S_{2,c^*} - S_{2,a}S_{1,c^*})\}, \tag{3.34}$$

$$B_g \otimes B_g: \quad \{(S_{1,a}S_{2,c^*} + S_{2,a}S_{1,c^*}),\ (-S_{1,a}S_{2,b} + S_{2,a}S_{1,b}),\ (-S_{1,c^*}S_{2,b} - S_{2,c^*}S_{1,b})\} \tag{3.35}$$

Identifying the prefactors within the spin Hamiltonian leads to the following possible contributions:

$$A_g \otimes A_g: \quad \{D_{c^*}, D_a\} \tag{3.36}$$

$$B_g \otimes B_g: \quad \{\Gamma_{ac^*}, D_{c^*}\}. \tag{3.37}$$

[2] Note, that spins transform as pseudo-vectors.

[3] Strictly speaking, a "-" indicates that the operation e.g. C_2 is not a symmetry of the magnetic space group, but instead C_2R, where R represents time reversal symmetry.

[4] For spin 1/2 in the quantum case, two-spin terms on a single site can only lead to a constant energy shift, since $\sigma_\alpha^2 = \mathbb{1}$ for all Pauli matrices. See also Chapter 4.

Therefore, the free energy in the absence of a magnetic field is a function of these parameters and the Heisenberg contribution, $\mathcal{F}(J, D_a, D_{c^*}, \Gamma_{ac^*})$. Consequently, the free energy is independent of the exchange parameters D_b, Γ_{ab}, and Γ_{bc^*}.

At finite field, we can approximate for uniform fields that the magnetic order parameter couples linearly to the field, $\mathcal{F} = c_1 (\mathbf{m}')^2 - c_2 \mathbf{H} \cdot \mathbf{m}'$, so that the free energy remains independent of D_b. Hence, for systems that are described by the C_{2h} point group with two magnetic sites per unit cell, the external magnetic field is "blind" towards the component along the 2_1 screw axis of the DM vector in this framework. Therefore, the framework discussed at the beginning of this section to gauge anisotropic interactions away, is applicable for κ-Cu.

3.4 Critical scenario in κ-Cu?

In Section 3.2, critical scenarios with exotic critical exponents for κ-Cu were discussed based on μSR, NMR and magnetic torque measurements. Given the very small energies involved, we began to wonder whether smaller terms such as the Dzyaloshinskii-Moriya interaction can be relevant for the interpretation. In this section, we first discuss a more natural explanation for the change of the critical exponent β observed in the μSR experiment based on the theoretical framework derived in the previous section. This analysis is published in Ref. [77]. However, we will then see that magnetic torque measurements on κ-Cu cannot be incorporated consistently in this picture, as we pointed out later in Ref. [78]. In Section 3.5, we discuss therefore an alternative scenario taking non-magnetic impurities in κ-Cu into account.

3.4.1 Theoretical magnetization expressions including SOC

In order to analyse the μSR data, we derive first theoretical expressions for the scaling of the magnetization with field in the framework of Section 3.3. The dominating sources for anisotropy in the spin Hamiltonian for κ-Cu are the g-tensor and the anisotropic terms in the bilinear contribution, $\mathbf{D}_{ij}$ and Γ_{ij}. As discussed in Section 2.5, the g-tensor is sublattice dependent and fulfils a (π, π) staggered pattern, illustrated also in Fig. 2.9. As detailed in Section 3.3, the stripy contribution of the DM vector does not couple to a magnetic field. Therefore, we will treat it as purely staggered. To take advantage of the effective picture with local coordinates, we generalize first the approach to include a staggered g-tensor. The local rotations of the spins lead then to an effective isotropic spin-spin description $\mathcal{H}_{(2)} = \sum_{ij} \tilde{J}_{ij} \tilde{\mathbf{S}}_i \cdot \tilde{\mathbf{S}}_j$, where the angle-dependence of the energy is captured only by the Zeeman term. In the unrotated basis it is given by

$$\mathcal{H}_{(1)} = -\mu_B \mathbf{H}^{\mathrm{T}} \cdot \sum_i \left(\mathbb{G}_{\mathrm{A}} \cdot \mathbf{S}_{i_{\mathrm{A}}} + \mathbb{G}_{\mathrm{B}} \cdot \mathbf{S}_{i_{\mathrm{B}}} \right), \tag{3.38}$$

where A and B indicate the two distinct sublattices in the κ-$(\mathrm{ET})_2\mathrm{X}$ materials. The Rodrigues' rotation formula can then be applied to the case with a local g-tensor $\mathbb{G}_i$:

$$\begin{aligned} \mathbf{H}^{\mathrm{T}} \cdot \mathbb{G}_i \cdot \mathbf{S}_i &= (1 - \cos\phi)[\mathbf{d} \cdot \tilde{\mathbf{S}}_i][(\mathbb{G}_i^{\mathrm{T}} \cdot \mathbf{H})^{\mathrm{T}} \cdot \mathbf{d}] + \cos\phi\, (\mathbb{G}_i^{\mathrm{T}} \cdot \mathbf{H})^{\mathrm{T}} \cdot \tilde{\mathbf{S}}_i + \eta_i \sin\phi\, (\mathbb{G}_i^{\mathrm{T}} \cdot \mathbf{H})^{\mathrm{T}} \cdot (\tilde{\mathbf{S}}_i \times \mathbf{d}) \\ &= [(1 - \cos\phi)((\mathbb{G}_i^{\mathrm{T}} \cdot \mathbf{H})^{\mathrm{T}} \cdot \mathbf{d})\mathbf{d} + \cos\phi\, (\mathbb{G}_i^{\mathrm{T}} \cdot \mathbf{H}) - \eta_i \sin\phi\, ((\mathbb{G}_i^{\mathrm{T}} \cdot \mathbf{H}) \times \mathbf{d})]^{\mathrm{T}} \cdot \tilde{\mathbf{S}}_i, \end{aligned} \tag{3.39}$$

where η_i is the sublattice dependent parameter defined in Eq. (3.7). As mentioned in Section 2.5, the g-tensor has a uniform ($\mathbb{G}_u$) and a staggered ($\mathbb{G}_s$) contribution:

$$\mathbb{G}_i = \mathbb{G}_u + \eta_i \mathbb{G}_s. \tag{3.40}$$

Using this explicit form of the local g-tensor in Eq. (3.39):

$$\begin{aligned} \mathbf{H}^{\mathrm{T}} \cdot \mathbb{G}_i \cdot \mathbf{S}_i = [(1 - \cos\phi)(((\mathbb{G}_u^{\mathrm{T}} + \eta_i \mathbb{G}_s^{\mathrm{T}}) \cdot \mathbf{H})^{\mathrm{T}} \cdot \mathbf{d})\mathbf{d} + \cos\phi\, (\mathbb{G}_u^{\mathrm{T}} + \eta_i \mathbb{G}_s^{\mathrm{T}}) \cdot \mathbf{H} \\ - \eta_i \sin\phi \left(((\mathbb{G}_u^{\mathrm{T}} + \eta_i \mathbb{G}_s^{\mathrm{T}}) \cdot \mathbf{H}) \times \mathbf{d} \right)]^{\mathrm{T}} \cdot \tilde{\mathbf{S}}_i, \end{aligned} \tag{3.41}$$

enables to identify an effective uniform, sublattice independent, field $\mathbf{H}_{\mathrm{eff},u}$ and a sublattice dependent, staggered field $\mathbf{H}_{\mathrm{eff},s}$:

$$\mathbf{H}_{\mathrm{eff},u} = (1-\cos\phi)(\mathbf{H}^{\mathrm{T}}\cdot\mathbb{G}_u\cdot\mathbf{d})\mathbf{d} + \cos\phi\,(\mathbb{G}_u^{\mathrm{T}}\cdot\mathbf{H}) - \sin\phi\,((\mathbb{G}_s^{\mathrm{T}}\cdot\mathbf{H})\times\mathbf{d}), \tag{3.42}$$

$$\mathbf{H}_{\mathrm{eff},s} = (1-\cos\phi)(\mathbf{H}^{\mathrm{T}}\cdot\mathbb{G}_s\cdot\mathbf{d})\mathbf{d} + \cos\phi\,(\mathbb{G}_s^{\mathrm{T}}\cdot\mathbf{H}) - \sin\phi\,((\mathbb{G}_u^{\mathrm{T}}\cdot\mathbf{H})\times\mathbf{d}). \tag{3.43}$$

For small canting angles ϕ, i.e. weak spin-orbit coupling, we can approximate $\cos\phi\approx 1$, $\sin\phi\approx\frac{|\mathbf{D}|}{2J}$ and neglect terms $\mathcal{O}(|\mathbb{G}_s\cdot\mathbf{D}|)$:

$$\mathbf{H}_{\mathrm{eff},u}\approx\mathbb{G}_u^{\mathrm{T}}\cdot\mathbf{H} \qquad\text{and}\qquad \mathbf{H}_{\mathrm{eff},s}\approx\mathbb{G}_s^{\mathrm{T}}\cdot\mathbf{H}-\frac{1}{2J}\,((\mathbb{G}_u^{\mathrm{T}}\cdot\mathbf{H})\times\mathbf{D}). \tag{3.44}$$

To simplify the notation, we define the following matrix:

$$\mathbb{R} = -\frac{1}{2J}\,\mathbb{G}_u\cdot\mathbb{D} = \frac{1}{2J}\,\mathbb{G}_u\cdot\begin{pmatrix} 0 & -D_z & D_y \\ D_z & 0 & -D_x \\ -D_y & D_x & 0\end{pmatrix}, \tag{3.45}$$

so that the effective fields have analogical forms:

$$\mathbf{H}_{\mathrm{eff},u} = \mathbb{G}_u^{\mathrm{T}}\cdot\mathbf{H} \qquad\text{and}\qquad \mathbf{H}_{\mathrm{eff},s} = (\mathbb{G}_s+\mathbb{R})^{\mathrm{T}}\cdot\mathbf{H}. \tag{3.46}$$

The Zeeman Hamiltonian, given by Eq. (3.38), can then be expressed in terms of these effective fields:

$$\mathcal{H}_{(1)} = -\mu_B\mathbf{H}_{\mathrm{eff},u}^{\mathrm{T}}\cdot\big(\sum_i\tilde{\mathbf{S}}_i\big) - \mu_B\mathbf{H}_{\mathrm{eff},s}^{\mathrm{T}}\cdot\big(\sum_i\eta_i\,\tilde{\mathbf{S}}_i\big). \tag{3.47}$$

The Hamiltonian up to bilinear contributions in the rotated framework is therefore:

$$\mathcal{H}_{(1)}+\mathcal{H}_{(2)} = -\mu_B\sum_i(\mathbf{H}_{\mathrm{eff},u}+\eta_i\mathbf{H}_{\mathrm{eff},s})^{\mathrm{T}}\cdot\tilde{\mathbf{S}}_i + \sum_{ij}\tilde{J}_{ij}\,\tilde{\mathbf{S}}_i\cdot\tilde{\mathbf{S}}_j. \tag{3.48}$$

In a critical scenario with the magnetic field as the tuning parameter, a universal scaling close to the QCP is described by $|\mathbf{m}| = \chi_0\,|\mathbf{H}|^{\beta}$, where $\mathbf{m}$ is the magnetization, χ_0 is the field-independent part of the susceptibility and β the critical exponent. Under the assumption that the ground state of κ-Cu in the absence of a magnetic field is a QSL state, the total magnetization vanishes, $\mathbf{m}|_{H=0}=0$. A magnetic field talks to a system described by the Hamiltonian Eq. (3.48) via the Zeeman term. The magnetization relates to the spin expectation value with the respective q-vector[5] via the following expressions:

$$\mathbf{m}_u = \mathbb{G}_u\cdot\langle\sum_i\mathbf{S}_i\rangle \qquad\text{and}\qquad \mathbf{m}_s = (\mathbb{G}_s+\mathbb{R})\cdot\langle\sum_i\eta_i\mathbf{S}_i\rangle. \tag{3.49}$$

The spin expectation value of a specific q-vector scales with the corresponding effective field given in Eq. (3.46) according to the general scaling relation:

$$\langle\sum_i\mathbf{S}_i\rangle = \chi_{0,u}\,|\mathbf{H}_{\mathrm{eff},u}|^{\beta_H-1}\mathbf{H}_{\mathrm{eff},u} \qquad\text{and}\qquad \langle\sum_i\eta_i\mathbf{S}_i\rangle = \chi_{0,s}\,|\mathbf{H}_{\mathrm{eff},s}|^{\beta_L-1}\mathbf{H}_{\mathrm{eff},s}. \tag{3.50}$$

Note, that this implies that the magnetization in Eq. (3.49) is neither parallel to the external field, nor the effective field. For the further analysis we approximate the uniform and staggered magnetization to be perpendicular. The norm of the local magnetization $|\mathbf{m}| = |\mathbf{m}_u+\mathbf{m}_s|$ is then within this framework:

$$|\mathbf{m}| = \sqrt{(\chi_{0,u}|\mathbf{H}_{\mathrm{eff},u}|^{\beta_H})^2|\mathbb{G}_u\cdot\mathbf{n}_{\mathrm{eff},u}|^2 + (\chi_{0,s}|\mathbf{H}_{\mathrm{eff},s}|^{\beta_L})^2|(\mathbb{G}_s+\mathbb{R})\cdot\mathbf{n}_{\mathrm{eff},s}|^2}, \tag{3.51}$$

where we introduced the unit vector $\mathbf{n}$ in the direction of the respective effective field.

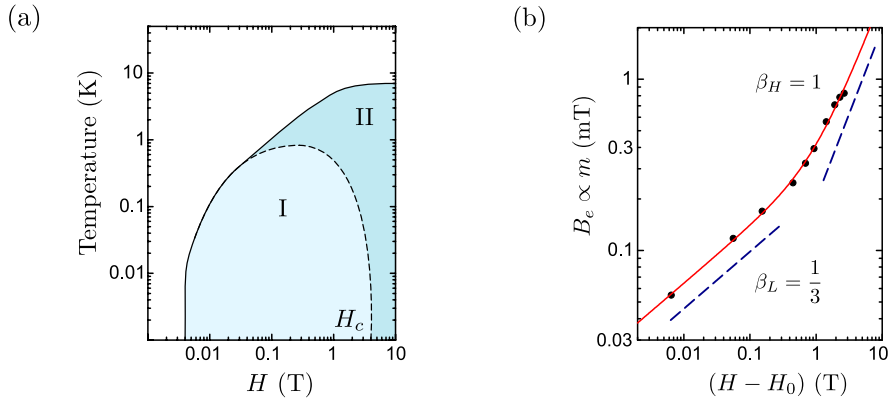

Figure 3.5: (a) Cartoon for an alternative phase diagram for κ-Cu, where a low-field region I and a high-field region II are identified for low temperatures. (b) Alternative fit of the μSR data under consideration of anisotropic effects [77]. Fig. (a,b) adapted from Ref. [77].

3.4.2 Fit of μSR linewidth including SOC

The form of Eq. (3.51) suggests a scenario, where the observed kink in the μSR linewidth does not represent a field-induced transition, but rather a smooth crossover between different regimes dominated by the staggered or the uniform effective field, illustrated as a cartoon phase diagram in Fig. 3.5(a). There, we illustrated a low-field region I below a critical field H_c for low temperatures. This region is dominated by the effective staggered field, i.e. by spin-orbit coupling effects. Above H_c, the high-field region II is in this framework dominated by the uniform effective field. Since the phase diagram proposed in Ref. [98] is based on the scaling behaviour of the μSR linewidth, we provide here an alternative fit considering SOC effects through the magnetization expression given by Eq. (3.51).

To fit the μSR linewidth B_e, following the assumption $B_e \propto |\mathbf{m}|$ proposed in Ref. [98], we take into account the explicit expressions of $\mathbb{G}_u$, $\mathbb{G}_s$ and $\mathbf{D}$ for κ-Cu, which follow directly from the *ab-initio* calculations in Section 2.5. We treat then the parameters $\chi_{0,u}$, $\chi_{0,s}$, β_H, and β_L in Eq. (3.51) as fit parameters. The uniform and staggered anisotropic g-tensors can be extracted from the calculations in the previous chapter and are given by

$$\mathbb{G}_u = \begin{pmatrix} 2.010 & 0 & -8 \cdot 10^{-4} \\ 0 & 2.005 & 0 \\ 7 \cdot 10^{-4} & 0 & 2.005 \end{pmatrix}, \tag{3.52}$$

and

$$\mathbb{G}_s = \begin{pmatrix} 0 & -4 \cdot 10^{-4} & 0 \\ -6 \cdot 10^{-4} & 0 & -26 \cdot 10^{-4} \\ 0 & -25 \cdot 10^{-4} & 0 \end{pmatrix}. \tag{3.53}$$

The matrix $\mathbb{R}$, defined in Eq. (3.45), is constructed by $\mathbb{G}_u$ and the DM vector $\mathbf{D} = (3.3, 0.9, 1.0)\,\mathrm{K}$ for κ-Cu. Note that due to the structure of $\mathbb{R}$, and of $\mathbb{G}_u$ and $\mathbb{G}_s$, the effective uniform and staggered field are orthogonal, $\mathbf{H}_{\mathrm{eff},u} \perp \mathbf{H}_{\mathrm{eff},s}$, for external fields in the ac^* plane.

Since the μSR experiment was performed with a powder sample of κ-Cu, the line width is proportional to the magnetization averaged over the space angles, $B_e \propto \int d\Omega\ |\mathbf{m}|$. In Fig. 3.5(b) we show a fit of this expression to the data points taken from Ref. [98], where we obtained the following scaling exponents:

$$\beta_L \approx 0.330 \qquad \text{and} \qquad \beta_H \approx 0.999. \tag{3.54}$$

[5] A uniform magnetization corresponds to $q = 0$, while we refer to a staggered magnetization for $\mathbf{q} = (\pi, \pi)$ with respect to the square lattice.

These values are not exotic. For the regime dominated by the uniform effective field, referred to as region II in Fig. 3.5(a), we find with $\beta_H \approx 1$ linear scaling of the magnetization with field, $|\mathbf{m}| \propto |\mathbf{H}_{\mathrm{eff},u}|$. This relation corresponds to the conventional field-dependence of the magnetization in a non-critical regime. For the low-field regime, region I in Fig. 3.5(a), dominated by the effective staggered field, we find with $\beta_H \approx 1/3$ very good agreement with the exponents calculated for one-dimensional chains in the framework of an effective staggered field. There, the staggered magnetization is known to be proportional to $H_0^{1/3}$ [144, 145]. Note, that for this fit we obtained a ratio $\chi_{0,s}/\chi_{0,u} \approx 1000$ at $H = 1\,\mathrm{T}$, which is consistent with a critical scenario where the staggered component is far within the diverging limit.

Therefore, the change in the scaling behaviour of the μSR linewidth corresponds in this framework rather to a smooth crossover between regimes dominated by SOC effects and conventional behaviour than to a signature of an exotic QCP. In Section 3.5, we propose, motivated by the magnetic torque response, a different scenario where the κ-Cu enters a valence bond glass state instead of a critical staggered regime. In the case of the μSR data, the kink would then correspond to a smooth crossover between a regime dominated by impurities and a regime dominated by the bulk properties.

3.4.3 Theoretical magnetic torque expressions

In the discussion of the magnetic torque response in Ref. [120], the authors stated that *"now there is no theory to explain the experimental values, to our best knowledge"*, referring to the observed critical exponents. After the apparent success of considering SOC effects in μSR observations, it was tempting to incorporate the torque data in this critical scenario with SOC effects as well. However, we will see that this scenario predicts a behaviour not seen by experiment.

First, we derive general expressions for the magnetic torque in terms of scaling exponents. We consider a situation, in which the investigated material is in equilibrium, the system has minimal energy, before an external field is switched on. In a case where the anisotropic contributions are given by the anisotropic g-tensor and the spin-spin interactions $\mathbf{D}_{ij}$ and Γ_{ij}, there are two mechanisms important for the response to a magnetic field. On the one hand, the crystal tries to rotate to adjust the relative spatial position of the g-tensor to optimize the energy gain. On the other hand, due to the DM vector and pseudo-dipolar tensor, the optimal spin configuration depends on the relative orientation to the crystal. The interplay of these two mechanisms determines which spin configuration and spatial crystal orientation minimize the energy in the presence of a magnetic field. The reorientation the crystal desires leads to the measured magnetic torque τ, and can be calculated as the derivative of the free energy $\mathcal{F}$ with respect to the angle θ between the crystal and a reference axis (see also Fig. 3.6(a)):

$$\tau = \frac{\mathrm{d}\mathcal{F}}{\mathrm{d}\theta} \qquad \text{and} \qquad \tau\,\big|_{T=0} = \frac{\mathrm{d}\langle\mathcal{H}\rangle}{\mathrm{d}\theta} \tag{3.55}$$

We restrict the analysis to the $T = 0$ expression, where entropic contributions are not considered and the free energy $\mathcal{F}$ corresponds to the expectation value of the Hamiltonian $\langle\mathcal{H}\rangle$.

Uniform case

We start with a case, where the g-tensor is anisotropic ($g_p \neq g_q \neq g_r$) on a uniform lattice, so that $\mathbb{G}_u$ is the g-tensor on all lattice sites i and the spin-spin correlations are described by an isotropic Heisenberg spin Hamiltonian $\mathcal{H}_{(2)} = J\sum_{\langle ij\rangle}\mathbf{S}_i \cdot \mathbf{S}_j$. For the spatial orientation of the crystal, the only relevant part of the Hamiltonian is in this case the Zeeman coupling:

$$\mathcal{H} = -\mu_B \mathbf{H}^{\mathrm{T}} \cdot \mathbb{G}_u \cdot \Big(\sum_i \mathbf{S}_i\Big), \tag{3.56}$$

since the reorientation of the spins resulting from spin-spin correlations are not observable in this experimental setup. In general, we assume a QSL bulk ground state for zero field, so that $\langle\sum_i \mathbf{S}_i\rangle = 0$. For simplicity, we describe the experiment as a rotation of the field in the negative direction, rather than rotating the g-tensor and the spins.

The Zeeman energy is minimized when the spins $\mathbf{S}_i$ are parallel to the effective field given by:

$$\mathbf{H}_{\mathrm{eff},u} = \mathbb{G}_u^{\mathrm{T}} \cdot \mathbf{H}. \tag{3.57}$$

Similar to the approach above, we relate the spin expectation value to the corresponding effective field. Here, via the introduction of the general - scalar - susceptibility χ_u:

$$\langle \sum_i \mathbf{S}_i \rangle = \chi_u \, \mathbf{H}_{\mathrm{eff},u}. \tag{3.58}$$

Consequently, the corresponding uniform magnetization $\mathbf{m}_u$ is influenced by the effective field through the appropriate g-tensor:

$$\mathbf{m}_u = \mathbb{G}_u \cdot \langle \sum_i \mathbf{S}_i \rangle = \chi_u \mathbb{G}_u \cdot \mathbf{H}_{\mathrm{eff},u}. \tag{3.59}$$

Without solving the Hamiltonian, we assume at this point that the spin expectation value scales with some exponent with field. The scaling can be encoded in the susceptibility:

$$\chi_u = \tilde{\chi}_{0,u} \, |\mathbf{H}_{\mathrm{eff},u}|^{-\zeta_u} \tag{3.60}$$

where we introduced the scaling exponent ζ_u.

With the scaling assumption given by Eq. (3.60), the expectation value of the Hamiltonian Eq. (3.56) can be expressed in terms of the effective field and the susceptibility:

$$\begin{aligned} \langle \mathcal{H} \rangle &= -\mu_B \, \mathbf{H}_{\mathrm{eff}}^{\mathrm{T}} \cdot \langle \sum_i \mathbf{S}_i \rangle \\ &= -\mu_B \, \mathbf{H}_{\mathrm{eff}}^{\mathrm{T}} \cdot \chi_u \, \mathbf{H}_{\mathrm{eff}} \\ &= -\mu_B \, \mathbf{H}_{\mathrm{eff}}^{\mathrm{T}} \cdot \chi_{0,u} \, |\mathbf{H}_{\mathrm{eff}}|^{-\zeta_u} \, \mathbf{H}_{\mathrm{eff}} \\ &= -\mu_B \, \chi_{0,u} \, |\mathbf{H}_{\mathrm{eff}}|^{2-\zeta_u}. \end{aligned} \tag{3.61}$$

To derive the torque expression from $\langle \mathcal{H} \rangle$, we use the following relation for a derivative of a vector norm to power α:

$$\begin{aligned} \frac{\mathrm{d}}{\mathrm{d}\theta} |\mathbf{r}(\theta)|^{\alpha} &= \frac{\mathrm{d}}{\mathrm{d}\theta} \big(x(\theta)^2 + y(\theta)^2 + z(\theta)^2 \big)^{\alpha/2} \\ &= \frac{\alpha}{2} \big(x(\theta)^2 + y(\theta)^2 + z(\theta)^2 \big)^{\alpha/2-1} \frac{\mathrm{d}\mathbf{r}(\theta)^{\mathrm{T}}}{\mathrm{d}\theta} \cdot 2\mathbf{r}(\theta) \\ &= \alpha |\mathbf{r}(\theta)|^{\alpha-2} \frac{\mathrm{d}\mathbf{r}(\theta)^{\mathrm{T}}}{\mathrm{d}\theta} \cdot \mathbf{r}(\theta). \end{aligned} \tag{3.62}$$

Using the expression for the expectation value of the Hamiltonian, Eq. (3.61), the torque is then given by:

$$\begin{aligned} \tau &= -\mu_B \, \chi_{0,u} \frac{\mathrm{d}}{\mathrm{d}\theta} |\mathbf{H}_{\mathrm{eff}}|^{2-\zeta_u} \\ &= -\mu_B \, \chi_{0,u} (2-\zeta_u) |\mathbf{H}_{\mathrm{eff}}|^{-\zeta_u} \frac{\mathrm{d}\mathbf{H}_{\mathrm{eff}}^{\mathrm{T}}}{\mathrm{d}\theta} \cdot \mathbf{H}_{\mathrm{eff}}. \end{aligned} \tag{3.63}$$

This expression can be sorted with respect to the angle-dependent terms and those dependent on the norm of the field $H = |\mathbf{H}|$:

$$\begin{aligned} \tau &= -\mu_B \, (2-\zeta_u) H^{2-\zeta_u} |\mathbb{G}_u^{\mathrm{T}} \cdot \mathbf{h}|^{-\zeta_u} \frac{\mathrm{d}(\mathbb{G}_u^{\mathrm{T}} \cdot \mathbf{h})^{\mathrm{T}}}{\mathrm{d}\theta} \mathbb{G}_u^{\mathrm{T}} \cdot \mathbf{h} \\ &\equiv H^2 \tilde{\chi}_u(H) f_u(\theta), \end{aligned} \tag{3.64}$$

where we introduced the unit vector $\mathbf{h} = \mathbf{H}/H$, the field-dependent susceptibility:

$$\tilde{\chi}_u(H) = \mu_B(2-\zeta_u)\tilde{\chi}_{0,u}H^{-\zeta_u}, \tag{3.65}$$

and the angle-dependent function:

$$f_u(\theta) = -\frac{1}{|\mathbb{G}_u^{\mathrm{T}}\cdot\mathbf{h}|^{\zeta_u}}\left(\frac{\mathrm{d}\mathbf{h}^{\mathrm{T}}}{\mathrm{d}\theta}\cdot\mathbb{G}_u\cdot\mathbb{G}_u^{\mathrm{T}}\cdot\mathbf{h}\right). \tag{3.66}$$

The definition of the field-dependent susceptibility in Eq. (3.65) is chosen such that in the limit $\zeta_u \to 0$ the conventional linear scaling of the magnetization with field is reproduced:

$$\mathbf{m}_u = \tilde{\chi}_{0,u}\mathbb{G}_u\cdot\mathbb{G}_u^{\mathrm{T}}\cdot\mathbf{H}. \tag{3.67}$$

In this limit, $\zeta_u \to 0$, the torque is known to scale $\propto H^2$, which is fulfilled by the definition in Eq. (3.64), since in this case $\tilde{\chi}_u$ is field-independent. In the conventional scaling limit $\zeta_u \to 0$, the angle dependence should follow a $\propto \sin 2\theta$ dependence. To demonstrate this, we can consider the torque in the ac^* plane, with θ as the angle between the a axis and field $\mathbf{H}$:

$$\begin{aligned}\tau_{a\text{-}c^*}(\theta) &= -\tilde{\chi}_u\left[\frac{\mathrm{d}}{\mathrm{d}\theta}\begin{pmatrix}H\cos\theta\\0\\H\sin\theta\end{pmatrix}\right]\cdot\mathbb{G}_u\cdot\mathbb{G}_u^{\mathrm{T}}\cdot\begin{pmatrix}H\cos\theta\\0\\H\sin\theta\end{pmatrix}\\ &= 2\mu_B\tilde{\chi}_{0,u}H^2\begin{pmatrix}\sin\theta\\0\\-\cos\theta\end{pmatrix}\cdot\mathbb{G}_u\cdot\mathbb{G}_u^{\mathrm{T}}\cdot\begin{pmatrix}\cos\theta\\0\\\sin\theta\end{pmatrix}.\end{aligned} \tag{3.68}$$

If the eigensystem of the g-tensor is equal to the crystal axes, the expression reduces to:

$$\tau_{a\text{-}c^*}(\theta) = \mu_B\tilde{\chi}_{0,u}H^2(g_{aa}^2 - g_{c^*c^*}^2)\sin(2\theta). \tag{3.69}$$

This expression is consistent with the expression used, for example, by Watanabe *et al.* [146], to which also Isono *et al.* [120] refer in their torque analysis for κ-Cu. Rotation of the g-tensor within the ac^* plane leads to an additional offset θ_0.

Staggered case

As mentioned in the μSR analysis above, an appropriate description of the response of κ-Cu to a magnetic field requires consideration of the staggered contribution to the g-tensor and anisotropic spin-spin interactions. The starting point for the derivation of the torque expressions in this case is the framework of locally rotated coordinate systems, such that the anisotropy is captured by an effective staggered field $\mathbf{H}_{\mathrm{eff},s}$, given by Eq. (3.46). In addition to a scaling assumption for the uniform spin expectation value, a scaling assumption for the staggered spin expectation value is necessary:

$$\mathbf{m}_s = (\mathbb{G}_s + \mathbb{R})\cdot\langle\sum_i \eta_i\mathbf{S}_i\rangle = \chi_s(\mathbb{G}_s+\mathbb{R})\cdot\mathbf{H}_{\mathrm{eff},s}. \tag{3.70}$$

The scaling assumption for the susceptibility in the staggered case depends on $\mathbf{H}_{\mathrm{eff},s}$ and the critical exponent ζ_s:

$$\chi_s = \tilde{\chi}_{0,s}|\mathbf{H}_{\mathrm{eff},s}|^{-\zeta_s}, \tag{3.71}$$

The isotropic, field-dependent contribution of the staggered susceptibility depends on the critical exponent:

$$\tilde{\chi}_s(H) = \mu_B(2-\zeta_s)\tilde{\chi}_{0,s}H^{-\zeta_s}, \tag{3.72}$$

and the staggered angle-dependent function depends on both, the staggered g-tensor $\mathbb{G}_s$ and the matrix $\mathbb{R}$, as defined in Eq. (3.45):

$$f_s(\theta) = -\frac{1}{|(\mathbb{G}_s+\mathbb{R})^{\mathrm{T}}\cdot\mathbf{h}|^{\zeta_s}}\left(\frac{\mathrm{d}\mathbf{h}^{\mathrm{T}}}{\mathrm{d}\theta}\cdot(\mathbb{G}_s+\mathbb{R})\cdot(\mathbb{G}_s+\mathbb{R})^{\mathrm{T}}\cdot\mathbf{h}\right). \tag{3.73}$$

Scalar spin chirality

Another possible source of anisotropy in the presence of an external field is a finite scalar spin chirality. For κ-Cu an exotic QSL with chiral order was proposed as an attempt to explain the mysterious $T_* = 6\,\mathrm{K}$ anomaly [147]. In Section 2.5.1, the scalar spin chirality was introduced as a consequence of the presence of an external field. Therefore, its influence on magnetic torque measurements has to be considered. In the rotated framework introduced in Section 3.3, this term can be expressed as:

$$\mathcal{H}_{(3)} = \mu_B \frac{1}{S} \sum_{\langle ijk \rangle} \tilde{J}_\chi^{ijk}\, \tilde{\mathbf{S}}_i \cdot (\tilde{\mathbf{S}}_j \times \tilde{\mathbf{S}}_k). \tag{3.74}$$

In Section 2.5.1, it was pointed out that the exchange term is for small fields linear in Φ, a quantity proportional to the magnetic flux. Motivated by that, we expressed this interaction in Section 2.5 in analogy to the Zeeman term:

$$\mathcal{H}_{(3)} = -\mu_B \tilde{j}_\Phi (\mathbf{H}^{\mathrm{T}} \cdot \mathbf{n}) \sum_{\langle ijk \rangle} \tilde{\mathbf{S}}_i \cdot (\tilde{\mathbf{S}}_j \times \tilde{\mathbf{S}}_k), \tag{3.75}$$

with the dimensionless plaquette operator $\tilde{j}_\Phi$. The source for anisotropy of the three-spin term is in leading order the dependence on the direction of the magnetic field through the prefactor $\mathbf{H}^{\mathrm{T}} \cdot \mathbf{n}$, where $\mathbf{n}$ is the normal vector to the plane of the $\langle ijk \rangle$ plaquette enclosing the flux $\frac{q}{\hbar}\Phi$.

In analogy to the Zeeman term, the minimization of $\mathcal{H}_{(3)}$ depends on the spatial relation of the field $\mathbf{H}$ to the normal vector $\mathbf{n}$, so that we can introduce the scalar effective field:

$$|\mathbf{H}_{\mathrm{eff},\Phi}| = \tilde{j}_\Phi (\mathbf{n}^{\mathrm{T}} \cdot \mathbf{H}). \tag{3.76}$$

Following the strategy above, we introduce a chiral susceptibility like expression χ_Φ via:

$$\langle \sum_{\langle ijk \rangle} \tilde{\mathbf{S}}_i \cdot (\tilde{\mathbf{S}}_j \times \tilde{\mathbf{S}}_k) \rangle = \chi_\Phi\, |\mathbf{H}_{\mathrm{eff},\Phi}|. \tag{3.77}$$

The scalar chirality scales then as:

$$\mathbf{m}_\chi = (j_\phi \mathbf{n})\, \langle \sum_{\langle ijk \rangle} \tilde{\mathbf{S}}_i \cdot (\tilde{\mathbf{S}}_j \times \tilde{\mathbf{S}}_k) \rangle = \chi_\Phi |\mathbf{H}_{\mathrm{eff},\Phi}| (j_\phi \mathbf{n}). \tag{3.78}$$

Note, that we have defined here $\mathbf{m}_\chi$ as a vector for convenience. It is always oriented parallel to $\mathbf{n}$, and only its norm $|\mathbf{m}_\chi|$ plays a role for the physics. The torque induced by the scalar spin chirality τ_Φ is then given by the following expression:

$$\begin{aligned} \tau_\Phi &= -\mu_B \tilde{\chi}_{0,\Phi} (2 - \zeta_\Phi) |\mathbf{H}_{\mathrm{eff},\Phi}|^{-\zeta_\Phi} \frac{\mathrm{d}|\mathbf{H}_{\mathrm{eff},\Phi}|}{\mathrm{d}\theta} |\mathbf{H}_{\mathrm{eff},\Phi}| \\ &= H^2 \tilde{\chi}_\Phi(H) f_\Phi(\theta). \end{aligned} \tag{3.79}$$

Here, we defined the field-dependent chiral "susceptibility":

$$\tilde{\chi}_\Phi(H) = \mu_B (2 - \zeta_\Phi) \tilde{\chi}_{0,\Phi} H^{-\zeta_\Phi} \tag{3.80}$$

and the angle-dependent function as follows:

$$f_\Phi(\theta) = -\frac{1}{|(j_\Phi \mathbf{n}) \cdot \mathbf{h}|^{\zeta_\Phi}} \left(\frac{\mathrm{d}\mathbf{h}^{\mathrm{T}}}{\mathrm{d}\theta} (j_\Phi \mathbf{n})^{\mathrm{T}} (j_\Phi \mathbf{n}) \cdot \mathbf{h} \right). \tag{3.81}$$

Total generalized torque contribution

The expectation value of the Hamiltonian is determined by the scaling assumptions given by Eq. (3.60), Eq. (3.70), and Eq. (3.77):

$$\langle \mathcal{H} \rangle = -\mu_B \tilde{\chi}_{0,u} |\mathbf{H}_{\mathrm{eff},u}|^{2-\zeta_u} - \mu_B \tilde{\chi}_{0,s} |\mathbf{H}_{\mathrm{eff},s}|^{2-\zeta_s} - \mu_B \tilde{\chi}_{0,\Phi} |\mathbf{H}_{\mathrm{eff},\Phi}|^{2-\zeta_\Phi}. \tag{3.82}$$

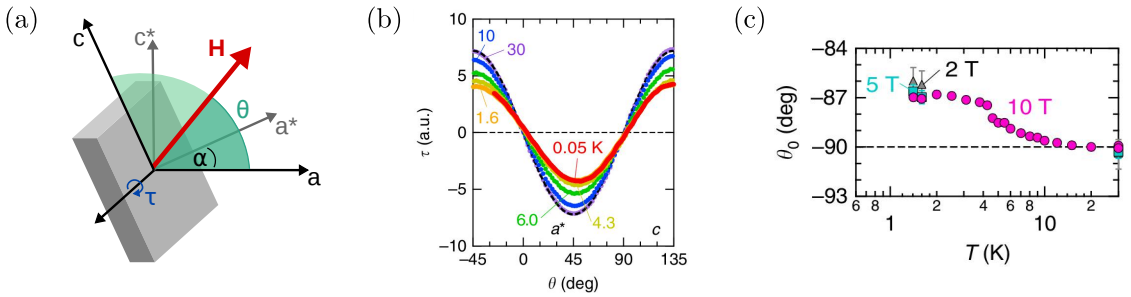

Figure 3.6: (a) Parameter definitions in magnetic torque response, with the field $\mathbf{H}$ rotated in the ac plane of κ-Cu, and θ as the angle between $\mathbf{H}$ and the crystallographic a axis. (b) Experimental angle-dependence of magnetic torque at $H = 10\,\mathrm{T}$, showing a $\tau \propto \sin 2(\theta - \theta_0)$ behaviour [120]. (c) Fig. (a) adapted from Ref. [78], Fig. (b,c) reprinted from Ref. [120].

Hence, the torque expression for a "clean" bulk consists of the sum of the various anisotropic contributions:

$$\begin{aligned}\tau_\mathrm{B} &= \tau_u + \tau_s + \tau_\Phi \\ &= H^2\tilde{\chi}_u(H)f_u(\theta) + H^2\tilde{\chi}_s(H)f_s(\theta) + H^2\tilde{\chi}_\Phi(H)f_\Phi(\theta).\end{aligned} \tag{3.83}$$

Note, that our *ab-initio* estimates for κ-Cu suggest a significant ring-exchange contribution $K/J \sim 0.1$ to the spin Hamiltonian. The isotropic expression for the four-spin term, discussed in Section 2.5, does not contribute to magnetic torque. In principle, including spin-orbit coupling effects leads also in $\mathcal{H}_{(4)}$ to anisotropic ring-exchange terms. However, the leading order contributions to these terms can be "gauged" away the local coordinate transformation $\mathbf{S} \to \tilde{\mathbf{S}}$ detailed in Section 3.3, so that the effects by $\mathcal{H}_{(4)}$ do not explicitly contribute to the torque at lowest order. Similarly, the three-spin term $\mathcal{H}_{(3)}$ contributes through the dependence on the direction of the magnetic field via $(\mathbf{H}\cdot\mathbf{n})$ in lowest order. The spin-spin interaction term, however, does not contribute in lowest order, since anisotropic terms due to SOC are gauged away by the local coordinate transformations and the three-spin term can be expressed in terms of isotropic scalar products $4(\mathbf{a}\cdot\mathbf{S}_i)(\mathbf{b}\cdot\mathbf{S}_i) = \frac{1}{2}\mathbf{a}\cdot\mathbf{b} + i(\mathbf{a}\times\mathbf{b})\cdot\mathbf{S}_i$, as detailed in Appendix A.

3.4.4 Theoretical magnetic torque in κ-Cu

With the generalized torque expression Eq. (3.83) and the *ab-initio* derived spin Hamiltonian for κ-Cu (see Section 2.5), the magnetic angle- and field-dependence of the torque response can be predicted for various critical scenarios. The magnetic torque setup considered below is illustrated as a cartoon in Fig. 3.6(a), with a magnetic field $\mathbf{H}$ rotated in the ac^* plane.

The torque response of these scenarios can then be compared to the main experimental features [120]: (i) The $\tau \propto \sin 2(\theta - \theta_0)$ angle-dependence, shown in Fig. 3.6(b), (ii) the field-dependent angle shift $\theta_0(H)$ shown in Fig. 3.6(c), and (iii) the consistently observed $T_* = 6\,\mathrm{K}$ anomaly [36–38, 120], also observable in Fig. 3.6(c). From the theoretical side, the free parameters are the critical exponents ζ_u, ζ_s, ζ_Φ and the field-independent susceptibility contributions $\tilde{\chi}_{0,u}$, $\tilde{\chi}_{0,s}$, $\tilde{\chi}_{0,\Phi}$. The effective fields $\mathbf{H}_{\mathrm{eff},u}$ and $\mathbf{H}_{\mathrm{eff},s}$ are fully determined by $\mathbb{G}_u$, $\mathbb{G}_s$ and $\mathbb{R}$, which depend solely on the *ab-initio* determined parameters for κ-Cu given in Section 2.5. For the effective field $|\mathbf{H}_{\mathrm{eff},\Phi}|$, we use the field-independent parameter j_ϕ from the same section, and choose $\mathbf{n}$ in the direction of the crystallographic a axis. The angle θ is defined similarly to the angle used by Isono *et al.* [120], where θ is the angle between $\mathbf{H}$ and the long axis of an ET molecule. Here, we approximate this axis with the principal axis of $(\mathbb{G}_u\cdot\mathbb{G}_u^\mathrm{T})$, which is very close to the a axis, as shown in Fig. 3.6(a).

The non-critical case with $\zeta_u = 0$, $\zeta_s = 0$ and $\chi_\Phi = 0$ leads, as mentioned above, the conventional $\propto \sin 2\theta$ angle-dependence for the torque, shown in Fig. 3.7(a). This case corresponds to a material

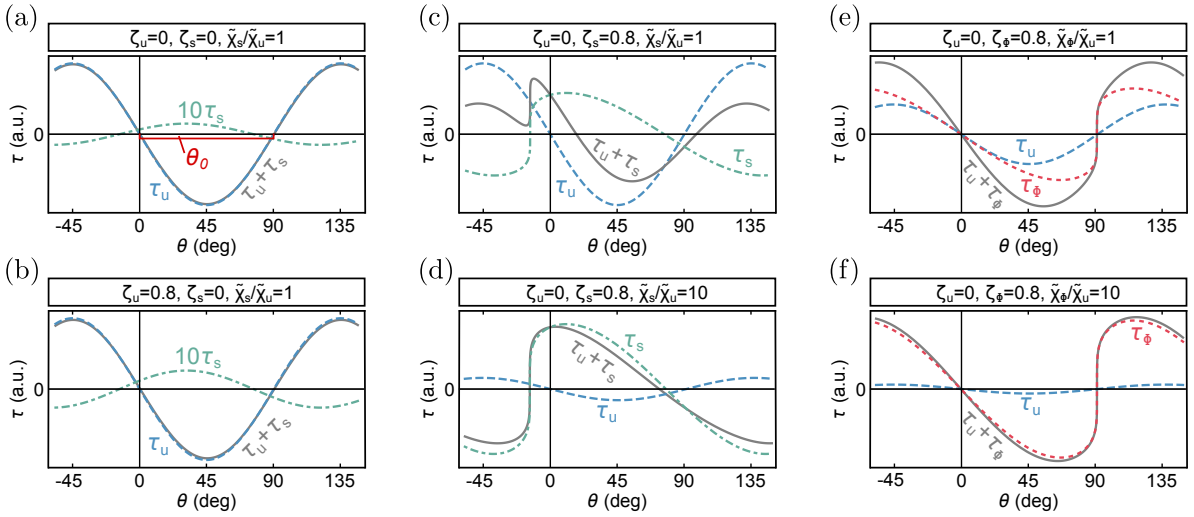

Figure 3.7: Angle-dependence of the magnetic torque, resolved with respect to the uniform (τ_u), staggered (τ_s), and chiral (τ_Φ) contributions, given by Eq. (3.83) for various critical scenarios for the indicated parameters. (a) Non-critical scenario ($\zeta_u = \zeta_s = \zeta_\Phi = 0$), (b) diverging uniform susceptibility ($\zeta_u = 0.8$), (c) diverging staggered susceptibility ($\zeta_s = 0.8$) at intermediate field ($\tilde{\chi}_s/\tilde{\chi}_u = 1$), (d) diverging staggered susceptibility ($\zeta_s = 0.8$) at for fields close to the QCP ($\tilde{\chi}_s/\tilde{\chi}_u = 10$), (e) diverging chiral susceptibility ($\zeta_\Phi = 0.8$) at intermediate field ($\tilde{\chi}_s/\tilde{\chi}_u = 1$), and (f) diverging chiral susceptibility ($\zeta_\Phi = 0.8$) for fields close to the QCP ($\tilde{\chi}_s/\tilde{\chi}_u = 10$). Fig. adapted from Ref. [78].

deep in a QSL state and is consistent with the experimental observation for temperatures above the $T_* = 6\,\mathrm{K}$ anomaly by Isono *et al.* [120]. The staggered contribution τ_s is essentially negligible, and the angle-dependence of the torque stems primarily from anisotropy of the uniform g-tensor $\mathbb{G}_u$. The torque follows a $\sin 2(\theta - \theta_0)$ dependence, with a field-independent angle-shift $\theta_0 \approx 90°$, defined in Fig. 3.7(a). However, for $T < T_*$, the magnetic torque measurements [120] revealed a diverging torque susceptibility instead. Therefore, we considered different critical scenarios and compared the characteristic features to the experimental observation of (i) a $\sin 2(\theta - \theta_0)$ angle-dependence and (ii) a field-dependent angle shift $\theta_0(H)$ [120].

In Fig. 3.7(b) we show the case of a diverging *uniform* susceptibility with a critical exponent of $\zeta_u = 0.8$, matching the experimentally fitted value (see also Fig. 3.6(c)). In this case, we found the experimentally observed $\sin 2(\theta - \theta_0)$ behaviour. This follows directly from the fact, that the uniform g-tensor, see Eq. (3.52), is approximately isotropic, leading to no singularities in the denominator of the angle-dependent function $f_u(\theta)$ given by Eq. (3.66). However, since the total torque corresponds essentially to the uniform contribution of the torque, $\tau \sim \tau_u$, a field-dependent angle-shift $\theta_0(H)$ cannot be obtained within this scenario. Moreover, as pointed out in the context of the μSR analysis above, a critical uniform scenario seems unlikely for κ-Cu. Given the dominant antiferromagnetic interactions, as calculated in Section 2.5, a coupling of a staggered order-parameter to a uniform external field seems counter-intuitive.

In Fig. 3.7(c,d) we show therefore the more intuitive case of a diverging *staggered* susceptibility with a critical exponent $\zeta_s = 0.8$. This scenario would be consistent with the one discussed in the context of the μSR analysis above, that the material is very close to (π, π) order. In this case, we observed a strong dependence of the shape of the total torque curve on the ratio $\tilde{\chi}_s/\tilde{\chi}_u$. The staggered contribution τ_s shows a saw-tooth like angle dependence due to singularities for certain angles in the denominator of $f_s(\theta)$, defined in Eq. (3.73). These singularities stem from the strong anisotropic character of $\mathbb{G}_s + \mathbb{R}$ (see Eq. (3.53) and Eq. (3.45)). For the same order of magnitude, $\tilde{\chi}_s = \tilde{\chi}_u$, i.e. at intermediate field, the linear combination of the sawtooth-shape from the staggered contribution, with the sinusoidal shape from the uniform contribution, lead to a highly unsymmetrical angle-dependence of $\tau = \tau_u + \tau_s$ (shown

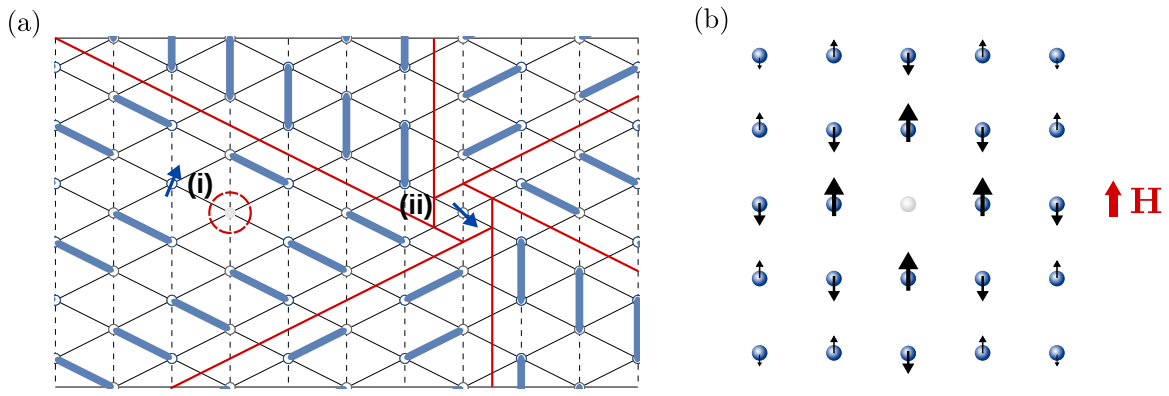

Figure 3.8: (a) Mechanisms in a valence bond glass that lead to localized orphan spins. Singlet bonds are illustrated in blue, domain walls between different valence bond patterns are indicated in red: (i) Anion layer vacancies, emphasized by the red circle, may cause a singlet bond to break, giving rise to an orphan spin, and (ii) domain wall pattern defects may also lead to orphan spins. (b) Impurity cloud with field-induced moments surrounding the bare impurity parallel to the external field and decreasing with distance from the impurity. Fig. (a) adapted from Ref. [78].

in Fig. 3.7(c)). For small fields closer to the QCP, leading to e.g. the ratio $\tilde{\chi}_s = 10\tilde{\chi}_u$, the total shape is dominated by the sawtooth character of the staggered contribution, illustrated in Fig. 3.7(d). Both cases are not consistent with the experimentally observed $\sin 2(\theta - \theta_0)$ angle-dependence [120] and therefore rule out the previously proposed scenario of a staggered critical case [77].

Finally, we considered the case of a diverging *scalar chiral* susceptibility with a critical exponent $\zeta_\Phi = 0.8$, shown in Fig. 3.7(e,f). Similarly to the case of a diverging staggered susceptibility, the chiral contribution leads to a sawtooth shape of the magnetic torque. In this case, the reason are singularities in the angle-dependent function $f_\Phi(\theta)$ given by Eq. (3.81) for in-plane field directions with $\mathbf{H} \cdot \mathbf{n} = 0$. Hence, the steep slope of τ_Φ is located at $\theta = 90°$, corresponding to the c^* direction. For both field regimes, $\tilde{\chi}_\Phi = \tilde{\chi}_u$ (see Fig. 3.7(e)) and $\tilde{\chi}_\Phi = 10\tilde{\chi}_u$ (see Fig. 3.7(f)), it was impossible to obtain the experimentally observed $\sin 2(\theta - \theta_0)$ angle-dependence, thus excluding a chiral critical scenario as well.

On this basis, we concluded that any critical scenario for κ-Cu under field is inconsistent with the experimentally observed magnetic torque response [120].

3.5 κ-Cu as a Valence Bond Glass

After ruling out a critical scenario as a possible explanation for the observed behaviour in κ-Cu, we considered a scenario in which κ-Cu enters a Valence Bond Glass (VBG) state below T_*. This scenario was motivated by works on disorder-induced effects [42, 148] and hints on significant influence of disorder especially from the inhomogeneous NMR response [36], discussed in Section 2.3. The main results presented in this section are published in Ref. [78].

If the bulk material is described by a VBG state, the magnetic response may be dominated by isolated magnetic moments due to disorder. Before we demonstrate the implications on the magnetic torque response, we first discuss the mechanisms, which may lead to the appearance of so-called "orphan" spins.

3.5.1 Orphan spins in κ-Cu

There are two sources, which are likely to induce localized magnetic moments in κ-Cu below T_*, which rely on the ground state being close to a valence bond solid (VBS) phase.

One possible source are reported defects in the anion layer of κ-Cu [134, 149]. Such defects hamper the charge transfer between the anion and the organic layer, so that non-magnetic vacancies emerge. The influence of such a vacancy onto the magnetic response of a system depends on the nature of its ground state. In a vanilla QSL, such as the resonating valence bond (RVB) phase, excitations can be described with spinon quasiparticles, as detailed in Chapter 1. The spinons can travel in the lattice over large distances without additional energy costs, they are deconfined. In this case, the presence of a non-magnetic vacancy has negligible influence onto the magnetic response of the system and the total magnetic behaviour is dominated by the bulk properties of the system [150, 151] . The situation differs strongly if the host system is in a valence bond solid phase, where the valence bonds are frozen in a specific pattern. In this case, the spinons are confined, since their propagation would lead to a rearrangement of the valence bond pattern that costs energy. It has been shown that in this case a non-magnetic vacancy may induce a localized magnetic moment by breaking a valence bond [150–155]. In Fig. 3.8(a) such a situation is illustrated with case (i). Therefore, the magnetic response of the system would be dominated in this case by the impurity induced orphan spins instead of the bulk properties.

A second possible source for orphan spins are inhomogeneities in the interaction parameters between the magnetic sites. Possible microscopic reasons for such a situation in κ-Cu are disorder in the conformations of terminal ethylene groups of the ET molecules [156, 157], randomized orientations within of the anions [158], and local charge distributions within the ET dimers [102, 159, 160]. If the system is in a valence bond solid state, randomized interactions of the host system may induce domain wall patterns, as shown in Fig. 3.8(a). These interplay of these patterns may lead to the emergence of orphan spins, as it is illustrated with case (ii). For a significant number of domain walls, the state is conventionally referred to as a valence bond glass instead of a valence bond solid, in analogy to the conventional glass systems. Recently, Kimchi and coworkers [42, 148] proposed the emergence of a such valence bond glass state in frustrated two-dimensional systems due to these kind of randomized interactions in the framework of a strong disorder renormalization group (SDRG) analysis.

We propose as a possible scenario that κ-Cu enters a VBG phase below $T_* = 6\,\mathrm{K}$, where its magnetic response is dominated by the disorder induced orphan spins due to the confinement in the ground state. Starting with this scenario as an assumption, we will show below, that this it offers, in contrast to the previously discussed criticality, a consistent explanation for the experimentally observed phenomena by μSR and magnetic torque.

3.5.2 Theoretical local moment torque expressions

Starting from the assumption that localized magnetic moments are present in κ-Cu, generalized magnetic torque expressions on the basis of localized magnetic $S = 1/2$ moments in analogy to the bulk expressions in Section 3.4.3 can be derived. Since we consider the case where the magnetic response is dominated by the localized moments, we assume conventional bulk susceptibilities with $\zeta_u = \zeta_s = 0$. At lowest order, impurity effects are independent of the scalar spin chirality. We will therefore neglect the corresponding effects below.

In general, in the regime of orphan spins, the magnetic moment can be effectively described by a localized magnetic moment. However, this magnetic moment belongs usually to an impurity cloud of induced magnetic moments in the host system by e.g. a non-magnetic vacancy, due to fluctuations of the valence bonds around the impurity. In Fig. 3.8(b), we illustrate such an broad screening cloud, where the impurity acquires a moment that is distributed around the impurity with a localization length that scales inversely to the bulk gap. In contrast to the bulk case, where the uniform magnetic moment was approximately perpendicular to the staggered magnetic moment, in the case of the induced defect magnetization, all moments associated with q-vectors are approximately parallel to the external magnetic field [154]. Hence, the effective magnetic moment can be described by a single effective impurity spin variable $\tilde{\mathbf{S}}_\mathrm{I}$. In this approach, the screening cloud is described by the same Hamiltonian as the bulk, where we index the sites inside the screening cloud with i' and the site with the localized moment with m. The uniform contribution corresponds then to the sum over sites i' in the vicinity of site m:

$$\sum_{i' \sim m} \langle \tilde{\mathbf{S}}_{i'} \rangle = c_u \langle \tilde{\mathbf{S}}_{\mathrm{I},m} \rangle, \tag{3.84}$$

where we introduced with c_u a constant that reflects the weight of the uniform Fourier contribution. Similarly, the staggered contribution contains of the sublattice dependent sum over sites i' in the vicinity of site m:

$$\sum_{i' \sim m} \eta_{i'} \langle \tilde{\mathbf{S}}_{i'} \rangle = c_s \langle \tilde{\mathbf{S}}_{\mathrm{I},m} \rangle, \tag{3.85}$$

where we introduced with c_s constant that reflects the staggered (π, π) Fourier contribution. These expressions can be absorbed into an effective impurity g-tensor as a linear combination of the bulk g-tensor:

$$\mathbb{G}_{\mathrm{I}} \approx (c_u \mathbb{G}_u + c_s(\mathbb{G}_s + \mathbb{R})). \tag{3.86}$$

The effective impurity Zeeman term consists then of a sum over the impurity clouds at site m, where the induced moments are encoded in the effective impurity g-tensor:

$$\mathcal{H}_{\mathrm{Zee,I}} = -\mu_B \, \mathbf{H}^{\mathrm{T}} \cdot \sum_m \mathbb{G}_{\mathrm{I},m} \cdot \tilde{\mathbf{S}}_{\mathrm{I},m}. \tag{3.87}$$

This impurity g-tensor generally differs from the bulk g-tensor, depending on the ratio of the induced moments at different wave vectors c_s/c_u in Eq. (3.86). The effective field for a specific localized impurity cloud can be defined analogously to the bulk case in terms of the impurity g-tensor, where we drop the index m of the impurity site for clarity:

$$\mathbf{H}_{\mathrm{eff,I}} = \mathbb{G}_{\mathrm{I}}^{\mathrm{T}} \cdot \mathbf{H}. \tag{3.88}$$

The corresponding impurity magnetization scales then in the known fashion with the effective impurity field:

$$\mathbf{m}_{\mathrm{I}} = \mathbb{G}_{\mathrm{I}} \cdot \langle \tilde{\mathbf{S}}_{\mathrm{I}} \rangle = \chi_{\mathrm{I}} \, \mathbb{G}_{\mathrm{I}} \cdot \mathbf{H}_{\mathrm{eff,I}}. \tag{3.89}$$

The scaling assumption for the susceptibility introduces a scaling exponent for the impurity case:

$$\chi_{\mathrm{I}} = \tilde{\chi}_{0,\mathrm{I}} |\mathbf{H}_{\mathrm{eff,I}}|^{-\zeta_{\mathrm{I}}}, \tag{3.90}$$

and the isotropic contribution follows the general form:

$$\tilde{\chi}_{\mathrm{I}}(H) = \mu_B (2 - \zeta_{\mathrm{I}}) \tilde{\chi}_{0,\mathrm{I}} H^{-\zeta_{\mathrm{I}}}, \tag{3.91}$$

as well as the angle-dependent function:

$$f_{\mathrm{I}}(\theta) = -\frac{1}{|\mathbb{G}_{\mathrm{I}}^{\mathrm{T}} \cdot \mathbf{h}|^{\zeta_{\mathrm{I}}}} \left(\frac{\mathrm{d}\mathbf{h}^{\mathrm{T}}}{\mathrm{d}\theta} \cdot \mathbb{G}_{\mathrm{I}} \cdot \mathbb{G}_{\mathrm{I}}^{\mathrm{T}} \cdot \mathbf{h} \right). \tag{3.92}$$

The impurity torque is in this framework therefore fully determined by the impurity susceptibility $\tilde{\chi}_{\mathrm{I}}(H)$ and the angle-dependent function that depends on the impurity scaling exponent ζ_{I} and the effective impurity g-tensor $\mathbb{G}_{\mathrm{I}}$:

$$\tau_{\mathrm{I}} = H^2 \tilde{\chi}_{\mathrm{I}}(H) f_{\mathrm{I}}(\theta) \tag{3.93}$$

The total torque of the system is the sum of the bulk torque τ_{B}, given by Eq. (3.83), and the impurity torque τ_{I}:

$$\tau = \tau_{\mathrm{B}} + \tau_{\mathrm{I}}. \tag{3.94}$$

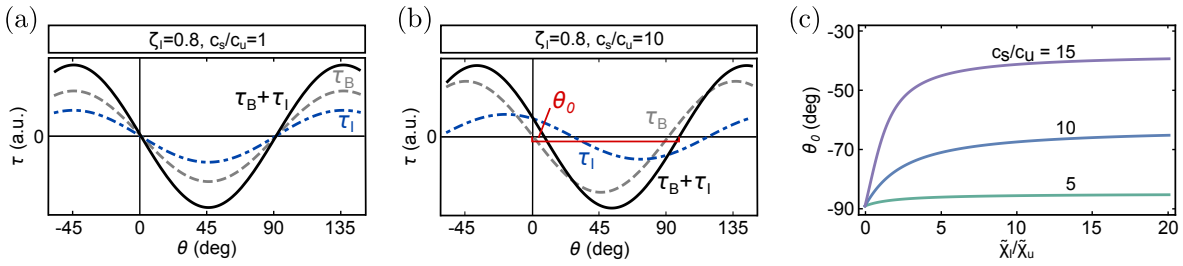

Figure 3.9: Torque features including bulk (τ_{B}) and impurity (τ_{I}) effects with impurity exponent $\zeta_{\mathrm{I}} = 0.8$. (a) Angle-dependence with equal contributions from uniform and staggered moments ($c_s/c_u = 1$), (b) angle-dependence for $c_s > c_u$ with induced angle-shift θ_0 indicated, (c) angle-shift θ_0 as a function of the ratio $\tilde{\chi}_{\mathrm{I}}/\tilde{\chi}_{\mathrm{u}}$ for indicated c_s/c_u. Fig. adapted from Ref. [78].

3.5.3 Total torque response of κ-Cu

On the basis of the theoretical expressions above, the experimental observation of (i) a $\tau \propto \sin 2(\theta - \theta_0)$ angle-dependence, (ii) a field-dependent angle shift $\theta_0(H)$ [120] for temperatures below T_* can be tested against the scenario of orphan spins dominating the magnetic torque response in κ-Cu.

In Fig. 3.9(a) we show the angle-dependence of the torque with an impurity scaling exponent $\zeta_{\mathrm{I}} = 0.8$. We assumed conventional scaling of the bulk susceptibility ($\zeta_u = \zeta_s = \zeta_\Phi = 0$), and assumed the same order of magnitude from the bulk with $\tilde{\chi}_{\mathrm{I}} = \tilde{\chi}_u = \tilde{\chi}_s$ for simplicity. For identical contributions from the staggered and uniform magnetic moments, $c_s/c_u = 1$, we obtained, in agreement with experiment, a sinusoidal angle-dependence of the total torque. However, the second experimental feature, the field dependence of the angle shift θ_0, could not be obtained within this parameter set. This follows directly from the fact, that in this case the denominator in the angle-dependent functions $f(\theta)$ is the exactly same from the bulk and the impurity contributions. The same would be true for $c_s < c_u$, where the dominant part in the impurity g-tensor would be the approximately isotropic uniform part.

In contrast, if $c_s > c_u$, a field-dependent angle shift is possible. The sum with the uniform contribution prevents singularities in the angle-dependent function $f_{\mathrm{I}}(\theta)$, which ensures a sinusoidal shape of the total angle-dependent torque. In Fig. 3.9(b), we show the torque for $c_s/c_u = 10$, which shows both of the discussed experimental features. Hence, the presence of a large staggered magnetic moment together with an unconventional scaling in field of the impurity part meets both of the experimental observations regarding the field-dependence.

As illustrated in Fig. 3.9(c), a significant angle shift for $\zeta_{\mathrm{I}} = 0.8$ can already be observed for moderate ratios of $\tilde{\chi}_{\mathrm{I}}/\tilde{\chi}_u$. A more important factor is the ratio between the staggered and uniform magnetic moments c_s/c_u. To meet the experimentally observed angle shift [120], we expect $c_s/c_u \approx 5 - 10$. For such a large ratio, the system has to be close to a quantum critical point toward Néel phase in terms of magnetic parameter ratios (e.g. J/J' or K/J). Which ratio can be expected for the appropriate material parameters would have to be determined via solving directly the spin expectation values with other methods.

3.5.4 Outlook: Interacting orphan spins

The remaining question for this framework is whether the experimentally observed scaling exponents are consistent with the proposed valence bond glass scenario. Intuitively, it may be expected that scaling exponents are significantly sample dependent in the case of impurities as the most important feature. In order to address this issue, interactions between the orphan spins have to be considered. This analysis was done with Stephen M. Winter in Ref. [78], here we briefly summarize the most important findings.

In general, the broad screening clouds that surround orphan spins overlap, leading to an interaction between the localized moments. This situation has been tackled in the framework of strong disorder renormalization group (SDRG) formalism [161–164]. Since the effective interaction between the impurity

clouds depends on their distance, in general there are randomized ferromagnetic and antiferromagnetic interactions expected. Lowering the temperature below the effective interaction of these clouds, the interacting impurities can be described by clusters of strongly correlated spins that grow with decreasing temperature. Such a situation can be described in the framework of a finite randomness large-spin fixed point (LSFP) [161, 162]. The properties of such a system can be described with the following effective energy scale:

$$\Omega = \Omega_0 \max(k_B T, \mu_B S_{\text{eff}}^{\text{avg}} |\mathbb{G}_{\text{I}}^{\text{T}} \cdot \mathbf{H}|), \tag{3.95}$$

which is either dominated by the thermal energy $k_B T$, or by the approximated impurity Zeeman energy $\mu_B S_{\text{eff}}^{\text{avg}} |\mathbb{G}_{\text{I}}^{\text{T}} \cdot \mathbf{H}|$. Here, we introduced the average magnetic moment per cluster $S_{\text{eff}}^{\text{avg}} = S_0 \Omega^{-\kappa}$ with $\kappa \geq 0$ with the non-universal exponent κ that defines the scaling of the effective moment with the effective field and the average cluster spin at fixed temperature and field S_0. In the case of a LSFP, it has been argued [161, 162], that the number of impurity clusters N_C scales as $N_C = N_0 \Omega^{2\kappa}$, where N_0 is the average cluster density at fixed temperature and field. In this case, the non-universal exponent fulfils the inequality $2\kappa \leq 1$, since the number of clusters should decrease with the effective energy scale. Together with the constraint above that $\kappa \geq 0$, the non-universal exponent κ is restricted by the following inequality:

$$1 \leq (2\kappa)^{-1} \leq \infty. \tag{3.96}$$

The localized magnetic moments can be described in this framework with a modified Brillouin function $\mathcal{B}(S, x)$, which results in the following impurity torque expression:

$$\tau_{\text{I}} \approx H g(\theta) N_C S_{\text{eff}}^{\text{avg}} \mathcal{B}\left(S_{\text{eff}}^{\text{avg}}, \frac{\mu_B |\mathbb{G}_{\text{I}}^{\text{T}} \cdot \mathbf{H}|}{k_B T} \right), \tag{3.97}$$

where the angle-dependent function $g(\theta)$ is defined as the limit of $f_{\text{I}}(\theta)$ in Eq. (3.92) with $\zeta_{\text{I}} = 0$.

In the low-temperature limit $k_B T \ll \mu_B S_{\text{eff}}^{\text{avg}} |\mathbb{G}_{\text{I}}^{\text{T}} \cdot \mathbf{H}|$, the Brillouin function can be approximated as $\mathcal{B}(S, x \to \infty) \approx 1$, while the effective energy scale in Eq. (3.95) is dominated by the Zeeman contribution, $\Omega = \Omega_0 \mu_B S_{\text{eff}}^{\text{avg}} |\mathbb{G}_{\text{I}}^{\text{T}} \cdot \mathbf{H}|$. Since the average magnetic moment per cluster depends also on the effective energy scale, $S_{\text{eff}}^{\text{avg}} = S_0 \Omega^{-\kappa}$, Ω scales with field as $\Omega^{1+\kappa} = \Omega_0 \mu_B S_0 |\mathbb{G}_{\text{I}}^{\text{T}} \cdot \mathbf{H}|$. The field-dependence of the torque expression Eq. (3.97) in the low temperature limit follows directly:

$$\tau_{\text{I}} \propto H N_C S_{\text{eff}}^{\text{avg}} = H N_0 S_0 \Omega^{\kappa} = H N_0 S_0 (\Omega_0 \mu_B S_0 |\mathbb{G}_{\text{I}}^{\text{T}} \cdot \mathbf{H}|)^{\frac{\kappa}{1+\kappa}}. \tag{3.98}$$

Comparing this expression with the single local moment case, given by Eq. (3.93), leads to a relation between the scaling exponents in the two frameworks: $\frac{\kappa}{1+\kappa} - 1 = -\zeta_{\text{I}}$. Together with the inequality for the non-universal scaling exponent κ in Eq. (3.96), this leads to a restriction of the scaling exponent ζ_{I} in a narrow window at low temperatures:

$$2/3 \lesssim \zeta_{\text{I}} \leq 1. \tag{3.99}$$

In addition to the sinusoidal behaviour of the torque and the field-dependent angle shift $\theta_0(\theta)$, consideration of interaction between the localized moments provided therefore a relatively narrow range for possible critical exponents in field, explaining the weak variation between samples. We therefore concluded, see Ref. [78], that disorder effects could explain, in principle, the observed torque response.

3.6 Summary

This chapter was devoted to two scenarios dealing with the mysterious magnetic behaviour of the triangular lattice organic κ-Cu (κ-$(\text{ET})_2\text{Cu}_2(\text{CN})_3$). Not only seemed experiments to contradict each other, where specific heat suggested a gapless QSL state, while thermal transport gave evidence for a gapped QSL. Also, the puzzling $T_* = 6\,\text{K}$ anomaly lacked any satisfying explanation.

One scenario proposed to explain some of these aspects was exotic criticality with the magnetic field as a tuning parameter. After a brief introduction of the concept of criticality and a review of

the experimentally observed critical exponents, we investigated the coupling mechanisms of κ-Cu to a magnetic field. Starting from the dominant anisotropic interaction terms including their orientation pattern determined in Chapter 2, we could follow a well-known strategy to "gauge" anisotropic terms away with local spin rotations. In this case, all anisotropy effects are captured in the single-spin term in the Hamiltonian in terms of an effective field $\mathbf{H}_{\mathrm{eff},s}$. Symmetries in the $P2_1/c$ space group determined that a magnetic field couples to the magnetic model Hamiltonian such that this strategy is applicable.

We presented then two scenarios in the context of the experimentally observed behaviour of κ-Cu. A critical scenario under the consideration of spin-orbit coupling effects could be tested with the observations in powder μSR measurements. The change in the scaling of field-dependent μSR linewidth $B_e \propto m$ at a field H_0 could indeed be explained consistently in this framework. For this, we did not calculate the spin expectation value in the magnetization expression explicitly, but took advantage of general scaling behaviour in critical scenarios with the scaling exponents as fit parameters. The finding of a critical scenario with a diverging staggered contribution at low fields met the intuitive expectation for a system with antiferromagnetic interaction bordering Néel order. However, while this scenario seemed promising, it removed the exotic aspect of the original proposal and left therefore the seemingly contradicting experiments and the T_* anomaly unexplained.

We then checked the theory of criticality including anisotropic terms against magnetic torque data and their key features of sinusoidal angle-dependence and a field and temperature-dependent angle-shift. After the derivation of generalized expressions for the magnetic torque at $T = 0$, we tested a variety of critical scenarios, with diverging uniform, staggered and chiral contributions. However, none of the scenarios could match the key experimental features. Therefore, we had to dismiss criticality as the central answer for the puzzling behaviour of κ-Cu.

Instead, we considered a situation in which orphan spins dominate the magnetic response of κ-Cu below the infamous $T_* = 6\,\mathrm{K}$ anomaly. In this scenario, κ-Cu is considered a "vanilla" QSL, where the valence bonds freeze at $T_* = 6\,\mathrm{K}$ and enter a valence bond glass (VBG) state. In a host system with confined spinons, as it is the case for a VBG, non-magnetic vacancies or randomized interactions may lead to localized magnetic moments, or "orphan spins". The effects of isolated magnetic moments in a bulk system described by the model Hamiltonian determined in Chapter 2, implied a torque behaviour with both experimental features, $\tau \propto \sin 2(\theta - \theta_0)$ and $\theta_0(H)$. As pointed out in the outlook, the additional consideration of interaction between the orphan spins offered also an explanation for the temperature-dependence of θ_0 and why the exponents in the torque susceptibility are not strongly sample dependent.

Moreover, the framework of orphan spins may also explain the seemingly contradicting experiments of thermal conductivity and specific heat. In the proposed scenario, low-lying excitations can be pictured as local domain wall fluctuations. This restructuring of the VGB domain wall pattern does not have an energy gap, leading to a linear temperature dependence of the specific heat [165–167], as it is also predicted for conventional structural glasses [168]. On the other hand, since these excitations are *local* domain wall fluctuations, there is no contribution to the thermal conductivity κ_T in the $T \to 0$ limit.

As a next step it would be interesting to see, what the specific solution of the Hamiltonian in the framework of orphan spins would be. A detailed and careful analysis, e.g. with SDRG, would certainly help to enlighten whether this scenario is robust against further consistency checks. For example, it would be very helpful to develop a theory for the response in the μSR experiment taking localized moments into account.

Chapter 4

Anisotropic magnetic interactions in the pyrochlore lattice

4.1 Introduction

In this chapter, we discuss in more detail the hybrid method to determine magnetic interactions from a combination of *ab-initio* methods with exact diagonalization on the example of pyrochlore compounds. The pyrochlore geometry is arguably the most prominent example of a geometrically frustrated system in three dimensions. It is composed of tetrahedra, illustrated in Fig. 4.1(a), the three-dimensional version of triangular units which inspired Anderson to his proposal of spin liquid states due to frustration [2]. The high symmetry of the pyrochlore lattice leads to strong constraints onto anisotropic interactions, so that this geometry is especially convenient to detail and test the hybrid method.

From a theoretical point of view, the pyrochlore lattice offers a rich play ground for various exotic magnetic ground states [3, 169, 170]. For antiferromagnetic nearest-neighbour Heisenberg interactions, there have been suggestions for a quantum spin-liquid (QSL) ground state [171–173], that were later discussed for more complicated, experimentally motivated, models as a so-called quantum spin-ice state [174]. Interestingly, for a ferromagnetic coupling of classical Ising spins along the cubic [111] direction, i.e. towards the center of the tetrahedra, frustration arises as well [3, 5, 169]. These types of interaction are often discussed in the context of a "classical" spin ice, where the two-in, two-out spin configurations in the pyrochlore lattice are similar to the proton positions in water ice [175]. Recently, Liu *et al.* [176] picked up the initial motivation of putative QSL states, with a systematic classification of $\mathbb{Z}_2$ spin-liquid states on the pyrochlore lattice on the basis of various mean-field ansätze.

In the real materials, one of the most famous class of pyrochlores consists of the rare-earth pyrochlore oxides, which are described usually with the formular $A_2B_2O_7$, where A is a $4f$ rare-earth trivalent ion [169]. A famous example is the spin-ice material $Dy_2Ti_2O_7$, for which it was possible to derive from thermodynamic arguments that the ice rules are obeyed [177]. It has then drawn much attention in the late 2000s, when its experimental data have been interpreted in terms of the first measurement of magnetic monopoles [178–180]. Recent interest was devoted the family of ytterbium pyrochlores with A = Yb, where AFM and FM ground states have been observed by modifying the B element and hence a close competition amongst weakly ordered states is suspected [170]. Especially $Yb_2Ti_2O_7$, previously discussed as a QSL candidate [169], seems to be puzzling to date, although it was recently proposed to be a weak ferromagnet with strong sample variations due to disorder [181]. Other observed phenomena related to magnetic order in pyrochlore compounds were, for example, an order-by-disorder mechanism in the XY antiferromagnet $Er_2Ti_2O_7$ [182] and a debated noncollinear all-in-all-out order in $Y_2Ir_2O_7$ [183, 184].

In this chapter, we discuss two spin 1/2 pyrochlore materials that seem to share most microscopic properties at first glance, but possess very different ground states. $Lu_2V_2O_7$ orders ferromagnetically [185–187], while $Lu_2Mo_2O_5N_2$ is a QSL candidate [188]. In both cases, spin-orbit coupling (SOC) effects play an important role. In the QSL candidate, this can be assigned straightforwardly to the heavy

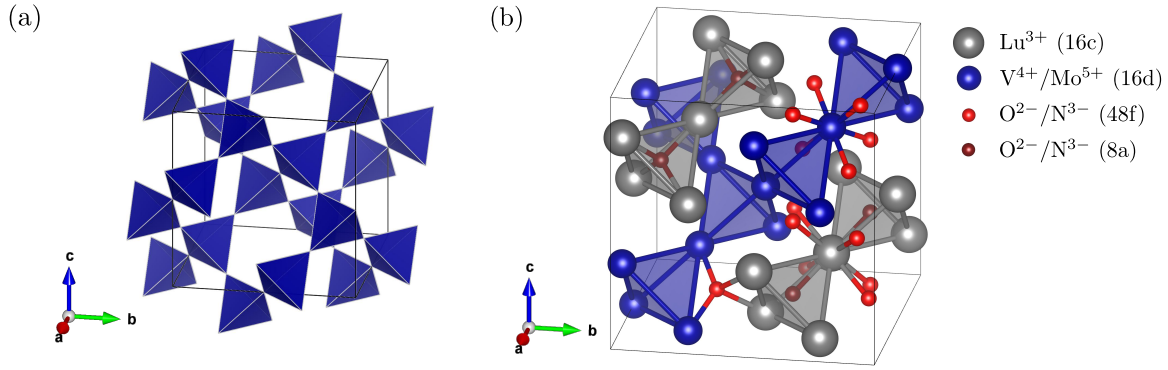

Figure 4.1: (a) Network of corner-sharing tetrahedra by A or B sites in cubic pyrochlore oxides $A_2B_2O_7$. (b) Crystal structure of $Lu_2V_2O_7$ and $Lu_2Mo_2O_5N_2$. Illustrated are the corner-sharing tetrahedra of Lu^{3+} ions with Wyckoff position 16c, the corner-sharing tetrahedra of V4+ or Mo5+ ions on 16d, the sixfold coordination of the magnetic site by O^{2-} or N^{3-} ions on 48f, and the eightfold coordination of Lu with two additional O/N ions on the 8a Wyckoff position. The crystal environment of the 48f O/N ions consists of two V/Mo ions and two Lu ions, while the environment of the 8a O/N ion are always four Lu ions.

magnetic ion Mo^{5+}. In the ferromagnet this is less obvious, where the magnetism is carried by the lighter V^{4+} ion. However, in this case, the isotropic exchange is suppressed by competing mechanisms of AFM contributions with Hund's coupling, thus the significance of usually smaller terms is increased. In order to investigate the SOC effects in the magnetic model, we focused on the bilinear magnetic Hamiltonian, which is in the most general form for spin-1/2 ions given by the following expression:

$$\mathcal{H}_{\text{spin}} = \sum_{\langle ij \rangle} J_{ij} \left(\mathbf{S}_i \cdot \mathbf{S}_j\right) + \mathbf{D}_{ij} \cdot \left(\mathbf{S}_i \times \mathbf{S}_j\right) + \mathbf{S}_i \cdot \Gamma_{ij} \cdot \mathbf{S}_j, \tag{4.1}$$

with the SOC induced Dzyaloshinskii-Moriya vector $\mathbf{D}_{ij}$ and the pseudo-dipolar tensor Γ_{ij}.

This chapter is organized as follows. In order to provide context for the desired exchange parameters and their specific properties on pyrochlore lattices, we discuss the related symmetry constraints due to Moriya's rules in Section 4.2. Then, in Section 4.3, we introduce the extended Hubbard Hamiltonian for d block electrons to obtain the starting point for the exact diagonalization step in the hybrid method. Then, in Section 4.4, we discuss the hybrid method at the example of the ferromagnet $Lu_2V_2O_7$. In Section 4.5 we apply the same method to the QSL candidate $Lu_2Mo_2O_5N_2$. Finally, we summarize the main conclusions presented in this chapter in Section 4.6. The results for the two materials are published in Ref. [79, 80]. The hybrid method was also discussed in the feature article Ref. [60].

4.2 Magnetic exchange parameters in pyrochlores

In this chapter, we focus on the influence of anisotropic interactions on spin 1/2 pyrochlore compounds. These systems are highly symmetric and crystallize in a face-centered cubic space group. However, the absence of bond inversion symmetry allows for a finite nearest-neighbour Dzyaloshinskii-Moriya interaction [189]. A classical Monte Carlo study of nearest neighbour AFM Heisenberg exchange with DM interaction on the pyrochlore lattice by Elhajal *et al.* [189] revealed a strong influence of the DM interaction on the ground state even for small DM values. For a DM arrangement referred to as the "direct" case, further detailed below, the QSL ground state was lifted in favour of an all-in-all-out ordering at a transition temperature on the order of the DM interaction. For the "indirect" case, "order by disorder" effects favoured a coplanar ordering also below a temperature $T_c \approx |\mathbf{D}|/k_B$. It is an open question how much influence quantum fluctuations for spin 1/2 cases have on these findings, although Elhajal *et al.* [189] argued that, due to the high dimensionality and similar findings of a quantum

Atom	Wyckoff position	Coordinates	$Lu_2V_2O_7$	$Lu_2Mo_2O_5N_2$	(ideal) environment
A	16d	$(\frac{1}{2},\frac{1}{2},\frac{1}{2})$	V^{4+}	Mo^{5+}	(O,O/N) octahedra
B	16c	$(0,0,0)$	Lu^{3+}	Lu^{3+}	eight (O,O/N)
C	48f	$(x,\frac{1}{8},\frac{1}{8})$	O^{2-}	O^{2-}/N^{3-}	Lu/(V,Mo) tetrahedra
C′	8a	$(\frac{1}{8},\frac{1}{8},\frac{1}{8})$	O^{2-}	O^{2-}	Lu tetrahedra

Table 4.1: Crystallographic positions for the space group $Fd\bar{3}m$ for a pyrochlore $A_2B_2C_6C'$ with origin at 16*c*. The specific atoms for $Lu_2V_2O_7$ and $Lu_2Mo_2O_5N_2$ are also given, illustrated in Fig. 4.1(b).

mechanical treatment with different approximations [190], at least the qualitative statement should also hold for the extreme quantum case with $S = 1/2$.

In this section, we first introduce the pyrochlore lattice and its symmetries in more detail. Then we discuss Moriya's rules for the DM interaction based on symmetry considerations for the pyrochlore case and reproduce with that results by Elhajal *et al.* [189]. Based on that, we extend this framework to obtain restrictions onto the pseudo-dipolar tensor in $\mathcal{H}_{\mathrm{PD}} = \mathbf{S}_1 \cdot \Gamma_{12} \cdot \mathbf{S}_2$. We will see that, in the case of the pyrochlore lattice, very few parameters remain independent.

4.2.1 The pyrochlore lattice

As mentioned above, cubic pyrochlore oxides can usually be described with the formula $A_2B_2O_7$, where the A and the B ions form two interpenetrating lattices of corner-sharing tetrahedra. In Fig. 4.1(a) we illustrate such a network for one sublattice of A or B sites. To refer to every lattice of corner-sharing tetrahedra as a "pyrochlore" lattice has been established for around thirty years. Originally, the expression stems from the compound $NaCaNb_2O_6F$, which produces a green flame when burned and was therefore named after the Greek translation of "green fire" in 1930 by von Gaertner [169]. Most pyrochlore materials crystallize in the highly symmetric face-centred cubic space group $Fd\bar{3}m$. They possess a C_3 three-fold rotational symmetry about the axes toward the tetrahedra centres, commonly referred to as local $\hat{z}$, or cubic [111], axes. In Fig. 4.1(b) we show the generalized crystal structure of the two compounds discussed in this chapter, $Lu_2V_2O_7$ and $Lu_2Mo_2O_5N_2$, with emphasis on the electronic environment of the atoms at the different Wyckoff positions. The typical trivalent rare-earth ion is in both cases Lu^{3+} on the A site, here assigned to Wyckoff position 16c, and the magnetism is varied by V^{4+} or Mo^{5+} on the B site, assigned to the Wyckoff position 16d. Note, that there is only one adjustable positional parameter x for the O or N atom at position 48f, given in Table 4.1. This parameter controls the coordination geometry of the magnetic site.

4.2.2 Moriya's rules: Symmetry constraints in the pyrochlore lattice

In 1960, Tôru Moriya formulated rules constraining the direction of DM vectors in $\mathcal{H}_{\mathrm{DM}} = \mathbf{D}_{12} \cdot (\mathbf{S}_1 \times \mathbf{S}_2)$ based only on the symmetries of the material [49]. In the case of two ions located at points A and B with the point C bisecting the straight line A-B (illustrated on the example of one tetrahedron in the pyrochlore lattice in Fig. 4.2(a)), Moriya's rules [49] can be summarized with the following five points:

1. Inversion center at C: $\mathbf{D} = 0$
2. Mirror plane $\perp$ A-B, through C: $\mathbf{D} \parallel$ mirror plane or $\mathbf{D} \perp$ A-B
3. A, B $\in$ mirror plane: $\mathbf{D} \perp$ mirror plane
4. Two-fold rotation axis $\perp$ A-B, through C: $\mathbf{D} \perp$ two-fold axis
5. n-fold axis ($n \geq 2$) $\parallel$ A-B: $\mathbf{D} \parallel$ A-B

Below, we discuss the resulting constraints onto the anisotropic interaction parameters in the pyrochlore lattice, that were for the DM interaction already pointed out in Ref. [189]. The specific derivation of the symmetrically allowed contributions is mainly based on the fact that a magnetic state has to be energetically degenerate with every other magnetic state related via a symmetry operation of the

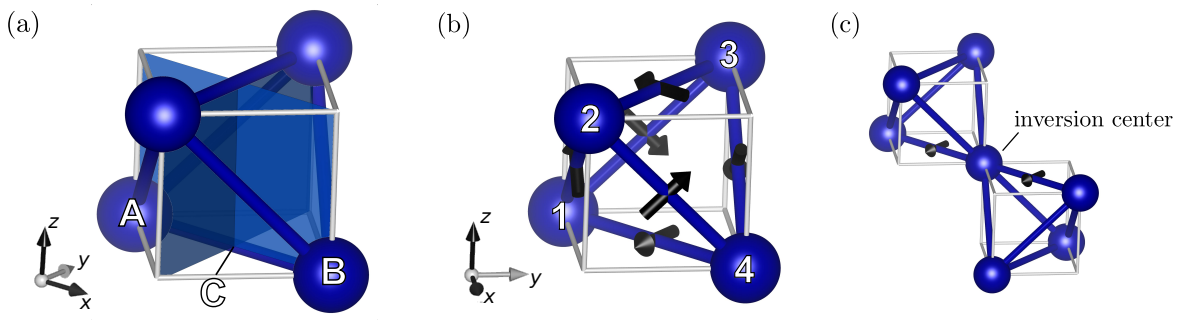

Figure 4.2: (a) Tetrahedron of magnetic sites with the two (perpendicular) mirror planes with respect to the A-B bond. The point C intersects the A-B bond in the middle. (b) Dzyaloshinksii-Moriya vectors within a tetrahedron of the pyrochlore lattice. Bond 1-2 is related to the bond A-B from (a) by rotation. The other vectors in the tetrahedron follow from the symmetry restrictions on the pyrochlore lattice. (c) Connection of two tetrahedra in the pyrochlore lattice by inversion center. Fig. (a,b) adapted from Ref. [79].

crystallographic space group. The detailed derivations for the DM vector and the pseudo-dipolar tensor are given in Appendix B. Here, we discuss the most important implications for the magnetic Hamiltonian.

DM orientations in the pyrochlore lattice

The most relevant symmetry elements for one bond in the pyrochlore lattice are the two mirror planes, illustrated in Fig. 4.2(a) for bond A-B, intersected at point C. Under consideration of point 2 and 3 of Moriya's rules we confirmed in Appendix B that in this case there is only one independent component in the DM vector:

$$\mathbf{D}_{\mathrm{AB}} = \begin{pmatrix} 0 \\ D^{y}_{\mathrm{AB}} \\ 0 \end{pmatrix}, \tag{4.2}$$

in the coordinate system shown in Fig. 4.2(a). Therefore, the only material specific degrees of freedom are the sign of the DM vector and its order of magnitude $|\mathbf{D}_{\mathrm{AB}}|$. Both depend on microscopic details like the filling, the occupied orbitals or the crystal field. Once one bond is determined quantitatively, the sign and the order of magnitude of the DM vectors on other bonds in the crystal are determined by symmetry. For example, the DM vector on bond 1-2 in Fig. 4.2(b) follows from $\mathbf{D}_{14}$ via a rotation of $2/3\pi$ about the [111] axis. For all six bonds in one pyrochlore tetrahedron we obtained then the following expressions:

$$\begin{aligned}
\mathbf{D}_{12} &= \frac{1}{\sqrt{2}} \begin{pmatrix} -D^{y}_{\mathrm{AB}} \\ 0 \\ +D^{y}_{\mathrm{AB}} \end{pmatrix}, \quad \mathbf{D}_{13} = \frac{1}{\sqrt{2}} \begin{pmatrix} 0 \\ +D^{y}_{\mathrm{AB}} \\ -D^{y}_{\mathrm{AB}} \end{pmatrix}, \quad \mathbf{D}_{14} = \frac{1}{\sqrt{2}} \begin{pmatrix} +D^{y}_{\mathrm{AB}} \\ -D^{y}_{\mathrm{AB}} \\ 0 \end{pmatrix}, \\
\mathbf{D}_{23} &= \frac{1}{\sqrt{2}} \begin{pmatrix} -D^{y}_{\mathrm{AB}} \\ -D^{y}_{\mathrm{AB}} \\ 0 \end{pmatrix}, \quad \mathbf{D}_{24} = \frac{1}{\sqrt{2}} \begin{pmatrix} 0 \\ +D^{y}_{\mathrm{AB}} \\ +D^{y}_{\mathrm{AB}} \end{pmatrix}, \quad \mathbf{D}_{34} = \frac{1}{\sqrt{2}} \begin{pmatrix} -D^{y}_{\mathrm{AB}} \\ 0 \\ -D^{y}_{\mathrm{AB}} \end{pmatrix}.
\end{aligned} \tag{4.3}$$

For each bond, the DM vector is perpendicular to the corresponding bond and within the surface of the enclosing cube. For $D^{y}_{\mathrm{AB}} > 0$ the above expresseions correspond to the so-called "indirect" case, an expression introduced by Elhajal*et al.* [189] to distinct between the two possible DM configurations on a pyrochlore lattice. Such an indirect case is illustrated in Fig. 4.2(b), corresponding to the coordinate systems used for the expressions above. Since two tetrahedra are connected by an inversion center at the common site, illustrated in Fig. 4.2(c), the DM vectors in the entire crystal can be constructed by symmetry. Within this chapter we discuss with the hybrid method a possibility to determine both, the sign and the order of magnitude, for a given crystal structure based on *ab-initio* methods.

Pseudo-dipolar tensor in the pyrochlore lattice

The same considerations as for the DM interaction based on Moriya's rules are also valid for the pseudo-dipolar tensor, detailed in Appendix B. The general pseudo-dipolar contribution $\mathcal{H}_{\mathrm{PD}}$ is defined as follows:

$$\mathcal{H}_{\mathrm{PD}} = \begin{pmatrix} S_{\mathrm{A}}^x & S_{\mathrm{A}}^y & S_{\mathrm{A}}^z \end{pmatrix} \begin{pmatrix} \Gamma_{\mathrm{AB}}^{xx} & \Gamma_{\mathrm{AB}}^{xy} & \Gamma_{\mathrm{AB}}^{xz} \\ \Gamma_{\mathrm{AB}}^{xy} & \Gamma_{\mathrm{AB}}^{yy} & \Gamma_{\mathrm{AB}}^{yz} \\ \Gamma_{\mathrm{AB}}^{xz} & \Gamma_{\mathrm{AB}}^{yz} & -(\Gamma_{\mathrm{AB}}^{xx} + \Gamma_{\mathrm{AB}}^{yy}) \end{pmatrix} \begin{pmatrix} S_{\mathrm{B}}^x \\ S_{\mathrm{B}}^y \\ S_{\mathrm{B}}^z \end{pmatrix}. \tag{4.4}$$

The symmetrically allowed components of the pseudo-dipolar tensor Γ_{AB} for the coordinate system for bond A-B shown in Fig. 4.2(a), contains only two independent contributions:

$$\Gamma_{\mathrm{AB}} = \begin{pmatrix} \Gamma_{\mathrm{AB}}^{xx} & 0 & 0 \\ 0 & \Gamma_{\mathrm{AB}}^{yy} & 0 \\ 0 & 0 & -(\Gamma_{\mathrm{AB}}^{xx} + \Gamma_{\mathrm{AB}}^{yy}) \end{pmatrix}. \tag{4.5}$$

From the same symmetry relations as used in the case of the DM vectors, the pseudo-dipolar tensor is fully determined by rotations into the coordinate system depicted in Fig. 4.2(b):

$$\Gamma_{12} = \begin{pmatrix} \frac{\Gamma_{\mathrm{AB}}^{xx}+\Gamma_{\mathrm{AB}}^{yy}}{2} & 0 & \frac{\Gamma_{\mathrm{AB}}^{xx}-\Gamma_{\mathrm{AB}}^{yy}}{2} \\ 0 & -(\Gamma_{\mathrm{AB}}^{xx}+\Gamma_{\mathrm{AB}}^{yy}) & 0 \\ \frac{\Gamma_{\mathrm{AB}}^{xx}-\Gamma_{\mathrm{AB}}^{yy}}{2} & 0 & \frac{\Gamma_{\mathrm{AB}}^{xx}+\Gamma_{\mathrm{AB}}^{yy}}{2} \end{pmatrix}, \; \Gamma_{13} = \begin{pmatrix} -(\Gamma_{\mathrm{AB}}^{xx}+\Gamma_{\mathrm{AB}}^{yy}) & 0 & 0 \\ 0 & \frac{\Gamma_{\mathrm{AB}}^{xx}+\Gamma_{\mathrm{AB}}^{yy}}{2} & \frac{\Gamma_{\mathrm{AB}}^{xx}-\Gamma_{\mathrm{AB}}^{yy}}{2} \\ 0 & \frac{\Gamma_{\mathrm{AB}}^{xx}-\Gamma_{\mathrm{AB}}^{yy}}{2} & \frac{\Gamma_{\mathrm{AB}}^{xx}+\Gamma_{\mathrm{AB}}^{yy}}{2} \end{pmatrix},$$

$$\Gamma_{14} = \begin{pmatrix} \frac{\Gamma_{\mathrm{AB}}^{xx}+\Gamma_{\mathrm{AB}}^{yy}}{2} & \frac{\Gamma_{\mathrm{AB}}^{xx}-\Gamma_{\mathrm{AB}}^{yy}}{2} & 0 \\ \frac{\Gamma_{\mathrm{AB}}^{xx}-\Gamma_{\mathrm{AB}}^{yy}}{2} & \frac{\Gamma_{\mathrm{AB}}^{xx}+\Gamma_{\mathrm{AB}}^{yy}}{2} & 0 \\ 0 & 0 & -(\Gamma_{\mathrm{AB}}^{xx}+\Gamma_{\mathrm{AB}}^{yy}) \end{pmatrix}, \; \Gamma_{23} = \begin{pmatrix} \frac{\Gamma_{\mathrm{AB}}^{xx}+\Gamma_{\mathrm{AB}}^{yy}}{2} & \frac{\Gamma_{\mathrm{AB}}^{yy}-\Gamma_{\mathrm{AB}}^{xx}}{2} & 0 \\ \frac{\Gamma_{\mathrm{AB}}^{yy}-\Gamma_{\mathrm{AB}}^{xx}}{2} & \frac{\Gamma_{\mathrm{AB}}^{xx}+\Gamma_{\mathrm{AB}}^{yy}}{2} & 0 \\ 0 & 0 & -(\Gamma_{\mathrm{AB}}^{xx}+\Gamma_{\mathrm{AB}}^{yy}) \end{pmatrix},$$

$$\Gamma_{24} = \begin{pmatrix} -(\Gamma_{\mathrm{AB}}^{xx}+\Gamma_{\mathrm{AB}}^{yy}) & 0 & 0 \\ 0 & \frac{\Gamma_{\mathrm{AB}}^{xx}+\Gamma_{\mathrm{AB}}^{yy}}{2} & \frac{\Gamma_{\mathrm{AB}}^{yy}-\Gamma_{\mathrm{AB}}^{xx}}{2} \\ 0 & \frac{\Gamma_{\mathrm{AB}}^{yy}-\Gamma_{\mathrm{AB}}^{xx}}{2} & \frac{\Gamma_{\mathrm{AB}}^{xx}+\Gamma_{\mathrm{AB}}^{yy}}{2} \end{pmatrix}, \; \Gamma_{34} = \begin{pmatrix} \frac{\Gamma_{\mathrm{AB}}^{xx}+\Gamma_{\mathrm{AB}}^{yy}}{2} & 0 & \frac{\Gamma_{\mathrm{AB}}^{yy}-\Gamma_{\mathrm{AB}}^{xx}}{2} \\ 0 & -(\Gamma_{\mathrm{AB}}^{xx}+\Gamma_{\mathrm{AB}}^{yy}) & 0 \\ \frac{\Gamma_{\mathrm{AB}}^{yy}-\Gamma_{\mathrm{AB}}^{xx}}{2} & 0 & \frac{\Gamma_{\mathrm{AB}}^{xx}+\Gamma_{\mathrm{AB}}^{yy}}{2} \end{pmatrix}. \tag{4.6}$$

Therefore, the bilinear spin Hamiltonian on the pyrochlore lattice consists of four independent parameters. For example, the bilinear interaction on bond A-B is fully determined by the isotropic Heisenberg exchange J_{AB}, one contribution in the DM interaction D_{AB}^y, and two independent contributions in the pseudo-dipolar tensor $\Gamma_{\mathrm{AB}}^{xx}$ and $\Gamma_{\mathrm{AB}}^{yy}$.

4.2.3 Pyrochlore spin Hamiltonian representations in the literature

Unfortunately, there are several parametrization schemes customary in the literature discussing pyrochlore compounds. This can lead to confusion, since the naming of exchange parameters is not always unique. For this reason, it is crucial to define the complete Hamiltonian carefully, before the magnitude of certain parameters can be compared between different studies. Here, we review the three most common parametrization schemes for pyrochlores.

In this chapter, we expressed the Hamiltonian with nine parameters in terms of the most general bilinear spin 1/2 Hamiltonian:

$$\mathcal{H}_{\mathrm{gen}} = \begin{pmatrix} S_1^x & S_1^y & S_1^z \end{pmatrix} \cdot \begin{pmatrix} J + \Gamma^{xx} & \Gamma^{xy} + D^z & \Gamma^{xz} - D^y \\ \Gamma^{xy} - D^z & J + \Gamma^{yy} & \Gamma^{yz} + D^x \\ \Gamma^{xz} + D^y & \Gamma^{yz} - D^x & J - (\Gamma^{xx} + \Gamma^{yy}) \end{pmatrix} \cdot \begin{pmatrix} S_2^x \\ S_2^y \\ S_2^z \end{pmatrix} \tag{4.7}$$

This representation has the advantage of generality. Therefore, it can be easily compared to parameters in different geometries and is familiar to a wider audience than the pyrochlore community. However, it has the disadvantage that the independent parameters within the pyrochlore lattice are difficult to identify. As discussed above, the pyrochlore lattice has in principle only four independent parameters.

For example, for bond 1-2 in Fig. 4.2(b) and following the notation in Eq. (4.3) and Eq. (4.6), this matrix would reduce to the following expression:

$$\mathcal{H}_{\text{gen}} = \begin{pmatrix} S_1^x & S_1^y & S_1^z \end{pmatrix} \cdot \begin{pmatrix} J_{12} + \Gamma_{12}^{xx} & \frac{1}{\sqrt{2}} D_{12}^x & \Gamma_{12}^{xz} \\ -\frac{1}{\sqrt{2}} D_{12}^x & J_{12} - 2\Gamma_{12}^{xx} & -\frac{1}{\sqrt{2}} D_{12}^x \\ \Gamma_{12}^{xz} & \frac{1}{\sqrt{2}} D_{12}^x & J_{12} + \Gamma_{12}^{xx} \end{pmatrix} \cdot \begin{pmatrix} S_2^x \\ S_2^y \\ S_2^z \end{pmatrix}. \tag{4.8}$$

This insight is somewhat hidden in the parametrization by Eq. (4.7).

In contrast, Thompson *et al.* [191] took advantage of the high symmetry in the pyrochlore lattice using the following parametrization:

$$\mathcal{H}_{\text{ex}} = \mathcal{H}_{\text{Ising}} + \mathcal{H}_{\text{iso}} + \mathcal{H}_{\text{pd}} + \mathcal{H}_{\text{DM}}. \tag{4.9}$$

The Ising like term $\mathcal{H}_{\text{Ising}}$ contains the spin projection on local $\hat{z}$ axes[1], which point toward the middle of the tetrahedron:

$$\mathcal{H}_{\text{Ising}} = -J_{\text{Ising}} \sum_{\langle ij \rangle} (\mathbf{S}_i \cdot \hat{z}_i)(\mathbf{S}_j \cdot \hat{z}_j), \tag{4.10}$$

the isotropic Heisenberg term $\mathcal{H}_{\text{iso}}$ has the well-known form:

$$\mathcal{H}_{\text{iso}} = -J_{\text{iso}} \sum_{\langle ij \rangle} \mathbf{S}_i \cdot \mathbf{S}_j, \tag{4.11}$$

the pseudo-dipolar term $\mathcal{H}_{\text{pd}}$ contains in addition to a Heisenberg contribution the spin projection on the bond $\hat{r}_{ij}$ connecting site i and j:

$$\mathcal{H}_{\text{pd}} = -J_{\text{pd}} \sum_{\langle ij \rangle} (\mathbf{S}_i \cdot \mathbf{S}_j - 3(\mathbf{S}_i \cdot \hat{r}_{ij})(\mathbf{S}_j \cdot \hat{r}_{ij})), \tag{4.12}$$

and finally the Dzyaloshinskii-Moriya contribution $\mathcal{H}_{\text{DM}}$ of the usual form, where $\hat{\Omega}_{\text{DM}}^{ij}$ is the unit vector in the direction of the DM vector:

$$\mathcal{H}_{\text{DM}} = -J_{\text{DM}}\, \hat{\Omega}_{\text{DM}}^{ij} \cdot (\mathbf{S}_i \times \mathbf{S}_j). \tag{4.13}$$

For bond 1-2 defined in Fig. 4.2(b) we use the following local $\hat{z}$ axes, bond vector $\hat{r}_{12}$ and DM direction:

$$\hat{z}_1 = \frac{1}{\sqrt{3}} \begin{pmatrix} 1 \\ 1 \\ 1 \end{pmatrix}, \; \hat{z}_2 = \frac{1}{\sqrt{3}} \begin{pmatrix} -1 \\ 1 \\ -1 \end{pmatrix}, \; \hat{r}_{12} = \frac{1}{\sqrt{2}} \begin{pmatrix} 1 \\ 0 \\ 1 \end{pmatrix}, \; \hat{\Omega}_{12} = \frac{1}{\sqrt{2}} \begin{pmatrix} -1 \\ 0 \\ 1 \end{pmatrix}. \tag{4.14}$$

Then, the parametrization according to Ref. [191] leads to the following spin Hamiltonian for bond 1-2:

$$\mathcal{H}_{\text{ex}} = \begin{pmatrix} S_1^x & S_1^y & S_1^z \end{pmatrix} \cdot \begin{pmatrix} \frac{1}{3} J_{12}^{\text{Ising}} - J_{12}^{\text{iso}} + \frac{1}{2} J_{12}^{\text{pd}} & -\frac{1}{3} J_{12}^{\text{Ising}} - \frac{1}{\sqrt{2}} J_{12}^{\text{DM}} & \frac{1}{3} J_{12}^{\text{Ising}} + \frac{3}{2} J_{12}^{\text{pd}} \\ \frac{1}{3} J_{12}^{\text{Ising}} + \frac{1}{\sqrt{2}} J_{12}^{\text{DM}} & -\frac{1}{3} J_{12}^{\text{Ising}} - J_{12}^{\text{iso}} - J_{12}^{\text{pd}} & \frac{1}{3} J_{12}^{\text{Ising}} + \frac{1}{\sqrt{2}} J_{12}^{\text{DM}} \\ \frac{1}{3} J_{12}^{\text{Ising}} + \frac{3}{2} J_{12}^{\text{pd}} & -\frac{1}{3} J_{12}^{\text{Ising}} - \frac{1}{\sqrt{2}} J_{12}^{\text{DM}} & \frac{1}{3} J_{12}^{\text{Ising}} - J_{12}^{\text{iso}} + \frac{1}{2} J_{12}^{\text{pd}} \end{pmatrix} \cdot \begin{pmatrix} S_2^x \\ S_2^y \\ S_2^z \end{pmatrix} \tag{4.15}$$

Although the Heisenberg and the DM term obey the same form in both representations, the different definitions of the additional terms influence the actual values of the exchange parameters for all terms. The relation between the two parametrization schemes is bond dependent. For example, for bond 1-2 we found the following expressions:

$$\begin{aligned} J_{12} &= -J_{\text{iso}} + \frac{1}{9} J_{12}^{\text{Ising}}, \quad |\mathbf{D}_{12}| = -J_{\text{DM}} - \frac{\sqrt{2}}{3} J_{\text{Ising}}, \\ \Gamma_{12}^{xx} &= \frac{1}{2} J_{\text{pd}} + \frac{2}{9} J_{\text{Ising}}, \quad \Gamma_{12}^{xz} = \frac{3}{2} J_{\text{pd}} + \frac{1}{3} J_{\text{Ising}}. \end{aligned} \tag{4.16}$$

[1] For appropriate local coordinates in pyrochlore systems see also Section 4.3.

Hence, comparing "the" Heisenberg or "the" DM interaction of specific materials is only meaningful if all contributing terms are taken into account.

Ross *et al.* [174] introduced a third way of parametrization using only four parameters, but without reference to local $\hat{z}$ axes or bond directions. For bond 1-3 in Fig. 4.2(b) the matrix is explicitly given in Ref. [174]:

$$J_{\text{par}} = \begin{pmatrix} J_2 & J_4 & J_4 \\ -J_4 & J_1 & J_3 \\ -J_4 & J_3 & J_1 \end{pmatrix}. \tag{4.17}$$

Note, that the relation to the notation used by Thompson *et al.* [191] was pointed out in the appendix of Ref. [174]. The relation to the notation used in this thesis is given by the following expressions:

$$\begin{aligned} J_{13} &= \frac{2}{3}J_1 + \frac{1}{3}J_2, \qquad |\mathbf{D}_{13}| = -\sqrt{2}\,J_4, \\ \Gamma_{13}^{xx} &= -\frac{2}{3}J_1 + \frac{2}{3}J_2, \quad \Gamma_{13}^{yz} = J_3. \end{aligned} \tag{4.18}$$

The diagonal part of the pseudo-dipolar tensor Γ is in this case mixed with the Heisenberg exchange via the parameters J_1 and J_2, while the off-diagonal component of Γ is simply replaced by the parameter J_3. The comparison with parameter J_4 contains the somewhat dangerous point that they only differ in the normalization convention.

The relation for the other bonds follow for both of the alternative parametrization schemes accordingly from Eq. (4.3) and Eq. (4.6) and the local coordinate systems given in Section 4.3.

4.3 Extended Hubbard Hamiltonian for *d* block electrons

In the two pyrochlore materials investigated in this chapter, $Lu_2V_2O_7$ and $Lu_2Mo_2O_5N_2$, the magnetism is mainly determined by the $3d$ electrons in V^{4+} and $4d$ electrons Mo^{5+} respectively. In this section, we discuss the form and physical implications of the contributing terms to the generalized multi-orbital Hubbard Hamiltonian for d block electrons, including spin-orbit coupling:

$$\mathcal{H}_{\text{tot}} = \mathcal{H}_{\text{hop}} + \mathcal{H}_{\text{soc}} + \mathcal{H}_{\text{int}}. \tag{4.19}$$

This Hamiltonian provides the electronic information for the investigated materials and an effective low-energy Hamiltonian can then be extracted from corresponding clusters via exact exact diagonalization and projection onto the low-energy subspace.

4.3.1 Hopping parameters from *ab-initio* calculations

The hopping term $\mathcal{H}_{\text{hop}}$ contains the kinetic energy, encoded in the hopping parameters $t_{i\alpha,j\beta}$:

$$\mathcal{H}_{\text{hop}} = \sum_{ij}\sum_{\alpha\beta}\left[t_{i\alpha,j\beta}\, d_{i\alpha}^{\dagger} d_{j\beta} + \text{H.c.}\right]. \tag{4.20}$$

As mentioned in Chapter 1, the hopping parameters depend on the orbital overlap integrals of the investigated material and can be obtained from *ab-initio* calculations. Numerical details for the two cases discussed in this chapter are given in Section 4.4 and Section 4.5. In general, those calculations should be performed for a non-magnetic, non-relativistic case in order reduce double counting of these effects. Since first principles calculations always contain an exchange-correlation contribution, it is, however, not possible to avoid double counting completely.

To preserve the symmetry of the pyrochlore lattice it is crucial to work with local coordinate systems for the magnetic sites such that every ion "feels" the same crystallographic environment. Here, we follow the local coordinate systems introduced in Ref. [174] and illustrated in Fig. 4.3(a). In this arrangement, the local $\hat{z}$ axes point toward the center of the tetrahedron, and hence into the center of the cube

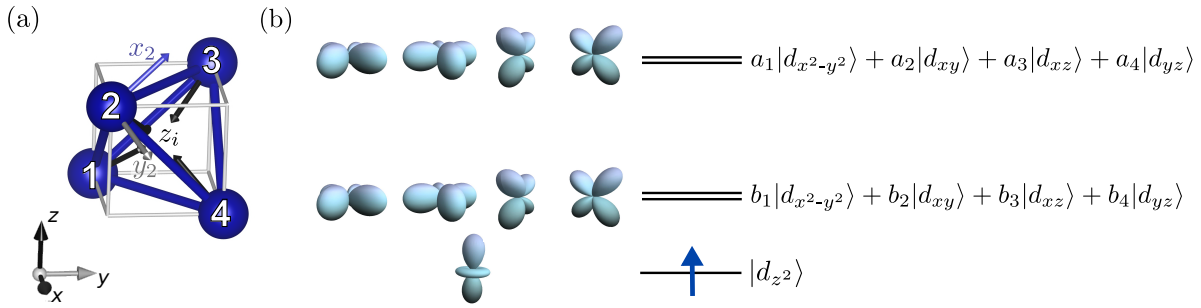

Figure 4.3: (a) Local coordinate systems as given in Eq. (4.21) in one tetrahedron employed within the tight-binding approximation. (b) Trigonal crystal field splitting in d^1 pyrochlore systems like $Lu_2V_2O_7$ and $Lu_2Mo_2O_5N_2$ using the local coordinate systems shown in (a). The energetically lowest orbital is in this case the d_{z^2} orbital, the two higher energy levels correspond to linear combinations of $d_{x^2-y^2}$, d_{xy}, d_{xz} and d_{yz}, where the coefficients depend on the microscopic details of the materials. Both high energy levels are two-fold degenerate.

enclosing this tetrahedron. The $\hat{x}$ axes are parallel to a bond on an opposite side of the tetrahedron, in the direction of the cubes face diagonal, so two axes are always parallel to each other. In the global coordinate system defined in Fig. 4.3(a) the local coordinate axes are defined as follows:

$$\begin{aligned}
\hat{x}_1 &= \frac{1}{\sqrt{2}}\begin{pmatrix}0\\1\\-1\end{pmatrix}, \hat{x}_2 = \frac{1}{\sqrt{2}}\begin{pmatrix}0\\1\\1\end{pmatrix}, \quad \hat{x}_3 = \frac{1}{\sqrt{2}}\begin{pmatrix}0\\-1\\1\end{pmatrix}, \hat{x}_4 = \frac{1}{\sqrt{2}}\begin{pmatrix}0\\-1\\-1\end{pmatrix}, \\
\hat{y}_1 &= \frac{1}{\sqrt{6}}\begin{pmatrix}-2\\1\\1\end{pmatrix}, \hat{y}_2 = \frac{1}{\sqrt{6}}\begin{pmatrix}2\\1\\-1\end{pmatrix}, \hat{y}_3 = \frac{1}{\sqrt{6}}\begin{pmatrix}-2\\-1\\-1\end{pmatrix}, \hat{y}_4 = \frac{1}{\sqrt{6}}\begin{pmatrix}2\\-1\\1\end{pmatrix}, \\
\hat{z}_1 &= \frac{1}{\sqrt{3}}\begin{pmatrix}1\\1\\1\end{pmatrix}, \quad \hat{z}_2 = \frac{1}{\sqrt{3}}\begin{pmatrix}-1\\1\\-1\end{pmatrix}, \hat{z}_3 = \frac{1}{\sqrt{3}}\begin{pmatrix}1\\-1\\-1\end{pmatrix}, \hat{z}_4 = \frac{1}{\sqrt{3}}\begin{pmatrix}-1\\-1\\1\end{pmatrix}.
\end{aligned} \tag{4.21}$$

Using this framework of local coordinates leads to a trigonal crystal field splitting, illustrated in Fig. 4.3(b). For the two compounds discussed in this chapter, the lowest energy level corresponds to the d_{z^2} orbital occupied by a single electron in the ground state. The two energetically higher levels consist of linear combinations of the other four orbitals, e.g. $a_1|d_{x^2-y^2}\rangle + a_2|d_{xy}\rangle + a_3|d_{xz}\rangle + a_4|d_{yz}\rangle$. The specific coefficients in the linear combination depend on the microscopic details of the specific materials, as we will demonstrate in Section 4.4 and Section 4.5.

4.3.2 Two-particle interaction term

Following, for example, Ref. [56] the typical generalized two-particle interaction term is given by the following expression:

$$\begin{aligned}
\mathcal{H}_{\text{int}} = &\sum_i \sum_{\alpha\beta} U_{\alpha\beta}\, n_{i\alpha\uparrow} n_{i\beta\downarrow} + \frac{1}{2}\sum_{i\sigma}\sum_{\alpha\neq\beta}(U_{\alpha\beta} - J_{\alpha\beta})\, n_{i\alpha\sigma} n_{i\beta\sigma} \\
&+ \sum_i \sum_{\alpha\neq\beta} J_{\alpha\beta}\,(d^\dagger_{i\alpha\uparrow} d^\dagger_{i\beta\downarrow} d_{i\alpha\downarrow} d_{i\beta\uparrow} + d^\dagger_{i\alpha\uparrow} d^\dagger_{i\alpha\downarrow} d_{i\beta\downarrow} d_{i\beta\uparrow})
\end{aligned} \tag{4.22}$$

where $\{i, j\}$ are site and $\{\alpha, \beta\}$ orbital indices. The covered two-particle processes by this equation are illustrated in Fig. 4.4(a). Double occupation on the same site and orbital are punished with the on-site energy U_0 of the Coulomb interaction tensor $U_{\alpha\beta}$. The off-diagonal elements describe the punishment for electrons on different orbitals with opposite spin, indicated with "Coulomb AFM" in Fig. 4.4(a).

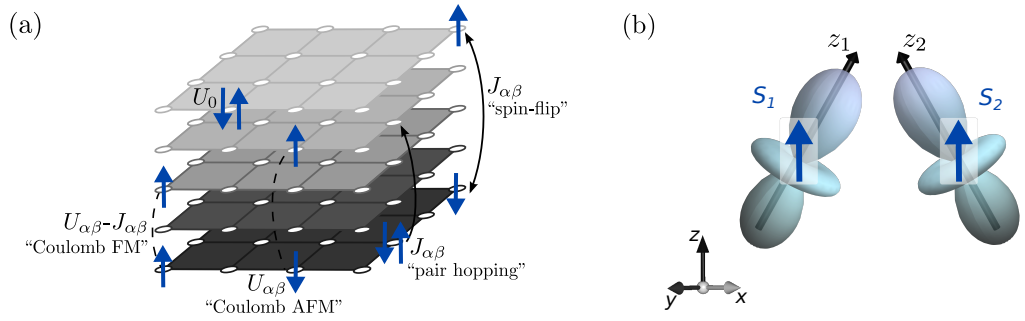

Figure 4.4: (a) Two-particle interaction processes present in the generalized multi-orbital Hubbard Hamiltonian according to Eq. (4.22). Sites are indicated as white dots, orbitals are illustrated as planes. Phrases conventionally used to refer to indicated processes are given in quotation marks. (b) Illustration of the coordinate discrepancy between the spin and orbital space before addition local rotations are applied. Fig. (b) adapted from Ref. [79].

In the case of the same spin direction this is reduced by the Hund's coupling tensor $J_{\alpha\beta}$, indicated by "Coulomb FM". In the rotational invariant case of the generalized Hubbard Hamiltonian, $J_{\alpha\beta}$ describes in addition "pair hopping" and "spin-flip" exchange processes.

In the case of d block electrons, the Coulomb interaction tensor can be derived from Slater integrals F_k [192] and relates the Coulomb interaction for the involved orbitals as follows:

$$\begin{array}{cccccc} U_{\alpha\beta} & |d_{x^2\text{-}y^2}\rangle & |d_{z^2}\rangle & |d_{xy}\rangle & |d_{yz}\rangle & |d_{xz}\rangle \\ \langle d_{x^2\text{-}y^2}| & U_0 & U_0-2j_2 & U_0-2j_3 & U_0-2j_1 & U_0-2j_1 \\ \langle d_{z^2}| & U_0-2j_2 & U_0 & U_0-2j_2 & U_0-2j_4 & U_0-2j_4 \\ \langle d_{xy}| & U_0-2j_3 & U_0-2j_2 & U_0 & j_1 & U_0-2j_1 \\ \langle d_{yz}| & U_0-2j_1 & U_0-2j_4 & U_0-2j_1 & U_0 & U_0-2j_1 \\ \langle d_{xz}| & U_0-2j_1 & U_0-2j_4 & U_0-2j_1 & U_0-2j_1 & U_0 \end{array} \tag{4.23}$$

With those Slater integrals it is also possible express the Hund's coupling tensor $J_{\alpha\beta}$:

$$\begin{array}{cccccc} J_{\alpha\beta} & |d_{x^2\text{-}y^2}\rangle & |d_{z^2}\rangle & |d_{xy}\rangle & |d_{yz}\rangle & |d_{xz}\rangle \\ \langle d_{x^2\text{-}y^2}| & U_0 & j_2 & j_3 & j_1 & j_1 \\ \langle d_{z^2}| & j_2 & U_0 & j_2 & j_4 & j_4 \\ \langle d_{xy}| & j_3 & j_2 & U_0 & j_1 & j_1 \\ \langle d_{yz}| & j_1 & j_4 & j_1 & U_0 & j_1 \\ \langle d_{xz}| & j_1 & j_4 & j_1 & j_1 & U_0 \end{array} \tag{4.24}$$

The above expressions contain in fact only two independent model parameters. One possible choice for these model parameters is for example U_0 and the average Hund's coupling J_{avg} defined[2] as follows:

$$J_{\text{avg}} = \frac{1}{2l(2l+1)} \sum_{\alpha \neq \beta} J_{\alpha\beta}. \tag{4.25}$$

The relation to the Slater integrals F_i is given by [56]:

$$J_{\text{avg}} = \frac{5}{7}\frac{(F_2+F_4)}{14}, \quad j_1 = \frac{3}{49}F_2 + \frac{20}{9}\frac{1}{49}F_4, \quad U_0 = F_0 + \frac{8}{5}J_{\text{avg}}. \tag{4.26}$$

For d block transition metals a typical approximation is the relation $F_4 = \frac{5}{8}F_2$, eliminating the third independent parameter. In this case j_1 is fully determined by J_{avg}:

$$j_1 \approx 0.77\, J_{\text{avg}}, \tag{4.27}$$

[2]Note, that the parameter referred to as J_{avg} in this thesis corresponds to the parameter $\mathcal{J}_{\text{avg}}$ in Ref. [56], which is therein distinguished from a different parameter J_{avg}.

as well as the remaining interaction parameters j_n:

$$j_2 = -2J_{\text{avg}} + 3j_1 \approx 0.32\, J_{\text{avg}}, \tag{4.28}$$

$$j_3 = +6J_{\text{avg}} - 5j_1 \approx 2.91\, J_{\text{avg}}, \tag{4.29}$$

$$j_4 = +4J_{\text{avg}} - 3j_1 \approx 1.68\, J_{\text{avg}}. \tag{4.30}$$

Note, that the smallest contribution in the Hubbard interaction tensor is hence $U_0 - 3j_2$, for the "Coulomb FM" case with the corresponding energy $U_{\alpha\beta} - J_{\alpha\beta}$. In our parameter-dependent studies, we therefore excluded parameter combinations which lead to $U_0 - 3j_2 < 0$ as the strictest requirement for a physical meaningful description. If this requirement is not fulfilled, it would lead to unphysical processes conflicting with Hund's rules.

4.3.3 Spin-orbit coupling term

The spin-orbit coupling contribution to the spin Hamiltonian

$$\mathcal{H}_{\text{soc}} = \lambda \sum_i \sum_{\alpha\beta} \sum_{\sigma\sigma'} \langle\, i\,\alpha\,\sigma|\mathbf{L}\cdot\mathbf{S}|\, i\,\beta\,\sigma'\rangle\, d^\dagger_{i\alpha\sigma} d_{i\beta\sigma'}, \tag{4.31}$$

with the SOC parameter λ, has in the case of d electrons a well-known analytical expression. Using the Kronecker product, the matrix elements of the scalar product $\mathbf{L}\cdot\mathbf{S} = \sum_{r_i} L_{r_i} S_{r_i}$ can be evaluated in the spin and angular momentum space separately:

$$\sum_{r_i} \langle i\alpha\,\sigma|(L_{r_i} S_{r_i})|i\beta\,\sigma'\rangle = \sum_{r_i} \langle \alpha_i|L_{r_i}|\beta_i\rangle \otimes \langle\sigma|S_{r_i}|\sigma'\rangle. \tag{4.32}$$

Here, we indicate with the indices $\{\alpha_i, \beta_i\}$ that the orbitals may be site dependent through the local coordinates $r_i = \{x_i, y_i, z_i\}$. As discussed above, this is indeed the case for the pyrochlore lattice.

While the spin operators for spin 1/2 are with $\mathbf{S} = \frac{1}{2}\vec{\sigma}$ given by the Pauli matrices $\vec{\sigma}$, the angular momentum can be evaluated through the expression of the d orbitals in terms of the angular quantum number $l = 2$ in terms of spherical harmonics $|l;\, m_l\rangle$:

$$\begin{array}{lllll} |d_{xz}\rangle & = \frac{1}{\sqrt{2}}\big(|2;\,-1\rangle - |2;\,1\rangle\big), & |d_{yz}\rangle & = \frac{i}{\sqrt{2}}\big(|2;\,-1\rangle + |2;\,1\rangle\big), \\ |d_{x^2-y^2}\rangle & = \frac{1}{\sqrt{2}}\big(|2;\,-2\rangle + |2;\,2\rangle\big), & |d_{xy}\rangle & = \frac{i}{\sqrt{2}}\big(|2;\,-2\rangle - |2;\,2\rangle\big), \\ |d_{z^2}\rangle & = |2;\,0\rangle. & & \end{array} \tag{4.33}$$

The expression for the operators L_x, L_y, L_z in the basis of d orbitals follows directly from the action on the spherical harmonics:

$$L_z|l\; m_l\rangle = m_l\,|l\; m_l\rangle, \tag{4.34}$$

$$L_\pm|l\; m_l\rangle = \sqrt{(l \mp m_l)(l \pm m_l + 1)}\,|l\; m_l \pm 1\rangle, \tag{4.35}$$

with the relation $L_\pm = L_x \pm iL_y$. The explicit expressions for the angular momentum operators in the basis of d orbitals are then for the z component:

$$\begin{array}{r|ccccc} L_z & |d_{x^2\text{-}y^2}\rangle & |d_{z^2}\rangle & |d_{xy}\rangle & |d_{yz}\rangle & |d_{xz}\rangle \\ \hline \langle d_{x^2\text{-}y^2}| & 0 & 0 & -2i & 0 & 0 \\ \langle d_{z^2}| & 0 & 0 & 0 & 0 & 0 \\ \langle d_{xy}| & 2i & 0 & 0 & 0 & 0 \\ \langle d_{yz}| & 0 & 0 & 0 & 0 & i \\ \langle d_{xz}| & 0 & 0 & 0 & -i & 0 \end{array} \tag{4.36}$$

The explicit expression for the x component is:

$$\begin{array}{r|ccccc} L_x & |d_{x^2\text{-}y^2}\rangle & |d_{z^2}\rangle & |d_{xy}\rangle & |d_{yz}\rangle & |d_{xz}\rangle \\ \hline \langle d_{x^2\text{-}y^2}| & 0 & 0 & 0 & i & 0 \\ \langle d_{z^2}| & 0 & 0 & 0 & i\sqrt{3} & 0 \\ \langle d_{xy}| & 0 & 0 & 0 & 0 & -i \\ \langle d_{yz}| & -i & -i\sqrt{3} & 0 & 0 & 0 \\ \langle d_{xz}| & 0 & 0 & i & 0 & 0 \end{array} \tag{4.37}$$

and for the y component:

$$\begin{array}{r|ccccc} L_y & |d_{x^2\text{-}y^2}\rangle & |d_{z^2}\rangle & |d_{xy}\rangle & |d_{yz}\rangle & |d_{xz}\rangle \\ \hline \langle d_{x^2\text{-}y^2}| & 0 & 0 & 0 & 0 & i \\ \langle d_{z^2}| & 0 & 0 & 0 & 0 & -i\sqrt{3} \\ \langle d_{xy}| & 0 & 0 & 0 & i & 0 \\ \langle d_{yz}| & 0 & 0 & -i & 0 & 0 \\ \langle d_{xz}| & -i & i\sqrt{3} & 0 & 0 & 0 \end{array} \tag{4.38}$$

As mentioned above, the spin-orbit coupling matrix elements are site dependent due to the site-dependent coordinate systems of the angular momentum. In Fig. 4.4(b) we illustrate the relation, i.e. the product, of the d_{z^2} orbital to the spin. From Eq. (4.32) it follows directly that the product is site-dependent as well. The spin expectation value $\langle\sigma|S_{r_i}|\sigma'\rangle$ is therefore not simply given by Pauli matrices, but follows from an additional rotation into the global coordinate system. For example, for site 1 in Fig. 4.3(a) the local axis $\hat{z}_1$, expressed in the global coordinate system, is given by:

$$\hat{z}_1 = \frac{1}{\sqrt{3}} \begin{pmatrix} 1 \\ 1 \\ 1 \end{pmatrix}. \tag{4.39}$$

Therefore, the operator measuring the z component of the spin on this site is accordingly a linear combination of the spin operators:

$$S_{z_1} = \frac{1}{\sqrt{3}}(S_x + S_y + S_z). \tag{4.40}$$

At this point, the multi-orbital Hubbard Hamiltonian for d block electrons is fully determined. The material-specific parameters are given by the overlap integrals $t_{i\alpha,j\beta}$ in the kinetic energy in $\mathcal{H}_{\text{hop}}$, while the two-particle interaction $\mathcal{H}_{\text{int}}$ and spin-orbit coupling contribution $\mathcal{H}_{\text{SOC}}$ are given by analytical expressions for d orbitals. However, the description of relatively small clusters still requires calculations in a large Hilbert space, challenging the solution of such systems in most cases. Since we are interested in the description of Mott insulators with localized electrons, it is reasonable to use this additional information to reduce the Hilbert space further with a low-energy description in terms of pseudo-spins.

4.4 The pyrochlore ferromagnet $Lu_2V_2O_7$

Kira Riedl, Daniel Guterding, Harald O. Jeschke, Michel J. P. Gingras, and Roser Valentí,
Ab initio determination of spin Hamiltonians with anisotropic exchange interactions: The case of the pyrochlore ferromagnet $Lu_2V_2O_7$,
Phys. Rev. B **94**, 014410 (2016)
[79]

In this section, we demonstrate with the hybrid method the determination of the complete bilinear spin 1/2 Hamiltonian by a combination of *ab-initio* methods and exact diagonalization on the example of the pyrochlore ferromagnet $Lu_2V_2O_7$. The corresponding results are published in Ref. [79].

From experiment it is known that $Lu_2V_2O_7$ is a ferromagnetic Mott insulator, with a Curie temperature $T_c \approx 70\,\text{K}$ [185–187]. However, from the microscopic details of this spin 1/2 pyrochlore structure it is not obvious that the exchange between nearest neighbours is ferromagnetic. For example, in 2004 Ichikawa *et al.* [193] stated that the origin of the ferromagnetism in $Lu_2V_2O_7$ still remained unsolved. Spin-polarized neutron diffraction suggested, via comparison with theoretically obtained magnetic form factors, an "orbital ordering" such that the energetically lowest orbitals all point to the center of one tetrahedron [193]. It was argued [185, 193, 194] that this "orbital ordering" is responsible for the ferromagnetism observed in $Lu_2V_2O_7$.

A controversy regarding the anisotropic spin-spin interactions emerged in 2011, when Xiang *et al.* [195] presented a DFT total energy study. In this work, the authors suggested for $Lu_2V_2O_7$ and its sister compound $Y_2V_2O_7$ not only a Heisenberg and DM interaction, but also a finite single-ion anisotropy $\mathcal{H}_{\text{ani}} = A\sum_i(\mathbf{S}_i \cdot \hat{z}_i)^2$. Although the magnetism in both of these compounds is carried by the spin 1/2 V^{4+} ions, the additional splitting of the t_{2g} levels would lead to the emergence of single-ion anisotropy with $A = -3.64\,\text{meV}$. However, the presence of such a term is inconsistent with the quantum mechanical description of a spin 1/2 particle. A term quadratic in Pauli matrices should only lead to a constant contribution to the spin Hamiltonian due to the relation $(\sigma_r)^2 = \mathbb{1}_{2\times 2}$. The anisotropy due to the DM interaction was estimated with the total energy calculations to be much smaller than the single-ion anisotropy ($|\mathbf{D}_{ij}| = 0.34\,\text{meV}$) with a DM to Heisenberg ratio $|\mathbf{D}_{ij}/J_{ij}| = 0.048$. Another natural source for anisotropy in spin 1/2 systems is the pseudo-dipolar tensor Γ, which was not addressed in Ref. [195]. Note, that in order to determine the DM interaction, Xiang *et al.* had to consider energies of non-collinear magnetic configurations that may have been far from the true ground state energy of $Lu_2V_2O_7$. In this compound it was pointed out, that ferromagnetic collinearity is stable against the finite DM interaction [187]. Therefore, the hybrid method seems to be preferable in this situation. Based on inelastic neutron scattering measurements, Mena *et al.* [196] reevaluated the spin model for $Lu_2V_2O_7$ experimentally. Simulations of the scattering data within mean-field random-phase approximation revealed a Heisenberg exchange $J_{ij} = -8.1\,\text{meV}$, in agreement with the isotropic term in the *ab-initio* study [195]. Simulations in specific regions in reciprocal space revealed for the anisotropic DM interaction a ratio $|\mathbf{D}_{ij}|/|J_{ij}| \approx 0.18$, an order of magnitude larger than the ratio suggested from the total energy calculations [195].

Experimentally, $Lu_2V_2O_7$ regathered attention, when in 2010 Onose *et al.* [187] reported the observation of a magnon Hall effect. A finite DM interaction was argued to act like an effective vector potential ϕ_{ij} for propagating magnons. For a quantization axis in the direction of the DM vector, the spin Hamiltonian can be rewritten as $J_{ij}(\mathbf{S}_i \cdot \mathbf{S}_j) + \mathbf{D}_{ij} \cdot (\mathbf{S}_i \times \mathbf{S}_j) = \tilde{J}_{ij}(\mathrm{e}^{i\phi_{ij}}\, S_i^+ S_j^- + \mathrm{e}^{-i\phi_{ij}}\, S_i^- S_j^+) + J_{ij} S_i^z S_j^z$, where we defined $\tilde{J}_{ij} = \frac{1}{2}(J_{ij}^2 + |\mathbf{D}_{ij}|^2)^{1/2}$ and $\tan\phi_{ij} = |\mathbf{D}_{ij}|/J_{ij}$. A finite DM vector leads therefore to a phase factor in the spin wave picture, similar to the Peierls phase caused by the vector potential for electrons (see also Chapter 2). Onose *et al.* performed magnetization, resistivity, and thermal conductivity measurements. The authors argued that, below $T = 100\,\text{K}$, the electric contribution of thermal conductivity is negligible and hence the observed heat current can only be carried by phonons and magnons for low temperatures. Due to a decrease of the thermal Hall conductivity in the high-field region $H \sim 10\,\text{T}$, they ruled out phonons as a possible source, since higher fields should reduce their scattering by magnetic fluctuations. A fit of magnetic specific heat and transverse thermal conductivity data suggested an extremely strong DM interaction with $|\mathbf{D}_{ij}/J_{ij}| \approx 0.32$ for a nearest neighbour Heisenberg interaction $J_{ij} \approx -3.4$ meV[3]. In this context, $Lu_2V_2O_7$ was suggested to be a candidate topological magnon insulator with chiral edge states [197–200]. In analogy to electronic topological insulators, the propagation of a magnon leads in this picture to an accumulation of a phase ϕ_{ij} that induces a nonzero Berry curvature [198].

Since the magnitude $|\mathbf{D}|$ seemed to be hotly debated, a reliable microscopic procedure to estimate anisotropic exchange couplings appeared to be highly beneficial. In the hybrid method, detailed below, only quantum mechanically allowed terms appear by construction, avoiding complications like the finite single-ion anisotropy for spin 1/2 systems in Ref. [195]. Moreover, all quantum mechanically allowed terms are determined, at least up to the considered order. Somewhat complicated terms like the symmetric pseudo-dipolar tensor Γ_{ij}, which is often neglected due to the number of independent parameters and numerical effort, are considered naturally in the hybrid method. The discrepancy between experimentally and theoretically estimated exchange parameters suggests that those additional anisotropic terms might play a more important role than initially assumed. Elhajal *et al.* [189] already pointed out that in the case of a collinear ground state the cross product $\mathbf{S}_i \times \mathbf{S}_j$ is reduced to $\mathcal{O}(\lambda)$, so that the DM interaction might be with $\mathcal{O}(\lambda^2)$ of similar importance as the symmetric contributions with $\mathcal{O}(\lambda^2)$.

[3] Onose *et al.* [187] estimated a spin stiffness $D_s = 21\,\text{meV}\cdot\text{Å}^2$ from fitting the magnon contribution to specific heat at low temperatures. The superexchange $J = -3.4\,\text{meV}$ can then be obtained from the relationship $|J|S = 8D_s/a^2$ derived in the supplemental material of Ref. [187], where $S = 1/2$ is the spin value and $a = 9.94\,\text{Å}$ is the lattice constant of $Lu_2V_2O_7$.

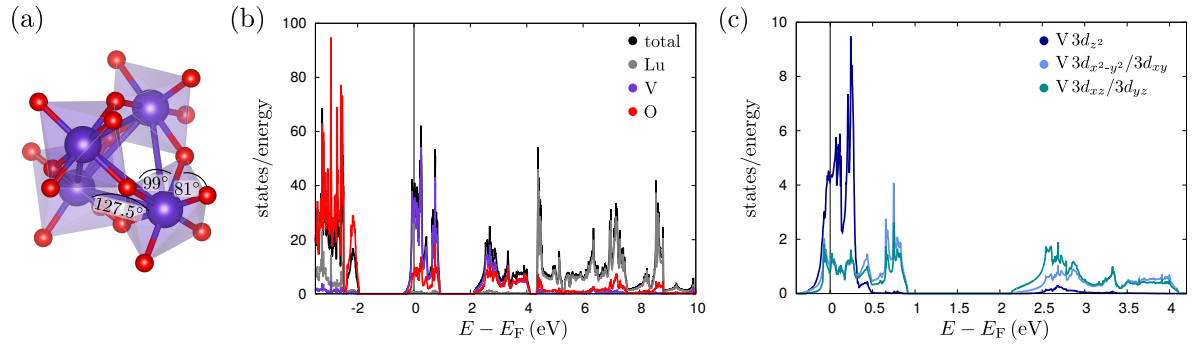

Figure 4.5: (a) V tetrahedron with oxygen environment causing the observed trigonal crystal field splitting. (b) Density of states of $Lu_2V_2O_7$ resolved with respect to the elements in the crystal structure. (c) DOS resolved with respect to the $3d$ V characters in the relevant energy window close to the Fermi energy E_F.

4.4.1 *Ab-initio* determination of hopping and spin-orbit parameters

As a first step, we performed a non-magnetic, non-relativistic band structure calculation within an all-electron full-potential local orbital (FPLO) [201] basis and used for the exchange-correlation functional the generalized gradient approximation (GGA) [202]. In Fig. 4.5 we show the *ab-initio* density of states (DOS) for $Lu_2V_2O_7$ from the experimental structure determined in Ref. [203]. The total DOS, shown in Fig. (b), reveals a dominant vanadium weight close to the Fermi level. Therefore, a description in terms of localized vanadium orbitals is suitable to capture the physics relevant in this energy range. Note, that there is in addition oxygen weight mixed in, on which we elaborate further below. In Fig. 4.5(c), we show the density of states in a more narrow energy window close the Fermi level, resolved with respect to the $3d$ vanadium orbitals. In addition to the confirmation of the d block orbital character in this energy range, it shows the expected trigonal crystal field splitting for a pyrochlore structure. For the determination of the orbital characters of the density of states, we employed the local coordinate systems introduced in Section 4.3.

Next, we obtained the hopping parameters $t_{i\alpha,j\beta}$ from projective Wannier functions as implemented in FPLO [204]. We found that in the energy window between $E - E_F = -0.5\,\text{eV}$ and $E - E_F = 3.0\,\text{eV}$,

	$t_{1\alpha,1\beta}$					$t_{1\alpha,2\beta}$				
	$d_{x^2-y^2}$	d_{z^2}	d_{xy}	d_{yz}	d_{xz}	$d_{x^2-y^2}$	d_{z^2}	d_{xy}	d_{yz}	d_{xz}
$d_{x^2-y^2}$	+1.58	0	0	-1.26	0	-0.14	+0.07	-0.09	-0.01	+0.11
d_{z^2}	0	+0.24	0	0	0	+0.07	-0.04	+0.12	-0.09	-0.15
d_{xy}	0	0	+1.58	0	-1.26	-0.09	+0.12	-0.24	+0.11	+0.12
d_{yz}	-1.26	0	0	+1.83	0	-0.01	-0.09	+0.11	-0.03	+0.04
d_{xz}	0	0	-1.26	0	+1.83	+0.11	-0.15	+0.12	+0.04	+0.01

	$t_{1\alpha,3\beta}$					$t_{1\alpha,4\beta}$				
	$d_{x^2-y^2}$	d_{z^2}	d_{xy}	d_{yz}	d_{xz}	$d_{x^2-y^2}$	d_{z^2}	d_{xy}	d_{yz}	d_{xz}
$d_{x^2-y^2}$	-0.30	-0.14	0	+0.18	0	-0.14	+0.07	+0.09	-0.01	-0.11
d_{z^2}	-0.14	-0.04	0	+0.17	0	+0.07	-0.04	-0.12	-0.09	+0.15
d_{xy}	0	0	-0.09	0	-0.07	0.09	-0.12	-0.24	-0.11	+0.12
d_{yz}	+0.18	+0.17	0	+0.03	0	-0.01	-0.09	-0.11	-0.03	-0.04
d_{xz}	0	0	-0.07	0	-0.06	-0.11	+0.15	+0.12	-0.04	+0.01

Table 4.2: On-site energies $t_{1\alpha,1\beta}$ (in eV) and nearest neighbor hopping parameters $t_{1\alpha,j\beta}$ (in eV) between vanadium site 1 and j as defined in Fig. 4.2(b) via Wannier orbitals illustrated in Fig. 4.6. The parameters for the other three vanadium ions in one tetrahedron follow from symmetry considerations.

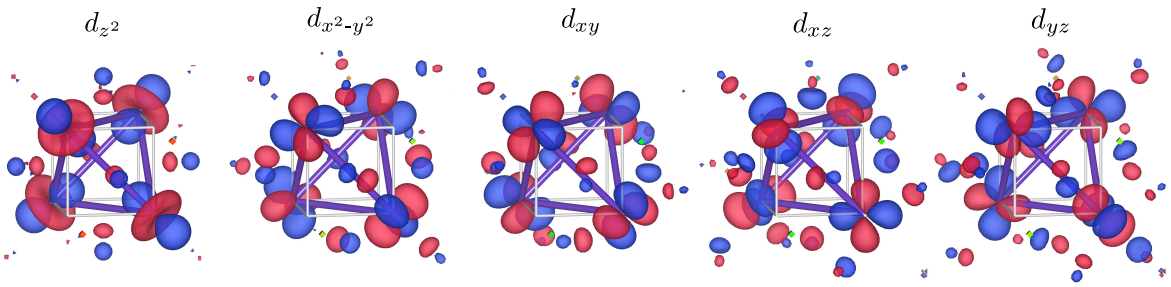

Figure 4.6: $3d$ Wannier orbitals in one vanadium tetrahedron in $Lu_2V_2O_7$ determined by the projective Wannier function with FPLO [204]. The orbital lowest in energy ($\varepsilon_0 = 0.24\,\text{eV}$) corresponds to d_{z^2}. The two energetically higher levels ($\varepsilon_1 = 0.44\,\text{eV}$ and $\varepsilon_2 = 2.97\,\text{eV}$) are each two-fold degenerate and correspond to linear combinations of the remaining four orbitals. Fig. depicting d_{z^2} adapted from Ref. [60].

where the vanadium d orbitals are dominant, the reduced description only in terms of the vanadium d orbitals leads to a good agreement with the DFT result, which includes all elements and orbitals in $Lu_2V_2O_7$. That implies, that the energy levels obtained from the determined hopping parameters in the model Hamiltonian given by Eq. (4.20) reproduce almost perfectly the non-relativistic electronic band structure. In Table 4.2 we show the on-site energies and the nearest neighbour hopping parameters, representing the dominant parameters in the kinetic part of the Hubbard Hamiltonian.

The on-site energies $t_{1\alpha,1\beta}$ confirm d_{z^2} as the orbital lowest in energy. The corresponding Wannier orbitals are shown for one tetrahedron in Fig. 4.6. In agreement with the experimental finding [193], the d_{z^2} orbitals point into the center of the tetrahedron, along the local $\hat{z}$ axes. Additional weights from the oxygen p orbitals are features of the hybridization, as already indicated by the density of states in Fig. 4.5(c). The overlap of d_{z^2} orbitals between different sites is with $t_{1z^2,jz^2} = -0.04\,\text{eV}$ surprisingly small. This might be an effect of hopping via oxygen orbitals, where nodes along the hopping paths reduce the final effective hopping. The two energetically higher levels are given by linear combinations of the other four orbitals, d_{xy}, $d_{x^2\text{-}y^2}$, d_{xz} and d_{yz}, as indicated by the large on-site off-diagonal contributions in $t_{1\alpha,1\beta}$ in Table 4.2. The hopping integrals between sites with the lowest orbital are with e.g. $t_{1z^2,2x^2\text{-}y^2} = -0.14\,\text{eV}$ also rather large. The large hopping into empty orbitals enables a stronger influence of Hund's coupling effects, which plays in the case of $Lu_2V_2O_7$ an important role, as discussed below.

Having determined $t_{i\alpha,j\beta}$, we proceeded to compute the spin-orbit coupling parameter λ. We used the analytical expressions derived in Section 4.3 for the spin 1/2, d orbital SOC matrix elements, leaving only the spin-orbit coupling strength λ as a material-specific parameter. The value of λ is mainly determined by the nature of the involved magnetic ion, vanadium in the case of $Lu_2V_2O_7$. The corresponding SOC constant of an isolated ion V^{4+} is experimentally known with $\lambda_{\text{exp}} = 248\,\text{cm}^{-1} = 30.75\,\text{meV}$ [205]. To a smaller degree, the crystal environment of the ion is expected to modify this value. In order to estimate the crystallographic influence, we considered a fully relativistic band structure. Via a numerical fitting procedure we determined the value of λ in the sum of $\mathcal{H}_{\text{hop}}$, Eq. (4.20), and $\mathcal{H}_{\text{SOC}}$, Eq. (4.31), that reproduces the relativistic band structure with the most accuracy.

In Fig. 4.7 we demonstrate this procedure for $Lu_2V_2O_7$. Along a certain path in reciprocal space, shown in Fig. 4.7(a), where the most important reciprocal high-symmetry points are illustrated, we calculated with FPLO the fully relativistic band structure, shown in Fig. 4.7(b). The relativistic effects cause a band splitting in certain regions in reciprocal space. In Fig. 4.7(c) we show the energy bands for such a case with various methods along the path L-W in a small energy window close to the Fermi level, emphasized by the grey window in Fig. (b). The fully relativistic energy bands are indicated in dark blue, as shown for the wider region in Fig. (b). In purple, we illustrated the non-relativistic band structure from the tight-binding (TB) model given by Eq. (4.20) with the parameters given in Table 4.2 and further neighbour hopping parameters. The absence of the band splitting in this case is clearly visible. In red, we show the energy bands obtained from the sum $\mathcal{H}_{\text{hop}} + \mathcal{H}_{\text{SOC}}$ with λ as the only

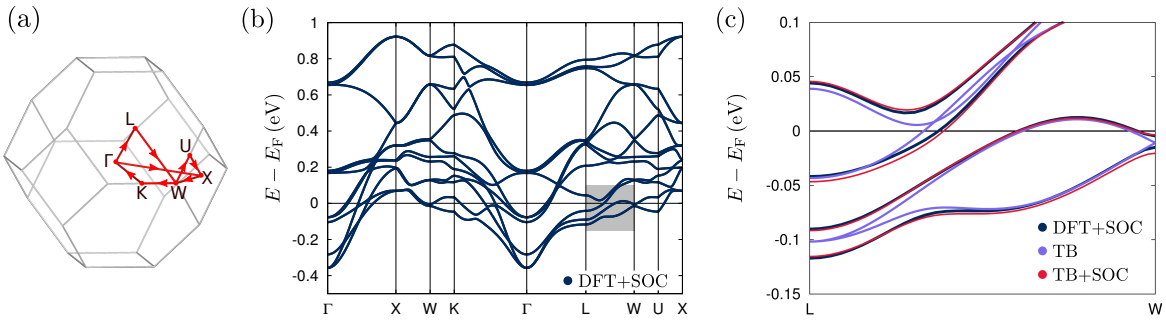

Figure 4.7: (a) Brillouin zone of the FCC space group corresponding to the pyrochlore structure with the high symmetry k points used in the brand structure calculations indicated. (b) Band structure from relativistic density functional theory (DFT+SOC) of $Lu_2V_2O_7$ along the k-path indicated in (a). (c) Band structure from DFT+SOC, from a non-relativistic tight-binding model (TB), and from a tight-binding model including spin-orbit coupling (TB+SOC) with $\lambda = 30.0\,\text{meV}$. The chosen k-path and energy window is indicated in gray in (b). Fig. adapted from Ref. [79].

free parameter, determined by a numerical optimization procedure. The band structure shown in red is computed with the following spin-orbit coupling parameter:

$$\lambda = 30\,\text{meV}, \tag{4.41}$$

in good agreement with the single-ion value for vanadium V^{4+}.

4.4.2 Importance of Hund's coupling and all five *d* orbitals

With $\mathcal{H}_{\text{hop}} + \mathcal{H}_{\text{SOC}}$ we determined the material specific contributions to the Hamiltonian available from *ab-initio* calculations. As discussed in Section 4.3, for d orbitals the two-particle interaction term $\mathcal{H}_{\text{int}}$, Eq. (4.22), is fully determined by Slater integrals, except for two model parameters. For the project discussed in this section we chose U_0 and J_{avg} as free model parameters within reasonable parameter ranges for vanadium. Note, that we considered a cluster of two sites, which allows to extract the bilinear spin exchange parameters, but without higher-order corrections. While this approach is able to provide a good picture about the orders of magnitude and importance of the various allowed parameters, the specific values should be considered with healthy caution. Before we present the determination of the low-energy subspace of $Lu_2V_2O_7$ via cluster diagonalization, we next discuss important contributions to $\mathcal{H}_{\text{tot}}$, Eq. (4.19).

Especially in the analysis of a system in terms of perturbation theory, it might be tempting to omit terms describing Hund's coupling due to the somewhat complicated analytic expressions and increased computational demands. However, for $Lu_2V_2O_7$ it is not possible to find a suitable low-energy description without taking this effect into account. The fact, that the ground state of $Lu_2V_2O_7$ is ferromagnetic [185], suggests strongly that Hund's coupling is important. The ferromagnetic ground state cannot stem from conventional Goodenough-Kanamori rules, since the angle between two vanadium atoms with the nearest oxygen atom is $\theta = 127.5°$ (see also Fig. 4.5(a)), which is far from the 90° that would predict ferromagnetic coupling in this framework [206]. Note, that conventional Goodenough-Kanamori rules were formulated for the case of $d_{x^2\text{-}y^2}$ orbitals in a square lattice. In this case, the geometry influences whether the antiferromagnetic contribution to the Heisenberg exchange $J_{\text{AFM}} \approx \frac{4t^2}{U}$ contribution is large. If the angle-independent Hund's coupling contributes to the Heisenberg interaction significantly, the relative magnitude of J is less influenced by the geometry. For $Lu_2V_2O_7$, the prediction of a ferromagnetic or antiferromagnetic Heisenberg coupling seems to require therefore more sophisticated calculations. As mentioned above, another tempting simplification of the Hamiltonian $\mathcal{H}_{\text{tot}}$ is the reduction onto the three lowest orbitals, sometimes referred to as the t_{2g} orbitals in the literature. However, the strong mixing of the orbitals in the two higher energy levels and the consideration of SOC effects

$\mathbf{L}\cdot\mathbf{S} = \frac{1}{2}(L_-S_+ + L_+S_-) + L_zS_z$ that stem from interaction between orbitals with $\Delta m_l = \pm 1$, suggests the importance of all five orbitals.

The proposal of an "orbital ordering" mechanism in $Lu_2V_2O_7$ as the responsible mechanism for the ferromagnetic ground state [194] was based on the argument that the hopping process between the lowest and the energetically highest d orbitals induces a ferromagnetic ground state for much lower Hund's couplings than with only t_{2g} levels. Including this hopping process therefore shifts $Lu_2V_2O_7$ for realistic Hund's coupling and crystal field splitting into the ferromagnetic region of the phase diagram. While in Ref. [194] a simplified version of the $3d$ Hubbard Hamiltonian [56] interaction was used, it nevertheless emphasizes that a description of the correct ferromagnetic interaction is only possible taking Hund's coupling effects and all five d orbitals into account.

4.4.3 Projection onto low-energy subspace

With the extended Hamiltonian $\mathcal{H}_{\text{tot}}$ established, we next diagonalized it on a two-site cluster with five d orbital and two spin degrees of freedom. We constrained the considered states to those containing two electrons per cluster in order to satisfy the filling of $Lu_2V_2O_7$ with one electron per magnetic site. In second quantization this implies $\binom{20}{2} = 190$ states. Consequently, the Hamiltonian can be represented by a 190×190 matrix, which we diagonalized numerically. For parameter sets with $U_0 - 3J_{\alpha\beta} > 0$ the low-energy subspace of the system is captured by four singly occupied states. Since spin-orbit coupling is small compared to the Hubbard parameters, $\lambda \ll U_{\alpha\beta}$ and $\lambda \ll J_{\alpha\beta}$, mixing of the orbital lowest in energy (d_{z^2}) with other orbitals should be weak. Therefore, we defined the low-energy state $|\chi\rangle$ in terms of a linear combination of the d_{z^2} singly occupied states:

$$|\chi\rangle = c_{\uparrow\uparrow}\,|\uparrow_{i,z^2}\uparrow_{j,z^2}\rangle + c_{\uparrow\downarrow}\,|\uparrow_{i,z^2}\downarrow_{j,z^2}\rangle + c_{\downarrow\uparrow}\,|\downarrow_{i,z^2}\uparrow_{j,z^2}\rangle + c_{\downarrow\downarrow}\,|\downarrow_{i,z^2}\downarrow_{j,z^2}\rangle. \tag{4.42}$$

For finite hopping and spin-orbit coupling, these ground states are modified by mixing with other states. Since in the case of $Lu_2V_2O_7$ we expect this mixing to be small, it is nevertheless instructive to analyse the low-energy states in terms of the coefficients $c_{\sigma\sigma'}$ in various limits. Here, we choose the parameters $U_0 = 3.3\,\text{eV}$ and $J_{\text{avg}} = 0.845\,\text{eV}$ for presentation purpose. Below, we discuss the influence of the model parameter choice onto the resulting spin Hamiltonian in more detail.

Low-energy states in various limits

With $t_{i\alpha,j\beta} = 0$ and $\lambda = 0$ there is no mixing of the orbitals and no exchange between sites. Therefore, the ground state is four-fold degenerate with the pure d_{z^2} orbital occupied for the four possible spin orientations. The ground state energy $\varepsilon_0 = 0.4702\,\text{eV}$ is twice the on-site energy of the d_{z^2} orbital $\varepsilon_{z^2} = 0.2351\,\text{eV}$, as given in Table 4.2. Exact diagonalization of $\mathcal{H}_{\text{tot}}$ confirmed these expectations. Due to the degeneracy, the ground states are not uniquely defined, but can be rotated such that $c_{\sigma\sigma'} = 1$ in Eq. (4.42) for each ground state:

$\varepsilon^{\text{pure}}$	$c_{\uparrow\uparrow}$	$c_{\uparrow\downarrow}$	$c_{\downarrow\uparrow}$	$c_{\downarrow\downarrow}$
0.4702 eV	1	0	0	0
0.4702 eV	0	1	0	0
0.4702 eV	0	0	1	0
0.4702 eV	0	0	0	1

(4.43)

Since there is no exchange between the orbitals, a finite Hund's coupling has no influence in this case.

With $t_{i\alpha,j\beta} = 0$ and a finite spin-orbit coupling, $\lambda \neq 0$, the eigenenergies are shifted due to the mixing of orbitals and spins. Hence, it is more meaningful to describe the states in terms of pseudo-orbitals $\tilde{\alpha}$, which result from linear combinations of the mixed states. The energies of the four lowest states correspond then to a pseudo-orbital labelled as $d_{\tilde{z}^2}$ to emphasize the close character to the original low energy orbital. Since the electrons on different sites cannot "talk" to each other, spin-orbit coupling does not lift the four-fold degeneracy and only shifts the total ground state energy, for the chosen parameter set to $\varepsilon^{\text{SO}} = 0.4685\,\text{eV}$.

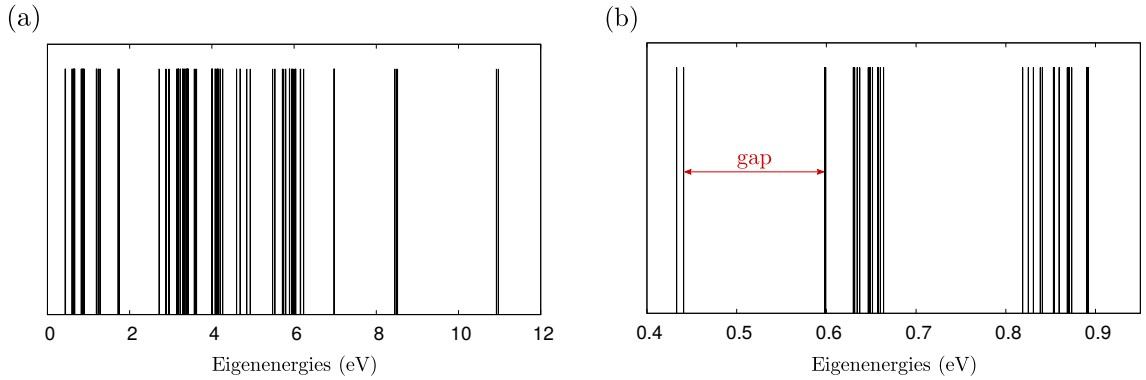

Figure 4.8: (a) Complete energy spectrum of a two-site cluster in $Lu_2V_2O_7$ with the model parameters $U_0 = 3.3$ eV, $J_{\text{avg}} = 0.845\,\text{eV}$, and $\lambda = 30\,\text{meV}$. (b) Zoomed in energy spectrum with indication of the gap between the four low-energy states, serving as a basis for the effective spin Hamiltonian, and the next higher eigenenergy.

In contrast, with finite hopping, $t_{i\alpha,j\beta} \neq 0$, and no spin-orbit coupling, $\lambda = 0$, the orbitals on different sites influence each other. In this case, exchange terms including Hund's coupling effects become important and cause a splitting into a triplet and a singlet state:

ε^{hop}	$c_{\uparrow\uparrow}$	$c_{\uparrow\downarrow}$	$c_{\downarrow\uparrow}$	$c_{\downarrow\downarrow}$
0.4391 eV	1	0	0	0
0.4391 eV	0	0	0	1
0.4391 eV	0	0.70	0.70	0
0.4477 eV	0	0.70	−0.70	1

(4.44)

Note, that the triplet states are in this case lower in energy, indicating already a ferromagnetic ground state.

Finally, with finite hopping $t_{i\alpha,j\beta} \neq 0$ and finite spin-orbit coupling $\lambda \neq 0$, the degeneracy of the four lowest eigenenergies is completely lifted. Next to the singlet-triplet splitting caused by Hund's coupling effects, the mixing of orbital and spin states due to spin-orbit coupling leads to additional small splitting of the three lowest states in energy:

$\varepsilon^{\text{SO+hop}}$	$c_{\uparrow\uparrow}$	$c_{\uparrow\downarrow}$	$c_{\downarrow\uparrow}$	$c_{\downarrow\downarrow}$
0.43300 eV	+0.69	0	0	+0.69
0.43306 eV	+0.49	−0.49	−0.49	−0.49
0.43307 eV	$+0.49 - 0.02i$	+0.49	$+0.49 - 0.05i$	$-0.49 - 0.02i$
0.44104 eV	0	$+0.70 - 0.03i$	$-0.70 + 0.06i$	0

(4.45)

The full energy spectrum for $Lu_2V_2O_7$ with the chosen parameters $U_0 = 3.3\,\text{eV}$, $J_{\text{avg}} = 0.845\,\text{eV}$, and $\lambda = 30\,\text{meV}$ is shown in Fig. 4.8. In Fig. (b), the spectrum for a narrow energy window close to the ground state energy illustrates the gap between the four lowest eigenenergies and the next excited state. The fact, that these states are well separated allows for a description solely in terms of this low-energy subspace. Since a simple neglection of the small contributions in other orbitals would generate a non-orthonormal basis, a procedure to recover an orthonormal basis, such as the Löwdin orthonormalization, is required before the effective spin Hamiltonian can be extracted [207].

Löwdin orthonormalization

To construct the effective spin Hamiltonian we first projected with $\mathbb{O}$ the four lowest eigenstates $|\psi_n\rangle$ onto linear combinations $|\chi_n\rangle$ of the singly occupied states with one electron in each d_{z^2} orbital $|s_n\rangle$:

$$|\chi_n\rangle = \mathbb{O}|\psi_n\rangle = \sum_m c_{nm}|s_m\rangle, \tag{4.46}$$

where the coefficients c_{nm} are those defined in Eq. (4.42) and the singly occupied states are defined as $|s_n\rangle = |\sigma_n\ \sigma'_n\rangle$ in the case of a two-site cluster. Due to the truncation of the Hilbert space, the constructed basis is not orthonormal resulting in a finite off-diagonal overlap matrix of the basis states:

$$\mathbb{S} = \sum_{n=1}^{N}\sum_{m=1}^{N} |\chi_n\rangle\langle\chi_m| \neq \mathbb{1}, \tag{4.47}$$

where N is the number of low-energy states. In the case a two-site cluster with one electron per site it is therefore $N = 2^2$.

Now, we consider hypothetical orthonormal basis states $|\tilde{\chi}\rangle$ in terms of the non-orthonormal basis via a yet unknown projector $\mathbb{X}$:

$$|\chi'\rangle = \mathbb{X}|\chi\rangle = \sum_m c'_{nm}|s_m\rangle. \tag{4.48}$$

The projector $\mathbb{X}$ can be related to the overlap matrix via the complete orthonormal basis states $|\tilde{\chi}\rangle$ and Eq. (4.47):

$$\mathbb{1} = \sum_{n=1}^{N}\sum_{m=1}^{N} |\chi'_n\rangle\langle\chi'_m| = \sum_{n=1}^{N}\sum_{m=1}^{N} \mathbb{X}|\chi_n\rangle\langle\chi_m|\mathbb{X}^\dagger = \mathbb{X}\cdot\mathbb{S}\cdot\mathbb{X}^\dagger, \tag{4.49}$$

and therefore:

$$\mathbb{S} = (\mathbb{X}^\dagger\cdot\mathbb{X})^{-1}. \tag{4.50}$$

In principle, there is an infinite number of projection possibilities for $\mathbb{X}$ [208]. However, Löwdin [209] proposed the symmetric orthogonalization procedure with the specific choice:

$$\mathbb{X} = \mathbb{S}^{-1/2}. \tag{4.51}$$

It has been shown [210] that this choice fulfils the maximal overlap criterium in the least-squares sense with $\sum_i\langle\chi'_i - \chi_i|\tilde{\chi}_i - \chi_i\rangle = \min$. With the normalization condition $\langle\tilde{\chi}_i|\tilde{\chi}_i\rangle = 1$ and a finite overlap $\langle\chi_i|\chi_i\rangle = \text{const}$, this is equivalent to the criterium:

$$\sum_i(\langle\tilde{\chi}_i|\chi_i\rangle + \langle\chi_i|\tilde{\chi}_i\rangle) = \max, \tag{4.52}$$

which is the mathematical expression of maximal overlap of the orthonormal and the original basis states.

The orthonormal basis states can now be determined directly from the overlap matrix and the projection onto the subspace as defined in Eq. (4.46):

$$|\chi'_n\rangle = \mathbb{S}^{-1/2}|\chi_n\rangle. \tag{4.53}$$

The coefficients in the orthonormal basis c' follow directly from this choice together with Eq. (4.48):

$$\sum_m c'_{nm}|s_m\rangle = \mathbb{S}^{-1/2}\sum_m c_{nm}|s_m\rangle. \tag{4.54}$$

The main advantage of the orthogonalization method is the conservation of the eigenenergies of the full system within the description of the reduced Hilbert space.

The overlap matrix for $Lu_2V_2O_7$ with the *ab-initio* determined hopping and SOC parameters and the model parameters $U_0 = 3.3\,\text{eV}$ and $J_{\text{avg}} = 0.845\,\text{eV}$ is:

$$\mathbb{S} = \begin{pmatrix} 0.962 & 0 & 0 & 0 \\ 0 & 0.958 & 0 & 0 \\ 0 & 0 & 0.959 & 0 \\ 0 & 0 & 0 & 0.959 \end{pmatrix}, \tag{4.55}$$

where the off-diagonal elements are on the order of 10^{-5}. The deviations from the identity matrix are a measure for the approximation quality to describe a system in terms of the chosen subspace. In this case, the deviations are rather small and the choice of subspace is with that rather well justified. The coefficients $c'_{\sigma\sigma'}$ according to the orthonormal states defined in Eq. (4.48), are modified compared to the naive description with Eq. (4.45):

ε	$c'_{\uparrow\uparrow}$	$c'_{\uparrow\downarrow}$	$c'_{\downarrow\uparrow}$	$c'_{\downarrow\downarrow}$
0.43300 eV	$+0.7071$	0	0	$+0.7071$
0.43306 eV	$+0.4997$	-0.4997	-0.4997	-0.4997
0.43307 eV	$-0.4995 + 0.0245i$	$+0.4999$	$+0.4975 + 0.0493i$	$-0.4995 - 0.0245i$
0.44104 eV	$+0.0175$	$+0.0189 - 0.7067i$	$+0.0162 + 0.7067i$	-0.0175

(4.56)

4.4.4 Effective Spin Hamiltonian for $Lu_2V_2O_7$

At this point, the effective Hamiltonian is known in terms of the low energy states introduced above:

$$\mathcal{H}_{\text{eff}} = \sum_{nm} c'_{nm}\, |s_n\rangle\langle s_m|. \tag{4.57}$$

A more intuitive description can be achieved with the help of spin projectors, which allow an expression of the effective Hamiltonian in terms of spin operators.

In Chapter 1 we introduced the Abrikosov pseudo-fermion representation for spin 1/2 operators $\mathbf{S} = \underline{d}^\dagger \vec{\sigma} \underline{d}$. Operators in second quantization can generally be expressed as follows:

$$\hat{A} = \sum_{\mu\nu\mu'\nu'} \langle \mu\nu|\hat{A}|\mu'\nu'\rangle\, d^\dagger_{1\mu} d^\dagger_{2\nu} d_{2\nu'} d_{1\mu'}. \tag{4.58}$$

With the help of this relation we transformed the effective Hamiltonian in Eq. (4.57) in second quantization into an expression in terms of spin operators. For example, the operator with both spins up in both states can be expressed in second quantization:

$$|\uparrow_{iz^2}\uparrow_{jz^2}\rangle\langle\uparrow_{iz^2}\uparrow_{jz^2}| = d^\dagger_{i,z^2\uparrow} d^\dagger_{j,z^2\uparrow} d_{j,z^2\uparrow} d_{i,z^2\uparrow}, \tag{4.59}$$

and therefore be connected to spin operators S^z, where we omitted the orbital index for simplicity:

$$d^\dagger_{i,z^2\uparrow} d^\dagger_{j,z^2\uparrow} d_{j,z^2\uparrow} d_{i,z^2\uparrow} = (\frac{1}{2} + S^z_i)(\frac{1}{2} + S^z_j). \tag{4.60}$$

The $N \times N$ (here 4×4) dimensional effective Hamiltonian in terms of second quantization reads then as follows:

$$\mathcal{H}_{\text{eff}} = \sum_{n=1}^{N}\sum_{m=1}^{N} c'_{nm}|s_n\rangle\langle s_m| = \sum_{n=1}^{4}\sum_{m=1}^{4} c'_{nm}\, d^\dagger_{i,z^2\sigma_n} d^\dagger_{j,z^2\sigma'_n} d_{j,z^2\sigma'_m} d_{i,z^2\sigma_m}, \tag{4.61}$$

and can therefore be expressed as an effective Hamiltonian in terms of spin operators:

$$\mathcal{H}_{\text{eff}} = \sum_{\alpha}\sum_{\beta} \gamma_{\alpha\beta} S^\alpha_i S^\beta_j, \tag{4.62}$$

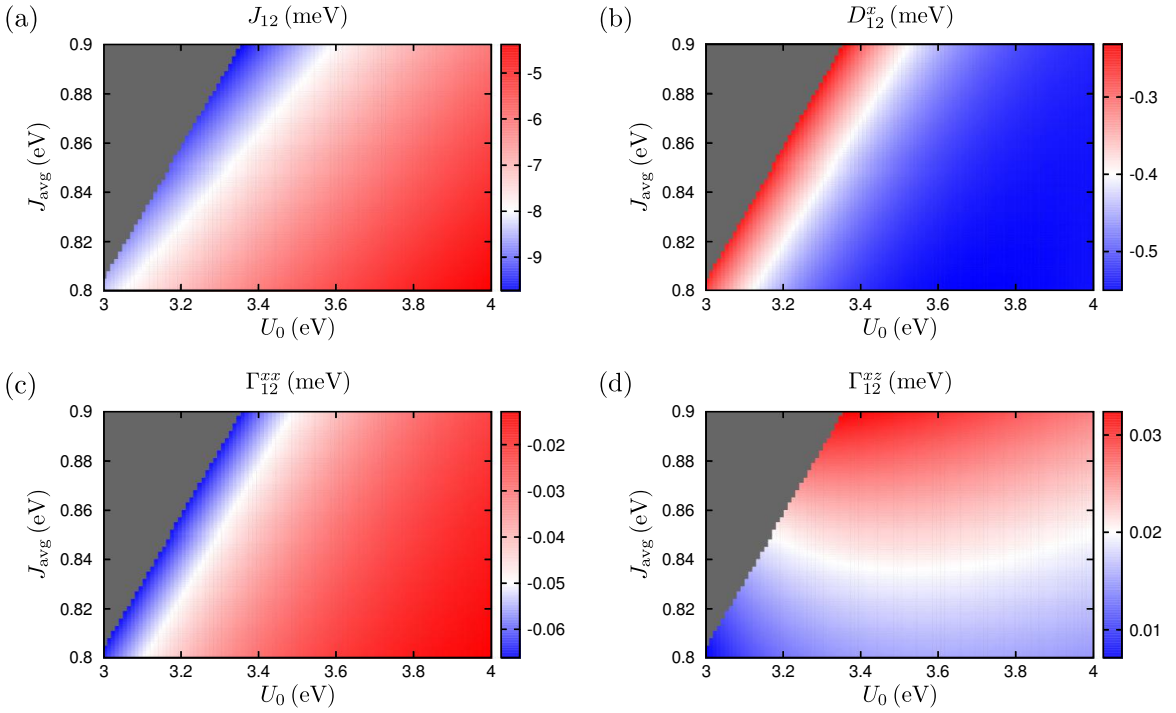

Figure 4.9: Magnetic parameters for $Lu_2V_2O_7$ on bond 1-2 within a range of parameters U_0 and $J_{\rm avg}$. (a) Heisenberg exchange, (b) x component of the DM vector, (c) Γ^{xx}_{12} and (d) Γ^{xz}_{12} components of the pseudo-dipolar tensor. Fig. adapted from Ref. [79].

with $\alpha, \beta = \{0, x, y, z\}$, where we refer to the identity matrix with $\alpha = 0$ in order to parametrize the constant contributions in the spin Hamiltonian. Due to time reversal symmetry, odd spin terms vanish unless an external magnetic field is present.

As discussed in Section 4.2, the bilinear spin Hamiltonian for pyrochlore systems consists of four independent parameters. In the parametrization chosen in this chapter, these independent parameters are the Heisenberg exchange J, one independent parameter in the Dzyaloshinskii-Moriya interaction $\mathbf{D}$, and two independent parameters in the symmetric pseudo-dipolar tensor Γ. With the method described above, we determined the bilinear spin Hamiltonian of $Lu_2V_2O_7$ with the *ab-initio* hopping and SOC parameters given in Table 4.2 and Eq. (4.41). With the parameter choice $U_0 = 3.3\,\text{eV}$ and $J_{\rm avg} = 0.845\,\text{eV}$ we obtained:

$$J_{12} = -7.99\,\text{meV}, \quad \mathbf{D}_{12} = \begin{pmatrix} -0.4 \\ 0 \\ 0.4 \end{pmatrix} \text{meV}, \quad \Gamma_{12} = \begin{pmatrix} -0.05 & 0 & 0.02 \\ 0 & 0.1 & 0 \\ 0.02 & 0 & -0.05 \end{pmatrix} \text{meV}. \tag{4.63}$$

This parameter set leads to a reasonably good agreement of the calculated Heisenberg exchange with the value $J = -8.22\,\text{meV}$ determined from inelastic neutron scattering experiments [196]. The philosophy behind this choice is, that a Heisenberg parameter fine-tuned to experiment may allow then to predict the higher order terms for a working parameter set. However, to track the dependencies of the exchange parameters, we computed them for a range of model parameters U_0 and $J_{\rm avg}$, as shown in Fig. 4.9. A reasonable parameter range for the Hund's coupling is $J_{\rm avg} = 0.8$–$0.9\,\text{eV}$ in transition metals with $3d$ orbitals [206]. For the Coulomb repulsion we considered $U_0 = 3$–$4\,\text{eV}$ as a reasonable parameter range. Parameter combinations that would give unphysical $U_{\alpha\beta} - 3J_{\alpha\beta} < 0$ were excluded from the parameter scan and indicated as a grey background.

In Fig. 4.9(a) we show the computed values for the Heisenberg exchange on bond 1-2 as defined in Fig. 4.2(b). A value close to neutron scattering experiment [196], $J_{12} = -8\,\text{meV}$, is indicated in white. The monotonic increase of the Heisenberg parameter as a function of U_0 and $J_{\rm avg}$ is promising

in the sense that modifications of the model parameters lead to directly predictable modifications of the exchange parameters. We will see in the next section, for the case of $Lu_2Mo_2O_5N_2$, that this is not necessarily the case. For all reasonable model parameters U_0 and J_{avg} we obtained a ferromagnetic result, in agreement with the experimental observation. Reasonable model parameters lead to a Heisenberg exchange between $J_{12} = -5\,\text{meV}$ and $-9\,\text{meV}$.

The numerical results for the x component of the Dzyaloshinskii-Moriya interaction D_{12}^x on bond 1-2 are shown in Fig. 4.9(b). Note, that this exchange parameter is renormalized in comparison to the total interaction parameter with $|\mathbf{D}_{12}| = \sqrt{2}D_{12}^x$. The numerical results obey the constraints given by Moriya's rules, introduced in Section 4.2. With that they confirmed the employed local coordinates, given by Eq. (4.21) and the rotations in the analytical part of the spin-orbit coupling matrix elements introduced in Section 4.3. One of the numerical results, as a consequence of the material specific parameters, is already the sign of the DM vector, which corresponds for the whole range of model parameters to the indirect case as defined by Elhajal *et al.* [189]. The value $D_{12}^x = -0.4\,\text{meV}$, given in Eq. (4.63), is indicated in white in Fig. 4.9(b) and corresponds to the following ratio with the Heisenberg exchange:

$$\frac{|\mathbf{D}|}{|J|} \approx 0.07. \tag{4.64}$$

The slope of the parameter dependence does not follow the slope in the Heisenberg exchange. Therefore, the ratio $|\mathbf{D}/J|$ is not uniquely determined, even for a fixed Heisenberg exchange. For model parameters corresponding to a Heisenberg exchange window $J = -8 \pm 0.5\,\text{meV}$, we obtained ratios between 4% and 9%. Even this range of results is lower than the two available experimental results with $|\mathbf{D}/J| \simeq 0.32$ from transport data fits [187] and $|\mathbf{D}/J| \simeq 0.18$ from inelastic neutron scattering [196]. We comment further on this discrepancy below.

In Fig. 4.9(c,d) the two independent parameters Γ_{12}^{xx} and Γ_{12}^{xz} of the pseudo-dipolar tensor on bond 1-2 are illustrated. While the diagonal component Γ_{12}^{xx} shows a similar dependence on U_0 and J_{avg} as the DM vector, the off-diagonal component can lead to a much larger range of parameter ratios. For the parameter set $U_0 = 3.3\,\text{eV}$, $J_{\text{avg}} = 0.845\,\text{eV}$, as chosen for Eq. (4.63), the white regions in the figure indicate to the ratio:

$$\frac{||\Gamma||}{|J|} = 0.02, \tag{4.65}$$

where $||\Gamma|| \equiv \sqrt{\sum_{ij} |\Gamma_{ij}|^2}$ corresponds to the so-called Frobenius norm of the pseudo-dipolar tensor. For model parameters leading to a Heisenberg exchange window $J = -8 \pm 0.5\,\text{meV}$, we computed ratios between 1% and 2%. Although these corrections are rather small, it is questionable whether they are entirely negligible in the analysis of the magnetic exchange in $Lu_2V_2O_7$. We comment on this issue further below.

Second order perturbation theory

As an alternative approach for constructing the effective spin Hamiltonian, and as a check for consistency, we also applied second order perturbation theory [51] to the two-site cluster Hubbard Hamiltonian for $Lu_2V_2O_7$. For that we followed the general scheme introduced in Chapter 1 with

$$\mathcal{H}_{\text{eff}} = \mathbb{P}\mathcal{H}_1\mathbb{R}\mathcal{H}_1\mathbb{P}, \qquad \text{with} \quad \mathbb{P} = \sum_n |s_n\rangle\langle s_n|, \quad \mathbb{R} = \sum_{m\neq n} \frac{|\phi_m\rangle\langle\phi_m|}{\langle s_n|\mathcal{H}_0|s_n\rangle - \langle\phi_m|\mathcal{H}_0|\phi_m\rangle}, \tag{4.66}$$

generalized to the five-orbital case. The resulting effective spin Hamiltonian can then be directly compared with the Hamiltonian obtained via cluster diagonalization. Here, we consider the single-site Hamiltonian as $\mathcal{H}_0$:

$$\mathcal{H}_0 = \sum_i \mathcal{H}_i + \mathcal{H}_{\text{int}}, \tag{4.67}$$

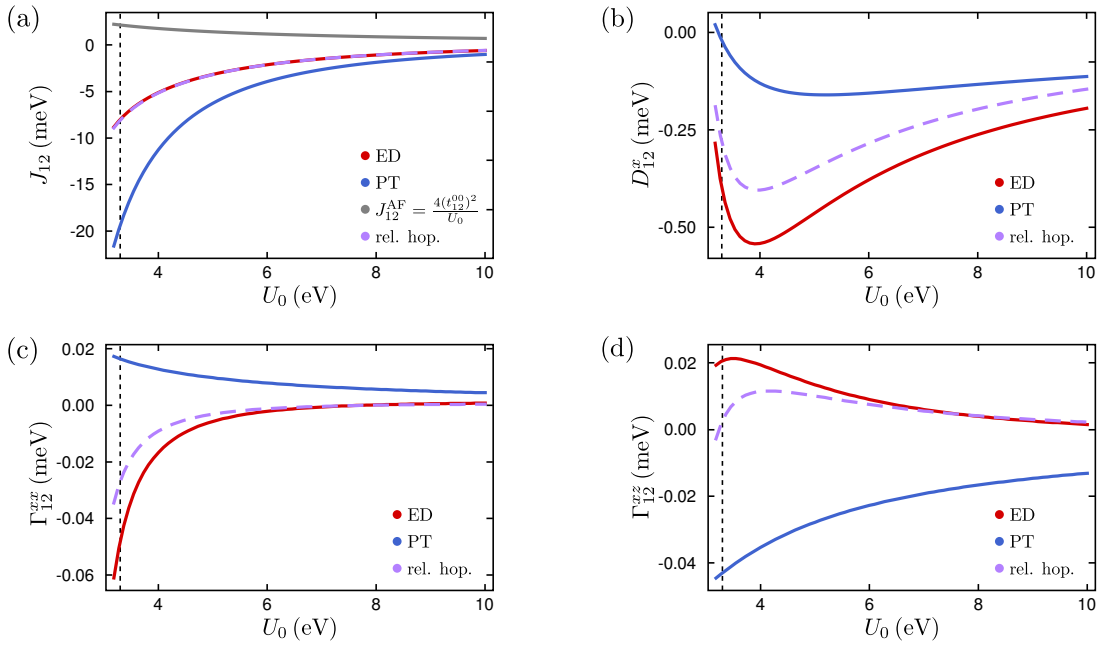

Figure 4.10: Magnetic parameters from exact diagonalization (ED), perturbation theory (PT) and relativistic hopping parameters obtained directly from DFT (rel. hop.) for $Lu_2V_2O_7$ on bond 1-2 with fixed $J_{\mathrm{avg}} = 0.845\,\mathrm{eV}$ and within a range of parameters U_0. The proposed model parameter set for $Lu_2V_2O_7$ with $U_0 = 3.3\,\mathrm{eV}$ is indicated with a black dashed line.

given by Eq. (1.3) and Eq. (4.22) respectively. The hopping contribution, given by Eq. (4.20), is then the perturbative part:

$$\mathcal{H}_1 = \mathcal{H}_{\mathrm{hop}}. \tag{4.68}$$

Spin-orbit coupling is included in the single-site Hamiltonian $\mathcal{H}_i$ and treated exact in this approach.

The perturbation theory results are shown in Fig. 4.10, with fixed Hund's coupling $J_{\mathrm{avg}} = 0.845\,\mathrm{eV}$. As expected, the perturbation theory results approach the exact diagonalization results in the limit of strong correlations $U_0 \gg t_{i\alpha,j\beta}$. However, for $U_0 = 3.3\,\mathrm{eV}$, indicated by the dashed line, strong higher-order corrections are evident. This becomes more pronounced for terms of higher order in spin-orbit coupling. For example, Γ_{12}^{xx} and Γ_{12}^{xz} even change sign. In the case of the Heisenberg exchange, shown in Fig. 4.10(a) we also show the antiferromagnetic contribution $J_{12}^{\mathrm{AF}} = \frac{4(t_{12}^{00})^2}{U_0}$ which is in competition with the Hund's coupling effects and therefore reduces the absolute value of the Heisenberg exchange. This effect promotes the importance of the smaller spin-orbit caused exchange parameters. Since $t_{iz^2,jz^2} = -0.04\,\mathrm{eV}$ for different sites $i \neq j$ is not the dominant overlap between orbitals on different sites, it is on the other hand not surprising that the final result for the nearest neighbour Heisenberg exchange is ferromagnetic.

Relativistic *ab-initio* hopping parameters

In more complicated cases than d block orbitals, analytic expressions for the SOC matrix elements might not be available. One example for this are organic charge transfer salts, discussed in Chapter 2. As a consequence, it can be impossible to reduce the spin-orbit coupling description $\mathcal{H}_{\mathrm{SOC}}$ to only one free parameter λ. With certain DFT codes, e.g. FPLO, it is implemented to directly compute complex hopping parameters with projective Wannier functions. Within this approach, the optimization step for the parameter λ is omitted. However, this strategy represents a stronger approximation than the procedure presented above. As detailed in Chapter 1, a complex spin-dependent hopping term stems

from spin-orbit coupling effects through a basis transformation into the eigenbasis of the single-particle Hamiltonian. In this case, the interaction part $\mathcal{H}_{\text{int}}$ should be transformed into the same basis for consistency. However, for cases with unknown analytical expressions of the SOC matrix elements this proves to be difficult. Due to the overlap matrix $\mathbb{S}$ in Eq. (4.55) we know that the eigenbasis of the full system does not differ strongly from the basis with singly occupied states. Therefore, the error introduced by calculating with $\mathcal{H}_{\text{int}}$ in a different basis than the hopping part should be comparably small. This is true for systems with small spin-orbit coupling $\lambda \ll t_{i\alpha,j\beta}$, e.g. in the case of organic charge transfer salts.

Since we have the opportunity to check the results within both approaches, we calculated the exchange parameters for $Lu_2V_2O_7$ in a second approach via exact cluster diagonalization with complex hoppings obtained directly from FPLO. The results are shown in Fig. 4.10, indicated by the dashed purple lines. Although the interaction Hamiltonian is expressed in a different basis than the single-particle Hamiltonian, the deviations from the calculations with a consistent basis, shown in red, are surprisingly small. As expected, the Heisenberg exchange is almost not influenced by this approximation. While we see corrections in the case of the DM and the pseudo-dipolar tensor, the uncertainty due to the choice of model parameters U_0 and J_{avg} seems to influence the relative ratio to the Heisenberg exchange much stronger than the approximation in the choice of basis sets.

4.4.5 Discussion of $Lu_2V_2O_7$ spin Hamiltonian

The hybrid method detailed in this section allowed to obtain with $J_{ij} = -8\,\text{meV}$ a nearest-neighbour Heisenberg interaction close to the experimental value obtained from inelastic neutron scattering [196]. Fitting from magnetic specific heat [187] on the other hand suggested with $J_{ij} = -3.4\,\text{meV}$ a much smaller value. Due to the more indirect determination and subtleties in the substraction of phonon contributions, we focused on the INS results for comparison. The value of $J_{ij} = -7.09\,\text{meV}$ for the isotropic exchange determined from total energy DFT calculations by Xiang *et al.* [195] is also in relatively good agreement. Note, that the total energy method depends on the choice of the model parameters representing Hubbard repulsion and Hund's coupling as well. Due to dependencies on the specific implementation techniques in the DFT code and the construction of the Hubbard Hamiltonian, it is unfortunately not possible to directly compare the results for a given model parameter set. The overall agreement of the total energy calculations with the hybrid method in the dominating energy scale is generally not surprising, since the isotropic parameters do not depend strongly on the details of the non-collinear spin arrangements and the consideration of relativistic effects. Note, that the results in Ref. [195] are given for calculations for $Y_2V_2O_7$, which is symmetrically equivalent to $Lu_2V_2O_7$, but the different rare earth ion might influence the details of the exchange to a small degree.

Unfortunately, the DM to Heisenberg ratio presented in this chapter, $|\mathbf{D}_{ij}/J_{ij}| = 0.07$, differs rather strongly from the ratio extracted from INS fits $|\mathbf{D}_{ij}/J_{ij}| = 0.18$. Note, that the discrepancy to the transport data is with $|\mathbf{D}_{ij}/J_{ij}| = 0.32$ even larger, although this finding is of course not independent from the much smaller Heisenberg exchange. The discrepancy to the INS result may have a number of reasons. For example, the fit to the INS data neglected the pseudo-dipolar tensor, which might shift some anisotropic features to a larger DM interaction. Also, longer-range isotropic Heisenberg exchange might lead to higher-order corrections, which are absent in both, the INS and the theoretical calculation in this chapter. It is however not clear, whether they would enter in the same way, so that errors in different directions might have been caused on both sides. That larger cluster sizes could improve the theoretical result is already hinted by the overlap integrals given in Table 4.2. While the hopping between d_{z^2} orbitals on different sites is rather small, higher order hopping processes might influence the nearest neighbour exchange in a non-negligible way. Moreover, in the case of $Lu_2Mo_2O_5N_2$, discussed in the next section, total energy DFT calculations suggested a significant contribution from third nearest neighbour Heisenberg exchange J_{3a}. Further studies should therefore investigate the influence of higher-order terms in $Lu_2V_2O_7$.

The discrepancy of our finding with the total energy result [195] of the somewhat smaller ratio $|\mathbf{D}_{ij}/J_{ij}| = 0.048$, is stronger than it might seem at first glance. The Heisenberg exchange from total energies is estimated to be smaller than in our approach. This disagreement most certainly stems from the different treatment of the total spin Hamiltonian in the two approaches. While Xiang *et al.* [195]

neglected the pseudo-dipolar tensor in their chosen parametrization scheme, we found that these terms provide a finite correction to the total spin Hamiltonian. More importantly, in Ref. [195] the inclusion of single-ion anisotropy differs significantly from the approach presented in this chapter. As pointed out in Chapter 1, the possible magnetic configurations in DFT have to be described in the single-particle picture and correspond therefore mainly to broken-symmetry states. Mixing of energetically higher eigenstates of the quantum mechanical spin Hamiltonian with low-energy eigenstates might therefore result in an artificial finite single-ion anisotropy. However, as soon as the description is reduced to a spin 1/2 model Hamiltonian, inclusion of such a term hampers a meaningful treatment. In order to avoid this issue, we chose an approach in which only quantum mechanically allowed terms are finite by construction in the model Hamiltonian.

In general, it is not obvious why the determination of the defining magnetic exchange contributions in $Lu_2V_2O_7$ turned out to be so challenging. With an ordering temperature of $T_c \approx 70\,\mathrm{K}$ [185–187] to a ferromagnetic ground state, the energy scales in the system did not seem to be of alarmingly small size. However, discrepancies between the available experiments and theoretical calculations remain to some extent unsolved. Especially with regard to the topological aspects of magnon excitations [187, 197–200] a progress in understanding the magnetic properties quantitatively in $Lu_2V_2O_7$ is however desirable. For example, we computed the sign of its DM interaction and classified it with that as an indirect pyrochlore. This may explain the different sign of the transverse thermal conductivity in $In_2Mn_2O_7$ [211], which was suggested to be related to the sign of the DM interaction [198]. Calculations of the spin Hamiltonian including the DM interaction for $In_2Mn_2O_7$ would be required to check this hypothesis. On the other hand, the number of edge states in the framework of $Lu_2V_2O_7$ as an topological magnon insulator would depend on the ratio $|\mathbf{D}_{ij}/J_{ij}|$ [197, 199], which remains to be debated. Therefore, the determination of the appropriate spin Hamiltonian for $Lu_2V_2O_7$ should be further pursued with theoretical studies of higher-order and long-range contributions.

4.5 The pyrochlore gearwheel QSL candidate $Lu_2Mo_2O_5N_2$

Yasir Iqbal, Tobias Müller, **Kira Riedl**, Johannes Reuther, Stephan Rachel, Roser Valentí, Michel J. P. Gingras, Ronny Thomale, and Harald O. Jeschke,
Signatures of a gearwheel quantum spin liquid in a spin-1/2 pyrochlore molybdate Heisenberg antiferromagnet,
Phys. Rev. Mater. **1**, 071201 (2017)
[80]

In this section we discuss, in contrast to the pyrochlore ferromagnet $Lu_2V_2O_7$, the pyrochlore quantum spin-liquid candidate $Lu_2Mo_2O_5N_2$. This compound is a pyrochlore antiferromagnet with Mo^{5+} S=1/2 moments that fail to develop long-range order or spin freezing down to $T^* \approx 0.5\,\mathrm{K}$, despite a significant Curie-Weiss temperature[4] $\Theta_{\mathrm{CW}} = -121\,\mathrm{K}$ [188]. In three dimensions, the pyrochlore lattice is due to the strong geometrical frustration among the most promising structures in the search for QSL states. However, most materials in these two families either develop long-range magnetic order or display a spin-glass-like freezing at low temperature [169]. The parent compound $Lu_2Mo_2O_7$ is a S=1 system with the magnetic ion Mo^{4+}. This material was proposed as a spin-glass candidate by Clark *et al.* [188]. The authors argued then that a substitution of O for N could tune the nature of the ground state from a spin glass to a quantum spin liquid. The observed linear temperature dependence in the heat capacity $C_{\mathrm{mag}} \propto T$, together with the fact that $Lu_2Mo_2O_5N_2$ is an insulator, were interpreted as signatures of a spinon Fermi surface. However, such a dependence can also be assigned to glass like behaviour [168].

Another important issue is that it is not clear at this point how the observed non-magnetic random site O/N disorder influences the magnetic response of $Lu_2Mo_2O_5N_2$. Additional experiments and re-

[4]Note, however, that in the case of strong spin-orbit coupling the effective moment μ_{eff} in the Curie-Weiss law is temperature-dependent. This was pointed out already in 1949 by Kotani [212], and expanded to more complicated symmetries by Kamimura a decade later [213]. A naive Curie-Weiss fit of susceptibility data might therefore lead to misleading results. Clark *et al.* [188] mentioned themselves the large deviation of their fitted $\mu_{\mathrm{eff}} = 1.11\,\mu_B$ compared to the expected $\mu_{\mathrm{eff}} = 1.73\,\mu_B$ for a pure, temperature-independent spin 1/2 system.

Atom	Wyckoff position	Coordinates	Occupancy [188]	Occupancy (theory)
Lu	16d	$(0.5, 0.5, 0.5)$	1.0	1.0
Mo	16c	$(0.0, 0.0, 0.0)$	1.0	1.0
O/N	48f	$(0.3477, 0.125, 0.125)$	0.663/0.257	0.695/0.305
O'/N'	8b	$(0.375, 0.375, 0.375)$	0.831/0.169	0.831/0.169

Table 4.3: Refined atomic coordinates of $Lu_2Mo_2O_5N_2$ reported by Ref. [188] and occupancy used in the theoretical *ab-initio* calculations to preserve a 5:2 O:N ratio.

finement of the crystal growth towards single crystals might enlighten whether the observed response should be assigned to a "dirty" version of a clean sample with a QSL ground state or whether disorder effects dominate the compounds behaviour. In this case it might be necessary to analyse the system in a similar fashion as was discussed in Chapter 3 in the context of the organic charge transfer salt κ-$(ET)_2Cu_2(CN)_3$.

Instead of pinpointing the precise spin Hamiltonian for a clean crystal, the goal of this project was rather to gain intuition about the mechanisms that could play a dominant role in the magnetic response of $Lu_2Mo_2O_5N_2$. *Ab-initio* studies determining anisotropic contributions in Ref. [80] were performed as part of the completion of this thesis and are presented here. In Ref. [80], the total energy DFT calculations were performed by Harald O. Jeschke and the $S = 1/2$ pseudofermion functional renormalization group (PFFRG) calculations by Yasir Iqbal.

4.5.1 Theoretical modelling of O/N occupation

The conventional situation for pyrochlore oxides is realized in $Lu_2V_2O_7$, with two crystallographically inequivalent oxygen atoms O and O′, corresponding to the formula $A_2B_2O_6O'$, where the O′ atoms are located at the centers of the non-magnetic Lu^{3+} tetrahedra (see also Fig. 4.1(b)), and the magnetism is carried by spin 1/2 V^{4+} ions. Consequently, the Lu site is eightfold coordinated by oxygen, in contrast to the sixfold coordination of V [214]. In the more complicated case of $Lu_2Mo_2O_5N_2$, there are two of the oxygen atoms replaced by nitrogen atoms. To keep a non-magnetic Lu^{3+} site and a spin 1/2 Mo^{5+} magnetic site, the doping should ideally only affect the oxygens on the 48f positions. However, in reality the N doping cannot be controlled as precisely.

For the *ab-initio* calculations we used the crystal structure determined from powder samples in Ref. [188], given in Table 4.3. The occupancy of the oxygen/nitrogen atoms with Wyckoff position 48f do not add up to one, hinting at a O/N deficiency in $Lu_2Mo_2O_5N_2$. To circumvent issues with the charge distribution, we used in the *ab-initio* calculations theoretical occupancies for this position, normalized to one and preserving the stoichiometry of $Lu_2Mo_2O_5N_2$. Considering the multiplicity of the Wyckoff positions, the ideal occupancies can be determined by the following two equations:

$$\frac{8 \cdot 0.831 + 48 \cdot n_O}{8 \cdot 0.169 + 48 \cdot n_N} = \frac{5}{2} \qquad \text{and} \qquad n_O + n_N = 1. \tag{4.69}$$

The resulting theoretical occupancies used in the *ab-initio* calculations are presented in Table 4.3.

With occupation numbers providing a charge distribution with Mo^{5+}, i.e. spin 1/2 at the magnetic sites, the first step towards a meaningful model is accomplished. A second issue for the theoretical treatment is the random O/N occupation in $Lu_2Mo_2O_5N_2$. A subject of future work could be the question, whether it is possbile to synthesize single crystals with an ordered O/N distribution. Since this would break the high pyrochlore symmetry it might not be possible to accomplish. Therefore, we decided to use a O/N distribution as close as possible to the experimental refinement. In the DFT calculations, the random O/N occupation was modeled using virtual crystal approximation [215]. This corresponds to a crystal structure where nuclear charges of $Z = 8 \cdot 0.663 + 7 \cdot 0.257 = 7.6948$ and $Z = 8 \cdot 0.831 + 7 \cdot 0.169 = 7.831$ are assigned to the atoms at Wyckoff positions 48f and 8b, respectively.

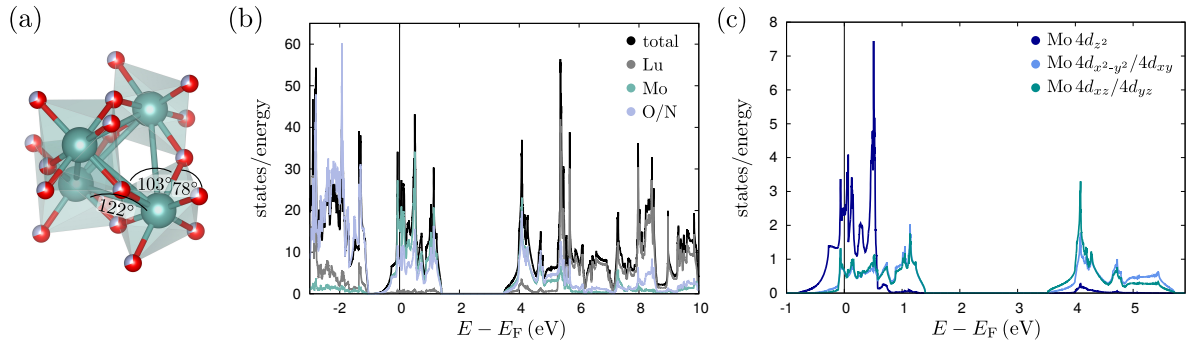

Figure 4.11: (a) Mo tetrahedron with O/N environment causing the observed trigonal crystal field splitting. (b) Density of states of $Lu_2Mo_2O_5N_2$ resolved with respect to the elements in the crystal structure. (c) DOS resolved with respect to the $4d$ Mo characters in the relevant energy window.

4.5.2 *Ab-initio* determination of hopping and spin-orbit parameters

For $Lu_2Mo_2O_5N_2$, we employed the same strategy as presented in the previous Section 4.4 to determine the anisotropic exchange parameters in a spin 1/2 pyrochlore lattice. The first step was to perform non-magnetic, non-relativistic density functional theory calculations with the FPLO code [201] to obtain the *ab-initio* density of states.

In Fig. 4.11(a) we show the oxygen/nitrogen environment within one molybdenum tetrahedron. The angles determining the distortion of the O/N octahedra, which are among others responsible for details of the trigonal crystal field splitting, differ slightly from those observed in $Lu_2V_2O_7$ (see also Fig. 4.5(a)). However, we show below that the consequences of small differences can be rather strong. In Fig. 4.11(b) we show the DFT density of states with respect to the contributing elements. Since we used for the *ab-initio* calculations the virtual crystal approximation, it is not possible to distinguish oxygen from nitrogen contributions. Similarly to $Lu_2V_2O_7$, the states close to the Fermi level are dominated by the magnetic sites, here Mo $4d$ orbitals. The orbital resolved DOS of molybdenum character within the local coordinate systems given in Section 4.3 is shown in Fig. 4.11(c). The partial density of states reveals the expected trigonal crystal field splitting for the pyrochlore structure, encouraging a description within a tight-binding approximation with restriction to the five Mo $4d$ orbitals. In this case, both, the oxygen and nitrogen weights, are effectively integrated out within the energy window of the Wannier projection.

			$t_{1\alpha,1\beta}$					$t_{1\alpha,2\beta}$		
	$d_{x^2-y^2}$	d_{z^2}	d_{xy}	d_{yz}	d_{xz}	$d_{x^2-y^2}$	d_{z^2}	d_{xy}	d_{yz}	d_{xz}
$d_{x^2-y^2}$	+2.58	0	0	-1.84	0	-0.17	+0.11	-0.13	-0.03	+0.12
d_{z^2}	0	+0.29	0	0	0	+0.11	-0.11	+0.19	-0.10	-0.17
d_{xy}	0	0	+2.58	0	-1.84	-0.13	+0.19	-0.33	+0.12	+0.11
d_{yz}	-1.84	0	0	+2.51	0	-0.03	-0.10	+0.12	-0.01	+0.10
d_{xz}	0	0	-1.84	0	+2.51	+0.12	-0.17	+0.11	+0.10	+0.11
			$t_{1\alpha,3\beta}$					$t_{1\alpha,4\beta}$		
	$d_{x^2-y^2}$	d_{z^2}	d_{xy}	d_{yz}	d_{xz}	$d_{x^2-y^2}$	d_{z^2}	d_{xy}	d_{yz}	d_{xz}
$d_{x^2-y^2}$	-0.40	-0.22	0	+0.17	0	-0.17	+0.11	+0.13	-0.03	-0.12
d_{z^2}	-0.22	-0.11	0	+0.20	0	+0.11	-0.11	-0.19	-0.10	+0.17
d_{xy}	0	0	-0.10	0	-0.10	+0.13	-0.19	-0.33	-0.12	+0.11
d_{yz}	+0.17	+0.20	0	+0.16	0	-0.03	-0.10	-0.12	-0.01	-0.10
d_{xz}	0	0	-0.10	0	-0.07	-0.12	+0.17	+0.11	-0.10	+0.11

Table 4.4: Onsite energies $t_{1\alpha,1\beta}$ (in eV) and nearest neighbor hopping parameters $t_{1\alpha,j\beta}$ (in eV) between molybdenum site 1 and j as defined in Fig. 4.2(b). The parameters for the other three molybdenum ions in one tetrahedron follow from symmetry considerations.

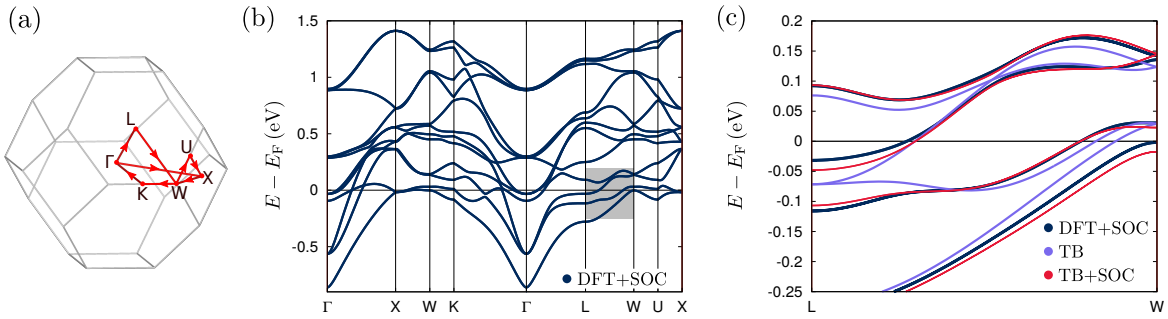

Figure 4.12: (a) High-symmetry path in reciprocal space used along which the band structures are computed. (b) Relativistic band structure from DFT along the k-path indicated in (a). (c) Band structure from DFT+SOC, from a non-relativistic tight-binding model (TB) and from a tight binding model including spin-orbit coupling (TB+SOC) with $\lambda = 88.7\,\text{meV}$. The illustrated region is indicated in (b) by the gray rectangle.

The hopping parameters $t_{i\alpha,j\beta}$, corresponding to $\mathcal{H}_{\text{hop}}$ in Eq. (4.20), were obtained from projective Wannier functions with the FPLO code [204]. The resulting band structure agrees well with the total non-magnetic, non-relativistic DFT band structure. We show the dominating on-site and nearest-neighbour hopping parameters in Table 4.4. The hopping integral t_{iz^2,jz^2} for different sites $i \neq j$ is almost three times larger than it is for $Lu_2V_2O_7$. Consequently, the antiferromagnetic contribution $J_{ij}^{\text{AF}} = \frac{4(t_{12}^{00})^2}{U_0}$ is expected to be a much stronger competitor to ferromagnetic contributions than it is the case for the vanadium compound. Therefore, an antiferromagnetic magnetic exchange between nearest neighbours in $Lu_2Mo_2O_5N_2$ is expected. This is in agreement with the theoretical finding of a QSL ground state of antiferromagnetic nearest neighbour exchange on the pyrochlore lattice [189] and the lack of experimentally observed magnetic ordering in $Lu_2Mo_2O_5N_2$ down to very low temperatures.

With the hopping parameters $t_{i\alpha,j\beta}$ at hand, we were then able to determine the spin-orbit coupling strength λ with the optimization approach introduced in the previous section. The relativistic band structure obtained with the FPLO code is shown in Fig. 4.12(b) along the path shown in Fig. (a). In a second step, we optimized the parameter λ with the analytic expressions for the SOC matrix elements introduced in Section 4.3 so that the energy bands of $\mathcal{H}_{\text{hop}} + \mathcal{H}_{\text{SOC}}$ matched the relativistic DFT band structure considering the full crystal. Within the optimization procedure, we found the following SOC constant:

$$\lambda = 88.7\,\text{meV}, \tag{4.70}$$

leading to a good agreement of the band structures from DFT+SOC with TB+SOC, shown in Fig. 4.12(c). For comparison, the spin-orbit coupling strength was measured for a neutral Mo atom, in contrast to the Mo^{5+} ion, and was determined to be similar with $\lambda_{\text{exp}} = 678\,\text{cm}^{-1} = 84.1\,\text{meV}$ [216].

4.5.3 Effective Anisotropic Spin Hamiltonian for $Lu_2Mo_2O_5N_2$

Next, we followed the strategy to determine the effective spin Hamiltonian introduced in the previous section, for the compound $Lu_2Mo_2O_5N_2$. The nearest-neighbour bilinear spin Hamiltonian including anisotropic exchange parameters

$$\mathcal{H} = \sum_{\langle ij \rangle} J_{ij}\mathbf{S}_i \cdot \mathbf{S}_j + \mathbf{D}_{ij} \cdot (\mathbf{S}_i \times \mathbf{S}_j) + \mathbf{S}_i \cdot \Gamma_{ij} \cdot \mathbf{S}_j \tag{4.71}$$

follows from diagonalization of the full extended Hubbard Hamiltonian on clusters of two sites, five d-orbitals and two spin degrees of freedom with projection onto the low-energy subspace, consisting of four states. With the Abrikosov pseudo-fermion representation this low-energy Hamiltonian can be mapped,

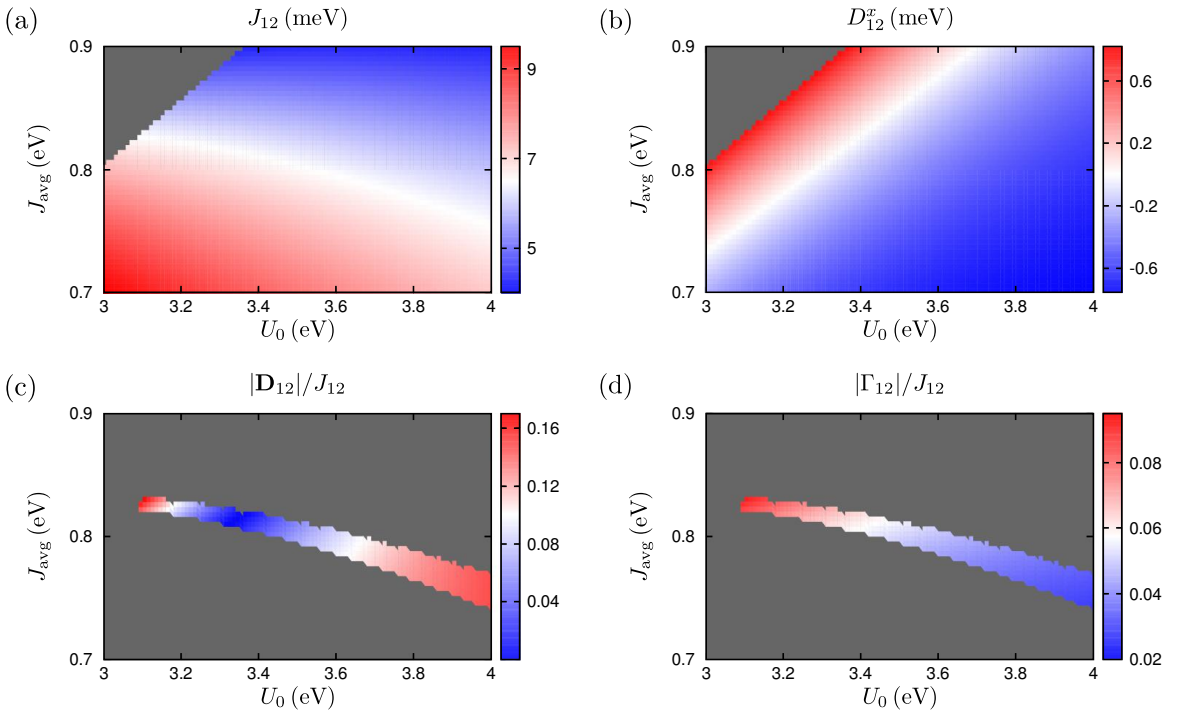

Figure 4.13: Magnetic parameters for $Lu_2Mo_2O_5N_2$ on bond 1-2 within a range of parameters U_0 and J_{avg}. (a) Heisenberg exchange, (b) x component of the DM vector. Relative results in the parameter range leading to $J_{12} = 6.5 \pm 0.2\,\text{meV}$ with (c) $|\mathbf{D}_{12}|/J_{12}$ and (d) $||\Gamma_{12}||/J_{12}$.

after Löwdin orthonormalization, onto an effective spin Hamiltonian. The only model parameters of this approach are U_0 and J_{avg}.

The total energy calculations by Harald O. Jeschke determined a spin Hamiltonian considering isotropic Heisenberg contributions up to third nearest neighbours. For the calculation of the anisotropic contributions to the nearest-neighbour bilinear spin Hamiltonian, we focused on model parameters U_0 and J_{avg} which reproduce the nearest neighbour Heisenberg exchange suggested by the total energy calculations $J_1 = 75\,\text{K} = 6.5\,\text{meV}$.

In Fig. 4.13(a) we show the computed bilinear nearest-neighbour Heisenberg exchange, with the *ab-initio* parameters given in Table 4.4 and by Eq. (4.70) for $Lu_2Mo_2O_5N_2$ in a range of parameters U_0 and J_{avg}, on a bond 1-2 as defined in Fig. 4.2(b). For U_0 we focused on the same range as successfully employed in case of $Lu_2V_2O_7$, while we considered an even wider range for possible Hund's coupling interactions. Unfortunately, the dependence of the Heisenberg exchange on the model parameters is in the case of $Lu_2Mo_2O_5N_2$ far from monotonic. Compared to the DM interaction, shown in Fig. 4.13(b), the dependence differs significantly. Therefore, a parameter set leading to the experimentally expected Heisenberg exchange matches a wide range of DM interaction parameters. To illustrate this effect, we show in Fig. 4.13(c) the ratio $|\mathbf{D}_{12}|/J_{12}$ only for parameter combinations which lead to the expected Heisenberg exchange in the window $J_{12} = 6.5 \pm 0.2\,\text{meV}$. This corresponds to possible ratios of $|\mathbf{D}_{12}|/J_{12}$ between 0% and 18%. Moreover, the high ratio regions appear in relatively low as well as relatively high regions of a Hubbard repulsion U_0. Therefore, it is not insightful to choose a specific parameter set as we did in the case of $Lu_2V_2O_7$ to propose a possible spin Hamiltonian for $Lu_2Mo_2O_5N_2$. Instead, the method employed for this compound rather offers some upper limit for possible DM interactions relative to the Heisenberg exchange.

In the case of the pseudo-dipolar tensor, the possible ratios $||\Gamma_{12}||/J_{12}$ are not as drastically as it is the case for the DM interaction, with ratios between 2% and 9% and a more straightforward behaviour with scaling the model parameters. Due to the stronger spin-orbit coupling parameter $\lambda = 88.7\,\text{meV}$, the influence of the pseudo-dipolar tensor becomes en par more pronounced.

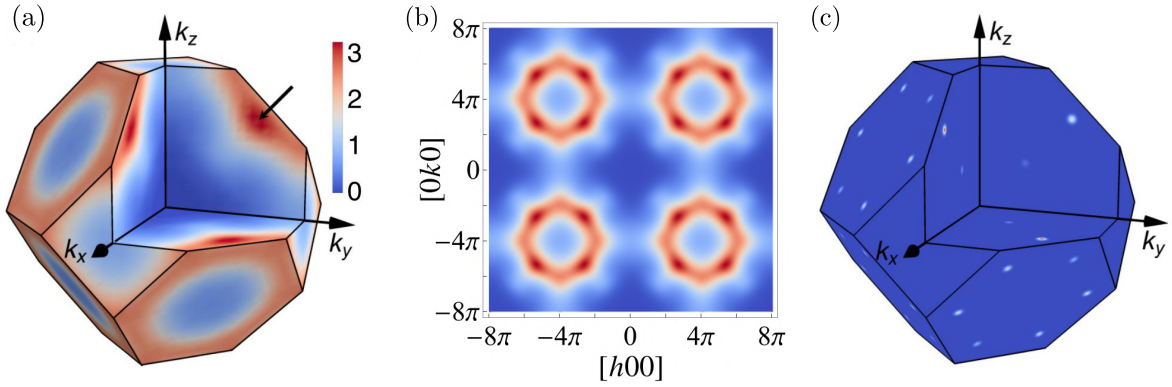

Figure 4.14: Spectral weight from PFFRG and classical energy minization calculations performed by Yasir Iqbal and depicted from Ref. [80]. (a) PFFRG spectral weight in the Brillouin zone of $Lu_2Mo_2O_5N_2$. (b) PFFRG "gearwheel" signatures in the spectral weight in a 2D cut in the $[hk0]$ plane. (c) Classical spectral weight in the Brillouin zone of the pyrochlore structure. Fig. adapted from Ref. [80].

4.5.4 Discussion of $Lu_2Mo_2O_5N_2$ spin Hamiltonian

In the search for quantum spin liquid candidates, a commonly accepted approach is to consider materials with a Hamiltonian $\mathcal{H}_0 + \mathcal{H}'$, where $\mathcal{H}_0$ is known to have a QSL ground state from theory and the hope is that the material specific modification $\mathcal{H}'$ does not alter the magnetic response too strongly. In this context $Lu_2Mo_2O_5N_2$ challenges with the two tasks to (i) identify proper descriptions in terms of $\mathcal{H}_0$ and $\mathcal{H}'$ and to (ii) determine the response of $\mathcal{H}_0$ theoretically. In Ref. [80] the proposal was to consider further neighbour isotropic Heisenberg exchange interactions:

$$\mathcal{H} = J_1 \sum_{\langle i,j\rangle_1} \mathbf{S}_i \cdot \mathbf{S}_j + J_2 \sum_{\langle i,j\rangle_2} \mathbf{S}_i \cdot \mathbf{S}_j + J_{3a} \sum_{\langle i,j\rangle_{3a}} \mathbf{S}_i \cdot \mathbf{S}_j + J_{3b} \sum_{\langle i,j\rangle_{3b}} \mathbf{S}_i \cdot \mathbf{S}_j, \tag{4.72}$$

with $\langle i,j\rangle_{(1,2)}$ indexing nearest neighbour (second nearest neighbour) pairs of sites. There exist two inequivalent third neighbour bonds in the pyrochlore structure, where two magnetic sites are connected with a nearest-neighbour site in-between ($\langle i,j\rangle_{3a}$) or across an empty hexagon ($\langle i,j\rangle_{3b}$). Total energy DFT calculations by Harald O. Jeschke suggested a parameter set with AFM Heisenberg interactions $(J_1, J_2, J_{3a}, J_{3b}) = (74.8, 0.6, 17.2, -5.8)\,\mathrm{K}$. This implies that J_{3a} with 22% of J_1 should be considered as the strongest modification in $Lu_2Mo_2O_5N_2$ compared to a simple nearest-neighbour Heisenberg model. In order to gain intuition about the influence of these modifications, Yasir Iqbal performed PFFRG calculations for the isotropic model and found no magnetic order down to $T^* \approx |\Theta_{\mathrm{CW}}|/100$.

In Fig. 4.14 we show the spectral weight computed with PFFRG in Fig. (a) the whole Brillouin zone and Fig. (b) in a two-dimensional cut in the $[hk0]$ plane. The "gearwheel" pattern of the spectral weight shown in Fig. (b) served as the inspiration for the title in Ref. [80], where $Lu_2Mo_2O_5N_2$ is referred to as a gearwheel QSL candidate. The diffused spectral weight pattern suggests a picture, in which the possible QSL is a molten version of a parent classical magnetic order with the corresponding sharp features. With an iterative minimization of the classical Hamiltonian [217] an incommensurate non-coplanar spiral order was revealed. The corresponding spectral weight in reciprocal space is shown in Fig. 4.14(c). The maxima match the diffused maxima obtained with PFFRG shown in Fig. (a).

An open question is, of course, the influence of the anisotropic spin-spin interactions, which were treated so far as part of the not too influencial $\mathcal{H}'$ contribution to the true Hamiltonian of $Lu_2Mo_2O_5N_2$. Currently, a PFFRG treatment of anisotropic contributions like the Dzyaloshinskii-Moriya interaction is computationally expensive [218]. Therefore, the only possible treatment at the moment is a classical optimization calculation at $T = 0$. It showed that a DM interaction between 8% and 10% would not significantly alter the nature of the classical parent state. In the picture of the QSL being the molten version of the classical state this would imply a weak influence of the DM interaction. However, to ensure

the persistence of a QSL ground state in the spin 1/2 material, a quantum mechanical treatment should be pursued in future studies. In addition, it remains to be determined whether the DM interaction is indeed smaller than 10% of the strongest Heisenberg interaction. On the other hand, tackling issues like the O/N randomness and current deficiency in the available powder samples are probably of higher priority. However, the results presented in Ref. [80] hint strongly that it is worth the effort to continue investigating $Lu_2Mo_2O_5N_2$ experimentally and theoretically.

4.6 Discussion

In this chapter, we detailed the hybrid method to determine the bilinear spin 1/2 Hamiltonian including anisotropic contributions on small clusters in the pyrochlore structure.

In this approach, spin-orbit coupling effects of the *d*-block orbitals are treated exactly, up to "infinite order". In this sense, the spin and orbital angular momenta are mixed in the low energy eigenstates. Since we considered the full extended Hubbard Hamiltonian up to this point of the calculation, the choice of the basis states does *not* influence the physical properties of the system. The crucial point is the projection onto the low-energy subspace. In both investigated materials, $Lu_2V_2O_7$ in Section 4.4 and $Lu_2Mo_2O_5N_2$ in Section 4.5, spin-orbit coupling is small compared to the Hubbard repulsion. Hence, a projection onto a basis that consists almost only of the spin operators of the lowest orbital is justified. Since the basis is not orthonormal if the contributions from the other states are naively thrown away, we employed a symmetric orthonormalization procedure. This preserved the determined eigenenergies of the full system. In that sense the resulting spin operators describe a pseudo-spin operator. In the end what we called S_{i,z^2}, with d_{z^2} being the lowest orbital, was a low energy pseudo-spin operator that has maximal overlap with the true S_{i,z^2} operator. Since we considered the full Hubbard Hamiltonian in the diagonalization procedure and preserved the eigenvalues in the orthonormalization step, the resulting effective Hamiltonian still gives the true, exact, eigenvalues of the full Hamiltonian up to two sites.

In comparison, in perturbation theory as introduced in Chapter 1, the effective Hamiltonian is projected onto the eigenstates of $\mathcal{H}_0$. In this case it is important to distinguish which terms are treated perturbatively and which are treated exactly. This problem is not present in the exact diagonalization approach. However, since spin-orbit coupling is small in the two investigated materials, the error introduced by projecting on the single occupied lowest orbital states was small. In Section 4.4 we compared results from perturbation theory to the exact diagonalization and found a good agreement for large Hubbard repulsion $U_0 \approx 10\,\mathrm{eV}$.

In Section 4.4 we applied this procedure to the pyrochlore ferromagnet $Lu_2V_2O_7$ and summarized the findings published in Ref. [79]. In this case the advantage to restrict the spin Hamiltonian to quantum mechanically allowed terms is strongly emphasized due to the controversy about a finite single-ion anisotropy raised by Xiang *et al.* [195]. A full resolution to all allowed terms in the nearest-neighbour bilinear spin 1/2 Hamiltonian was demonstrated. Especially the non-negligible contribution of the pseudo-dipolar tensor was an aspect not addressed by other methods discussing this compound before. On the other hand, discrepancies with results from inelastic neutron scattering [196] and transport data [187] could not be fully resolved. Further calculations taking higher-order terms including further neighbour Heisenberg exchange and anisotropic contributions, maybe even beyond bilinear terms, might therefore be helpful to understand the underlying mechanisms in this compound better.

In Section 4.5 we then used the procedure in the context of the QSL candidate $Lu_2Mo_2O_5N_2$. While in this chapter we concentrated on the estimation of the anisotropic contributions to the bilinear spin 1/2 Hamiltonian, in Ref. [80] the focus was the analysis of the isotropic Hamiltonian. In order to judge how well this approximation is justified, a knowledge about the anisotropic terms is indispensable. We found that it is unfortunately difficult to pinpoint a specific parameter set that is suitable to describe the material and we could only suggest the range for the DM interaction, to be between 0% and 18% of the main Heisenberg exchange J_1. This includes the QSL region for a clean parent compound suggested by PFFRG calculations. However, further calculations, taking the O/N disorder more careful into account and with respect to higher order terms are certainly necessary to give a detailed insight into the low-energy physics of this material. The goal to motivate further investigations and to demonstrate the need to synthesize clean single crystals on the other hand was certainly achieved.

Chapter 5

Magnetic excitations in the honeycomb Kitaev material α-$RuCl_3$

Stephen M. Winter, **Kira Riedl**, Pavel A. Maksimov, Alexander L. Chernyshev, Andreas Honecker, and Roser Valentí,
Breakdown of Magnons in a Strongly Spin-Orbital Coupled Magnet,
Nat. Commun. **8**, 1152 (2017)
[81]

5.1 Introduction

The last geometry discussed in this thesis is the honeycomb structure, a two-dimensional lattice which is, among others, famous for hosting an exactly solvable spin model with a QSL ground state. In 2006, Kitaev published a seminal paper [6], in which he introduced the honeycomb Kitaev model that consists of bond-dependent Ising interactions, shown in Fig. 5.1, between spin 1/2 particles on the honeycomb lattice. In this paper, he demonstrated the exact solution of the model in terms of the Majorana fermion formalism. While an exactly solvable spin-liquid model in two dimensions is already exciting itself, additional attention was sparked in 2009, when Jackeli and Khaliullin [219] proposed a possible realization of the Kitaev model in real materials. The authors discussed a mechanism for materials that are structured in the honeycomb lattice, with edge-sharing octahedra surrounding heavy transition metal ions, resulting in the pure Kitaev honeycomb model. Since then, extensive research has been devoted to the Kitaev model and its extensions [220–223]. In real materials, the most prominent two-dimensional Kitaev compounds are α-$RuCl_3$, Na_2IrO_3, and α-Li_2IrO_3 [43, 44, 224–230]. However, to date all of the Kitaev candidate materials order magnetically at low temperatures, dismissing the option to be a realization of a perfect Kitaev spin-liquid (KSL). In this situation, the enigma to solve is how far away are the realized materials from the pure KSL limit and which parameters could be tuned to design materials in the Kitaev spin-liquid regime.

The Kitaev candidate materials mentioned above are Mott insulators, which order in an antiferromagnetic zigzag order in the case of Na_2IrO_3 [43, 44] and α-$RuCl_3$ [46, 231, 232] and in an incommensurate phase in the case of α-Li_2IrO_3 [233, 234]. The magnetic order is a consequence of additional magnetic interactions next to the Kitaev exchange. Several *ab-initio* studies have investigated the effective spin Hamiltonian for these materials [224–229]. Among them, Winter *et al.* [224] applied the hybrid method, used in Chapter 2 and Chapter 4, and identified for Na_2IrO_3, in addition to the Kitaev interaction, a significant contribution from nearest and third nearest neighbour antiferromagnetic Heisenberg exchange. In the case of α-Li_2IrO_3, the authors found significant second neighbour interactions including a non-negligible Dzyaloshinskii-Moriya exchange.

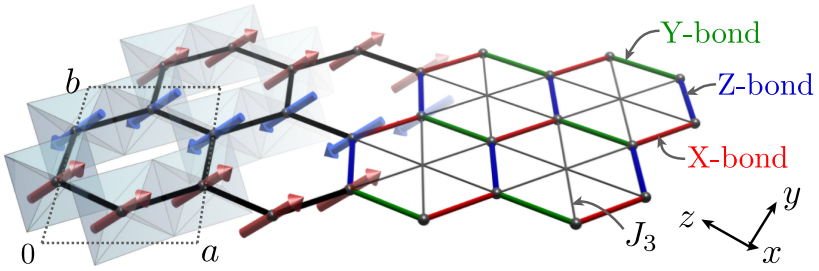

Figure 5.1: 2D honeycomb layer in α-$RuCl_3$, with the edge-sharing Cl octahedra surrounding the magnetic Ru ions, which order in the illustrated antiferromagnetic zigzag order as illustrated, in low temperatures on the left side. On the right side we illustrate the definition of the underlying magnetic model Hamiltonian with respect to the inequivalent bonds. Fig. reprinted from Ref. [81].

The iridate compounds consist of heavier magnetic ions than α-$RuCl_3$, consequently they are subject to stronger spin-orbit coupling and expected to have a more pronounced Kitaev interaction. However, the neutron absorption rate of iridium in inelastic neutron scattering (INS) experiments is very strong, so that such experiments are extremelly challenging [44, 231]. This eliminates one of the most powerful experimental tools to investigate magnetic interactions in real materials for the iridate samples. In contrast, in the case of α-$RuCl_3$, INS experiments are not significantly hampered by the absorption rate [46, 47, 231], which allows systematic experimental studies of the magnetic interactions. With available experimental data to compare to, we chose α-$RuCl_3$ as the subject of our theoretical investigation in this chapter, as a representative case of the Kitaev candidate materials. In Fig. 5.1, we illustrate one 2D honeycomb layer of α-$RuCl_3$, including the antiferromagnetic zigzag order, observed below $T_N = 7\,K$ [46, 231, 232]. In this chapter, we will specifically address the inelastic neutron scattering (INS) measurements [46, 231], which revealed a continuum of excitations that was interpreted in terms of fractionalized excitations due to proximity to the Kitaev spin-liquid state.

In order to provide a context for this interpretation, we will first discuss briefly, in Section 5.2, the exact solution of the "pure" Kitaev honeycomb model and its possible realization in real materials. Then, in Section 5.3, we establish the framework of extended Kitaev models, including the expected additional magnetic interactions, *ab-initio* predictions for α-$RuCl_3$ from the literature, and the corresponding phase diagram. In Section 5.4, we review the key experimental features observed in INS experiments, which should be reproduced by the appropriate model Hamiltonian for α-$RuCl_3$. Then, in Section 5.5, we introduce the method of exact diagonalization for correlations functions, which we apply in Section 5.6 to the specific case of α-$RuCl_3$. This section is devoted to the resolution of the nature of the excitation continuum observed in α-$RuCl_3$. In order to achieve that, we first predicted theoretically INS intensities for a series of model Hamiltonians and compared the results to the key experimental features. This allowed us to determine the most appropriate spin Hamiltonian for α-$RuCl_3$, which was controversially discussed before [224–227]. Based on that Hamiltonian, we then proposed magnon-decay processes in the case of strong anisotropic bond-dependent interactions and the absence of certain symmetries as the reason for excitation continua, which are conventionally interpreted as a signature of QSL's.

The results presented in this chapter are published in Ref. [81].

5.2 The honeycomb Kitaev model

5.2.1 Exact solution of the honeycomb Kitaev model

In 2006, Alexei Kitaev published the exact solution for a spin 1/2 quantum compass model, on the honeycomb lattice, which carries nowadays his name [6]. In such models, the interactions along a bond are anisotropic and depend on the orientation of the bond. Kitaev wrote in the article that he was originally interested in anyonic systems that provide a realization of quantum memory protected

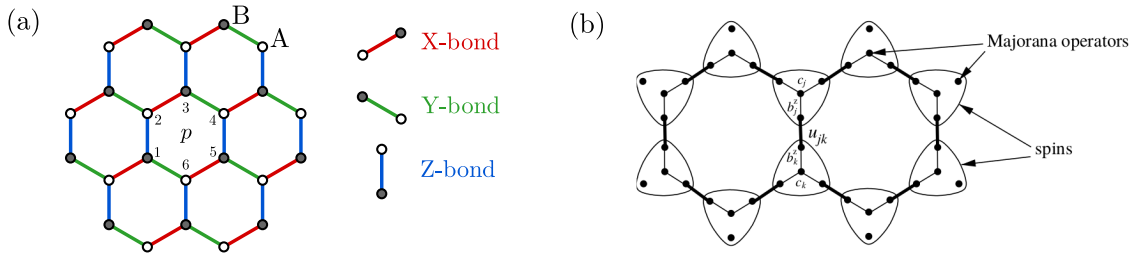

Figure 5.2: (a) Honeycomb lattice with the different bond types illustrated in red, green, and blue. The sublattices are labelled with A and B and one six-site plaquette is indicated by p. (b) Effective representation of the spins in terms of Majorana operators introduced by Kitaev [6]. Fig. (b) reprinted from Ref. [6].

from decoherence. This is not the case in the Kitaev honeycomb model, which was in this sense a disappointment. In contrast, the reaction of the community of quantum spin-liquid models was very different. The quasiparticles in this model may be characterized as fermions and $\mathbb{Z}_2$ vortices, with that the Kitaev model is one of the rare examples of an exactly solvable system, in more than one dimension, that hosts a quantum spin liquid ground state. In this section, we briefly sketch the exact solution as presented in Ref. [6], a more detailed derivation can be found, for example, in Ref. [235].

The Kitaev model lives on the honeycomb lattice, illustrated in Fig. 5.2(a), and its corresponding Hamiltonian is given by the following expression:

$$\mathcal{H} = -J_x \sum_{\text{X-bonds}} \sigma_j^x \sigma_k^x - J_y \sum_{\text{Y-bonds}} \sigma_j^y \sigma_k^y - J_z \sum_{\text{Z-bonds}} \sigma_j^z \sigma_k^z, \tag{5.1}$$

where σ are the spin 1/2 Pauli matrices. Hence, it can be described as a bond-dependent Ising model, where the component of the Ising interaction depends on the bond type of the honeycomb lattice. Since it is classically not possible to minimize all bond interactions with the same configuration, this is a frustrated system according to the definition introduced in Chapter 1. Below, we use the following, abbreviated notation:

$$\mathcal{H} = -\sum_{jk} J_\alpha \sigma_j^\alpha \sigma_k^\alpha, \tag{5.2}$$

where we omitted the indices in $\alpha = \alpha_{jk}$ for clarity, and defined $\alpha_{jk} = x$ if the sites j and k are connected by an X-bond, $\alpha_{jk} = y$ for a Y-bond, and $\alpha_{jk} = z$ for a Z-bond.

Hilbert space reduction with plaquette operator

One important ingredient to solve the honeycomb Kitaev model in Eq. (5.1) is the so-called plaquette operator $\hat{W}_p$:

$$\hat{W}_p = (\sigma_1^z \sigma_2^z)(\sigma_2^x \sigma_3^x)(\sigma_3^y \sigma_4^y)(\sigma_4^z \sigma_5^z)(\sigma_5^x \sigma_6^x)(\sigma_6^y \sigma_1^y), \tag{5.3}$$

which connects the spin 1/2 particles around a six-site plaquette as defined in Fig. 5.2(a). With the property of the Pauli matrices $\sigma^\alpha \sigma^\beta = i\varepsilon_{\alpha\beta\gamma}\sigma^\gamma$, the plaquette operator can be simplified to the following expression:

$$\hat{W}_p = \sigma_1^x \sigma_2^y \sigma_3^z \sigma_4^x \sigma_5^y \sigma_6^z. \tag{5.4}$$

This operator commutes with the Hamiltonian Eq. (5.1), and plaquette operators on other plaquettes, hence it corresponds in this model to a constant of motion. Its eigenvalues are $w_p = \pm 1$, which follow directly from the property $\hat{W}_p^2 = 1$. With two degrees of freedom, these are $\mathbb{Z}_2$ operators, commonly

called flux operators due to the connection of the spins in one plaquette. Here, we follow the convention that a plaquette with $w_p = +1$ is called flux free, while $w_p = -1$ indicates a finite flux.

Since the plaquette operator commutes with the Hamiltonian, the Hilbert space $\mathcal{L}$ is block diagonal in the eigenspace of the plaquette operator $\hat{W}_p$:

$$\mathcal{L} = \bigoplus_{w_1,\dots,w_m} \mathcal{L}_{w_1,\dots w_m}, \tag{5.5}$$

where w_i is the eigenvalue of the plaquette operator on the i^{th} plaquette, and m is the number of plaquettes. Therefore, the Hilbert space can be divided into sectors according to each plaquette, which reduces the Hilbert space from 2^N dimensions for a spin 1/2 system to $2^{N/2}$ dimensions, since the honeycomb lattice contains 1/2 plaquette per site.

Expression in terms of free Majorana fermions

Next, we transform the model into a basis in terms of Majorana fermions, which are particles that fulfill the fermion anticommutation relations and are their own antiparticle, $c^\dagger = c$. The strategy to transform a spin system to a fermionic representation and gain an approximate solution in a mean-field fashion is not unusual [5]. The exciting property of the honeycomb Kitaev model is, however, that the mean-field solution turns out to be exact.

Kitaev labelled the Majorana operators he introduced as b^x, b^y, b^z, and c, see also Fig. 5.2(b). These Majorana operators act on the four-dimensional Fock space $\tilde{\mathcal{M}}$ at each site, while a spin operator lives in the two-dimensional subspace $\mathcal{M} \subset \tilde{\mathcal{M}}$. Hence, it is crucial to restrict the solution to the physically relevant solutions of the subspace $\mathcal{M}$. In the extended space, it is possible to express the spin operators as follows:

$$\tilde{\sigma}^x = ib^x c, \qquad \tilde{\sigma}^y = ib^y c, \qquad \tilde{\sigma}^z = ib^z c, \tag{5.6}$$

where the "charge" and the "bond" character are carried by different Majorana particles. This transformation can be directly used to express the original Hamiltonian, given by Eq. (5.2), in the enlarged Hilbert space:

$$\mathcal{H} = -\sum_{jk} J_\alpha (ib_j^\alpha c_j)(ib_k^\alpha c_k). \tag{5.7}$$

With the bond operator $\hat{u}_{jk} = ib_j^\alpha b_k^\alpha$, the Hamiltonian can be further simplified:

$$\mathcal{H} = i\sum_{jk} J_\alpha \hat{u}_{jk} c_j c_k. \tag{5.8}$$

The bond operators $\hat{u}_{jk} = ib_j^\alpha b_k^\alpha$ commute with the Hamiltonian and with each other, so that the (extended) Hilbert space is also block diagonal in the eigenspace of $\hat{u}_{jk}$:

$$\tilde{\mathcal{L}} = \bigoplus_u \tilde{\mathcal{L}}_u, \tag{5.9}$$

where u stands for the collection of all $\hat{u}_{jk}$. The corresponding eigenvalues of the bond operator are $u_{jk} = \pm 1$. The restriction to the subspace with respect to the bond eigenvalues is obtained by the replacement of the bond operator with a number ± 1. This corresponds to a mean-field ansatz, which is in this case exact, since the bond operator commutes with the Hamiltonian. The resulting Hamiltonian,

$$\mathcal{H} = i\sum_{jk} J_\alpha \langle \hat{u}_{jk} \rangle c_j c_k, \tag{5.10}$$

has the form of a free fermion problem and is hence exactly solvable. For a given configuration of $\langle \hat{u}_{ij} \rangle$ this quadratic Hamiltonian can be exactly solved, defining the states in this system together with the "matter" fermions c_i completely. Note, that not all configurations of $\langle \hat{u}_{ij} \rangle$ correspond to physically distinct states, due to the enlarged Hilbert space.

Exact solution with Lieb theorem

Based on this insight, Kitaev proposed to interpret the operators $\hat{u}_{jk}$ as a $\mathbb{Z}_2$ gauge field and the number w_p as a magnetic flux through the plaquette p. In this convention, he proposed to think of $w_p = -1$ as the plaquette carrying a flux, while $w_p = 1$ for all plaquettes corresponds to the flux free state. According to the Lieb theorem [236], the energy minimum of Eq. (5.10) corresponds to the vortex-free field configuration with $w_p = 1$ for all plaquettes p. One gauge option to ensure that this is fulfilled, is to choose $\langle \hat{u}_{jk} \rangle = 1$ for all bonds. This relationship is fulfilled, since the plaquette operator, starting from Eq. (5.3) can be expressed, with the definition of the spin operators in Eq. (5.6), as follows (compare Fig. 5.2(a)):

$$\hat{W}_p = \hat{u}_{21}\hat{u}_{23}\hat{u}_{43}\hat{u}_{45}\hat{u}_{65}\hat{u}_{61}, \tag{5.11}$$

where we followed Kitaev's convention to express the bond operators with the "even" sublattice sites first, in order to avoid ambiguity in the signs.

With the configuration $\langle \hat{u}_{jk} \rangle = 1$ for all bonds, the Hamiltonian in Eq. (5.10) can be simplified to the following expression:

$$\mathcal{H} = i \sum_{\langle ij \rangle_x} J_x c_i c_j + i \sum_{\langle ij \rangle_y} J_y c_i c_j + i \sum_{\langle ij \rangle_z} J_z c_i c_j. \tag{5.12}$$

This field configuration introduced translational symmetry into the system, allowing for a Fourier transformation equivalent to the graphene honeycomb tight-binding case, sketched in Appendix C:

$$c_{\tau u} = \frac{1}{\sqrt{N}} \sum_{\mathbf{k}} \mathrm{e}^{-i\mathbf{k}\cdot\mathbf{r}_u} c_{\tau\mathbf{k}}, \tag{5.13}$$

where $\tau = \{\mathrm{A}, \mathrm{B}\}$ is the sublattice index in Fig. 5.2(a) and u indexes the unit cell. The Hamiltonian in reciprocal space can then be expressed as follows:

$$\mathcal{H} = \sum_{\mathbf{k}} \begin{pmatrix} c_{A,-\mathbf{k}} & c_{B,-\mathbf{k}} \end{pmatrix} \begin{pmatrix} 0 & if(\mathbf{k}) \\ -if^*(\mathbf{k}) & 0 \end{pmatrix} \begin{pmatrix} c_{A,\mathbf{k}} \\ c_{B,\mathbf{k}} \end{pmatrix}, \tag{5.14}$$

with $f(\mathbf{k}) = J_z + J_x \, \mathrm{e}^{i\mathbf{k}\cdot\mathbf{n}_1} + J_y \, \mathrm{e}^{i\mathbf{k}\cdot\mathbf{n}_2}$, with the two lattice vectors of the honeycomb unit cell $\mathbf{n}_{1/2}$, and where we used the property of Majorana fermions $c^\dagger_{\tau,\mathbf{k}} = c_{\tau,-\mathbf{k}}$. This Hamiltonian has the eigenvalues $\varepsilon_{1/2}(\mathbf{k}) = \pm|f(\mathbf{k})|$ with the following quasiparticles:

$$\alpha_{\mathbf{k}} = \frac{1}{\sqrt{2}}\left(i\frac{f(\mathbf{k})}{|f(\mathbf{k})|}c_{A,\mathbf{k}} + c_{B,\mathbf{k}}\right) \qquad \text{and} \qquad \beta_{\mathbf{k}} = \frac{1}{\sqrt{2}}\left(-i\frac{f(\mathbf{k})}{|f(\mathbf{k})|}c_{A,\mathbf{k}} + c_{B,\mathbf{k}}\right). \tag{5.15}$$

The excitations of the pure Kitaev system can therefore be expressed in terms of linear combinations of Majorana fermions. With respect to the spin basis, these excitations are fractionalized quasiparticles and hence fulfill a defining criterion for a quantum spin liquid, as discussed in Chapter 1. Moreover, from the analogy to the tight-binding Hamilonian for the honeycomb material graphene, it is immediately clear, that at least for $J_x = J_y = J_z$ the spectrum is gapless, with a Dirac point at the high symmetry K-point in reciprocal space[1]. As Knolle pointed out [235], for increasing anisotropy of the exchange constants, the Dirac points move in the Brillouin zone until they merge and annihilate for $|J_z| > |J_x| + |J_y|$ and permutations. In that phase, the Kitaev model is gapped.

5.2.2 Kitaev interaction in real materials

The pure Kitaev model arises from the general spin 1/2 Hamiltonian, given by the following expression:

$$\mathcal{H}_{\text{spin}} = \sum_{ij} \left[J_{ij}\mathbf{S}_i \cdot \mathbf{S}_j + \mathbf{D}_{ij} \cdot (\mathbf{S}_i \times \mathbf{S}_j) + \mathbf{S}_i \cdot \Gamma_{ij} \cdot \mathbf{S}_j) \right], \tag{5.16}$$

[1] For a definition of the K-point for specific unit vectors on the honeycomb lattice and a discussion of the tight binding solution for nearest neighbour hopping on the honeycomb lattice, see Appendix C.

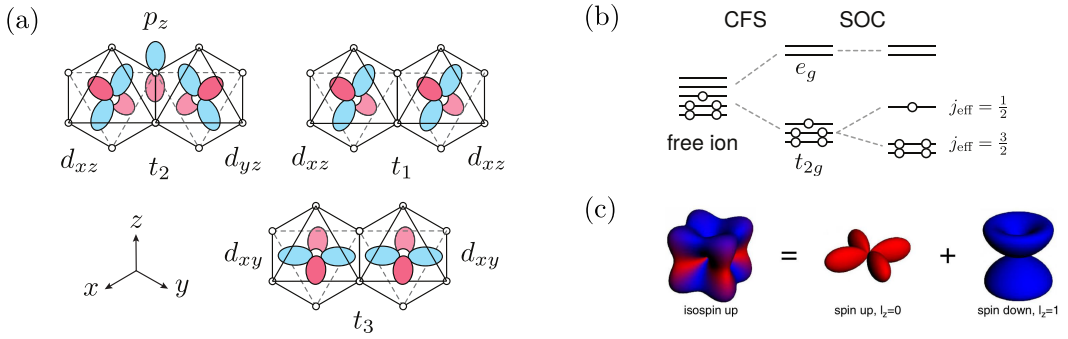

Figure 5.3: (a) Indirect and direct hopping integrals for a perfect octahedral environment along the Z-bond. Positive phases are illustrated in red, negative phases in blue. For a 3D illustration of the local coordinate system see also Fig. 5.4. t_2 represents the metal-ligand-metal hopping considered in Ref. [219]. In real materials direct metal-metal hoppings of nature t_1 and t_3 contribute as well. For distorted octahedra there is an additional t_4, not shown here. (b) Splitting of d^5 orbitals due to octahedral environment (crystal field splitting "CFS") into e_g and t_{2g} orbitals and in the limit of strong spin-orbit coupling into $j_{\text{eff}} = 1/2$ and $j_{\text{eff}} = 3/2$ levels. (c) Isospin in the limit of strong spin-orbit coupling as a linear combiation of spin and orbital degrees of freedom, captured in the j_{eff} basis. Fig. (a,b) reprinted from Ref. [222], Fig. (c) reprinted from Ref. [219].

in the limit of a vanishing Heisenberg interaction $J_{ij} = 0$, no DM interaction $|\mathbf{D}_{ij}| = 0$, and a finite, bond-dependent contribution of one component of the pseudo-dipolar tensor Γ_{ij}. For example, for the Z-bond defined in Fig. 5.2(a), the pseudo-dipolar contribution in the diagonal z component corresponds to the Kitaev interaction, $K_1 = \Gamma_{zz}$. How such a model can be achieved in real materials, was proposed by Jackeli and Khaliullin in 2009 [219]. Here, we summarize the main features of this mechanism, following, among others, explanations provided in Ref. [221, 222].

The starting point for such a mechanism are Mott insulators in the strong spin-orbit coupling limit with transition metal ions such as Ir, Os, Rh, or Ru. In the case of d^5 magnetic ions in a perfect environment of edge-sharing octahedra of ligand atoms, hopping mechanisms including metal-ligand-metal and direct metal-metal paths are present[2]. In Fig. 5.3(a) such hopping mechanisms are illustrated for the case of edge-sharing octahedra. Note, that in Ref. [219] the only considered hopping path is the indirect metal-ligand-metal path, labelled as t_2. The octahedral ligand environment causes a crystal field splitting (CFS) into t_{2g} and e_g orbitals, illustrated in Fig. 5.3(b). In the following, we assume that the e_g levels are high enough in energy to neglect their contribution to the low-energy description. However, one should keep in mind that this is an approximation.

Possible hopping paths between $\{d_{xy}, d_{yz}, d_{xz}\} \in t_{2g}$ metal orbitals and $\{p_x, p_y, p_z\} \in p$ ligand orbitals, such as t_2, are restricted strongly by symmetry. A perfect octahedral environment implies an angle $\theta = 90°$ of the metal-ligand bonds adjacent to each other. According to Slater-Koster integrals, see e.g. Ref. [57], the overlap between p and d orbitals, with the bond direction $\hat{b}$, is restricted by symmetry as follows:

$\hat{b} = \hat{x}$	$\lvert d_{xy}\rangle$	$\lvert d_{yz}\rangle$	$\lvert d_{xz}\rangle$
$\langle p_x\rvert$	0	0	0
$\langle p_y\rvert$	$V_{dp\pi}$	0	0
$\langle p_z\rvert$	0	$V_{dp\pi}$	0

and

$\hat{b} = \hat{y}$	$\lvert d_{xy}\rangle$	$\lvert d_{yz}\rangle$	$\lvert d_{xz}\rangle$
$\langle p_x\rvert$	$V_{dp\pi}$	0	0
$\langle p_y\rvert$	0	0	0
$\langle p_z\rvert$	0	0	$V_{dp\pi}$

. (5.17)

Here, $V_{dp\pi}$ reflects that the formed bond of the d and p orbitals includes one shared nodal plane of the original orbitals to which the bond axis belongs, referred to as a π-bond.

[2]Note, that the α polytype of $RuCl_3$ consists of such (distorted) edge-sharing octahedra in stacked honeycomb layers, while the β polytype consists of face-sharing $RuCl_6$ octahedra arranged in chains [237].

The effective spin exchange Hamiltonian can then be determined, for example, by perturbation theory. In order to obtain a dominant Kitaev type interaction, the usually dominant isotropic Heisenberg interaction has to be suppressed. Here, we demonstrate that this is the case in the framework of second-order perturbation theory. In the limit of strong spin-orbit coupling, the SOC contribution is considered as part of $\mathcal{H}_0$, and the perturbation, in the d orbital picture, stems solely from the real hopping $\mathcal{H}_1 = \sum_{\langle ij\rangle}\sum_{\alpha\beta}\sum_{\sigma} t_{i\alpha,j\beta} c^{\dagger}_{i\alpha\sigma} c_{j\beta\sigma}$+H.c., where α, β are the orbital indices and we consider only hopping over nearest neighbour sites $\langle ij\rangle$. Since spin-orbit coupling is not considered in the perturbation, the spin is preserved during hopping processes. For a Z-bond, the plaquette including the ligand is in the xy plane for the edge-sharing geometry. In this case, the only finite hopping processes according to Eq. (5.17) are $d_{yz} \rightarrow p_z \rightarrow d_{xz}$ along the upper path of the plaquette (see t_2 in Fig. 5.3(a)), and along the lower path $d_{xz} \rightarrow p_z \rightarrow d_{yz}$. In both cases the hopping process obtains in total a negative phase.

Since we work in the framework of perturbation theory, a description in a basis that can capture the nature of the ground state correctly is essential. This is in contrast to the hybrid method, applied in Chapters 2 and 4, to determine the effective spin model for triangular lattice organics and pyrochlores. A proper basis in the strong spin-orbit coupling limit is given by the eigenbasis of the SOC matrix, the so-called j_{eff} basis. This approach was applied, for example, in Ref. [224]. Note, however, that in Ref. [219, 221] the perturbation theory was considered in the d-orbital basis. This is an approximation, due to the singly occupancy the main properties of the ground state might however still be captured. The j_{eff} states are in this case linear combinations of d orbitals and spin 1/2 states, which can be derived directly from Clebsch-Gordon coefficients:

$$|j_{1/2}\rangle = \begin{cases} \frac{1}{\sqrt{3}}(-|xy,\uparrow\rangle - i|xz,\downarrow\rangle - |yz,\downarrow\rangle) & (m_j = +\frac{1}{2}) \\ \frac{1}{\sqrt{3}}(+|xy,\downarrow\rangle + i|xz,\uparrow\rangle - |yz,\uparrow\rangle) & (m_j = -\frac{1}{2}) \end{cases} \tag{5.18}$$

$$|j_{3/2}\rangle = \begin{cases} \frac{1}{\sqrt{2}}(\quad\quad - i|xz,\uparrow\rangle - |yz,\uparrow\rangle) & (m_j = +\frac{3}{2}) \\ \frac{1}{\sqrt{6}}(2|xy,\uparrow\rangle - i|xz,\downarrow\rangle - |yz,\downarrow\rangle) & (m_j = +\frac{1}{2}) \\ \frac{1}{\sqrt{6}}(2|xy,\downarrow\rangle - i|xz,\uparrow\rangle + |yz,\uparrow\rangle) & (m_j = -\frac{1}{2}) \\ \frac{1}{\sqrt{2}}(\quad\quad - i|xz,\downarrow\rangle + |yz,\downarrow\rangle) & (m_j = -\frac{3}{2}) \end{cases} \tag{5.19}$$

In the hole picture, and with sufficient on-site correlation, the ground state consists of singly occupied $j_{1/2}$ states, illustrated in Fig. 5.3(b). In the following, we express the $|j_{1/2}\rangle$ states with $|\Uparrow\rangle$ and $|\Downarrow\rangle$ and the $|j_{3/2}\rangle$ states with $|\pm\frac{3}{2}\rangle$ and $|\pm\frac{1}{2}\rangle$. For the perturbation theory, we consider the hopping as a perturbation and the on-site Coulomb repulsion and the spin-orbit coupling as part of the unperturbed system:

$$\mathcal{H}_0 = \lambda \sum_{i,\alpha\beta} \langle \mathbf{L}\cdot\mathbf{S}\rangle c^{\dagger}_{i\alpha\sigma} c_{i\beta\sigma'} + \mathcal{H}_{\text{int}}, \tag{5.20}$$

$$\mathcal{H}_1 = -t \sum_{\sigma} \left[c^{\dagger}_{i,xz,\sigma} c_{j,yz,\sigma} + c^{\dagger}_{i,yz,\sigma} c_{j,xz,\sigma}\right] + \text{H.c.} \tag{5.21}$$

The explicit expression of the two-particle interaction term for d orbitals is given in Section 4.3 and resembles essentially the effects of on-site Hubbard repulsion and Hund's coupling. The effective Hamiltonian in second order perturbation theory, as discussed in detail in Section 1.2, is given by the product $\mathcal{H}_{\text{eff}} = \mathbb{P}\mathcal{H}_1\mathbb{R}\mathcal{H}_1\mathbb{P}$, where $\mathbb{P}$ projects onto the ground states of the system and $\mathbb{R}$ is the renormalized projector onto the excited states. A direct consequence of the form of the j_{eff} states given by Eq. (5.18) is that in a single-orbital model, here $|j_{1/2}\rangle$, all contributions exactly cancel, as pointed out by Jackeli *et al.* [219]:

$$\langle\Uparrow_i |\mathcal{H}_1| \Uparrow_j\rangle = \frac{1}{3}\big[- i\underbrace{\langle xz\downarrow |\mathcal{H}_1| yz\downarrow\rangle}_{=-t} + i\underbrace{\langle yz\downarrow |\mathcal{H}_1| xz\downarrow\rangle}_{=-t}\big] = 0 \tag{5.22}$$

$$\langle\Downarrow_i |\mathcal{H}_1| \Downarrow_j\rangle = \frac{1}{3}\big[+ i\underbrace{\langle xz\uparrow |\mathcal{H}_1| yz\uparrow\rangle}_{=-t} - i\underbrace{\langle yz\uparrow |\mathcal{H}_1| xz\uparrow\rangle}_{=-t}\big] = 0 \tag{5.23}$$

$$\langle\Uparrow_i |\mathcal{H}_1| \Downarrow_j\rangle = \langle\Downarrow_i |\mathcal{H}_1| \Uparrow_j\rangle = 0. \tag{5.24}$$

The simple mechanism to gain a dominant Heisenberg exchange, like it was demonstrated for the single-orbital case in Section 1.2, is therefore dismissed in this case. This is the first hint, that the Heisenberg exchange looses the commonly dominant role and rises only from higher order processes.

In a multi-orbital picture, including the $|j_{3/2}\rangle$ states, the only non-vanishing matrix elements of $\mathcal{H}_1$ are between the ground states and the $|\pm\frac{3}{2}\rangle$ states:

$$\begin{aligned}\mathcal{H}_{\text{eff}} = \sum_{\langle ij\rangle}\sum_{\sigma_j=\{\Uparrow_j,\Downarrow_j\}} \frac{1}{\mathbb{B}_{\sigma_j}} |\Uparrow_i \sigma_j\rangle \underbrace{\langle\Uparrow_i \sigma_j|\mathcal{H}_1|-\tfrac{3}{2}_i\sigma_j\rangle}_{=-i\sqrt{\frac{3}{2}}t} \underbrace{\langle-\tfrac{3}{2}_i\sigma_j|\mathcal{H}_1|\Uparrow_i \sigma_j\rangle}_{=i\sqrt{\frac{3}{2}}t} \langle\Uparrow_i \sigma_j| \\ + \frac{1}{\mathbb{B}_{\sigma_j}} |\Downarrow_i \sigma_j\rangle \underbrace{\langle\Downarrow_i \sigma_j|\mathcal{H}_1|+\tfrac{3}{2}_i\sigma_j\rangle}_{=-i\sqrt{\frac{3}{2}}t} \underbrace{\langle+\tfrac{3}{2}_i\sigma_j|\mathcal{H}_1|\Downarrow_i \sigma_j\rangle}_{=i\sqrt{\frac{3}{2}}t} \langle\Downarrow_i \sigma_j| \quad + \quad i\leftrightarrow j.\end{aligned} \tag{5.25}$$

Here, $\mathbb{B}_{\sigma_j}$ is a consequence of the normalization of the projection operator onto the excited states $\mathbb{R}$ and depends generally on (λ, U, J_H). For an exact expression including Hund's coupling, see e.g. Ref. [224]. The main effect, however, can already be seen from the expression in the limit of vanishing Hund's coupling.

In the limit of $J_H \to 0$, $\mathbb{B}$ is equal for all excited states, i.e. the relative spin orientation of the spin in the ground state and the spin transferred to the excited state is irrelevant, and we can directly evaluate Eq. (5.25):

$$\begin{aligned}\mathcal{H}_{\text{eff}} &= \frac{1}{\mathbb{B}}\frac{4}{3}t^2 \sum_{\langle ij\rangle} \left[|\Uparrow_i\Uparrow_j\rangle\langle\Uparrow_i\Uparrow_j| + |\Uparrow_i\Downarrow_j\rangle\langle\Uparrow_i\Downarrow_j| + |\Downarrow_i\Uparrow_j\rangle\langle\Downarrow_i\Uparrow_j| + |\Downarrow_i\Downarrow_j\rangle\langle\Downarrow_i\Downarrow_j|\right] \\ &= \frac{1}{\mathbb{B}}\frac{4}{3}t^2\mathbb{1}.\end{aligned} \tag{5.26}$$

Without Hund's coupling, the contribution is hence merely a constant contribution to the spin Hamiltonian.

With Hund's coupling, $\mathbb{B}_{\sigma_j}$ depends on the relative spin orientation of the excited state and the ground state. Therefore, $\mathbb{B}_{\sigma_j}$ is not an equal coefficient for all operators any more and the identity matrix cannot be identified. However, the nonvanishing matrix elements are all diagonal in spin projectors, as evident from Eq. (5.25). In Chapter 4 we defined the spin projectors as follows:

$$\begin{aligned}|\sigma\sigma'\rangle\langle\sigma\sigma'| &= \sum_{\mu\nu\mu'\nu'} \langle\mu\nu|\sigma\sigma'\rangle\langle\sigma\sigma'|\mu'\nu'\rangle c^\dagger_{1\mu}c^\dagger_{2\nu}c_{2\nu'}c_{1\mu'} \\ &= \sum_{\mu\nu\mu'\nu'} \delta_{\mu\sigma}\delta_{\nu\sigma'}\delta_{\mu'\sigma}\delta_{\nu'\sigma'}c^\dagger_{1\mu}c^\dagger_{2\nu}c_{2\nu'}c_{1\mu'} \\ &= c^\dagger_{1\sigma}c_{1\sigma}c^\dagger_{2\sigma'}c_{2\sigma'} \\ &= (\frac{1}{2}+\eta S^z_1)(\frac{1}{2}+\eta' S^z_2).\end{aligned} \tag{5.27}$$

where $\eta = +1$ ($\eta = -1$) for $\sigma = \Uparrow$ ($\sigma = \Downarrow$). Therefore, only terms $\propto S^z_i S^z_j$ contribute to $\mathcal{H}_{\text{eff}}$, resulting in an Ising spin exchange interaction term. On bonds with other spatial orientations, the non-vanishing matrix elements correspond to orthogonal orbital orientations, the Ising contribution differs therefore for every spatially differently oriented bond, which leads to the famous honeycomb Kitaev compass model.

Moreover, that Hund's coupling is the essential mechanism to obtain the Kitaev model follows also from another consideration. In the honeycomb lattice, there is bond inversion symmetry for nearest neighbour bonds. In Chapter 1, we showed that the pseudo-dipolar tensor $\Gamma \propto \mathbf{D}\otimes\mathbf{D}$ in the limit of $J_H \to 0$, so that in this case also $\Gamma = 0$. Since the Kitaev term is for the Z-bond equal to $-(\Gamma^{xx}+\Gamma^{yy})$, a finite Kitaev contribution can only be obtained from Hund's coupling effects, i.e. for a perturbation theory $\mathcal{O}(\frac{t^2 J_H}{U^2})$. This has been pointed out in many references previously [219, 221, 224]. Note also, that induced interaction by Hund's coupling is naturally ferromagnetic, suggesting a ferromagnetic Kitaev

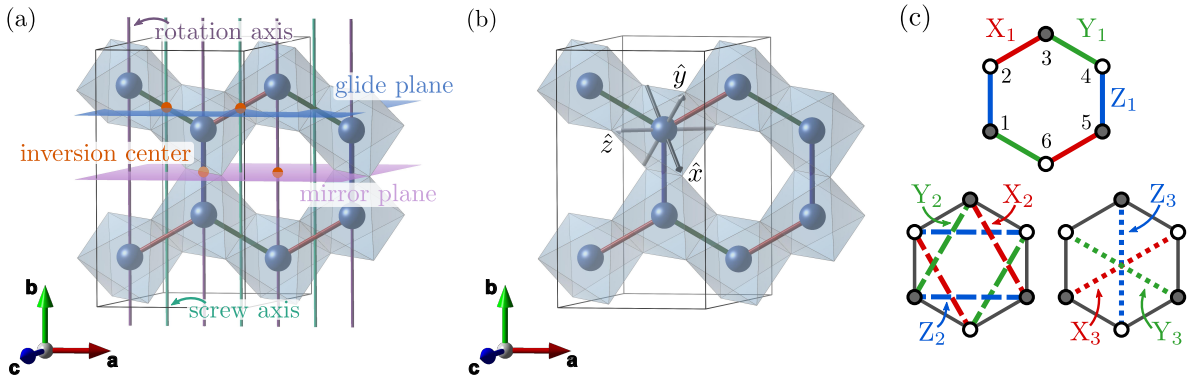

Figure 5.4: (a) Symmetries present in $C2/m$ Kitaev materials, including inversion centers, two-fold screw axes, two-fold rotation axes, glide planes and mirror planes on the example of α-$RuCl_3$. (b) Local coordinates $\hat{x}$, $\hat{y}$, $\hat{z}$ used in the spin model describing α-$RuCl_3$. Therefore, the a axis corresponds to $[11\bar{2}]$, the b axis to $[\bar{1}10]$ and the c^* axis to $[111]$. (c) Definition of first (X_1,Y_1,Z_1), second (X_2,Y_2,Z_2), and third (X_3,Y_3,Z_3) nearest neighbour bonds following the convention established by Winter *et al.* [224].

interaction for real materials. This insight will play an important role in the analysis of the microscopic mechanisms of α-$RuCl_3$ later in this chapter.

In real materials, direct hopping processes between the d-orbitals are in general finite, leading to finite Heisenberg and additional finite symmetric off-diagonal contributions, labelled as Γ and Γ'. These additional hopping processes are shown in Fig. 5.3(a), labelled as t_1 and t_3. If the octahedral environment is not perfect, there is an additional hopping contribution allowed, conventionally referred to as t_4. The labelling of the hopping processes $t_{1\ldots4}$ stems from the symmetry restrictions in real Kitaev materials, that allow for four distinct hopping processes, for a derivation see Appendix C. An expression for the effective Hamiltonian $\mathcal{H}_{\text{eff}}$ in second order perturbation theory under exact consideration of Hund's coupling and spin-orbit coupling is given in Ref. [224]. Interestingly, the authors found that under consideration of direct hopping, the optimal angle of a metal-ligand-metal plaquette is $\theta \approx 100°$, rather than $\theta = 90°$ corresponding to a perfect octahedral environment. In this case, nearest neighbour non-Kitaev interactions are almost perfectly suppressed.

5.3 Extended honeycomb Kitaev model for α-$RuCl_3$

5.3.1 Spin Hamiltonian representations for Kitaev materials

As discussed in Chapter 4, in some cases it can be convenient to parametrize a Hamiltonian differently than the most general expression. This is also the case for the Kitaev materials, where a very specific interaction term is desired to be dominant. The most general bilinear spin 1/2 Hamiltonian can be expressed as follows:

$$\mathcal{H}_{\text{gen}} = \begin{pmatrix} S_1^x & S_1^y & S_1^z \end{pmatrix} \begin{pmatrix} J+\Gamma^{xx} & \Gamma^{xy}+D^x & \Gamma^{xz}-D^y \\ \Gamma^{xy}-D^x & J+\Gamma^{yy} & \Gamma^{yz}+D^x \\ \Gamma^{xz}+D^y & \Gamma^{yz}-D^x & J-\Gamma^{xx}-\Gamma^{yy} \end{pmatrix} \begin{pmatrix} S_2^x \\ S_2^y \\ S_2^z \end{pmatrix} \tag{5.28}$$

However, due to the symmetry operations in the $C2/m$ space group, shown in Fig. 5.4(a), only four parameters are independent for a Z-bond. For example, if bond 1-2 is a nearest neighbour Z-bond, the inversion center implies the DM interaction to vanish, leaving only six independent parameters instead of the general nine. Additionally, we consider the mirror plane perpendicular to the b axis, which corresponds to the direction $[\bar{1}10]$ in the coordinate system of the spin Hamiltonian given in Fig. 5.4(b). Such a reflection can be expressed by the reflection matrix $\mathcal{R} \cdot \mathbf{S}_1 = \mathbf{S}_2$, which exchanges the spin index in addition to the reflection itself. For the symmetrical anisotropic contribution in the Hamiltonian,

such a symmetry implies the relation $\mathbf{S}_1^\dagger \cdot \Gamma \cdot \mathbf{S}_2 = \mathbf{S}_2^\dagger \cdot \mathcal{R}^{-1} \cdot \Gamma \cdot \mathcal{R} \cdot \mathbf{S}_1$. For the reflection matrix with respect to the $[\bar{1}10]$ axis, we obtain then the following equality[3]:

$$\begin{pmatrix} J_{12}+\Gamma_{12}^{xx} & \Gamma_{12}^{xy} & \Gamma_{12}^{xz} \\ \Gamma_{12}^{xy} & J_{12}+\Gamma_{12}^{yy} & \Gamma_{12}^{yz} \\ \Gamma_{12}^{xz} & \Gamma_{12}^{yz} & J_{12}-\Gamma_{12}^{xx}-\Gamma_{12}^{yy} \end{pmatrix} \stackrel{!}{=} \begin{pmatrix} J_{21}+\Gamma_{21}^{yy} & \Gamma_{21}^{xy} & \Gamma_{21}^{yz} \\ \Gamma_{21}^{xy} & J_{21}+\Gamma_{21}^{xx} & \Gamma_{21}^{xz} \\ \Gamma_{21}^{yz} & \Gamma_{21}^{xy} & J_{21}-\Gamma_{21}^{xx}-\Gamma_{21}^{yy} \end{pmatrix} \tag{5.29}$$

If bond 1-2 is a nearest neighbour Z-bond, this implies the relations $\Gamma_{12}^{xx} = \Gamma_{12}^{yy}$ and $\Gamma_{12}^{xz} = \Gamma_{12}^{yz}$, leaving only four independent parameters in the Hamiltonian:

$$\mathcal{H}_{\text{gen}} = \begin{pmatrix} S_1^x & S_1^y & S_1^z \end{pmatrix} \begin{pmatrix} J_{12}+\Gamma_{12}^{xx} & \Gamma_{12}^{xy} & \Gamma_{12}^{xz} \\ \Gamma_{12}^{xy} & J_{12}+\Gamma_{12}^{xx} & \Gamma_{12}^{xz} \\ \Gamma_{12}^{xz} & \Gamma_{12}^{xz} & J_{12}-2\Gamma_{12}^{xx} \end{pmatrix} \begin{pmatrix} S_2^x \\ S_2^y \\ S_2^z \end{pmatrix}. \tag{5.30}$$

In the case of the Kitaev materials, a different parametrization [221, 224] was followed, emphasizing the symmetry of the investigated compounds:

$$\mathcal{H}_{\mathcal{K}} = \begin{pmatrix} S_1^x & S_1^y & S_1^z \end{pmatrix} \begin{pmatrix} J_{\mathcal{K}} & \Gamma_{\mathcal{K}} & \Gamma'_{\mathcal{K}} \\ \Gamma_{\mathcal{K}} & J_{\mathcal{K}} & \Gamma'_{\mathcal{K}} \\ \Gamma'_{\mathcal{K}} & \Gamma'_{\mathcal{K}} & J_{\mathcal{K}}+K_{\mathcal{K}} \end{pmatrix} \begin{pmatrix} S_2^x \\ S_2^y \\ S_2^z \end{pmatrix}. \tag{5.31}$$

The relation between the two parametrizations is then easily obtained:

$$J_{\mathcal{K}} = J_{12} + \Gamma_{12}^{xx}, \qquad K_{\mathcal{K}} = -3\Gamma_{12}^{xx}, \qquad \Gamma_{\mathcal{K}} = \Gamma_{12}^{xy}, \qquad \Gamma'_{\mathcal{K}} = \Gamma_{12}^{xz}. \tag{5.32}$$

Hence, similarly to the pyrochlores in Chapter 4, the so-called "Heisenberg" exchange, refers to different exchange parameters in the two representations. From now on, we follow the Kitaev specific representation, omit the index $\mathcal{K}$ for readability and replace it with an index indicating the distance between neighbours, e.g. J_1 for nearest neighbours, J_3 for third nearest neighbours. Note, that for the X- and Y-bonds the symmetry restrictions are lower and allow for six independent parameters. The only constrained parameters are the vanishing Dzyaloshinskii-Moriya contributions due to bond inversion centers. However, in this chapter we work with an effective model that assumes C_3 symmetry and therefore neglects these additional degrees of freedom. This assumption is valid for negligible distortions in the lattice structure [224].

For the second nearest neighbours, illustrated in Fig. 5.4(c), there are no symmetry restrictions, leading to nine independent parameters for the X_2- and Y_2-bonds, which are related by symmetry, and seven for the Z_2-bond, where no inversion center forbids a finite DM vector, but the presence of the two-fold rotation axis, see Fig. 5.4(a), implies e.g. $\Gamma_{24}^{xx} = \Gamma_{24}^{yy}$ and $\Gamma_{24}^{xz} = \Gamma_{24}^{yz}$. On third nearest neighbour level, the symmetry situation is equivalent to the nearest neighbours, with six indepenent parameters for X_3-, Y_3-bonds and four for the Z_3-bond, where we followed the notation introduced in Ref. [224]. In total, this results in 36 free parameters to describe Kitaev materials with effective spin models.

5.3.2 *Ab-initio* studies of α-$RuCl_3$

Due to the large number of independent parameters allowed by symmetry for a spin model for α-$RuCl_3$, insight from *ab-initio* methods is crucial. It is certainly impossible to determine 36 parameters from fitting to experimental data. Therefore, we review here briefly the results from several *ab-initio* studies [224–227] to narrow down an appropriate minimal model. In Section 5.6, we then present our study of a series of parameter sets within the determined minimal parameter space established here.

One important struggle, which also played a role in the analysis of the experimental INS data, was initial uncertainty about the correct space group of α-$RuCl_3$. Unfortunately, due to the delicate cancelling mechanisms, mentioned in the previous section, and the similarity of involved parameters like the Hund's coupling, Hubbard repulsion, and SOC constant [222], small modifications lead in the case of α-$RuCl_3$ to significant changes in the spin model. To date, there have been three space groups discussed for the low temperature structure of α-$RuCl_3$: $P3_112$, $C2/m$, and $R\bar{3}$. To distinguish between those

[3] In this expression we already used that only symmetrical terms survive due to the bond inversion center. Note also, that the spin transforms as a pseudo-vector.

Structure	Method	J_1	K_1	Γ_1	J_3	Ref.
$P3_112$ [238]	DFT+2OPT	-3.5	$+4.6$	$+6.4$	–	[226]
$P3_112$ [239]	DFT+ED	-5.5	$+7.6$	$+8.4$	$+0.2$	[224]
$P3_112$ [238]	QC	-0.5	-1.2	-1.0	–	[225]
Relaxed [226]	DFT+2OPT	$-2.8/-1.0$	$-4.0/-8.8$	$+7.2/+3.9$	–	[226]
$C2/m$ [237]	DFT+ED	-1.7	-6.7	$+6.6$	-0.9	[224]
$C2/m$ [237]	QC	$+0.7$	-5.0	$+1.2$	–	[225]
$C2/m$ [232]	DFT	-1.8	-10.6	$+3.8$	$+1.25$	[227]

Table 5.1: Exchange parameters in meV determined by several methods based on *ab-initio* approaches for α-$RuCl_3$ for the first space group $P3_112$ and the later updated space group $C2/m$. 2OPT = second order perturbation theory, ED = exact diagonalization, QC = quantum chemistry, and DFT = density functional theory. The parameter values are averaged over X-, Y- and Z-bonds. Table adapted from Ref. [81].

space groups is challenging due to highly propable stacking faults between the honeycomb layers, which are only weakly coupled through van der Waals interactions [237, 240]. Early studies suggested the highly symmetric trigonal space group $P3_112$ [238, 239] with a Ru-Cl-Ru angle $\sim 88°$, very close to the ideal octahedral environment. In this case, most of the *ab-initio* studies identified an antiferromagnetic Kitaev interaction, $K_1 > 0$. In Table 5.1, we list various *ab-initio* studies based on the different proposed crystal structures, as well as a theoretically relaxed structure. For the $P3_112$ space group, the Kitaev interaction is either positive, or has a small negative value. Later studies then suggested a less symmetric $C2/m$ structure with a larger angle $\sim 94°$ [232, 237]. *Ab-initio* studies based on this more refined structure suggested consistently a ferromagnetic Kitaev interaction, $K_1 < 0$. Moreover, signatures for a structural phase transition at $T \approx 150\,\mathrm{K}$ were reported [46, 241], so that a crystal structure refinement at room temperature is questionable for studies of low temperature properties. This transition is thought to be of $C2/m \to R\bar{3}$ nature [242], but it has been difficult to pin down the influence on the local Ru-Cl-Ru bond geometry. Note, that we present bond averaged values in Table 5.1, although microscopic studies suggest an anisotropy between the X-, Y- and the Z-bond in α-$RuCl_3$ [224–227]. To reduce the parameter space, and since it was suggested that longer range interactions are more dicisive for the magnetic response [224], we decided to employ this as a first approximation. The *ab-initio* studies cited in Table 5.1 determined the effective spin Hamiltonian with different approximations, including second order perturbation theory based on *ab-initio* hopping parameters (DFT+2OPT) [226], the hybrid method as employed in Chapter 2 and Chapter 4 (DFT+ED) [224], quantum chemistry (QC) methods [225], and total energy DFT calculations [227]. A general observation is that the various methods agree in the trends for the exchange parameters rather well, as long as they are based on the same crystal structure.

On the electronic model level, Winter *et al.* [224] found for α-$RuCl_3$ a significant contribution from direct hopping with $|t_2/t_3| \sim 1$, in contrast to the metal-ligand-metal hopping proposed in Ref. [219] as a source for a pure Kitaev model in real materials. The bond angle $\sim 94°$ allows for large direct hopping t_3, on the Z-bonds, and t_3', on the X- and Y-bonds. To determine the spin model, the authors considered four- and six-spin ring-exchange interactions using the hybrid method. They found the ring-exchange terms to be small, but large longer-range couplings such as the third nearest neighbour Heisenberg exchange J_3. Due to the moderate Hubbard repulsion U, they also found significant modifications by the higher order terms. In most of the *ab-initio* studies, the off-diagonal term Γ' was found to be significantly smaller than the presented parameters in Table 5.1. For example, in Ref. [224] off-diagonal terms Γ' and second-neighbour interactions were consistently below 1 meV. This motivated us to choose as a minimal model the parameter space $(J_1, K_1, \Gamma_1, J_3)$:

$$\mathcal{H} = \sum_{\langle ij \rangle} J_1\ \mathbf{S}_i \cdot \mathbf{S}_j + K_1\ S_i^\gamma S_j^\gamma + \Gamma_1\ (S_i^\alpha S_j^\beta + S_i^\beta S_j^\alpha) + \sum_{\langle\langle\langle ij \rangle\rangle\rangle} J_3\ \mathbf{S}_i \cdot \mathbf{S}_j. \tag{5.33}$$

Future studies may consider bond anisotropy, additional off-diagonal terms Γ' and smaller long-range contributions, to settle on further details once the main magnetic mechanisms in α-$RuCl_3$ are established.

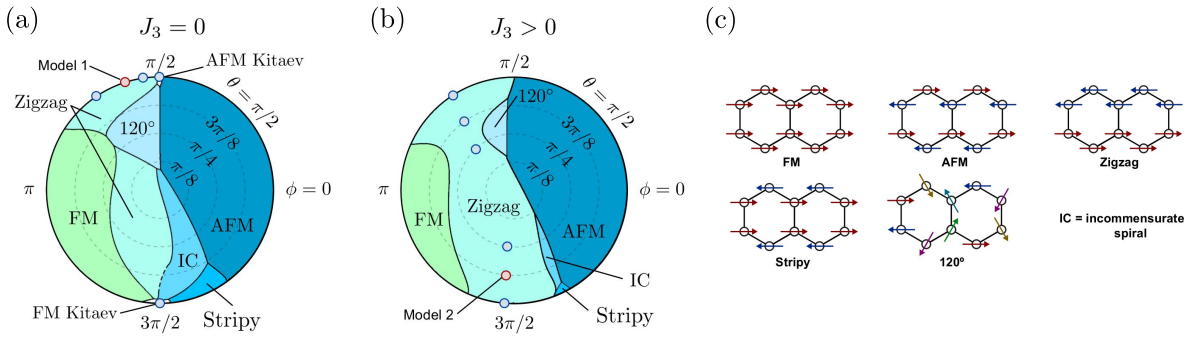

Figure 5.5: Phase diagrams for the minimal model $(J_1, K_1, \Gamma_1, J_3)$ calculated by Stephen M. Winter, where the phase boundaries were determined from second-order energy corrections to the classical state energies [243]. The parametrization $J_1 = \sin\theta\cos\phi$, $K_1 = \sin\theta\sin\phi$, $\Gamma_1 = \cos\theta$, as introduced in Ref. [221] and an overall constant J_3 is employed. The blue and red points indicate studied parameter sets presented at the end of this chapter and listed in Table 5.2. (a) Phase diagram for $(J_1, K_1, \Gamma_1, J_3 = 0)$. (b) Phase diagram for the minimal model $(J_1, K_1, \Gamma_1, J_3 > 0)$, with a constant ratio $J_3/\sqrt{J_1^2 + K_1^2 + \Gamma_1^2} = +0.088$, approximately consistent with the magnitude assumed in the studied models in this thesis. (c) Definition of the phases used in (a,b). Fig. adapted from Ref. [81]

5.3.3 Phase diagram of the minimal model for α-$RuCl_3$

The phase diagram of the extended Kitaev model has been subject of intense research [221, 224, 228]. Since the magnetic order of α-$RuCl_3$ is known from experiment [232, 237], a phase diagram for the extended Kitaev model can provide guidance which parameter sets should be considered as possible candidates. In 2014, Rau *et al.* [221] presented phase diagrams in the (J_1, K_1, Γ_1) space, determined classically and from exact diagonalization on a periodic 24-site cluster. In order to capture the effects of the longer range interaction J_3, Stephen M. Winter calculated the phase diagrams shown in Fig. 5.5 [81]. The phase boundaries were determined from second-order energy corrections to the classical state energies, based on a method introduced in Ref. [243].

As a parametrization scheme we followed Ref. [221] with normalized values to $J_1 = \sin\theta\cos\phi$, $K_1 = \sin\theta\sin\phi$ and $\Gamma_1 = \cos\theta$. In general, the extended Kitaev model hosts six distinct ordered phases [221, 224, 225, 228, 243–248]. On the outer circle, with $\theta = \pi/2$, there is no contribution from the off-diagonal term $\Gamma_1 = 0$, so that in this case the phases of the "pure" Heisenberg-Kitaev model are shown. Without long-range interaction, in Fig. 5.5(a), tuning the ratio of J_1/K_1 drives the system from an antiferromagnetic Néel order, for e.g. $J_1 = -1$ and $K_1 = 0$, through the Kitaev spin liquid ("AFM Kitaev", e.g. $J_1 = 0$, $K_1 = 1$), the antiferromagnetic zigzag order, ferromagnetic order (e.g. $J_1 = 1$, $K_1 = 0$), the Kitaev spin liquid ("FM Kitaev", e.g. $J_1 = 0$, $K_1 = -1$) and finally a stripy order. Towards the center of the circle, θ is reduced and a finite Γ_1 parameter is introduced. This induces an additional 120° order, illustrated in Fig. 5.5(c), where the name is inspired by the ground state of the isotropic triangular lattice. The second induced phase is an incommensurate order (IC), which is in certain regions energetically difficult to distinguish from the zigzag order, indicated by the dashed line in the phase diagram. For a finite long-range antiferromagnetic Heisenberg exchange $J_3 > 0$, the phase boundaries of the existing phases are essentially shifted around, shown in Fig. 5.5(b). Here, a relatively small constant ratio $J_3/\sqrt{J_1^2 + K_1^2 + \Gamma_1^2} = +0.088$ was applied, which is consistent with the suggestion by *ab-initio* studies. The main consequence of $J_3 > 0$ is an extended area of the zigzag phase, which stabilizes the experimentally observed magnetic order in α-$RuCl_3$.

In order to disentangle the effects of the exchange parameters in the extended model, we studied a series of models, presented in Section 5.6, all of them restricted to the zigzag region in the phase diagram. Unfortunately, various parameter combinations lead to the experimentally observed magnetic order. In Fig. 5.5(a,b), the parameter sets studied in Section 5.6 are indicated by blue and red dots in the phase diagrams and listed in Table 5.2. As initially proposed by experimental fitting, three models within the nearest neighbour Heisenberg Kitaev (nnHK) model family $(J_1 < 0, K_1 > 0, \Gamma_1 = 0, J_3 = 0)$

Model family	J_1	K_1	Γ_1	J_3	Name
nnHK	-4.6	+7.0	–	–	
	-2.4/-2.2	+8.0/+7.4	–	–	Model 1
	-1.2	+8.3	–	–	
AFM Kitaev	–	+8.4	–	–	
extended AFM Kitaev	-4.6	+7.0	–	+0.7	
	-4.6	+6.3	+3.1	+0.7	
	-4.6	+5.0	+5.0	+0.7	
extended FM Kitaev	-0.5	-4.0	+4.0	+0.5	
	-0.5	-5.0	+2.5	+0.5	Model 2
	-0.5	-5.6	–	+0.5	
FM Kitaev	–	-5.7	–	–	

Table 5.2: Exchange parameters in meV of the models indicated in Fig. 5.5 and studied in Section 5.6. The nearest-neighbour Heisenberg Kitaev (nnHK) are normalized to $\sqrt{J_1^2 + K_1^2} = 8.4\,\text{meV}$, note that Model 1 is renormalized in Fig. 5.11 to 7.7 meV, indicated by the second values in the table. The extended AFM Kitaev models are normalized to $\sqrt{J_1^2 + K_1^2 + \Gamma_1^2 + J_3^2} = 8.5\,\text{meV}$ and the extended FM Kitaev models are normalized to $\sqrt{J_1^2 + K_1^2 + \Gamma_1^2 + J_3^2} = 7.7\,\text{meV}$.

were studied. Model 1, indicated in red, was proposed by Banerjee *et al.* [231]. Then, we studied a series of models with long-range Heisenberg exchange and different signs of the Kitaev interaction, referred to as the extended AFM Kitaev models with $(J_1 < 0, K_1 > 0, \Gamma_1 > 0, J_3 > 0)$. Finally, we studied the extended FM Kitaev models with $(J_1 < 0, K_1 < 0, \Gamma_1 > 0, J_3 > 0)$, which contain with Model 2 the most promising parameter set, indicated in red as well.

5.4 Key experimental observations for α-$RuCl_3$

A detailed experimental and theoretical study of α-$RuCl_3$ was published in 2015 by Johnson *et al.* [237]. The authors reinvestigated the crystal structure, the magnetic order with susceptibility and magnetization measurements, and the electronic structure with *ab-initio* calculations. We revisit the results regarding the behaviour of α-$RuCl_3$ under magnetic field in Chapter 6. The authors derived from X-ray diffraction patterns of untwinned α-$RuCl_3$ crystals Bragg reflections that are consistent with the $C2/m$ space group at room temperature and down to $T = 80\,\text{K}$. From magnetic neutron powder diffraction and additional symmetry considerations, the authors deduced the onset of long-range magnetic order below $T_N \approx 13\,\text{K}$ and identified the order as an antiferromagnetic zigzag order. With this method it was, however, not possible to determine the specific orientation of the magnetic moments. Cao *et al.* [232] confirmed later the antiferromagnetic zigzag order and determined the magnetic moments to lie in the *ac*-plane from experimentally determined static magnetic structure factors.

In 2016, Banerjee *et al.* [231] discussed inelastic neutron scattering (INS) experiments on powder samples of α-$RuCl_3$. In the framework of a nearest neighbour Heisenberg-Kitaev (nnHK) model, where INS results were analysed in terms of linear spin-wave theory (LSWT). In this work, the authors stated that it *"has turned out that the signature of the Majorana fermion in the response function measured by means of inelastic neutron scattering is perhaps one of the most direct ways of pinning down the excitation's existence"*. With neutron diffraction on a powder sample, they determined magnetic order below $T_N = 14\,\text{K}$. The authors also observed two magnetic orders at different $\mathbf{q}$ vectors, hinting toward stacking faults along the c^* axis between the honeycomb planes, where one magnetic order was assigned to ABAB stacking, and the other one to ABCABC. Nevertheless, both phases showed signatures of the in-plane antiferromagnetic zigzag order. Based on these observations the authors argued that a Heisenberg-Kitaev Hamiltonian can satisfactorily capture the magnetic properties of α-$RuCl_3$. Although this compound magnetically orders at low temperatures, they argued that signatures of fractionalization may be present in collective magnetic excitations. With the observation of a minimum M_1 in the powder INS data at a $\mathbf{q}$ vector corresponding to the M-point, shown in Fig. 5.6(a), they confirmed

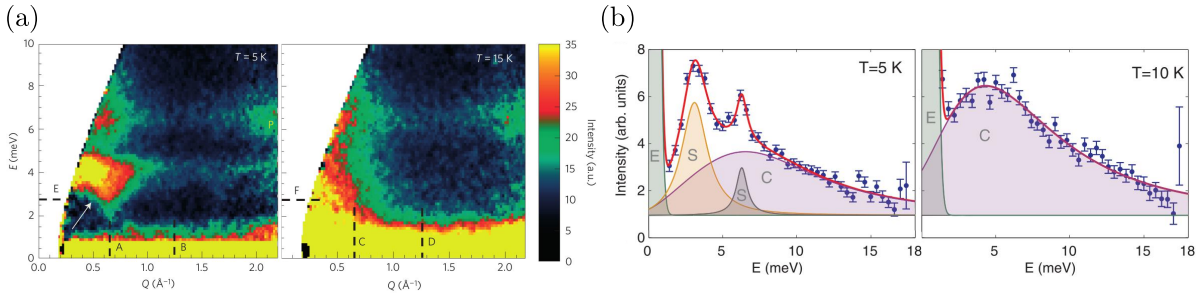

Figure 5.6: (a) Powder INS results by Banerjee *et al.* [231] at $T = 5\,\mathrm{K}$ and $T = 15\,\mathrm{K}$ for an average $\mathbf{q}$ vector in reciprocal space. For the low-temperature data the authours assign two magnetic modes M_1 (at $E = 4\,\mathrm{meV}$) and M_2 (at $E = 6\,\mathrm{meV}$). (b) Single crystal INS results at the Γ point by Banerjee *et al.* [46] at $T = 5\,\mathrm{K}$ and $T = 10\,\mathrm{K}$. Contributions are assigned by the authors to an elastic component (E), spin-wave contributions (S) and a continuum (C). Fig. (a) reprinted from Ref. [231], Fig. (b) reprinted from Ref. [46].

the zigzag order. In addition, they observed a second feature M_2 at higher energies. Based on the differing temperature dependence of these two modes, observable in Fig. 5.6(a), they argued in favour of an interpretation in terms of Majorana fermions. For a temperature above the ordering temperature $T = 15\,\mathrm{K}$, the feature at higher energies remains intact. To gain further insight, they fitted the $T = 5\,\mathrm{K}$ data with Gaussians and interpreted the two obtained peaks at $E_1 = 4.1\,\mathrm{meV}$ and $E_2 = 6.5\,\mathrm{meV}$ with the help of LSWT for zigzag order. The authors pointed out that LSWT is inapplicable for strongly quantum fluctuating systems, but was nevertheless chosen due to the lack of appropriate alternatives. Since it is not possible to assign unambiguously the peaks in the experimental data to the peaks in LSWT, they offered two possible models: $(J_1 = -4.6, K_1 = +7.0)\,\mathrm{meV}$ or $(J_1 = -2.9, K_1 = +8.1\,)\mathrm{meV}$. Since at that time *ab-initio* studies for spin Hamiltonians were mainly based on the $P3_112$ structure, the qualitative tendencies seemed to be consistent with the microscopic results. Due to the proximity to the QSL state in the phase diagram, the authors argued, that M_2 was a feature of the spin liquid state, and that hence its behaviour could not be captured within LSWT. They used therefore the approach, to describe the high-energy feature in terms of the pure, analytically solvable Kitaev model, and the low-energy feature in terms of the semi-classical LSWT.

A more refined analysis was available in 2017, with INS data on single crystals by Banerjee *et al.* [46]. The authors argued to have a low contribution from stacking faults due to the observation of a single magnetic ordering transition at $T_N = 7\,\mathrm{K}$. The availability of single crystals allowed a resolution in reciprocal space in contrast to the averaged results in Ref. [231]. In the measured neutron scattering intensity at the Γ-point in the Brillouin zone, shown in Fig. 5.6(b), the authors assigned a continuum contribution, denoted by "C", at temperatures below and above T_N. Since the existence of a continuum below the ordering temperature is not a feature observed in LSWT, the authors drew the connection to a pure Kitaev model, where a continuum would be expected over large energy scales. In neutron scattering experiments it is only possible to excite multiples of quasiparticles such as Majorana fermions. Due to the various possibilities to distribute the energy between multiple fractionalized excitations, in INS experiments this would be observed as a continuum of excitations as a function of energy. In order to analyse the data, the authors worked in the framework of the pure Kitaev model in the high-energy limit and in terms of LSWT in the ordered limit. They argued that, while it was known that additional terms are relevant for α-$RuCl_3$, no reliable theory was available that can capture the physics in-between. Secondly, they pointed out the lack of agreement among the *ab-initio* studies, which was probably justified at that point, as discussed in Section 5.3. In Fig. 5.7(a), we show measured INS intensitites in reciprocal space. Note, that this figure was published later in Ref. [47] in the context of magnetic field experiments. However, the figure shows data at zero magnetic field and should, in spirit, correspond to results already obtained in 2017. Fig. 5.7(b) contains the data published in Ref. [46], which resembles integrated data over various energy windows in reciprocal space. As one of the central

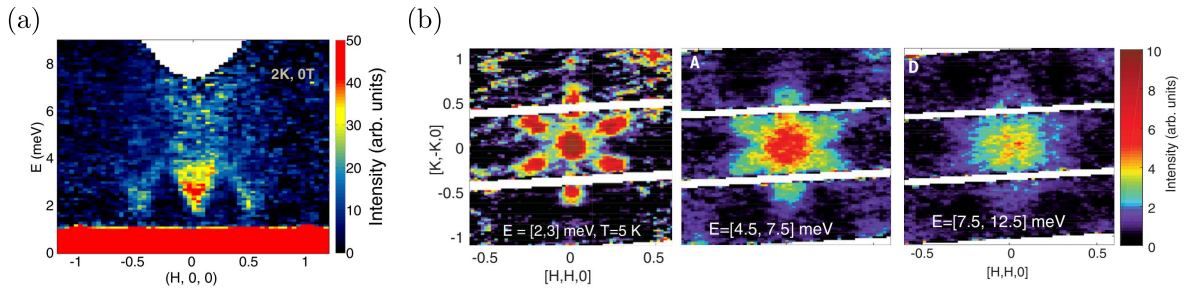

Figure 5.7: (a) INS results by Banerjee *et al.* [47] at $T = 2\,\mathrm{K}$ in reciprocal space along $[H, 0, 0]$, which corresponds to the k path Y-M-Γ-M-Y. Note the intensity at the Γ point and the washed out nature at higher energies. (b) INS results integrated over indicated energy windows by Banerjee *et al.* [46] at $T = 5\,\mathrm{K}$. Note the intensity at the Γ point at low temperatures, the six-fold star shape at intermediate energies and the disappearance of the star signature at higher energies. Fig. (a) reprinted from Ref. [47], Fig. (b) reprinted from Ref. [46].

results, Banerjee *et al.* stressed the robust contribution at the Γ-point for different energy windows and temperatures. As an indication for short range correlations, this is a consistent feature of the Kitaev model. Another important feature, which plays a prominent role later in this chapter, is the observation of the six-fold star shape at intermediate energies, shown in the middle panel of Fig. 5.7(b), which served as an identification tool for a correct reproduction of the INS data of spin models, next to the prominent weights at the Γ-point.

5.5 Dynamical correlation functions from exact diagonalization

As pointed out by Banerjee *et al.* [46, 231], the combination of anisotropic and long-range interactions in the effective spin Hamiltonian for α-$RuCl_3$ challenge common powerful methods like DMRG [249, 250] or Monte-Carlo methods [251, 252]. Symmetries that lower computational costs or low-dimensional effective representations, failed to date to be successfully applied to the extended Kitaev model. Therefore, we tackled this issue with the method of exact diagonalization (ED). With this method, all exchange terms in the spin Hamiltonian can be treated on equal footing. The main drawback of exact diagonalization is the restriction to small cluster sizes. Especially in the case of the honeycomb lattice, it is difficult to control the resulting finite-size effects quantitatively, since extrapolation to infinite cluster sizes requires a series of clusters with equal symmetry. We address this issue in more detail in Section 5.6. The theoretical quantity, which is necessary to predict INS intensities based on a spin Hamiltonian, is the dynamical spin structure factor $\mathcal{S}(\mathbf{q}, \omega)$. It can be calculated with exact diagonalization within the so-called Lanczos algorithm [253]. In this section, we introduce the general idea of this method and how dynamical correlation functions can be extracted. As a main guide for this section we followed the explanations in Ref. [254], where it is referred to as the "chain model".

5.5.1 Lanczos method

Generally, the method of exact diagonalization is hampered by the tremendous numerical effort at relatively small cluster sizes. Since the full energy spectrum of a given Hamiltonian is rarely necessary to address certain physical issues, methods to reduce the Hilbert space to a relevant subspace are very powerful. One example is the Lanczos method, which was formulated by Lanczos in the context of a computer algorithm in 1950 [253]. The Lanczos method is based on the fundamental insight that it is possible to express any Hermitian matrix in terms of a tridiagonal matrix via basis transformation. In a more abstract formulation, this is true for operators such as a given Hamiltonian $\mathcal{H}$:

$$\mathcal{H}|\phi_n\rangle = a_n|\phi_n\rangle + b_{n+1}|\phi_{n+1}\rangle + b_n|\phi_{n-1}\rangle. \tag{5.34}$$

Here, $|\phi_i\rangle$ are orthogonal states, such that the recurrence relation Eq. (5.34) is fulfilled. The coefficients a_i and b_i are yet to be determined parameters in the Lanczos algorithm. In matrix representation with the Lanczos states $|\phi_i\rangle$ as basis states, the tridiagonal form of the Hamiltonian is evident:

$$\mathcal{H} = \begin{pmatrix} a_0 & b_1 & 0 & 0 & \dots \\ b_1 & a_1 & b_2 & 0 & \dots \\ 0 & b_2 & a_2 & b_3 & \dots \\ 0 & 0 & b_3 & a_3 & \dots \\ \vdots & \vdots & \vdots & \vdots & \end{pmatrix}. \tag{5.35}$$

The states $|\phi_i\rangle$ are ordered, with the initial state $|\phi_0\rangle$ and the final state $|\phi_{l-1}\rangle$ in an l-dimensional Lanczos space, which is built with the recurrence relation Eq. (5.34). It is therefore a Krylov subspace $\mathcal{K}$, which is spanned by the images of $|\phi_0\rangle$ under increasing powers of $\mathcal{H}$:

$$\mathcal{K}_l(\mathcal{H}, |\phi_0\rangle) = \text{span}\,\{|\phi_0\rangle, \mathcal{H}|\phi_0\rangle, \mathcal{H}^2|\phi_0\rangle, \dots, \mathcal{H}^{l-1}|\phi_0\rangle\}. \tag{5.36}$$

As a consequence, the choice of the initial state $|\phi_0\rangle$ determines which physical phenomena can be described properly in the corresponding subspace. A poor relation of $|\phi_0\rangle$ to the problem at question results in a poor description in the chosen subspace.

If the initial state is an eigenstate of the Hamiltonian, the Lanczos procedure is immediately terminated due to the eigenequation $\mathcal{H}|\phi_0\rangle = a_0|\phi_0\rangle$. If $|\phi_0\rangle$ is not an eigenstate, the product $\mathcal{H}|\phi_0\rangle = a_0|\phi_0\rangle$ gives some contribution to the initial state due to the overlap of $|\phi_0\rangle$ with some eigenstates, and additional contributions to the eigenstates of the Hamiltonian which do not have an overlap with $|\phi_0\rangle$. These additional contributions can be summarized in an yet unknown state $|\phi_1\rangle$:

$$\mathcal{H}|\phi_0\rangle = a_0|\phi_0\rangle + b_1|\phi_1\rangle. \tag{5.37}$$

Note, that therefore the state $|\phi_1\rangle$ is orthogonal to $|\phi_0\rangle$ by construction. The coefficient a_0 can be identified directly as the diagonal matrix element of the Hamiltonian:

$$\langle\phi_0|\mathcal{H}|\phi_0\rangle = a_0\langle\phi_0|\phi_0\rangle + b_1\langle\phi_0|\phi_1\rangle = a_0. \tag{5.38}$$

The coefficient b_1 can be determined by rearranging Eq. (5.37) to $b_1|\phi_1\rangle = \mathcal{H}|\phi_0\rangle - a_0|\phi_0\rangle$ and from the norm of both sides of the equation:

$$|b_1|^2\langle\phi_1|\phi_1\rangle = ||\mathcal{H}|\phi_0\rangle - a_0|\phi_0\rangle||^2 \tag{5.39}$$

It is convenient to choose b_1 as the positive root of the norm, so that we obtain the following definition:

$$b_1 = ||\mathcal{H}|\phi_0\rangle - a_0|\phi_0\rangle||. \tag{5.40}$$

With the two coefficients a_0 and b_1 determined, the new state follows from rearranging Eq. (5.37):

$$|\phi_1\rangle = \frac{\mathcal{H}|\phi_0\rangle - a_0|\phi_0\rangle}{b_1}. \tag{5.41}$$

By construction, $|\phi_1\rangle$ is also normalized.

To generalize this approach, we assume that we have constructed a set of orthonormal Lanczos states $\{\phi_0, \dots, \phi_n\}$ with finite coefficients $\{a_0, \dots, a_n\}$ and $\{b_1, \dots, b_n\}$. This is a valid premise, since every Hermitian operator can be expressed in terms of a tridiagonal representation, as mentioned above. The objective is then to determine the next state in the chain, $|\phi_{n+1}\rangle$, together with the corresponding coefficients a_n and b_{n+1}. The coefficient a_n follows naturally from the orthonormalization of the states:

$$a_n = \langle\phi_n|\mathcal{H}|\phi_n\rangle. \tag{5.42}$$

Choosing the positive root of the squared norm of Eq. (5.34), the coefficient b_{n+1} is the norm of the new state $|\phi_{n+1}\rangle$:

$$b_{n+1} = ||\mathcal{H}|\phi_n\rangle - a_n|\phi_n\rangle - b_n|\phi_{n-1}\rangle||. \tag{5.43}$$

With a_n and b_{n+1} determined, the new state follows directly from the recurrence relation Eq. (5.34):

$$|\phi_{n+1}\rangle = \frac{\mathcal{H}|\phi_n\rangle - a_n|\phi_n\rangle - b_n|\phi_{n-1}\rangle}{b_{n+1}}. \tag{5.44}$$

By construction, $|\phi_{n+1}\rangle$ is orthogonal to $|\phi_n\rangle$ and $|\phi_{n-1}\rangle$. To show that it is also orthogonal to every other previous state, we consider a state of the orthonormal subspace $|\phi_m\rangle$ with $m < n-1$. From Eq. (5.44) follows:

$$\begin{aligned} b_{n+1}\langle\phi_m|\phi_{n+1}\rangle &= \langle\phi_m|\mathcal{H}|\phi_n\rangle - a_n\langle\phi_m|\phi_n\rangle - b_n\langle\phi_m|\phi_{n-1}\rangle \\ &= \langle\phi_m|\mathcal{H}|\phi_n\rangle. \end{aligned} \tag{5.45}$$

Here, we used that $|\phi_m\rangle$ is orthogonal to states with index $i < n+1$. Since the Hamiltonian is Hermitian, $\langle\phi_m|\mathcal{H}|\phi_n\rangle = \langle\phi_n|\mathcal{H}|\phi_m\rangle$, and with the recurrence relation Eq. (5.34) with respect to $|\phi_m\rangle$ on the right-hand side, we obtain:

$$b_{n+1}\langle\phi_m|\phi_{n+1}\rangle = \langle\phi_n|\big[a_m|\phi_m\rangle + b_{m+1}|\phi_{m+1}\rangle + b_m|\phi_{m-1}\rangle\big]. \tag{5.46}$$

Since $m < n-1$, every scalar product in this expression is between orthogonal states, which implies for $b_{n+1} \neq 0$ directly, that the new state $|\phi_{n+1}\rangle$ is orthogonal to every state $|\phi_m\rangle$ obtained before in the Lanczos procedure:

$$b_{n+1}\langle\phi_m|\phi_{n+1}\rangle = 0. \tag{5.47}$$

The Lanczos algorithm terminates when the norm of a new vector vanishes, $b_l = 0$. Neglecting numerical errors, this implies that the full invariant subspace is explored. The sum over the l-dimensional Lanczos subspace is therefore a complete sum:

$$\sum_{i=0}^{l-1} |\phi_i\rangle\langle\phi_i| = \mathbb{1}. \tag{5.48}$$

To prove this statement, we show that Eq. (5.48) follows from the initial assumption that $b_l = 0$. We start with the sum over the matrix elements of the Hamiltonian with the last state in the Lanczos subspace:

$$\begin{aligned} \sum_{i=0}^{l-1}\langle\phi_{l-1}|\mathcal{H}|\phi_i\rangle\langle\phi_i|\mathcal{H}|\phi_{l-1}\rangle &= \sum_{i=0}^{l-1} ||\langle\phi_i|\mathcal{H}|\phi_{l-1}\rangle||^2 \\ &= \sum_{i=0}^{l-1} ||a_{l-1}\langle\phi_i|\phi_{l-1}\rangle + b_{l-1}\langle\phi_i|\phi_{l-2}\rangle||^2, \end{aligned} \tag{5.49}$$

where we used the recurrence relation Eq. (5.34) and $b_l = 0$. Since $i \leq l-1$, the scalar products are between orthonormal states, the sum collapses and we find the following relation:

$$\sum_{i=0}^{l-1}\langle\phi_{l-1}|\mathcal{H}|\phi_i\rangle\langle\phi_i|\mathcal{H}|\phi_{l-1}\rangle = ||a_{l-1} + b_{l-1}||^2. \tag{5.50}$$

On the other hand, if we start with the matrix element of $\mathcal{H}^2$ of the outer Lanczos states and use Eq. (5.34) with $b_l = 0$, we find the same expression:

$$\begin{aligned} \langle\phi_{l-1}|\mathcal{H}\mathcal{H}|\phi_{l-1}\rangle &= ||a_{l-1}|\phi_{l-1}\rangle + b_{l-1}|\phi_{l-2}\rangle||^2 \\ &= ||a_{l-1} + b_{l-1}||^2. \end{aligned} \tag{5.51}$$

Comparing Eq. (5.50) with Eq. (5.51), we obtain the following relation:

$$\sum_{i=0}^{l-1}\langle\phi_{l-1}|\mathcal{H}|\phi_i\rangle\langle\phi_i|\mathcal{H}|\phi_{l-1}\rangle = \langle\phi_{l-1}|\mathcal{H}\mathcal{H}|\phi_{l-1}\rangle, \tag{5.52}$$

which is equivalent to the statement that the sum over Lanczos states up to the index with $b_l = 0$ is complete, as expressed in Eq. (5.48).

5.5.2 Correlation functions in the Lanczos subspace

In general, a dynamical correlation function $I_{\mathcal{O}}(\omega)$ measures the response of a system described by the Hamiltonian $\mathcal{H}$ in its ground state $|\psi_0\rangle$ to some operator $\mathcal{O}$ at a frequency ω:

$$I_{\mathcal{O}}(\omega) = \langle\psi_0|\mathcal{O}^\dagger\delta\big(\omega - (\mathcal{H} - E_0)\big)\mathcal{O}|\psi_0\rangle. \tag{5.53}$$

The δ-function of an operator is only evaluable for diagonal operators. In principle, the calculation of $I_{\mathcal{O}}(\omega)$ requires therefore full knowledge of the energy spectrum of $\mathcal{H}$. To keep the computational effort, in case of numerical approaches, minimal, the Hilbert space of the Hamiltonian should be reduced as much as possible. The Lanczos method introduced above is a suitable method to reduce the dimensions of $\mathcal{H}$ to a subspace of states, that are relevant to describe the response of a system described by $\mathcal{H}$ to an operator $\mathcal{O}$. If it was possible to determine the relevant subspace for the response to the operator $\mathcal{O}$ exactly, the reduction onto the l-dimensional Lanczos subspace would be exact as well. However, in practice the Hilbert space of the operator and numerical errors introduce usually an approximative aspect already at this point of the procedure.

In the following, we distinguish between the full $d\times d$ dimensional Hamiltonian $\mathcal{H}$ and the smaller $l\times l$ dimensional Lanczos Hamiltonian $\mathcal{H}^{\mathrm{L}}$, with l Lanczos vectors $|\phi_i\rangle$. We assume the ideal case, where the full invariant subspace is fully determined. In this case, a projector $\mathbb{L}$ connects the two representations:

$$\mathcal{H}^{\mathrm{L}} = \mathbb{L}^\dagger \cdot \mathcal{H} \cdot \mathbb{L}. \tag{5.54}$$

To find an expression for the correlation function given by Eq. (5.53) in the Lanczos subspace, we first express the ground state $|\psi_0\rangle$ in terms of the initial Lanczos state $|\phi_0\rangle$. As pointed out above, the choice of the initial vector $|\phi_0\rangle$ for the Lanczos method determines the physics possible to calculate within the invariant subspace. For the correlation function, we are interested in the response of the system in the ground state to a certain operator $\mathcal{O}$. Fortunately, the choice for the initial state is therefore straightforward:

$$|\phi_0\rangle = \frac{\mathcal{O}|\psi_0\rangle}{\sqrt{\langle\psi_0|\mathcal{O}^\dagger\mathcal{O}|\psi_0\rangle}}. \tag{5.55}$$

Note, that we assumed here that the ground state $|\psi_0\rangle$ is known. The contribution of the Hamilton operator in the correlation function Eq. (5.53) can then be evaluated with respect to the first Lanczos vector as follows:

$$I_{\mathcal{O}}(\omega) = \langle\psi_0|\mathcal{O}^\dagger\mathcal{O}|\psi_0\rangle\,\langle\phi_0|\delta\big(\omega - (\mathcal{H} - E_0)\big)|\phi_0\rangle. \tag{5.56}$$

The expression in the δ-function can then be related to the invariant Krylov subspace through the projection operator $\mathbb{L}$,

$$\langle\phi_0|\delta\big(\omega - (\mathcal{H} - E_0)\big)|\phi_0\rangle = \langle\phi_0|\mathbb{L}^\dagger\delta\big(\omega - (\mathcal{H} - E_0)\big)\mathbb{L}|\phi_0\rangle, \tag{5.57}$$

where the equality holds for a fully explored, exactly determined Krylov space. The energy spectrum in the full Hilbert space depends on the eigenvectors of the full Hamiltonian $|\psi_n\rangle$:

$$\mathcal{H} = \sum_{n=0}^{d-1} E_n|\psi_n\rangle\langle\psi_n|. \tag{5.58}$$

Then, it is possible to define a set of eigenstates $|\varphi_\alpha\rangle$ of the Hamiltonian that lives in the invariant Krylov space and span therefore the eigenbasis of the reduced Hamiltonian $\mathcal{H}^L$. The overlap with the full eigenbasis can be evaluated by the following rule:

$$\langle\varphi_\alpha|\psi_n\rangle = \begin{cases} 0 & \text{if} \quad |\psi_n\rangle \notin \mathcal{K}_l \\ \delta_{L(\alpha),n} & \text{if} \quad |\psi_n\rangle \in \mathcal{K}_l \end{cases}, \tag{5.59}$$

where we introduced a mapping $L(\alpha \in \{0,\ldots,l-1\} \to n \in \{0,\ldots,d-1\})$ of the indices in the eigenbasis of the full Hamiltonian onto the eigenbasis of the reduced Hamiltonian. The projection onto the Krylov subspace can be expressed in terms of those states:

$$\mathbb{L} = \sum_{\alpha=0}^{l-1} |\varphi_\alpha\rangle\langle\varphi_\alpha|. \tag{5.60}$$

The δ-function in Eq. (5.57) can then be evaluated with respect to the reduced Krylov space using the spectral representation Eq. (5.58) of the Hamiltonian $\mathcal{H}$ and the projection operator as expressed above:

$$\begin{aligned}\langle\phi_0|\delta\big(\omega-(\mathcal{H}-E_0)\big)|\phi_0\rangle &= \sum_{n=0}^{d-1}\sum_{\{\alpha,\beta\}=0}^{l-1} \langle\phi_0|\varphi_\alpha\rangle\langle\varphi_\alpha|\psi_n\rangle\langle\psi_n|\varphi_\beta\rangle\langle\varphi_\beta|\phi_0\rangle\,\delta\big(\omega-(E_n-E_0)\big)\\ &= \sum_{n'=0}^{l-1} \langle\phi_0|\varphi_{n'}\rangle\langle\varphi_{n'}|\phi_0\rangle\,\delta\big(\omega-(E_{n'}-E_0)\big),\end{aligned} \tag{5.61}$$

where $n' = L(\alpha)$ corresponds to the index in the Krylov space that matches the eigenstates in the full Hilbert space. The correlation function as defined in Eq. (5.53), can then be determined via the following expression:

$$I^{\mathrm{L}}_{\mathcal{O}}(\omega) = \sum_{n'=0}^{l-1} |c_{n'}|^2\,\delta\big(\omega-(E_{n'}-E_0)\big), \tag{5.62}$$

where we introduced the coefficients c'_n as the positive root:

$$c_{n'} = \sqrt{\langle\psi_0|\mathcal{O}^\dagger\mathcal{O}|\psi_0\rangle}\,\langle\varphi_{n'}|\phi_0\rangle. \tag{5.63}$$

The Lanczos procedure reduces then to the determination of (i) the overlap of the operator $\mathcal{O}$ with the ground state $|\psi_0\rangle$, (ii) the l eigenenergies of the reduced Hamiltonian $E_{n'}$, and (iii) the overlap of the eigenstates $|\varphi_{n'}\rangle$ with the initial Lanczos state $|\phi_0\rangle$.

In practice, the Lanczos procedure is terminated at some point, which is not necessarily at the boundary of the invariant Krylov space. That the convergence of the Lanczos procedure is well-defined, follows from the correlation function in time:

$$I_{\mathcal{O}}(\omega) = \frac{1}{2\pi}\int_{-\infty}^{\infty} \mathrm{d}t\,\mathrm{e}^{i\omega t}\langle\psi_0|\mathcal{O}^\dagger(t)\mathcal{O}|\psi_0\rangle. \tag{5.64}$$

The time evolution of the operator $\mathcal{O}^\dagger(t) = \mathrm{e}^{-i\mathcal{H}t}\,\mathcal{O}\,\mathrm{e}^{i\mathcal{H}t}$ can be expanded in powers of the Hamiltonian using $\mathrm{e}^{i\mathcal{H}t} \approx \mathbb{1} + i\mathcal{H}t - \frac{1}{2}\mathcal{H}^2t^2 + \ldots$, so that the above expectation value hence consists of the squared norm of the state $(\mathbb{1} + i\mathcal{H}t - \frac{1}{2}\mathcal{H}^2t^2 + \ldots)\mathcal{O}|\psi_0\rangle$. This expression corresponds directly to sub-sequential construction of the Krylov subspace following the definition in Eq. (5.36), with the initial vector $|\phi_0\rangle$ as defined in Eq. (5.55). Terminating the Lanczos procedure corresponds therefore to a termination in the expansion of the time evolution operator. With typical values of $l = 100$, the accuracy of the expansion is in most cases sufficient from experience.

Off-diagonal spin correlation functions

We will see below that dynamical spin-spin correlation functions are needed to predict inelastic neutron scattering intensities theoretically. In the case of materials where spin-orbit coupling is important, off-diagonal spin correlation functions have to be considered. We generally describe a spin-spin correlation function, following the definition in Eq. (5.53), as follows:

$$\mathcal{S}_{\alpha\beta}(\mathbf{q},\omega) = \langle\psi_0|\hat{S}^\dagger_\alpha(\mathbf{q})\delta(\omega-(\mathcal{H}-E_0))\hat{S}_\beta(\mathbf{q})|\psi_0\rangle, \tag{5.65}$$

where the operators $\mathcal{O}$ are q-dependent spin operators $\hat{S}(\mathbf{q})$ with $\alpha, \beta = \{x, y, z\}$. However, to implement off-diagonal cases $\alpha \neq \beta$ in the Lanczos procedure directly is computationally very demanding. Instead, it is possible to determine off-diagonal correlation functions with a simple trick. Numerically, enough diagonal spin-spin correlations can be computed to create a system of equations that allows to determine all six, since they should be symmetrical, independent spin-spin correlation functions. Next to $\mathcal{S}_{xx}(\mathbf{q}, \omega)$, $\mathcal{S}_{yy}(\mathbf{q}, \omega)$ and $\mathcal{S}_{zz}(\mathbf{q}, \omega)$ we also considered:

$$\mathcal{S}_{x+y}(\mathbf{q}, \omega) = \langle\psi_0|(\hat{S}_x(\mathbf{q}) + \hat{S}_y(\mathbf{q}))^\dagger \delta(\omega - (\mathcal{H} - E_0))(\hat{S}_x(\mathbf{q}) + \hat{S}_y(\mathbf{q}))|\psi_0\rangle, \tag{5.66}$$

$$\mathcal{S}_{x+z}(\mathbf{q}, \omega) = \langle\psi_0|(\hat{S}_x(\mathbf{q}) + \hat{S}_z(\mathbf{q}))^\dagger \delta(\omega - (\mathcal{H} - E_0))(\hat{S}_x(\mathbf{q}) + \hat{S}_z(\mathbf{q}))|\psi_0\rangle, \tag{5.67}$$

$$\mathcal{S}_{y+z}(\mathbf{q}, \omega) = \langle\psi_0|(\hat{S}_y(\mathbf{q}) + \hat{S}_z(\mathbf{q}))^\dagger \delta(\omega - (\mathcal{H} - E_0))(\hat{S}_y(\mathbf{q}) + \hat{S}_z(\mathbf{q}))|\psi_0\rangle. \tag{5.68}$$

The off-diagonal structure factor with different operators acting on the right-hand and left-hand side of the correlation function in Eq. (5.53), follows then from the relation:

$$\mathcal{S}_{x+y}(\mathbf{q}, \omega) = \mathcal{S}_{xx}(\mathbf{q}, \omega) + \mathcal{S}_{xy}(\mathbf{q}, \omega) + \mathcal{S}_{yx}(\mathbf{q}, \omega) + \mathcal{S}_{yy}(\mathbf{q}, \omega). \tag{5.69}$$

With $\mathcal{S}_{xx}(\mathbf{q}, \omega)$ and $\mathcal{S}_{yy}(\mathbf{q}, \omega)$ known, the symmetrical off-diagonal contribution $\mathcal{S}_{xy}(\mathbf{q}, \omega) + \mathcal{S}_{yx}(\mathbf{q}, \omega)$ is fully determined. The same is true for the other off-diagonal contributions:

$$\mathcal{S}_{xz}(\mathbf{q}, \omega) + \mathcal{S}_{zx}(\mathbf{q}, \omega) = \mathcal{S}_{x+z}(\mathbf{q}, \omega) - \mathcal{S}_{xx}(\mathbf{q}, \omega) - \mathcal{S}_{zz}(\mathbf{q}, \omega), \tag{5.70}$$

$$\mathcal{S}_{yz}(\mathbf{q}, \omega) + \mathcal{S}_{zy}(\mathbf{q}, \omega) = \mathcal{S}_{y+z}(\mathbf{q}, \omega) - \mathcal{S}_{yy}(\mathbf{q}, \omega) - \mathcal{S}_{zz}(\mathbf{q}, \omega). \tag{5.71}$$

As we will see below, it is absolutely crucial to work with off-diagonal dynamical structure factors in order to be able to relate any theoretical result to INS experiments due to the off-diagonal Γ and Γ' terms in the spin Hamiltonian of α-$RuCl_3$. This is not true for systems that can be well described solely by Heisenberg interactions. For this reason, sometimes correlation functions like $\mathcal{S}_{zz}(\mathbf{q}, \omega)$ are directly compared to INS results, which only justified in specific cases.

5.5.3 Correspondence to INS intensity

Inelastic neutron scattering is a powerful experimental tool to analyze the magnetic properties of materials. Here, we briefly sketch how the INS intensity $\mathcal{I}(\mathbf{q}, \omega)$ can be related to the theoretically available dynamical spin structure factor $\mathcal{S}_{\alpha\beta}(\mathbf{q}, \omega)$. Details of the derivation are, for example, available from Refs. [255, 256].

In neutron scattering experiments, neutrons of a specific energy pass through a target, which is the subject of the study. Most neutrons do not participate in more than one scattering event, which allows them to penetrate the sample deeply without disturbing the magnetic properties too much. Neutrons interact with the sample via interaction of their spin with the magnetic field caused by unpaired electrons in the sample. The scattered neutrons may be resolved according to the scattered direction, but independently of their final energy. In this case, the experiment is referred to as neutron diffraction. This allows to determine, for example, magnetic ordering, or more general the mean values of the magnetic-moment vectors on different atomic sites. With additional energy resolution, the experiment is referred to as inelastic neutron scattering and allows, through the additional energy and momentum conservation, to measure the dispersion relation of magnetic excitations.

Since the interaction of neutrons with matter is in general relatively weak, an appropriate starting point is Fermi's Golden Rule as a result of time-dependent perturbation theory in the first Born approximation. Fermi's Golden Rule states that the scattering probability, or differential cross-section, is proportional to the square of the matrix element of the interaction operator $\mathcal{H}_{\text{int}}$ of the neutron with the sample, sandwiched in the initial ($|i\rangle$) and the final ($|f\rangle$) state of the sample:

$$\frac{\mathrm{d}^2\sigma}{\mathrm{d}\Omega \mathrm{d}\omega} = \left(\frac{m}{2\pi}\right)^2 \frac{k'}{k} \sum_{i,\sigma} \sum_{f,\sigma'} p_i |\langle \mathbf{k}\sigma; i|\mathcal{H}_{\text{int}}(\mathbf{q})|\mathbf{k}'\sigma'; f\rangle|^2 \delta(\omega + E_i - E_f), \tag{5.72}$$

where $\{\mathbf{k}\sigma, \mathbf{k}'\sigma'\}$ are the spin and momentum states of the incoming and scattered neutrons respectively, and p_i is the thermal population factor. The δ-function ensures energy conservation and the prefactor

$\left(\frac{m}{2\pi}\right)^2 \frac{k'}{k}$ stems essentially from momentum conservation. The interaction operator of the scattering wave vector follows from Fourier transformation over the neutron positions, $\mathcal{H}_{\text{int}}(\mathbf{q}) = \int \mathcal{H}_{\text{int}}\, \mathrm{e}^{-i\mathbf{q}\cdot\mathbf{r}_n}\, \mathrm{d}\mathbf{r}_n$.

As mentioned above, the neutron spin interacts with the sample through the magnetic field caused by moving unpaired electrons. The magnetic dipole moment due to the electron at $\mathbf{r}_e$ generates at the neutron position $\mathbf{r}_n$ a vector potential $\mathbf{A}_n = \vec{\mu}_n \times \mathbf{r}/r^3$, with $\mathbf{r} = \mathbf{r}_e - \mathbf{r}_n$. The magnetic interaction of a neutron with a single electron with momentum $\mathbf{p}$ and spin $\mathbf{s}$ can be approximated[4] by minimal coupling and the Zeeman interaction:

$$\mathcal{H}_{\text{int}} = 2\mu_B \left(\mathbf{A}_n \cdot \mathbf{p} + \mathbf{s} \cdot (\nabla \times \mathbf{A}_n)\right). \tag{5.73}$$

Using the expression for $\mathbf{A}_n$, Fourier transformation and algebraic rearrangements [255], lead to an interaction Hamiltonian in terms of the scattering wave vector $\mathbf{q}$:

$$\mathcal{H}_{\text{int}}(\mathbf{q}) = 8\pi\mu_B \vec{\mu}_n \cdot \left(\frac{i}{q}\hat{\mathbf{q}} \times \mathbf{p} + \hat{\mathbf{q}} \times \mathbf{s} \times \hat{\mathbf{q}}\right) \mathrm{e}^{-i\mathbf{q}\cdot\mathbf{r}_e}, \tag{5.74}$$

where $\hat{\mathbf{q}}$ is the unit vector in the direction of $\mathbf{q}$. To evaluate the matrix element $\langle \mathbf{k}\sigma; i|\mathcal{H}_{\text{int}}(\mathbf{q})|\mathbf{k}'\sigma'; f\rangle$, we assume that $|i\rangle$ and $|f\rangle$ are linear combinations of states of the form $|(nls)m_l m_s\rangle$, where the quantum numbers (nls) are approximated to be constant. Expanding the plane wave $\mathrm{e}^{-i\mathbf{q}\cdot\mathbf{r}_e}$ in terms of spherical Bessel functions $j_\alpha(q)$ allows to identify the form factor $F(q) = \langle j_0(q)\rangle + \frac{1}{g}(2-g)\langle j_2(q)\rangle$ and leads to the following expression:

$$\langle \mathcal{H}_{\text{int}}(\mathbf{q})\rangle = 8\pi\mu_B \sum_j [\frac{1}{2} g F(q)]_j \, \langle \mathrm{e}^{-i\mathbf{q}\cdot\tilde{\mathbf{R}}_j}\, \vec{\mu}_n \cdot (\hat{\mathbf{q}} \times \mathbf{J}_j \times \hat{\mathbf{q}})\rangle, \tag{5.75}$$

where g is the Landé factor, $\mathbf{J} = \frac{1}{g}(\mathbf{L} + 2\mathbf{S})$ is the total angular momentum, and $\tilde{\mathbf{R}}_j = \mathbf{r}_e - \mathbf{r}$ the position of the j^{th} atom.

For unpolarized neutrons, the excited spin states $|\sigma'\rangle$ should be summed up, therefore the cross-section is proportional to the following expression:

$$\begin{aligned}\sum_{\sigma\sigma'} p_\sigma |\langle\sigma|\vec{\mu}_n \cdot (\hat{\mathbf{q}} \times \mathbf{J}_j \times \hat{\mathbf{q}})|\sigma'\rangle|^2 &= \sum_\sigma p_\sigma \langle\sigma|(\vec{\mu}_n \cdot (\hat{\mathbf{q}} \times \mathbf{J}_j \times \hat{\mathbf{q}}))(\vec{\mu}_n \cdot (\hat{\mathbf{q}} \times \mathbf{J}_{j'} \times \hat{\mathbf{q}}))|\sigma\rangle \\ &= \left(\frac{1}{2} g_n \mu_N\right)^2 \sum_{\alpha\beta} (\delta_{\alpha\beta} - \frac{q_\alpha q_\beta}{q^2}) J_{j\alpha} J_{j'\beta}.\end{aligned} \tag{5.76}$$

The term $\sum_{\alpha\beta}(\delta_{\alpha\beta} - \frac{q_\alpha q_\beta}{q^2})$ in the final line is commonly referred to as the polarization factor. Using Eq. (5.76) and Eq. (5.75) as concrete expressions for the interaction operator in the differential cross-section given by Eq. (5.72), we obtain:

$$\begin{aligned}\frac{\mathrm{d}^2\sigma}{\mathrm{d}\Omega \mathrm{d}\omega} = \frac{k'}{k}\left(\frac{\gamma e^2}{mc^2}\right)^2 &\sum_{\alpha\beta} (\delta_{\alpha\beta} - \frac{q_\alpha q_\beta}{q^2}) \sum_{jj'} [\frac{1}{2} g F(q)]_j [\frac{1}{2} g F(q)]_{j'} \\ &\times \sum_{i,f} p_i \langle i|J_{j\alpha}\, \mathrm{e}^{-i\mathbf{q}\cdot\tilde{\mathbf{R}}_j}\, |f\rangle\langle f|J_{j'\beta}\, \mathrm{e}^{i\mathbf{q}\cdot\tilde{\mathbf{R}}_{j'}}\, |i\rangle \delta(\omega + E_i - E_f),\end{aligned} \tag{5.77}$$

where γ the gyromagnetic ratio of the neutron. If the magnetic atoms are identical, the magnetic form factor does not depend on j, j', and we can identify the Fourier transform to reciprocal space of the angular momentum operators, such as $\sum_j \mathrm{e}^{-i\mathbf{q}\cdot\tilde{\mathbf{R}}_j} J_{j\alpha} = J_\alpha(\mathbf{q})$.

Next, we draw the connection to the pseudo-spin Hamiltonian of the sample by approximating the angular momentum operator with the pseudo-spin operator, and with the initial state as the ground

[4] Here, we assume no external field and the interaction with a single electron. For a more detailed derivation see Ref. [255].

state in pseudo-spin space $|i\rangle = |\psi_0\rangle$ with $p_i = 1$. Via rearrangement of the spin-spin correlation function given in Eq. (5.65):

$$\begin{aligned}\mathcal{S}_{\alpha\beta}(\mathbf{q},\omega) &= \langle\psi_0|\hat{S}^\dagger_\alpha(\mathbf{q})\delta(\omega-(\mathcal{H}-E_0))\hat{S}_\beta(\mathbf{q})|\psi_0\rangle \\ &= \langle\psi_0|\hat{S}^\dagger_\alpha(\mathbf{q})\delta(\omega-(\sum_n E_n|n\rangle\langle n|-E_0))\hat{S}_\beta(\mathbf{q})|\psi_0\rangle \\ &= \sum_n \langle\psi_0|\hat{S}^\dagger_\alpha(\mathbf{q})|n\rangle\langle n|\hat{S}_\beta(\mathbf{q})|\psi_0\rangle\delta(\omega-(E_n-E_0)),\end{aligned} \tag{5.78}$$

we can identify the theoretically accessible dynamical spin structure factor in Eq. (5.77) and relate it to the differential cross-section. The differential cross-section is for the assumptions above equal to the neutron scattering intensity for unpolarized neutrons and hence proportional to the following expression:

$$\mathcal{I}(\mathbf{q},\omega) \propto F^2(\mathbf{q}) \sum_{\alpha,\beta}\left(\delta_{\alpha\beta}-\frac{q_\alpha q_\beta}{q^2}\right)\mathcal{S}_{\alpha\beta}(\mathbf{q},\omega). \tag{5.79}$$

5.6 Magnetic excitations in α-$RuCl_3$

With a method available to predict theoretically inelastic neutron scattering intensities based on different spin models, we gained a powerful tool to combine *ab-initio* insights based on crystal structures with experimental observations. ED studies prior to the one presented in this chapter [81] focused mainly on static properties or on a specific choice of parameter sets [221, 225, 228, 247, 257]. Here, we focused on the dynamical response observed in α-$RuCl_3$. In this case, the observation of a broad continuum in the INS spectra caused speculations about proximity to the Kitaev spin-liquid. On the other hand, it is known that α-$RuCl_3$ magnetically orders at low temperatures, raising the question which additional terms are relevant in an effective spin Hamiltonian and how far away the material actually is from the desired QSL state. As pointed out before, the conventional approach to interpret INS spectra with linear spin wave theory (LSWT) is questionable, since quantum fluctuations beyond LSWT should naturally play an important role in a spin-liquid state. The option to include these quantum fluctuations with the method of exact diagonalization provides the option to check possible models, guided by *ab-initio* insights. In order to judge the influence of quantum fluctuation systematically, we compared the ED intensities with LSWT intensities, calculated by Stephen M. Winter. Note, that in principle three patterns of the AFM zigzag order are realizable. On finite clusters in the ED calculations, the ground state consists of a linear combination of these three domains, with ordering wave vector $\mathbf{Q} = \{\mathrm{Y}, \mathrm{M}, \mathrm{M}'\}$ (see also Fig. 6.10(a)), since spontaneous symmetry breaking is not possible away from the thermodynamic limit. In the case of the LSWT calculations, in principle one of these orders has to be chosen. In order to enable comparison with ED results, the LSWT results were therefore averaged over the three ordering wave vectors.

In this section, we present the investigation of a series of models, which can be divided in three groups, according to the restrictions on the parameter sets in the extended Kitaev model given by Eq. (5.33):

$$\mathcal{H} = \sum_{\langle ij\rangle} J_1\ \mathbf{S}_i\cdot\mathbf{S}_j + K_1\ S_i^\gamma S_j^\gamma + \Gamma_1\ (S_i^\alpha S_j^\beta + S_i^\beta S_j^\alpha) + \sum_{\langle\langle\langle ij\rangle\rangle\rangle} J_3\ \mathbf{S}_i\cdot\mathbf{S}_j. \tag{5.80}$$

Note, that in this model we assumed a C_3 symmetry that is not present in the real material α-$RuCl_3$. This strategy was chosen in order to reduce the number of free parameters.

First, we started with AFM Kitaev models with the nearest neighbour Heisenberg exchange J_1 as the only additional parameter (nnHK models). This parameter space was proposed in the original analysis of the powder INS data [231]. In the second group of models, we considered additionally nearest neighbour Γ_1 and third nearest neighbour Heisenberg exchange J_3 (AFM extended Kitaev models). Finally, we investigated models with FM Kitaev interaction, inspired by *ab-initio* results and consistent with the Jackeli-Khalliulin mechanism (FM extended Kitaev models). All of these models were checked against

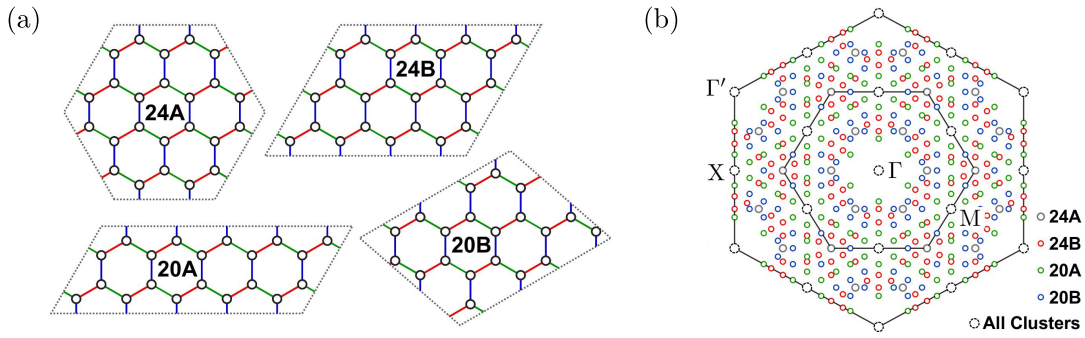

Figure 5.8: (a) Clusters used with periodic boundary conditions for the exact diagonalization calculations. (b) **q**-points according to the respective clusters shown in (a), high-symmetry points which result from all clusters are indicated with All Clusters. Figure (a,b) adapted from Ref. [81].

key experimental features, shown in Fig. 5.6 and Fig. 5.7: (i) The broad continuum of excitations at the Γ-point, (ii) the six-fold star in reciprocal space at intermediate energies, (iii) the two significant features of the Γ-point intensity at $E = 4\,\text{meV}$ and $E = 6\,\text{meV}$. Additionally, we considered only models that have the zigzag magnetic order as a ground state according to the phase diagram in Fig. 5.5. In this figure, the studied models are indicated as blue and red dots. The red dots indicate Model 1 and Model 2, discussed in more detail below. All of the studied models are also listed in Table 5.2. The main results presented in this section are published in Ref. [81].

5.6.1 Details of Exact Diagonalization Calculations

The general expression for inelastic neutron scattering intensity $\mathcal{I}(\mathbf{q},\omega)$ for a specific spin Hamiltonian is given by Eq. (5.79), where we employed the atomic form factor $F(\mathbf{q})$ for Ru^{3+} from Ref. [258].

The exact diagonalization calculations presented in this section were performed for the six spin-spin correlation functions necessary to capture all off-diagonal contributions to $\mathcal{I}(\mathbf{q},\omega)$. Next to the diagonal contributions $\mathcal{S}_{xx}(\mathbf{q},\omega)$, $\mathcal{S}_{yy}(\mathbf{q},\omega)$, and $\mathcal{S}_{zz}(\mathbf{q},\omega)$, we calculated therefore $\mathcal{S}_{xy}(\mathbf{q},\omega)+\mathcal{S}_{yx}(\mathbf{q},\omega)$, $\mathcal{S}_{xz}(\mathbf{q},\omega)+\mathcal{S}_{zx}(\mathbf{q},\omega)$, and $\mathcal{S}_{yz}(\mathbf{q},\omega)+\mathcal{S}_{zy}(\mathbf{q},\omega)$ via the system of equations given by Eq. (5.69), Eq. (5.70), and Eq. (5.71). The spin-spin correlation functions were calculated with the Lanczos method for dynamical correlation functions introduced in Section 5.5 in a pseudo-spin basis. The ground state of the full system $|\psi_0\rangle$ and the exact diagonalization of the reduced Hamiltonian $\mathcal{H}^L$ were calculated with the scipy library in python. For the ED calculations, we considered four different cluster shapes, shown in Fig. 5.8(a) and employed periodic boundary conditions. The cluster referred to as 24A consists of 24 sites and contains the full symmetry of the honeycomb lattice. In contrast, the clusters 24B, 20A, and 20B break this symmetry. For the simplified model we employed the D_{3d} point group, which contains the symmetry operations $\{E, 2C_3, 3C_2', i, 2S_6, 3\sigma_d\}$. With these symmetry operations we generated symmetry related clusters to 24B, 20A, and 20B, improving the resolution in reciprocal space, as shown in Fig. 5.8(b). The results for the q-points that live on all clusters were averaged.

In contrast to early studies using the dynamical Lanczos method, computational techniques allow to exactly diagonalize the reduced Hamiltonian in the invariant subspace $\mathcal{H}^L$. In general, we considered a Lanczos space with 100 Lanczos vectors. We also checked selected results with up to 1000 vectors and ensured that the presented INS intensities were converged. The method introduced in Section 5.5 was formulated for the ideal case of exactly determined Lanczos vectors. However, in practice numerical uncertainties cause the well-known problem of non-orthogonality between the Lanczos vectors. Since the orthogonality is only guaranteed for the three "connected" Lanczos vectors, the non-orthogonality can be inherited by new Lanczos vectors dramatically. Fortunately, it turns out that the eigenvalues are in general not strongly modified by this issue. Also, when the invariant Lanczos subspace would be, in principle, fully explored, in practice the eigenvalues are determined multiple times with the sum of the weights — in terms of the coefficients c_n — constant. The much reduced size of $\mathcal{H}_L$ has the consequence

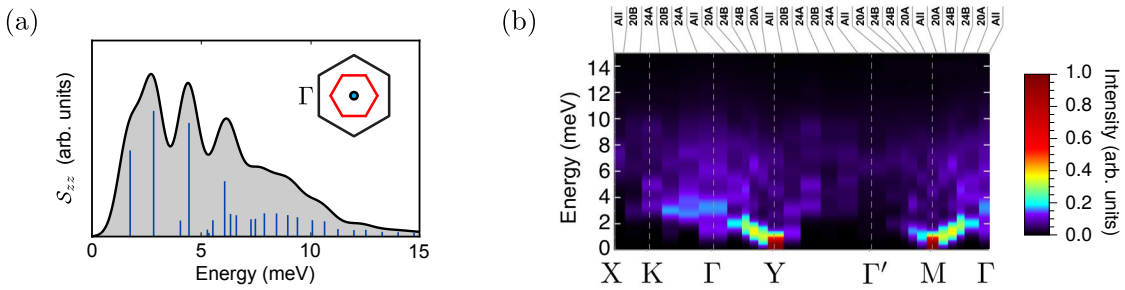

Figure 5.9: Procedure to extract INS intensity from ED calculations on the example of Model 2. (a) Spin-spin correlation function $\mathcal{S}_{zz}(\mathbf{q} = \Gamma, \omega)$ on cluster 24A, with Gaussian broadening with $\sigma = 0.5\,\text{meV}$ shown in black. The delta peaks from ED are shown in blue, scaled in terms of the intensity $\langle\psi_0|\hat{S}^\dagger_\alpha(\mathbf{q})\hat{S}_\alpha(\mathbf{q})|\psi_0\rangle|c_n(\mathbf{q})|^2$, compare with Eq. (5.81), and rescaled by a factor of 3. (b) Example case of INS intensity $\mathcal{I}(\mathbf{k}, \omega)$ with the intensity colour-coded, along the indicated path in reciprocal space. The clusters used in the ED calculation are indicated. For high-symmetry points living on all cluster, the intensities were averaged. Fig. (b) adapted from Ref. [81].

that it is not a technical challenge to directly diagonalize the matrix representing the correlation function. As a consequence, the numerical results are δ-peaks, which can then be broadened with any method of choice. In order to keep the results as close as possible to the experimental conditions, we employed a Gaussian broadening of the δ-peaks determined by the Lanczos method:

$$\mathcal{S}_{\alpha\alpha}(\mathbf{q}, \omega) = \sum_n \langle\psi_0|\hat{S}^\dagger_\alpha(\mathbf{q})\hat{S}_\alpha(\mathbf{q})|\psi_0\rangle|c_n(\mathbf{q})|^2 \frac{1}{\sigma\sqrt{2\pi}} \mathrm{e}^{-\frac{1}{2}((\omega-(E_n-E_0))/\sigma)^2}, \tag{5.81}$$

where we chose the broadening factor $\sigma = 0.5\,\text{meV}$, consistent with the width in experiment. In Fig. 5.9(a) we show as an example the broadening procedure for $\mathcal{S}_{zz}(\mathbf{q}, \omega)$ at the Γ-point for Model 2.

In Fig. 5.9(b), we show an example figure of a calculated INS intensity based on the broadened spectra from spin-spin correlation functions used in the general expression for INS intensities in Eq. (5.79). The colour scheme for the INS intensities were chosen to match the experimental colour scheme in Ref. [46, 231]. The intensities for each q-point could be obtained from at least one of the four clusters, as illustrated in Fig. 5.9(b). Finite size effects cause that the intensities are not entirely smoothly connected between different cluster shapes.

The figures in reciprocal space, where the intensities were integrated over specific energy windows $E = 1.3$–2.3, 5.5–8.5, and 10.5+ meV (e.g. Fig. 5.10(c), Fig 5.13(c)), were based only on results obtained from cluster 24A, in order to avoid kinks due to the integration process on different cluster shapes. The out-of-plane momentum arises in theory only from the atomic form factor and was integrated over the same range as in experiment. The energy window for the integration of the energy was chosen differently from the ones used in experiment in Ref. [231]. However, due to finite size effects, which modify the energy gap from the thermodynamic limit, a reasonable comparison was only possible for shifted energy windows. Note, that we also checked different energy windows and were not able to reproduce the experiment better within the AFM Kitaev term models.

In general, it is very difficult to perform a controlled finite size scaling for the presented calculations. Especially for models that include third nearest neighbour interactions, 20-site clusters suffer already from relatively strong finite size effects. Therefore, it is not reasonable to include clusters with a lower site number in the analysis. Another requirement is that a zigzag antiferromagnetic order can be realized on the cluster, so that the experimental ground state is, in principle, considered in the calculations. This restricts the possible periodic clusters to a site number with a multiple of four sites. Numerical costs and time, on the other hand, increase substantially for clusters with more than 24 sites, so that there are simply not enough data points to obtain a reasonable scaling in terms of system size. Nevertheless, on high-symmetry points like the Γ- and the M-point, which live on all considered clusters, it is possible to check trends, see e.g. Fig. 5.11(d,h,l,p). In general, we found that the lowest peak positions are

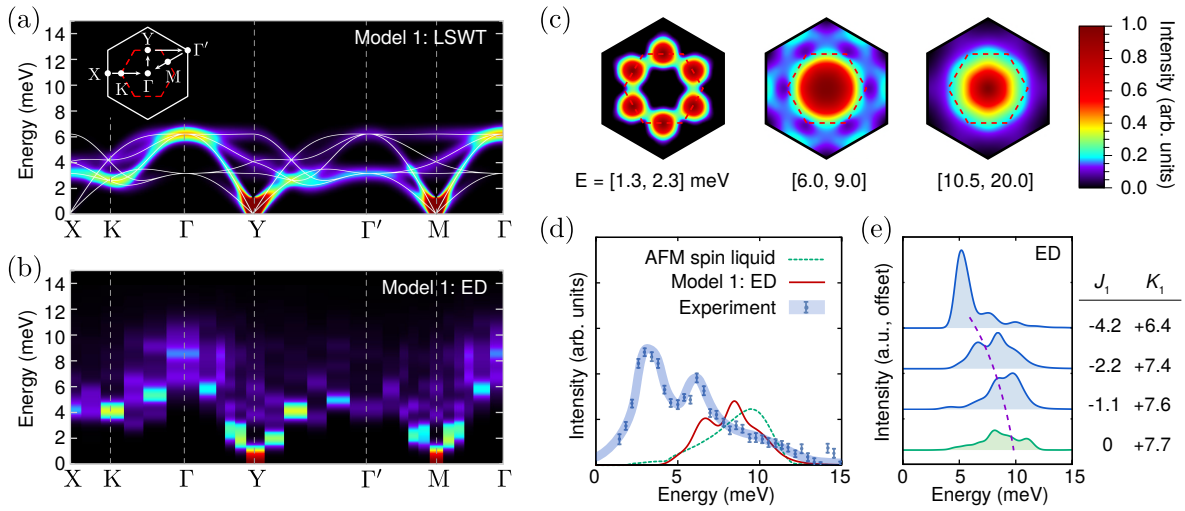

Figure 5.10: INS intensity $\mathcal{I}(\mathbf{k},\omega)$ for Model 1 $(J_1, K_1, \Gamma_1, J_3) = (-2.2, +7.4, 0.0, 0.0)$ meV as an example for the nnHK models. In each figure, the color scale is independently normalized. (a) INS intensity from LSWT for indicated path in reciprocal space, (b) $\mathcal{I}(\mathbf{k},\omega)$ from ED, (c) ED intensity integrated over the indicated energies windows, obtained from cluster 24A with the first Brillouin zone indicated by the dashed red line, (d) comparison of Γ-point intensity for AFM spin liquid, Model 1, and experiment [231], (e) Γ-point intensities for indicated model parameters. Fig. adapted from Ref. [81].

relatively well converged, especially in comparison to the Gaussian broadening factor of 0.5 meV. We observed deviations for the higher-energy peaks, which could be partly compensated by averaging. Note, however, that this is only possible at the high-symmetry points in reciprocal space.

5.6.2 Nearest neighbour Heisenberg-Kitaev (nnHK) models

When it was realized that the pure Kitaev honeycomb model could be realized in real materials such as α-$RuCl_3$, it was a reasonable approach to model the magnetic properties of α-$RuCl_3$ as close as possible to the desired "pure" case. However, it was clear that additional magnetic interactions terms are important, since the compound magnetically orders. According to the phase diagram in Section 5.3, a nearest neighbour Heisenberg exchange J_1 could drive the system into the ordered zigzag phase for an AFM Kitaev term with $K_1 > 0$. This motivated also the first proposal obtained via spin-wave fitting from Banerjee *et al.* [231]. We investigated one of their proposed models and discuss it in detail further below.

Model 1

In Fig. 5.10, we show with Model 1 $(J_1, K_1, \Gamma_1, J_3) = (-2.2, +7.4, 0.0, 0.0)$ meV the results for a representative of the nnHK models. In contrast to the hope that quantum fluctuations would induce a strong continuum of excitations at the Γ-point, the LSWT calculations, shown in Fig. 5.10(a), agree relatively well with the ED calculations, shown in Fig. (b). The spectrum reveals sharp features, especially in the environment of the q-points that correspond to the pseudo-Goldstone modes of zigzag order, Y and M. With that, the correct ground state was confirmed. With the theoretical INS intensity for Model 1 predicted, the experimental features observed in Ref. [46, 231] could be tested. (i) The continuum at the Γ-point is not well reproduced. In addition, the ED intensity at the Γ-point is located at high energies with $E > 5$ meV, in contrast to experiment. This becomes more clear considering the integrated INS intensity shown in Fig. 5.10(c). For the lowest energy window, $E = [1.3, 2.3]$ meV, there is no intensity at the Γ-point, while in experiment there is a very strong feature (see Fig. 5.7(b)). (ii) The six-fold star at the intermediate energy window, $E = [6.0, 9.0]$ meV, is not reproduced as well. In this energy region,

the Γ-point intensity dominates the first Brillouin zone almost entirely. (iii) The two significant features of the Γ-point are in principle reproduced, shown in Fig. (d). However, they are shifted to much higher energies and resemble more the pure AFM spin liquid case, as shown in Fig. (e).

In order to obtain more insight how the interplay of the two parameters K_1 and J_1 influence the spectrum, we performed these calculations for a series of models in the nnHK family. The Γ-point intensity obtained from ED calculations is shown in Fig. 5.10(e) for three models and the exact AFM Kitaev solution [220, 259]. These models are normalized to $\sqrt{J_1^2 + K_1^2} = 7.7\,\text{meV}$, below we motivate this choice. Note, that condition (iii) is less fulfilled the closer the parameter ratio $|J_1/K_1|$ approaches the Kitaev spin-liquid limit.

Series of nnHK models

In order to check systematically for the experimental features (i), (ii), and (iii) and to gain intuition about the interplay of the exchange parameters, we show detailed results for four models, including the AFM spin-liquid, in Fig. 5.11. To include the model proposed originally in Ref. [231], we normalized in these cases the parameters to $\sqrt{J_1^2 + K_1^2} = 8.4\,\text{meV}$. However, the parameter ratio $|J_1/K_1|$ matches the models shown in Fig. 5.10(e). An overall feature of this type of models is the surprsingly good agreement between ED and LSWT calculations. This can be explained with a dual transformation relation at $K_1 = -2J_1$ noted in Ref. [248].

The results for the model proposed by Banerjee *et al.* [231] with $(J_1, K_1) = (-4.6, +7.0)\,\text{meV}$ are shown in Fig. 5.11(a-d). Then, we tuned the parameter ratio $|J_1/K_1|$ toward the pure AFM Kitaev model, shown in Fig. (m-p). Note, that Fig. (m) and (o) show exact solutions from Ref. [220, 259]. As validated by the pseudo-Goldstone modes at Y- and M-points, all models — except for those with the KSL ground state — have the AFM zigzag order as their ground state. Next, we discuss the evolution of the desired experimental features approaching the spin-liquid case. (i) The broad excitation continuum at the Γ-point is not observable in Fig. (b), instead the ED intensity shows sharp signatures for the originally proposed model. Approaching the pure Kitaev limit, the excitations become more washed out, but are also lifted to higher energies, see Fig. (f,j,n). In Fig. (a,e,i,m), this is illustrated by the consistent absence of Γ-point intensity in the low-energy window. (ii) In the second Brillouin-zone a six-fold star feature is observable in Fig. (a), but with the low intensities at the Y- and M-points and high intensities at the X-point. Approaching the pure Kitaev limit, these features gain a circular shape, loosing the star feature altogether. This becomes also evident from Fig. (d,h,l,p), where the weight on the X-point at intermediate energies is very pronounced, in contrast to the weight on the M-, and Y-point for all models. The Γ-point intensity is shifted towards higher energies, approaching the AFM KSL limit. The most significant case with two distinct features is obtained in Fig. (h) for $(J_1, K_1) = (-2.4, +8.0)\,\text{meV}$. This is the reason why we discussed the rescaled version of this model above in more detail. However, the energy range does not match the experiment, and an interpretation in terms of underlying Majorana excitations seems questionable in the context of the broad continuum at much higher energies for the AFM Kitaev spin-liquid case.

As mentioned above, the low-energy peaks for the high-symmetry points are relatively well converged between the different clusters 24A, 24B, 20A, and 20B. In order to illustrate this, and also to draw attention to the limitations of the approach presented here, we show in Fig. (d,h,l,p) the INS intensities at high-symmetry points resolved according to the cluster they are obtained from.

In summary, for the nnHK models none of the experimentally observed key features of α-$RuCl_3$ could be reproduced, and the trends seem to become worse for parameter sets approaching the spin-liquid limit. This observation suggests that the parameter space of the nnHK models was chosen too small and additional terms, as suggested consistently from *ab-initio* studies, should be taken into account.

5.6.3 Extended AFM Kitaev models

According to the phase diagram in Fig. 5.5, the zigzag ground state can be stabilized over an extended region for a finite $J_3 > 0$, under consideration of a finite Γ_1 term. Next, we investigated the type of models suggested by *ab-initio* studies based on the early $P3_112$ space group, see also Table 5.1, with an antiferromagnetic Kitaev term within an extended spin Hamiltonian: $(J_1, K_1 > 0, \Gamma_1, J_3)$. To

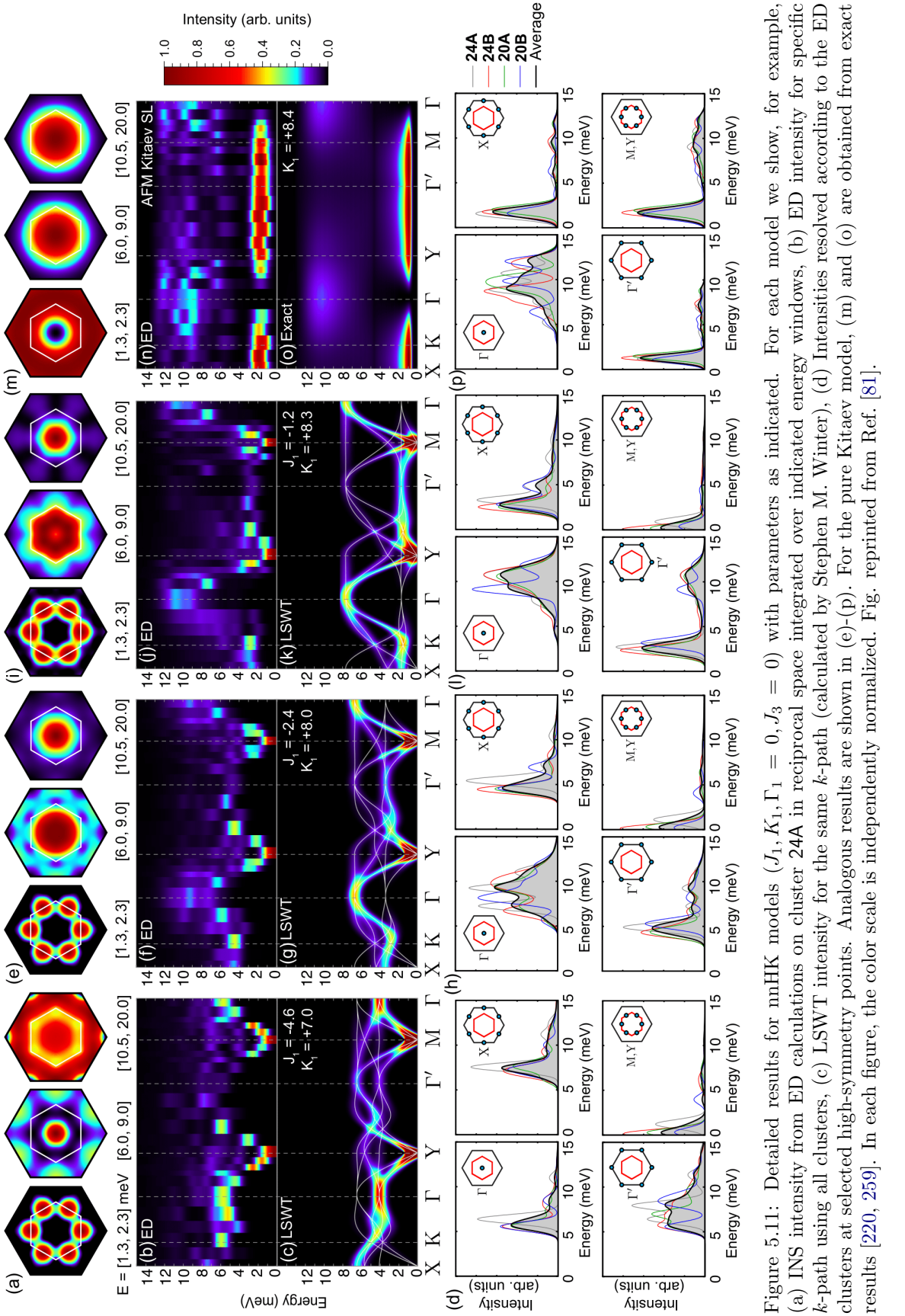

Figure 5.11: Detailed results for nnHK models ($J_1, K_1, \Gamma_1 = 0, J_3 = 0$) with parameters as indicated. For each model we show, for example, (a) INS intensity from ED calculations on cluster 24A in reciprocal space integrated over indicated energy windows, (b) ED intensity for specific k-path using all clusters, (c) LSWT intensity for the same k-path (calculated by Stephen M. Winter), (d) Intensities resolved according to the ED clusters at selected high-symmetry points. Analogous results are shown in (e)-(p). For the pure Kitaev model, (m) and (o) are obtained from exact results [220, 259]. In each figure, the color scale is independently normalized. Fig. reprinted from Ref. [81].

study the consequences of the involved parameters, we started from the nnHK model suggested by Banerjee *et al.* [231] and tuned the parameters towards a model with $K_1 = \Gamma_1$ and finite $J_3 = 0.7\,\text{meV}$, which was kept constant during the tuning process. For all models with finite J_3 we kept the norm $\sqrt{J_1^2 + K_1^2 + \Gamma_1^2 + J_3^2} = 8.5\,\text{meV}$ fixed.

An overall observation is the poor agreement of LSWT and ED intensities tuning away from the pure nnHK model limit. This is consistent with the explanation above, that the nnHK models are close to a SU(2) dual transformation that vanishes for a significant Γ_1 interaction. One important conclusion at this point was already, that for the analysis of models with strong off-diagonal contributions other methods than LSWT, which take quantum fluctuations properly into account, are necessary. On the LSWT level, the two models with finite Γ_1, shown in Fig. 5.12(k,o) have no pseudo-Goldstone modes at the M(Y)-points, although the ED results in Fig. (j,n) suggest a strong intensity at these points in agreement with the ground state suggested by the phase diagram. A possible explanation for this observation is the proximity to the 120° order, where quantum fluctuations are probably important to capture the extension of the zigzag order.

Next, we analysed the features of the different models with respect to the experimental key features. (i) To study the existence of a broad continuum at the Γ-point, we considered the ED intensities shown in Fig. 5.12(b,f,j,n). Adding a finite $J_3 = 0.7\,\text{meV}$ pushes the Γ-point intensity to higher energies and additionally sharpens it. In contrast, increasing Γ_1 lowers the Γ-point intensity and leads to the desired washout as observed in experiment. Note, that we observed a more pronounced broadening going *away* from the Kitaev spin-liquid. In this case, the anisotropic off-diagonal coupling effects seem to have an influence onto the excitation continuum, similarly to the one expected from fractionalized excitations, such as Majorana fermions. We will elaborate on this insight further below. While the two models with finite off-diagonal terms meet the criterion of a broad continuum, this continuum seems to be located at too low energies to reproduce the experimental observation. The high-energy window in Fig. 5.12(i,m) shows vanishing intensity at the center of the Brillouin zone, in contrast to experiment, see Fig. 5.7(b). (ii) The star-shape feature observed in experiment for intermediate energies is reproduced with intensity at the M- and Y-points for the model with $K_1 = \Gamma_1$, while the intensity seems to be more pronounced at the X-points for the other three models. The six-fold star shape seems to be a consequence of the importance of the Γ_1 term in this particular honeycomb geometry. (iii) While there are features at the Γ-point intensity in Fig. 5.12(d,h,l,p), the two features observed in experiment are not clearly observed in the ED results. The model with $K_1 = \Gamma_1$ seems the closest to experiment, but the tail at high energies is not pronounced enough.

Since the extended AFM Kitaev models are not consistent with *ab-initio* predictions for the updated $C2/m$ structure and the intensity at the Γ-point for high energies is absent for all models with a washed out continuum of excitations, we excluded this family of models as a possibility to capture the effects in α-$RuCl_3$. However, we emphasize the gained insight, that going away from the Kitaev spin-liquid limit by adding finite off-diagonal terms actually *promotes* a continuum of excitations.

5.6.4 Extended FM Kitaev models

As indicated by Table 5.1, *ab-initio* studies based on the $C2/m$ crystal structure for α-$RuCl_3$ suggest models with a ferromagnetic Kitaev interaction, finite anisotropic off-diagonal contributions and a small AFM third nearest neighbour Heisenberg interaction: $(J_1, K_1 < 0, \Gamma_1, J_3)$. As a starting point, we first discuss one example of these models, Model 2, and then analyse the influence of tuning the parameters in more detail in a series of calculations.

Model 2

In Fig. 5.13, we show with $(J_1, K_1, \Gamma_1, J_3) = (-0.5, -5.0, +2.5, +0.5)\,\text{meV}$ the results for Model 2, indicated by the red dot in the phase diagram in Fig. 5.5. As speculated above, the finite Γ_1 terms cause a continuum of excitations, which are only absent in the vicinity of the q-points corresponding to the magnetic order Y and M. While the LSWT calculations capture the ED calculations in this environment, the LSWT calculations fail, away from these reciprocal points, to capture the continuum character. The experimental features can be reproduced relatively well. (i) The broad continuum at

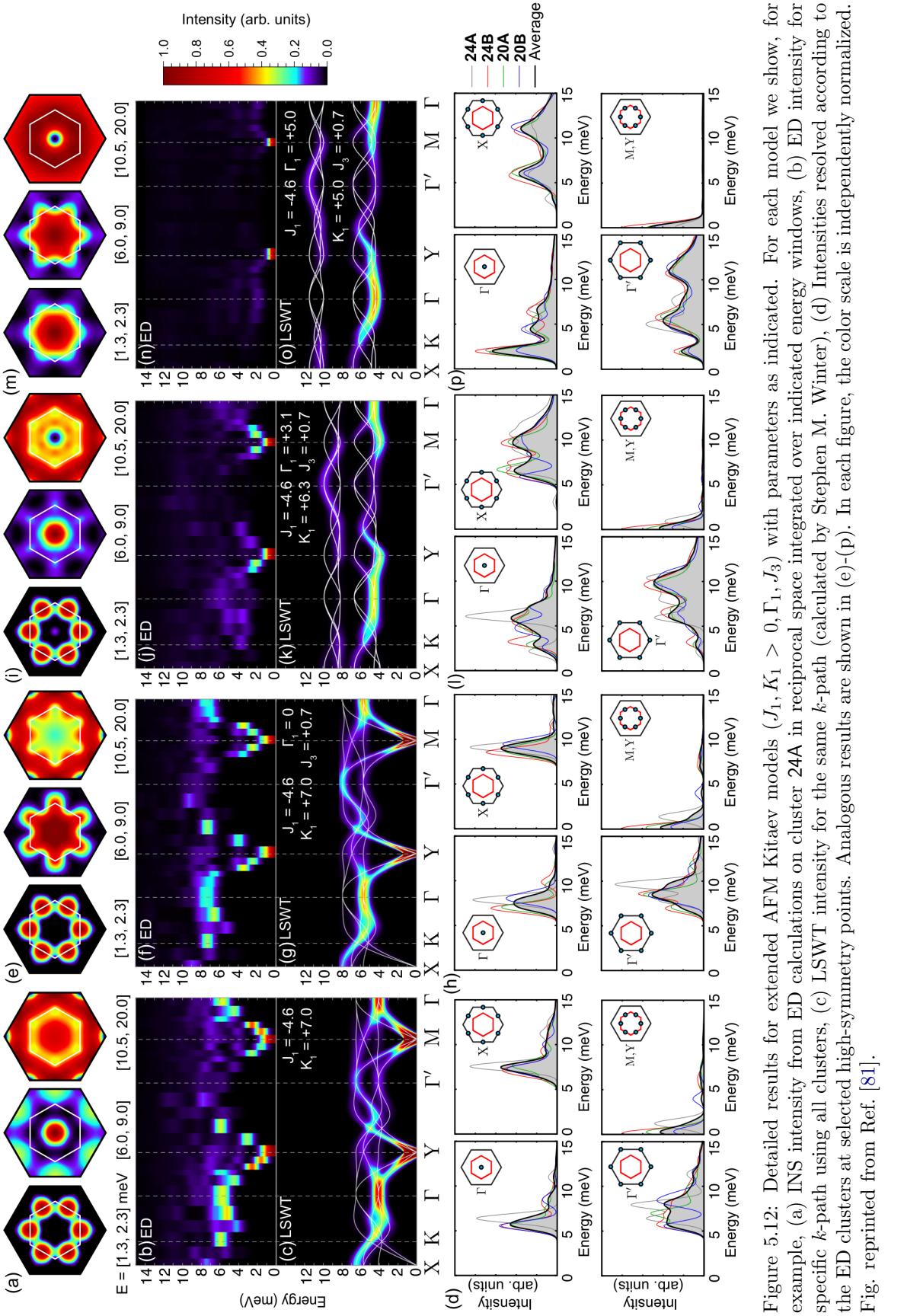

Figure 5.12: Detailed results for extended AFM Kitaev models ($J_1, K_1 > 0, \Gamma_1, J_3$) with parameters as indicated. For each model we show, for example, (a) INS intensity from ED calculations on cluster 24A in reciprocal space integrated over indicated energy windows, (b) ED intensity for specific k-path using all clusters, (c) LSWT intensity for the same k-path (calculated by Stephen M. Winter), (d) Intensities resolved according to the ED clusters at selected high-symmetry points. Analogous results are shown in (e)-(p). In each figure, the color scale is independently normalized. Fig. reprinted from Ref. [81].

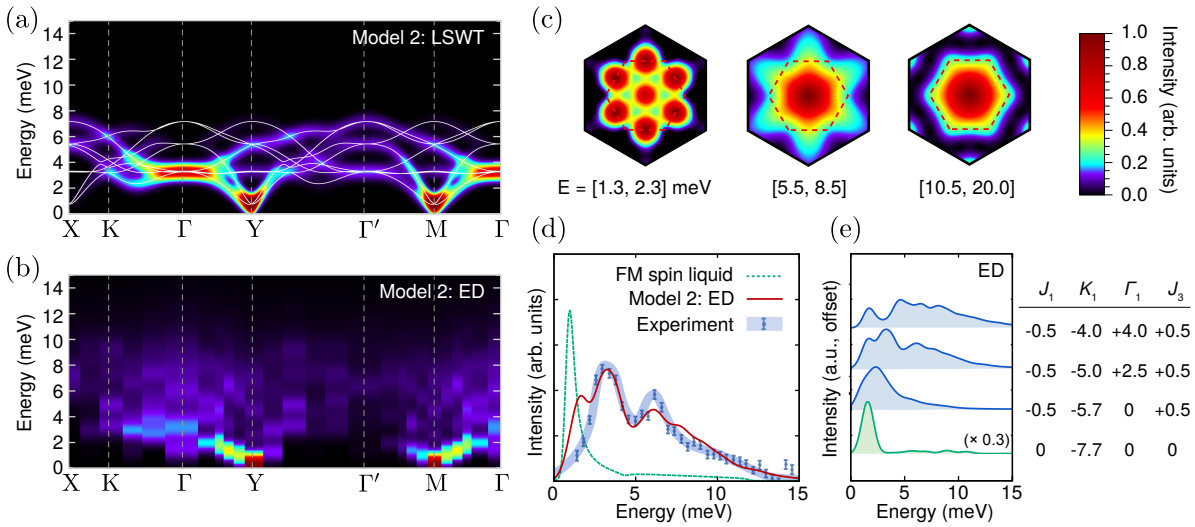

Figure 5.13: INS intensity $\mathcal{I}(\mathbf{k},\omega)$ for Model 2 $(J_1, K_1, \Gamma_1, J_3) = (-0.5, -5.0, +2.5, +0.5)\,\text{meV}$ as an example for the extended FM Kitaev models. In each figure, the color scale is independently normalized. (a) INS intensity from LSWT in reciprocal space, (b) $\mathcal{I}(\mathbf{k},\omega)$ from ED, (c) ED intensity integrated over the indicated energies windows, obtained from cluster 24A with the first Brillouin zone indicated by the dashed red line, (d) comparison of Γ point intensity for FM spin liquid, Model 2, and experiment [231], (e) Γ-point intensities for indicated model parameters. Figure adapted from Ref. [81].

the Γ-point is indeed present in the ED calculations shown in Fig. 5.13(b). In Fig. (c), the integrated intensities are shown, where in the low-energy window there is a significant contribution in the center of the Brillouin zone. (ii) The six-fold star shape at intermediate energy windows, is reproduced as well. (iii) The two significant features at the Γ-point, shown in comparison to experiment and the FM spin liquid limit in Fig. (d), are reproduced qualitatively, although a third feature seems to appear in the ED intensity. Whether this is a consequence of the cluster average or finite size effects, or indeed a sign that Model 2 is not optimized yet to describe α-$RuCl_3$, should be subject of future studies. Interestingly, the FM spin liquid limit, shown in green, differs dramatically from the experimental observation. In Fig. (e), we show the Γ-point intensity for a variety of models with constant $\sqrt{J_1^2 + K_1^2 + \Gamma_1^2 + J_3^2} = 7.7\,\text{meV}$ to obtain a first impression where Model 2 should be located relative to the FM Kitaev spin-liquid. This comparison suggests that the broad continuum at higher energies is not a consequence of the spin-liquid, but rather of the contribution from the Γ_1 term. While Model 2 seems to resemble the three significant experimental features, the reason for this seems to be different than proximity to the KSL limit.

Note, that a feature from experiment, which could not be reproduced with the LSWT or ED calculations of Model 2, is the excitation gap at the M(Y) points of $\Delta \approx 2\,\text{meV}$ [231, 260]. However, LSWT calculations by Stephen M. Winter for Model 2 under considertation of a bond-dependent anisotropy with $K_1^Z = -5.0 + \delta, K_1^{XY} = -5.0 - \delta, \Gamma_1^Z = +2.5 + \delta/2, \Gamma^{XY} = +2.5 - \delta/2$ could reproduce the correct gap for $\delta = 0.1K_1$, see also Supplementary Information of Ref. [81].

Series of extended FM Kitaev models

Finally, we investigated a series of extended FM Kitaev models, as indicated by the dots in the lower part of the phase diagram in Fig. 5.5 and also listed in Table 5.2. In this case, we kept the norm $\sqrt{J_1^2 + K_1^2 + \Gamma_1^2 + J_3^2} = 7.7\,\text{meV}$ fixed and equal to the models shown in Fig. 5.14(e). The Heisenberg parameters J_1 and J_3 were kept constant as well and we decreased the ratio $|\Gamma_1/K_1|$ toward the Kitaev spin-liquid limit, where we used exact results from Ref. [220, 259] instead of LSWT. The detailed results for all four models are shown in Fig. 5.14. For the three models with zigzag ground state, the pseudo-Goldstone modes are indeed located at the Y- and M-points in both cases, for LSWT and ED intensities.

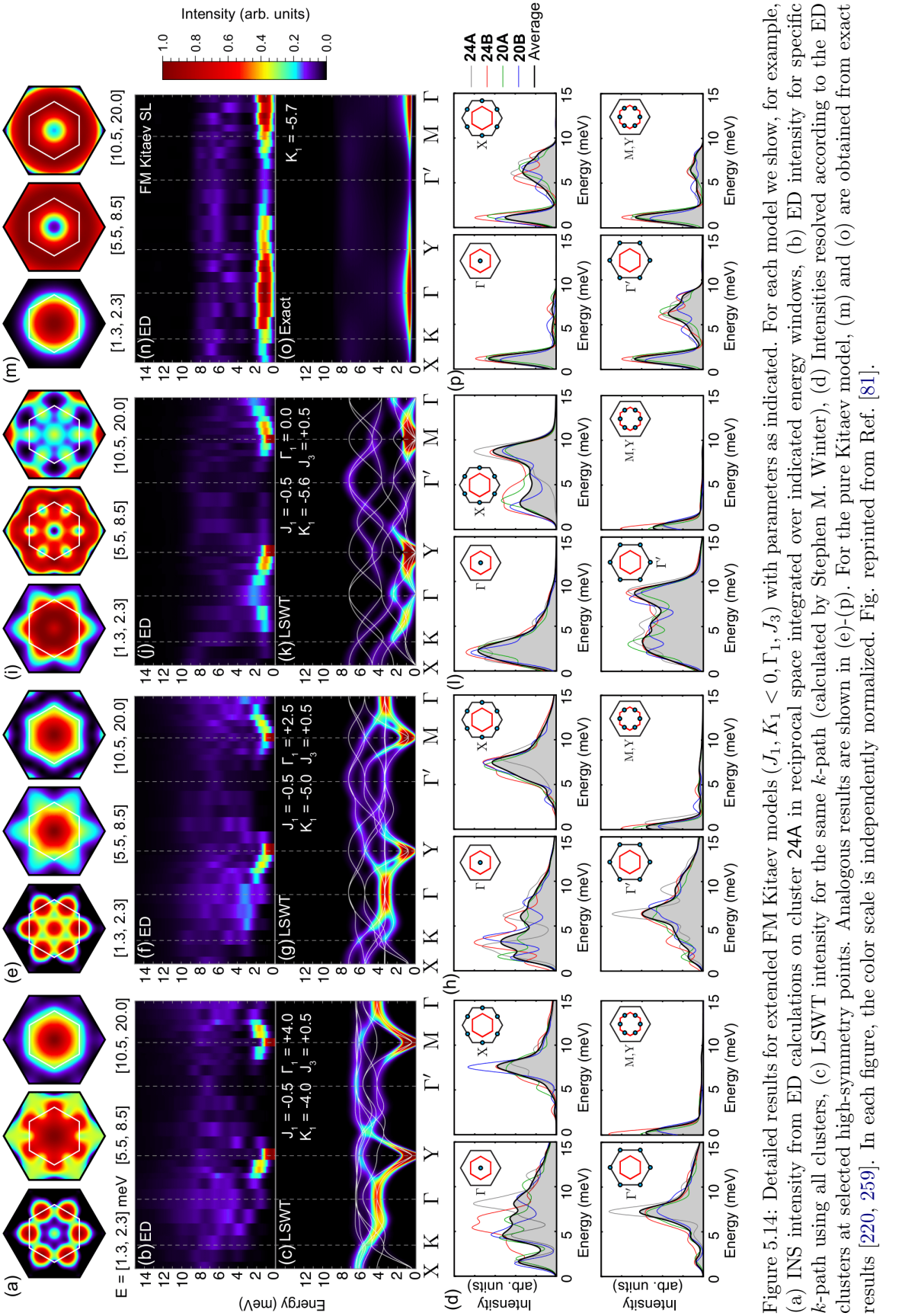

Figure 5.14: Detailed results for extended FM Kitaev models ($J_1, K_1 < 0, \Gamma_1, J_3$) with parameters as indicated. For each model we show, for example, (a) INS intensity from ED calculations on cluster 24A in reciprocal space integrated over indicated energy windows, (b) ED intensity for specific k-path using all clusters, (c) LSWT intensity for the same k-path (calculated by Stephen M. Winter), (d) Intensities resolved according to the ED clusters at selected high-symmetry points. Analogous results are shown in (e)-(p). For the pure Kitaev model, (m) and (o) are obtained from exact results [220, 259]. In each figure, the color scale is independently normalized. Fig. reprinted from Ref. [81].

The effect of the anisotropic off-diagonal contribution to wash out the excited states, away from the Y- and M-points, is a consistent observation over all models. Interestingly, the LSWT intensity with an AFM Kitaev interaction, shown in Fig. 5.11(c), is very similar to the LSWT intensity with an FM Kitaev interaction and off-diagonal anisotropic interactions, shown in Fig. 5.14(c). However, the ED results, shown in Fig. 5.11(b) and Fig. 5.14(b), differ significantly. The experimental feature of (i) the broad continuum at the Γ-point is a feature which seems present in all ED intensities, see Fig. (b,f,j). In this case, decreasing $|\Gamma_1/K_1|$ pushes the intensities down in energy, so that the model with $|\Gamma_1| = |K_1|$ lacks intensity at the center of the Brillouin zone, shown in Fig. (a). For the other models, the intensity increases, see Fig. (e,i,m), until it is finally a very intense low-energy mode in the Kitaev spin-liquid limit. The experimental feature (ii) of the six-fold star at intermediate energy windows is in the interplay with the ferromagnetic Kitaev interaction only present for Model 2, shown in Fig. (e). For stronger Γ_1 interaction, the weights are located at the X-points, as well as for $\Gamma_1 = 0$, so that $2\Gamma_1 = |K_1|$ seems to capture the optimal ratio. (iii) The two features at the Γ-point, see Fig. (d,h,l,p), are captured most accurately by Model 2, although in the case of equal contribution form Γ_1 and K_1, the strong tail might also be comparable to the observed features. Approaching the Kitaev spin-liquid limit by decreasing Γ_1 eliminates this feature.

In summary, the off-diagonal Γ_1 term induced for a series of models a washout of the excitation spectrum, even within the ordered phase. This questions the common concept to treat an excitation continuum as a smoking gun signature of fractionalized excitations and therefore of the existence of a spin liquid. With Model 2, we found a model that resembled most of the experimentally observed features, although proximity to the spin-liquid limit seemed not to be reason for that. Therefore, we next investigated alternative explanations for excitation continuum.

5.6.5 Magnon stability beyond LSWT

The discrepancy between LSWT and ED intensities in the extended Kitaev models hints towards a correspondence of the term $\Gamma_1 > 0$ with the instability of linear spin-wave theory. For this, we revisit first insights about the ordered (pseudo-)spin direction, dependent on the participating exchange terms in the magnetic model Hamiltonian by Chaloupka *et al.* [257]. For the considerations below we assumed a magnetic order with ordering wave vector $\mathbf{Q} = \mathrm{Y}$, so that the antiferromagnetic configuration in the zigzag chain is along the Z-bonds, see also Fig. 6.10(a). For models like the nnHK models, i.e. with $K_1 > 0$, $J_1 < 0$ and $\Gamma_1 = 0$, the spins are oriented along the cubic $\hat{z}$ axis, shown in Fig. 5.15(a). In contrast, for extended FM Kitaev models, i.e. with $K_1 < 0$, $J_1 > 0$, $J_3 > 0$ and $\Gamma_1 > 0$, the spins are along the $\hat{x}+\hat{y}$ direction and pushed toward the crystallographic ac^* plane for increasing Γ_1, illustrated in Fig. 5.15(b). Hence, in this case less symmetries are present than they were for the nnHK models.

These symmetry considerations have important consequences for the magnon bands observed in INS experiments. This can be demonstrated with the Holstein-Primakoff transformation, which relates spin operators with quasi-particle creation and annihilation operators, i.e. $a^\dagger$ and a, as follows:

$$\hat{S}^z = (S - a^\dagger a), \qquad \hat{S}^+ = \sqrt{2S}a^\dagger\sqrt{1-\frac{a^\dagger a}{2S}}, \qquad \hat{S}^- = \sqrt{2S}\sqrt{1-\frac{a^\dagger a}{2S}}a, \tag{5.82}$$

where S is the spin quantum number, so $S = 1/2$ for α-$RuCl_3$.

In the case of nnHK models, a convenient quantization axis is the $\hat{z}$ axis, along the direction of the magnetic moments. The Hamiltonian in terms of the above introduced quasi-particle operators contains then terms of the following type:

$$S_i^z S_j^z = (S - a_i^\dagger a_i)(S - a_j^\dagger a_j), \tag{5.83}$$

$$S_i^x S_j^x = \frac{2S}{4}\left(\sqrt{1-\frac{a_i^\dagger a_i}{2S}}a_i + a_i^\dagger\sqrt{1-\frac{a_i^\dagger a_i}{2S}}\right)\left(\sqrt{1-\frac{a_j^\dagger a_j}{2S}}a_j + a_j^\dagger\sqrt{1-\frac{a_j^\dagger a_j}{2S}}\right), \tag{5.84}$$

where we used that $S_i^x = \frac{1}{2}(S_i^+ + S_i^-)$. Note, that all terms contain an even number of quasi-particle operators, considering the square root expansion $\sqrt{1-x} \approx 1 - \frac{1}{2}x - \frac{1}{8}x^2 + \ldots$ in terms of small x, i.e. large S.

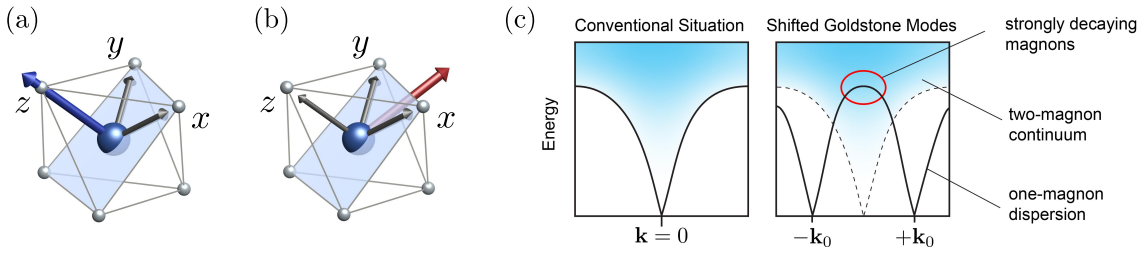

Figure 5.15: (a) Ordered moment with respect to cubic axes in nnHK models for ordering wave vector $\mathbf{Q} = \mathrm{Y}$, (b) ordered moment with respect to cubic axes in extended FM Kitaev models for ordering wave vector $\mathbf{Q} = \mathrm{Y}$, (c) cartoon of two-magnon continuum and one-magnon dispersion in a conventional (Heisenberg) situation vs. a situation with shifted Goldstone modes due to anisotropic bond-dependent interactions. Fig. (a,b,c) reprinted from Ref. [81].

In contrast, in the case of the extended FM Kitaev models, the magnetic moments are rotated away from the cubic axes [257]. With the quantization axis along the magnetic moments, shown in Fig. 5.15(b), the Hamiltonian contains also terms of the following type:

$$S_i^x S_j^z = \frac{1}{2}\sqrt{2S}\left(\sqrt{1-\frac{a_i^\dagger a_i}{2S}}a_i + a_i^\dagger\sqrt{1-\frac{a_i^\dagger a_i}{2S}}\right)\left(S - a_j^\dagger a_j\right). \tag{5.85}$$

Considering the series expansion of the square root $\sqrt{1-x} \approx 1 - \frac{1}{2}x - \frac{1}{8}x^2 + \ldots$, this type of term contains also odd numbers of quasi-particle operators.

In linear spin-wave theory, the effective Hamiltonian is expressed terms of magnon creation and annihilation operators in reciprocal space, i.e. $a_{\mathbf{q},m}^\dagger$ and $a_{\mathbf{q},m}$ respectively. In general, these magnon operators are related to the above introduced quasi-particles by termination of the square root expansion $\sqrt{1-x} \approx 1$ in Eq. (5.82) and a Bogoliubov transformation. The magnon Hamiltonian in LSWT is strictly quadratic and the magnon particle number is conserved:

$$\mathcal{H}_2 = \sum_{\mathbf{q},m} \varepsilon_{\mathbf{q},m} a_{\mathbf{q},m}^\dagger a_{\mathbf{q},m}. \tag{5.86}$$

Beyond the level of LSWT, anharmonic terms enter the magnon Hamiltonian for both model types, allowing in general for magnon decay processes in which the magnon particle number is not conserved.

In the case of nnHK models, with AFM Kitaev and FM Heisenberg interaction, the lowest decay process in the zigzag ground state beyond the single-magnon picture is given by processes with a change in the magnon number $\Delta N = \pm 2$, described by e.g. the following Hamiltonian:

$$\mathcal{H}_4 = \sum_{\mathbf{1-4}} V_{\mathbf{123}}^{\mathbf{4}}\; a_{\mathbf{1}}^\dagger a_{\mathbf{2}}^\dagger a_{\mathbf{3}}^\dagger a_{\mathbf{4}}\; \delta(\mathbf{q}_1 + \mathbf{q}_2 + \mathbf{q}_3 - \mathbf{q}_4) + \mathrm{H.c.}, \tag{5.87}$$

where the bold index labels momentum and magnon band ($\mathbf{i} \equiv \mathbf{q}_i, m_i$). The matrix element $V_{\mathbf{123}}^{\mathbf{4}}$ determines the weight of the decay process, where one-magnon states are mixed with the three-magnon continuum, leading to $\Delta N = \pm 2$. These decay processes depend, among others, on the energetic availability of the three-magnon continuum for the one-magnon states to decay into. Stephen M. Winter estimated the density of states of the three-magnon continuum based on momentum-dependent combinations of the one-magnon states known from LSWT calculations and found that $E_3^{\min} \geq \varepsilon_{\mathbf{q},1}$ everywhere in reciprocal space. Therefore, on the LSWT level, a stable description for nnHK models is guaranteed. Only at very high energies, where multiple-magnon states overlap, so that higher order decay processes are possible, a continuum deviating from the LSWT level can be observed.

The situation is very different for the extended FM Kitaev models. In this case, decay processes between the two-magnon continuum and the one-magnon states with $\Delta N = \pm 1$ are symmetrically

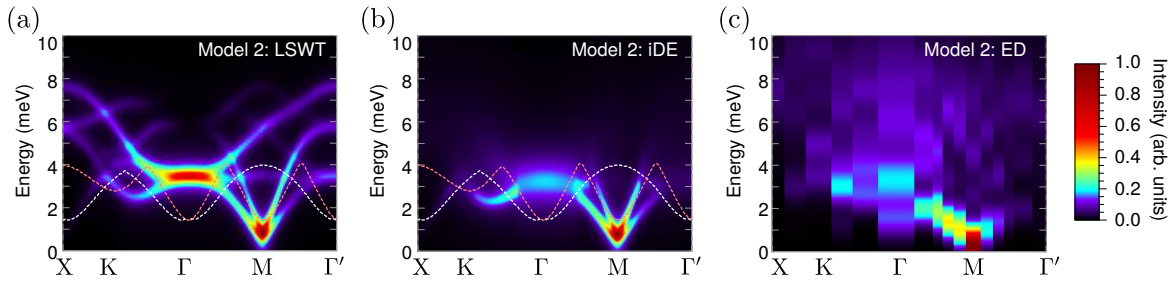

Figure 5.16: (a) LSWT intensity for Model 2 in reciprocal space, (b) INS intensity obtained form the imaginary self-consistent Dyson equation (iDE) approach obtained by Pavel A. Maksimov and Alexander L. Chernychev, (c) ED intensity along the same path in reciprocal space. Fig. adapted from Ref. [81].

allowed, as suggested by Eq. (5.85):

$$\mathcal{H}_3 = \sum_{\mathbf{1-3}} \Lambda^{\mathbf{3}}_{\mathbf{12}}\; a^\dagger_{\mathbf{1}} a^\dagger_{\mathbf{2}} a_{\mathbf{3}}\; \delta(\mathbf{k}_1 + \mathbf{k}_2 - \mathbf{k}_3) + \text{H.c.} \tag{5.88}$$

According to the estimates by Stephen M. Winter, the two-magnon density of states fulfills over an extended region in the Brillouin zone the condition $E_2^{\min} < \varepsilon_{\mathbf{q},1}$. This is a consequence of the antiferromagnetic zigzag order due to the anisotropic bond-dependent terms and differs with that strongly from a conventional Heisenberg situation, where the coupling is restricted by symmetry. The difference is illustrated as a cartoon in Fig. 5.15(c). In Heisenberg models, Goldstone modes must appear at the Γ-point and the ordering wave vector $\mathbf{Q}$, which correspond to a uniform rotation of the ordered moment direction. The two-magnon density of states is in this situation located above the one-magnon dispersion. In the case of strongly anisotropic bond-dependent interactions generally an energy cost for uniform spin rotations is induced, which leads to gaps at the Γ-point and the ordering wave vector. However, amazingly, the zigzag order still features pseudo-Goldstone modes elsewhere in the Brillouin zone, as explained e.g. in Ref. [261]. We will revisit this issue in Chapter 6 in the context of magnetic field effects in α-$RuCl_3$. In this case, the lower bound of the two-magnon density of states is obtained by one particle at an M-point and the second particle at $\mathbf{k}_2 = \mathbf{q} - \mathrm{M}$, moving the low-energy states away from the ordering wave vector. In principle, a magnon decay into energetically low-lying multiple-magnon states is therefore, in the presence of spin-orbit coupling, possible. This process causes the observation of an excitation continuum, as it is commonly assigned to spin-liquid materials.

iDE approach

With the speculation that the excitation continuum is caused by multiple-magnon decay processes instead of Majorana fermions, a method designed for this issue could further check this scenario. Therefore, Pavel A. Maksimov and Alexander L. Chernychev performed calculations with the self-consistent imaginary Dyson equation (iDE) [262] for Model 2. In this approach, the decay matrix element is approximately determined, where it is assumed that the real part of the magnon self-energy is captured on the LSWT level and the imaginary part is then calculated self-consistently. While this is still a rough approximation, it helps to gain intuition for descriptions between the LSWT approach, where decay processes are neglected completely, and the ED calculations, where all processes are present, but are difficult to be tracked to their origin. The result in comparison with the LSWT and ED calculations is shown in Fig. 5.16. Indeed, while the sharp signatures at the M-point are present in all three methods, the washout at the Γ-point is observable at the iDE level. Magnon-decay seems to be therefore — at least for the extended FM Kitaev models — the probable source for the excitation continuum.

5.7 Discussion

Due to the lack of a smoking gun experiment to identify a spin-liquid state directly and independent of its classification, the search for such exotic states is very challenging. Hope was gained with the mechanism proposed by Jackeli and Khalilluin, where promising candidate materials were identified as honeycomb transition metals with strong spin-orbit coupling, and the possibility to compare experimental data with the aid of an exact solution of the pure Kitaev honeycomb model. The experimental observation in INS measurements of an excitation continuum was therefore, not surprisingly, assigned quickly to excitations in terms of Majorana fermions. However, materials with anisotropic bond-dependent couplings are still difficult to treat theoretically, causing a lack of intuition about related expected effects.

In order to test the Majorana fermion scenario, we performed extensive exact diagonalization (ED) calculations for a series of models. This enabled us to gain more insight about the influence of the magnetic exchange parameters and benchmark with the exact solutions of the pure Kitaev model. We found that the originally proposed nnHK model is not appropriate to reproduce the observed key experimental features of α-$RuCl_3$. Moreover, approaching the AFM Kitaev limit pushes the response of the models away from experiment. Hence, an interpretation of the excitation continuum in α-$RuCl_3$ in terms of proximity to the AFM Kitaev spin liquid seems not appropriate. In contrast, a description of α-$RuCl_3$ in terms of extended FM Kitaev models seemed to be more successful. Interestingly, the observed features were also not caused by proximity to the FM Kitaev spin-liquid. Instead, consideration of reduced symmetries in magnon-decay processes due to the presence of strong anisotropic bond-dependent couplings provided a promising framework for the interpretation of the experimentally observed features.

To summarize, we gained two main insights in this chapter. For the specific material α-$RuCl_3$, we identified a minimal model which seems to reproduce the key experimental features consistently. Since this material was and is the subject of intensive attention in the community of frustrated magnetism, it is certainly beneficial to determine an appropriate magnetic model for this particular material. Second, we gained intuition what to expect from the magnetic excitations in systems with strong spin-orbit coupling. We found that the consideration of induced magnon-decay terms, which are observable at surprisingly low energies, explain the observation of a continuum of excitations. Hence, this feature cannot be treated as a smoking gun feature for fractionalized excitations. Instead, a possible breakdown of the single-magnon picture even in the ordered phase should be considered. In the case of α-$RuCl_3$, we found that proximity to the solution with fractionalized excitations seems unlikely to explain the experimental observations. Due to the continuum of excitations, is is also clearly not possible to describe the system on the LSWT level. Hence, a description of the excitations in terms of "non-interacting" particles could not be determined and may not be possible. Considering decay terms up to infinite order on the other hand enables always a perfect description of the system. The question up to which order of a basis, the basis can still be interpreted as the "appropriate" for a material, might be more of philosophical nature.

Chapter 6

Beyond order: α-$RuCl_3$ under magnetic field

6.1 Introduction

In the previous chapter we presented a possible framework for the interpretation of the magnetic response of α-$RuCl_3$ in terms of magnon-decay processes rather than proximity to the Kitaev spin-liquid phase. However, the significant Kitaev interaction in the model Hamiltonian raises the question, whether the material could be driven into a QSL state under certain conditions. Hence, in the search for a QSL state in α-$RuCl_3$, alternative routes were pursued by tuning of external parameters that may lead to a suppression of magnetic order, such as increasing temperature [263, 264], pressure [265, 266] or a magnetic field [47, 48].

In this chapter, we discuss the response of α-$RuCl_3$ in the presence of an external magnetic field based on the previously introduced extended FM Kitaev Model 2. The magnetic field represents an external parameter that guarantees to suppress the spontaneous AFM zigzag magnetic order at a critical value, since the magnetic interactions become naturally irrelevant for the magnetic order in the fully polarized limit at infinite field. The highly debated question is then, which phases the system passes with tuning between the zero-field limit of AFM zigzag order and the paramagnetic phase in the infinite-field limit. In Fig. 6.1(a), we show a cartoon of a possible phase diagram for α-$RuCl_3$ under field. The low-temperature antiferromagnetic zigzag order remains stable up to a critical field H_c, where the magnetic order is suppressed in favour of a quantum paramagnetic state, which has no spontaneous broken symmetry, but is trivial in the sense that it is adiabatically connected to the fully polarized state. A characterization regarding the nature of this state is one of the goals of this chapter. Experimentally, it was observed consistently that the magnetic order in α-$RuCl_3$ is suppressed for fields within the honeycomb plane at $H_c = 6 - 8\,\mathrm{T}$ [267–272]. Above the critical field $H \gtrsim H_c$, a number of exotic phases have been proposed for α-$RuCl_3$ [269, 271, 272] including interpretations based on the unconventional persistent Γ-point continuum in proximity to the critical field in INS [47, 273] and ESR experiments [274, 275]. Moreover, on the basis of thermal transport measurements it was argued that a finite field in specific directions induces the Kitaev spin-liquid state with Majorana edge-states [48]. Exotic field-induced phases were also predicted for a number of variations of the extended Kitaev models, under consideration of specific field orientations [225, 251, 276, 277].

In order to investigate this regime in the context of the theoretical model proposed for α-$RuCl_3$ in Chapter 5, we concentrated on two experimental setups. First, we present the investigation of the magnetic torque response under a rotated magnetic field away from the honeycomb plane. In Chapter 3, we derived theoretical expressions that allow to determine the magnetic torque for a specific spin Hamiltonian based on its expectation value $\langle \mathcal{H} \rangle$. For α-$RuCl_3$, we could then compare the theoretical predictions based on Model 2 with the recently measured torque response [278, 279]. Since the magnetic torque is a thermodynamic probe, such a response is predestined to identify phase transitions as a function of magnetic field. For ED calculations, we could resolve only one phase transition upon increasing

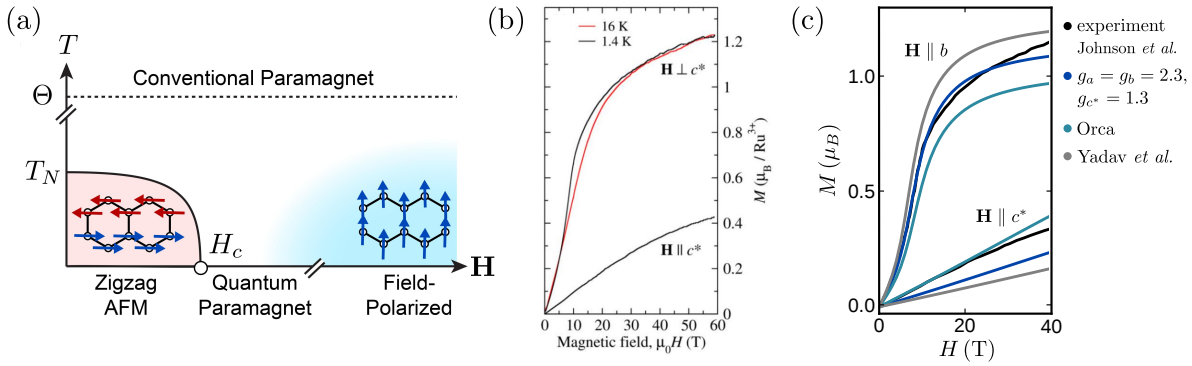

Figure 6.1: (a) Schematic H-T phase diagram of α-$RuCl_3$ with magnetic order at low temperature and fields, as well as field-polarized limit indicated. The regime indicated as Quantum Paramagnet indicates a regime with magnetic order suppressed before the polarized regime is reached. (b) Experimentally measured magnetization for in-plane ($\mathbf{H} \perp c^*$) and out-of-plane ($\mathbf{H} \parallel c^*$) field. (c) Magnetization by Johnson *et al.* [237], compared to curves obtained from ED calculations with $(g_{ab}, g_{c^*}) = (2.3, 1.3)$, from the Orca package with $(g_{ab}, g_{c^*}) = (2.1, 1.7)$, and from Yadav *et al.* [225] with $(g_{ab}, g_{c^*}) = (2.5, 1.1)$. Fig. (a) adapted from Ref. [83], Fig. (b) reprinted from Ref. [237].

field, suggesting that the quantum paramagnetic state in Fig. 6.1(a) is adiabatically connected to the fully polarized phase. To further characterize the nature of the quantum paramagnetic state, we investigated also the magnetic excitations under the influence of a magnetic field within the honeycomb plane. Unconventional shifting of INS intensity under magnetic field was interpreted in terms of exotic features of a possible field-induced QSL state [47]. In order to test this interpretation in the framework of the extended FM Kitaev model, we extended the tools for theoretical prediction of INS intensities from the previous chapter to include a magnetic field. We found that the intensity shifts and Γ-point continuum in the presence of a magnetic field can be captured in this framework. In order to further dissect the nature of this continuum, we also calculated the ESR response, which probes specific contributions of the dynamical structure factor at the Γ-point with respect to its transverse and longitudinal channels. We found good agreement with experimental ESR intensities [274, 275] and could assign intensities to one- and multi-magnon modes. The results presented in this chapter are published in Ref. [82, 83].

6.2 Extended model under magnetic field

In order to find an appropriate magnetic model for α-$RuCl_3$ under field, we use the experimental investigation by Johnson *et al.* [237] as orientation. In this work, the authors measured the magnetization at low temperatures, shown in Fig. 6.1(b), using static and pulsed fields up to $H = 60\,\mathrm{T}$. They could identify a pronounced steepening at $H_c = 8\,\mathrm{T}$ for fields in the honeycomb plane, i.e. $\mathbf{H} \perp c^*$, and assigned the anisotropy of the saturation magnetization to ruthenium g-anisotropy. The asymptotic approach of the magnetization towards saturation was interpreted as a signature for strong anisotropic terms in the spin Hamiltonian, where the total spin is not a good quantum number, and therefore quantum fluctuations are only suppressed in the asymptotic limit of infinite field.

The presence of a magnetic field influences the spin Hamiltonian, as detailed in Chapter 2. To leading order, a magnetic field induces a Zeeman term that includes a single spin operator:

$$\mathcal{H}_{(1)} = -\mu_B \mathbf{H}^{\mathrm{T}} \cdot \mathbb{G} \cdot \sum_i \mathbf{S}_i. \tag{6.1}$$

In the case of α-$RuCl_3$, the g-tensor is equivalent for all magnetic sites. From the magnetization experiments it follows that the magnetic model Hamiltonian should include anisotropy of the magnetic response to in-plane and out-of-plane fields. Unfortunately, the anisotropic response in the magnetization can stem from several sources. As suggested in Ref. [237], an anisotropic g-tensor offers a reasonable

explanation. In the previous chapter we also suggested significant anisotropic off-diagonal exchange contributions through the exchange term Γ_1. Since this contribution causes the honeycomb plane to be an easy plane [261], so that the effects in the magnetization curve are impossible to distinguish from an anisotropic g-tensor with a stronger in-plane contribution.

In the case of α-$RuCl_3$, the most probable scenario is an interplay of both mechanisms. While we were able to estimate $\Gamma_1 \approx 2.5\,\text{meV}$ from comparison with the zero-field INS intensity, we estimated the anisotropic g-tensor with guidance from *ab-initio* and from comparison with the magnetization curves by Johnson *et al.* [237]. Based on quantum chemistry calculations on a $[RuCl_6]^{3-}$ molecule Yadav *et al.* [225] reported an anisotropic g-tensor with $g_a = g_b = 2.51$, and $g_{c^*} = 1.09$. Based on these values, we calculated the magnetization with exact diagonalization of Model 2, determined in Chapter 5, with the parameters $(J_1, K_1, \Gamma_1, J_3) = (-0.5, -5.0, +2.5, +0.5)\,\text{meV}$ in addition to the Zeeman term given in Eq. (6.1). The corresponding magnetization curves are shown in Fig. 6.1(c) in grey, in comparison to the experimental curves, illustrated in black. While the in-plane magnetization for $\mathbf{H} \parallel b$ seems to be overestimated in comparison to experiment, the out-of-plane contribution seems too small.

We then determined the g-tensor of an isolated $[RuCl_6]^{3-}$ molecule with the quantum chemistry ORCA package at the PBE0/IGLO-III level [128, 129], as it was successfully applied in Chapter 2 for the organic charge transfer salts. With this method, we obtained a less anisotropic g-tensor than in Ref. [225], with $g_a = 2.04$, $g_b = 2.10$, and $g_{c^*} = 1.68$. The corresponding ED magnetization curve is shown in Fig. 6.1(c) in green. Note, that we averaged $g_{ab} = (g_a + g_b)/2$ to maintain the C_3 symmetry of Model 2. In this case, the anisotropy seems to be underestimated, which should be assigned to the stronger influence of the crystal environment compared to the more extended organic molecules.

An alternative option is, to follow the hybrid approach used in Chapters 2 and 4 for the Zeeman term as an effective spin Hamiltonian which may be calculated based on a Hubbard model. Unfortunately, this approach suffers in this case also from various issues. For example, the resulting g-values depend strongly on small changes of the crystal field splitting, so that uncertainties on the level of accuracy in the DFT level may have disproportional strong effects on the effective model[1]. In order to obtain nevertheless some intuition, we discuss this approach where the crystal-field parameter plays the role of a tuning parameter rather than an *ab-initio* value. The single-site Hubbard Hamiltonian including SOC and coupling to an external field can be expressed as follows:

$$\mathcal{H} = \sum_{i\alpha}\sum_{\sigma} \varepsilon_{i\alpha} c^\dagger_{i\alpha\sigma} c_{i\alpha\sigma} + \mathbf{H}^{\mathrm{T}} \cdot \sum_{i\alpha}\sum_{\sigma\sigma'} \langle \alpha\sigma|\mathbf{L} + 2\mathbf{S}|\alpha\sigma'\rangle c^\dagger_{i\alpha\sigma} c_{i\alpha\sigma'} + \lambda \sum_{i\alpha}\sum_{\sigma\sigma'} \langle \alpha\sigma|\mathbf{L}\cdot\mathbf{S}|\alpha\sigma'\rangle c^\dagger_{i\alpha\sigma} c_{i\alpha\sigma'}. \tag{6.2}$$

Since we restricted the calculations onto singly occupied states without hopping, the two-particle interaction term is naturally irrelevant. A suggested value for the SOC constant in α-$RuCl_3$ is $\lambda = 0.15\,\text{meV}$ [280]. For the crystal field splitting we assumed a simplified version of trigonal splitting in the d orbitals:

ε_i	$\lvert d_{xy}\rangle$	$\lvert d_{yz}\rangle$	$\lvert d_{xz}\rangle$
$\langle d_{xy}\rvert$	0	Δ	Δ
$\langle d_{yz}\rvert$	Δ	0	Δ
$\langle d_{xz}\rvert$	Δ	Δ	0

(6.3)

In the absence of crystal-field splitting, $\Delta = 0$, this approach would result in the isotropic conventional g-tensor with $g_a = g_b = g_{c^*} = 2$. The negligence of the differences in-between the crystal field terms as a uniform Δ leads to the relation $g_a = g_b$, due to the assumed perfect trigonal splitting. This is not exact for α-$RuCl_3$, however, we already committed to this approximation in the previous chapter by employing C_3 symmetry for the model. Analogously to the approach detailed in Chapter 4, the effective Hamiltonian obtained from a single-site Hubbard Hamiltonian with singly occupied states $|s_n\rangle$ reads as:

$$\mathcal{H}_{\text{eff}} = \sum_{n=1}^{N}\sum_{m=1}^{N} c'_{nm} |s_n\rangle\langle s_m| = \sum_{n=1}^{2}\sum_{m=1}^{2} c'_{nm} a^\dagger_{i,\sigma_n} a_{i,\sigma_m}, \tag{6.4}$$

[1] Note, that we neglect in the following the effects of the e_g levels, which may also play a non-negligible role. However, the crystal field splitting term would introduce in this case even more free parameters suffering from the DFT accuracy problem, so that we neglected this issue for clarity.

where we introduced the creation, $a^\dagger_{i,\sigma_n}$, and annihilation operators, a_{i,σ_n}, in the $j_{1/2}$ basis, where $\sigma_n = \pm 1/2$ represents the j_{eff} equivalent to the conventional spin up and spin down. The effective Hamiltonian can then be expressed in terms of spin operators, using the relation $\hat{A} = \sum_{\mu\nu}\langle\mu|\hat{A}|\nu\rangle a^\dagger_\mu a_\nu$ and the Abrikosov pseudo-spin representation detailed in Chapter 4:

$$\mathcal{H}_{\text{eff}} = \sum_\alpha \sum_\beta \gamma_{\alpha\beta} H^\alpha S_i^\beta . \tag{6.5}$$

The effective g-tensor is included in the prefactor $\gamma_{\alpha\beta}$ through the relation $\gamma_{\alpha\beta} = -\mu_B g_{\alpha\beta}$. For different field directions and in the limit $H \to 0$, we could then determine the g-tensor for a variety of crystal field splitting (CFS) parameters Δ. In Fig. 6.1(c) we show the ED magnetization for an effective g-tensor obtained with the CFS parameter $\Delta = 17\,\text{meV}$, illustrated in blue. This crystal field value leads for our model to a magnetization curve close to the experimental curve and corresponds to the following effective g-tensor:

$$g_a = g_b = 2.3 \qquad \text{and} \qquad g_{c^*} = 1.3. \tag{6.6}$$

Note that these values represent, roughly, the average of the quantum chemistry and DFT estimates for an isolated $[RuCl_3]^{3+}$ molecule. In the projects presented in this chapter, we worked with this g-tensor for the theoretical modelling of α-$RuCl_3$.

6.3 Magnetic torque in α-$RuCl_3$

Kira Riedl, Ying Li, Stephen M. Winter, and Roser Valentí,
Sawtooth Torque in Anisotropic $j_{\text{eff}} = 1/2$ Magnets: Application to α-$RuCl_3$,
Phys. Rev. Lett. **122**, 197202 (2019)
[82]

With the extension of a spin model for α-$RuCl_3$ under field, it was then possible to investigate the corresponding magnetic torque response theoretically. Since the phases in the limits of vanishing field, with the ordered AFM zigzag phase, and of infinite field, with the fully polarized state, are known, the number of phase transitions with increasing field is a direct evidence whether a much discussed intermediate phase [47, 48, 269–275] exists. From a theoretical perspective, we detailed the $T = 0$ magnetic torque expressions in Chapter 3, based on the anisotropy of the expectation value of the Hamiltonian:

$$\tau(\theta) = \frac{\mathrm{d}\langle\mathcal{H}\rangle}{\mathrm{d}\theta}. \tag{6.7}$$

In-plane field rotations in torque [267] and susceptibility [276] measurements revealed monoclinic symmetry, which is not included in our simplified C_3 symmetrical model for α-$RuCl_3$. Therefore, we restricted our analysis to out-of-plane rotations of the magnetic field, where the magnetic field is rotated away from the honeycomb ab plane, toward the out-of-plane c^* axis, sketched in Fig. 6.3(a). The angle θ defines the angle between the honeycomb plane and the field and takes the role of the reference angle introduced in Chapter 3. Leahy *et al.* [267] investigated the magnetic torque of α-$RuCl_3$ already in 2017, but focused on the torque field-dependence induced by in-plane field rotations. They observed a mysterious peak-dip structure and interpreted it as a signature of a field-induced phase transition. In the supplemental material, they also show the field dependence of the torque magnetization for out-of-plane field rotations, where a sawtooth angle-dependence is shown.

In 2018, Modic *et al.* [278] investigated the magnetic torque response of α-$RuCl_3$ for out-of-plane field rotations systematically, shown in Fig. 6.2(a) with θ defined as in Fig. 6.3(a). The authors observed consistently a sawtooth angle-dependence, in agreement with Ref. [267], for a variety of field strengths and analyzed the angle-dependence with a fit to the expression $\tau(\theta)/H = A \sin\theta\,\mathrm{sgn}\cos\theta + A_2 \sin 2\theta$, indicated by the solid lines in Fig. 6.2(a). This work was an extension of previous work on α-$RuCl_3$, where some of the authors measured the field-dependence for a fixed out-of-plane angle $\theta = 10°$ and observed

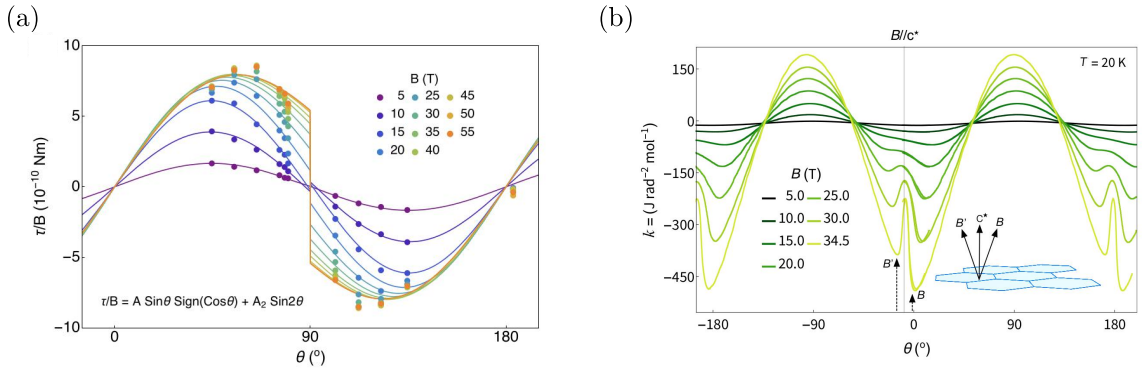

Figure 6.2: (a) Angle-dependent magnetic torque measured by Modic *et al.* [278] with fit to the indicated equation at different field strengths. (b) Angle-dependent magnetotropic coefficient $k = \mathrm{d}\tau/\mathrm{d}\theta$ for different field strenghts measured by Modic *et al.* [279]. Fig. (a) reprinted from Ref. [278], Fig. (b) reprinted from Ref. [279].

one pronounced phase transition [281]. Note, that the observation of a sawtooth angle-dependence at high fields was also observed in the 3D Kitaev material γ-Li_2IrO_3 [278, 282], as well as related anomalies in the torque field-dependence in the two-dimensional Kitaev material Na_2IrO_3 [230] as well as in the 3D materials γ-Li_2IrO_3 [278, 282, 283] and β-Li_2IrO_3 [284].

A second aspect is the angle-dependence of the critical field $H_c(\theta)$ at which the AFM zigzag order is suppressed. For α-$RuCl_3$, it is known that an out-of-plane field rotation pushes the critical field H_c to higher fields [285]. The data resolution in the out-of-plane torque measurements [278] was not sufficient to track the phase transitions accurately. However, later some of the authors presented torque data with a higher field resolution in Ref. [279]. In Fig. 6.2(b) we show the corresponding magnetotropic coefficient $k = \mathrm{d}\tau/\mathrm{d}\theta$. By measurement of k it is possible to identify, for example, second order phase transitions through finite jumps Δk. These jumps can be related to thermodynamic entities like, for example, the specific heat, $\Delta k \propto -\Delta C \left[\left(\frac{\partial T_c}{\partial H}\right)_\theta \left(\frac{\partial H_c}{\partial \theta}\right)_T\right]^2$, with the critical temperature T_c. Note that in the measured data, the symmetry with respect to the c^* axis seems violated and the integration of the curves would lead to an unexpected offset. However, we used the experimental data as a guide for the qualitative features of the α-$RuCl_3$ torque, which we identified as (i) the sawtooth angle-dependence of τ and (ii) the appearance of minima in k in the vicinity of a field direction $\mathbf{H} \parallel c^*$. Note, that in Fig. 6.2(b) the definition of θ is shifted by 90° compared to Fig. 6.2(a) and Fig. 6.3(a).

The magnetic torque of extended Kitaev models was previously studied with ED calculations with focus on the torque field-dependence of the Kitaev material Na_2IrO_3 [230]. Here, we concentrated on the parameters relevant for α-$RuCl_3$ and the sawtooth angle-dependence. In order to assign the proper phase transitions for field rotations, we first determined the phase diagram as a function of the field angle θ for Model 2, defined in Chapter 5, with an anisotropic g-tensor, suggested in Section 6.2. Then we analyzed the angle- and field-dependence of the magnetic torque response and studied the parameter contributions in the context of limiting models. The results presented in this section are published in Ref. [82], the classical results were determined by Stephen M. Winter.

6.3.1 Anisotropic field-dependent phase diagram for α-$RuCl_3$

We determined the angle-dependent phase diagram under field for α-$RuCl_3$ assuming that is described by Model 2, with the parameters $(J_1, K_1, \Gamma_1, J_3) = (-0.5, -5.0, +2.5, +0.5)\,\mathrm{meV}$, and under consideration of the g-tensor $(g_a, g_b, g_{c^*}) = (2.3, 2.3, 1.3)$. The phase diagram was determined based on ED calculations on the 24-site cluster 24A, defined in Section 5.6. We estimated the phase transitions from a combination of the extrema of the ground state energy derivates $\partial^2 E/\partial H^2$ and $\partial^2 E/\partial \theta^2$. Using these two criteria enabled us to compensate numerical convergence issues for field directions very close to the honeycomb layer or very close to the c^* axis. In Fig. 6.3(b), we show the resulting anisotropic field-dependent phase

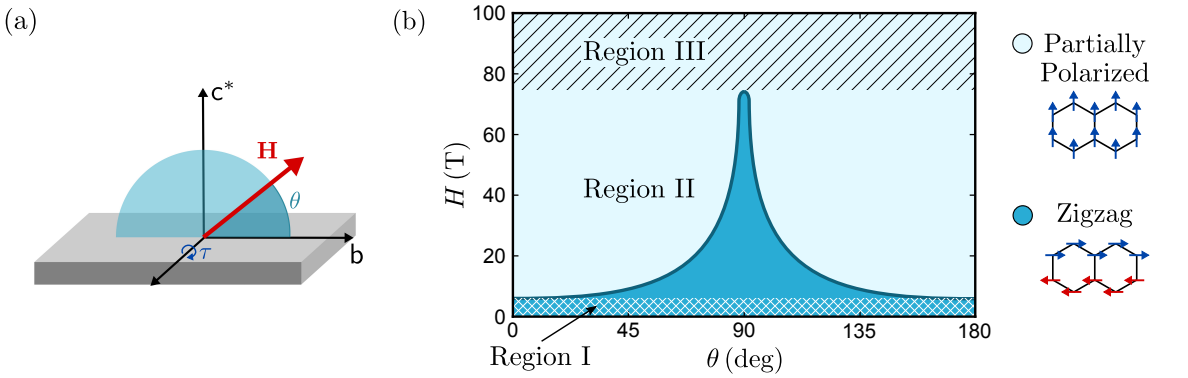

Figure 6.3: (a) Cartoon of magnetic torque setup used in the theoretical analysis in this chapter. The field is rotated away from the honeycomb ab plane in α-$RuCl_3$, towards the out-of-plane crystallographic c^* axis. The angle θ is between the honeycomb plane and the magnetic field $\mathbf{H}$. (b) Angle-dependent phase diagram for the model with parameters $(J_1, K_1, \Gamma_1, J_3) = (-0.5, -5.0, +2.5, +0.5)$ meV and $(g_a, g_b, g_{c^*}) = (2.3, 2.3, 1.3)$. We identified a Region I, where the ground state is the antiferromagnetic zigzag order for all angles θ, a Region II where for a fixed $H = |\mathbf{H}|$ both phases, the zigzag phase and the partially polarized phase, exist, dependent on the orientation of the field, parametrized by θ. Finally, in Region III, the model is for all field orientations in the polarized phase. Fig. (a,b) reprinted from Ref. [82].

diagram, where we found in agreement with experiment [285] a very strong dependence of the critical field on the field direction. For a magnetic field within the honeycomb plane, i.e. $\theta = 0°$, we determined a critical field $H_c(0°) \approx 6\,\mathrm{T}$, consistent with the experimental $H_c = 6 - 8\,\mathrm{T}$ [267–272]. For a magnetic field perpendicular to the honeycomb plane, i.e. $\theta = 90°$, we determined a much larger critical field of $H_c(90°) \approx 75\,\mathrm{T}$. In classical calculations, performed by Stephen M. Winter, the anisotropic effect was reduced, with a higher in-plane critical field $H_c(0°) \approx 11\,\mathrm{T}$ and a lower out-of-plane critical field $H_c(90°) \approx 51\,\mathrm{T}$.

For the discussion of the magnetic torque behaviour, it turned out to be useful to identify three distinct field regions. For fields with $|\mathbf{H}| < H_c(0°)$, the model is in the magnetically ordered AFM zigzag phase, independent of the magnetic field orientation. We labelled this region in the phase diagram in Fig. 6.3(b) as "Region I". For intermediate fields, with $H_c(0°) \leq |\mathbf{H}| < H_c(90°)$, the ground state of Model 2 depends on the orientation of the magnetic field. While for fields close the honeycomb plane, the polarized phase is entered for relatively low fields, away from the honeycomb plane the zigzag ordered phase becomes more robust against external fields. We associated this situation with the so-called "Region II". Finally, for fields with $|\mathbf{H}| \geq H_c(90°)$, we identified with "Region III" a regime where the model is in the polarized ground state for all field orientations.

After identification of the phase boundaries, we characterized the phases through static spin-spin correlations $\mathcal{S}(\mathbf{q}, \omega = 0) = \sum_\alpha \langle \hat{S}^\dagger_\alpha(\mathbf{q}) \hat{S}_\alpha(\mathbf{q}) \rangle$, where $\alpha = \{x, y, z\}$, determined by ED calculations on cluster 24A. The correlation functions for high-symmetry points in reciprocal space are shown in Fig. 6.4 for different field strengths within Region II. The wave vector $\mathbf{q}$ of the strongest $\mathcal{S}(\mathbf{q})$ characterizes the dominant features of the magnetic ground state as a function of angle θ. On finite clusters spontaneous symmetry breaking cannot be captured and in the absence of a magnetic field, the ground state shows strong correlations at all of the possible zigzag wave vectors, corresponding to the ordering wave vectors Y, M, and M′. In the presence of a magnetic field, such a symmetry is lifted and the energy of the three possible zigzag domains generally differ[2]. However, the correlations that correspond to the three possible ordered states are due to finite size effects still close to each other. For a field almost perpendicular to the honeycomb plane, at $\theta \lesssim 90°$ and $\theta \gtrsim 90°$, the correlation $\mathcal{S}(\mathrm{Y})$ dominates over the correlations of the other ordering wave vectors. Such a zigzag pattern is uniquely stabilized for fields in the bc^* plane.

[2]One exception for fields in the bc^* plane is the orientation with $\theta = 90°$, where the C_3 symmetry is restored and all zigzag domains are energetically equivalent.

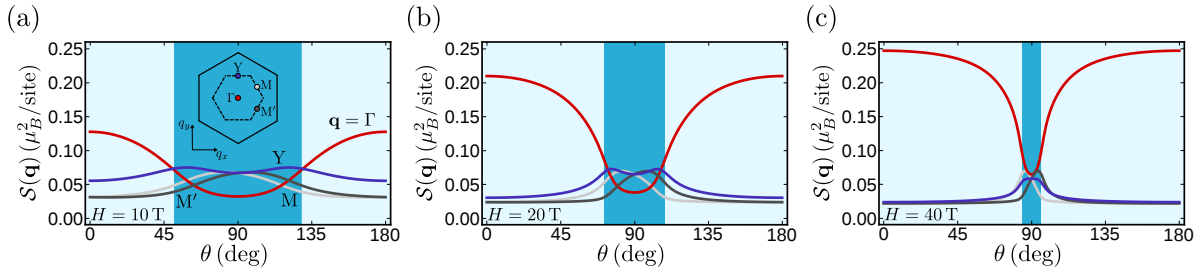

Figure 6.4: Static spin-spin correlations $\mathcal{S}(\mathbf{q}, \omega = 0) = \sum_\alpha \langle \hat{S}_\alpha^\dagger(\mathbf{q}) \hat{S}_\alpha(\mathbf{q}) \rangle$ for high-symmetry points Γ, Y, M, M′, obtained with ED calculations on cluster 24A as a function of the angle θ between the magnetic field and the honeycomb plane. The phases identified in the phase diagram in Fig. 6.3(b) are indicated by the matching background colour for the field strengths within Region II, with calculations at (a) $H = 10\,\mathrm{T}$, (b) $H = 20\,\mathrm{T}$, and (c) $H = 40\,T$. Fig. adapted from Ref. [82].

Within Region II, a field rotation towards the honeycomb plane drives then the system through a phase transition, entering the field-polarized phase. The polarized phase, indicated in Fig. 6.4 with a light-blue background, is characterized by a dominant $\mathcal{S}(\Gamma)$, with the strongest contributions for field directions close to the b axis ($\theta = 0°$, $\theta = 180°$). This observation was consistently confirmed numerically for low magnetic fields in Region II with $H = 10\,\mathrm{T}$ (Fig. 6.4(a)), intermediate fields with $H = 20\,\mathrm{T}$ (Fig. (b)), and fields close to the upper bound of Region II with $H = 40\,\mathrm{T}$ (Fig. (c)).

6.3.2 Torque and Magnetotropic Coefficient in α-$RuCl_3$

Next, we calculated the angle-dependence of the spin expectation value $|\langle \mathbf{S} \rangle|$, magnetic torque τ, and magnetotropic coefficient k for Model 2 with an anisotropic g-tensor, shown in Fig. 6.5. The results shown in Fig. (a,c,e) were obtained with exact diagonalization on the symmetric 24A cluster, while the results shown in Fig. (b,d,f) were obtained from classical calculations by Stephen M. Winter. The field regimes of Region I, Region II, and Region III, as defined in Fig. 6.3(b), are indicated for the respective field strengths for the ED and the classical case.

In the low-field Region I, with $|\mathbf{H}| < H_c(0°)$, the ground state is the AFM zigzag order for all field orientations. As discussed in Chapter 5, the orientation of the magnetic moments is for models with sufficient $\Gamma_1 > 0$ and an ordering wave vector $\mathbf{Q} = \mathrm{Y}$ located in the ac^* plane [257]. Therefore, fields along the b axis, i.e. $\theta = 0°$, are perpendicular to the zero-field ordered moments. We will revisit this issue in more detail in Section 6.4. In this case, the magnetic moments are most influenced by the presence of a field, in contrast to field orientations that correspond to other angles θ. This effect is enhanced by the g-tensor anisotropy, since the contribution within the honeycomb plane is larger than along the c^* axis, $g_{ab} > g_{c^*}$. Such a mechanism is reflected in the minimum of the spin expectation value at $\theta = 90°$, shown in Fig. 6.5(a,b) for ED and classical results respectively, where due to the absence of a phase transition in Region I the curve is smooth for all angles. The magnetic torque response, shown in Fig. (c,d), follows approximately the conventional $\tau \propto \sin 2\theta$ angle-dependence and the magnetotropic coefficient $k = \mathrm{d}\tau/\mathrm{d}\theta$, shown in Fig. (e,f), is smooth, confirming the absence of phase transitions in Region I.

In fields within Region II, with $H_c(0°) \leq |\mathbf{H}| < H_c(90°)$, effects of the phase transitions between the zigzag and the polarized phase are observable. Classically, the phase transition manifests through kinks in the spin expectation value, Fig. (b), which are smooth in the ED results in Fig. (a). These kinks are also observable in the magnetic torque in the classical calculations, see Fig. (d), and smoothed out as well for the ED calculations shown in Fig. (c). This corresponds to a deviation from the conventional $\tau \propto \sin 2\theta$ angle-dependence, with additional features in vicinity of the phase transition. In case of the magnetotropic coefficient k, these phase transitions cause pronounced features for both, the classical results in Fig. (f), and the ED results shown in Fig. (e), consistent with experiment [279], see also Fig. 6.2(b).

In the high-field Region III, i.e. $|\mathbf{H}| \geq H_c(90°)$, the system is in the polarized phase for all field

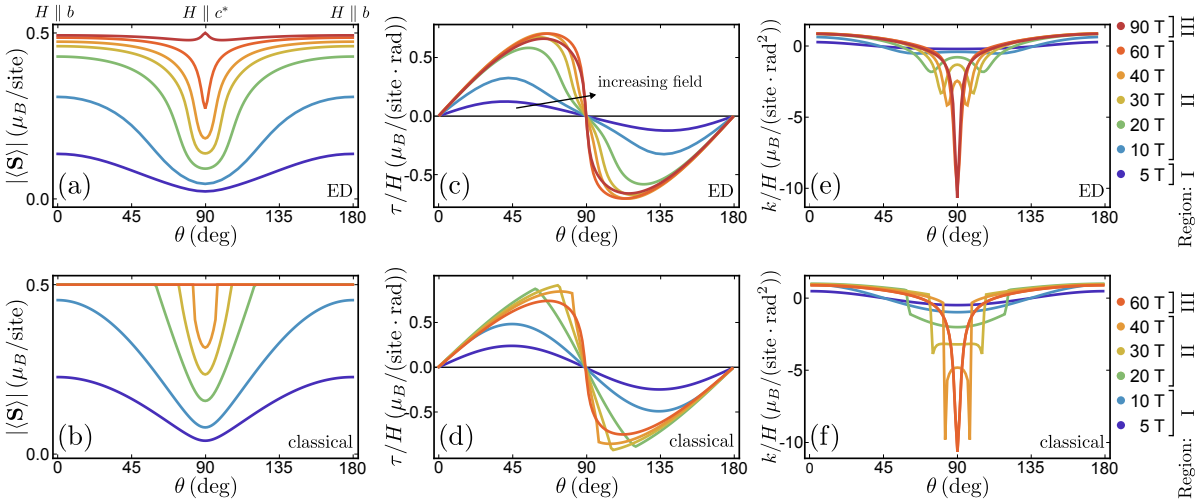

Figure 6.5: Angle-dependence of various quantities calculated based on the parameter set $(J_1, K_1, \Gamma_1, J_3) = (-0.5, -5.0, +2.5, +0.5)$ meV and $(g_a, g_b, g_{c^*}) = (2.3, 2.3, 1.3)$ for various magnetic field values as indicated. Region I, II, III as defined in Fig. 6.3(b) are indicated for ED and classical cases. (a) Spin expectation value from ED, (b) $|\langle \mathbf{S} \rangle|$ from classical calculations, (c) magnetic torque normalized with field from ED, (d) from classical calculations, (e) magnetotropic coefficient $k = \mathrm{d}\tau/\mathrm{d}\theta$ normalized with filed from ED, and (f) classical calculations. Fig. adapted from Ref. [82].

angles. Consequently, the classical spin expectation value is constant for all angles, Fig. (b), while there appears a small dip in the ED calculations for out-of-plane field orientations, Fig. (a). This can be related to suppressed quantum fluctuations in the case of high symmetry field orientations, like it is the case for $\mathbf{H} \parallel c^*$. The magnetic torque follows a sawtooth angle-dependence for both, ED and classical calculations shown in Fig. (c) and (d) respectively. This can be interpreted as a consequence of the crystallographic c^* axis being a hard axis due to the $\Gamma_1 > 0$ exchange term and the g-tensor anisotropy with $g_{ab} > g_{c^*}$. Close to the hard axis, the system is more susceptible towards changes in the field orientation, reflected in the rapid changes in the magnetic torque. The magnetotropic coefficient is characterized by one sharp minimum at the hard axis c^*, consistent with the considerations above.

Finally, we computed the field-dependence of the magnetic torque τ and magnetotropic coefficient k for Model 2 at various fixed field angles, presented in Fig. 6.6, in order to compare with the experimental results by Leahy *et al.* [267] and Modic *et al.* [281]. Consistent with experiment and previous ED studies [230], we observed for field strengths corresponding to Region II a kink in the torque, as a signature

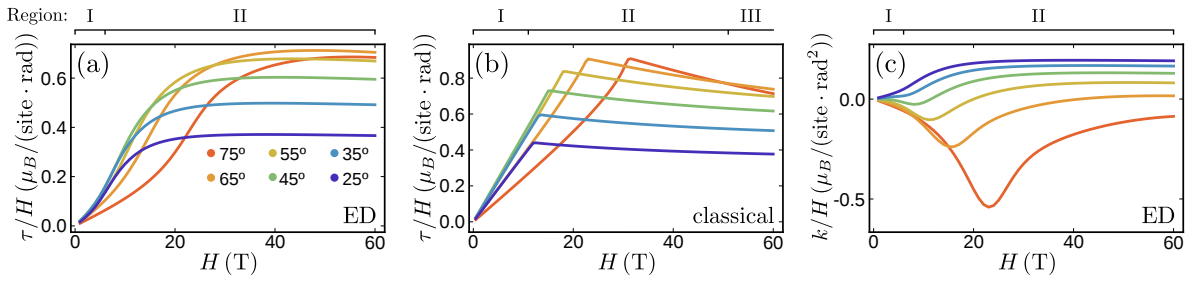

Figure 6.6: Field-dependence of various quantities calculated based on the parameter set $(J_1, K_1, \Gamma_1, J_3) = (-0.5, -5.0, +2.5, +0.5)$ meV and $(g_a, g_b, g_{c^*}) = (2.3, 2.3, 1.3)$ for several angles between field and honeycomb plane, as indicated. (a) Magnetic torque from ED calculations, normalized with field, (b) magnetic torque from classical calculations, (c) magnetotropic coefficient, normalised with field, from ED calculations. Fig. adapted from Ref. [82].

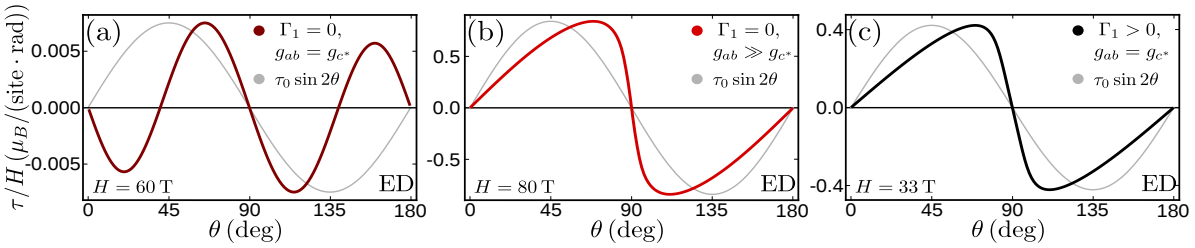

Figure 6.7: Angle-dependence of normalized magnetic torque τ/H for indicated parameter sets with $\tau = \tau_0 \sin 2\theta$ as a reference shown in gray for each model. (a) Kitaev term as the only source for anisotropy with $(J_1, K_1, \Gamma_1, J_3) = (-0.5, -5.6, 0, +0.5)$ meV and $(g_a, g_b, g_{c^*}) = (2.0, 2.0, 2.0)$ at $H = 60$ T, (b) g-anisotropy as the main anisotropy source with $(J_1, K_1, \Gamma_1, J_3) = (-0.5, -5.6, 0, +0.5)$ meV and $(g_a, g_b, g_{c^*}) = (2.0, 2.0, 0.2)$ at the critical field for the out-of-plane orientation $H = 80$ T, (c) Γ_1 effects as the main anisotropy source with $(J_1, K_1, \Gamma_1, J_3) = (-0.5, -5.6, +2.5, +0.5)$ meV and $(g_a, g_b, g_{c^*}) = (2.0, 2.0, 2.0)$ for $H = H_c(90°) = 33$ T. Fig. adapted from Ref. [82].

for the phase transition between the zigzag and the polarized phase, see Fig. 6.6(b) for the classical results. The ED results, shown in Fig. (a), are consistent with smoothed features. In both cases, the location of the kink is pushed to higher fields for higher angles, i.e. fields further away from the honeycomb plane. For fields above the critical field, $H > H_c$, the torque magnitude is essentially saturated, showing a slow decrease towards the $H \to \infty$ limit, especially visible in the classical calculations in Fig. (b). We elaborate on that limit further below. In the magnetotropic coefficient k, determined by ED and shown in Fig. (c), the phase transition is indicated as a single dip. This observation is consistent with only one phase transition, suggesting the absence of an intermediate field phases. However, it should be noted that this statement relies on the accuracy of the chosen Model 2 as an accurate description of α-$RuCl_3$ and relies on the field resolution of the calculations $\Delta H = 1$ T for the numerically determined second derivative of the ground state energy in the ED calculations.

6.3.3 Magnetic torque in limiting models

In order to gain intuition about the interplay of the different anisotropic contributions in Model 2, we calculated the magnetic torque response with exact diagonalization for various limits, shown in Fig. 6.7. For comparison, we indicated the conventional case with $\tau \propto \sin 2\theta$ to simplify the identification of the sawtooth features. The magnetic torque response can be expanded in terms of even order sine functions:

$$\frac{\tau}{H} = \sum_{n=1}^{\infty} c_{2n} \sin(2n\theta) = c_2 \sin(2\theta) + c_4 \sin(4\theta) + \dots \tag{6.8}$$

The contribution of the coefficients c_{2n} is in this framework a convenient criterium for the deviation of the torque angle-dependence from the conventional case with $c_{2n} = 0$ for $n > 1$.

The case, where the anisotropy solely stems from the Kitaev term is shown in Fig. 6.7(a) with $(J_1, K_1, \Gamma_1, J_3) = (-0.5, -5.6, 0, +0.5)$ meV and $(g_a, g_b, g_{c^*}) = (2.0, 2.0, 2.0)$. As mentioned in Chapter 5, the ferromagnetic Kitaev model is isotropic on the classical level. Quantum order-by-disorder mechanisms [286], however, choose the cubic axes as easy axes in the quantum limit. This results in a $\tau \propto \sin 4\theta$ angle-dependence, determined by ED calculations in the high-field regime at $H = 60$ T. ED calculations in Region III reveal that $|c_2|, |c_4| \propto H^{-2}$, and $|c_6|, |c_8| \propto H^{-4}$, corresponding to an anomalous scaling of the coefficients in the torque expansion in Eq. (6.8). However, in the known Kitaev materials to date, these order-by-disorder mechanism are overshadowed by effects of the other anisotropic contributions in the effective magnetic Hamiltonian.

One example for the dominance of other anisotropic contributions is the torque response shown in Fig. 6.7(b), determined for identical spin-spin parameters to the pure K_1 anisotropy case, $(J_1, K_1, \Gamma_1, J_3) = (-0.5, -5.6, 0, +0.5)$ meV, but with strong g-anisotropy, $g_{ab} \gg g_{c^*}$ at the field $H = H_c(90°)$. In this case, the $\sin 4\theta$ contribution is suppressed and a sawtooth angle-dependence emerges, showing clear

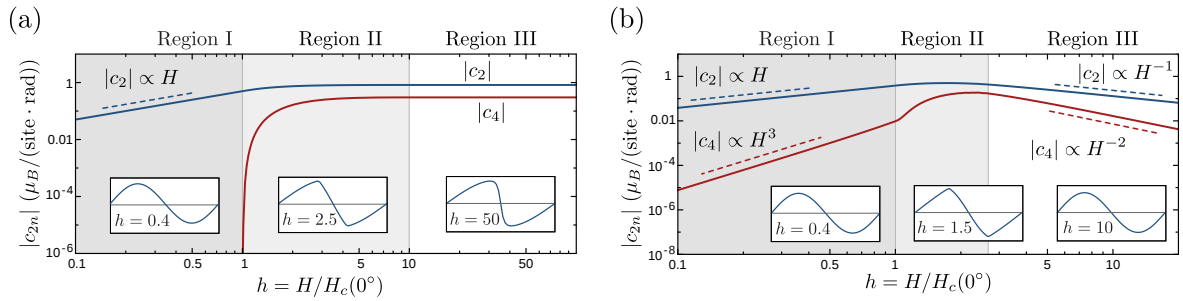

Figure 6.8: Fits of the coefficients in the magnetic torque expansion given in Eq. (6.8) to classically obtained curves, over a wide field range for (a) g-anisotropy as the main anisotropic source for the parameter set $(J_1, K_1, \Gamma_1, J_3) = (-0.5, -5.6, 0, +0.5)$ meV and $(g_a, g_b, g_{c^*}) = (2.0, 2.0, 0.2)$, (b) $\Gamma_1 > 0$ as the main anisotropic source for the parameter set $(J_1, K_1, \Gamma_1, J_3) = (-0.5, -5.6, +2.5, +0.5)$ meV and $(g_a, g_b, g_{c^*}) = (2.0, 2.0, 2.0)$. Fig. adapted from Ref. [82].

deviations from the $\sin 2\theta$ angle-dependence. In order to analyse the deviations more systematically, we fitted the leading order coefficients in the expansion Eq. (6.8) with torque curves obtained from classical calculations by Stephen M. Winter. Since the quantum order-by-disorder mechanism of the Kitaev term is suppressed in the presence of g-anisotropy, classical calculations are sufficient to hint the qualitative behaviour of the torque angle-dependence. In Fig. 6.8(a) we show the scaling with field of the fitted coefficients $|c_2|$ and $|c_4|$. In the ordered phase, Region I, the conventional torque angle-dependence with $c_{2n} = 0$ for $n > 1$ is confirmed. The scaling of $\tau/H \propto H$ implies the conventional quadratic dependence $\tau \propto H^2$, as discussed in Chapter 3. Increasing the field towards Region II, a finite c_4 contribution enters the torque expression, so that the angle-dependence deviates from the conventional behaviour and develops sawtooth features. Then, for fields in Region III, both coefficients are field-independent, so that the high-field torque exhibits consistently a sawtooth angle-dependence over wide field ranges. Such a behaviour can be assigned to the fact that the anisotropy stems solely from the anisotropic angle-dependent effective field $\mathbf{H}_{\text{eff}} = \mathbb{G}^{\text{T}} \cdot \mathbf{H}$. This effect is still present in the limit of the fully polarized phase, where the underlying bulk susceptibility is isotropic and does not contribute to the magnetic torque. Note, that this statement relies on the approximation that the g-tensor is independent of the magnetic field.

If the only anisotropy source is the off-diagonal spin-spin exchange $\Gamma_1 > 0$ term in Model 2, $(J_1, K_1, \Gamma_1, J_3) = (-0.5, -5.6, +2.5, +0.5)$ meV, and the g-tensor is isotropic, the angle-dependence at $H = H_c(90°)$ develops a sawtooth angle-dependence as well, shown in Fig. 6.7(c). Therefore, it is difficult in these intermediate field regimes to distinguish magnetic torque response due to g-anisotropy from anisotropy caused by $\Gamma_1 > 0$. To systematically analyse the angle-dependence, we fitted again classical torque curves to Eq. (6.8), the corresponding field scaling of the coefficients is shown in Fig. 6.8(b). In the low-field regime, Region I, higher order coefficients with $n > 1$, such as c_4, are in this case finite. However, due to the strong suppression at low fields $|c_4| \propto H^3$, signatures of these contributions are barely visible and the torque angle-dependence appears similar to the conventional $\sin 2\theta$ angle-dependence. In Region II, for intermediate fields, the interplay of second and fourth power coefficients lead to a sawtooth shape consistent with the ED result shown in Fig. 6.7(c). In contrast to the g-anisotropy case, in the high-field Region III, the coefficients remain field-dependent and scale as $|c_2| \propto H^{-1}$ and $|c_4| \propto H^{-2}$. This implies a suppression of the magnetic torque in the infinite-field limit $H \to \infty$. For an isotropic g-tensor, the spins are in this limit polarized along the field direction, so that a derivative with respect to θ vanishes in the fully polarized case. The spins follow the field and are aligned perfectly parallel to it.

In Ref. [278] it was proposed that chirality is the reason for the observation of the sawtooth angle-dependence in α-$RuCl_3$. To comment shortly on that, the scalar spin chirality term $\langle \mathbf{S}_i \cdot (\mathbf{S})_j \times \mathbf{S}_k) \rangle$ in the Hamiltonian may be induced by the presence of an external field, as discussed in Chapter 2. However, the spin Hamiltonian of α-$RuCl_3$ should be determined in the limit of strong spin-orbit coupling in terms of the j_{eff} basis. The perturbation theory results presented in Chapter 2 refer therefore not to

the appropriate basis for α-$RuCl_3$. For this reason, Ying Li determined the effective spin Hamiltonian with the hybrid method in the strong SOC limit and found such terms to be weak, generally, but also to differ from the expression $\langle \mathbf{S}_i \cdot (\mathbf{S})_j \times \mathbf{S}_k) \rangle$. Moreover, as pointed out in Chapter 2, the anisotropy in the scalar spin chirality stems from the magnetic flux that penetrates the three-site plaquette, which is proportional to the projection of the field onto the normal vector of the plaquette, $\mathbf{H} \cdot \mathbf{n}$. Consequently, the system should be most susceptible to in-plane fields, with $\theta = 0°$, in contrast to the experimental observations [278]. In other words, direct coupling of the field to three-spin terms would result in sawtooth features centred around $\theta = 0°$ instead of the observed $\theta = 90°$.

6.3.4 Summary

To summarize, the experimentally observed magnetic torque could be reproduced successfully with ED calculations using Model 2, which reproduces the zero-field INS data of α-$RuCl_3$, together with an anisotropic g-tensor determined from comparison with magnetization measurements in Section 6.2. Due to anisotropy of the critical field $H_c(\theta)$, we distinguished between three different field regimes with qualitatively different torque response. While in the low-field Region I a conventional $\sin 2\theta$ behaviour is predicted, the magnetic torque in the intermediate field Region II is dominated by signatures of the phase transitions between the AFM zigzag order and partially polarized phases. At high-fields in Region III with $H \gtrsim H_c$, a sawtooth torque is expected as a result of the honeycomb plane being an easy plane in the spin Hamiltonian.

Therefore, we concluded that a sawtooth torque, outside of field regions with various phase transitions or strong influence of the zero-field magnetic order, is a direct consequence of the presence of SOC induced terms like $\Gamma_1 > 0$ and an anisotropic g-tensor with $g_{ab} > g_{c^*}$. In contrast to interpretations in terms of exotic chiral contributions [278], this seems to be a rather general property of the Kitaev materials. A possible distinction between the two mechanisms may be magnetic torque measurements for $H \gg H_c$, where effects of the g-anisotropy are predicted to be field-independent, while magnetic torque due to spin interaction terms should be suppressed and eventually vanish.

6.4 Magnetic excitations in α-$RuCl_3$ under magnetic field

Stephen M. Winter, **Kira Riedl**, David Kaib, Radu Coldea, and Roser Valentí,
Probing α-$RuCl_3$ Beyond Magnetic Order: Effects of Temperature and Magnetic Field,
Phys. Rev. Lett. **120**, 077203 (2018)
[83]

In the previous section we found for Model 2 only one phase transition in the magnetic torque response. The remaining question is whether this framework can also consistently explain the magnetic excitations in the presence of a magnetic field. In 2018, Banerjee *et al.* [47] performed neutron scattering experiments on α-$RuCl_3$ with a magnetic field along the crystallographic a direction. From neutron diffraction, they determined a dominance of the Bragg peak at both ordering wave vectors $\mathbf{Q} = \{\mathrm{M}, \mathrm{M}'\}$ and a suppression at $\mathbf{Q} = \mathrm{Y}$ with increasing field up to $H = 6\,\mathrm{T}$. The authors measured then the inelastic neutron scattering along a path Γ'-Y-Γ-Y-Γ', shown in Fig. 6.9(a) for an intermediate field at $H = 4\,\mathrm{T}$ and a field close to the critical field with $H = 8\,\mathrm{T}$. Upon increasing field, the INS intensities reveal a softening of the gap at the Γ-point, together with a persistent Γ-point continuum over wide field ranges. In a conventional situation, such as antiferromagnetic Heisenberg interactions on a square lattice, Goldstone modes appear at all fields below H_c at the ordering wave vector $\mathbf{Q}$ [287]. In contrast, the INS experiments in α-$RuCl_3$ show intensity away from the ordering wave vector, but instead at the Y-point for small fields, which then disappears for increasing fields that are still much smaller than H_c. Banerjee *et al.* interpreted these observations as a signature for another field-induced transition, hinting at a field-induced QSL state that evolved from the zero-field Kitaev QSL.

A further characterization of the Γ-point continuum was possible via terahertz electron spin resonance (ESR) by Wang *et al.* [274]. In such an experiment, the excitations are induced with an oscillatory field $\mathbf{h}_\omega$ that is polarized longitudinal or transverse to the steady external field $\mathbf{H}$. In Fig. 6.9(b), we show

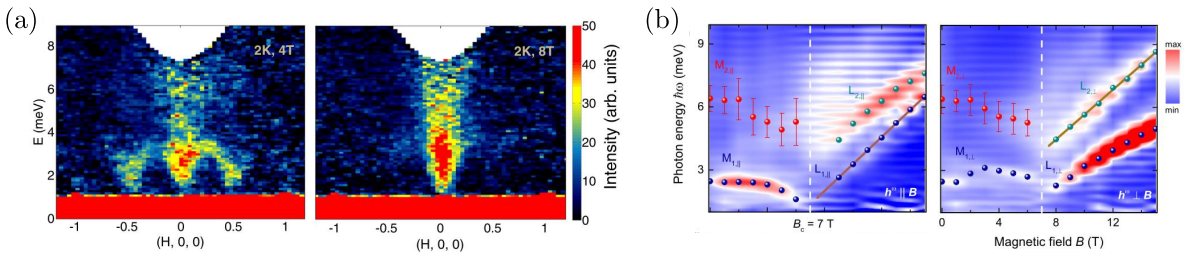

Figure 6.9: (a) INS intensity of α-$RuCl_3$ measured by Banerjee *et al.* [47] under magnetic field at $H = 4\,\mathrm{T}$, below H_c, and at $H = 8\,$, where the zigzag magnetic order is suppressed. The path in reciprocal space corresponds to Γ'-Y-Γ-Y-Γ' in the notation used in this chapter. (b) Terahertz spectroscopy intensity of α-$RuCl_3$ measured by Wang *et al.* [274] for a longitudinal and a transverse oscillating field. Fig. (a) reprinted from Ref. [47], Fig. (b) reprinted from Ref. [274].

the intensities in these two channels measured in Ref. [274]. The authors interpret the softening in the longitudinal channel of the lowest mode $M_{1,\parallel}$ close to the critical field as an indication that the spin gap closes approaching H_c. They argued that another spin gap is then reopened above the critical field, where the lowest mode $L_{1,\parallel}$ increases linearly with field, which may be assigned to a one-magnon excitation with $\Delta S = \pm 1$. As mentioned by the authors, this assignment would result in an in-plane g-value of $g_{ab} = 11.1$. This questions the correct assignment of that mode, especially since the intensity in the transverse channel allows for a lower scaling with field of the $\Delta S = \pm 1$ excitation. At higher energies, a continuum emerges in the longitudinal channel above H_c. In contrast, in the transverse channel the mode $M_{1,\perp}$ shows no signatures of gap closing at the critical field and the lowest channel above the critical field, $L_{1,\perp}$, shows a more pronounced continuum character than it is the case for the longitudinal channel. From a theoretical perspective, the evolution of these modes as a function of field allows to identify the active modes in terms of ΔS, so that one-magnon and multi-magnon processes may be identified. Note, that Ponomaryov *et al.* [275] published consistent experimental observations, where their particular experimental setup should contain excitations with both polarizations $\mathbf{h}_\omega || \mathbf{B}$ and $\mathbf{h}_\omega \perp \mathbf{B}$ and may therefore be compared to an average of our results discussed below.

In this section, we present the magnetic excitations under field determined by ED calculations for Model 2 with the anisotropic g-tensor proposed in Section 6.2. The study of the magnetic response in INS experiments in the presence of a magnetic field to "dissect" the continuum of excitations according to the field dependence has recently been demonstrated for the pyrochlore $Yb_2Ti_2O_7$ [288], which also features anisotropic bond-dependent interactions. Our main goal is to determine, whether the shifting of INS weight under field can be explained within the previously proposed framework of magnon-decay processes and whether an assignment of the observed modes in the terahertz spectroscopy is possible for theoretical predictions based on Model 2.

6.4.1 AFM zigzag domains and influence of in-plane field directions

Before we analyze the magnetic excitations under field, we address first a subtle issue regarding the AFM zigzag patterns and the corresponding influence of the field orientation within the honeycomb ab plane. In the previous section, we considered field rotations in the bc^* plane away from the honeycomb layer. Since the INS experiments were performed for fields along the crystallographic a axis, we had to consider the implicated differences for such a field orientation. For $\mathbf{H} \parallel a$, mean-field calculations identified a first-order transition between the AFM zigzag order and the polarized phase, in contrast to a second-order transition for $\mathbf{H} \parallel b$ [252]. On the level of exact diagonalization, the type of phase transition is difficult to identify due to finite size effects. Whether the difference in the transition is a mean-field artefact or appears also in experiment remains therefore an open question, but should be kept in mind below.

Another issue is raised by the three energetically degenerate zigzag domains on the honeycomb lattice for Model 2, shown in Fig. 6.10(a) with the corresponding ordering wave vectors $\mathbf{Q} = \{\mathrm{Y}, \mathrm{M}, \mathrm{M}'\}$ in

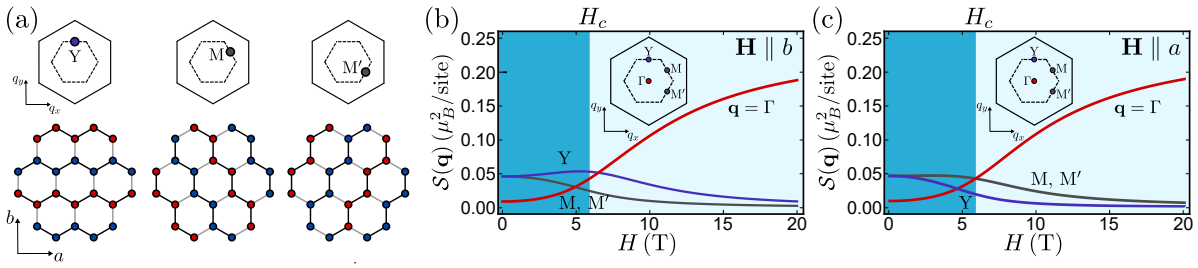

Figure 6.10: (a) Correspondence of zigzag ordering wave vectors Y, M, M′ in reciprocal space to real-space zigzag patterns, where spin up is indicated in red and spin down is indicated in blue. Bonds with a AFM spin configuration are indicated in grey. (b) Static spin-spin correlations $\mathcal{S}(\mathbf{q})$ as a function of field for $\mathbf{H} \parallel b$ and (c) as a function of field for $\mathbf{H} \parallel a$. The phases AFM zigzag phase for $H < H_c$ is distinguished from the partially polarized phase by the matching background colour with the phase diagram in Fig. 6.3(b). The static spin-spin correlations $\mathcal{S}(\mathbf{q}, \omega = 0) = \sum_\alpha \langle \hat{S}^\dagger_\alpha(\mathbf{q}) \hat{S}_\alpha(\mathbf{q}) \rangle$ were obtained with ED calculations for the parameter set $(J_1, K_1, \Gamma_1, J_3) = (-0.5, -5.0, +2.5, +0.5)$ meV and $(g_a, g_b, g_{c^*}) = (2.3, 2.3, 1.3)$. Fig. (b,c) adapted from Ref. [83].

reciprocal space. In the absence of a magnetic field, a magnetic order with AFM configuration along the Z-bond ($\mathbf{Q} = \mathrm{Y}$), is energetically degenerate with zigzag orders with AFM configurations along the X- or Y-bonds ($\mathbf{Q} = \mathrm{M}$, $\mathbf{Q} = \mathrm{M}'$ respectively). As mentioned in Section 6.3, in the presence of a magnetic field this degeneracy is lifted and specific AFM zigzag domains are energetically favoured.

For a zigzag order that corresponds to an ordering wave vector $\mathbf{Q} = \mathrm{Y}$ and in the presence of a FM Kitaev interaction $K_1 < 0$, the off-diagonal spin-spin interaction $\Gamma_1(S_i^x S_j^y + S_i^y S_j^x)$ is minimized (for $\Gamma_1 > 0$) for magnetic moments along $\hat{x} + \hat{y} \parallel \hat{a} + \sqrt{2}\hat{c}^*$, with the cubic axes defined as in Fig. 5.4(b). For sufficient $\Gamma_1 > 0$, Chaloupka *et al.* [257] found this moment orientation indeed energetically favourable. In such a case, an external field $\mathbf{H} \parallel b$ is perpendicular to the magnetic moments, so that this magnetic order is energetically favoured over zigzag patterns where the magnetic moments have a larger overlap with the field direction. We confirmed this with ED calculations of the static correlations $\mathcal{S}(\mathbf{q})$ at high-symmetry points as a function of field. In Fig. 6.10(b), we show $\mathcal{S}(\mathbf{q})$ for a field along the b direction, where the correlations at ordering wave vector $\mathbf{Q} = \mathrm{Y}$ are indeed higher than at order wave vectors $\mathbf{Q} = \{\mathrm{M}, \mathrm{M}'\}$. In neutron diffraction experiments with a field along the crystallographic b direction, we would therefore predict a Bragg peak at the Y-point in the Brillouin zone.

In contrast, for a zigzag domain with the AFM configuration along an X-bond, corresponding to $\mathbf{Q} = \mathrm{M}$, the off-diagonal spin-spin interaction along that bond is given by $\Gamma_1(S_i^y S_j^z + S_i^z S_j^y)$. In this case, the bond energy is minimized for magnetic moments along $\hat{y} + \hat{z} \parallel -\hat{a} + \sqrt{3}\hat{b} + 2\sqrt{2}\hat{c}^*$. A field $\mathbf{H} \parallel a$ overlaps less with these moments than with the moments for $\mathbf{Q} = \mathrm{Y}$. Ordering corresponding to $\mathbf{Q} = \mathrm{M}$ is therefore expected to be energetically favoured in this situation. This is confirmed by the ED calculations, where the correlations with ordering wave vector $\mathbf{Q} = \mathrm{M}$ are stronger for $\mathbf{H} \parallel a$, shown in Fig. 6.10(c), than those for $\mathbf{Q} = \mathrm{Y}$. An AFM configuration along the Y-bond corresponds to an ordering wave vector $\mathbf{Q} = \mathrm{M}'$ and is equal to the correlations at $\mathbf{Q} = \mathrm{M}$ for both field directions. In neutron diffraction experiments with $\mathbf{H} \parallel a$, we would therefore predict Bragg peaks at M and M′. This is in agreement with the experimental observation by Banerjee *et al.* [47].

6.4.2 Magnetic excitations in the Brillouin zone

For the analysis of the dynamic properties of Model 2 we have to consider a somewhat counterintuitive phenomenon present in the family of the extended Kitaev models. It can be shown through dual transformations that the low-energy excitations, in form of pseudo-Goldstone modes, appear at the wave vectors that do *not* correspond to the ordering wave vector [261]. For example, for a zigzag domain with ordering wave vector $\mathbf{Q} = \mathrm{Y}$, the pseudo-Goldstone modes are located at $\mathbf{q} = \mathrm{M}$ and $\mathbf{q} = \mathrm{M}'$ in the Brillouin zone. A pair of pseudo-Goldstone modes, that represents the low-energy boundary of the two-magnon continuum, is than located at $\Gamma = \mathrm{M} - \mathrm{M} = \mathrm{M}' - \mathrm{M}'$ or $\mathrm{Y} = \mathrm{M} - \mathrm{M}'$. Such a situation is

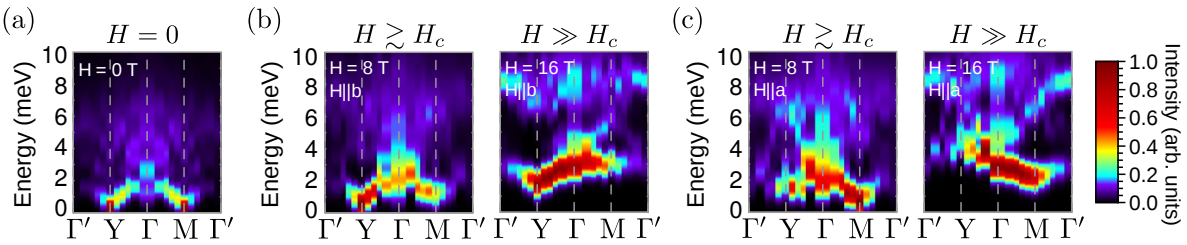

Figure 6.11: Theoretical INS intensities from ED calculations with the parameter set $(J_1, K_1, \Gamma_1, J_3) = (-0.5, -5.0, +2.5, +0.5)$ meV and $(g_a, g_b, g_{c^*}) = (2.3, 2.3, 1.3)$. In each figure, the color scale is independently normalized. (a) Zero-field intensity along indicated path in reciprocal space, (b) INS intensity for in-plane fields $\mathbf{H} \parallel b$ for field strengths close to the critical field ($H = 8\,\mathrm{T}$) and well above the critical field ($H = 16\,\mathrm{T}$), (c) INS intensity for in-plane fields $\mathbf{H} \parallel a$ for $H = 8\,\mathrm{T}$ and $H = 16\,\mathrm{T}$. Fig. adapted from Ref. [83].

expected for small fields with $\mathbf{H} \parallel b$. For small fields parallel to a, the ordering wave vectors $\mathbf{Q} = \mathrm{M}$ and $\mathbf{Q} = \mathrm{M}'$ are energetically degenerate, so that the pseudo-Goldstone modes are expected at $\mathbf{q} = \{\mathrm{Y}, \mathrm{M}'\}$ for M and at $\mathbf{q} = \{\mathrm{Y}, \mathrm{M}\}$ for M′. The low-energy bound of the two-magnon continuum can be located at $\{\Gamma = \mathrm{Y} - \mathrm{Y} = \mathrm{M}' - \mathrm{M}', \mathrm{M} = \mathrm{Y} - \mathrm{M}'\}$ for M and at $\{\Gamma = \mathrm{Y} - \mathrm{Y} = \mathrm{M} - \mathrm{M}, \mathrm{M}' = \mathrm{Y} - \mathrm{M}\}$ for M′. In order to analyse the influence of fields beyond the low-field limit, we calculated the INS response with exact diagonalization. The ED intensities were obtained from the four clusters introduced in Fig. 5.8. However, note that the presence of an external field, in principle, breaks the C_3 symmetry, so that the mapping from the real-space clusters to the reciprocal points shown in Fig. 5.8 is in this case only approximative. In all calculations, the spectra were Gaussian broadened with $\sigma = 0.5\,\mathrm{meV}$ and intensities were integrated over the out-of-plane contribution as discussed in Chapter 5.

In Fig. 6.11, we show the the ED intensities along the indicated path in reciprocal space. In the absence of an external field, the three zigzag domains are symmetrically equivalent on the finite size cluster of our numerical calculations, and the corresponding ED intensity shown in Fig. 6.11(a) is symmetrical with respect to the Γ-point. As detailed in the previous chapter, the Γ-point continuum is indeed captured by calculations based on Model 2 and has been discussed in terms of magnon-decay processes in the presence of off-diagonal Γ_1 interactions.

The ED intensity in the presence of a magnetic field along the crystallographic b direction is shown in Fig. 6.11(b). For $H \gtrsim H_c$, the weight at the M-point is pushed to higher energies, while the lowest energy excitation at the Y-point gains intensity. Additional weight can be also observed at the Γ-point. While the pseudo-Goldstone modes for the ordering wave vector $\mathbf{Q} = \mathrm{Y}$ were located for low fields $H \ll H_c$ at $\mathbf{q} = \{\mathrm{M}, \mathrm{M}'\}$, the situation is different for higher fields $H \gtrsim H_c$, where the lowest energy mode is shifted to be identical to the zero-field ordering wave vector and hence the two-magnon continuum is only located at the Γ-point. This observation is in agreement with LSWT calculations by Stephen M. Winter, shown in the supplemental information of Ref. [83]. This meets the intuitive picture from the square-lattice AFM Heisenberg situation [287] that a phase transition from the polarized to the ordered phase is realized by closing the gap at the ordering wave vector. The important difference in the presence of anisotropic bond-dependent interaction terms is that this picture is only true in the vicinity of the critical field $H \approx H_c$. Upon further lowering of the field, the rotation of the magnetic moments cause that the system enters a regime in which the ordering wave vector and the low-energy modes are not identical anymore due to the dual transformations [261] mentioned above.

The ED intensities in the presence of a magnetic field along the crystallographic a direction is shown in Fig. 6.11(c). In this case, there appears a low-energy mode at the M-point for $H \gtrsim H_c$, identical to one of the energetically degenerate ordering wave vectors $\mathbf{Q} = \{\mathrm{M}, \mathrm{M}'\}$ for this field direction. Additional weight is also observed at the Γ-point with an even more pronounced continuum than it was the case for $\mathbf{H} \parallel b$. In the case of $\mathbf{H} \parallel a$, there are low-energy modes expected at all three zigzag ordering wave vectors due to the degeneracy of the AFM zigzag order along the X- and Y-bond. Close to the critical field, the intensity is shifted toward the ordering wave vector at $\mathbf{Q} = \mathrm{M}$ and $\mathbf{Q} = \mathrm{M}'$ and the intensity

at $\mathbf{q} = \mathrm{Y}$ is suppressed. The loss of intensity at the Y-point observed in the INS experiment [47], which was performed along the path Γ'-Y-Γ-Y-Γ', also shown in Fig. 6.9(a), was assigned solely to an intensity shift to the Γ-point. In our ED calculations, we captured the loss of intensity at the Y-point, but predicted also a shift to the M-point, which was not probed in the experiment. We would therefore assign the intensity shift to a change of the field regime, where the low-energy modes become identical to the ordering wave vector. An exotic field-induced QSL phase is in this case not necessary to explain the measured INS intensity shift.

For higher fields, $H \gg H_c$, the INS intensities are pushed consistently to higher energies for both field directions, reflecting the energy gap induced by the external magnetic field. The lowest magnon at the Y- and the M-point remain sharply defined and are shifted to even higher energies. In contrast, the continuum character remains present at the Γ-point and is hence expected to be a feature even above H_c.

6.4.3 Dissection of the Γ-point continuum

Further dissection of the excitations under field is possible via electron spin resonance (ESR) absorption. In this case, the investigated compound is probed at the Γ point, where due to the polarization of the oscillatory field $\mathbf{h}_\omega$ only specific contributions of the spin structure factor are probed:

$$\omega\,\chi''(\omega) \propto \omega\,\mathcal{S}_{\alpha\alpha}(\mathbf{q} = \Gamma, \omega) \qquad \text{with} \qquad \alpha \parallel \mathbf{h}_\omega. \tag{6.9}$$

The theoretical ESR intensities for Model 2 with the g-tensor from Section 6.2 can then be directly compared to the experimental results by Wang *et al.* [274], shown in Fig. 6.9(b).

In Fig. 6.12 we show the ESR response for Model 2 from ED calculations, compared to LSWT intensities determined by Stephen M. Winter. The LSWT intensities were evaluated for an ordering wave vector $\mathbf{Q} = \mathrm{Y}$ for fields along the b direction, and were taken as an average of the intensities with ordering wave vectors $\mathbf{Q} = \{\mathrm{M}, \mathrm{M}'\}$ for field along the a direction. Therefore, the energetically favoured zigzag domains for the respective field directions were considered, which is advantageous compared to the ED calculations were a contribution from all zigzag domains is unavoidable.

In Fig. 6.12(a) we show the ESR intensities for $\mathbf{H} \parallel b$. For fields below the phase transition, $H < H_c$, the Γ point continuum is confirmed in the ESR response. The LSWT intensity reveals a one-magnon mode around $E \approx 3\,\mathrm{meV}$ labelled $m_1^\perp$ for an oscillatory field transverse to the external field $\mathbf{h}_\omega \perp \mathbf{H}$ with low intensity, and a magnon mode with strong intensity at the same energy labelled $m_1^\parallel$ for longitudinal excitations $\mathbf{h}_\omega \parallel \mathbf{H}$. These modes also appear in the ED intensities, where the similar response in both polarization channels may be an artefact of the absence of symmetry breaking due to finite size effects, as discussed above. These one-magnon modes were observed in experiment [274], shown in Fig. 6.9(b), and assigned as $M_{1,\parallel}$, with strong intensity, and $M_{1,\perp}$, with low intensity matching the LSWT predictions. In the ED calculations we found additional continuum modes $m_2^\perp$ and $m_2^\parallel$ around $E \approx 6\,\mathrm{meV}$, consistent with the experimentally observed modes $M_{2,\parallel}$ and $M_{2,\perp}$ [274].

For a field above the critical field, $H > H_c$, LSWT calculations revealed a one-magnon mode only in the transverse channel, labelled $l_1^\perp$, while there is no intensity in the longitudinal channel, see Fig. 6.12(a). In the ED case, it is possible to assign three distinct magnon modes, labelled $l_{1\ldots3}^\perp$ for the transverse and $l_{1\ldots3}^\parallel$ for the longitudinal channel. In agreement with the LSWT result, the most intense mode is $l_1^\perp$. In this case, the energy gap scales approximately linear with the external field H. In experiment, such transverse high-field one-magnon excitations appears as well, indicated as $L_{1,\perp}$ in Fig. 6.9(b). In the ED calculations, we observed a second intense transverse mode $l_2^\perp$ at higher energies with larger slope than $l_1^\perp$ as a function of field H, suggesting a multi-magnon origin with $\Delta S \geq 1$. This mode can be assigned to the experimentally measured $L_{2,\perp}$ in Fig. 6.9(b). In the longitudinal channel, the excitation energy of the lowest mode $l_1^\parallel$ from ED calculations scales faster with field than its transverse counterpart, in agreement with experiment. The higher energy mode $l_2^\parallel$ may be assigned to $L_{2,\parallel}$, although it should be noted that the slope seems to differ.

For fields with $\mathbf{H} \parallel a$, shown in Fig. 6.12(b), the ED observations are similar. This is not surprising, since the main differences in the INS intensities were at the Y, M, and M$'$ points, while the Γ point continuum was not influenced strongly by the specific in-plane field direction. In the ESR response,

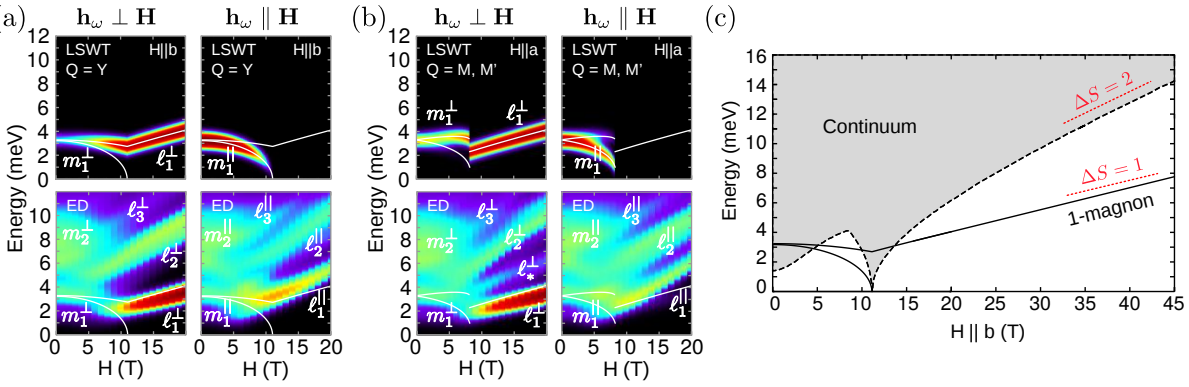

Figure 6.12: Polarized ESR intensities according to Eq. (6.9) obtained from ED and LSWT (by Stephen M. Winter) calculations, resolved with respect to the transverse ($\mathbf{h}_\omega \perp \mathbf{H}$) and longitudinal ($\mathbf{h}_\omega \parallel \mathbf{H}$) channel for an external field with (a) $\mathbf{H} \parallel b$ and (b) $\mathbf{H} \parallel a$. In each figure, the color scale is independently normalized. (c) Cartoon of ESR intensity in terms of a one-magnon mode and a two-magnon continuum. Fig. (a,b,c) adapted from Ref. [83].

essentially the same modes as for a field along the b axis can be assigned, with the exception of an additional mode $l_*^\perp$. This origin of this mode is unclear, but it may be an artefact of finite size effects, due to artificial persistence of zigzag modes in the polarized phase for this particular field direction. The semi-classical LSWT calculations face the above mentioned issue that the phase transition at H_c is classically a first order transition. This is reflected in the LSWT intensities, where the one-magnon bands jump discontinuously at the critical field. However, the main features with a dominant $m_1^\parallel$ mode below H_c and a dominant $l_1^\perp$ mode above H_c are conserved.

Finally, we address the magnon-decay picture discussed in the previous section, illustrated by a cartoon in Fig. 6.12(c). This figure shows the lowest one-magnon excitations and two-magnon continuum at the level of LSWT. The continuum overlaps with the one-magnon modes at low-field and near H_c, suggesting strongest deviations from LSWT occur at these field ranges. The symmetry allowed coupling of the one-magnon modes and, for example, the two-magnon continuum may modify the scaling with field significantly in field regions where they are located at similar energies. Consequently, the slope $\Delta E/\Delta B$ may only correspond to the expression $g_{ab}\mu_B\Delta S$ in the high-field limit, where the overlap of the two branches is sufficiently suppressed. Measurements for much higher fields $H \gg H_c$ could enlighten this issue, since in this regime the decay-processes could be avoided and finite size effects in the ED calculations are expected to be less important than it is the case for $H \sim H_c$. Our calculations suggest this regime should be at fields $H > 20\,\mathrm{T}$.

6.4.4 Summary

The magnetic excitations in the presence of a magnetic field in Model 2 with the anisotropic g-tensor introduced in Section 6.2 captured the experimental observations in INS intensities [47] and polarized ESR intensities [274]. In the case of the INS response, we were able to study alternative paths in the Brillouin zone compared to experiment. Therefore, we could track the pseudo-Goldstone modes in comparison to the ordering wave vectors for fields close to H_c, where they are at identical points in the Brillouin zone, in contrast to the case of small fields where they differ. Therefore, the picture of the higher order magnon-decay processes as the reason for the continuum of excitations proposed in the previous chapter is also consistent with the INS response under magnetic field. In the direct (second order) phase transition from the zigzag to the polarized phase, we highlighted that the mechanism is a closure of the gap at the ordering wave vectors. This mechanism cannot yet be verified, because the existing data corresponds to a field direction that may be first order and along the wrong path in reciprocal space. Therefore, while a direct transition can explain the existing INS intensities, more data is needed.

In the case of the ESR intensities, a dissection of the transverse and longitudinal channels of the dynamic spin structure factor could provide further insight into the microscopic processes observed in α-$RuCl_3$ and predicted for Model 2 under field. In this case, the theoretical predictions agreed qualitatively with the experimental observations. Magnon modes in the different channels and the various energy regimes could be assigned to the experimentally observed modes. In order to identify quantitative predictions, for example for the anisotropic g-tensor, higher field experiments above $H \sim 20\,\mathrm{T}$ may be insightful.

6.5 Discussion

In this chapter, we investigated the magnetic field response of α-$RuCl_3$ under the assumption that its main features can be captured within the two-dimensional extended FM Kitaev Model 2 proposed in the previous chapter. Since there is experimental evidence that the g-tensor is anisotropic, we first determined model parameters for g_{ab} and g_{c^*} guided by *ab-initio* and by comparison with experimentally determined magnetization curves [237].

Based on these model parameters, we investigated then the magnetic torque response of α-$RuCl_3$. We identified the sawtooth angle-dependence for out-of-plane field rotations as a characteristic feature for models with an easy plane. This character is caused in the case of α-$RuCl_3$ by the finite $\Gamma_1 > 0$ exchange in the spin Hamiltonian, as well as the anisotropic g-tensor with $g_{ab} > g_{c^*}$. We predicted that these two mechanisms cause similar torque response at intermediate fields. In contrast, the torque magnetization τ/H due to Γ_1 should vanish in the infinite-field limit, while it should become field-independent if it is caused by g anisotropy. Experiments at sufficiently high fields may therefore distinguish between these two mechanisms and provide a more accurate estimation of the g-tensor values, which is also desirable in the context of the interpretation of other field-dependent studies.

These studies under field are especially interesting in light of the much discussed putative intermediate phase in α-$RuCl_3$ for fields that suppress the magnetic zigzag order. In the framework of the magnetic torque response, we could resolve, within the numerical resolution, only one phase transition. Therefore, additional exotic phases, next to the magnetically ordered zigzag phase and the polarized phase, seem to be absent in the theoretical description based on Model 2. This picture is also consistent with inelastic neutron scattering intensities, where we could explain the shift of low-energy INS intensity upon increasing field with effects of the bond-dependent anisotropic interactions. They lead to the somewhat counter-intuitive phenomenon that at low fields the lowest energy modes are located away from the ordering wave vector, while they are located at the ordering wave vector for higher fields close to H_c. Further INS experiments along a path that includes both, the Y and the M point, may confirm or falsify this prediction. The theoretical calculation of ESR intensities allowed for specific probing of certain contributions of the dynamical structure factor at the Γ point and revealed one- and multi-magnon characteristics that could be assigned to the features observed in experiment. Further experiments at higher fields may give additional hints toward the anisotropic g-tensor and whether the speculated coupling of one-magnon modes with the two-magnon continuum can be confirmed.

The discussed experiments in this chapter, with the magnetic torque, and the INS and ESR intensities are consistently explainable in the framework of the proposed Model 2. However, the simplifications within the determination of the model may hamper eventually the interpretation of experimental observations that depend on specific details. For example, according to recent INS measurements by Balz *et al.* [273], there is a stronger out-of-plane dispersion of the one-magnon modes than originally suggested [46, 231]. The authors speculated that an additional three-dimensionl order may be entered upon increasing field. Such a phase naturally exceeds the predictive power of the two-dimensional Model 2. An appropriate three-dimensional extension of the magnetic model may therefore be desirable. Moreover, it is not clear how to explain the observed thermal transport measurements [48], which show signatures of fractionalized excitations, within the framework of Model 2. Whether this challenging experiment can be reproduced, and whether it is possible to find a model that consistently explains the known experimental facts as well as a field-driven Kitaev phase seems to remain a critical open question. No doubt, resolving this question will require further inputs from experiment and theory, as well as refinement of the magnetic Hamiltonian.

Chapter 7

Summary and Outlook

In this thesis, we presented the theoretical description of the magnetic properties of various frustrated spin systems. Especially in search of exotic states, such as quantum spin liquids, magnetically frustrated systems have been subject of intense research within the last four decades. Relating experimental observations in real materials with theoretical models that capture those exotic magnetic phenomena has been one of the great challenges within the field of magnetism in condensed matter.

In order to build such a bridge between experimental observations and theoretical models, we followed two complementary strategies in this thesis. One strategy was based on first principles methods that enable the theoretical prediction of electronic properties of real materials without further experimental input than the crystal structure. Based on these predictions, low-energy models that describe magnetic interactions can be extracted and, through further theoretical modelling, can be compared to experimental observations. The second strategy was to establish low-energy models through comparison of data from experiments, such as inelastic neutron scattering intensities, with calculated predictions based on a variety of plausible magnetic models guided by microscopic insights. Both approaches allow to relate theoretical magnetic models with real materials and may provide guidance for the design of new frustrated materials or the investigation of promising models related to exotic magnetic states.

The projects presented in this thesis were discussed in the publications in Ref. [60, 77–83].

At the beginning of this thesis, in Chapter 1, we introduced the basic underlying concepts that are relevant for the projects discussed in Chapter 2–6. As one of the main motivations to study frustrated spin systems, we discussed the concept of quantum spin liquids focussed on fractionalized excitations as one of their defining properties. Such fractionalized excitations may be observed indirectly in experiments or appear as the solution of certain spin models. As a standard theoretical method to obtain such a spin model, we introduced perturbation theory, in which the kinetic energy of the electrons is treated perturbatively. We reviewed then the concept of density functional theory as a powerful tool to extract the electronic properties of specific materials and concluded the chapter with the discussion of possibilities to extract a magnetic model from first principles.

In Chapter 2 and Chapter 3, we investigated the magnetic properties of organic charge transfer salt compounds. In these materials, it is possible to map their complicated crystal structure onto the well-studied anisotropic triangular lattice. In Chapter 2, we investigated the magnetic interactions of four κ-$(ET)_2X$ salts, where their magnetic properties can be tuned by replacement of the anion X. To obtain a magnetic low-energy model, we used a "hybrid" method in which we built an electronic Hubbard Hamiltonian based on *ab-initio* DFT calculations and extracted the effective magnetic Hamiltonian via exact diagonalization and projection onto the corresponding low-energy subspace. In this approach interaction parameters with different orders of magnitude are treated on equal footing, which allowed us to study especially smaller interaction parameters that arise from spin-orbit coupling (SOC), such as the Dzyaloshinskii-Moriya (DM) interaction, or higher-order spin terms, such as the four-spin ring exchange. The extracted spin Hamiltonians confirmed, in the context of the known phases in the anisotropic lattice from literature, the observed square lattice Néel order and quasi one-dimensional behaviour for the respective materials and the absence of magnetic order for two QSL candidates. In

Chapter 3, we then investigated in more detail one of the charge transfer salts with the QSL candidate κ-$(ET)_2Cu_2(CN)_3$ (κ-Cu), in the context of μSR and magnetic torque data. While it was possible to theoretically model the μSR response in the framework of a critical scenario considering anisotropic SOC effects, this picture failed to explain the magnetic torque response of κ-Cu. Instead, we proposed a scenario, in which κ-Cu can be described as a valence bond glass, where orphan spins, arising from disorder effects in the crystal, dominate the magnetic response. This scenario could also explain the consistently observed mysterious $T_* = 6\,\mathrm{K}$ anomaly as a signature for a transition into the valence bond glass state. Seemingly contradicting experiments of specific heat and thermal transport, that were so far interpreted in terms of gapped and gapless QSL states, may also be consistently explained within the valence bond glass scenario.

After the successful extraction of magnetic model parameters for the anisotropic lattice organics, we discussed the hybrid method in more detail in the context of anisotropic magnetic interactions in the three-dimensional pyrochlore lattice in Chapter 4. This lattice is formed of corner-sharing tetrahedra and is known to be a highly symmetric host for a variety of exotic magnetic properties caused by frustration. The high symmetry of this lattice leads to strong restrictions onto anisotropic interaction parameters such as the DM interaction. We then demonstrated the hybrid method in detail for an example of the ferromagnet $Lu_2V_2O_7$. In this case, the low-energy spin Hamiltonian obeyed the previously derived symmetry restrictions and could give insight about the previously debated isotropic ferromagnetic exchange, as well as the quantitative determination of the DM interaction. However, not all discrepancies with other studies could be resolved, and further investigation under consideration of further neighbour exchange, as well as higher order contributions in the hybrid method, should be considered in order to resolve a more refined magnetic model. These considerations are relevant for observations such as the magnon Hall effect. We then applied the method to determine the anisotropic spin-spin contributions to the QSL candidate $Lu_2Mo_2O_5N_2$. For this compound only powder samples are available to date, which are suspected to suffer from strong disorder effects. In this case we determined a magnetic model for a hypothetical clean parent compound that displays, according to pseudofermion functional renormalization group calculations, also a spin-liquid ground state. Therefore, further studies, and especially the growth of single crystals, seem to be a promising experimental pursuit.

In Chapter 5 and Chapter 6, we then investigated with the Kitaev material α-$RuCl_3$ a different kind of frustration. While the honeycomb lattice is not geometrically frustrated, the so-called honeycomb Kitaev model contains frustrated bond-dependent compass interaction terms. In Chapter 5, we followed the second strategy mentioned above and used available experimental data as a starting point to determine an appropriate low-energy spin Hamiltonian in the context of inelastic neutron scattering (INS) measurements. These experiments revealed signatures of a continuum of excitations, which had been interpreted in terms of fractionalized excitations to a proximate spin-liquid phase. This observation was especially exciting, since the ground state of the exactly solvable Kitaev honeycomb model corresponds to a Majorana spin liquid. On the other hand it was known that α-$RuCl_3$ magnetically orders at low temperatures. Guided by the microscopic insights from previous *ab-initio* studies, we therefore theoretically modelled the INS intensity via exact diagonalization calculations for a variety of magnetic models. We determined, in qualitative agreement with first principles, a model for α-$RuCl_3$ that contains a dominant ferromagnetic Kitaev interaction, but also additional isotropic Heisenberg interactions and bond-dependent off-diagonal terms. The observed continuum could be explained in terms of magnon-decay processes, which produce a continuum of excitations in the INS spectrum and cannot be assigned uniquely to a QSL feature. In Chapter 6, we considered a regime in which the magnetic order in α-$RuCl_3$ is suppressed through magnetic field effects. An experimentally observed sawtooth magnetic torque response could be reproduced in the framework of the previously determined magnetic model and the sawtooth feature could be classified as a general property of materials that contain an easy plane due to bond-dependent anisotropic interactions or an anisotropic gyromagnetic tensor. The field-induced intensity shifts observed in INS experiments could be reproduced with exact diagonalization calculations were related to the off-diagonal bond-dependent anisotropic interactions. An agreement between polarized electron spin resonance intensities and theory enabled the assignment of various excitations observed at high field, allowing the high-field phase to be identified as an asymptotically polarized regime. In general, the discussed observations in the Kitaev material α-$RuCl_3$ seem therefore to be consistent with the picture of magnon-decay processes due to the bond-dependent

anisotropic spin-spin interaction terms. However, whether Majorana fermions or magnons have a more significant overlap with the real physical excitations remains an open question to date.

To conclude, we investigated the magnetic properties of a number of frustrated materials that became directly or indirectly relevant in the search for a quantum spin liquid state. Due to the lack of a smoking gun experiment, it revealed to be notoriously difficult to pinpoint the ground state solely based on experimental observations. On the other hand, the theoretical modelling of complicated low-energy spin models is certainly equally challenging. Since a quantum spin-liquid state is naturally related to low-temperature physics, small interaction parameters such as spin-orbit coupling cannot be neglected *a priori*. We studied the significant influence of spin-orbit coupling effects in materials with strong SOC, such as the honeycomb α-$RuCl_3$, with intermediate SOC, such as the pyrochlore vanadate, and with small SOC, such as the organic materials. The induced anisotropic magnetic response turned out to be, in most cases, challenging to handle and resulted in complicated low-energy models. In the future, further studies should help to build a better intuition for such anisotropic interaction terms, so that typical features like the excitation continuum can be identified quickly. Moreover, an intuitive handling of such terms may also enable to discover new mechanism, such at it was pioneered by Kitaev with his exact solution of a model that can only be realized in materials with strong spin-orbit coupling.

Another issue that was discussed in detail, especially for the organic materials, were disorder effects. In real materials, disorder is often difficult to avoid completely. However, the majority of theoretical approaches, including most *ab-initio* studies, work under the assumption of an ideal situation with a clean parent compound. One important counter-example may be the organic QSL candidate κ-Cu, where the low-temperature response seems to be dominated by disorder effects. This implies the somewhat discouraging insight that the effects of disorder could be more important than often assumed. However, it also allows for the more optimistic insight that it may be worthwhile to invest in the further development of theories that treat disorder effects appropriately. While a theoretical description is challenging, already developed frameworks such as the strong disorder renormalization group seem promising. A further development of these methods may certainly open routes to explain unresolved puzzles and may open the possibility to discover new phenomena in the field of frustrated magnetism.

Appendix A

Useful relations

A.1 Useful relations of spinor operators

In this appendix, we present useful relations of spinor operators that were used throughout the thesis. In general, these relations are based on the Abrikosov pseudo-fermion representation for spin 1/2 operators $\mathbf{S}_i = \frac{1}{2}\underline{c}_i^\dagger \vec{\sigma} \underline{c}_i$. Products of scalar products with Pauli matrices can be simplified as follows:

$$(\mathbf{a}\cdot\vec{\sigma})(\mathbf{b}\cdot\vec{\sigma}) = (\mathbf{a}\cdot\mathbf{b})\mathbb{1}_2 + i(\mathbf{a}\times\mathbf{b})\cdot\vec{\sigma}, \tag{A.1}$$

$$(\mathbf{a}\cdot\vec{\sigma})(\mathbf{b}\cdot\vec{\sigma})(\mathbf{c}\cdot\vec{\sigma}) = (\mathbf{a}\cdot\mathbf{b})(\mathbf{c}\cdot\vec{\sigma}) + i(\mathbf{a}\times\mathbf{b})\cdot\mathbf{c}\;\mathbb{1}_2 - (\mathbf{a}\cdot\mathbf{c})(\mathbf{b}\cdot\vec{\sigma}) + (\mathbf{c}\cdot\vec{\sigma})(\mathbf{a}\cdot\mathbf{b}). \tag{A.2}$$

For the projection onto singly occupied states of a product of spinors, in the formalisms introduced in Chapter 1 expressed as $\mathbb{P}\underline{c}_i\underline{c}_i^\dagger\mathbb{P}$, the spinor product can be related to the spin operator on that side multiplied with a Pauli matrix:

$$\begin{aligned}\underline{c}_i\underline{c}_i^\dagger &= \begin{pmatrix} c_{i\uparrow}c_{i\uparrow}^\dagger & c_{i\uparrow}c_{i\downarrow}^\dagger \\ c_{i\downarrow}c_{i\uparrow}^\dagger & c_{i\downarrow}c_{i\downarrow}^\dagger \end{pmatrix} = \begin{pmatrix} 1-c_{i\uparrow}^\dagger c_{i\uparrow} & -c_{i\downarrow}^\dagger c_{i\uparrow} \\ -c_{i\uparrow}^\dagger c_{i\downarrow} & 1-c_{i\downarrow}^\dagger c_{i\downarrow} \end{pmatrix} = \mathbb{1}_2 - \begin{pmatrix} \frac{1}{2}+S_i^z & S_i^x - iS_i^y \\ S_i^x + iS_i^y & \frac{1}{2}-S_i^z \end{pmatrix} \\ &= \frac{1}{2}\mathbb{1}_2 - \mathbf{S}_i\cdot\vec{\sigma}. \end{aligned} \tag{A.3}$$

The commutator of spinor pairs is in general given by the following expression:

$$\begin{aligned}[\underline{c}_1^\dagger\underline{c}_2, \underline{c}_3^\dagger\underline{c}_4] &= [c_{1\uparrow}^\dagger c_{2\uparrow}, c_{3\uparrow}^\dagger c_{4\uparrow}] + [c_{1\downarrow}^\dagger c_{2\downarrow}, c_{3\downarrow}^\dagger c_{4\downarrow}] \\ &= \sum_\sigma [c_{1\sigma}^\dagger c_{2\sigma}, c_{3\sigma}^\dagger] c_{4\sigma} + c_{3\sigma}^\dagger [c_{1\sigma}^\dagger c_{2\sigma}, c_{4\sigma}] \\ &= \sum_\sigma (c_{1\sigma}^\dagger \{c_{3\sigma}^\dagger, c_{2\sigma}\} - \{c_{1\sigma}^\dagger, c_{3\sigma}^\dagger\}) c_{4\sigma} + c_{3\sigma}^\dagger (c_{1\sigma}^\dagger \{c_{2\sigma}, c_{4\sigma}\} - \{c_{1\sigma}^\dagger, c_{4\sigma}\} c_{2\sigma}) \\ &= \sum_\sigma c_{1\sigma}^\dagger c_{4\sigma}\delta_{23} - c_{3\sigma}^\dagger c_{2\sigma}\delta_{14} \\ &= \underline{c}_1^\dagger\underline{c}_4\delta_{23} - \underline{c}_3^\dagger\underline{c}_2\delta_{14}, \end{aligned} \tag{A.4}$$

where the site indices were expressed as $\{1\ldots4\}$ for clarity.

A.2 Isotropy of spin contribution in scalar spin chirality

The scalar spin chirality $\mathcal{H}_{(3)} = \frac{1}{S}\sum_{\langle ijk\rangle} J_\chi^{ijk}\mathbf{S}_i\cdot(\mathbf{S}_j\times\mathbf{S}_k)$, derived from perturbation theory in Chapter 2, is anisotropic since the exchange parameter depends on the direction of the external magnetic field. In contrast, the spin contribution itself is isotropic. This can be seen from an expression in terms

of scalar products, where we use the Pauli matrix relations given by Eq. (A.1) and Eq. (A.2):

$$\begin{aligned} 4(\mathbf{a}\cdot\mathbf{S}_i)(\mathbf{b}\cdot\mathbf{S}_i) &= \underline{c}_i^\dagger(\mathbf{a}\cdot\vec{\sigma})\underline{c}_i\underline{c}_i^\dagger(\mathbf{b}\cdot\vec{\sigma})\underline{c}_i \\ &= \underline{c}_i^\dagger(\mathbf{a}\cdot\vec{\sigma})(\frac{1}{2}\mathbb{1}_2-\mathbf{S}_i\cdot\sigma)(\mathbf{b}\cdot\vec{\sigma})\underline{c}_i \\ &= \frac{1}{2}\mathbf{a}\cdot\mathbf{b}+i(\mathbf{a}\times\mathbf{b})\cdot\mathbf{S}_i. \end{aligned} \tag{A.5}$$

The term with three Pauli matrices vanishes, since the relation via Eq. (A.2) gives terms of the type $\langle\psi_{ij}|\underline{c}_i^\dagger(\ldots\mathbf{S}_i\ldots)\underline{c}_i|\psi'_{ij}\rangle = \langle\psi_{ij}|2\underline{c}_i^\dagger(\ldots\underline{c}_i^\dagger\vec{\sigma}\underline{c}_i\ldots)\underline{c}_i|\psi'_{ij}\rangle$ that vanish in the case of singly occupied sites in the ground state $|\psi_{ij}\rangle$ as long as $\ldots$ does not contain terms dependent on site i or contain a Pauli matrix $\vec{\sigma}$.

A.3 Permutation operator and ring exchange

The four-spin ring exchange term discussed in Chapter 2 can be related to the plaquette permutation operator:

$$\hat{P}_{ijkl} = \hat{P}_{ij}\hat{P}_{jk}\hat{P}_{kl} \tag{A.6}$$

where the two-spin permutation operator defined as $\hat{P}_{ij} = 2\mathbf{S}_i\cdot\mathbf{S}_j+\frac{1}{2}$, results in the four spin ring-exchange term through summation with its Hermitian conjugate, $(\hat{P}_{ijkl})^\dagger = \hat{P}_{lkji}$. This can be shown, for example, using the relations of the Pauli matrices given by Eq. (A.1) and Eq. (A.2):

$$\begin{aligned} \hat{P}_{ijkl}+\hat{P}_{lkji} &= (1+\vec{\sigma}_i\cdot\vec{\sigma}_j)(1+\vec{\sigma}_j\cdot\vec{\sigma}_k)(1+\vec{\sigma}_k\cdot\vec{\sigma}_l)+\text{H.c.} \\ &= 1+(\vec{\sigma}_i\cdot\vec{\sigma}_j)+(\vec{\sigma}_j\cdot\vec{\sigma}_k)+(\vec{\sigma}_k\cdot\vec{\sigma}_l)+(\vec{\sigma}_i\cdot\vec{\sigma}_j)(\vec{\sigma}_j\cdot\vec{\sigma}_k)+(\vec{\sigma}_i\cdot\vec{\sigma}_j)(\vec{\sigma}_k\cdot\vec{\sigma}_l) \\ &\quad +(\vec{\sigma}_j\cdot\vec{\sigma}_k)(\vec{\sigma}_k\cdot\vec{\sigma}_l)+(\vec{\sigma}_i\cdot\vec{\sigma}_j)(\vec{\sigma}_j\cdot\vec{\sigma}_k)(\vec{\sigma}_k\cdot\vec{\sigma}_l)+\text{H.c.} \\ &= 1+(\vec{\sigma}_i\cdot\vec{\sigma}_j)+(\vec{\sigma}_j\cdot\vec{\sigma}_k)+(\vec{\sigma}_k\cdot\vec{\sigma}_l)+(\vec{\sigma}_i\cdot\vec{\sigma}_k)+i(\vec{\sigma}_i\times\vec{\sigma}_k)\cdot\vec{\sigma}_j+(\vec{\sigma}_i\cdot\vec{\sigma}_j)(\vec{\sigma}_k\cdot\vec{\sigma}_l) \\ &\quad +(\vec{\sigma}_j\cdot\vec{\sigma}_l)+i(\vec{\sigma}_j\times\vec{\sigma}_l)\cdot\vec{\sigma}_k+(\vec{\sigma}_i\cdot\vec{\sigma}_j)[(\vec{\sigma}_j\cdot\vec{\sigma}_l)+i(\vec{\sigma}_j\times\vec{\sigma}_l)\cdot\vec{\sigma}_k]+\text{H.c.} \\ &= 1+(\vec{\sigma}_i\cdot\vec{\sigma}_j)+(\vec{\sigma}_j\cdot\vec{\sigma}_k)+(\vec{\sigma}_k\cdot\vec{\sigma}_l)+(\vec{\sigma}_i\cdot\vec{\sigma}_k)+(\vec{\sigma}_i\cdot\vec{\sigma}_j)(\vec{\sigma}_k\cdot\vec{\sigma}_l) \\ &\quad +(\vec{\sigma}_j\cdot\vec{\sigma}_l)+(\vec{\sigma}_i\cdot\vec{\sigma}_l)+i(\vec{\sigma}_i\times\vec{\sigma}_l)\cdot\vec{\sigma}_j+i(\vec{\sigma}_i\cdot\vec{\sigma}_j)[(\vec{\sigma}_l\times\vec{\sigma}_k)\cdot\vec{\sigma}_j]+\text{H.c.} \\ &= 1+(\vec{\sigma}_i\cdot\vec{\sigma}_j)+(\vec{\sigma}_j\cdot\vec{\sigma}_k)+(\vec{\sigma}_k\cdot\vec{\sigma}_l)+(\vec{\sigma}_i\cdot\vec{\sigma}_k)+(\vec{\sigma}_i\cdot\vec{\sigma}_j)(\vec{\sigma}_k\cdot\vec{\sigma}_l) \\ &\quad +(\vec{\sigma}_j\cdot\vec{\sigma}_l)+(\vec{\sigma}_i\cdot\vec{\sigma}_l)+i[\vec{\sigma}_i\cdot(\vec{\sigma}_l\times\vec{\sigma}_k)+i(\vec{\sigma}_i\times(\vec{\sigma}_l\times\vec{\sigma}_k)\cdot\vec{\sigma}_j]+\text{H.c.} \\ &= 1+(\vec{\sigma}_i\cdot\vec{\sigma}_j)+(\vec{\sigma}_j\cdot\vec{\sigma}_k)+(\vec{\sigma}_k\cdot\vec{\sigma}_l)+(\vec{\sigma}_i\cdot\vec{\sigma}_k)+(\vec{\sigma}_i\cdot\vec{\sigma}_j)(\vec{\sigma}_k\cdot\vec{\sigma}_l) \\ &\quad +(\vec{\sigma}_j\cdot\vec{\sigma}_l)+(\vec{\sigma}_i\cdot\vec{\sigma}_l)-[\vec{\sigma}_l\cdot(\vec{\sigma}_i\cdot\vec{\sigma}_k)-\vec{\sigma}_k\cdot(\vec{\sigma}_i\cdot\vec{\sigma}_l)]\cdot\vec{\sigma}_j+\text{H.c.} \\ &= 2\big[(\vec{\sigma}_i\cdot\vec{\sigma}_j)(\vec{\sigma}_k\cdot\vec{\sigma}_l)+(\vec{\sigma}_i\cdot\vec{\sigma}_l)(\vec{\sigma}_j\cdot\vec{\sigma}_k)-(\vec{\sigma}_i\cdot\vec{\sigma}_k)(\vec{\sigma}_j\cdot\vec{\sigma}_l) \\ &\qquad +(\vec{\sigma}_i\cdot\vec{\sigma}_j)+(\vec{\sigma}_j\cdot\vec{\sigma}_k)+(\vec{\sigma}_k\cdot\vec{\sigma}_l)+(\vec{\sigma}_i\cdot\vec{\sigma}_k)+(\vec{\sigma}_j\cdot\vec{\sigma}_l)+(\vec{\sigma}_i\cdot\vec{\sigma}_l)+1\big]. \end{aligned} \tag{A.7}$$

Here we used, that the purely imaginary terms cancel in the sum with the Hermitian conjugate, indicated by H.c. This relation was famously mentioned by Thouless [118] in 1965 in the context of the exchange in solid ^{3}He.

Appendix B

Anisotropy in pyrochlores

B.1 DM orientations in the pyrochlore lattice

In Chapter 4 we discussed the symmetry constraints onto the anisotropic interaction terms on the pyrochlore lattice. Here, we explicitly derive the free parameters for the example bond A-B, illustrated in Fig. 4.2(a), under consideration of Moriya's rules given in Section 4.2.

For simplicity, we chose a coordinate system with the x axis parallel to the A-B bond and the z axis parallel to the edge perpendicular to the bond of the cube enclosing the tetrahedron, see Fig. 4.2(a). Note, that the spin is a pseudo-vector and transforms therefore like a vector under a proper rotation, but gains an additional sign change under an improper rotation such as a reflection. Next, we evaluate Moriya's rules in the case of the pyrochlore lattice:

1. Inversion center at C:

   - This is not the case in the pyrochlore lattice. However, since this is arguably the most important insight from Moriya's rules, we show below how a bond inversion center implies directly a vanishing DM interaction.

     As a pseudo-vector the spin is invariant under inversion ($\mathbf{S}_\mathrm{A} \rightarrow \mathbf{S}_\mathrm{B}$, $\mathbf{S}_\mathrm{B} \rightarrow \mathbf{S}_\mathrm{A}$). Then, it follows directly from the symmetry invariance of the Hamiltonian that the DM interaction cannot be finite:

$$D^x_\mathrm{AB}(S^y_\mathrm{A}S^z_\mathrm{B} - S^z_\mathrm{A}S^y_\mathrm{B}) \stackrel{!}{=} D^x_\mathrm{AB}(S^y_\mathrm{B}S^z_A - S^z_\mathrm{B}S^y_\mathrm{A}) \rightarrow D^x_\mathrm{AB} = 0 \tag{B.1}$$

$$D^y_\mathrm{AB}(S^z_\mathrm{A}S^x_\mathrm{B} - S^x_\mathrm{A}S^z_\mathrm{B}) \stackrel{!}{=} D^y_\mathrm{AB}(S^z_\mathrm{B}S^x_A - S^x_\mathrm{B}S^z_\mathrm{A}) \rightarrow D^y_\mathrm{AB} = 0 \tag{B.2}$$

$$D^z_\mathrm{AB}(S^x_\mathrm{A}S^y_\mathrm{B} - S^y_\mathrm{A}S^x_\mathrm{B}) \stackrel{!}{=} D^z_\mathrm{AB}(S^x_\mathrm{B}S^y_A - S^y_\mathrm{B}S^x_\mathrm{A}) \rightarrow D^z_\mathrm{AB} = 0 \tag{B.3}$$

   - $\mathbf{D}_\mathrm{AB} = 0$ (This is not realized in the pyrochlore lattice.)

2. Mirror plane $\perp$ A-B, through C:

   - A mirror plane perpendicular to A-B passing through C in the chosen coordinate system is the yz plane. This symmetry operation leaves the x component of the spin invariant ($S^x_\mathrm{A} \rightarrow S^x_\mathrm{B}$, $S^x_\mathrm{B} \rightarrow S^x_\mathrm{A}$) and leads to a sign change of the y and z component ($S^{y/z}_\mathrm{A} \rightarrow -S^{y/z}_\mathrm{B}$, $S^{y/z}_\mathrm{B} \rightarrow -S^{y/z}_\mathrm{A}$). Consequently, the x component of the DM vector vanishes:

$$D^x_\mathrm{AB}(S^y_\mathrm{A}S^z_\mathrm{B} - S^z_\mathrm{A}S^y_\mathrm{B}) \stackrel{!}{=} D^x_\mathrm{AB}(S^y_\mathrm{B}S^z_\mathrm{A} - S^z_BS^y_\mathrm{A}) \rightarrow D^x_\mathrm{AB} = 0 \tag{B.4}$$

$$D^y_\mathrm{AB}(S^z_\mathrm{A}S^x_\mathrm{B} - S^x_\mathrm{A}S^z_B) \stackrel{!}{=} D^y_\mathrm{AB}(-S^z_\mathrm{B}S^x_\mathrm{A} + S^x_BS^z_\mathrm{A}) \quad \checkmark \tag{B.5}$$

$$D^z_\mathrm{AB}(S^x_\mathrm{A}S^y_\mathrm{B} - S^y_\mathrm{A}S^x_B) \stackrel{!}{=} D^z_\mathrm{AB}(-S^x_\mathrm{B}S^y_\mathrm{A} + S^y_BS^x_\mathrm{A}) \quad \checkmark \tag{B.6}$$

   - $\mathbf{D}_\mathrm{AB} \parallel yz$ (mirror) plane

3. A, B $\in$ mirror plane:

   - While a mirror plane including A-B is in general not a unique requirement, there is only one realization in the case of the pyrochlore lattice. In the chosen coordinate system it corresponds to the xz plane. In this case, the y component of the spin is invariant ($S^y_{\mathrm{A}} \to S^y_{\mathrm{B}}$, $S^y_{\mathrm{B}} \to S^y_{\mathrm{A}}$), while there is a sign change of the x and z component ($S^{x/z}_{\mathrm{A}} \to -S^{x/z}_{\mathrm{B}}$, $S^{x/z}_{\mathrm{B}} \to -S^{x/z}_{\mathrm{A}}$). This allows only for a finite contribution to the y component of the DM vector:

$$D^x_{\mathrm{AB}}(S^y_{\mathrm{A}}S^z_{\mathrm{B}} - S^z_{\mathrm{A}}S^y_{\mathrm{B}}) \stackrel{!}{=} D^x_{\mathrm{AB}}(-S^y_{\mathrm{A}}S^z_{B} + S^z_{\mathrm{A}}S^y_{\mathrm{B}}) \to D^x_{\mathrm{AB}} = 0 \tag{B.7}$$

$$D^y_{\mathrm{AB}}(S^z_{\mathrm{A}}S^x_{\mathrm{B}} - S^x_{\mathrm{A}}S^z_{\mathrm{B}}) \stackrel{!}{=} D^y_{\mathrm{AB}}(S^z_{\mathrm{A}}S^x_{B} - S^x_{\mathrm{A}}S^z_{\mathrm{B}}) \quad \checkmark \tag{B.8}$$

$$D^z_{\mathrm{AB}}(S^x_{\mathrm{A}}S^y_{\mathrm{B}} - S^y_{\mathrm{A}}S^x_{\mathrm{B}}) \stackrel{!}{=} D^z_{\mathrm{AB}}(-S^x_{\mathrm{A}}S^y_{B} + S^y_{\mathrm{A}}S^x_{\mathrm{B}}) \to D^z_{\mathrm{AB}} = 0 \tag{B.9}$$

   - $\mathbf{D}_{\mathrm{AB}} \parallel$ y axis , therefore $\mathbf{D}_{\mathrm{AB}} \perp$ mirror plane

4. Two-fold rotation axis $\perp$ A-B, through C:

   - This is not realized in the pyrochlore lattice.

5. n-fold axis ($n \geq 2$) $\parallel$ A-B:

   - This is not realized in the pyrochlore lattice.

Consequently, the DM vector in the pyrochlore lattice has indeed in general only one independent component, in agreement with Ref. [189]:

$$\mathbf{D}_{\mathrm{AB}} = \begin{pmatrix} 0 \\ D^y_{\mathrm{AB}} \\ 0 \end{pmatrix}. \tag{B.10}$$

B.2 Pseudo-dipolar tensor in the pyrochlore lattice

With Moriya's rules successfully applied for the DM interaction, we can now derive the symmetrically independent parameters in the pseudo-dipolar tensor, given by Eq. (4.4) for the general case, based on the same strategy. For this, we work in the same coordinate system as defined in Fig. 4.2(a). Following Moriya's rules, we obtain then for the pseudo-dipolar tensor on the pyrochlore lattice:

1. Inversion center at C:

   - Since the spin is invariant under inversion and the pseudo-dipolar tensor is a symmetric object, this condition does not lead to restrictions onto the pseudo-dipolar tensor.
   - No constraints to Γ_{AB} (and this is not realized in the pyrochlore lattice)

2. Mirror plane $\perp$ AB, through C:

   - The mirror plane is the yz plane and leaves the x component of the spin invariant. Consequently, $\Gamma^{xy}_{\mathrm{AB}}$ and $\Gamma^{xz}_{\mathrm{AB}}$ vanish:

$$\Gamma^{xx}_{\mathrm{AB}}(S^x_{\mathrm{A}}S^x_{\mathrm{B}} - S^x_{\mathrm{A}}S^x_{\mathrm{B}}) \stackrel{!}{=} \Gamma^{xx}_{\mathrm{AB}}(S^x_{\mathrm{B}}S^x_{\mathrm{A}} - S^x_{\mathrm{B}}S^x_{\mathrm{A}}) \quad \checkmark \tag{B.11}$$

$$\Gamma^{yy}_{\mathrm{AB}}(S^y_{\mathrm{A}}S^y_{\mathrm{B}} - S^y_{\mathrm{A}}S^y_{\mathrm{B}}) \stackrel{!}{=} \Gamma^{yy}_{\mathrm{AB}}(S^y_{\mathrm{B}}S^y_{\mathrm{A}} - S^y_{\mathrm{B}}S^y_{\mathrm{A}}) \quad \checkmark \tag{B.12}$$

$$\Gamma^{xy}_{\mathrm{AB}}(S^x_{\mathrm{A}}S^y_{\mathrm{B}} + S^y_{\mathrm{A}}S^x_{\mathrm{B}}) \stackrel{!}{=} \Gamma^{xy}_{\mathrm{AB}}(-S^x_{\mathrm{B}}S^y_{\mathrm{A}} - S^y_{\mathrm{B}}S^x_{\mathrm{A}}) \to \Gamma^{xy}_{\mathrm{AB}} = 0 \tag{B.13}$$

$$\Gamma^{xz}_{\mathrm{AB}}(S^x_{\mathrm{A}}S^z_{\mathrm{B}} + S^z_{\mathrm{A}}S^x_{\mathrm{B}}) \stackrel{!}{=} \Gamma^{xz}_{\mathrm{AB}}(-S^x_{\mathrm{B}}S^z_{\mathrm{A}} - S^z_{\mathrm{B}}S^x_{\mathrm{A}}) \to \Gamma^{xz}_{\mathrm{AB}} = 0 \tag{B.14}$$

$$\Gamma^{yz}_{\mathrm{AB}}(S^y_{\mathrm{A}}S^z_{\mathrm{B}} + S^z_{\mathrm{A}}S^y_{\mathrm{B}}) \stackrel{!}{=} \Gamma^{yz}_{\mathrm{AB}}(S^y_{\mathrm{B}}S^z_{\mathrm{A}} + S^z_{\mathrm{B}}S^y_{\mathrm{A}}) \quad \checkmark \tag{B.15}$$

3. A, B $\in$ mirror plane:

   - In this case the mirror plane is the xz plane and leaves the y component of the spin invariant under reflection. Therefore, $\Gamma^{xy}_{\mathrm{AB}}$ and $\Gamma^{yz}_{\mathrm{AB}}$ vanish:

$$\Gamma^{xx}_{\mathrm{AB}}(S^x_{\mathrm{A}}S^x_{\mathrm{B}} - S^x_{\mathrm{A}}S^x_{\mathrm{B}}) \stackrel{!}{=} \Gamma^{xx}_{\mathrm{AB}}(S^x_{\mathrm{B}}S^x_{\mathrm{A}} - S^x_{\mathrm{B}}S^x_{\mathrm{A}}) \quad \checkmark \tag{B.16}$$

$$\Gamma^{yy}_{\mathrm{AB}}(S^y_{\mathrm{A}}S^y_{\mathrm{B}} - S^y_{\mathrm{A}}S^y_{\mathrm{B}}) \stackrel{!}{=} \Gamma^{yy}_{\mathrm{AB}}(S^y_{\mathrm{B}}S^y_{\mathrm{A}} - S^y_{\mathrm{B}}S^y_{\mathrm{A}}) \quad \checkmark \tag{B.17}$$

$$\Gamma^{xy}_{\mathrm{AB}}(S^x_{\mathrm{A}}S^y_{\mathrm{B}} + S^y_{\mathrm{A}}S^x_{\mathrm{B}}) \stackrel{!}{=} \Gamma^{xy}_{\mathrm{AB}}(-S^x_{\mathrm{B}}S^y_{\mathrm{A}} - S^y_{\mathrm{B}}S^x_{\mathrm{A}}) \rightarrow \Gamma^{xy}_{\mathrm{AB}} = 0 \tag{B.18}$$

$$\Gamma^{xz}_{\mathrm{AB}}(S^x_{\mathrm{A}}S^z_{\mathrm{B}} + S^z_{\mathrm{A}}S^x_{\mathrm{B}}) \stackrel{!}{=} \Gamma^{xz}_{\mathrm{AB}}(S^x_{\mathrm{B}}S^z_{\mathrm{A}} + S^z_{\mathrm{B}}S^x_{\mathrm{A}}) \quad \checkmark \tag{B.19}$$

$$\Gamma^{yz}_{\mathrm{AB}}(S^y_{\mathrm{A}}S^z_{\mathrm{B}} + S^z_{\mathrm{A}}S^y_{\mathrm{B}}) \stackrel{!}{=} \Gamma^{yz}_{\mathrm{AB}}(-S^y_{\mathrm{B}}S^z_{\mathrm{A}} - S^z_{\mathrm{B}}S^y_{\mathrm{A}}) \rightarrow \Gamma^{yz}_{\mathrm{AB}} = 0 \tag{B.20}$$

In general, the pseudo-dipolar tensor of a bond in the pyrochlore lattice has therefore only two independent contributions:

$$\Gamma_{\mathrm{AB}} = \begin{pmatrix} \Gamma^{xx}_{\mathrm{AB}} & 0 & 0 \\ 0 & \Gamma^{yy}_{\mathrm{AB}} & 0 \\ 0 & 0 & -(\Gamma^{xx}_{\mathrm{AB}} + \Gamma^{yy}_{\mathrm{AB}}) \end{pmatrix}. \tag{B.21}$$

Appendix C

Hopping on the honeycomb lattice

C.1 Tight binding model on the honeycomb lattice

The general hopping Hamiltonian in real space was extensively used in this thesis:

$$\mathcal{H} = \sum_{ij} t_{ij} c_i^\dagger c_j + \text{H.c.} \tag{C.1}$$

It can be diagonalized by a Fourier transformation into reciprocal space. For this we introduce the following Fourier components:

$$t_{ij} = t(\mathbf{r}_i - \mathbf{r}_j) = \frac{1}{N} \sum_{\mathbf{k}} \mathrm{e}^{i\mathbf{k}\cdot(\mathbf{r}_i - \mathbf{r}_j)}\, t_{\mathbf{k}} \tag{C.2}$$

$$c_i = \frac{1}{\sqrt{N}} \sum_{\mathbf{k}} \mathrm{e}^{i\mathbf{k}\mathbf{r}_i}\, c_{\mathbf{k}}. \tag{C.3}$$

Inserting these expressions into the general Hamiltonian Eq. (C.1) leads to the following expression:

$$\mathcal{H} = \frac{1}{N^2} \sum_{ij} \sum_{\mathbf{k}\mathbf{k}'\mathbf{k}''} \mathrm{e}^{i\mathbf{k}\cdot(\mathbf{r}_i - \mathbf{r}_j)}\, t_{\mathbf{k}}\, \mathrm{e}^{-i\mathbf{k}'\mathbf{r}_i}\, c_{\mathbf{k}'}^\dagger\, \mathrm{e}^{i\mathbf{k}''\mathbf{r}_j}\, c_{\mathbf{k}''} + \text{H.c.} \tag{C.4}$$

With the series definition of the Kronecker delta,

$$\delta_{\mu\nu} = \frac{1}{N} \sum_{\lambda} \mathrm{e}^{i\lambda(\mu-\nu)}, \tag{C.5}$$

we can identify the following diagonal Hamiltonian in reciprocal space:

$$\begin{aligned} \mathcal{H} &= \sum_{\mathbf{k}\mathbf{k}'\mathbf{k}''} \underbrace{\frac{1}{N} \sum_{i} \mathrm{e}^{i\mathbf{r}_i\cdot(\mathbf{k}-\mathbf{k}')}}_{=\delta_{\mathbf{k}\mathbf{k}'}} \underbrace{\frac{1}{N} \sum_{j} \mathrm{e}^{i\mathbf{r}_j\cdot(\mathbf{k}''-\mathbf{k})}}_{\delta_{\mathbf{k}''\mathbf{k}}} t_{\mathbf{k}} c_{\mathbf{k}'}^\dagger c_{\mathbf{k}''} + \text{H.c.} \\ &= \sum_{\mathbf{k}} t_{\mathbf{k}} c_{\mathbf{k}}^\dagger c_{\mathbf{k}} + \text{H.c.} \end{aligned} \tag{C.6}$$

To demonstrate this example, we discuss this approach for nearest neighbour hopping on the honeycomb lattice. This case is relevant for the model for graphene and is helpful in the context of the exact solution of the Kitaev honeycomb model introduced in Chapter 5. In general, there are three distinct bonds on the honeycomb lattice, which we label as X-bonds, Y-bonds, and Z-bonds, consistent with the notation in Fig. 5.2. For this case, the real space Hamiltonian can be expressed as follows:

$$\mathcal{H} = t \sum_{\langle \tau u, \tau' u' \rangle_x} c_{\tau u}^\dagger c_{\tau' u'} + t \sum_{\langle \tau u, \tau' u' \rangle_y} c_{\tau u}^\dagger c_{\tau' u'} + t \sum_{\langle \tau u, \tau' u' \rangle_z} c_{\tau u}^\dagger c_{\tau' u'} + \text{H.c.}, \tag{C.7}$$

where u indexes the unit cell, $\tau \in \{\mathrm{A}, \mathrm{B}\}$ is the sublattice parameter and $\langle u\tau, u'\tau' \rangle_\alpha$ indicates the bond type with $\alpha \in \{\mathrm{X}, \mathrm{Y}, \mathrm{Z}\}$. The Fourier transformation into reciprocal space is performed in the case of a bipartite lattice with respect to the unit cell, therefore we keep the sublattice parameter:

$$c_{\tau u} = \frac{1}{\sqrt{N}} \sum_{\mathbf{k}} \mathrm{e}^{i\mathbf{k}\cdot\mathbf{r}_u} \, c_{\tau\mathbf{k}}. \tag{C.8}$$

With the following definition for unit cell vectors in the honeycomb lattice:

$$\mathbf{n}_1 = \begin{pmatrix} \cos(\frac{1}{3}\pi) \\ \sin(\frac{1}{3}\pi) \end{pmatrix} a \qquad \text{and} \qquad \mathbf{n}_2 = \begin{pmatrix} \cos(\frac{2}{3}\pi) \\ \sin(\frac{2}{3}\pi) \end{pmatrix} a, \tag{C.9}$$

and the fact that nearest neighbour hopping always implies a change of the sublattice parameter, the Hamiltonian in reciprocal space can be expressed as follows:

$$\begin{aligned} \mathcal{H} = \frac{1}{N} \sum_{\mathbf{k}\mathbf{k}'} \Big[& t \sum_{\langle \tau u, \tau' u' \rangle_x} \mathrm{e}^{i\mathbf{k}\cdot\mathbf{r}_u} \, c^\dagger_{\mathrm{A},\mathbf{k}} \, \mathrm{e}^{-i\mathbf{k}'\cdot(\mathbf{r}_u + \mathbf{n}_1)} \, c_{\mathrm{B},\mathbf{k}} + t \sum_{\langle \tau u, \tau' u' \rangle_y} \mathrm{e}^{i\mathbf{k}\cdot\mathbf{r}_u} \, c^\dagger_{\mathrm{A},\mathbf{k}} \, \mathrm{e}^{-i\mathbf{k}'\cdot(\mathbf{r}_u + \mathbf{n}_2)} \, c_{\mathrm{B},\mathbf{k}} \\ & + t \sum_{\langle \tau u, \tau' u' \rangle_z} \mathrm{e}^{i\mathbf{k}\cdot\mathbf{r}_u} \, c^\dagger_{\mathrm{A},\mathbf{k}} \, \mathrm{e}^{-i\mathbf{k}'\cdot\mathbf{r}_u} \, c_{\mathrm{B},\mathbf{k}} + \mathrm{H.c.} \Big] \end{aligned} \tag{C.10}$$

With the the series expansion $\delta_{\mathbf{k}\mathbf{k}'} = \frac{1}{N} \sum_{\langle \tau u, \tau' u' \rangle_\alpha} \mathrm{e}^{i\mathbf{r}_u \cdot (\mathbf{k}' - \mathbf{k})}$, the resulting Hamiltonian is diagonal in $\mathbf{k}$ and has only off-diagonal components with respect to the sublattice:

$$\mathcal{H} = \sum_{\mathbf{k}} \begin{pmatrix} c^\dagger_{\mathrm{A},\mathbf{k}} & c^\dagger_{\mathrm{B},\mathbf{k}} \end{pmatrix} \begin{pmatrix} 0 & t(\mathrm{e}^{i\mathbf{k}\cdot\mathbf{n}_1} + \mathrm{e}^{i\mathbf{k}\cdot\mathbf{n}_2} + 1) \\ t(\mathrm{e}^{-i\mathbf{k}\cdot\mathbf{n}_1} + \mathrm{e}^{-i\mathbf{k}\cdot\mathbf{n}_2} + 1) & 0 \end{pmatrix} \begin{pmatrix} c_{\mathrm{A},\mathbf{k}} \\ c_{\mathrm{B},\mathbf{k}} \end{pmatrix}. \tag{C.11}$$

The eigenenergies follow then directly:

$$\varepsilon_{1/2} = \pm \sqrt{3 + 4\cos(\frac{1}{2}k_x a)\cos(\frac{\sqrt{3}}{2}k_y a) + 2\cos(k_x a)}. \tag{C.12}$$

The energy bands in reciprocal space contain the famous Dirac point at the K-point[1], with approximately linear energy dispersion.

C.2 Symmetrically allowed hopping terms in Kitaev materials

Here, we demonstrate the symmetry restrictions onto the tight binding Hamiltonian on the example of a Z-bond in Kitaev materials. T

Without spin-orbit coupling, hopping parameters are generally real and, due to time-reversal invariance, the matrix representing the hopping integrals is symmetric. The most general expression for hopping in the t_{2g} orbitals for is therefore as follows:

$$\mathcal{H}_{12} = \begin{pmatrix} c^\dagger_{1,yz} & c^\dagger_{1,xz} & c^\dagger_{1,xy} \end{pmatrix} \cdot \begin{pmatrix} t_{11} & t_{12} & t_{13} \\ t_{12} & t_{22} & t_{23} \\ t_{13} & t_{23} & t_{33} \end{pmatrix} \cdot \begin{pmatrix} c_{2,yz} \\ c_{2,xz} \\ c_{2,xy} \end{pmatrix} \tag{C.13}$$

For a perfect octahedral environment, this Hamiltonian is invariant under symmetry operations including a center of inversion in the middle of the bond, as well as two-fold rotations about the symmetry axes [110], [1$\bar{1}$0], and [001], as pointed out e.g. in Ref. [221]. These screw axes are illustrated for the case of α-$RuCl_3$ in Fig. 5.4(a) and given in terms of the local coordinate system shown in Fig. 5.4(b).

[1] For a definition of the conventional naming of the high reciprocal space for the respective lattices see e.g. Ref. [289]. For the unit cell chosen in this case, the high symmetry points correspond to: $\Gamma = (0, 0)$, $\mathrm{K} = (\frac{4\pi}{3a}, 0)$, and $\mathrm{M} = (\frac{\pi}{a}, -\frac{\pi}{\sqrt{3}a})$.

A matrix $\mathbb{A}$ is invariant under a symmetry operation $\mathcal{R}$ if it fulfils the relation $\mathbb{A} = \mathcal{R}^{-1} \cdot \mathbb{A} \cdot \mathcal{R}$. Hence, the C_2 operation about [110] implies:

$$\begin{pmatrix} t_{11} & t_{12} & t_{13} \\ t_{12} & t_{22} & t_{23} \\ t_{13} & t_{23} & t_{33} \end{pmatrix} = \begin{pmatrix} t_{22} & t_{12} & -t_{23} \\ t_{12} & t_{11} & -t_{13} \\ -t_{23} & -t_{13} & t_{33} \end{pmatrix}. \tag{C.14}$$

The same considerations are valid for the other C_2 axes with $[1\bar{1}0]$:

$$\begin{pmatrix} t_{11} & t_{12} & t_{13} \\ t_{12} & t_{22} & t_{23} \\ t_{13} & t_{23} & t_{33} \end{pmatrix} = \begin{pmatrix} t_{22} & t_{12} & t_{23} \\ t_{12} & t_{11} & t_{13} \\ t_{23} & t_{13} & t_{33} \end{pmatrix}, \tag{C.15}$$

and finally for the last C_2 operation about [001]:

$$\begin{pmatrix} t_{11} & t_{12} & t_{13} \\ t_{12} & t_{22} & t_{23} \\ t_{13} & t_{23} & t_{33} \end{pmatrix} = \begin{pmatrix} t_{11} & t_{12} & -t_{13} \\ t_{12} & t_{22} & -t_{23} \\ -t_{13} & -t_{23} & t_{33} \end{pmatrix}. \tag{C.16}$$

The center of inversion does not add any additional constraints to the symmetric matrix. Together the Hamiltonian fulfils therefore the following expression:

$$\mathcal{H}_{12} = \begin{pmatrix} c^\dagger_{1,yz} & c^\dagger_{1,xz} & c^\dagger_{1,xy} \end{pmatrix} \cdot \begin{pmatrix} t_1 & t_2 & 0 \\ t_2 & t_1 & 0 \\ 0 & 0 & t_3 \end{pmatrix} \cdot \begin{pmatrix} c_{2,yz} \\ c_{2,xz} \\ c_{2,xy} \end{pmatrix}. \tag{C.17}$$

In the case of trigonal distortion, the octahedral environment is stretched along the $[1\bar{1}0]$ axis. Therefore, the only constraint still valid is the C_2 rotation about this axis. The general Hamiltonian contains therefore one additional free parameter:

$$\mathcal{H}_{12} = \begin{pmatrix} c^\dagger_{1,yz} & c^\dagger_{1,xz} & c^\dagger_{1,xy} \end{pmatrix} \cdot \begin{pmatrix} t_1 & t_2 & t_4 \\ t_2 & t_1 & t_4 \\ t_4 & t_4 & t_3 \end{pmatrix} \cdot \begin{pmatrix} c_{2,yz} \\ c_{2,xz} \\ c_{2,xy} \end{pmatrix}. \tag{C.18}$$

The notation $t_{1\ldots4}$ is consistent with the notation used in Chapter 5.

References

[1] P. W. Anderson. *More is Different*. Science **177**, 393–396 (1972).

[2] P. W. Anderson. *Resonating valence bonds: A new kind of insulator?* Mater. Res. Bull. **8**, 153 – 160 (1973).

[3] L. Balents. *Spin liquids in frustrated magnets*. Nature **464**, 199 (2010).

[4] A. P. Ramirez. *Strongly Geometrically Frustrated Magnets*. Annu. Rev. Mater. Sci. **24**, 453–480 (1994).

[5] C. Lacroix, P. Mendels, and F. Mila (Eds.). *Introduction to Frustrated Magnetism*, vol. 164 of *Springer Series in Solid-State Sciences*. Berlin, (2011).

[6] A. Kitaev. *Anyons in an exactly solved model and beyond*. Ann. Phys. **321**, 2–111 (2006).

[7] P. A. Lee, N. Nagaosa, and X.-G. Wen. *Doping a Mott insulator: Physics of high-temperature superconductivity*. Rev. Mod. Phys. **78**, 17–85 (2006).

[8] Y. Zhou, K. Kanoda, and T.-K. Ng. *Quantum spin liquid states*. Rev. Mod. Phys. **89**, 025003 (2017).

[9] F. Becca. *An introduction to quantum spin liquids: general defintions and physical properties*. Lecture Notes: International school by SFB/TR49, (2014).

[10] P. Fazekas and P. W. Anderson. *On the ground state properties of the anisotropic triangular antiferromagnet*. Phil. Mag. **30**, 423–440 (1974).

[11] X.-G. Wen. *Quantum orders and symmetric spin liquids*. Phys. Rev. B **65**, 165113 (2002).

[12] P. Mendels and F. Bert. *Quantum Kagome Antiferromagnet $ZnCu_3(OH)_6Cl_2$*. J. Phys. Soc. Jpn. **79**, 011001 (2010).

[13] P. Mendels and F. Bert. *Quantum kagome antiferromagnet $ZnCu_3(OH)_6Cl_2$*. J. Phys. Conf. Ser. **320**, 012004 (2011).

[14] P. Lecheminant, B. Bernu, C. Lhuillier, L. Pierre, and P. Sindzingre. *Order versus disorder in the quantum Heisenberg antiferromagnet on the kagomé lattice using exact spectra analysis*. Phys. Rev. B **56**, 2521–2529 (1997).

[15] A. M. Läuchli, J. Sudan, and E. S. Sørensen. *Ground-state energy and spin gap of spin-$\frac{1}{2}$ Kagomé-Heisenberg antiferromagnetic clusters: Large-scale exact diagonalization results*. Phys. Rev. B **83**, 212401 (2011).

[16] Y. Iqbal, F. Becca, and D. Poilblanc. *Valence-bond crystal in the extended kagome spin-$\frac{1}{2}$ quantum Heisenberg antiferromagnet: A variational Monte Carlo approach*. Phys. Rev. B **83**, 100404 (2011).

[17] S. Yan, D. A. Huse, and S. R. White. *Spin-liquid ground state of the S=1/2 Kagome Heisenberg antiferromagnet*. Science **332**, 1173 (2011).

[18] H.-C. Jiang, Z. Wang, and L. Balents. *Identifying topological order by entanglement entropy*. Nat. Phys. **8**, 902 (2012).

[19] Y. Iqbal, D. Poilblanc, and F. Becca. *Vanishing spin gap in a competing spin-liquid phase in the kagome Heisenberg antiferromagnet*. Phys. Rev. B **89**, 020407 (2014).

[20] P. Mendels, F. Bert, M. A. de Vries, A. Olariu, A. Harrison, F. Duc, J. C. Trombe, J. S. Lord, A. Amato, and C. Baines. *Quantum Magnetism in the Paratacamite Family: Towards an Ideal Kagomé Lattice*. Phys. Rev. Lett. **98**, 077204 (2007).

[21] M. A. de Vries, J. R. Stewart, P. P. Deen, J. O. Piatek, G. J. Nilsen, H. M. Rønnow, and A. Harrison. *Scale-Free Antiferromagnetic Fluctuations in the $s = 1/2$ Kagome Antiferromagnet Herbertsmithite*. Phys. Rev. Lett. **103**, 237201 (2009).

[22] T.-H. Han, J. S. Helton, S. Chu, D. G. Nocera, J. A. Rodriguez-Rivera, C. Broholm, and Y. S. Lee. *Fractionalized excitations in the spin-liquid state of a kagome-lattice antiferromagnet*. Nature **492**, 406 (2012).

[23] J. Merino, R. H. McKenzie, J. B. Marston, and C. H. Chung. *The Heisenberg antiferromagnet on an anisotropic triangular lattice: linear spin-wave theory*. J. Phys.: Condens. Matter **11**, 2965–2975 (1999).

[24] L. F. Tocchio, A. Parola, C. Gros, and F. Becca. *Spin-liquid and magnetic phases in the anisotropic triangular lattice: The case of κ-(ET)$_2X$*. Phys. Rev. B **80**, 064419 (2009).

[25] M. Holt, B. J. Powell, and J. Merino. *Spin-liquid phase due to competing classical orders in the semiclassical theory of the Heisenberg model with ring exchange on an anisotropic triangular lattice*. Phys. Rev. B **89**, 174415 (2014).

[26] E. Ghorbani, L. F. Tocchio, and F. Becca. *Variational wave functions for the $s = \frac{1}{2}$ Heisenberg model on the anisotropic triangular lattice: Spin liquids and spiral orders*. Phys. Rev. B **93**, 085111 (2016).

[27] R. Coldea, D. A. Tennant, A. M. Tsvelik, and Z. Tylczynski. *Experimental Realization of a 2D Fractional Quantum Spin Liquid*. Phys. Rev. Lett. **86**, 1335–1338 (2001).

[28] M. Kohno, O. A. Starykh, and L. Balents. *Spinons and triplons in spatially anisotropic frustrated antiferromagnets*. Nat. Phys. **3**, 790 (2007).

[29] O. A. Starykh and L. Balents. *Ordering in Spatially Anisotropic Triangular Antiferromagnets*. Phys. Rev. Lett. **98**, 077205 (2007).

[30] T. Herfurth, S. Streib, and P. Kopietz. *Majorana spin liquid and dimensional reduction in Cs_2CuCl_4*. Phys. Rev. B **88**, 174404 (2013).

[31] K. Kanoda and R. Kato. *Mott physics in organic conductors with triangular lattices*. Annu. Rev. Condens. Matter Phys. **2**, 167–188 (2011).

[32] Y. Shimizu, K. Miyagawa, K. Kanoda, M. Maesato, and G. Saito. *Spin liquid state in an organic mott insulator with a triangular lattice*. Phys. Rev. Lett. **91**, 107001 (2003).

[33] T. Itou, A. Oyamada, S. Maegawa, and R. Kato. *Instability of a quantum spin liquid in an organic triangular-lattice antiferromagnet*. Nat. Phys. **6**, 673 (2010).

[34] M. Yamashita, N. Nakata, Y. Senshu, M. Nagata, H. M. Yamamoto, R. Kato, T. Shibauchi, and Y. Matsuda. *Highly Mobile Gapless Excitations in a Two-Dimensional Candidate Quantum Spin Liquid*. Science **328**, 1246–1248 (2010).

[35] S. Yamashita, T. Yamamoto, Y. Nakazawa, M. Tamura, and R. Kato. *Gapless spin liquid of an organic triangular compound evidenced by thermodynamic measurements*. Nat. Commun. **2**, 275 (2011).

[36] Y. Shimizu, K. Miyagawa, K. Kanoda, M. Maesato, and G. Saito. *Emergence of inhomogeneous moments from spin liquid in the triangular-lattice Mott insulator κ-(ET)$_2$Cu$_2$(CN)$_3$*. Phys. Rev. B **73**, 140407 (2006).

[37] S. Yamashita, Y. Nakazawa, M. Oguni, Y. Oshima, H. Nojiri, Y. Shimizu, K. Miyagawa, and K. Kanoda. *Thermodynamic properties of a spin-1/2 spin-liquid state in a κ-type organic salt*. Nat. Phys. **4**, 459 (2008).

[38] M. Yamashita, N. Nakata, Y. Kasahara, T. Sasaki, N. Yoneyama, N. Kobayashi, S. Fujimoto, T. Shibauchi, and Y. Matsuda. *Thermal-transport measurements in a quantum spin-liquid state of the frustrated triangular magnet κ-(BEDT-TTF)$_2$Cu$_2$(CN)$_3$*. Nat. Phys. **5**, 44 (2009).

[39] Y. Shen, Y.-D. Li, H. Wo, Y. Li, S. Shen, B. Pan, Q. Wang, H. Walker, P. Steffens, M. Boehm, et al. *Evidence for a spinon Fermi surface in a triangular-lattice quantum-spin-liquid candidate*. Nature **540**, 559 (2016).

[40] J. A. Paddison, M. Daum, Z. Dun, G. Ehlers, Y. Liu, M. B. Stone, H. Zhou, and M. Mourigal. *Continuous excitations of the triangular-lattice quantum spin liquid YbMgGaO$_4$*. Nat. Phys. **13**, 117 (2017).

[41] Z. Zhu, P. A. Maksimov, S. R. White, and A. L. Chernyshev. *Disorder-Induced Mimicry of a Spin Liquid in YbMgGaO$_4$*. Phys. Rev. Lett. **119**, 157201 (2017).

[42] I. Kimchi, A. Nahum, and T. Senthil. *Valence Bonds in Random Quantum Magnets: Theory and Application to YbMgGaO$_4$*. Phys. Rev. X **8**, 031028 (2018).

[43] Y. Singh and P. Gegenwart. *Antiferromagnetic Mott insulating state in single crystals of the honeycomb lattice material Na$_2$IrO$_3$*. Phys. Rev. B **82**, 064412 (2010).

[44] S. K. Choi, R. Coldea, A. N. Kolmogorov, T. Lancaster, I. I. Mazin, S. J. Blundell, P. G. Radaelli, Y. Singh, P. Gegenwart, K. R. Choi, S.-W. Cheong, P. J. Baker, C. Stock, and J. Taylor. *Spin Waves and Revised Crystal Structure of Honeycomb Iridate Na$_2$IrO$_3$*. Phys. Rev. Lett. **108**, 127204 (2012).

[45] Y. Singh, S. Manni, J. Reuther, T. Berlijn, R. Thomale, W. Ku, S. Trebst, and P. Gegenwart. *Relevance of the Heisenberg-Kitaev Model for the Honeycomb Lattice Iridates A$_2$IrO$_3$*. Phys. Rev. Lett. **108**, 127203 (2012).

[46] A. Banerjee, J. Yan, J. Knolle, C. A. Bridges, M. B. Stone, M. D. Lumsden, D. G. Mandrus, D. A. Tennant, R. Moessner, and S. E. Nagler. *Neutron scattering in the proximate quantum spin liquid α-RuCl$_3$*. Science **356**, 1055–1059 (2017).

[47] A. Banerjee, P. Lampen-Kelley, J. Knolle, C. Balz, A. A. Aczel, B. Winn, Y. Liu, D. Pajerowski, J. Yan, C. A. Bridges, A. T. Savici, B. C. Chakoumakos, M. D. Lumsden, D. A. Tennant, R. Moessner, D. G. Mandrus, and S. E. Nagler. *Excitations in the field-induced quantum spin liquid state of α-RuCl$_3$*. npj Quantum Mater. **3**, 8 (2018).

[48] Y. Kasahara, T. Ohnishi, Y. Mizukami, O. Tanaka, S. Ma, K. Sugii, N. Kurita, H. Tanaka, J. Nasu, Y. Motome, T. Shibauchi, and Y. Matsuda. *Majorana quantization and half-integer thermal quantum Hall effect in a Kitaev spin liquid*. Nature **559**, 227 (2018).

[49] T. Moriya. *Anisotropic superexchange interaction and weak ferromagnetism*. Phys. Rev. **120**, 91–98 (1960).

[50] T. Yildirim, A. B. Harris, A. Aharony, and O. Entin-Wohlman. *Anisotropic spin hamiltonians due to spin-orbit and coulomb exchange interactions*. Phys. Rev. B **52**, 10239–10267 (1995).

[51] I. Lindgren and J. Morrison. *Atomic many-body theory*, vol. 3 of *Springer series on atoms + plasmas*. Berlin [u.a.], 2nd edition, (1986).

[52] I. Dzyaloshinskii. *A thermodynamic theory of "weak" ferromagnetism of antiferromagnetics*. J. Phys. Chem. Solids **4**, 241–255 (1958).

[53] S. Cottenier. *Density Functional Theory and the family of (L)APW-methods: a step-by-step introduction*. 2nd edition, (2002-2013). (freely available at http://susi.theochem.tuwien.ac.at/reg_user/textbooks).

[54] H. Eschrig. *The fundamentals of density functional theory*, vol. 2. Springer, (2003).

[55] R. M. Martin. *Electronic structure: basic theory and practical methods*. Cambridge University Press, (2004).

[56] E. Pavarini, E. Koch, A. Lichtenstein, and D. Vollhardt (Eds.). *The LDA+DMFT approach to strongly correlated materials*, vol. 1 of *Schriften des Forschungszentrums Jülich: Modeling and Simulation*. Jülich, (2011).

[57] E. Pavarini, E. Koch, F. Anders, and M. Jarrell (Eds.). *Correlated Electrons: From Models to Materials*, vol. 2 of *Schriften des Forschungszentrums Jülich: Modeling and Simulation*. Jülich, (2012).

[58] P. Hohenberg and W. Kohn. *Inhomogeneous Electron Gas*. Phys. Rev. **136**, B864–B871 (1964).

[59] W. Kohn and L. J. Sham. *Self-Consistent Equations Including Exchange and Correlation Effects*. Phys. Rev. **140**, A1133–A1138 (1965).

[60] K. Riedl, Y. Li, R. Valentí, and S. M. Winter. *Ab Initio Approaches for Low-Energy Spin Hamiltonians*. Phys. Status Solidi B (2019). doi:10.1002/pssb.201800684.

[61] H. Xiang, C. Lee, H.-J. Koo, X. Gong, and M.-H. Whangbo. *Magnetic properties and energy-mapping analysis*. Dalton Trans. **42**, 823–853 (2013).

[62] L. Noodleman. *Valence bond description of antiferromagnetic coupling in transition metal dimers*. J. Chem. Phys. **74**, 5737 (1981).

[63] L. Noodleman and E. R. Davidson. *Ligand spin polarization and antiferromagnetic coupling in transition metal dimers*. Chem. Phys. **109**, 131 (1986).

[64] A. A. Tsirlin and H. Rosner. *Extension of the spin-$\frac{1}{2}$ frustrated square lattice model: The case of layered vanadium phosphates*. Phys. Rev. B **79**, 214417 (2009).

[65] H. O. Jeschke, F. Salvat-Pujol, and R. Valentí. *First-principles determination of Heisenberg Hamiltonian parameters for the spin-$\frac{1}{2}$ kagome antiferromagnet $ZnCu_3(OH)_6Cl_2$*. Phys. Rev. B **88**, 075106 (2013).

[66] J. K. Glasbrenner, I. I. Mazin, H. O. Jeschke, P. J. Hirschfeld, R. M. Fernandes, and R. Valentí. *Effect of magnetic frustration on nematicity and superconductivity in iron chalcogenides*. Nat. Phys. **11**, 953 (2015).

[67] F. Illas, I. P. R. de Moreira, C. De Graaf, and V. Barone. *Magnetic coupling in biradicals, binuclear complexes and wide-gap insulators: a survey of ab initio wave function and density functional theory approaches*. Theor. Chem. Acc. **104**, 265 (2000).

[68] F. Neese. *Definition of corresponding orbitals and the diradical character in broken symmetry DFT calculations on spin coupled systems*. J. Phys. Chem. Solids **65**, 781 (2004).

[69] I. Rudra, Q. Wu, and T. Van Voorhis. *Accurate magnetic exchange couplings in transition-metal complexes from constrained density-functional theory*. J. Chem. Phys. **124**, 024103 (2006).

[70] E. Ruiz, J. Cano, S. Alvarez, and P. Alemany. *Broken symmetry approach to calculation of exchange coupling constants for homobinuclear and heterobinuclear transition metal complexes*. J. Comput. Chem. **20**, 1391 (1999).

[71] R. L. Martin and F. Illas. *Antiferromagnetic exchange interactions from hybrid density functional theory*. Phys. Rev. Lett. **79**, 1539–1542 (1997).

[72] C. Adamo, V. Barone, A. Bencini, F. Totti, and I. Ciofini. *On the calculation and modeling of magnetic exchange interactions in weakly bonded systems: the case of the ferromagnetic copper (II) μ2-azido bridged complexes*. Inorg. Chem. **38**, 1996 (1999).

[73] U. Tutsch, B. Wolf, S. Wessel, L. Postulka, Y. Tsui, H. O. Jeschke, I. Opahle, T. Saha-Dasgupta, R. Valentí, A. Brühl, K. Remović-Langer, T. Kretz, H.-W. Lerner, M. Wagner, and M. Lang. *Evidence of a field-induced Berezinskii-Kosterlitz-Thouless scenario in a two-dimensional spin-dimer system*. Nat. Commun. **5**, 5169 (2014).

[74] E. Pavarini, E. Koch, and U. Schollwöck (Eds.). *Emergent Phenomena in Correlated Matter*, vol. 3 of *Schriften des Forschungszentrums Jülich: Modeling and Simulation*. Jülich, (2013).

[75] E. Pavarini, S. Biermann, A. Poteryaev, A. I. Lichtenstein, A. Georges, and O. K. Andersen. *Mott Transition and Suppression of Orbital Fluctuations in Orthorhombic $3d^1$ Perovskites*. Phys. Rev. Lett. **92**, 176403 (2004).

[76] E. Pavarini, A. Yamasaki, J. Nuss, and O. K. Andersen. *How chemistry controls electron localization in $3d^1$ perovskites: a Wannier-function study*. New J. Phys. **7**, 188–188 (2005).

[77] S. M. Winter, K. Riedl, and R. Valentí. *Importance of spin-orbit coupling in layered organic salts*. Phys. Rev. B **95**, 060404(R) (2017).

[78] K. Riedl, R. Valentí, and S. M. Winter. *Critical spin liquid versus valence-bond glass in a triangular-lattice organic antiferromagnet*. Nat. Commun. **10**, 2561 (2019).

[79] K. Riedl, D. Guterding, H. O. Jeschke, M. J. P. Gingras, and R. Valentí. *Ab initio determination of spin Hamiltonians with anisotropic exchange interactions: The case of the pyrochlore ferromagnet $Lu_2V_2O_7$*. Phys. Rev. B **94**, 014410 (2016).

[80] Y. Iqbal, T. Müller, K. Riedl, J. Reuther, S. Rachel, R. Valentí, M. J. P. Gingras, R. Thomale, and H. O. Jeschke. *Signatures of a gearwheel quantum spin liquid in a spin-$\frac{1}{2}$ pyrochlore molybdate Heisenberg antiferromagnet*. Phys. Rev. Materials **1**, 071201 (2017).

[81] S. M. Winter, K. Riedl, P. A. Maksimov, A. L. Chernyshev, A. Honecker, and R. Valentí. *Breakdown of Magnons in a Strongly Spin-Orbital Coupled Magnet*. Nat. Commun. **8**, 1152 (2017).

[82] K. Riedl, Y. Li, S. M. Winter, and R. Valentí. *Sawtooth Torque in Anisotropic $j_{\mathit{eff}} = 1/2$ Magnets: Application to α-$RuCl_3$*. Phys. Rev. Lett. **122**, 197202 (2019).

[83] S. M. Winter, K. Riedl, D. Kaib, R. Coldea, and R. Valentí. *Probing α-$RuCl_3$ Beyond Magnetic Order: Effects of Temperature and Magnetic Field*. Phys. Rev. Lett. **120**, 077203 (2018).

[84] D. A. Huse and V. Elser. *Simple Variational Wave Functions for Two-Dimensional Heisenberg Spin-1/2 Antiferromagnets*. Phys. Rev. Lett. **60**, 2531–2534 (1988).

[85] P. Sindzingre, P. Lecheminant, and C. Lhuillier. *Investigation of different classes of variational functions for the triangular and kagomé spin-1/2 Heisenberg antiferromagnets*. Phys. Rev. B **50**, 3108–3113 (1994).

[86] L. Capriotti, A. E. Trumper, and S. Sorella. *Long-Range Néel Order in the Triangular Heisenberg Model*. Phys. Rev. Lett. **82**, 3899–3902 (1999).

[87] W. LiMing, G. Misguich, P. Sindzingre, and C. Lhuillier. *From Néel long-range order to spin liquids in the multiple-spin exchange model*. Phys. Rev. B **62**, 6372–6377 (2000).

[88] S. R. White and A. L. Chernyshev. *Neél Order in Square and Triangular Lattice Heisenberg Models*. Phys. Rev. Lett. **99**, 127004 (2007).

[89] W. Zheng, R. R. P. Singh, R. H. McKenzie, and R. Coldea. *Temperature dependence of the magnetic susceptibility for triangular-lattice antiferromagnets with spatially anisotropic exchange constants*. Phys. Rev. B **71**, 134422 (2005).

[90] O. I. Motrunich. *Variational study of triangular lattice spin-1/2 model with ring exchanges and spin liquid state in κ-(ET)$_2$Cu$_2$(CN)$_3$*. Phys. Rev. B **72**, 045105 (2005).

[91] S.-S. Lee and P. A. Lee. *U(1) Gauge Theory of the Hubbard Model: Spin Liquid States and Possible Application to κ-BEDT-TTF$_2$Cu$_2$CN$_3$*. Phys. Rev. Lett. **95**, 036403 (2005).

[92] M. S. Block, D. N. Sheng, O. I. Motrunich, and M. P. A. Fisher. *Spin Bose-Metal and Valence Bond Solid Phases in a Spin-1/2 Model with Ring Exchanges on a Four-Leg Triangular Ladder*. Phys. Rev. Lett. **106**, 157202 (2011).

[93] B. J. Powell and R. H. McKenzie. *Quantum frustration in organic mott insulators: from spin liquids to unconventional superconductors*. Rep. Prog. Phys. **74**, 056501 (2011).

[94] M. Dressel. *Quantum criticality in organic conductors? Fermi liquid versus non-Fermi-liquid behaviour*. J. Phys. Condens. Matter **23**, 293201 (2011).

[95] N. Toyota, T. Shimazu, T. Sasaki, K. Shibata, T. Kajitani, M. Lang, and S. Ikeda. *Low-lying vibrational states in superconducting κ-(BEDT-TTF)$_2$Cu(NCS)$_2$: Inelastic neutron scattering*. Synth. Met. **86**, 2009–2010 (1997).

[96] L. Pintschovius, H. Rietschel, T. Sasaki, H. Mori, S. Tanaka, N. Toyota, M. Lang, and F. Steglich. *Observation of superconductivity-induced phonon frequency changes in the organic superconductor kappa-(BEDT-TTF)$_2$Cu(NCS)$_2$*. EPL **37**, 627 (1997).

[97] H. Taniguchi, R. Sato, K. Satoh, A. Kawamoto, H. Okamoto, T. Kobayasi, and K. Mizuno. *Crystal Growth of 50mg-Class Single Crystals of β′-(BEDT-TTF)$_2$ICl$_2$ and Crystal Evaluation*. J. Low Temp. Phys. **142**, 441–444 (2006).

[98] F. L. Pratt, P. J. Baker, S. J. Blundell, T. Lancaster, S. Ohira-Kawamura, C. Baines, Y. Shimizu, K. Kanoda, I. Watanabe, and G. Saito. *Magnetic and non-magnetic phases of a quantum spin liquid*. Nature **471**, 612 (2011).

[99] H. Kino and H. Fukuyama. *Electronic States of Conducting Organic κ-(BEDT-TTF)$_2$X*. J. Phys. Soc. Jpn. **64**, 2726–2729 (1995).

[100] R. H. McKenzie. *A strongly correlated electron model for the layered organic superconductors κ-(BEDT-TTF)$_2$X*. Comments Cond. Matt. Phys. **18**, 309 (1998).

[101] D. Guterding, M. Altmeyer, H. O. Jeschke, and R. Valentí. *Near-degeneracy of extended $s+d_{x^2-y^2}$ and d_{xy} order parameters in quasi-two-dimensional organic superconductors*. Phys. Rev. B **94**, 024515 (2016).

[102] R. Kaneko, L. F. Tocchio, R. Valentí, and F. Becca. *Charge orders in organic charge-transfer salts*. New J. Phys. **19**, 103033 (2017).

[103] E. Gati, J. K. H. Fischer, P. Lunkenheimer, D. Zielke, S. Köhler, F. Kolb, H.-A. K. von Nidda, S. M. Winter, H. Schubert, J. A. Schlueter, H. O. Jeschke, R. Valentí, and M. Lang. *Evidence for electronically driven ferroelectricity in a strongly correlated dimerized bedt-ttf molecular conductor*. Phys. Rev. Lett. **120**, 247601 (2018).

[104] K. Miyagawa, A. Kawamoto, Y. Nakazawa, and K. Kanoda. *Antiferromagnetic ordering and spin structure in the organic conductor, κ-(BEDT-TTF)$_2$Cu[N(CN)$_2$]Cl*. Phys. Rev. Lett. **75**, 1174 (1995).

[105] D. F. Smith, S. M. De Soto, C. P. Slichter, J. A. Schlueter, A. M. Kini, and R. G. Daugherty. *Dzialoshinskii-Moriya interaction in the organic superconductor κ-(BEDT-TTF)$_2$Cu[N(CN)$_2$]Cl*. Phys. Rev. B **68**, 024512 (2003).

[106] D. F. Smith, C. P. Slichter, J. A. Schlueter, A. M. Kini, and R. G. Daugherty. *Precise Determination of the Orientation of the Dzialoshinskii-Moriya Vector in κ-(BEDT-TTF)$_2$Cu[N(CN)$_2$]Cl*. Phys. Rev. Lett. **93**, 167002 (2004).

[107] A. Antal, T. Fehér, A. Jánossy, E. Tátrai-Szekeres, and F. Fülöp. *Spin Diffusion and Magnetic Eigenoscillations Confined to Single Molecular Layers in the Organic Conductors κ-(BEDT-TTF)$_2$Cu[N(CN)$_2$]x (x =Cl,Br)*. Phys. Rev. Lett. **102**, 086404 (2009).

[108] Y. Yoshida, H. Ito, M. Maesato, Y. Shimizu, H. Hayama, T. Hiramatsu, Y. Nakamura, H. Kishida, T. Koretsune, C. Hotta, and G. Saito. *Spin-disordered quantum phases in a quasi-one-dimensional triangular lattice*. Nat. Phys. **11**, 679 (2015).

[109] Y. Shimizu, T. Hiramatsu, M. Maesato, A. Otsuka, H. Yamochi, A. Ono, M. Itoh, M. Yoshida, M. Takigawa, Y. Yoshida, and G. Saito. *Pressure-tuned exchange coupling of a quantum spin liquid in the molecular triangular lattice κ-(ET)$_2$Ag$_2$(CN)$_3$*. Phys. Rev. Lett. **117**, 107203 (2016).

[110] M. Q. Weng, D. N. Sheng, Z. Y. Weng, and R. J. Bursill. *Spin-liquid phase in an anisotropic triangular-lattice heisenberg model: Exact diagonalization and density-matrix renormalization group calculations*. Phys. Rev. B **74**, 012407 (2006).

[111] D. Heidarian, S. Sorella, and F. Becca. *Spin-$\frac{1}{2}$ heisenberg model on the anisotropic triangular lattice: From magnetism to a one-dimensional spin liquid*. Phys. Rev. B **80**, 012404 (2009).

[112] J. Reuther and R. Thomale. *Functional renormalization group for the anisotropic triangular antiferromagnet*. Phys. Rev. B **83**, 024402 (2011).

[113] R. Kaneko, S. Morita, and M. Imada. *Gapless Spin-Liquid Phase in an Extended Spin 1/2 Triangular Heisenberg Model*. J. Phys. Soc. Jpn. **83**, 093707 (2014).

[114] D. N. Sheng, O. I. Motrunich, and M. P. A. Fisher. *Spin Bose-metal phase in a spin-$\frac{1}{2}$ model with ring exchange on a two-leg triangular strip*. Phys. Rev. B **79**, 205112 (2009).

[115] H. C. Kandpal, I. Opahle, Y.-Z. Zhang, H. O. Jeschke, and R. Valentí. *Revision of Model Parameters for κ-Type Charge Transfer Salts: An Ab Initio Study*. Phys. Rev. Lett. **103**, 067004 (2009).

[116] T. Koretsune and C. Hotta. *Evaluating model parameters of the κ- and β′-type Mott insulating organic solids*. Phys. Rev. B **89**, 045102 (2014).

[117] K. Nakamura, Y. Yoshimoto, T. Kosugi, R. Arita, and M. Imada. *Ab initio Derivation of Low-Energy Model for κ-ET Type Organic Conductors*. J. Phys. Soc. Jpn. **78**, 083710 (2009).

[118] D. J. Thouless. *Exchange in solid ^{3}He and the Heisenberg Hamiltonian*. Proc. Phys. Soc. **86**, 893 (1965).

[119] A. H. MacDonald, S. M. Girvin, and D. Yoshioka. *$\frac{t}{U}$ expansion for the Hubbard model*. Phys. Rev. B **37**, 9753–9756 (1988).

[120] T. Isono, T. Terashima, K. Miyagawa, K. Kanoda, and S. Uji. *Quantum criticality in an organic spin-liquid insulator κ-(BEDT-TTF)$_2$Cu$_2$(CN)$_3$*. Nat. Commun. **7**, 13494 (2016).

[121] J. Oitmaa, C. Hamer, and W. Zheng. *Series expansion methods for strongly interacting lattice models*. Cambridge University Press, (2006).

[122] C. J. Morningstar and M. Weinstein. *Contractor renormalization group method: A new computational technique for lattice systems*. Phys. Rev. Lett. **73**, 1873–1877 (1994).

[123] C. J. Morningstar and M. Weinstein. *Contractor renormalization group technology and exact hamiltonian real-space renormalization group transformations*. Phys. Rev. D **54**, 4131–4151 (1996).

[124] H.-Y. Yang, A. F. Albuquerque, S. Capponi, A. M. Läuchli, and K. P. Schmidt. *Effective spin couplings in the mott insulator of the honeycomb lattice hubbard model*. New J. Phys. **14**, 115027 (2012).

[125] H.-Y. Yang, A. M. Läuchli, F. Mila, and K. P. Schmidt. *Effective Spin Model for the Spin-Liquid Phase of the Hubbard Model on the Triangular Lattice*. Phys. Rev. Lett. **105**, 267204 (2010).

[126] H. Y. Yang and K. P. Schmidt. *Effective models for gapped phases of strongly correlated quantum lattice models*. EPL **94**, 17004 (2011).

[127] K. Nakamura, Y. Yoshimoto, and M. Imada. *Ab initio two-dimensional multiband low-energy models of $EtMe_3Sb[Pd(dmit)_2]_2$ and κ-$(BEDT\text{-}TTF)_2Cu(NCS)_2$ with comparisons to single-band models*. Phys. Rev. B **86**, 205117 (2012).

[128] F. Neese. *The ORCA program system*. Wiley Interdiscip. Rev. Comput. Mol. Sci. **2**, 73–78 (2012).

[129] F. Neese. *Efficient and accurate approximations to the molecular spin-orbit coupling operator and their use in molecular g-tensor calculations*. J. Chem. Phys. **122**, 034107 (2005).

[130] K. Gregor and O. I. Motrunich. *Nonmagnetic impurities in a $s = \frac{1}{2}$ frustrated triangular antiferromagnet: Broadening of ^{13}C NMR lines in κ-$(ET)_2Cu_2(CN)_3$*. Phys. Rev. B **79**, 024421 (2009).

[131] M. Yamashita, T. Shibauchi, and Y. Matsuda. *Thermal-Transport Studies on Two-Dimensional Quantum Spin Liquids*. Chem. Phys. Chem. **13**, 74–78 (2012).

[132] R. S. Manna, M. de Souza, A. Brühl, J. A. Schlueter, and M. Lang. *Lattice Effects and Entropy Release at the Low-Temperature Phase Transition in the Spin-Liquid Candidate κ-$(BEDT\text{-}TTF)_2Cu_2(CN)_3$*. Phys. Rev. Lett. **104**, 016403 (2010).

[133] M. Poirier, M. de Lafontaine, K. Miyagawa, K. Kanoda, and Y. Shimizu. *Ultrasonic investigation of the transition at 6 K in the spin-liquid candidate κ-$(BEDT\text{-}TTF)_2Cu_2(CN)_3$*. Phys. Rev. B **89**, 045138 (2014).

[134] K. G. Padmalekha, M. Blankenhorn, T. Ivek, L. Bogani, J. A. Schlueter, and M. Dressel. *ESR studies on the spin-liquid candidate κ-$(BEDT\text{-}TTF)_2Cu_2(CN)_3$: Anomalous response below T= 8 K*. Physica B Condens. Matter **460**, 211–213 (2015).

[135] M. Vojta. *Quantum phase transitions*. Rep. Prog. Phys. **66**, 2069 (2003).

[136] B. K. Chakrabarti, A. Dutta, and P. Sen. *Quantum Ising phases and transitions in transverse Ising models*. Springer, (1996).

[137] P. Kopietz, L. Bartosch, and F. Schütz. *Introduction to the Functional Renormalization Group*. Springer, (2010).

[138] S. Sachdev. *Quantum phase transitions*. Cambridge University Press, Cambridge, 2nd edition, (2011).

[139] M. Continentino. *Quantum scaling in many-body systems*. Cambridge University Press, (2017).

[140] L. Shekhtman, O. Entin-Wohlman, and A. Aharony. *Moriya's anisotropic superexchange interaction, frustration, and Dzyaloshinsky's weak ferromagnetism*. Phys. Rev. Lett. **69**, 836–839 (1992).

[141] A. Authier. *International Tables for Crystallography: Vol. D, Physical Properties of Crystals*. International Union of Crystallography, (2003).

[142] M. Pinterić, M. Miljak, N. Biškup, O. Milat, I. Aviani, S. Tomić, D. Schweitzer, W. Strunz, and I. Heinen. *Magnetic anisotropy and low-frequency dielectric response of weak ferromagnetic phase in κ-(BEDT-TTF)$_2$Cu[N(CN)$_2$]Cl, where BEDT-TTF is Bis(ethylenedithio)tetrathiafulvalene*. Eur. Phys. J. B **11**, 217–225 (1999).

[143] *Point Group Symmetry Character Tables*, (2019). Webpage: https://www.webqc.org/symmetrypointgroup-c2h.html.

[144] M. Oshikawa and I. Affleck. *Field-Induced Gap in $s = 1/2$ Antiferromagnetic Chains*. Phys. Rev. Lett. **79**, 2883–2886 (1997).

[145] I. Affleck and M. Oshikawa. *Field-induced gap in Cu benzoate and other $s = \frac{1}{2}$ antiferromagnetic chains*. Phys. Rev. B **60**, 1038–1056 (1999).

[146] D. Watanabe, M. Yamashita, S. Tonegawa, Y. Oshima, H. Yamamoto, R. Kato, I. Sheikin, K. Behnia, T. Terashima, S. Uji, T. Shibauchi, and Y. Matsuda. *Novel pauli-paramagnetic quantum phase in a mott insulator*. Nat. Commun. **3**, 1090 (2012).

[147] G. Baskaran. *Novel local symmetries and chiral-symmetry-broken phases in s=1/2 triangular-lattice Heisenberg model*. Phys. Rev. Lett. **63**, 2524–2527 (1989).

[148] I. Kimchi, J. P. Sheckelton, T. M. McQueen, and P. A. Lee. *Scaling and data collapse from local moments in frustrated disordered quantum spin systems*. Nat. Commun. **9**, 4367 (2018).

[149] O. Drozdova, G. Saito, H. Yamochi, K. Ookubo, K. Yakushi, M. Uruichi, and L. Ouahab. *Composition and Structure of the Anion Layer in the Organic Superconductor κ-(BEDT-TTF)$_2$Cu$_2$(CN)$_3$: Optical Study*. Inorg. Chem. **40**, 3265–3266 (2001).

[150] A. Kolezhuk, S. Sachdev, R. R. Biswas, and P. Chen. *Theory of quantum impurities in spin liquids*. Phys. Rev. B **74**, 165114 (2006).

[151] R. L. Doretto and M. Vojta. *Quantum magnets with weakly confined spinons: Multiple length scales and quantum impurities*. Phys. Rev. B **80**, 024411 (2009).

[152] M. Vojta, C. Buragohain, and S. Sachdev. *Quantum impurity dynamics in two-dimensional antiferromagnets and superconductors*. Phys. Rev. B **61**, 15152–15184 (2000).

[153] S. Sachdev, C. Buragohain, and M. Vojta. *Quantum impurity in a nearly critical two-dimensional antiferromagnet*. Science **286**, 2479–2482 (1999).

[154] S. Sachdev and M. Vojta. *Quantum impurity in an antiferromagnet: Nonlinear sigma model theory*. Phys. Rev. B **68**, 064419 (2003).

[155] K. H. Höglund and A. W. Sandvik. *Anomalous Curie Response of Impurities in Quantum-Critical Spin-1/2 Heisenberg Antiferromagnets*. Phys. Rev. Lett. **99**, 027205 (2007).

[156] D. Guterding, R. Valentí, and H. O. Jeschke. *Influence of molecular conformations on the electronic structure of organic charge transfer salts*. Phys. Rev. B **92**, 081109 (2015).

[157] B. Hartmann, J. Müller, and T. Sasaki. *Mott metal-insulator transition induced by utilizing a glasslike structural ordering in low-dimensional molecular conductors*. Phys. Rev. B **90**, 195150 (2014).

[158] M. Pinterić, M. Čulo, O. Milat, M. Basletić, B. Korin-Hamzić, E. Tafra, A. Hamzić, T. Ivek, T. Peterseim, K. Miyagawa, K. Kanoda, J. A. Schlueter, M. Dressel, and S. Tomić. *Anisotropic charge dynamics in the quantum spin-liquid candidate κ-(BEDT-TTF)$_2$Cu$_2$(CN)$_3$*. Phys. Rev. B **90**, 195139 (2014).

[159] C. Hotta. *Quantum electric dipoles in spin-liquid dimer Mott insulator κ-ET$_2$Cu$_2$(CN)$_3$*. Phys. Rev. B **82**, 241104 (2010).

[160] M. Abdel-Jawad, I. Terasaki, T. Sasaki, N. Yoneyama, N. Kobayashi, Y. Uesu, and C. Hotta. *Anomalous dielectric response in the dimer mott insulator κ-(BEDT-TTF)$_2$Cu$_2$(CN)$_3$*. Phys. Rev. B **82**, 125119 (2010).

[161] E. Westerberg, A. Furusaki, M. Sigrist, and P. A. Lee. *Random Quantum Spin Chains: A Real-Space Renormalization Group Study*. Phys. Rev. Lett. **75**, 4302–4305 (1995).

[162] E. Westerberg, A. Furusaki, M. Sigrist, and P. A. Lee. *Low-energy fixed points of random quantum spin chains*. Phys. Rev. B **55**, 12578–12593 (1997).

[163] Y.-C. Lin, R. Mélin, H. Rieger, and F. Iglói. *Low-energy fixed points of random Heisenberg models*. Phys. Rev. B **68**, 024424 (2003).

[164] F. Iglói and C. Monthus. *Strong disorder RG approach of random systems*. Phys. Rep. **412**, 277–431 (2005).

[165] R. R. P. Singh. *Valence Bond Glass Phase in Dilute Kagome Antiferromagnets*. Phys. Rev. Lett. **104**, 177203 (2010).

[166] B. Frischmuth, M. Sigrist, B. Ammon, and M. Troyer. *Thermodynamics of random ferromagnetic-antiferromagnetic spin-1/2 chains*. Phys. Rev. B **60**, 3388–3399 (1999).

[167] K. Watanabe, H. Kawamura, H. Nakano, and T. Sakai. *Quantum spin-liquid behavior in the spin-1/2 random Heisenberg antiferromagnet on the triangular lattice*. J. Phys. Soc. Jpn. **83**, 034714 (2014).

[168] P. W. Anderson, B. I. Halperin, and C. M. Varma. *Anomalous low-temperature thermal properties of glasses and spin glasses*. Philos. Mag. **25**, 1–9 (1972).

[169] J. S. Gardner, M. J. P. Gingras, and J. E. Greedan. *Magnetic pyrochlore oxides*. Rev. Mod. Phys. **82**, 53–107 (2010).

[170] A. M. Hallas, J. Gaudet, and B. D. Gaulin. *Experimental Insights into Ground-State Selection of Quantum XY Pyrochlores*. Annu. Rev. Condens. Matter Phys. **9**, 105–124 (2018).

[171] M. Hermele, M. P. A. Fisher, and L. Balents. *Pyrochlore photons: The $U(1)$ spin liquid in a $S = \frac{1}{2}$ three-dimensional frustrated magnet*. Phys. Rev. B **69**, 064404 (2004).

[172] R. Moessner and J. T. Chalker. *Properties of a Classical Spin Liquid: The Heisenberg Pyrochlore Antiferromagnet*. Phys. Rev. Lett. **80**, 2929–2932 (1998).

[173] B. Canals and C. Lacroix. *Pyrochlore Antiferromagnet: A Three-Dimensional Quantum Spin Liquid*. Phys. Rev. Lett. **80**, 2933–2936 (1998).

[174] K. A. Ross, L. Savary, B. D. Gaulin, and L. Balents. *Quantum Excitations in Quantum Spin Ice*. Phys. Rev. X **1**, 021002 (2011).

[175] M. J. Harris, S. T. Bramwell, D. F. McMorrow, T. Zeiske, and K. W. Godfrey. *Geometrical Frustration in the Ferromagnetic Pyrochlore $Ho_2Ti_2O_7$*. Phys. Rev. Lett. **79**, 2554–2557 (1997).

[176] C. Liu, G. B. Halász, and L. Balents. *Competing orders in pyrochlore magnets from a $\mathbb{Z}_2$ spin liquid perspective*. arXiv preprint arXiv:1905.00460 (2019).

[177] A. P. Ramirez, A. Hayashi, R. J. Cava, R. Siddharthan, and B. S. Shastry. *Zero-point entropy in 'spin ice'*. Nature **399**, 333 (1999).

[178] L. D. C. Jaubert and P. C. W. Holdsworth. *Signature of magnetic monopole and Dirac string dynamics in spin ice*. Nat. Phys. **5**, 258 (2009).

[179] D. J. P. Morris, D. A. Tennant, S. A. Grigera, B. Klemke, C. Castelnovo, R. Moessner, C. Czternasty, M. Meissner, K. C. Rule, J.-U. Hoffmann, K. Kiefer, S. Gerischer, D. Slobinsky, and R. S. Perry. *Dirac strings and magnetic monopoles in the spin ice $Dy_2Ti_2O_7$*. Science **326**, 411–414 (2009).

[180] S. T. Bramwell, S. R. Giblin, S. Calder, R. Aldus, D. Prabhakaran, and T. Fennell. *Measurement of the charge and current of magnetic monopoles in spin ice*. Nature **461**, 956 (2009).

[181] D. F. Bowman, E. Cemal, T. Lehner, A. R. Wildes, L. Mangin-Thro, G. J. Nilsen, M. J. Gutmann, D. J. Voneshen, D. Prabhakaran, A. T. Boothroyd, D. G. Porter, C. Castelnovo, K. Refson, and J. P. Goff. *Role of defects in determining the magnetic ground state of ytterbium titanate*. Nat. Commun. **10**, 637 (2019).

[182] J. D. M. Champion, M. J. Harris, P. C. W. Holdsworth, A. S. Wills, G. Balakrishnan, S. T. Bramwell, E. Čižmár, T. Fennell, J. S. Gardner, J. Lago, D. F. McMorrow, M. Orendáč, A. Orendáčová, D. M. Paul, R. I. Smith, M. T. F. Telling, and A. Wildes. *$Er_2Ti_2O_7$: Evidence of quantum order by disorder in a frustrated antiferromagnet*. Phys. Rev. B **68**, 020401 (2003).

[183] W. Witczak-Krempa, G. Chen, Y. B. Kim, and L. Balents. *Correlated Quantum Phenomena in the Strong Spin-Orbit Regime*. Annu. Rev. Condens. Matter Phys. **5**, 57–82 (2014).

[184] J. G. Rau and M. J. Gingras. *Frustrated Quantum Rare-Earth Pyrochlores*. Annu. Rev. Condens. Matter Phys. **10**, 357–386 (2019).

[185] S. Shamoto, T. Nakano, Y. Nozue, and T. Kajitani. *Substitution effects on ferromagnetic Mott insulator $Lu_2V_2O_7$*. J. Phys. Chem. Solids **63**, 1047 – 1050 (2002).

[186] H. D. Zhou, E. S. Choi, J. A. Souza, J. Lu, Y. Xin, L. L. Lumata, B. S. Conner, L. Balicas, J. S. Brooks, J. J. Neumeier, and C. R. Wiebe. *Magnetic-polaron-driven magnetoresistance in the pyrochlore $Lu_2V_2O_7$*. Phys. Rev. B **77**, 020411 (2008).

[187] Y. Onose, T. Ideue, H. Katsura, Y. Shiomi, N. Nagaosa, and Y. Tokura. *Observation of the magnon hall effect*. Science **329**, 297–299 (2010).

[188] L. Clark, G. J. Nilsen, E. Kermarrec, G. Ehlers, K. S. Knight, A. Harrison, J. P. Attfield, and B. D. Gaulin. *From Spin Glass to Quantum Spin Liquid Ground States in Molybdate Pyrochlores*. Phys. Rev. Lett. **113**, 117201 (2014).

[189] M. Elhajal, B. Canals, R. Sunyer, and C. Lacroix. *Ordering in the pyrochlore antiferromagnet due to Dzyaloshinsky-Moriya interactions*. Phys. Rev. B **71**, 094420 (2005).

[190] V. N. Kotov, M. Elhajal, M. E. Zhitomirsky, and F. Mila. *Dzyaloshinsky-Moriya-induced order in the spin-liquid phase of the $s = 12$ pyrochlore antiferromagnet*. Phys. Rev. B **72**, 014421 (2005).

[191] J. D. Thompson, P. A. McClarty, H. M. Rønnow, L. P. Regnault, A. Sorge, and M. J. P. Gingras. *Rods of Neutron Scattering Intensity in $Yb_2Ti_2O_7$: Compelling Evidence for Significant Anisotropic Exchange in a Magnetic Pyrochlore Oxide*. Phys. Rev. Lett. **106**, 187202 (2011).

[192] A. I. Liechtenstein, V. I. Anisimov, and J. Zaanen. *Density-functional theory and strong interactions: Orbital ordering in mott-hubbard insulators*. Phys. Rev. B **52**, R5467–R5470 (1995).

[193] H. Ichikawa, L. Kano, M. Saitoh, S. Miyahara, N. Furukawa, J. Akimitsu, T. Yokoo, T. Matsumura, M. Takeda, and K. Hirota. *Orbital ordering in ferromagnetic $Lu_2V_2O_7$*. J. Phys. Soc. Jpn. **74**, 1020–1025 (2005).

[194] S. Miyahara, A. Murakami, and N. Furukawa. *Orbital ordering induced ferromagnetism in $Lu_2V_2O_7$*. J. Mol. Struct. **838**, 223 – 226 (2007).

[195] H. J. Xiang, E. J. Kan, M.-H. Whangbo, C. Lee, S.-H. Wei, and X. G. Gong. *Single-ion anisotropy, dzyaloshinskii-moriya interaction, and negative magnetoresistance of the spin-$\frac{1}{2}$ pyrochlore $R_2v_2o_7$*. Phys. Rev. B **83**, 174402 (2011).

[196] M. Mena, R. S. Perry, T. G. Perring, M. D. Le, S. Guerrero, M. Storni, D. T. Adroja, C. Rüegg, and D. F. McMorrow. *Spin-wave spectrum of the quantum ferromagnet on the pyrochlore lattice* $lu_2v_2o_7$. Phys. Rev. Lett. **113**, 047202 (2014).

[197] L. Zhang, J. Ren, J.-S. Wang, and B. Li. *Topological magnon insulator in insulating ferromagnet*. Phys. Rev. B **87**, 144101 (2013).

[198] A. Mook, J. Henk, and I. Mertig. *Magnon Hall effect and topology in kagome lattices: A theoretical investigation*. Phys. Rev. B **89**, 134409 (2014).

[199] M. Pereiro, D. Yudin, J. Chico, C. Etz, O. Eriksson, and A. Bergman. *Topological excitations in a kagome magnet*. Nat. Commun. **5**, 4815 (2014).

[200] A. Mook, J. Henk, and I. Mertig. *Tunable magnon weyl points in ferromagnetic pyrochlores*. Phys. Rev. Lett. **117**, 157204 (2016).

[201] K. Koepernik and H. Eschrig. *Full-potential nonorthogonal local-orbital minimum-basis band-structure scheme*. Phys. Rev. B **59**, 1743–1757 (1999).

[202] J. P. Perdew, K. Burke, and M. Ernzerhof. *Generalized Gradient Approximation Made Simple*. Phys. Rev. Lett. **77**, 3865–3868 (1996).

[203] A. Haghighirad, C. Gross, and W. Assmus. *Powder synthesis and crystal growth of $Y_2V_2O_7$ under high pressure and its physical properties*. J. Cryst. Growth **310**, 2277 – 2283 (2008).

[204] H. Eschrig and K. Koepernik. *Tight-binding models for the iron-based superconductors*. Phys. Rev. B **80**, 104503 (2009).

[205] M. Blume and R. Watson. *Theory of spin-orbit coupling in atoms, II. Comparison of theory with experiment*. Proc. Royal Soc. London, Ser. A **271**, 565–578 (1963).

[206] D. Khomskii. *Transition metal compounds*. Cambridge Univ. Press, Cambridge, (2014).

[207] J. des Cloizeaux. *Extension d'une formule de Lagrange à des problèmes de valeurs propres*. Nucl. Phys. **20**, 321 (1960).

[208] D. Szczepanik and J. Mrozek. *On several alternatives for löwdin orthogonalization*. Comput. Theor. Chem. **1008**, 15 – 19 (2013).

[209] P.-O. Löwdin. *On the Non-Orthogonality Problem Connected with the Use of Atomic Wave Functions in the Theory of Molecules and Crystals*. J. Chem. Phys. **18**, 365–375 (1950).

[210] I. Mayer. *On Löwdin's method of symmetric orthogonalization*. Int. J. Quant. Chem. **90**, 63–65 (2002).

[211] T. Ideue, Y. Onose, H. Katsura, Y. Shiomi, S. Ishiwata, N. Nagaosa, and Y. Tokura. *Effect of lattice geometry on magnon Hall effect in ferromagnetic insulators*. Phys. Rev. B **85**, 134411 (2012).

[212] M. Kotani. *On the Magnetic Moment of Complex Ions. (I)*. J. Phys. Soc. Jpn. **4**, 293–297 (1949).

[213] H. Kamimura. *On the Magnetic Moment and g-Value of Complex Ions*. J. Phys. Soc. Jpn. **11**, 1171–1181 (1956).

[214] G. T. Knoke, A. Niazi, J. M. Hill, and D. C. Johnston. *Synthesis, structure, and ferromagnetism of the oxygen defect pyrochlore system $Lu_2V_2O_{7-x}$ ($x = 0.40 - 0.65$)*. Phys. Rev. B **76**, 054439 (2007).

[215] L. Bellaiche and D. Vanderbilt. *Virtual crystal approximation revisited: Application to dielectric and piezoelectric properties of perovskites*. Phys. Rev. B **61**, 7877–7882 (2000).

[216] M. Montalti, A. Credi, L. Prodi, and M. T. Gandolfi. *Handbook of photochemistry*. CRC press, (2006).

[217] M. F. Lapa and C. L. Henley. *Ground states of the classical antiferromagnet on the pyrochlore lattice*. arXiv preprint arXiv:1210.6810 (2012).

[218] M. Hering and J. Reuther. *Functional renormalization group analysis of Dzyaloshinsky-Moriya and Heisenberg spin interactions on the kagome lattice*. Phys. Rev. B **95**, 054418 (2017).

[219] G. Jackeli and G. Khaliullin. *Mott Insulators in the Strong Spin-Orbit Coupling Limit: From Heisenberg to a Quantum Compass and Kitaev Models*. Phys. Rev. Lett. **102**, 017205 (2009).

[220] J. Knolle, D. L. Kovrizhin, J. T. Chalker, and R. Moessner. *Dynamics of a Two-Dimensional Quantum Spin Liquid: Signatures of Emergent Majorana Fermions and Fluxes*. Phys. Rev. Lett. **112**, 207203 (2014).

[221] J. G. Rau, E. K.-H. Lee, and H.-Y. Kee. *Generic Spin Model for the Honeycomb Iridates beyond the Kitaev Limit*. Phys. Rev. Lett. **112**, 077204 (2014).

[222] S. M. Winter, A. A. Tsirlin, M. Daghofer, J. van den Brink, Y. Singh, P. Gegenwart, and R. Valentí. *Models and materials for generalized Kitaev magnetism*. J. Phys.: Condens. Matter **29**, 493002 (2017).

[223] M. Hermanns, I. Kimchi, and J. Knolle. *Physics of the Kitaev Model: Fractionalization, Dynamic Correlations, and Material Connections*. Annu. Rev. Condens. Matter Phys. **9**, 17–33 (2018).

[224] S. M. Winter, Y. Li, H. O. Jeschke, and R. Valentí. *Challenges in design of Kitaev materials: Magnetic interactions from competing energy scales*. Phys. Rev. B **93**, 214431 (2016).

[225] R. Yadav, N. A. Bogdanov, V. M. Katukuri, S. Nishimoto, J. van den Brink, and L. Hozoi. *Kitaev exchange and field-induced quantum spin-liquid states in honeycomb α-$RuCl_3$*. Sci. Rep. **6**, 37925 (2016).

[226] H.-S. Kim and H.-Y. Kee. *Crystal structure and magnetism in α-$RuCl_3$: An ab initio study*. Phys. Rev. B **93**, 155143 (2016).

[227] Y. S. Hou, H. J. Xiang, and X. G. Gong. *Unveiling magnetic interactions of ruthenium trichloride via constraining direction of orbital moments: Potential routes to realize a quantum spin liquid*. Phys. Rev. B **96**, 054410 (2017).

[228] V. M. Katukuri, S. Nishimoto, V. Yushankhai, A. Stoyanova, H. Kandpal, S. Choi, R. Coldea, I. Rousochatzakis, L. Hozoi, and J. van den Brink. *Kitaev interactions between $j = 1/2$ moments in honeycomb Na_2IrO_3 are large and ferromagnetic: insights from ab initio quantum chemistry calculations*. New J. Phys. **16**, 013056 (2014).

[229] Y. Yamaji, Y. Nomura, M. Kurita, R. Arita, and M. Imada. *First-Principles Study of the Honeycomb-Lattice Iridates Na_2IrO_3 in the Presence of Strong Spin-Orbit Interaction and Electron Correlations*. Phys. Rev. Lett. **113**, 107201 (2014).

[230] S. D. Das, S. Kundu, Z. Zhu, E. Mun, R. D. McDonald, G. Li, L. Balicas, A. McCollam, G. Cao, J. G. Rau, H.-Y. Kee, V. Tripathi, and S. E. Sebastian. *Magnetic anisotropy of the alkali iridate Na_2IrO_3 at high magnetic fields: Evidence for strong ferromagnetic Kitaev correlations*. Phys. Rev. B **99**, 081101 (2019).

[231] A. Banerjee, C. A. Bridges, J.-Q. Yan, A. A. Aczel, L. Li, M. B. Stone, G. E. Granroth, M. D. Lumsden, Y. Yiu, J. Knolle, S. Bhattacharjee, D. L. Kovrizhin, R. Moessner, D. A. Tennant, G. Mandrus, and S. E. Nagler. *Proximate Kitaev quantum spin liquid behaviour in a honeycomb magnet*. Nat. Mater. **15**, 733–740 (2016).

[232] H. B. Cao, A. Banerjee, J.-Q. Yan, C. A. Bridges, M. D. Lumsden, D. G. Mandrus, D. A. Tennant, B. C. Chakoumakos, and S. E. Nagler. *Low-temperature crystal and magnetic structure of α-$RuCl_3$*. Phys. Rev. B **93**, 134423 (2016).

[233] I. Kimchi, R. Coldea, and A. Vishwanath. *Unified theory of spiral magnetism in the harmonic-honeycomb iridates α ,β, and gamma-Li_2IrO_3*. Phys. Rev. B **91**, 245134 (2015).

[234] S. C. Williams, R. D. Johnson, F. Freund, S. Choi, A. Jesche, I. Kimchi, S. Manni, A. Bombardi, P. Manuel, P. Gegenwart, and R. Coldea. *Incommensurate counterrotating magnetic order stabilized by Kitaev interactions in the layered honeycomb α-Li_2IrO_3*. Phys. Rev. B **93**, 195158 (2016).

[235] J. Knolle. *Dynamics of a Quantum Spin Liquid*. Springer, (2016).

[236] E. H. Lieb. *Flux Phase of the Half-Filled Band*. Phys. Rev. Lett. **73**, 2158–2161 (1994).

[237] R. D. Johnson, S. C. Williams, A. A. Haghighirad, J. Singleton, V. Zapf, P. Manuel, I. I. Mazin, Y. Li, H. O. Jeschke, R. Valentí, and R. Coldea. *Monoclinic crystal structure of α-$RuCl_3$ and the zigzag antiferromagnetic ground state*. Phys. Rev. B **92**, 235119 (2015).

[238] E. V. Stroganov and K. V. Ovchinnikov. *Crystal structure of ruthenium trichloride*. Vestn. Leningr. Univ. Fiz. Khim **12**, 152–157 (1957).

[239] J. M. Fletcher, W. E. Gardner, A. C. Fox, and G. Topping. *X-Ray, infrared, and magnetic studies of α- and β-ruthenium trichloride*. J. Chem. Soc. A pages 1038–1045 (1967).

[240] K. W. Plumb, J. P. Clancy, L. J. Sandilands, V. V. Shankar, Y. F. Hu, K. S. Burch, H.-Y. Kee, and Y.-J. Kim. *α-$RuCl_3$: A spin-orbit assisted Mott insulator on a honeycomb lattice*. Phys. Rev. B **90**, 041112 (2014).

[241] Y. Kubota, H. Tanaka, T. Ono, Y. Narumi, and K. Kindo. *Successive magnetic phase transitions in α-$RuCl_3$: XY-like frustrated magnet on the honeycomb lattice*. Phys. Rev. B **91**, 094422 (2015).

[242] S. Reschke, F. Mayr, Z. Wang, S.-H. Do, K.-Y. Choi, and A. Loidl. *Electronic and phonon excitations in α-$RuCl_3$*. Phys. Rev. B **96**, 165120 (2017).

[243] D. Gotfryd, J. Rusnačko, K. Wohlfeld, G. Jackeli, J. Chaloupka, and A. M. Oleś. *Phase diagram and spin correlations of the Kitaev-Heisenberg model: Importance of quantum effects*. Phys. Rev. B **95**, 024426 (2017).

[244] J. Reuther, R. Thomale, and S. Trebst. *Finite-temperature phase diagram of the Heisenberg-Kitaev model*. Phys. Rev. B **84**, 100406 (2011).

[245] R. Schaffer, S. Bhattacharjee, and Y.-B. Kim. *Quantum phase transition in Heisenberg-Kitaev model*. Phys. Rev. B **86**, 224417 (2012).

[246] G. Baskaran, S. Mandal, and R. Shankar. *Exact Results for Spin Dynamics and Fractionalization in the Kitaev Model*. Phys. Rev. Lett. **98**, 247201 (2007).

[247] J. Chaloupka, G. Jackeli, and G. Khaliullin. *Kitaev-Heisenberg Model on a Honeycomb Lattice: Possible Exotic Phases in Iridium Oxides A_2IrO_3*. Phys. Rev. Lett. **105**, 027204 (2010).

[248] J. Chaloupka, G. Jackeli, and G. Khaliullin. *Zigzag Magnetic Order in the Iridium Oxide Na_2IrO_3*. Phys. Rev. Lett. **110**, 097204 (2013).

[249] M. Gohlke, R. Verresen, R. Moessner, and F. Pollmann. *Dynamics of the Kitaev-Heisenberg Model*. Phys. Rev. Lett. **119**, 157203 (2017).

[250] M. Gohlke, G. Wachtel, Y. Yamaji, F. Pollmann, and Y. B. Kim. *Quantum spin liquid signatures in Kitaev-like frustrated magnets*. Phys. Rev. B **97**, 075126 (2018).

[251] L. Janssen, E. C. Andrade, and M. Vojta. *Honeycomb-Lattice Heisenberg-Kitaev Model in a Magnetic Field: Spin Canting, Metamagnetism, and Vortex Crystals*. Phys. Rev. Lett. **117**, 277202 (2016).

[252] L. Janssen, E. C. Andrade, and M. Vojta. *Magnetization processes of zigzag states on the honeycomb lattice: Identifying spin models for α-$RuCl_3$ and Na_2IrO_3*. Phys. Rev. B **96**, 064430 (2017).

[253] C. Lanczos. *An Iteration Method for the Solution of the Eigenvalue Problem of Linear Differential and Integral Operators*. J. Res. Nat. Bur. Stand. **45**, 255–282 (1950).

[254] H. Ehrenreich, F. Seitz, and D. Turnbull (Eds.). *Solid State Physics: Advances in Research and Applications*, vol. 35. Academic Press, New York, (1980).

[255] J. Jensen and A. R. Mackintosh (Eds.). *Rare Earth Magnetism: Structures and Excitations*. Clarendon Press, Oxford, (1991).

[256] A. Furrer, J. Mesot, and T. Strässle. *Neutron Scattering in Condensed Matter Physics*, vol. 4 of *Series on Neutron Techniques and Applications*. World Scientific, Hackensack NJ, (2009).

[257] J. Chaloupka and G. Khaliullin. *Magnetic anisotropy in the Kitaev model systems Na_2IrO_3 and $RuCl_3$*. Phys. Rev. B **94**, 064435 (2016).

[258] D. T. Cromer and J. T. Waber. *Scattering Factors Computed from Relativistic Dirac-Slater Wave Functions*. Acta Cryst. **18**, 104–109 (1965).

[259] J. Knolle, D. L. Kovrizhin, J. T. Chalker, and R. Moessner. *Dynamics of fractionalization in quantum spin liquids*. Phys. Rev. B **92**, 115127 (2015).

[260] K. Ran, J. Wang, W. Wang, Z.-Y. Dong, X. Ren, S. Bao, S. Li, Z. Ma, Y. Gan, Y. Zhang, J. T. Park, G. Deng, S. Danilkin, S.-L. Yu, J.-X. Li, and J. Wen. *Spin-Wave Excitations Evidencing the Kitaev Interaction in Single Crystalline α-$RuCl_3$*. Phys. Rev. Lett. **118**, 107203 (2017).

[261] J. Chaloupka and G. Khaliullin. *Hidden symmetries of the extended Kitaev-Heisenberg model: Implications for the honeycomb-lattice iridates A_2IrO_3*. Phys. Rev. B **92**, 024413 (2015).

[262] P. A. Maksimov, M. E. Zhitomirsky, and A. L. Chernyshev. *Field-induced decays in XXZ triangular-lattice antiferromagnets*. Phys. Rev. B **94**, 140407(R) (2016).

[263] S.-H. Do, S.-Y. Park, J. Yoshitake, J. Nasu, Y. Motome, Y. S. Kwon, D. T. Adroja, D. J. Voneshen, K. Kim, T.-H. Jang, J.-H. Park, K.-Y. Choi, and S. Ji. *Majorana fermions in the Kitaev quantum spin system α-$RuCl_3$*. Nat. Phys. **13**, 1079 (2017).

[264] A. M. Samarakoon, A. Banerjee, S.-S. Zhang, Y. Kamiya, S. E. Nagler, D. A. Tennant, S.-H. Lee, and C. D. Batista. *Comprehensive study of the dynamics of a classical Kitaev spin liquid*. Phys. Rev. B **96**, 134408 (2017).

[265] Z. Wang, J. Guo, F. F. Tafti, A. Hegg, S. Sen, V. A. Sidorov, L. Wang, S. Cai, W. Yi, Y. Zhou, H. Wang, S. Zhang, K. Yang, A. Li, X. Li, Y. Li, J. Liu, Y. Shi, W. Ku, Q. Wu, R. J. Cava, and L. Sun. *Pressure-induced melting of magnetic order and emergence of a new quantum state in α-RuC_3*. Phys. Rev. B **97**, 245149 (2018).

[266] T. Biesner, S. Biswas, W. Li, Y. Saito, A. Pustogow, M. Altmeyer, A. U. B. Wolter, B. Büchner, M. Roslova, T. Doert, S. M. Winter, R. Valentí, and M. Dressel. *Detuning the honeycomb of α-$RuCl_3$: Pressure-dependent optical studies reveal broken symmetry*. Phys. Rev. B **97**, 220401 (2018).

[267] I. A. Leahy, C. A. Pocs, P. E. Siegfried, D. Graf, S.-H. Do, K.-Y. Choi, B. Normand, and M. Lee. *Anomalous Thermal Conductivity and Magnetic Torque Response in the Honeycomb Magnet α-$RuCl_3$*. Phys. Rev. Lett. **118**, 187203 (2017).

[268] J. A. Sears, Y. Zhao, Z. Xu, J. W. Lynn, and Y.-J. Kim. *Phase diagram of α-$RuCl_3$ in an in-plane magnetic field*. Phys. Rev. B **95**, 180411 (2017).

[269] A. U. B. Wolter, L. T. Corredor, L. Janssen, K. Nenkov, S. Schönecker, S.-H. Do, K.-Y. Choi, R. Albrecht, J. Hunger, T. Doert, M. Vojta, and B. Büchner. *Field-induced quantum criticality in the Kitaev system α-$RuCl_3$*. Phys. Rev. B **96**, 041405 (2017).

[270] R. Hentrich, A. U. B. Wolter, X. Zotos, W. Brenig, D. Nowak, A. Isaeva, T. Doert, A. Banerjee, P. Lampen-Kelley, D. G. Mandrus, S. E. Nagler, J. Sears, Y.-J. Kim, B. Büchner, and C. Hess. *Unusual Phonon Heat Transport in α-$RuCl_3$: Strong Spin-Phonon Scattering and Field-Induced Spin Gap*. Phys. Rev. Lett. **120**, 117204 (2018).

[271] J. Zheng, K. Ran, T. Li, J. Wang, P. Wang, B. Liu, Z.-X. Liu, B. Normand, J. Wen, and W. Yu. *Gapless Spin Excitations in the Field-Induced Quantum Spin Liquid Phase of α-$RuCl_3$*. Phys. Rev. Lett. **119**, 227208 (2017).

[272] S.-H. Baek, S.-H. Do, K.-Y. Choi, Y. S. Kwon, A. U. B. Wolter, S. Nishimoto, J. van den Brink, and B. Büchner. *Evidence for a Field-Induced Quantum Spin Liquid in α-$RuCl_3$*. Phys. Rev. Lett. **119**, 037201 (2017).

[273] C. Balz, P. Lampen-Kelley, A. Banerjee, J. Yan, Z. Lu, X. Hu, S. M. Yadav, Y. Takano, Y. Liu, D. A. Tennant, M. D. Lumsden, D. Mandrus, and S. E. Nagler. *Magnons, fractional excitations, and field-induced transitions in α-$RuCl_3$*. arXiv preprint arXiv:1903.00056 (2019).

[274] Z. Wang, S. Reschke, D. Hüvonen, S.-H. Do, K.-Y. Choi, M. Gensch, U. Nagel, T. Rõ om, and A. Loidl. *Magnetic Excitations and Continuum of a Possibly Field-Induced Quantum Spin Liquid in α-$RuCl_3$*. Phys. Rev. Lett. **119**, 227202 (2017).

[275] A. N. Ponomaryov, E. Schulze, J. Wosnitza, P. Lampen-Kelley, A. Banerjee, J.-Q. Yan, C. A. Bridges, D. G. Mandrus, S. E. Nagler, A. K. Kolezhuk, and S. A. Zvyagin. *Unconventional spin dynamics in the honeycomb-lattice material α-$RuCl_3$: High-field electron spin resonance studies*. Phys. Rev. B **96**, 241107 (2017).

[276] P. Lampen-Kelley, L. Janssen, E. C. Andrade, S. Rachel, J.-Q. Yan, C. Balz, D. G. Mandrus, S. E. Nagler, and M. Vojta. *Field-induced intermediate phase in α-$RuCl_3$: Non-coplanar order, phase diagram, and proximate spin liquid.* arXiv preprint arXiv:1807.06192 (2018).

[277] D. A. S. Kaib, S. M. Winter, and R. Valentí. *Kitaev honeycomb models in magnetic fields: Dynamical response and hidden symmetries*. arXiv preprint arXiv:1904.01025 (2019).

[278] K. A. Modic, B. J. Ramshaw, A. Shekhter, and C. M. Varma. *Chiral spin order in some purported Kitaev spin-liquid compounds*. Phys. Rev. B **98**, 205110 (2018).

[279] K. A. Modic, R. D. McDonald, J. P. C. Ruff, M. D. Bachmann, Y. Lai, J. C. Palmstrom, D. Graf, M. Chan, F. F. Balakirev, J. B. Betts, G. S. Boebinger, M. Schmidt, D. A. Sokoloc, P. J. W. Moll, B. J. Ramshaw, and A. Shekhter. *Scale-Invariance of a Spin Liquid in High Magnetic Fields*. arXiv preprint arXiv:1901.09245 (2019).

[280] H.-S. Kim, V. V. Shankar, A. Catuneanu, and H.-Y. Kee. *Kitaev magnetism in honeycomb $RuCl_3$ with intermediate spin-orbit coupling*. Phys. Rev. B **91**, 241110 (2015).

[281] K. A. Modic, M. D. Bachmann, B. J. Ramshaw, F. Arnold, K. R. Shirer, A. Estry, J. B. Betts, N. J. Ghimire, E. D. Bauer, M. Schmidt, M. Baenitz, E. Svanidze, R. D. McDonald, A. Shekhter, and P. J. W. Moll. *Resonant torsion magnetometry in anisotropic quantum materials*. Nat. Commun. **9**, 3975 (2018).

[282] K. A. Modic, B. J. Ramshaw, J. B. Betts, N. P. Breznay, J. G. Analytis, R. D. McDonald, and A. Shekhter. *Robust spin correlations at high magnetic fields in the harmonic honeycomb iridates*. Nat. Commun. **8**, 180 (2017).

[283] K. A. Modic, T. E. Smidt, I. Kimchi, N. P. Breznay, A. Biffin, S. Choi, R. D. Johnson, R. Coldea, P. Watkins-Curry, G. T. McCandless, J. Y. Chan, F. Gandara, Z. Islam, A. Vishwanath, A. Shekhter, R. D. McDonald, and J. G. Analytis. *Realization of a three-dimensional spin–anisotropic harmonic honeycomb iridate*. Nat. Commun. **5**, 4203 (2014).

[284] T. Takayama, A. Kato, R. Dinnebier, J. Nuss, H. Kono, L. S. I. Veiga, G. Fabbris, D. Haskel, and H. Takagi. *Hyperhoneycomb Iridate β-Li_2IrO_3 as a Platform for Kitaev Magnetism*. Phys. Rev. Lett. **114**, 077202 (2015).

[285] M. Majumder, M. Schmidt, H. Rosner, A. A. Tsirlin, H. Yasuoka, and M. Baenitz. *Anisotropic Ru^{3+} $4d^5$ magnetism in the $\alpha RuCl_3$ honeycomb system: Susceptibility, specific heat, and zero-field NMR*. Phys. Rev. B **91**, 180401 (2015).

[286] Y. Sizyuk, P. Wölfle, and N. B. Perkins. *Selection of direction of the ordered moments in Na_2IrO_3 and α-$RuCl_3$*. Phys. Rev. B **94**, 085109 (2016).

[287] M. Mourigal, M. E. Zhitomirsky, and A. L. Chernyshev. *Field-induced decay dynamics in square-lattice antiferromagnets*. Phys. Rev. B **82**, 144402 (2010).

[288] J. D. Thompson, P. A. McClarty, D. Prabhakaran, I. Cabrera, T. Guidi, and R. Coldea. *Quasiparticle Breakdown and Spin Hamiltonian of the Frustrated Quantum Pyrochlore $Yb_2Ti_2O_7$ in a Magnetic Field*. Phys. Rev. Lett. **119**, 057203 (2017).

[289] W. Setyawan and S. Curtarolo. *High-throughput electronic band structure calculations: Challenges and tools*. Comput. Mater. Sci. **49**, 299–312 (2010).